BIOMECHANICAL & BIOCHEMICAL CONTRIBUTIONS OF MATRIX METALLOPROTEINASES IN JOINT PAIN: MODELS, MECHANISMS, & PATIENTS

Meagan E. Ita

A DISSERTATION

in

Bioengineering

Presented to the Faculties of the University of Pennsylvania

in

Partial Fulfillment of the Requirements for the

Degree of Doctor of Philosophy

2021

Supervisor of Dissertation

_____

Beth A. Winkelstein,
Professor of Bioengineering

Graduate Group Chairperson

_____

Yale E. Cohen,
Professor of Bioengineering, Otorhinolaryngology

Dissertation Committee:

D. Kacy Cullen, Associate Professor of Neurosurgery
Eric J. Granquist, Assistant Professor of Oral & Maxillofacial Surgery/Pharmacology
Paul A. Janmey, Professor of Bioengineering, Physiology
David F. Meaney, Professor of Bioengineering

ACKNOWLEDGMENTS

First and foremost, I am incredibly grateful for my adviser, Beth Winkelstein, for her guidance and mentorship over the years. In thanks to her mentorship, I have experienced immense personal and professional growth throughout this experience. Thank you for supporting me in this opportunity and helping me to strengthen my critical thinking and to deepen my scientific thought process. I am confident that the skills and experience I have gained over the years with you as a role model will help me be successful in the years to come. I am truly appreciative that you have always made time for me, even during the hardest days of the pandemic.

Many thanks to the members of my committee, Dr. David Meaney, Dr. D. Kacy Cullen, Dr. Eric Granquist, and Dr. Paul Janmey. Your input has strengthened the work in this thesis and my training has been enhanced by your scientific expertise. Special thanks to Dr. Granquist, who made possible the clinical studies in this thesis, enhancing the clinical relevance of this body of work. I would also like to specially thank Dr. Meaney and Dr. Alexandra Modupe Adegoke, who helped me with the viral calcium imaging techniques. I am very grateful for the time Alex spent training me so that I could introduce these techniques to our lab. I am also grateful to Dr. Cullen and Kevin Browne who taught me how to harvest large animal specimens and provided precious samples that aided in early studies as this thesis was developing.

I am grateful for the rich resources and expertise of the Cell & Developmental Biology Microscopy Core and owe many thanks to Jasmine Zhao and Andrea Stout who

often helped me with confocal imaging studies on very short notice. Many of the assays in this thesis would not have been possible without your assistance.

I have been fortunate to have many “unofficial” mentors and advocates throughout this experience, including Dr. LeAnn Dourte and Dr. Victor Barocas. You have both been instrumental in my professional development and I am very grateful for my conversations with you both. LeAnn, thank you for the opportunity to teach with you for many years, you are an excellent role model as an educator, and I look forward to continuing our professional connection in the future. Thank you also to Renee Kelly, Sarah Gormley, and Sevile Mannickarottu for being a constant source of optimism and support. I regret that the pandemic kept me from enjoying your presence in my final months!

An enormous amount of thanks to all past and present members of the SPRL. To Jenell Volkov, Martha Zeeman, Sijia Zhang, and to Brianne Connizzo as my first graduate student mentor in this program, I learned many skills in the lab early on with your guidance, and you all continue to be role models and dear friends to me today. My gratitude goes to Sagar Singh, Prabesh Ghimire, Christine Weisshaar, Nick Stiansen, Harrison Troche, Rachel Welch, Gabrielle Leavitt, Patrisia DeAnda, and Olivia Leavitt, who all directly contributed to studies in this thesis. It was a privilege to work with you. To Megan Sperry, Julia Quindlen-Hotek, and Sonia Kartha, my daily life in the lab was made richer by your intelligence and friendship. I am so grateful to have shared many years with you through this PhD and made life-long friendships.

I owe debts of gratitude to my many generous friends, of which there are too many individuals to name. My Philly Surge Running family has truly become my Philadelphia family and I am so lucky to have you all in my life. Dorcas BF Huang, I do not deserve your unprecedented friendship! Lauren Beck, Sonia Kartha, Ravi Yelleswarapu, and Jessica Liu, I admire all of you and am so grateful to call you friends. To Mike Magaraci, Thomas Gilgenast, and Heling Zhao, I am so grateful to have landed in a home with you all and Lux, who is 200x smarter than any cat and has been a unifier and constant throughout the years, especially during these last few months. To Nishal Shah, I appreciate everything you do for me and your constant support and optimism. All of you make me a stronger, better, and happier person.

Finally, thank you to my incredibly loving and supportive family. Not a day goes by that I do think about you all. To Rebecca, Daniel, and my parents, I cannot articulate how important you are all to me and how much your support has helped me achieve this degree. Thank you for the constant perspective about what is important and the value of family. I love you all very much.

ABSTRACT

BIOMECHANICAL & BIOCHEMICAL CONTRIBUTIONS OF MATRIX METALLOPROTEINASES IN JOINT PAIN: MODELS, MECHANISMS, & PATIENTS

Meagan E. Ita

Beth A. Winkelstein

Chronic joint pain is a major healthcare challenge with a staggering socioeconomic burden. Pain from synovial joints is mediated by the innervated joint tissues. Due to its innervation, the collagenous capsular ligament that surrounds the joint encodes nociceptive signals and transmits them for pain perception. Although increases in the matrix metalloproteinases (MMPs) occur in painful synovial joints either from injury or degenerative disorders, whether and how MMPs may be mechanistically involved in joint pain is unknown. Since the interstitial collagenase MMP-1 has many roles in collagen degradation and signal transduction pathways, it may play a role in nociception from the joint capsular ligament, but this has not been evaluated. The studies in this thesis define the biomechanical and biochemical roles of MMP-1 in afferent signaling using complementary approaches in human, rat, and cell culture models to define fibroblast-neuron and collagen-neuron interactions in nociception, with and without tissue loading. MMPs in the innervated capsular tissue from patients with painful temporomandibular joint disorders are characterized and establish a role for both MMP-1,

and the gelatinase MMP-9, as positive correlates with pain symptoms. Studies in the rat show that excess intra-articular MMP-1 is sufficient to induce behavioral sensitivity which is paralleled by neuronal dysregulation in both the peripheral and central nervous systems. Moreover, nociception may be initiated by the microscale catabolism of collagen molecules in the capsular ligament and its subsequent effects on the multiscale biomechanical function of ligament tissues in the presence of MMP-1. To better understand those MMP-1-induced pain mechanisms, a novel co-culture model was designed to mimic the multicellular microenvironment of the capsular ligament incorporating both fibroblasts and peripheral neurons. Biomechanical loading and biochemical degradation each increase both MMP-1 expression and that of the nociceptive neurotransmitter substance P, suggesting possible mechanisms leading to increased MMP-1 in painful joints. Furthermore, since studies reveal that fibroblasts mediate the extent of load-induced MMP-1, fibroblast functionality have a substantive role in contributing to and/or mediating effects of MMP-1 on peripheral neurons. Collectively, studies in this thesis provide a foundational schema for MMP-1 as a biomechanical and biochemical regulator in painful joint disorders.

TABLE OF CONTENTS

Page

LIST OF TABLES

Page

LIST OF FIGURES

Page

Chapter 1

Introduction & Background

Portions of this chapter have been adapted from:

Ita ME, Winkelstein BA. Pain signaling systems from injured cervical facet joints. In: **Whiplash Injury: A Model for Development of Chronic Pain**. Jensen TS, Turk D, Kasch H, Eds., pg 15-33, 2016.

Ita ME, Zhang S, Holsgrove TP, Kartha S, Winkelstein BA. The physiological basis of cervical facet-mediated persistent pain: basic science and clinical challenges. *Journal of Orthopaedic & Sports Physical Therapy,* 47(7): 450-61, 2017.

Sperry MM, Ita ME, Kartha S, Zhang S, Yu YH, Winkelstein BA. The interface of mechanics and nociception in joint pathophysiology: insights from the facet and temporomandibular joints. *Journal of Biomechanical Engineering*, 139(2): 021003, 2017.

1.1. Introduction

Chronic joint pain is a costly and widespread problem, affecting a large proportion of the population at some point over the course of their lifetime, and, unfortunately, effective treatments are largely lacking (Hogg-Johnson et al. 2008; IBM Corporation 2019; Institute of Medicine 2011; National Academies of Sciences, Engineering, and Medicine 2020). Pain from synovial joints can result from an inciting injury event to peripheral tissues or from damage that accumulates over time, compromising the biomechanical properties of the joint's tissues and lowering the threshold for pain signaling from innervated joint tissues (Elliott et al. 2009; Gellhorn et al. 2013; Ita et al. 2017b; Loeser et

al. 2012; Sperry et al. 2017). In either case, loading of the joint's ligamentous capsule, in particular, can initiate pathophysiological cascades that lead to pain by activating the innervating nociceptive fibers embedded in the ligamentous matrix (Kallakuri et al. 2008; Lee et al. 2004; Lee et al. 2008; Lu et al. 2005).

This chapter provides a brief summary of relevant background information about the anatomy and innervation of synovial joints (Section 1.2.1) and an overview of mechanisms of nociception from the periphery to the central nervous system (Section 1.2.2). The anatomical review focuses on the facet joints of the spine due to their high susceptibility to injury and propensity to encode pain signals from the periphery (Elliott et al. 2009; Jaumard et al. 2011; Manchikanti et al. 2004). Section 1.2.3 then provides an overview specifically focused on pain associated with osteoarthritis (OA), and, in particular, OA in the facet joints of the spine and the temporomandibular joint (TMJ) in the jaw. The in vivo and in vitro studies in this thesis focus on, and are designed based on, the spinal facet joints. Yet, the studies in Chapter 3 use the temporomandibular joint (TMJ); a detailed anatomical description of the TMJ is found in Section 3.1. The biology and functional characteristic of matrix metalloproteinases (MMPs) are discussed with a focus on MMP-1 and MMP-9 (Section 1.2.4). Finally, techniques and assays used throughout this thesis are presented and reviewed as relevant to particular studies in later chapters (Section 1.2.5).

1.2. Background

1.2.1. Anatomy & Innervation of Synovial Joints

The cervical facet joints are bilateral joints in the posterolateral region of the spine, and are responsible for coupling rotations and bending in the neck, as well as transmitting axial load (Figure 1.1) (Jaumard et al. 2011). The articulating joint is innervated by the medial branches of the primary dorsal rami of the superior and inferior cervical levels of each joint (Bogduk and Marsland 1988). Pain signals are transmitted by nociceptive afferent fibers that innervate facet tissues, including the bone, joint capsule, and synovium (Kallakuri et al. 2012; Loeser et al. 2012). The afferent fibers that innervate the facet have their cell bodies in the dorsal root ganglia (DRG) and synapse with spinal dorsal horn neurons to transmit sensory information from the periphery (Figure 1.1) (Basbaum et al. 2009; Kallakuri et al. 2012; Loeser et al. 2012). Afferent nerve fibers include

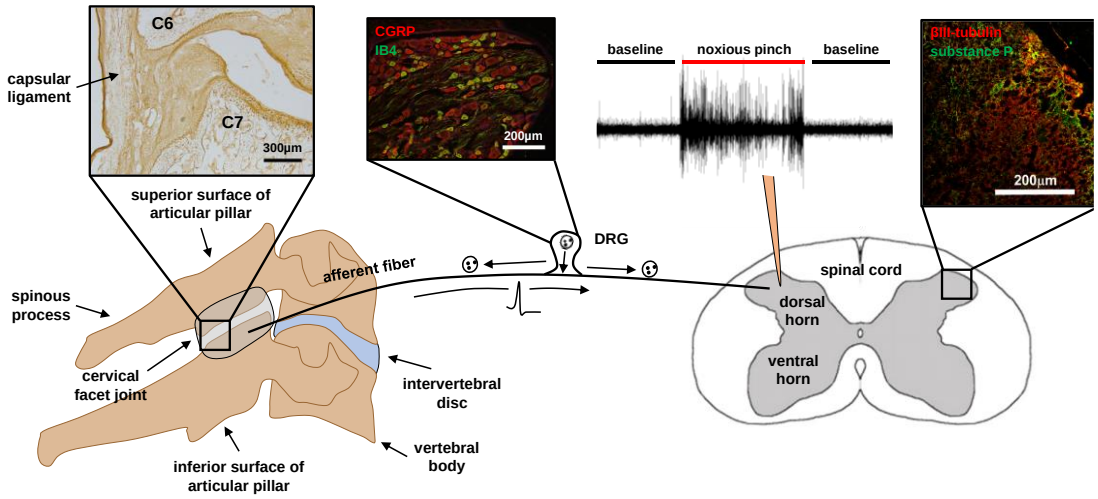

Figure 1.1. Schematic illustrating the anatomy in the periphery of the facet joint and the relevant neuronal connections to the central nervous system. Afferents that innervate the facet joint and its capsular ligament have cell bodies in the dorsal root ganglia (DRG) and synapse with neurons in the spinal dorsal horn. Nociceptive information is encoded by many types of afferent nerve fibers, including isolectin B4 (IB4)-positive non-peptidergic neurons and peptidergic fibers that produce neuropeptides, such as calcitonin gene-related peptide (CGRP) and substance P. Noxious stimuli are translated into electrical (e.g. action potentials) and biochemical (e.g. neurotransmitter) signals. In persistent pain, central sensitization occurs, with neuronal hyperexcitability and altered neurotransmitter production and release in the spinal dorsal horn. Figure adapted from Ita, et al. *J Orthop Sports Phys Ther*, 2017.

mechanoreceptive and nociceptive C- and Aδ- fibers (Chen et al. 2006; Crosby and Smith 2015; Jaumard et al. 2011; Kallakuri et al. 2004).

The joint capsule is made up primarily of collagen, with Type I collagen making up 80-99% of the total collagen (Burgeson and Nimni 1992) at a concentration of 30-40mg/mL (Miller and Rhodes 1982). The collagen network of the facet capsular ligament contains subregions of fibers with parallel and irregular orientations (Ban et al. 2017; Kallakuri et al. 2012; Yahia and Garzon 1993; Yamashita et al. 1996). Along with nerve fibers, fibroblast-like synoviocytes (FLS), also known as synovial fibroblasts or type B synoviocytes, reside in the capsule's extracellular matrix (ECM) (Bartok and Firestein 2010; Kallakuri et al. 2012; Yahia and Garzon 1993; Yamashita et al. 1996). Under normal physiologic conditions, synovial fibroblasts maintain the structural integrity of the capsule and synovium by controlling ECM composition (Bottini and Firestein 2013; Grinnell 2000). Resident fibroblasts can also be influenced by, and even alter, the collagen network (Grinnell 2000; Grinnell 2003; Provenzano et al. 2005; Provenzano et al. 2002); activated fibroblasts convert mechanical stimuli into biological responses via regulating genes, releasing growth factors, and remodeling the ECM (Camelliti et al. 2005; Grinnell 2000; Grinnell 2003; Wang et al. 2007).

Fibroblasts are stromal cells with roles in development, repair, wound healing, and ECM remodeling (Rinn et al. 2006). Fibroblasts are ubiquitous cells, found throughout the body, that are defined by their morphology, ability to adhere, and lack of lineage-specific markers; but, they are functionally and phenotypically diverse depending on their anatomical origin (Hinz 2013; Rinn et al. 2006). FLS are a unique class of fibroblast-like

cells found in the lining and capsular ligament of synovial joints (Bottini and Firestein 2013; Yamashita et al. 1996). FLS play a large role in propagating inflammation in joint tissues and secreting enzymes that remodel their surrounding ECM (Bartok and Firestein 2010; Bottini and Firestein 2013; Hardy et al. 2013). The functional role of FLS in inflammation and aberrant ECM remodeling is particularly important in the pathological cascades that mediate rheumatoid arthritis, which has been extensively described in the human and in rodent models of that disease (Ahn et al. 2008; Bartok and Firestein 2010; Bottini and Firestein 2013; Hardy et al. 2013; Hu et al. 2012). Despite the prevalence of studies describing the role of FLS in joint inflammation, little is known about the interactions between FLS and matrix mechanics and microstructure, nor about their interactions with peripheral neurons in the context of nociception.

1.2.2. Nociception & Pain Transmission

According to the International Association for the Study of Pain (IASP), nociception refers to activity that occurs in the nervous system in response to a noxious stimulus (Raja et al. 2020). Nociceptors are the subpopulation of peripheral nerve fibers that process the thermal, mechanical, and/or chemical stimuli in the noxious range (Basbaum et al. 2009). The two major classes of nociceptors are medium-diameter myelinated Aδ-afferents that mediate localized acute “fast” pain and small-diameter unmyelinated C-fibers that transmit poorly localized “slow” pain (Basbaum et al. 2009). A noxious stimulus is defined as an actual or potential tissue-damaging event; when that event is transduced by nociceptors then that noxious event is considered a *nociceptive* stimulus because it has relayed the signal of tissue damage to the nervous system (Loeser and Treede

2008; Raja et al. 2020). Nociceptive signaling can lead to sensitization, which is an increased responsiveness of neurons to their normal input or recruitment of a response to normally subthreshold inputs (Basbaum et al. 2009; Braz et al. 2005; Loeser and Treede 2008).

Sensitization can occur in the periphery or in the central nervous system (CNS). Peripheral sensitization leads to altered nociceptive responses at the injury site, including decreased thresholds to initiate afferent firing and increased responsiveness of peripheral nociceptive neurons (Latremoliere and Woolf 2009; Woolf et al. 1992). Central sensitization involves the enhancement of nociceptive pathways via the recruitment of previously subthreshold nociceptors in response to neural injury, aberrant activity, or inflammation (Latremoliere and Woolf 2009). Unlike peripheral sensitization, central sensitization is decoupled from the presence and/or intensity of the inciting peripheral stimulus (Latremoliere and Woolf 2009). Thus, a state of central sensitization represents a shift from "high-threshold nociception" to "low-threshold hypersensitivity" (Latremoliere and Woolf 2009). The host of changes in the CNS that occur with central sensitization have been extensively reviewed (Bettini and Moore 2016; Ji et al. 2018; Latremoliere and Woolf 2009); a few characteristics of dorsal horn neurons that are involved in central sensitization include their increased spontaneous activity and a reduction in their threshold for peripheral stimulation (Figure 1.1). Central sensitization can also produce an increase in nociceptor responsiveness to their normal subthreshold afferent input at *secondary* sites that have no tissue damage (Figure 1.1) (Basbaum et al. 2009; Latremoliere and Woolf 2009; Loeser and Treede 2008; Syx et al. 2018).

Although nociception is the physiological basis for the experience of pain, the human experience of pain includes both sensory and emotional components (Bushnell et al. 2013; Loeser and Treede 2008). Self-reported pain is commonly assessed using pain rating scales (Hawker et al. 2011; Hjermstad et al. 2011; Williamson and Hoggart 2005). Unidimensional scales such as the Visual Analog Scale (VAS), the Verbal Rating Scale (VRS), and the Numerical Rating Scale (NRS) collect self-reported patient pain scores on numeric Likert scales ranging from 10-points to 100-points, with the lowest scores taken as "no pain" and the highest scores indicating the "worst pain imaginable" (Hawker et al. 2011; Hjermstad et al. 2011; Williamson and Hoggart 2005). Multidimensional scales like the McGill Pain Questionnaire and the Chronic Pain Grade Scale provide categorized scores on subscales assessing more specific aspects of the pain experience, such as sensory pain, affective pain, and disability associated with pain (Hawker et al. 2011; Hjermstad et al. 2011; Williamson and Hoggart 2005). The manipulation of cognitive and emotional factors can impact the perception of pain (Bushnell et al. 2013). Moreover, descending pain pathways from the brain to the spinal cord are heavily implicated in modulating both of the psychological and physiological components of the pain experience (Braz et al. 2005; Bushnell et al. 2013; Crofford 2015; Sperry et al. 2020a).

1.2.3. Osteoarthritis & Degenerative Joint Pain

Pain from degenerative joint diseases like osteoarthritis represents one of the most common painful conditions (Institute of Medicine 2011; National Academies of Sciences, Engineering, and Medicine 2020; NIDCR 2014; Perrot 2015). The spinal facet joint and the temporomandibular joint (TMJ) are the two most common sources of chronic joint pain

(Hogg-Johnson et al. 2008; Institute of Medicine 2011; NIDCR 2014). Painful degeneration can arise in the spinal facet joints after trauma (referred to as post-traumatic osteoarthritis) or with age-related degeneration (Gellhorn et al. 2013; Hawellek et al. 2017; Kuyinu et al. 2016; Park et al. 2014; Suri et al. 2013). Painful TMJ disorder is often initiated by repeated atypical loading that can lead to joint degeneration (OA) or internal derangement (ID) (Scrivani et al. 2008; Tanaka et al. 2008). Internal derangement occurs with the displacement of the articular disc and is primarily considered as a soft-tissue disorder (National Academies of Sciences, Engineering, and Medicine 2020). Long-term and advanced ID develops into OA in 15% of patients with ID, with the progression to OA defined by the breakdown of cortical bone of the TMJ condyle (National Academies of Sciences, Engineering, and Medicine 2020). Current therapies for TMJ pain, including anesthetics, surgery, and medications, provide only temporary relief (Institute of Medicine 2011).

Degeneration is caused by a complex combination of biomechanical and biological cascades that initiate nociception in innervated joint tissues (i.e. bone, synovium, and ligaments and notably not the articular cartilage), resulting in pain and a loss of physical function (Loeser et al. 2012; Malfait and Miller 2016; Varady and Grodzinsky 2016). The mechanisms by which pathologic degeneration initiates pain is unclear; however, many animal models of joint degeneration, primarily in rodents, suggest that both neuropathic and inflammatory mechanisms play a role (Malfait et al. 2013). Many of those studies in the rodent utilize intra-articular injections to define the effects of chemical irritants on the structure and health of joint tissues and on the cellular responses of host cells, which is

discussed in more detail in Section 1.2.5.1 (Adães et al. 2015; Kras et al. 2015; Malfait et al. 2013; Nascimento et al. 2013; Nwosu et al. 2016). Additionally, there is evidence of both peripheral and central sensitization from degenerative pain (Havelin et al. 2015; Perrot 2015; Syx et al. 2018), including the dysregulation of ion channels which has been demonstrated in monosodium iodoacetate-induced knee degeneration in the rat (Rahman and Dickenson 2015). Although the facet joints are susceptible to degeneration (Gellhorn et al. 2013; Kim et al. 2015) and are a known source of pain, only a handful of studies have investigated degenerative cascades using intra-articular injections in the facet joint via collagenase (Yeh et al. 2008) or complete Freund's adjuvant (CFA) (Shuang et al. 2014).

Degeneration induces tissue degradation that can compromise the mechanical integrity of joint tissues, increasing their susceptibility to mechanical injury. Enzymes like the matrix metalloproteases (MMPs) and ADAMTSs (a disintegrin and a metalloprotease with thrombospondin motifs) degrade collagen and aggrecan/proteoglycans, respectively, both of which make up the ECM of the articular cartilage and capsular ligament (Mort and Billington 2001; Pearle et al. 2005; Song et al. 2007). Selective digestion of constitutive components of the ECM, such as collagen, elastin, or proteoglycans, has been shown to alter the mechanical properties and biomechanical responses in native tissue and in vitro systems (Barbir et al. 2010; Grant et al. 2015; Grenier et al. 2014; Griffin et al. 2014; Henninger et al. 2013; Rojas et al. 2014; Smith et al. 2008; Sperry et al. 2017). Collectively, these studies suggest that joint tissues may have a lower threshold for mechanical injury during degenerative states.

Although abnormal capsular ligament kinematics can initiate pain signaling (Crosby et al. 2015; Lee et al. 2006; Quinn et al. 2007), and degeneration alters tissue mechanics (Grenier et al. 2014; Henninger et al. 2013; Lee et al. 2001; Sperry et al. 2017; Varady and Grodzinsky 2016), excessive mechanical injury is not required for degeneration-induced pain. Indeed, macroscopic tears and joint space narrowing are evident in ligaments following clinical diagnosis of "degeneration" in the absence of any direct trauma (Hill et al., 2005). Moreover, pain that accompanies degeneration is not always correlated with the extent of joint degradation in patients (Finan et al. 2013; Hunter et al. 2013; Malfait and Schnitzer 2013; National Academies of Sciences, Engineering, and Medicine 2020; Perrot 2015). That lack of correlation has led to recent work investigating whether or not the many other molecular pathways that are also altered in degeneration directly contribute to pain generation. Such pathophysiological pathways include, for example, the many inflammatory cytokines and chemokines that are detected in the synovial fluid of osteoarthritis patients (Miller et al. 2014). It is likely that a combination of abnormal kinematics and pathologic biochemical cascades contributes to nociception that drives pain in degenerative joint disease.

1.2.4. Matrix Metalloproteinases

The matrix metalloproteinases (MMPs), of which 24 have been identified in human tissues (Sbardella et al. 2012; Visse and Nagase 2003), are proteinases that degrade components of the ECM and have roles in many physiological and pathological processes (Huntley 2012; Kawasaki et al. 2008; Rosenberg 2002; Visse and Nagase 2003), including joint and/or nervous system diseases (Huntley 2012; Kawasaki et al. 2008; Lo et al. 2003;

Loeser et al. 2012; Rosenberg 2002; Sbardella et al. 2012; Visse and Nagase 2003). MMPs are categorized on the basis of their substrate specificity, sequence similarity, and domain organization (Visse and Nagase 2003). In vertebrates, MMPs are divided into six groups: collagenases, gelatinases, stromelysins, matrilysins, membrane-type MMPs, and other MMPs (Visse and Nagase 2003). This section focuses on the collagenases and gelatinases since those two MMP subgroups are investigated in the studies of this thesis; the functions and characteristics of all MMPs are extensively reviewed elsewhere (Murphy and Nagase 2009; Sbardella et al. 2012; Visse and Nagase 2003).

The human collagenases, MMP-1, MMP-8, and MMP-13 have identical ECM substrates to one another and preferentially degrade the triple helical collagen that composes most of the capsule's ECM network (Burgeson and Nimni 1992; Fields 2013; Konttinen et al. 1999; Visse and Nagase 2003). The gelatinases, MMP-2 and MMP-9 preferentially degrade denatured collagen (i.e. gelatin) (Visse and Nagase 2003). Although collagenases and gelatinases have high affinities to triple helical collagen and gelatin, respectively, each subgroup of MMPs has many other ECM and non-ECM substrates (Murphy and Nagase 2009; Sbardella et al. 2012; Visse and Nagase 2003).

The exact substrates that an MMP can interact with at a given moment depend on whether the MMP is in its latent zymogen form or in its catabolically active state. MMPs are secreted as catabolically inactive zymogens ("pro-forms") that are extracellularly activated through disruption of their cysteine-zinc interaction by proteases like plasmin or other MMPs (Sbardella et al. 2012; Visse and Nagase 2003). In most cases, MMPs can only cleave ECM substrates *after* they are activated and cannot participate in matrix

remodeling in their pro-forms. However, in both the active and pro- forms, many MMPs can interact with cell-surface receptors and/or cell-signaling molecules (Murphy and Nagase 2009; Sbardella et al. 2012; Visse and Nagase 2003). MMP activity is tightly regulated at the level of transcription, extracellular pro-MMP activation, and by the endogenous tissue inhibitors of metalloproteinases (TIMPs) (Löffek et al. 2011; Visse and Nagase 2003). When those MMP regulatory mechanisms are disrupted, the role of MMPs transitions from normal to pathological (Agrawal et al. 2008; Löffek et al. 2011; Rosenberg 2002; Sbardella et al. 2012; Yong et al. 2001).

MMP levels are altered in the joint capsule and synovial fluid of painful joint conditions (Cohen et al. 2007; Haller et al. 2015; Kim et al. 2015; Konttinen et al. 1999; Lattermann et al. 2017; Tchetverikov et al. 2005), but have not been investigated for their mechanistic relationship with nociceptive pathways. The human interstitial collagenases, MMP-1, -8, and -13, and the transmembrane protein MMP-14 (Visse and Nagase 2003), have all been detected in joints; MMP-1, in particular, increases in the joint capsule after elbow trauma (Cohen et al. 2007) and with facet degeneration (Kim et al. 2015). Its concentration has also been shown to increase in synovial fluid after knee trauma (Chockalingam et al. 2013; Haller et al. 2015; Konttinen et al. 1999; Tchetverikov et al. 2005). MMP-1 may also mediate nociception via its role in catalyzing Type I collagen remodeling on a microscale. The local biomechanical environment of neurons in a collagen network mediates their signaling (Zarei et al. 2017; Zhang et al. 2016; Zhang et al. 2017a; Zhang et al. 2018), and degradation of a collagen network alters its network reorganization under load (Sperry et al. 2017). Because a degraded matrix reorganizes differently under

load than a non-degraded matrix (Sperry et al. 2017), it follows that collagen degradation driven by MMP-1 *may* alter the capsule's collagen network, which activates resident afferents or lowers their threshold for activation by stretch. However, if and how MMP-1-driven degradation alters the relationship between the collagen structure and composition with cell activation is not known.

MMP-1 may also sensitize neurons through ECM-independent mechanisms in addition to its ability to degrade collagen. Both catabolically active and inactive forms of MMP-1 can serve as neuronal signaling proteins via receptors involved in nociception (Allen et al. 2016; Boire et al. 2005; Conant et al. 2002; Conant et al. 2004; Dumin et al. 2001). Both forms also have substrates to pain-related molecules (Basbaum et al. 2009; Kawasaki et al. 2008; Visse and Nagase 2003; Zhou et al. 2014). For example, MMP-1 binds to several receptors implicated in nociception, including β1-integrin and protease activated receptor-1 (PAR-1), even when catabolically inactive (Allen et al. 2016; Boire et al. 2005; Conant et al. 2002; Conant et al. 2004; Dumin et al. 2001). The non-ECM substrates of MMP-1 include pro-inflammatory cytokines (i.e. interleukin-1β (IL-1β) and tumor necrosis factor α (TNFα)) and substance P, and it is expressed in neurons and glial cells, which are involved in pain (Basbaum et al. 2009; Kallakuri et al. 2004; Lee et al. 2008; Miller et al. 2014; Visse and Nagase 2003; Zhou et al. 2014). MMP-9 is downstream of MMP-1 (Conant et al. 2002; Visse and Nagase 2003), sensitizes peripheral neurons (Ji et al. 2008), is necessary for early-phase neuropathic pain (Kawasaki et al. 2008), and has roles in blood brain barrier breakdown and neurodegeneration (Rosenberg 2002; Sbardella et al. 2012). MMP-1 and MMP-9 have been identified *together* in joints after trauma

(Haller et al. 2015; Konttinen et al. 1999; Lattermann et al. 2017), further supporting that *both* may play a role in altered joint states that cause pain.

In addition to the human collagenases, bacterial collagenase from the bacterium *Clostridium histolyticum* can cleave Type I triple helical collagen, but by a more aggressive cleavage mechanism that the human collagenases (Fields 2013). Although collagenases derived from bacteria are devoid of the many other pathophysiological roles of native MMPs (Sbardella et al. 2012; Visse and Nagase 2003), their collagenolytic activity can be harnessed to answer question about collagen catabolism in isolation.

1.2.5. Relevant Models & Techniques

1.2.5.1. Intra-Articular Injection in Animal Models & Quantification of Behavioral Sensitivity

Experimental animal models using the intra-articular injection of various agents into the joint space have defined the downstream effects of irritants on behavioral and physiological outcomes. For example, intra-articular injection of the inflammatory irritant CFA is commonly used to produce joint pain and inflammation. Intra-articular CFA produces peripheral behavioral sensitivity and joint degeneration, as well as increases in the expression of synaptophysin, a protein involved in synaptic transmission, in the dorsal horn of the spinal cord (Malfait et al. 2013; Nascimento et al. 2013; Zhang et al. 2012). Intra-articular injection of nerve growth factor (NGF), a known inflammatory mediator that also contributes to inflammation in the facet joint after mechanical injury (Kras et al. 2015), transiently induces evoked neuronal firing of spinal neurons at one day after its injection

in parallel with evidence of behavioral sensitivity (Kras et al. 2015), suggesting that acute inflammatory pain can play a role in rodent models of facet joint pain.

Specific investigation of pain resulting from joint cartilage degeneration often utilizes intra-articular injections of monosodium iodoacetate (MIA), a disruptor of chondrocyte glycolysis, both in the spinal facet joint and TMJ (Gong et al. 2011; Kim et al. 2011; Wang et al. 2016). Those studies report that MIA induces severe cartilage damage defined by proteoglycan loss and surface fissures in subchondral bone that progress in severity out to seven weeks after MIA injection (Gong et al. 2011; Kim et al. 2011; Wang et al. 2016). Intra-articular MIA in the facet joint induces biphasic mechanical hyperalgesia, with injected rats exhibiting behavioral sensitivity at days 1 and 3 after injection, and then not again until day 21 (Gong et al. 2011). That biphasic pain response induced by intra-articular MIA is paralleled by early increases in the cytokines IL-1β and TNFα (Gong et al. 2011), suggesting that inflammation may drive the initiation of pain in early stages of joint degeneration. Moreover, the dysregulation of MMPs and chemokines in joint tissues may contribute to later stage pain after an inflammatory stimulus, since the chemokine stromal cell-derived factor-1 (SDF-1), its receptor CXC chemokine receptor 4 (CXCR4), MMP-3, and MMP-9 increase in chondrocytes four weeks after MIA injection into the TMJ (Wang et al. 2016). Although those studies define the effects of a severe inflammatory agent on pain, joint degeneration, and chondrocyte physiology (Gong et al. 2011; Kim et al. 2011; Wang et al. 2016), they do not assess changes in peripheral nerves or in spinal tissues.

Several animal studies of intra-articular collagenase have demonstrated that a crude formulation of bacterial collagenase induces severe joint degeneration marked by chondrocyte disorganization, cartilage thinning and fibrillation, bone defects, and joint space narrowing (Adães et al. 2014; Gou et al. 2019; Yeh et al. 2008). Notably, intra-articular injection of CFA, MIA, and crude bacterial collagenase all produce evident structural degeneration (Adães et al. 2014; Gong et al. 2011; Gou et al. 2019; Kim et al. 2011; Malfait and Schnitzer 2013; Nascimento et al. 2013; Wang et al. 2016; Yeh et al. 2008; Zhang et al. 2012). As such, they correspond to the clinical scenario in which joint damage is severe and radiographically detectable (Gellhorn et al. 2013; Suri et al. 2013). Yet, those studies do not fully explain the clinical cases in which patients do not present with imaging evidence of joint destruction (van der Donk et al. 1991; Kjaer et al. 2005).

Sensitization can occur within a nociceptive neuron's receptive field in the periphery or to neurons in the CNS (Loeser and Treede 2008; Raja et al. 2020); that sensitization can manifest symptomatically as hyperalgesia and/or allodynia (Loeser and Treede 2008; Raja et al. 2020). Allodynia is that pain elicited by a normally non-noxious (non-painful) stimulus and hyperalgesia is a heighted response to a noxious (painful) stimulus (Loeser and Treede 2008; Raja et al. 2020). These signs are quantifiable and have been used in both clinical studies (Curatolo et al. 2015; Elliott et al. 2009; Lluch et al. 2014; Sterling et al. 2008; Sterling 2010) and animal models (Crosby et al. 2015; Lee et al. 2004; Sperry et al. 2020b; Winkelstein 2011) of pain, using dermatomal mapping between species (Takahashi and Nakajima 1996). Behavioral sensitivity is assessed by measuring a subject's reflex threshold in response to a mechanical stimulus (Loeser and Treede 2008).

In the rat, mechanical hyperalgesia is commonly quantified using von Frey filaments that apply a calibrated force to the skin local to the source of pain or in nearby regions (Figure 1.2A) (Loeser and Treede 2008). Since the same cervical spinal nerves innervate the capsular ligaments of the facet joints and distribute innervations to the forepaw of the rat

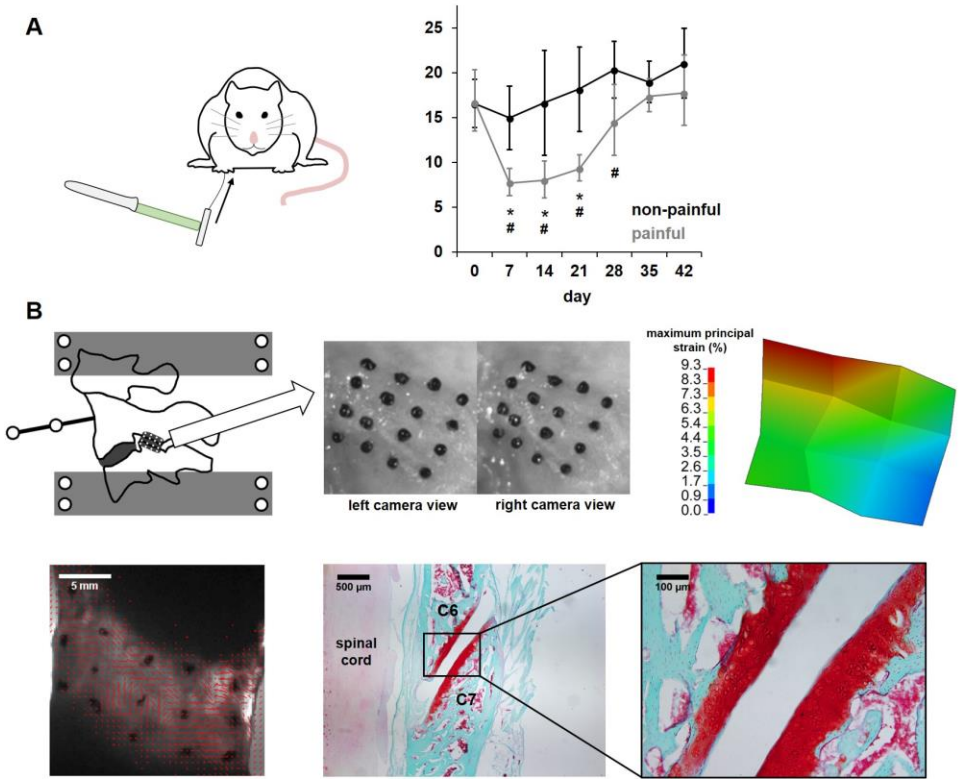

Figure 1.2. (A) Mechanically evoked pain is detectable using behavioral assays in rodent models of facet-mediated pain. The withdrawal threshold of the forepaw is significantly reduced (*p<0.002) in response to stimulation with von Frey filaments after a supraphysiologic facet capsule stretch (painful; grey) compared to physiologic non-painful facet capsule stretch (black) (#p<0.008), with a lower threshold indicating increased mechanical hyperalgesia. **(B)** Biomechanical measurements and imaging measures of collagen fiber microstructural realignment of the cervical facet joint. Schematic of a C1-C3 human cervical spine specimen in a mechanical testing system with vertebral markers projecting anteriorly and a grid of markers attached to the C2/C3 facet joint for kinematic analysis of the capsular surface strains during loading. The grid on the capsular surface is tracked by cameras which are used to estimate capsule deformation during vertebral loading. A fiber alignment map (shown in red lines), generated by polarized light imaging, shows collagen fiber alignment and its reorganization during facet loading, which alters the local biomechanical environment of any resident afferents in the ligament's collagen matrix. Safranin O staining of the rat C6/C7 facet six weeks after facet joint distraction simulating physiological loading shows the proteoglycan content of the facet joint cartilage (red); the close-up (inset) shows that facet cartilage does not exhibit signs of joint degeneration after non-painful facet capsule loading. Figure adapted from Ita, et al. *J Orthop Sports Phys Ther*, 2017.

(Lee et al. 2008; Takahashi and Nakajima 1996; Winkelstein 2011), mechanical hyperalgesia evoked in the forepaw can indicate a noxious stimulus from the facet joints (Figure 1.2A). Importantly, mechanically evoked behavioral sensitivity does not fully capture the affective components of pain in the human, such as spontaneous pain (Bushnell et al. 2013; Loeser and Treede 2008).

1.2.5.2. Mechanical Testing & Imaging of Collagen Networks

Mechanical testing of human cadaveric and rodent facet capsular ligaments has defined the biomechanical responses of the capsular ligament under load (Panjabi et al. 1998; Pearson et al. 2004; Quinn and Winkelstein 2007; Quinn and Winkelstein 2008; Quinn and Winkelstein 2011; Winkelstein et al. 2000). Full-field strain measurements made across the surface of the facet capsule during mechanical testing provide context to the biomechanical responses (Figure 1.2B). That dimensionless measure describes the deformation of a body by changes in length and line segments and the changes in the angles between them (Figure 1.2B). Strain is a helpful and common injury metric across species due to its relationship to deformation and because it is unitless. For example, strains during ligament stretch that induce pain in the rat (8-31% at 500%/s) (Dong et al. 2012) align with those measured in cadavers during simulated whiplash injury (29-40%) (Panjabi et al. 1998; Pearson et al. 2004).

Quantitative polarized light imaging (QPLI) can be integrated with mechanical testing to provide kinematic data of collagen in capsular ligaments (Figure 1.2B). Polarized light is an optical technique that exploits the natural birefringence of collagen molecules to quantify the dynamic reorganization of collagen fibers during mechanical loading, and has

been used extensively to evaluate soft tissue biomechanics and other collagenous tissue equivalents (Lake et al. 2011; Quinn and Winkelstein 2009; Sander et al. 2009; Tower et al. 2002). Briefly, in a QPLI system, light from a fiber-optic illuminator is polarized by a rotating polarizer, travels through the ligament (or other birefringent tissue), and is received by a circular analyzer mounted on a high-speed camera (Quinn and Winkelstein 2008; Tower et al. 2002).

Using that approach, reorganization of the collagen fibers in human cadaveric capsular ligaments has been found to co-localize with regions of unrecovered tissue strain after a posterior-vertebral retraction (Quinn and Winkelstein 2011) and to coincide with decreases in tissue stiffness in posterior retraction (Lee and Winkelstein 2012) and in tension (Quinn and Winkelstein 2009). The reorganization of collagen fibers also coincides with a decrease in ligament stiffness in isolated rat facet capsular ligaments during tension (Quinn et al. 2010). Moreover, that anomalous fiber reorganization in the rat occurs at strain magnitudes that also produce pain (Quinn et al. 2007; Quinn et al. 2010), suggesting that anomalous fiber realignment may explain the development of pain from facet capsular injury. Fiber alignment maps generated by harmonic analysis of the acquired QPLI images also reveal that there is a spatial variation in the cervical and lumbar facet capsule and a high degree of inter-sample heterogeneity of the collagen organization across the surface of a capsular ligament (Figure 1.2B) (Ban et al. 2017). Collectively, that work emphasizes that the effects of loading on the physiological responses in the facet capsule may vary regionally with the varied collagen microstructure. Those studies also suggest that atypical fiber reorganization during loading may be associated with local failures in the collagen

network of the ligament and be a possible mechanism involved in the development of stretch-induced pain

1.2.5.3. Tissue-Level Structural Degeneration

Histological methods are extensively used as tools to evaluate degradation in joint tissue sections in the context of joint degeneration (Schmitz et al. 2010). Hematoxylin-Eosin stains cell nuclei blue-purple and cartilage matrix pinkish with bluish aspect in areas of high proteoglycan content and is used for the overall assessment of cell and tissue morphology (Schmitz et al. 2010). Safranin O staining visualizes the articular cartilage by staining proteoglycans and glycosaminoglycans (Figure 1.2B), and is a sensitive indicator of pathological decreases in proteoglycan content due to degenerative changes in the joint (Sperry et al. 2019; Yeh et al. 2008). Histochemical staining with Picrosirius Red stains the collagen fibers in joint tissues, enabling tissue-level assessment of collagen orientation (Sander and Barocas 2009; Schmitz et al. 2010). Histology stains have been used to demonstrate that the progression of degradation in joint tissues due to intra-articular MIA, intra-articular bacterial collagenase, and instability-inducing surgery in animal models of joint degeneration (Kim et al. 2011; Malfait et al. 2013; Wang et al. 2016; Yeh et al. 2008) replicate the evidence of joint degradation that is observed in some patients with severe osteoarthritis (Kim et al. 2015). Although histological stains enable visualization of joint tissues in single tissue slices and can inform about the structural health of joint tissues, they do not enable measuring the dynamic responses of the tissues to load. As such, study designs integrating histology assays together with mechanical testing are needed to define the structure-function relationships of tissues (Grant et al. 2015; Lake and Barocas 2012;

Miller et al. 2012; O'Leary et al. 2018).

1.3. Summary

Owing to their innervation, the capsular ligaments of synovial joints are sources of pain (Barnsley et al. 1993; Basbaum et al. 2009; Bogduk and Marsland 1988; Kallakuri et al. 2012; Loeser et al. 2012). Although the mechanisms by which traumatic joint loading causes pain are beginning to emerge (Crosby et al. 2014; Crosby et al. 2015; Ita et al. 2017a; Kras et al. 2015; Lee et al. 2008; Sperry et al. 2017; Zarei et al. 2017; Zhang et al. 2016; Zhang et al. 2017b; Zhang et al. 2018), the mechanisms by which pain is initiated in degenerated joints are not as clear. Furthermore, MMP-1 has not been studied for its role in nociceptive transmission from innervated joint tissues, despite its known involvement in the degenerative processes that accompany painful joint diseases (Fields 2013; Loeser et al. 2012; Sbardella et al. 2012; Visse and Nagase 2003).

The studies in this thesis examine the role(s) of MMP-1 in nociceptive transmission from the capsular ligament by defining its role in mediating collagen-neuron and fibroblast-neuron interactions in the context of loading. Integrated approaches in patients, in a rodent model, and in cells are used to study the relevant questions most comprehensively. The first studies presented in this thesis provide clinical context for the relevance of MMPs in painful joint disease by quantifying MMPs in innervated soft tissues of degenerated TMJs from patients and probing their relationships to clinical signs and symptoms of disease progression. In order to define the effect of MMP-1 on pain, joint structure-function relationships, and neuronal dysregulation, studies in the rodent utilize intra-articular

injections of bacterial collagenase and MMP-1 integrated with techniques to quantify behavioral sensitivity. Finally, a neuron-fibroblast co-culture model is developed to recapitulate the microenvironment of the capsular ligament and it is used in studies to define the mechanistic role of MMP-1 in the context of stretch-induced nociceptive signaling. In studies in the animal and in the co-culture model of the capsular ligament, QPLI techniques are integrated with immunolabeling of proteins in order to enable answering questions about local relationships between the microstructural reorganization of collagen fibers and the dysregulation of MMPs and neuropeptides in fibroblasts and peripheral neurons.

Chapter 2

Rationale, Context, Hypothèses, & Aims

2.1. Rationale & Context

Chronic pain affects 100 million adults in the United States at an annual cost of $560-635 billion, negatively impacting the daily lives of at least 18% of Americans (IBM Corporation 2019; Institute of Medicine 2011). Joint pain from trauma and/or degeneration is a leading cause of chronic pain (Institute of Medicine 2011). Synovial joints like those of the spine, jaw, knee, hip, elbow, wrist, ankle, and hand can become painful with aging or from trauma due to repeated and/or supra-physiologic loading that can initiate tissue damage and degeneration (Mow et al. 1993; Neogi 2013). Neck and low back pain are among the most prevalent chronic syndromes (Hogg-Johnson et al. 2008; Institute of Medicine 2011), and can be due to pathology of the spinal facet joints which are susceptible to trauma (Elliott et al. 2009; Manchikanti et al. 2004; Norris and Watt 1983; Sterling et al. 2003) and degeneration (Gellhorn et al. 2013; Hawellek et al. 2017; Park et al. 2014; Suri et al. 2013) in both the cervical and lumbar regions. Disorders of the TMJ make up the second most common musculoskeletal condition resulting in pain and disability after chronic low back pain (National Academies of Sciences, Engineering, and Medicine 2020; NIDCR 2014). Current therapies for joint pain, including anesthetics, surgical

interventions, and medications, provide only temporary relief (Institute of Medicine 2011; National Academies of Sciences, Engineering, and Medicine 2020). Development of effective treatments remains hampered by an incomplete understanding of the mechanisms that initiate and maintain joint pain.

Abnormal traumatic and/or repeated loading of the innervated capsular ligament can cause aberrant changes to the ligament's collagen network and initiate signal transduction in host FLS cells (Bartok and Firestein 2010; Kallakuri et al. 2008; Lee et al. 2004; Zhang et al. 2016). Load-induced effects on the collagen microstructure and FLS physiology can lead to nociceptive signaling in afferent fibers (Yamashita et al. 1996; Zhang et al. 2016; Zhang et al. 2017). Yet, the interactions between afferents, FLS, and collagen fibers in the context of injurious loading is not well understood. MMP-1 interacts directly with collagen fibers via collagen catabolism and also interacts both directly and indirectly with host FLS cells and innervating afferents. MMP-1 may mediate nociception via Type I collagen catabolism that alters the local biomechanical environment of the ligament (Sperry et al. 2017; Visse and Nagase 2003). MMP-1 can also sensitize neurons by binding directly to neuronal receptors and/or acting as a signaling protein in nociceptive-related pathways, including regulation of MMP-9 (Allen et al. 2016; Conant et al. 2002; Visse and Nagase 2003). Furthermore, very little is known about the interactions of afferent fibers and FLS with each other and their surrounding collagen network in the context of joint pain, despite their both being present in capsular ligaments (Provenzano et al. 2005; Yamashita et al. 1996). Despite evidence for MMP-1's involvement in ECM-dependent mechanotransduction and non ECM-dependent nociception pathways including via MMP-

9, it is not clear if, or how, MMP-1 acts as a mechanical and/or biologic regulator of nociception in the capsular ligament. Therefore, the **overall goal** of this thesis is to define how the *biomechanical* and *biochemical* actions of MMP-1 contribute to nociceptive transmission from the capsular ligament.

An in vitro neuron-seeded 3D collagen gel model has been developed to replicate the sensory innervation and network microstructures of the facet capsule and used to define neuron-ECM interactions under different loads (Zhang et al. 2016; Zhang et al. 2017; Zhang et al. 2018). In that model, DRGs containing cell bodies of the sensory neurons that innervate the capsule (Basbaum et al. 2009; Kras et al. 2013) are embedded in a 3D collagen network to mimic the local anatomy of the capsular ligaments. While that system enables the investigation of afferent-collagen interactions under injurious loading, it does not fully mimic the local cellular contributions and interactions present in capsular ligaments since it does not include FLS (Bartok and Firestein 2010; Provenzano et al. 2002; Valencia et al. 2004; Yahia and Garzon 1993; Yamashita et al. 1996). Furthermore, since synovial fibroblasts interact with MMP-1 (Jenkins et al. 1999; Sorsa et al. 1992), including their effects in a model is critical to more fully understand how MMP-1 may mediate nociception in joints. In addition to the spinal facets, other synovial joints like the TMJ also contain multicellular environments with FLS cells embedded along with afferents (Kido et al. 1993); in fact, FLS cells likely play a role in the degenerative and inflammatory etiologies of chronic and painful TMJ disorders (Scrivani et al. 2008; Tanaka et al. 2008), where MMP-1 levels are also both detectable and elevated (Kanyama et al. 2000; Srinivas et al. 2001). As such, existing models have limited utility to evaluate afferent-fibroblast

interactions in the context of nociception. A major goal of this thesis was to create a more physiologic in vitro model of the capsular ligament and use it to study MMP-1's role in nociception on a cellular level in parallel with studies in the human and the animal. Together with studies in the human (Aim 1), and the rat (Aim 2), studies utilizing the co-culture collagen gel model (Aims 3 & 4) provide evidence that supports a role for MMP-1 in joint pain across scales.

The mechanisms by which traumatic joint loading causes pain are beginning to be defined (Crosby et al. 2014; Crosby et al. 2015; Ita et al. 2017; Kras et al. 2015a; Zhang et al. 2016; Zhang et al. 2017; Zhang et al. 2018), but the mechanisms by which pain is initiated and/or mediated in *degenerated joints* are not as clear. Despite trauma severity and pain being correlated (Chen et al. 2006; Crosby et al. 2015; Dong et al. 2012; Lu et al. 2005; Panjabi et al. 1998; Pearson et al. 2004; Quinn et al. 2010), mixed reports show both positive and negative associations between the severity of structural degeneration and joint pain (Hall et al. 2017; Hunter et al. 2013; Loeser et al. 2012; Suri et al. 2013; Torres et al. 2006). Furthermore, pain scores from patients are rarely correlated with degradative enzymes in the joint (Kim et al. 2011; Konttinen et al. 1999; Lattermann et al. 2017), hampering the ability to understand molecular changes in protein expression, particularly with respect to MMPs, in the context of clinically-relevant pain. Studies measuring MMP-1 and/or MMP-9 in joints with chronic pain conditions are also scarce (Lafeber and van Spil 2013), and are primarily limited to the knee (Haller et al. 2015; Konttinen et al. 1999; Lafeber and van Spil 2013; Lattermann et al. 2017; Tchetverikov et al. 2005). Aim 1 addresses these gaps by quantifying protein levels of MMPs in innervated joint tissues from

patients with chronic, painful disorders of the TMJ, commonly caused by atypical loading (Scrivani et al. 2008; Tanaka et al. 2008). Studies in that aim assess relationships between MMP levels and metrics of both structural degeneration and patient-reported pain scores that are currently limited in the literature. Findings in Aim 1 also help set up the cellular-level mechanistic studies of MMP-1 and MMP-9 in the rest of this thesis by characterizing the relationship between MMP-1 and MMP-9 in human tissue, contextualizing their physiological relevance.

Animal studies injecting intra-articular bacterial collagenase report more severe joint degeneration with higher doses and longer follow-up times after injection, hypothesizing that structural damage mediates pain (Adães et al. 2014; Gou et al. 2019; Yeh et al. 2008). Yet, the progression and extent of joint damage in those studies depends on the type of bacterial collagenase injected. Most studies use a crude bacterial collagenase that also contains high levels of secondary proteases; intra-articular crude bacterial collagenase in the knee and lumbar facet joints in rats mimics the clinical scenario in which joint damage, particularly to cartilage and bone, is severe (Adães et al. 2014; Gou et al. 2019; Yeh et al. 2008). Yet, the outcomes of those studies do not explain clinical cases in which patients do not present with imaging evidence of joint destruction (van der Donk et al. 1991; Gellhorn et al. 2013; Hunter et al. 2013; Kjaer et al. 2005; Suri et al. 2013). On the contrary, *purified* bacterial collagenase, which lacks the proteolytic enzymes capable of degrading cartilage (Fields 2013), induces more subtle changes to the ECM of joint tissues (van der Kraan et al. 1990; van Osch et al. 1994; van Osch et al. 1995); intra-articular purified bacterial collagenase increases joint laxity (van Osch et al. 1994),

suggesting that collagenase-mediated degradation of Type I collagen-rich tissues, like the capsular ligament, can destabilize the joint and potentially trigger pathological cascades in the resident cells.

Purified collagenase from bacteria partially captures the collagenolytic function of the human interstitial collagenase MMP-1, rendering collagenase a useful tool for interrogating the collagenolytic effect of MMP-1 in isolation. But, it lacks the other myriad roles of MMP-1 in healthy and pathologic physiology. For example, bacterial collagenase lacks all non-ECM substrates of MMP-1 (Fields 2013; Zhang et al. 2015) and breaks down Type I collagen via a more aggressive mechanism by catabolizing all Y-Gly bonds versus cleavage into one-quarter and three-quarter segments like MMP-1 (Fields 2013; Zhang et al. 2015). Experiments in Aim 2 define the effect of both intra-articular purified bacterial collagenase and intra-articular MMP-1, in separate studies, on joint structure-function relationships and peripheral neuron function in the context of pain in the rat (Ita and Winkelstein 2019; Kras et al. 2015a; Kras et al. 2015b).

The majority of patients diagnosed with degenerative joint pain do not report a significant injury to the painful joint (Hill et al. 2005), and often report pain with every-day, physiologic activities including walking, standing, and climbing stairs (Neogi 2013), suggesting that joint degeneration may lower the threshold for mechanically-evoked pain. It is possible that increased MMP-1 in degenerated joints (Chockalingam et al. 2013; Kim et al. 2015; Loeser et al. 2012; Tchetverikov et al. 2005) may degrade the joint's capsule and, as such, alter its response to loads. The intra-articular injection of exogenous collagenases in Aim 2, whether bacterial or MMP-1, provides insight into possible

mechanical and/or chemical mechanisms of MMP-1's role in mediating joint pain by increasing joint levels of collagenases in the absence of traumatic injury.

Studies in Aims 3 and 4 describe the development and characterization of a DRG-FLS co-culture collagen gel model and use it to begin to define the mechanism of MMP-1 involvement in loading-induced nociception. In those studies, our existing 3D neuron-collagen culture system (Zhang et al. 2017; Zhang et al. 2018) is modified to more closely mimic an innervated ligamentous joint capsule by incorporating biologically-relevant fibroblasts to better match the multicellular state of the capsular ligament. Since synovial fibroblasts have a distinct phenotype and function compared to other fibroblasts (Bartok and Firestein 2010; Hinz 2013; Vandenabeele et al. 2003), primary FLS cells were harvested from the knee joint capsular ligaments and characterized with and without DRG co-culture in the 3D collagen gel environment (Aim 3a).

Non-physiologic loading mediates neuronal nociceptive signaling (Zarei et al. 2017; Zhang et al. 2016; Zhang et al. 2017; Zhang et al. 2018) and initiates pathological ECM remodeling by fibroblasts, including MMP-1 secretion (Petersen et al. 2012), and fibroblast collagen deposition (Bartok and Firestein 2010; Camelliti et al. 2005; Hsieh et al. 2000; Kim et al. 2002; Provenzano and Vanderby 2006; Wang et al. 2007). In collagen networks, those load-induced cellular responses are triggered by reorganization of the local fiber network surrounding the embedded cells (Grinnell 2000; Sander et al. 2009; Zhang et al. 2016). Although those load-induced cellular responses are known, how collagen network degradation alters the relationship between load and cell-cell interactions is not known. Furthermore, if, and how, FLS integration alters mechanical and/or physiological

behavior in the neuron-collagen system has also not been investigated. Collectively, the studies in Aim 3 examine nociception, DRG- and FLS-localized MMP expression, network composition and microstructure, and multiscale biomechanics of the co-culture collagen gel model in response to a degradative chemical exposure (Aim 3b) and a mechanical stretch-to-gel failure in uniaxial tension (Aim 3c). Throughout this thesis, nociceptive response is measured by changes in substance P expression since that neurotransmitter is involved in transmitting nociceptive signals (Basbaum et al. 2009; Cheng and Ji 2008; Zhang et al. 2017) and facet joint pain (Kras et al. 2015b). Calcium signaling is also utilized as a proxy for action potentials and neuronal activity (Chen et al. 2013; Patel et al. 2015), since increased neuronal firing is characteristic of afferent activity in pain resulting from joint trauma (Crosby et al. 2015).

Strain magnitude directly relates to the extent of pain (Dong et al. 2012; Panjabi et al. 1998; Pearson et al. 2004), neuronal expression of substance P and activated signaling kinase phosphorylated ERK (pERK) (Zhang et al. 2016; Zhang et al. 2017), and neuronal activity (Chen et al. 2006; Crosby et al. 2015; Lu et al. 2005; Quinn et al. 2010). In neuron-collagen gels, a strain threshold of 14-40% (at 1%-7% strain/sec) increases substance P and pERK expression (Zhang et al. 2016; Zhang et al. 2017; Zhang et al. 2018). Experiments in Aim 4a expand on that prior work, as well as on stretch experiments in Aim 3c, by characterizing the expression of substance P, MMP-1, and MMP-9 in DRG and FLS cells, network microstructure, and multiscale biomechanical metrics after a sub-failure stretch. In Aim 4a, experiments test whether the strain thresholds that increase neuronal regulators like substance P and pERK (Zhang et al. 2016; Zhang et al. 2017; Zhang et al.

2018) also have nociceptive effects in the DRG-FLS co-culture model. The sub-failure stretch used in Aim 4 models the clinically-reported sub-failure joint trauma that produces sustained behavioral sensitivity in the rat (Dong et al. 2012; Ita et al. 2017; Winkelstein and Santos 2008) and is imposed using an equibiaxial mechanical test configuration to simulate the constrained anatomy of the spinal facet joint capsule (Jaumard et al. 2011; Sperry et al. 2017; Yahia and Garzon 1993; Yamashita et al. 1996). In addition to characterizing neuronal expression of substance P, that study quantifies MMP-1 and MMP-9 expression in both DRG and FLS cells after stretch. Although MMP-1 is upstream of MMP-9 and substance P in signaling cascades (Conant et al. 2004; Visse and Nagase 2003; Zhang et al. 2017), it is not known if MMP-1 regulates either or both of MMP-9 and/or substance P in traumatic ligament loading or if their interactions depend on load. To investigate this, Aims 4b and 4c integrate MMP-1 inhibition with a painful, sub-failure stretch and test whether inhibiting MMP-1 alters MMP-9 expression, substance P expression, or the collagen network in injury modalities that cause chronic joint pain. Studies inhibiting MMP-1 provide mechanistic context to the outcomes of exogenous MMP-1 in the joint (Aim 2), as well as to the MMP levels quantified in painful joint disease (Aim 1).

2.2. Overall Hypotheses & Specific Aims

The studies in this thesis combine complementary approaches in the human, rat, and cells to define the role of MMPs, and particularly MMP-1, in joint pain by integrating outcomes in both the musculoskeletal and nervous systems. The **overall hypothesis** is that

MMP-1 mediates afferent signaling by regulating fibroblast-neuron and collagen-neuron interactions in the capsular ligament of synovial joints in the context of loading by changing the biomechanical environment of the ligament and acting as a biochemical mediator of MMP-9. The central hypothesis has four sub-hypotheses that are each tested in the following associated specific aims.

Hypothesis 1. MMPs play a role in the degeneration and pain accompanying chronic joint diseases. MMP-1 and MMP-9 are detectable in innervated soft tissues from painful joints, with the signal for MMP-1 being higher than that of MMP-9. Since MMP-1 degrades collagen in joint tissues (Visse and Nagase 2003), but MMP-9 does not, MMP-1 is predicted to correlate with measures of joint damage. Since both MMP-1 and MMP-9 are linked to nociception (Allen et al. 2016; Conant et al. 2002; Kawasaki et al. 2008), both of those MMPs correlate with pain.

Aim 1. Characterize the pro- and active forms of MMP-1 and MMP-9 protein expression in the Type I collagen-rich and innervated capsular ligament and disc tissues from human TMJs with painful internal derangement and/or osteoarthritis. Relate MMP levels to each other and to clinical data, including pain scores, magnetic resonance imaging (MRI), scores of degenerative severities, and function.

> **1a.** Quantify the pro- and active forms of MMPs, separately, to compare relative amounts of catabolically active and inactive MMPs in joint tissues and test the relationships between MMP-1 and MMP-9.

1b. Test relationships between MMPs and patient-reported pain scores using a Likert scale, and also with function measured by maximal incisal opening. Quantify joint damage using MRI data and the EuroTMjoint scoring system to evaluate relationships between MMPs and damage that is evident on clinical imaging. Test differences in MMP levels by Wilkes stage as a metric of overall joint degeneration at the time of surgery.

1c. Evaluate if MMPs differ with tissue type (capsular ligament or disc) or the type of surgery (total joint replacement or discectomy).

Hypothesis 2. Exogenous intra-articular collagenase induces immediate and sustained behavioral sensitivity via its mediation of the collagen network and signaling pathways. Because collagenases have strong collagenolytic activity and break down Type I collagen (Fields 2013), intra-articular collagenase, including bacterial collagenase and human MMP-1, degrades the ligament's collagen network rendering its microstructure sparser and reorganizing it, which results in tissue-level joint degeneration and altered joint kinematics under load at later times. Intra-articular MMP-1 also increases expression of nociceptive mediators, including MMP-9, given its myriad roles in non-matrix dependent signaling pathways (Allen et al. 2016; Conant et al. 2002; Dumin et al. 2001; Visse and Nagase 2003).

Aim 2. Utilize a rodent model of intra-articular C6/C7 facet injection to evaluate the effects of intra-articular collagenases on joint structure, joint biomechanics, and peripheral

neuronal function in the context of behavioral sensitivity at later times. Utilize purified bacterial collagenase to isolate the collagenolytic functions of collagenases and MMP-1 to test the collagenolytic and non-collagenolytic functions collectively.

2a. Measure the effect of intra-articular purified bacterial collagenase on immediate and sustained behavioral sensitivity. Quantify joint tissue structure using histology stains of the cartilage and capsular ligament and the physiological health of the cartilage using a HIF-1α label to assess chondrocyte homeostasis. In the DRG, measure nociceptive neuropeptide expression using an immunolabel to substance P and stimuli-evoked signaling transduction using an immunolabel to pERK. Determine if MMP-1 is increased in the DRG in parallel with changes in behavioral sensitivity, joint health, and the expression of substance P and pERK.

2b. Measure the effect of intra-articular MMP-1 on immediate and sustained behavioral sensitivity. Quantify joint tissue structure using histology as described in **Aim 2a**. Test whether intra-articular MMP-1 changes the collagen microstructure and/or composition of the capsular ligament using polarized light imaging and biochemical assays. Investigate MMP-1-induced changes to tissue and microstructural ligament kinematics by assessing mechanical responses and ligament collagen fiber alignment maps during stretch to failure. Evaluate substance P and MMP-9 expression in the DRG to investigate nociceptive responses in the rat.

2c. Integrate findings from **Aims 2a** and **2b** to infer how the collagenolytic and the non-collagenolytic functions of exogenous intra-articular collagenases affect behavioral sensitivity, joint structure-function, nociception, and inflammation.

Hypothesis 3. Fibroblast-like synoviocytes regulate the microstructure of their surrounding collagen network during non-constrained culture and under stretch. Fibroblast-mediated collagen reorganization results in stronger biomechanical properties of the bulk matrix when stretched. Fibroblasts secrete low levels of MMPs at baseline; mechanical and chemical collagen-altering stimuli increase MMP levels. Fibroblasts regulate the cellular localization of MMPs to peripheral neurons and non-fibroblast cells in their local environment and influence neuronal expression of nociceptive neuropeptides.

Aim 3. Develop and characterize a physiologically relevant co-culture collagen gel model incorporating peripheral neurons and fibroblasts that mimics the multicellular environment and collagen network of an innervated ligamentous joint capsule. Characterize the cellular and collagen network response of that co-culture collagen gel system to biochemical and biomechanical stimuli.

3a. Characterize the phenotype and morphology of fibroblasts harvested from rat capsular ligaments using immunolabels of the structural protein vimentin and the cell-surface specific protein CD90. Compare the function of capsular ligament-derived fibroblasts to the more broadly studied 3T3 fibroblast cell line using matched fibroblast-seeded gels and stretch-to-failure experiments to define the

physiology of primary-sourced fibroblasts relative to immortalized cells. Assess the viability and health of both peripheral neurons and capsular fibroblasts during their co-culture.

3b. Expose the co-culture collagen gel system to purified bacterial collagenase and measure collagen network composition and microstructure. Measure peripheral neuronal firing using calcium signaling as a proxy for action potentials. Quantify MMP-1 expression in peripheral neurons and fibroblasts. Compare MMP-1 expression in neurons in vitro with in vivo intra-articular-induced changes in DRG-localized MMP-1 measured in studies in the rat in **Aim 2a**.

3c. Impose a tensile failure stretch to the co-culture collagen gel model and measure neuropeptide expression of substance P in peripheral neurons, and MMP-1 and MMP-9 expression in neurons and fibroblasts, immediately after gel failure. Define macroscale biomechanics and collagen network microstructural kinematics using quantitative polarized light imaging during loading. Compare the cellular physiological and multiscale biomechanical behavior of the co-culture collagen gels to collagen gels containing only peripheral neurons to test if fibroblasts regulate how neurons and collagen fibers respond to stretch.

Hypothesis 4. Sub-failure stretch of neuron-fibroblast co-culture gels above the magnitude that increases substance P expression in peripheral neurons also regulates MMP-1 and MMP-9 expression in both peripheral neurons and fibroblasts. MMP-1 mediates stretch-induced nociceptive responses via its regulation of MMP-9. Under load, MMP-1 regulates

the reorganization of collagen fibers on a microscale but does not regulate macroscopic biomechanical properties of its environment. Inhibiting MMP-1 decreases stretch-induced MMP-9 and substance P expression in peripheral neurons and alters the microstructural reorganization of collagen fibers during a sub-failure mechanical exposure.

Aim 4. Using the in vitro model from **Aim 3**, evaluate if, and how, MMP-1 and MMP-9 mediate relationships between neurons and fibroblasts, and their surrounding collagen network, in response to a stretch that mimics the sub-failure, painful injuries that occur in vivo. Integrate quantitative polarized light imaging techniques to test if MMP-1 inhibition alters network kinematics during painful loading. Assay protein expression 24 hours after stretch since MMP transcriptional and translation regulation occurs after many hours.

4a. Measure neuronal substance P expression, and neuronal and fibroblast-localized MMP-1 and MMP-9 expression, network microstructure, and macroscale biomechanics of co-culture collagen gels in response to a biaxial stretch that induces strains greater than those that induce pain in vivo.

4b. Optimize an MMP-1 inhibition protocol based on dose magnitude and frequency that decreases MMP-1 expression across cell types. Compare MMP-1 levels between regimens that use different magnitudes of the inhibitor ilomastat either given: daily, only during every media change, only prior to stimuli known to increase MMP-1, or only immediately after stimuli. Test the effectiveness of MMP-1 inhibition on blocking MMP-1 expression using a biochemical exposure to

bacterial collagenase comparable to that used in **Aim 3b** and a sub-failure stretch used in **Aim 4a** as stimuli known to increase MMP-1.

4c. Perform the same experiments as in **Aim 4a** with the MMP-1 inhibition protocol optimized from **Aim 4b** to determine if, and how, MMP-1 inhibition alters neuronal expression of substance P and MMP-9 expression in peripheral neurons and fibroblasts, after a painful, sub-failure, biaxial stretch. Define relationships between expression of MMP-1, MMP-9, and substance P with changes in microstructural reorganization.

2.3. Overview of Thesis Organization

The aims of this thesis are organized into chapters corresponding to the individual studies. The studies from Aim 1 are presented first in Chapter 3 because they evaluate the role of MMPs in painful joint diseases in a human population, which provides a clinical context for questions investigated in the rest of the thesis. Chapter 4 summarizes studies from Aim 2a that investigate the effects of intra-articular bacterial collagenase on pain as well as joint and neural outcomes. Although that study demonstrates that a collagenase with the collagenolytic-function of human MMP-1 is sufficient to induce pain, many questions remained unanswered about the underlying mechanism of how a collagen-degrading stimulus mediates nociception. Chapter 5 details the development of a novel neuron-fibroblast co-culture collagen gel model (Aim 3a), and characterizes that model's response to exposure to the same bacterial collagenase (Aim 3b) used by the intra-articular

in vivo studies in Chapter 4 to better understand how a collagen-degrading agent in the joint mediates nociception. Chapter 6 summarizes experiments characterizing the cellular and network responses of the co-culture model to tensile failure (Aim 3c), elaborating on how integrating fibroblasts into the neuron-collagen gel model influences neuronal responses and collagen kinematics in the context of loading. The stretch experiments in the co-culture model of the capsular ligament presented in Chapter 6 demonstrate a novel role for MMP-1 in nociception and motivate asking whether and how intra-articular MMP-1 *alone* is sufficient to induce pain. As such, Chapter 7 presents the studies from Aim 2b that utilize intra-articular MMP-1 in the rat and demonstrate that MMP-1 is sufficient to induce pain-like behaviors, further supporting that MMP-1 is directly involved in the nociceptive signaling presented in the in vitro work in Chapter 6. Lastly, Chapter 8 details experiments that test the effect of inhibiting MMP-1 on nociceptive signaling due to a sub-failure, painful stretch in the co-culture model. Those studies first test whether a painful stretch defined using the neuron-only collagen gel model is enough to initiate nociceptive responses in the modified co-culture model (Aim 4a), and then assess cellular and collagen network responses during painful stretch with MMP-1 inhibition (Aims 4b & 4c). Lastly, Chapter 9 integrates the main findings of the overall thesis in the broader context of painful joint conditions, addresses limitations and implications of this work, and proposes directions for future research.

Chapter 3

Characterization of MMPs & Their Relationships to Clinical Data in a Patient Population with Painful TMJ Disorders

This chapter has been adapted from:

Ita ME, Ghimire P, Granquist EJ, Winkelstein BA. MMPs in tissues from TMJ disorders relate to pain more than joint damage. *Journal of Orthopaedic Research*, under revision.

3.1. Overview

Orofacial pain has been identified as one of the six most common clinically relevant chronic pain conditions and is often caused by temporomandibular disorders (TMDs) (National Academies of Sciences, Engineering, and Medicine 2020; Treede et al. 2019). In a prospective study with over 3,000 adults, participants developed clinically verified TMD at a rate of 4% per year and reported orofacial pain symptoms at a rate of 18.8% per year (Slade et al. 2016). Painful TMDs include pathologies of the TMJ and its tissues and include internal derangement (ID) of the articular disc and degenerative joint diseases like osteoarthritis (OA) (National Academies of Sciences, Engineering, and Medicine 2020). For the TMJ, internal derangement of the disc refers to the displacement of the articular disc from its normal functional relationship with the mandibular condyle (National Academies of Sciences, Engineering, and Medicine 2020). Long-term and advanced

derangement develops into OA in 15% of patients with ID, with the progression to OA defined by the breakdown of cortical bone of the TMJ condyle (National Academies of Sciences, Engineering, and Medicine 2020). Pain from TMJ disorders is more often caused by repeated atypical loading than by an acute traumatic injury (Scrivani et al. 2008; Sperry et al. 2017; Tanaka et al. 2008), unlike the etiologies for other synovial joints like the cervical facets (Elliott et al. 2009; Ita et al. 2017). Such functional overloading, as is associated with parafunctional habits like jaw clenching and grinding, causes pathological changes that lead to degenerative and/or inflammatory cascades that can sensitize pain fibers in the TMJ (Scrivani et al. 2008; Sperry et al. 2017; Tanaka et al. 2008).

The bilateral TMJs function together as a complex to connect the mandible to the temporal bone of the skull and allow for the rotational and translational movements of the mandible (National Academies of Sciences, Engineering, and Medicine 2020; Sperry et al. 2017). The articular disc lies entirely within the joint capsule, positioned between the mandibular condyle and the glenoid fossa of the temporal bone (Figure 3.1). (National Academies of Sciences, Engineering, and Medicine 2020). The capsular ligament provides stability to the TMJ and encloses the joint's synovial fluid (Figure 3.1) (National Academies of Sciences, Engineering, and Medicine 2020). The mandibular branch of the trigeminal nerve supplies the sensory innervation of the TMJ, with nociceptive fibers innervating the capsular ligament, the peripheral articular disc, the synovial membrane, and the periosteum (Kido et al. 1993; Sessle 2011). The nociceptor innervation of the capsular ligament and disc vary regionally, with the anterior portion of the joint capsule most densely innervated, followed by the posterior, lateral, and medial portions. The disc has

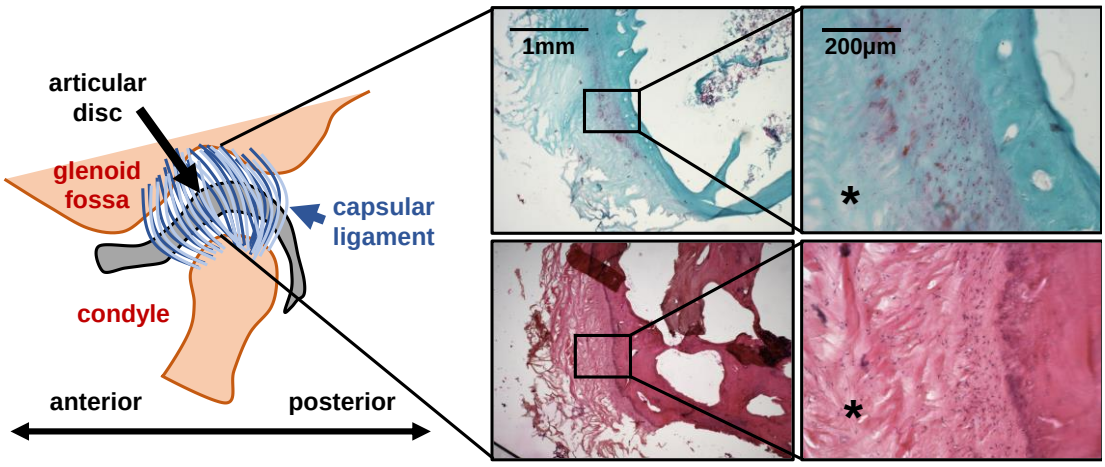

Figure 3.1. Schematic of a unilateral TMJ and its anatomy showing the capsular ligament that surrounds the joint space and the articular disc. Histology images show low and high magnification Safranin O-Fast Green staining (top; red=cartilage, green=underlying bone, black=nuclei) and Hematoxylin-Eosin staining (bottom; pale pink=collagen, black=nuclei) of a human TMJ excised during a total joint replacement surgery. The collagenous fibers of the capsular ligament (black stars) are observed in images from both stains lateral to the cartilage and bone. Scale bars apply to both stains.

more nerves in the peripheral portion and no fibers in the central disc band (Kido et al. 1993).

Although the TMJ is like other synovial joints in its overall anatomy, having a bony articulation and synovial fluid encapsulated by a ligamentous capsule (Figure 3.1), there are several differences between the TMJ and other synovial joints (National Academies of Sciences, Engineering, and Medicine 2020; Wadhwa and Kapila 2008). For example, the articular surfaces of the TMJ consist of Type I and Type II collagen-rich fibrocartilage which differs from the hyaline cartilage that lines the articular surfaces of synovial joints in the limbs, which does not typically contain Type I collagen (National Academies of Sciences, Engineering, and Medicine 2020; Wadhwa and Kapila 2008). The higher Type I collagen content of the TMJ fibrocartilage may make it more prone to collagenase-degradation than other synovial joints since a greater proportion of the cartilage is prone to

degradation with elevated collagenase levels in painful TMDs (Kanyama et al. 2000; Srinivas et al. 2001). Also, the articular disc of the TMJ separates the joint cavity into two fluid-filled compartments and it governs the rotational and translational movements in the lower and upper compartments, respectively (National Academies of Sciences, Engineering, and Medicine 2020). Although the disc is attached on its sides to the mandibular condyle, the anterior and posterior portions are free from attachment (National Academies of Sciences, Engineering, and Medicine 2020), which may contribute to overall mechanical vulnerability of the TMJ due to disc instability and subsequent ID and OA.

Although this thesis focuses on the role of MMPs in pain signaling in the capsular ligament, the articular disc of the TMJ is also susceptible to degradation by collagenases and can act as a pain sensor in that joint because of its nociceptive innervation (Kido et al. 1993). Type I collagen does make up less of the total matrix distribution in the disc than in the capsule due to higher levels of glycosaminoglycans in the TMJ disc; but Type I collagen is still the primary matrix component (Milam et al. 1991). So, MMP-1 may mediate nociception via degradation of Type I collagen or via its role in signaling pathways in the disc just as it may in capsular ligament tissue. Accordingly, this chapter includes all studies from Aim 1 that quantify MMPs in the capsular ligament and also presents parallel MMP quantification and analyses in the articular disc. MMP levels from both ligament and disc tissues are combined in correlation analyses with clinical pain scores and imaging to provide additional insight.

MMP-1 is hypothesized to mediate afferent signaling in the capsular ligament, in part, by acting as a biochemical mediator of the gelatinase MMP-9. This notion is

supported by evidence of MMP-1's regulation of MMP-9 (Conant et al. 2002; Visse and Nagase 2003) as well as the established role of MMP-9 in neuropathic pain (Ji et al. 2008; Kawasaki et al. 2008). The other member of the gelatinase MMP subgroup is MMP-2, which, like MMP-9, is also regulated by MMP-1 and implicated in neuropathic pain (Conant et al. 2002; Ji et al. 2008; Kawasaki et al. 2008; Visse and Nagase 2003). Yet, the role of the gelatinases in neuropathic pain differs in that MMP-9 is required for the early (on the scale of days in the rodent) pain *initiation* phase and MMP-2 is necessary for late stage (on the scale of weeks or more in the rodent) pain *maintenance* (Ji et al. 2008; Kawasaki et al. 2008). The capsular ligament and disc tissues probed in the studies in this chapter are from a patient population diagnosed with *late-stage chronically painful* TMJ disorders. Since MMP-2 is implicated in late-stage pain transmission, and MMPs are probed in tissues from joints with late-state painful joint disease, the studies outlined in this chapter probe MMP-2 in parallel with MMP-1 and MMP-9. Indeed, both of those gelatinases are detected together in the synovial fluid of TMJs with internal derangement (Srinivas et al. 2001) and osteoarthritis (Kanyama et al. 2000), supporting that an increase in both gelatinases may be mechanistically due to upstream MMP-1 and/or mediate pain.

Correlations between MMP-1 and MMP-2, and relationships between MMP-2 and clinical data, are tested in the studies in this chapter as well. The relationships of MMP-1, MMP-9, and MMP-2 with the clinical data that are investigated in this chapter were expected to differ based on the extracellular matrix (ECM) substrates and signaling roles of each MMP (Ji et al. 2008; Kawasaki et al. 2008; Sbardella et al. 2012; Visse and Nagase 2003). Only MMP-1 was hypothesized to relate to measures of generalized disease

progression and clinical imaging because it directly catabolizes the primary ECM component of both the ligament and disc tissue, unlike MMP-9 and MMP-2 (Visse and Nagase 2003). All MMPs were expected to relate to patient-reported pain scores and function, since all three MMPs have roles in nociceptive-related pathways (Allen et al. 2016; Ji et al. 2008; Kawasaki et al. 2008; Visse and Nagase 2003).

3.2. Relevant Background

Chronic pain is a substantial public health challenge and is commonly associated with diseases of synovial joints (Institute of Medicine 2011). TMDs arise from pathologies of the TMJ, are the second leading musculoskeletal condition resulting in pain, and occur with degenerative diseases like ID and osteoarthritis OA (National Academies of Sciences, Engineering, and Medicine 2020; Slade et al. 2016; Treede et al. 2019). The TMJ forms the articulation between the mandibular glenoid fossa and the condyle, is separated into two synovial cavities by a fibrocartilaginous disc, and is encapsulated by a ligamentous capsule (Figure 3.1). Pathologic repeated loading that occurs in ID and OA activates the trigeminal nerve fibers that innervate TMJ tissues such as the disc and capsular ligament (Kido et al. 1993; Scrivani et al. 2008); as such, innervated tissues act as pain sensors in TMJ disorders. The resulting persistent pain and severe jaw dysfunction that occur with TMJ degeneration and end-stage disease can be treated surgically with open joint arthroplasty, discectomy, and/or total joint replacement (TJR) (National Academies of Sciences, Engineering, and Medicine 2020). Although patients experience positive outcomes and long-term stability after surgical intervention (Abramowicz and Dolwick

2010; Wolford et al. 2015), invasive surgery is *only* used after other treatments fail (National Academies of Sciences, Engineering, and Medicine 2020). Pharmacologic treatments often fall short since they are adapted from other musculoskeletal and/or pain disorders rather than derived from evidence-based studies of individuals with painful TMJ disorders (National Academies of Sciences, Engineering, and Medicine 2020). Defining those molecular mechanisms that sustain and exacerbate severe TMJ degeneration can identify better therapeutic targets for earlier intervention and disease prediction (Kusiak et al. 2018).

MMPs have many roles in physiological and pathological processes including degenerative pathogenesis with painful TMDs (Kartha et al. 2016; Sbardella et al. 2012; Visse and Nagase 2003). MMPs are broadly categorized into subgroups based on their substrate specificity and domain structure (Visse and Nagase 2003); the collagenases (MMP-1, MMP-8, MMP-13) and gelatinases (MMP-2, MMP-9) increase in TMJs with both ID and OA (Almeida et al. 2015; Fujita et al. 2009; Gho et al. 2018; Kanyama et al. 2000; Kubota et al. 1998; Marchetti et al. 1999; Mizui et al. 2001; Srinivas et al. 2001; Tanaka et al. 2001). Although there is overlap in the extracellular matrix substrates across MMPs, collagenases and gelatinases preferentially degrade fibrillar (triple-helical) and denatured collagens, respectively (Visse and Nagase 2003). MMPs are classically described for their catabolism of ECM constituents and, thus, in association with tissue destruction in TMJ disorders. Yet, MMPs are also implicated in diseases of the nervous system (Yong et al. 2001), pain transmission (Kawasaki et al. 2008), and in receptor-mediated and intercellular signaling pathways that regulate nociception (Conant et al.

2002; Dumin et al. 2001). Accordingly, although MMPs may drive TMD pain and/or joint tissue degeneration, their role is unknown.

MMP-1 is a likely mediator of TMJ pain given its role in nociception and its elevated levels in TMDs. MMP-1 is secreted as a catabolically inactive zymogen, pro-MMP-1, that is extracellularly activated through disruption of its cysteine-zinc interaction by proteases like plasmin or other MMPs (Sbardella et al. 2012; Visse and Nagase 2003). Since MMPs can only cleave ECM substrates *after* they are activated, they cannot participate in matrix remodeling in their pro-forms. However, in both active and pro-forms, many MMPs have non-ECM regulatory roles. This is true for MMP-1, which binds to receptors implicated in nociception, including β1-integrin and proteinase activated receptor-1 (PAR-1) (Conant et al. 2002; Dumin et al. 2001) and non-ECM substrates, like pro-inflammatory cytokines and neuropeptides, involved in pain signaling (Sbardella et al. 2012; Visse and Nagase 2003). Moreover, MMP-1 activates gelatinases (pro-MMP-9, pro-MMP-2) that are heavily implicated in pain transmission (Kawasaki et al. 2008; Visse and Nagase 2003; Yong et al. 2001). MMP-1, MMP-9, and MMP-2 are detected together in TMJ synovial fluid (SF) with ID (Srinivas et al. 2001) and OA (Kanyama et al. 2000), supporting that an increase in gelatinases may be mechanistically due to extracellular activation by MMP-1. Yet if, and how, MMP-1 relates to pain in TMJ disorders, via MMP-9, MMP-2, or other pathways, is unknown.

Although MMPs and their relationship to joint damage have been probed (Almeida et al. 2015; Fujita et al. 2009; Kubota et al. 1998; Mizui et al. 2001; Srinivas et al. 2001; Tanaka et al. 2001), results are mixed and depend on the damage metric used. In most

cases, analyses compare patients by disease severity using Wilkes staging, which combines clinical, radiologic, and surgical findings on a gross anatomical level (Wilkes 1989). Overall, those studies show that MMP-9 and MMP-2 generally increase in joint tissues with the presence of pathology compared to asymptomatic states (Almeida et al. 2015; Kubota et al. 1998); but, MMP levels do not always increase with disease severity (Fujita et al. 2009; Srinivas et al. 2001). For instance, MMP-9 and MMP-2 are reported to be higher in the synovial fluid from TMJs with mild ID than in those with severe ID (Srinivas et al. 2001). Yet, other studies report the opposite result, with increased gelatinase levels in more severe disease states (Mizui et al. 2001; Tanaka et al. 2001). Unlike tissue damage metrics, very few studies have assessed MMPs in the context of pain scores despite patient-reported pain being the primary reason that patients seek treatment. There is some evidence of elevated MMP-3 levels in TMJ synovial fluid with greater pain (Fujita et al. 2009). If and how MMPs relate to pain and clinical degenerative signs in TMDs is unknown.

This study defined the extent of MMP-1, MMP-9, and MMP-2 in the innervated capsular ligament and disc of TMJs from patients undergoing TJR or arthroplasty discectomy surgery for painful TMJ disorder. Despite those tissues being innervated and acting as pain sensors (Kido et al. 1993; Sessle 2011), most studies characterizing MMPs in TMJ disorders evaluate synovial fluid levels (Fujita et al. 2009; Kanyama et al. 2000; Kubota et al. 1998; Mizui et al. 2001; Srinivas et al. 2001; Tanaka et al. 2001). Given the different tissue compositions and innervation patterns (Burgeson and Nimni 1992; Kido et al. 1993; Milam et al. 1991), and factors used in surgical decision making about recommending TJR or discectomy (National Academies of Sciences, Engineering, and

Medicine 2020; Scrivani et al. 2008), MMPs were evaluated by tissue and surgery type. Severity of disease progression using Wilkes staging (Wilkes 1989) and dysfunction by quantification of maximal incisal opening (MIO) (Scrivani et al. 2008) were also included in analyses. The pro- and active forms were probed since both forms are involved in joint destruction and/or nociception (Conant et al. 2002; Dumin et al. 2001; Kawasaki et al. 2008; Visse and Nagase 2003; Yong et al. 2001). Since active MMP-1 converts pro-MMP-9 and pro-MMP-2 to active protease states (Sbardella et al. 2012; Visse and Nagase 2003), active MMP-1 was hypothesized to correlate with active MMP-9 and MMP-2. It was also hypothesized that MMPs are involved in ECM catabolism and pain transmission in painful TMDs; so, we tested relationships separately between each MMP and each of clinical pain score, Wilkes stage (Wilkes 1989) and MRI damage scores (Kellenberger et al. 2018). Since there is still debate about whether structural degeneration and pain are related (Emshoff et al. 2003; Koh et al. 2009), we tested that relationship using MRI damage and pain scores for these subjects.

3.3. Methods

3.3.1. Patient Recruitment & Population Details

This study was designed as a retrospective cohort study of evidence level three in the Level of Evidence classification utilized to determine the clinical value of a study in evidence-based medicine (Moore 2020). All procedures were performed with approval from the Institutional Review Board (protocol #828997) of the University of Pennsylvania. Written informed consent was granted from all subjects undergoing either TJR (n=6) or

arthroplasty surgery for discectomy (ART) (n=3) (Table 3.1). Inclusion criteria were age older than 18 years, surgery for OA and/or ID, and failing prior medical management of at least six weeks of physical therapy, medication, and use of an occlusal appliance (Scrivani et al. 2008). Individuals were excluded from the study if they underwent TMJ surgery for conditions other than ID or OA and/or had surgical site infection, history of facial congenital abnormalities, or prior acute facial fractures. Patient-reported pain scores were collected before surgery and quantified by a Likert scale from 0 (no pain) to 10 (most severe pain) (Leonardi et al. 2016). Maximal incisal opening (MIO) was measured to quantify functional range of motion (Scrivani et al. 2008). At the time of surgery, a Wilkes stage was assigned based on TMJ gross pathology, with scores from 1 (least severe) to 5

Table 3.1. Summary of subject clinical & imaging data

Subject ID	Age (yrs)	Sex	Surgery type	Tissue type	Wilkes stage	Pain score	MIO (mm)	MRI total	MRI osseous
S01	53	M	TJR	disc	5	10	20	2**	2
S02	52	F	ART	ligament	4	9	48		
S03	61	F	TJR	disc	5	6	40	4**	2
S04	39	F	ART	disc ligament	5	8	26		
S06	33	F	TJR	ligament	5	10	28	3	3
S09	29	F	ART	ligament disc	3	6	28	0^^	0
S10	66	F	TJR	ligament	5	6	35		
S12	44	F	TJR	disc	5	8	33		
S13	29	F	TJR	ligament disc	5	9	44	3^^	3

M, male; F, female; TJR, total joint replacement; ART, arthroplasty; MIO, maximal incisal opening. Shading indicates no MRI report available.
All MRI reports contain evaluation of bone; ****** indicates MRI reports with comments on inflammation.
^^ MR score for these subjects are correlated to MMP levels for ligament & disc samples, separately.

(most severe) (Wilkes 1989). Details regarding the past medical history and medication usage of each subject were collected and are summarized in Appendix A. TMJ tissue samples were extracted at the time of surgery; ligament and/or disc tissue (Figure 3.1) was immediately finely dissected separately based on tissue type and stored at -80°C until protein extraction was performed.

3.3.2. Tissue Processing, MMP Western Blot & Analyses

Tissue (n=12 from nine subjects; Table 3.1) was finely chopped, homogenized in T-PER protein extraction buffer with 1X Halt protease inhibitor cocktail (Thermo Fisher; Waltham, MA), and centrifuged to isolate supernatant for 5 minutes at 10,000g. A BCA kit (Thermo Fisher) quantified protein. Human recombinant forms of MMP-1 (Anaspec; Fremont, CA), MMP-9, and MMP-2 (both R&D Systems; Minneapolis, MN) were fully activated by incubation with 1mM 4-Aminophenylmercuric acetate (APMA) at 37ºC for 3, 5, and 2 hours, respectively. Pro-MMP-1 (30ng/µL), APMA-activated MMP-1 (30ng/µL), pro-MMP-9 (50ng/µL), APMA-activated MMP-9 (400ng/µL), pro-MMP-2 (20ng/µL), and APMA-activated MMP-2 (50ng/µl) were loaded as positive controls (15mg/mL) and underwent SDS gel electrophoresis at 150V for 80 minutes. Protein was transferred to a PVDF membrane using the iBlot2 system (Thermo Fisher), blocked for 1 hour in Intercept blocking buffer (Li-Cor; Lincoln, NE), and triple-washed in TBS-T for 5 minutes each. Separate membranes were incubated in either a primary antibody for MMP-1 (4µg/mL), MMP-9 (4µg/mL), or MMP-2 (1µg/mL) (all from R&D Systems) overnight at 4ºC. The next day membranes underwent several TSB-T washes and were incubated in

secondary antibody (1:10,000; Li-Cor) for 2 hours at room temperature. After additional TSB-T washes, membranes were imaged using an Odyssey imaging system (Li-Cor). To account for any variation in sample loading, membranes were stripped in stripping buffer (Li-Cor), labeled with β-actin (1:1,000; Cell Signaling; Danvers, MT) using the same protocol, and imaged again. Protein expression was quantified using the pixel intensity of bands matching the positive controls using Image Studio Lite (VR5.2; Li-Cor) and normalized to β-actin intensity for each sample (Figure 3.2).

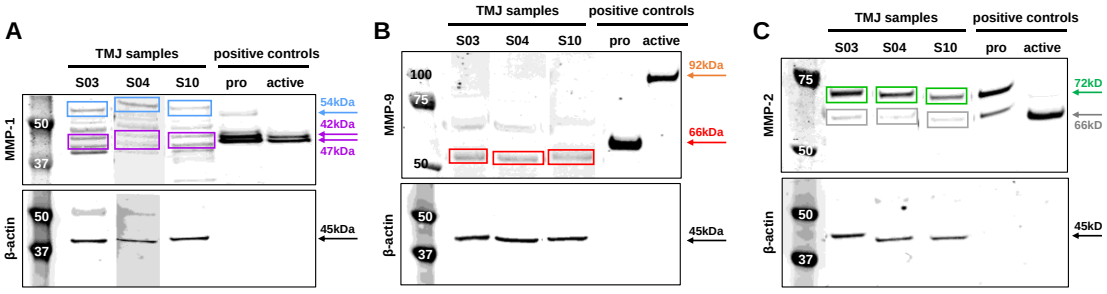

Figure 3.2. Representative Western Blots showing labeling for **(A)** MMP-1, **(B)** MMP-9, or **(C)** MMP-2. For each blot **(A-C)**, the left-most lane shows the molecular weight standards (in kDa) and the next three lanes show exemplary protein bands, grouped together for visualization and taken from different gels, from a TMJ disc sample (S03) and ligament sample (S10) taken from TJR surgeries and a ligament sample taken from an arthroplasty discectomy (S04). All brightness adjustments applied for visualization were applied equally for each gel image. Labeling for β-actin (45kDa) is shown under each MMP label and was used to normalize MMP labeling intensity for each sample. Also shown are the pro- and APMA-activated recombinant proteins that serve as positive controls. Sample band intensity is quantified using the positive controls of (A) pro-MMP-1 (54kDa), active MMP-1 (double bands at 42kDa & 47kDa; purple), (B) pro-MMP-9 (92kDa; orange), active MMP-9 (66kDa), (C) pro-MMP-2 (72kDa), and active MMP-2 (66kDa). (A) The intensity of both bands of active MMP-1 (42kDa & 47kDa) were summed. (B) Active MMP-9 was quantified at 60kDa based on differences in intracellular post-processing between the human and recombinant protein, as confirmed by the manufacturer. All pro- and active MMPs were detectable except for pro-MMP-9 at 92kDa.

3.3.3. Scoring of MRI Reports

MRI reports were available only for some patients (n=5 subjects) and rated using the EuroTMjoint research network progressive score (Kellenberger et al. 2018) (Table 3.1 & Appendix A). That semiquantitative grading scale separately assesses inflammation and osseous deformity, with each domain evaluated from 0 (normal) to 4 (severe pathology)

(Kellenberger et al. 2018). Although bone abnormalities were evaluated in all reports, only two reports contained comments on inflammation (Table 3.1); the absence of comments about inflammation was taken as normal (grade 0). For each subject with an MRI report, scores were tallied for each domain separately, as well as summed for a total MRI score (scale of 0-8).

3.3.4. Statistical Analyses

All statistical analyses were performed with $\alpha=0.05$ using JMP-Prov14 (SAS Institute Inc.; Cary, NC). Since a Shapiro-Wilk test revealed non-normal distribution for MMP protein data, they were treated as non-normal continuous numeric variables and compared using non-parametric statistics. Both pain and MRI scores were treated as ordinal numeric variables. A Kendall's τ correlation tested significance of relationships between active MMP-1 and each of active MMP-9 and active MMP-2, and between each MMP and pain score.

A non-parametric Wilcoxon signed rank test tested differences in MMPs between disc and ligament tissues; the same analysis compared surgery type (TJR, ART). A Wilcoxon signed rank test assessed MMP differences between joints with most severe Wilkes rating (stage 5) and all other scores. Separate Kendall's correlations tested relationships between each MMP and MRI scores, and between pain and MRI scores. Because imaging reports contained more detailed bone findings, the osseous and total MRI scores were separately correlated.

3.4. Results

Nearly all joints (from subjects age 45.1±13.7years) have the most severe Wilkes score (5), with only 2 subjects exhibiting lower stages (Table 3.1). All patients report pain scores in the top half of the Likert scale and have a MIO of 33.55±9.11mm before surgery (Table 3.1). All clinical information, including medical history and medication information for each patient is compiled in Appendix A.

MMPs are detected in nearly all samples, with MMP-1 detected in 10 samples and MMP-9 and MMP-2 in 11 samples. Although both pro- and active forms of MMP-1 and MMP-2 are detected across samples, only active MMP-9 is evident (Figures 3.2 & 3.3). Expression is greatest for active MMP-1 (5.96±10.84), active MMP-9 (5.49±6.32), and

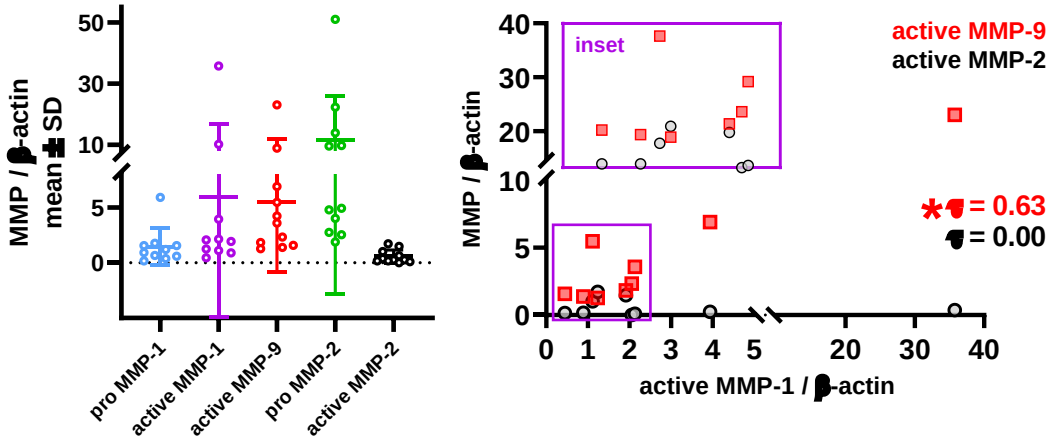

Figure 3.3. Relative MMP expression for each tissue sample. The pro- and active forms of MMP-1 and MMP-2, and the active form of MMP-9, are expressed in most tissue samples, with single data points shown for each sample along with the mean and standard deviation (SD). Active MMP-1 and active MMP-9 are significantly correlated (*p=0.01; τ=0.63; squares); but, there is no correlation between active MMP-1 and active MMP-2 (p=1.00; τ=0.00; circles). The τ correlation coefficient, ranging from -1 indicating a negative association to +1 indicating a positive association, between active MMP-1 and MMP-9 is 0.63 and indicates an increase in MMP-9 with greater expression of MMP-1. The τ correlation coefficient between active MMP-1 and MMP-2 is 0.00 and indicates no relationship between the two variables. The inset shows a close-up of the data points closest to the origin.

pro-MMP-2 (11.57±14.43), although each exhibit substantial variation (Figure 3.3). In contrast, pro-MMP-1 (1.46±1.65) and active MMP-2 (0.55±0.58) are more tightly clustered across samples (Figure 3.3). Quantification of the protein expression of each MMP for each sample is detailed in Appendix A.

Active MMP-1 and active MMP-9 are significantly positively correlated (p=0.01, τ=0.63) to each other (Figure 3.3). Yet, active MMP-1 and active MMP-2 are not correlated (p=1.00, τ=0.00) (Figure 3.3). Although MMP levels appear higher in disc than ligament, with increases from 1.06-4.97-fold (Figure 3.4A), those increases are not significant.

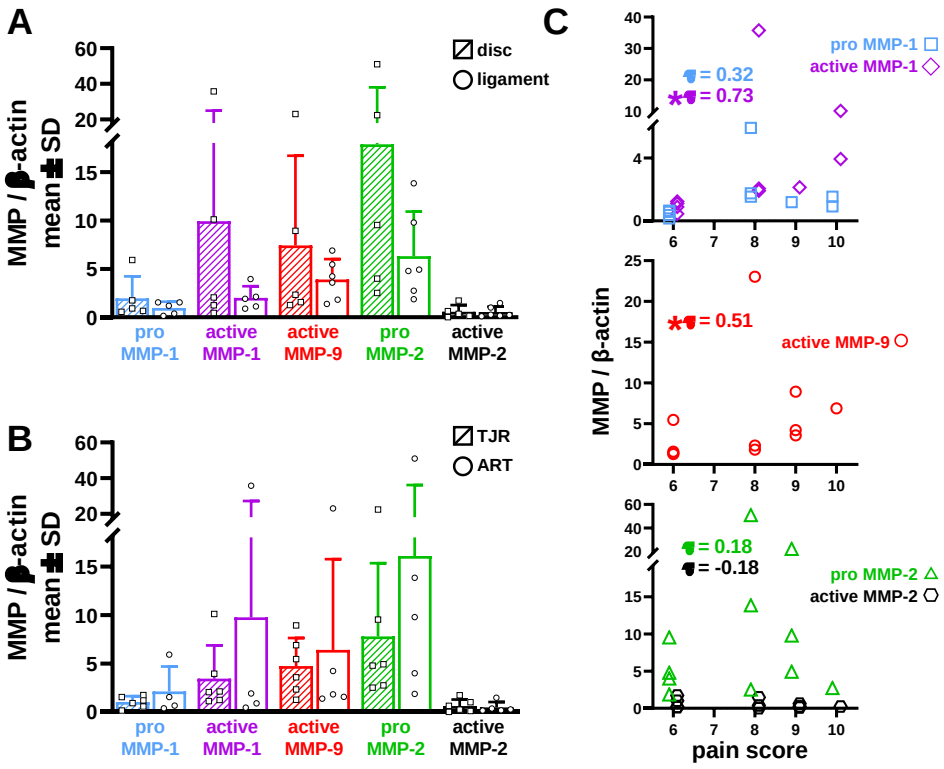

Figure 3.4. MMP levels for data clustered by **(A)** tissue type (disc (hashed squares); ligament (unfilled circles)) and by **(B)** surgery type (TJR (hashed squares); ART (unfilled circles)) show no differences for any MMPs by a Wilcoxon rank sum test. Bar plots depict mean±standard deviation (SD) of data with single data points for each sample superimposed. **(C)** Both active MMP-1 (*p<0.01; τ=0.73) and active MMP-9 (*p=0.04; τ=0.51) correlate with patient-reported pain. The plots for MMP-1 and MMP-2 against pain score show data points staggered on either side of the ordinal pain scores to enable visualizing each of the data points for the pro- and active forms.

Similarly, expression levels of each MMP are not different whether extracted during arthroplasty discectomy or a TJR procedure (Figure 3.4B).

Although MMP levels do not differ by tissue or surgery type, some MMPs are related to clinical and imaging data (Figure 3.5). Active MMP-1 is significantly correlated with pain score ($p<0.01$, $\tau=0.73$); the same relationship is also detected between pain and active MMP-9 ($p=0.04$, $\tau=0.51$) (Figure 3.4C). However, only MMP-1 varies with

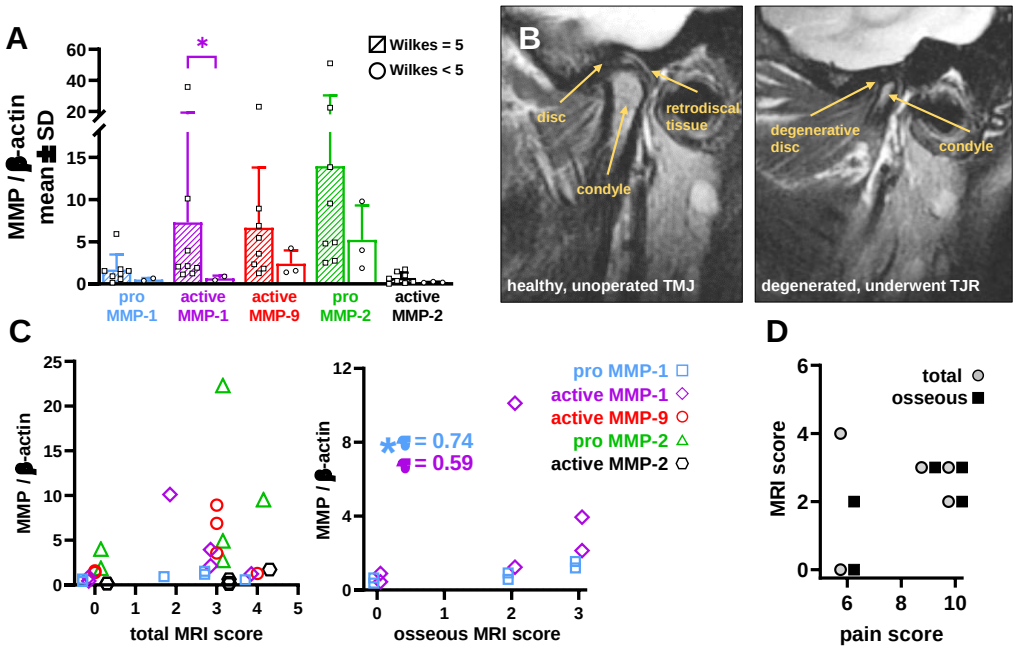

Figure 3.5. (A) MMP levels for samples from joints with a most severely degenerated Wilkes stage of 5 (hashed bars; squares) and those with a Wilkes stage less than 5 (unfilled bars; circles). Tissues from joints with a Wilkes stage 5 score have greater expression of active MMP-1 than tissues from less degenerated joints (*p=0.04; Wilcoxon rank sum test). Bar plots depict mean±standard deviation (SD) of data with single data points shown for each sample. **(B)** Exemplary T2-weighted MR images (for subject S06) in the closed position of the healthy, unoperated right TMJ and degenerated left TMJ prior a TJR. Substantial condylar degeneration and flattening is evident on the degenerated TMJ which was assigned a Wilkes score of 5, an osseous MRI score of 3 (out of 4), and a total MRI score of 3 (out of 4); no inflammatory changes were noted. **(C)** Scatter plots of MMP level versus the EuroTMjoint total score and osseous score, separately, from subjects (n=5) with MR imaging. MMP levels for each sample with an accompanying MR report were included separately; so, MMP levels of both the ligament and disc samples for subjects S09 and S13 were included as unique data points in correlation analyses with MR scores. Data points are staggered around discrete MRI scores for data visualization. Although there are no correlations detected with total MRI score ($p\geq0.1502$; $\tau\leq0.54$), pro-MMP-1 increases significantly with osseous MRI score (*$p=0.04$; $\tau=0.74$). **(D)** There is no relationship between total (circles) or osseous (squares) MRI score with pain.

measures of joint damage (Figure 3.5). MMP levels in samples with the most severe stage of Wilkes pathology are higher than those from joints with less severe pathology (Figure 3.5A). While this trend exists for all MMPs, it is only significant for active MMP-1 ($p=0.04$) (Figure 3.5A). Despite substantial degeneration evident on MR images and quantified by the EuroTMJoint scoring (Table 3.1 & Figure 3.5B), total MRI score is not correlated with any of the MMPs (Figure 3.5C). If only the osseous domain score is considered (Table 3.1), a significant positive correlation ($p=0.04$, $\tau=0.74$) is detected with pro-MMP-1 (Figure 3.5C). Of note, MRI scores do not correlate with pain, regardless of whether inflammation is used in the scoring (Figure 3.5D).

3.5. Discussion

MMP-1, MMP-9, and MMP-2 are detected in both the TMJ disc and capsular ligament, with MMP-1 and MMP-2 detected in both pro- and active forms (Figures 3.2 & 3.3). Although immunolabeling has shown MMP-1 in the ligament and MMP-9 and MMP-2 in the disc of TMD patients (Almeida et al. 2015; Gho et al. 2018; Marchetti et al. 1999), those studies did not distinguish between the pro- and active forms, limiting their ability to determine the degree to which MMP levels are catabolically active. In fact, detecting more active forms of MMP-1 and MMP-9 than their catabolically inactive pro-forms (Figure 3.3) suggests a majority of those MMPs may be available to cleave triple helical collagen and gelatin, respectively (Visse and Nagase 2003). Since triple helical Type I collagen is the primary ECM component, with negligible gelatin, of both the disc and ligament (Burgeson and Nimni 1992; Milam et al. 1991), both tissues are susceptible to degradation

by active MMP-1 (Figure 3.4A). MMP-1 degradation of Type I collagen may affect the tissue's macro- and microenvironment; tissue degradation can lead to whole joint destabilization and subsequent degeneration resulting in severe-stage Wilkes' scores (Table 3.1) (Otterness et al. 2000; Varady and Grodzinsky 2016). Since tissue-level degradation by MMP-1 can produce joint instability (Varady and Grodzinsky 2016; Visse and Nagase 2003), elevated active MMP-1 may cause the more severe degeneration that is evident in the Wilkes stage 5 joints (Figure 3.5A). On a microscale, MMP-1-cleavage of Type I collagen could disrupt the matrix surrounding innervating afferents embedded in TMJ tissues (Kido et al. 1993), breaking afferent-collagen binding sites like integrin adhesions. Since axonal nociceptive signaling depends on β1-integrin binding sites (Zhang et al. 2017), collagen degradation by MMP-1 could initiate and/or mediate pain signaling, and may explain the correlation between active MMP-1 and pain (Figure 3.4A).

Although all MMPs are detected, MMP-9's pro-form is not detected (Figures 3.2 & 3.3) and only the active forms of MMP-1 and MMP-9 relate to pain (Figure 3.4C). The positive correlation between active MMP-1 and MMP-9 further suggests their mechanistic relationship in painful TMJ disorders (Figure 3.3). Since active MMP-1 catalyzes pro-MMP-9 by cleaving its bait region (Visse and Nagase 2003), upstream regulation of MMP-9 by MMP-1 may be responsible for their correlation (Figure 3.3). It is also possible that MMP-1 activates any of the pro-MMP-9 that is present in soft tissues to an extent that makes *only* the active form detectable, which may explain why pro-MMP-9 is not detected (Figure 3.2B). The lack of pro-MMP-9 could also be an artefact of this sample population's

late stage degeneration (Table 3.1), since pro-MMP-9 in the synovial fluid is higher in mildly degenerated TMJs than those with severe degeneration (Srinivas et al. 2001).

The ECM-independent and nociceptive-related mechanisms by which active MMP-1 and MMP-9 directly bind to neuronal receptors may explain their relationships to pain (Figure 3.4C) (Basbaum et al. 2009; Conant et al. 2002; Dumin et al. 2001; Kawasaki et al. 2008; Sbardella et al. 2012; Visse and Nagase 2003). For example, MMP-1 stimulates intracellular calcium-dependent signaling via Gi protein-coupled receptors on neurons (Conant et al. 2002), which can stimulate neurotransmitter release (Basbaum et al. 2009), propagating neuronal excitability and sensitivity (Table 3.1) (Slade et al. 2016). Co-localizing MMPs to neuronal receptors in TMJ disc and ligament would help determine regulatory pathways in these soft tissues. Furthermore, although MMPs are quantified in whole tissue homogenates in this study, localization by anatomical tissue region also would provide insight into whether MMPs aggregate in nerve-rich regions (Kido et al. 1993).

The association between MMP-9, but not MMP-2, and pain (Figure 3.4C) may reveal that inflammatory stimuli to afferents drives TMJ pain. This notion is supported by MMP-9 being rapidly upregulated in the dorsal root ganglion after nerve injury (Kawasaki et al. 2008) and in the trigeminal ganglion after an injection of an inflammatory agent in the TMJ (Nascimento et al. 2013). No association between MMP-2 and pain score (Figure 3.4C) contradicts our original hypothesis since MMP-2 maintains chronic pain (Kawasaki et al. 2008) and every subject has chronic pain based on their high pain scores (Table 3.1) and the inclusion criteria of our study. Although active MMP-2 levels are low (Figure 3.3), a relationship between pro-MMP-2 and pain could exist with more samples (Figure 3.4C).

Indeed, a power analysis using sample size charts for Kendall's τ correlations indicates that approximately 35 samples are required to disprove the null hypothesis (May and Looney 2020), which is three times the sample size (n=12) used in this study. It is also likely that MMP-9 and MMP-2 vary with disease progression since expression levels and functional roles of MMPs vary according to degenerative stage (Mizui et al. 2001; Srinivas et al. 2001; Tanaka et al. 2001).

The greater pro-MMP-1 with greater osseous MRI scores (Figure 3.5C) suggests MMP-1 may have a role in pathological TMJ bone remodeling. Since MMP-1 is undetectable during healthy homeostasis, its presence indicates pathological remodeling in joint tissues (Sbardella et al. 2012). Pro-MMP-1 is catabolically inactive (Visse and Nagase 2003); its association with osseous damage (Figure 3.5C) like condylar flattening and erosions (Kellenberger et al. 2018) is likely due to its interaction with its non-ECM substrates. Pro-MMP-1 regulates inflammatory cytokines that regulate joint tissue destruction, including bone (Ernberg 2017). Despite increased MMP-1 in more structurally damaged joints (Figure 3.5), the lack of association between damage scores and pain (Figure 3.5D) is consistent with the discordance between imaging evidence of joint pathology and pain clinically (Emshoff et al. 2003; Koh et al. 2009). Together, these results (Figures 3.4C & 3.5) suggest that MMP-1's role in pain may be independent of its mediation of joint damage.

Overall, none of the MMPs relate to total MRI scores (Figure 3.5C), which may be due to disparities in resolution between tissue homogenization techniques and semiquantitative MRI scoring. These correlations relate MMP levels in specific tissues to

whole joint imaging metrics (Figure 3.5C) (Kellenberger et al. 2018). However, since MMP-3 levels in synovial fluid and arthroscopically-detected joint synovitis are related (Fujita et al. 2009), it is possible that the imaging features and tissue assays used here are too coarse to detect relationships. Analyses of these MMPs in the context of higher specificity imaging features would be helpful. Although the EuroTMjoint scale was originally developed for juvenile idiopathic arthritis, it was used here because it includes inflammatory features (e.g. edema, effusion) (Kellenberger et al. 2018). However, the MRI reports are themselves limited by the documented practitioner impressions and their details. Nevertheless, results show correlations against even coarse MR features reveal distinct relationships between MMPs and joint damage (Figure 3.5C).

Collectively, these results suggest that MMPs in innervated soft tissues may have a role in TMJ pain in addition to mediating ECM destruction. Specifically, MMP-1 and MMP-9 may be useful indicators of painful disease and may be helpful as diagnostic predictors of pain (National Academies of Sciences, Engineering, and Medicine 2020). It is possible that medications taken at the time, or in advance, of surgery could alter MMPs and may confound findings; for example, all but one of these subjects reported using NSAIDs (Appendix A), which could alter MMPs (Visse and Nagase 2003). Since probing MMPs in soft tissues requires invasive surgery, evaluating more accessible physiological samples (SF, serum, saliva) could not only help elucidate mechanistic pathways, but also aid in prognosis and treatment. Regardless, findings implicate MMPs in pain mediation and highlight them as useful clinical tools and/or targets for painful TMJ, and possibly other, disorders.

3.6. Integration & Conclusions

The experiments presented in this chapter corroborate prior reports of detectable MMP-1, MMP-9, and MMP-2 in joint tissues with painful diseases (Almeida et al. 2015; Fujita et al. 2009; Kubota et al. 1998; Mizui et al. 2001; Srinivas et al. 2001; Tanaka et al. 2001) and provides evidence that both MMP-1 and MMP-9 correlate with pain (Figures 3.3 & 3.4). These results suggest MMP-1 and MMP-9 involvement in peripheral nociception and support the overall hypothesis associated with Aim 1 that MMPs play a role in the degeneration and pain accompanying chronic joint disease in the context of a clinically relevant population. The positive correlation between MMP-1 and MMP-9 (Figure 3.3) also indicates that those two catabolic enzymes are related in nociceptive mechanisms underlying painful joint disease. Although a *mechanistic* relationship between MMP-1 and MMP-9 is not established based on their correlation (Figure 3.3), studies in Chapter 8 investigate the mechanistic regulation of MMP-9 by MMP-1 using the synthetic MMP inhibitor ilomastat in vitro.

Although MMP-2 is necessary for chronic neuropathic pain (Ji et al. 2008; Kawasaki et al. 2008), it was not found to correlate with pain for these chronic TMJ disorders (Figure 3.4), despite the late-stage disease in the chronic pain patients included in this study (Table 3.1). Further, MMP-9 is only implicated in the *initiation* of neuropathic pain (Ji et al. 2008; Kawasaki et al. 2008), but is detectable (Figures 3.2 & 3.3) and follows pain severity (Figure 3.4). This relationship between this protease and pain may indicate ongoing noxious input from the joint even in chronic stages (Nascimento et al. 2013;

Winkelstein and Santos 2008), and underscores that MMPs have roles in joint-mediated pain transmission that are distinct from neuropathic pain.

The significant relationships detected between MMP-1 and general disease progression measured by Wilkes staging (Figure 3.5A), and MMP-1 and bone damage indicated by MRI (Figure 3.5) support the hypothesis that MMP-1 correlates with measures of joint damage. However, it is not clear whether the variability of MMP-1 with joint damage influences afferent signaling mechanisms in those same joint tissues, especially since patient-reported pain score does not correlate with the overall MRI scores (Figure 3.5D). Further, only the pro-form of MMP-1 correlates with osseous MRI scores (Figure 3.5C); since pro-MMP-1 does not possess collagenolytic activity, this positive correlation between pro-MMP-1 and osseous damage may suggest that the non-collagenolytic functions of pro-MMP-1 somehow compromise TMJ bone health. Whether MMP-1 acts as a collagen-degrading catalyst, cell signaling protein, or both is also unclear. Studies in Chapter 4 exploit a purified bacterial collagenase that has the collagenolytic activity of MMP-1 to parse out how the collagenolytic role of MMP-1, in isolation from its other functions, may influence the development of pain and/or joint degeneration in a rat model.

Although these studies provide clinical context in support of broader questions investigated in this thesis, the retrospective cohort design of this investigation has several limitations. The MMP levels and clinical data evaluated here are from a single timepoint, late in disease progression, and thus do not enable assessment of how MMP levels, joint structure-function outcomes, nor neuronal outcomes may develop in parallel with pain. Further, because capsular ligament and disc tissue can only be acquired during late-stage

disease surgery or post-mortem, control groups are lacking either a healthy patient cohort or tissues samples obtained prior to disease progression. Indeed, MMPs were assayed in tissues from patients that were experiencing unmanageable pain for at least six weeks, biasing the findings. In vivo studies in Chapter 4 utilize a bacterial collagenase as a provocative stimulus and measure behavioral sensitivity as an outcome, allowing the assessment of pain development over time. Moreover, peripheral neural tissue that is unable to be probed in this clinical study is assayed in the studies with the animal model in Chapter 4 to investigate changes in protein expression of relevant neuronal regulators. Although studies in Chapter 4 only assay joint and neural tissue outcomes at a single timepoint, they allow for a control group not available in this clinical study. Further, studies in Chapter 7 use an intra-articular MMP-1 injection in the facet joint of rats to directly test the effect of elevated intra-articular MMP-1 (Figures 3.2-3.4) on behavioral, joint, and neural outcomes. Studies in Chapters 5, 6, and 8 more deeply investigate interactions between MMP-1 and MMP-9 on a cellular level in the context of injuries and/or degeneration that lead to painful joint diseases, and provide insight into possible mechanisms.

Chapter 4

Effects of Intra-Articular Bacterial Collagenase on Pain, Joint Structure, & Neuronal Dysregulation In Vivo

This chapter has been adapted from:

Ita ME, Ghimire P, Welch R, Troche HR, Winkelstein BA. Intra-articular collagenase in the spinal facet joint induces pain, neuronal dysregulation, & increased MMP-1, in the absence of joint destruction. *Scientific Reports*, in press.

4.1. Overview

Pathologies of joints are a leading cause of chronic pain and present a substantial socioeconomic burden (IBM Corporation 2019; Institute of Medicine 2011; National Academies of Sciences, Engineering, and Medicine 2020). Effective therapies for joint pain have been hindered by difficulties in diagnosing joint disease and the inability of diagnostic criteria to track with patient symptoms (Finan et al. 2013; Hunter et al. 2013; National Academies of Sciences, Engineering, and Medicine 2020). For example, although the diagnostic criteria for temporomandibular disorders are generally good for acute disc displacement and subluxation, they are extremely poor for other displacements of the disc and degenerative joint disease (National Academies of Sciences, Engineering, and Medicine 2020). The poor performance of diagnostic criteria for joint disease is rooted in the fact that characteristic radiographical features, like osteophytes, bone sclerosis, and

joint space narrowing, and *not* patient self-reported symptoms, more often define the presence of osteoarthritis "disease" (Hunter et al. 2013; Pereira et al. 2011), which is problematic because anatomic elements of joint disease do not always parallel pain symptoms (van der Donk et al. 1991; Kjaer et al. 2005). Indeed, the main foci of the studies in this thesis investigate molecular and physiologic elements of joint disease (Kraus et al. 2015), in addition to the anatomic changes, that can result in chronic pain. Recent advances in imaging techniques, particularly magnetic resonance imaging (MRI), show promise in detecting features in joint tissues that better parallel symptoms (Emshoff et al. 2003; Hunter et al. 2013), but they remain imperfect. In fact, the lack of association between pain and MRI damage scores observed in the clinical study reported in Chapter 3 also supports this sentiment (Ita et al. 2020). Recently, studies imaging synaptic activity in the brain demonstrate the ability to differentiate between joint loading that leads to persistent versus transient pain (Sperry et al. 2020a), suggesting that focusing imaging efforts at the level of the brain, in addition to, or instead of, imaging at the level of the joint, may be a useful prognostic tool to predict which pathologies will develop into chronic conditions.

Collagenase is hypothesized to regulate the biomechanical environment of the ligament via its mediation of the collagen network. Even subtle, microscopic changes to a nerve-embedded collagen network can initiate afferent signaling (Zarei et al. 2017; Zhang et al. 2016; Zhang et al. 2017), and microscopic changes to collagen structure may not be detected by current diagnostic methods (Hunter et al. 2013; Kraus et al. 2015). Therefore, collagenase-induced degradation, and subsequent influences on nociceptive signaling, *may* be one mechanism of molecular dysregulation that leads to joint pain and disability absent

accompanying gross structural deficiencies (van der Donk et al. 1991; Kjaer et al. 2005). The studies in this chapter investigate this hypothesis using intra-articular collagenase in a rat model and measuring effects on pain-related behaviors, joint structure, and neuronal dysregulation.

Although there have been several animal studies of intra-articular collagenase (Adães et al. 2014; Gou et al. 2019; Yeh et al. 2008), they use a crude bacterial collagenase, ranging in dose from 1U to 50U, that induces severe joint degeneration marked by chondrocyte disorganization, cartilage thinning and fibrillation, bone defects, and joint space narrowing; notably, many of these characteristics match the criteria of osteoarthritis diagnosis (Hunter et al. 2013). Thus, those studies characterize the clinical scenario in which joint damage is severe and radiographically detectable (Gellhorn et al. 2013; Suri et al. 2013). Studies in this chapter build off those studies by utilizing a *purified* bacterial collagenase, which only cleaves Type I collagen, unlike the crude collagenases that also degrade cartilage components. This study tests the hypothesis that, in isolation, the collagenolytic function of collagenases initiates nociceptive cascades in joint afferents by changing the capsule's collagen network and manifests in pain-like behavior. Since the collagenase used in the studies in this chapter is purified and less aggressive than prior studies in its catabolism of joint tissues (Adães et al. 2014; Gou et al. 2019; Yeh et al. 2008), a dose at the top of the range for crude collagenases (1-50U) was expected to cause *only* mild degradation. As such, 60U of purified bacterial collagenase was selected intentionally. Studies in this chapter utilize histology stains of facet joint ligament, cartilage, and bone tissue to assess the effects of intra-articular bacterial collagenase on

anatomic structure and to place behavioral and neural outcomes in the context of various clinical signs of joint disease.

Since the overall goal of this thesis is to define nociceptive transmission from the capsular ligament, peripheral responses are investigated here since the axonal projections from the peripheral DRG neuronal cell bodies innervate joint tissues (Basbaum et al. 2009; Kras et al. 2013a). However, changes to central pain processing are also associated with chronic joint and painful diseases; there is evidence of central pain processing after joint trauma (Crosby et al. 2015) in experimental osteoarthritis models (Rahman and Dickenson 2015) and in patients with osteoarthritis knee pain (Finan et al. 2013; Lluch et al. 2014). Although there is evidence that peripheral joint tissue inputs are necessary for joint-mediated pain (Winkelstein and Santos 2008), the relative contributions of peripheral and central sensitization vary by patient and may explain the disagreement between pain severity and overt tissue degeneration, whereby patients with little damage exhibit greater physiological evidence of changes in central processing and vice versa (Finan et al. 2013; Malfait and Schnitzer 2013). Studies in this chapter evaluate expression of relevant regulators in the spinal cord as well as in peripheral neurons to test if there is any collagenase-induced dysregulation in pain processing pathways. Substance P, pERK, and MMP-1 are immunolabeled in the superficial dorsal horn of the spinal cord, where afferent fibers synapse (Basbaum et al. 2009).

4.2. Relevant Background

Chronic pain poses a substantial public health challenge, with 18% of Americans

reporting pain interfering with daily life and annual costs in the United States exceeding those for cancer and diabetes combined (IBM Corporation 2019; Institute of Medicine 2011). A primary source of chronic pain is joint disease associated with osteoarthritis (Institute of Medicine 2011; Loeser et al. 2012). Neck and low back pain are among the most prevalent chronic syndromes (Institute of Medicine 2011), and can result from pathology of the spinal facet joints which are susceptible to trauma (Manchikanti et al. 2004) and degeneration (Gellhorn et al. 2013). Innervated joint tissues, like the capsular ligament that surrounds the spinal facet (Kallakuri et al. 2012), facilitate pain transmission. Since nerve fibers and resident fibroblast-like synoviocytes (FLS) in the facet capsule are mechanosensitive (Bartok and Firestein 2010; Zhang et al. 2017), load-induced disruption of the capsule's Type I collagen network can initiate pathological cellular cascades (Lu et al. 2005). Collagen fiber deformation also activates nociceptive afferents (Ita and Winkelstein 2019; Zhang et al. 2016), which have their cell bodies in the dorsal root ganglia (DRG) and synapse with spinal dorsal horn neurons to transmit noxious stimuli (Basbaum et al. 2009).

Degeneration is a hallmark of painful joint disease and is mediated by a host of proteolytic enzymes that degrade joint tissues. Collagenases, for example, are matrix metalloproteinases (MMPs) that degrade the extracellular matrix (ECM) of the cartilage and/or capsular ligament, altering joint structure and mechanics (Fields 2013; Visse and Nagase 2003). The interstitial collagenases, MMP-1, -8, and -13, and the transmembrane protein MMP-14, degrade triple helical collagen (Visse and Nagase 2003). MMP-1 protein levels increase in the joint capsule after elbow trauma (Cohen et al. 2007) and with facet

degeneration (Kim et al. 2015), and MMP-1 concentration increases in synovial fluid after knee trauma (Haller et al. 2015). Intra-articular injection of MMP-1 and MMP-13 in hamster knees produces collagen fragments indicative of Type I collagen cleavage within even 15 minutes (Otterness et al. 2000), demonstrating that interstitial collagenases can quickly initiate collagen damage. Collagenase-injected knees also exhibit increased laxity (van Osch et al. 1995), suggesting a decrease in their biomechanical integrity. Since the facet capsular ligament is primarily triple helical Type I collagen, it is especially susceptible to degradation by collagenases (Visse and Nagase 2003). Although it is possible that pathological levels of collagenases could trigger nociceptive cascades in the afferents embedded in the capsule's collagen network via degradation of the fibers surrounding the nerves, the mechanistic involvement of collagenases in degenerative joint pain is unclear.

There is a known discordance between radiographic signs of facet joint degeneration and pain symptoms (Hunter et al. 2013), with some studies reporting positive relationships between pain and evidence of joint degeneration (Gellhorn et al. 2013; Suri et al. 2013), and others finding weak or no correlations between damage and symptoms (van der Donk et al. 1991; Kjaer et al. 2005). Animal studies injecting intra-articular bacterial collagenase find more severe joint degeneration with higher doses and longer time after the injection (Adães et al. 2014; Gou et al. 2019; Yeh et al. 2008). Further, the progression and extent of joint damage depends on the *type* of bacterial collagenase. Most studies use a crude bacterial collagenase that also contains high levels of secondary proteases like trypsin and clostripain; intra-articular crude bacterial collagenase in the knee

and lumbar facet joints in animal models mimics the clinical scenario in which joint damage, particularly to cartilage and bone, is severe (Adães et al. 2014; Gellhorn et al. 2013; Gou et al. 2019; Suri et al. 2013; Yeh et al. 2008). Crude collagenases induce chondrocyte disorganization, cartilage thinning and fibrillation, subchondral bone defects, and proteoglycan loss (Adães et al. 2014; Gou et al. 2019; Yeh et al. 2008). Movement-induced pain-like behaviors and tactile allodynia are evident as early as three days after injection and lasts for eight weeks (Adães et al. 2014; Gou et al. 2019), and are hypothesized to be mediated by the severe progression of joint damage and subsequent exposure of nerve fibers in eroded subchondral bone (Gou et al. 2019).

Although studies of intra-articular crude collagenase posit a mechanism by which structural damage may mediate sensitivity (Adães et al. 2014; Gou et al. 2019), that mechanism does not explain clinical cases in which patients do not present with imaging evidence of joint destruction (van der Donk et al. 1991; Kjaer et al. 2005). As such, it is possible that in some cases of chronic joint pain, nociception may be mediated by mechanisms *other* than structural damage detected radiographically. Given the elevated levels of interstitial collagenases in joint disease (Cohen et al. 2007; Haller et al. 2015; Kim et al. 2015), and the potential for the innervated capsular ligament to undergo collagen degradation (Visse and Nagase 2003), bacterial collagenase is hypothesized to initiate nociceptive cascades in joint afferents by changing the capsule's collagen network, which alters the local microstructural environment of afferents. Indeed, injecting *purified* bacterial collagenase, which lacks the proteolytic enzymes capable of degrading cartilage, induces increased joint laxity and suggests that collagenase-mediated degradation of Type

I collagen-rich tissues, like the capsular ligament, can destabilize the joint and trigger pathological mechanotransduction cascades (van Osch et al. 1994). Although that study supports the notion that collagenase-mediated collagen degradation alone might play a role in joint disease, effects on pain were not investigated.

These studies tested whether intra-articular purified bacterial collagenase in cervical facets induces pain-like behaviors and investigated degenerative and nociceptive pathways in the peripheral and central nervous systems in the rat. Behavioral sensitivity was quantified by measuring mechanical hyperalgesia, which is a component of the complex human experience of pain in the human (Loeser and Treede 2008). Mechanical hyperalgesia was measured for 21 days after bilateral injection into the C6/C7 cervical facets. A 60U dose of bacterial collagenase was chosen based on prior reports using crude bacterial collagenase injected into lumbar facet joints that found severe joint degradation accompanied by tactile allodynia (Gou et al. 2019; Yeh et al. 2008). The 60U dose has also been shown to increase neuronal expression of biochemical regulators of injury and nociception in DRG neurons (Sperry et al. 2017) and cause a 3.8-fold increase in the amount of degraded collagen in the capsular ligament measured with collagen hybridizing peptide (CHP) after two hours of digestion (Figure 4.1). CHP selectively hybridizes with degraded, unwound collagen chains (Hwang et al. 2017; Lin et al. 2019) and can be correlated to the relative amount of degraded collagen compared to total collagen using the hydroxyproline assay to measure degraded Type I helical collagen (Figure 4.1) (Bank et al. 1997). Thus, an increase in CHP with a 60U dose of purified bacterial collagenase

demonstrates that enzyme's ability to degrade the collagen comprising the capsular ligament (Figure 4.1).

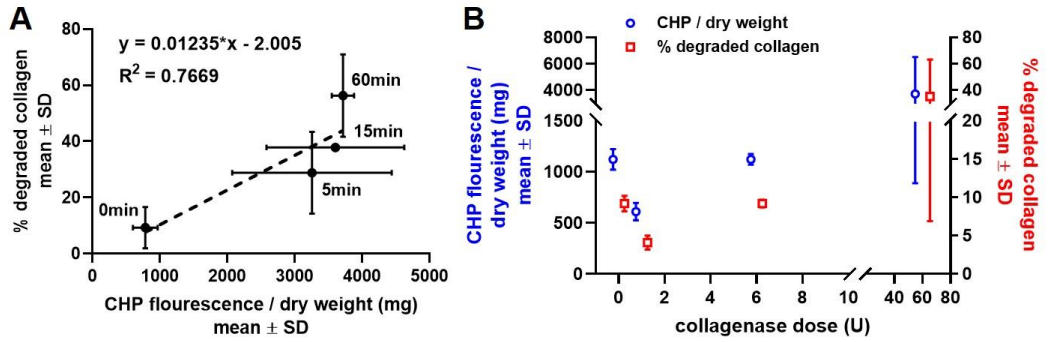

Figure 4.1. (A) Facet capsular ligaments were heated for different times to induce graded collagen degradation and assayed for absolute degraded collagen or CHP fluorescence to create a calibration curve between the two outcomes. Each data point represents 4 measurements taken from 2 ligaments for each group. **(B)** A 2-hour digestion in 60U purified bacterial collagenase produces 35% degraded collagen that is 3.8-fold higher than that from 6U collagenase and 8.5-fold higher than the degradation by 1U. Data in **(B)** are staggered on the x-axis to better visualize CHP fluorescence and degraded collagen together.

Effects on joint structure were quantified using histology of the capsular ligament and cartilage at day 21, a timepoint that allows for any detectable joint damage to develop (Yeh et al. 2008). Hypoxia-inducible factor 1α (HIF-1α), a protein that regulates chondrocyte survival in pathologically hypoxic environments, was also probed for its role in homeostatic maintenance in the cartilage (Kartha et al. 2016; Sperry et al. 2020b). Substance P, a neuropeptide involved in nociception (Basbaum et al. 2009; Zhang et al. 2017), and phosphorylated ERK (pERK), a mitogen-activated kinase indicative of noxious injury (Dai et al. 2002; Ji et al. 1999), were assayed in the DRG and spinal cord. MMP-1 protein responses were also evaluated in the DRG and spinal cord since it has been shown recently to have a role in joint pain and in diseased joints with severe-to-very mild degeneration (Cohen et al. 2007; Haller et al. 2015; Kim et al. 2015).

4.3. Methods

4.3.1. Intra-Articular Injection & Tissue Harvest

All procedures were approved by the University of Pennsylvania Institutional Animal Care and Use Committee (IACUC) and performed under the Committee for Research and Ethical Issues of the IASP guidelines (Zimmermann 1983). Male Holtzman rats (Envigo; Indianapolis, IN; 476±41g at tissue harvest) were pair-housed with 12-hour light/dark cycles and randomly assigned to groups for injection (collagenase n=12; vehicle n=6). Under inhalation isoflurane anesthesia (4% induction; 2.5% maintenance), a midline incision over the back of the neck exposed the paraspinal musculature of the C4-T2 vertebrae (Figure 4.2). The C6/C7 facet joints were cleared, and injected bilaterally with either purified bacterial collagenase (collagenase n=12) dissolved in saline (10µL; 60U; CLSPANK; Worthington Biochemical Corporation; Lakewood, NJ) or saline (10µL;

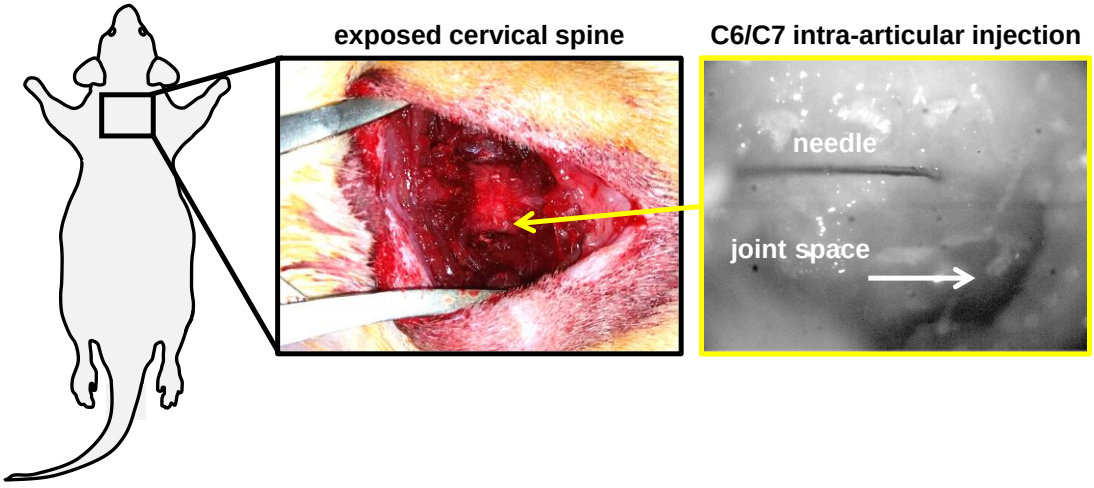

Figure 4.2. Bilateral intra-articular injection is performed in the C6/C7 facet joints of the rat. To perform the injection, the paraspinal musculature of the C4-T1 vertebrae are exposed and the C6/C7 facet joints cleared. Either purified bacterial collagenase (n=12) dissolved in saline (10µL; 60U) or saline only (10µL; vehicle n=6) is injected directly into the lateral aspect of the C6/C7 joint using a 33-gauge beveled needle for both the right and left joints.

vehicle n=6) (Figure 4.2). Wounds were sutured and stapled; rats were recovered in room air. Surgical staples were removed after 14 days, and weight gain was continuously monitored.

After behavioral testing on day 21, cervical spinal facet joints (collagenase n=6; vehicle: n=3) or neural tissues (collagenase n=6; vehicle: n=3) were harvested from separate groups of rats. On day 21, rats were anesthetized with sodium pentobarbital (65mg/kg; i.p.) and transcardially perfused with phosphate-buffered saline (PBS; 250ml) followed by 4% paraformaldehyde (PFA; 250ml). The C4-T1 spinal columns were harvested from half of the cohort (collagenase n=6; vehicle n=3) and post-fixed in 4% PFA for 24 hours, held in sucrose (Sigma; St. Louis, MO) dissolved in PBS (30%) for seven days, and decalcified in 10% EDTA (Thermo Fisher; Waltham, MA) for 3-4 weeks (Kras et al. 2015). The C6/C7 segment was embedded in Tissue-Tek OCT Compound (Fisher Scientific; Waltham, MA), coronally cryosectioned (16μm), and thaw-mounted onto Superfrost Plus slides (Fisher Scientific). DRGs and spinal cord at C6/C7 were harvested from the remaining rats (collagenase n=6; vehicle n=3), post-fixed in PFA for 24 hours, held in 30% sucrose for seven days, and embedded in OCT. Axial cryosections (14μm; 6-8/rat) were thaw-mounted. Tissue sections from naïve rats (n=2) were included in all analyses to provide un-operated control tissue.

4.3.2. Behavioral Testing

To assess whether intra-articular bacterial collagenase induces pain-like behaviors, behavioral sensitivity was quantified before, and for 21 days after, intra-articular injection (Kras et al. 2015). Since the rat C6/C7 dermatome extends to the forepaw (Takahashi and

Nakajima 1996), paw withdrawal threshold (PWT) in the forepaw was measured to quantify mechanical hyperalgesia (Kras et al. 2015). Von Frey filaments of ascending strengths (Stoelting; Wood Dale, IL) were applied to each rat's forepaw and responses identified using thresholding methods (Kras et al. 2015). PWTs were quantified before surgery (baseline; BL) and on days 1, 3, 5, 7, 11, 14, 17, and 21. Three rounds of testing were completed each day, separated by 10 minutes; all rounds were averaged bilaterally to obtain the daily PWT for each rat. Groups were evaluated simultaneously; all quantitative analyses were performed without group identification to eliminate bias.

4.3.3. Histology Staining of Facet Joint

Tissue sections were stained with Picrosirius Red/Alcian Blue (Schmitz et al. 2010) (Sigma) to visualize collagen fibers in the capsular ligament, and imaged using an EVOS FL Auto Imaging microscope with a 20x Olympus objective (5-6 images/rat). Separate regions of interest (ROIs) containing only the ligament were randomly selected (2-4 ROIs/image) and fiber orientation was analyzed using a Fourier transform method, which computes the magnitude and direction of the principal orientation axes of the image (Figure 4.3A) (Sander and Barocas 2009). The anisotropy index was calculated from the ratio of the principal axes to describe orientation on a continuous scale from isotropic (random; 0) to aligned (1) (Sander and Barocas 2009) and averaged across ROIs for each rat (Figure 4.3A).

Cartilage structure was evaluated using Safranin O/Fast Green staining (Sigma) to visualize cartilage and bone (Schmitz et al. 2010). Joint sections were prepared and imaged as described above for the ligament. Stained articular surfaces (6-8 images/rat) were scored

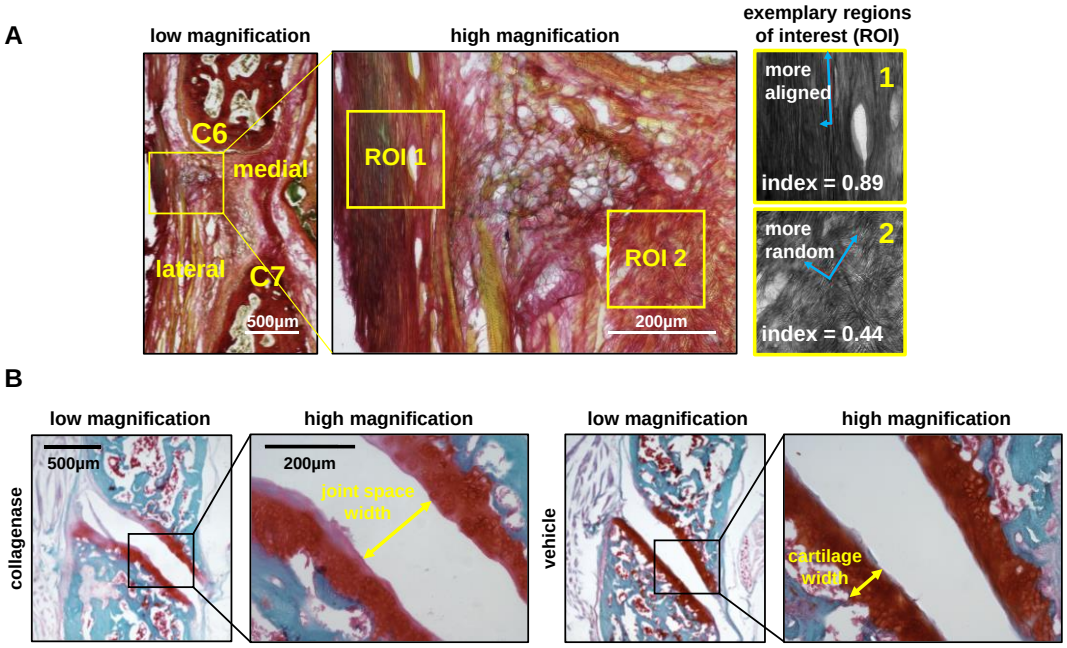

Figure 4.3. Structural assessment of the facet joint's capsular ligament, cartilage, and bone at 21 days after intra-articular injection of collagenase or vehicle. **(A)** A low magnification image of collagen fibers stained with Picrosirius Red/Alcian blue depicts the anatomical orientation of a C6/C7 joint. A high magnification image of the capsule in the lateral-to-middle region shows two separate regions of interest (ROIs) from a ligament after collagenase injection with principal orientation axes (blue arrows) and their anisotropy indices (white text) overlaid. ROI 1 demonstrates collagen fibers with highly aligned orientation and ROI 2 demonstrates fibers with a less aligned, more isotropic orientation. **(B)** Low and high magnification images of bone and cartilage staining with Safranin O/Fast Green reveals a mild decrease in cartilage staining and slight fibrillation in some collagenase-injected joints. Joint space width is defined as the the perpendicular distance between the articular surfaces; cartilage width is defined by the length of the Safranin O staining perpendicular to the subchondral bone. Scale bars in collagenase images apply to vehicle images.

by two blinded graders using a modified Mankin scale to assess cartilage degradation (Table 4.1) (Xu et al. 2009), based on cellular and background staining, chondrocyte arrangement, and structural surface condition, with scores ranging from normal (0) to maximally degenerate (10) (Xu et al. 2009), and averaged across all images for each rat.

Joint space and cartilage width were measured using FIJI (NIH; Bethesda, MD) to evaluate joint space narrowing and cartilage degradation (Gellhorn et al. 2013). Joint space width was quantified as the perpendicular distance between the articular surfaces; cartilage

Table 4.1. Modified Mankin scoring system (adapted from Xu et al 2009)

Category	Grading notes	Description	Score
pericellular Safranin-O staining	Pericellular refers to the area directly surrounding cells.	normal slightly enhanced intensely enhanced	0 1 2
background Safranin-O staining	Background refers to areas outside of and between cells. Changes in staining are evident in the more superficial layers of the cartilage and as cells become less dense.	normal slight increase or decrease severe increase or decrease no staining	0 1 2 3
chondrocyte arrangement	Hypocellularity refers to a decrease in cells present. Clustering and hypocellularity together is a 2.	normal chondrocyte clustering hypocellularity	0 1 2
cartilage structure	Fibrillation is the formation of clefts between cartilage cells.	normal superficial fibrillation fibrillation past superficial missing cartilage	0 1 2 3

width was defined by the length of the Safranin O staining perpendicular to the subchondral bone (Figure 4.3B). Both measurements were made in triplicate for each image (3-4 images/rat) from the lateral to medial end of the joint and averaged.

4.3.4. HIF-1α Immunolabeling in Articular Cartilage

HIF-1α expression was assayed using immunolabeling to evaluate the health of chondrocytes in the C6/C7 articular cartilage (Kartha et al. 2016; Sperry et al. 2020b). Immunohistochemical protocols are described previously (Sperry et al. 2020b) and used a primary antibody for rabbit anti-HIF-1α (1:250; Abcam Cambridge, MA) and a biotinylated horse anti-rabbit IgG secondary antibody (1:1,000; Vector Laboratories; Burlingame, CA). Coronal tissue sections without primary antibodies were included as negative controls and to verify antibody specificity for all immunolabeling assays. Articular cartilage was imaged using an EVOS FL Auto Imaging microscope with a 40x Olympus objective. The acquired 40x images (5 sections/rat) were cropped in FIJI to areas of 1000x450 pixels to include regions with chondrocytes. An assessor blinded to groups

counted both the number of HIF-1α-positive and the total number of cells in each image (Sperry et al. 2020b); the percentage HIF-1α-positive cells was taken as an average for each animal.

4.3.5. Substance P, phosphorylated ERK, & MMP-1 Immunolabeling in Neural Tissue

To assess substance P, pERK, and MMP-1 in the peripheral and central nervous systems, axial cryosections of C7 DRGs and spinal cord (6-8/rat) were immunolabeled. Neural tissue was triple-labeled for the microtubule-associated protein 2 (MAP-2) to visualize neuronal somata and dendrites (chicken; 1:500; Abcam) (Cullen et al. 2012), substance P (guinea pig; 1:400; Neuromics; Edina, MN), and pERK (mouse; 1:500; Cell Signaling; Danvers, MT). Sections were triple washed in TBS (Thermo Fisher Scientific) with Triton X-100 (0.03%; Bio-Rad; Hercules, CA), blocked in TBS with normal goat serum (10%; Vector) and bovine serum albumin (BSA) (1%; Sigma) for 2 hours at room temperature, and incubated overnight at 4°C with primary antibodies in TBS with 1% BSA. Sections underwent three washes and were incubated for 2 hours at room temperature with the Alexa Fluor secondary antibodies goat anti-chicken 488, anti-guinea pig 633, and anti-mouse 568 (all 1:1,000; Thermo Fisher) in TBS with BSA (1%). After washing in TBS and deionized water, slides were cover-slipped with Fluorogel (Electron Microscopy Sciences; Hatfield, MA).

Sections that were fluorescently labeled for MAP-2, substance P, and pERK were imaged at 20x with a Leica TCS SP8 confocal microscope. To quantify substance P and pERK labeling intensity in neurons, MAP-2 positive cells (n=10/image) were first

identified by a blinded grader (n=5-7 images/rat) to select neurons (Figure 4.4); then, the signal intensity of substance P and pERK labeling in the MAP-2 selected neurons was separately quantified by manually outlining the neurons and quantifying the average pixel brightness, using FIJI (Figure 4.4). Substance P and pERK expression in DRG neurons was further assessed by neuronal size by calculating the cell diameter as the average of the length and width of each selected cell using FIJI. Neurons were categorized as small- (<21μm), medium- (21-40μm), and large- (>40μm) diameter neurons (Kras et al. 2014; Weisshaar et al. 2010), based on the known different functional roles across neurons of different sizes (Basbaum et al. 2009; Dai et al. 2002). To quantify substance P and pERK in the superficial dorsal horn where nociceptors synapse (Basbaum et al. 2009), spinal cord images were cropped to include only the superficial dorsal horn which correspond to an area of 700x300 pixels. Substance P and pERK were quantified, separately, by counting

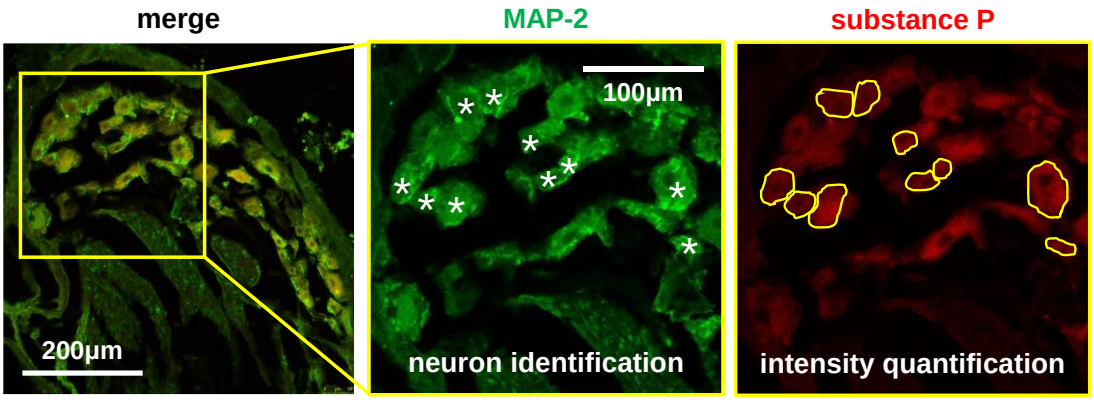

Figure 4.4. Substance P quantification in the DRG by neuronal size; the same approach was used for pERK as well. The low magnification image in the first image shows a merged MAP-2 (green) and substance P (red) immunolabel with blown out insets of the separated MAP-2 and substance P channels. Substance P is quantified in the isolated confocal image channels by first identifying 10 randomly selected MAP-2 positive cells in the MAP-2 imaged channel (white asterisks) and then manually outlining those same neurons in protein-labeled imaged channel using the FIJI software; the substance P channel is shown with selected neurons outlined in yellow. The average pixel intensity within, and the major and minor diameter of, the elliptical regions were then measured in the outlined neurons using FIJI to quantify signal intensity and neuronal size, respectively.

the number of pixels above the threshold for expression in naïve tissue using a custom MATLAB densitometry (Appendix B) (Lee and Winkelstein 2009). DRG signal intensities and the percentage of positive pixels in spinal cord were quantified for each image and averaged by rat.

To quantify MMP-1 in neural tissue, separate cryosections (6-8/rat) were washed in distilled water, incubated in Dako Target Retrieval Solution (Agilent; Santa Clara, CA) for 30 minutes at 95°C, cooled, and processed as described for HIF-1α (Sperry et al. 2020b) using a primary antibody for MMP-1 (rabbit; 1:400; Proteintech; Rosemont, IL). MMP-1 labeled tissues were imaged using an EVOS FL Auto Imaging microscope with a 40x (DRG) or 20x (spinal cord) Olympus objective. Areas of 600x600 pixels were cropped from the raw 40x DRG images to exclude connective tissue. Areas of 1500x500 pixels were cropped from the raw 20x spinal cord images to include only the superficial dorsal horn. Using the MATLAB script (details in Appendix B), MMP-1 expression was quantified using densitometry in the cropped 600x600 pixel DRG images and in the cropped 1500x500 pixel spinal cord images (Lee and Winkelstein 2009). The percentage of positively labeled pixels was separately calculated in DRG and spinal cord and averaged by rat.

4.3.6. Statistical Analyses

All statistical analyses were performed with $\alpha=0.05$ using JMP Pro v14 (SAS Institute Inc.; Cary, NC). Normality was tested using a Shapiro-Wilk goodness-of-fit test for a normal continuous fit on the residuals of all outcomes. Differences in paw withdrawal thresholds between groups over time were compared using repeated-measures ANOVA

and post-hoc Tukey HSD tests, with a single rat as an experimental unit. Anisotropy index, joint space width, cartilage width, and HIF-1α expression were compared by two-tailed t-tests. Since the Mankin score and all immunolabeling outcomes had non-normal distributions ($p<0.05$; Shapiro-Wilk test), differences were tested with a non-parametric Wilcoxon (Mann-Whitney) test to test differences between collagenase and vehicle groups. The effect of neuron size within groups was tested with a three-way ANOVA and post-hoc Tukey HSD tests.

4.4. Results

Collagenase decreases the PWT from baseline un-injected responses as early as one day after its injection ($p<0.001$), with collagenase-injected rats exhibiting increased sensitivity and significantly ($p<0.001$) decreased PWT for the full 21-day period after injection (Figure 4.5). Although a bilateral injection of saline vehicle also produces an initial decrease in PWT on day 1 ($p=0.009$), that decrease does not persist (Figure 4.5); the PWT of collagenase-injected rats is significantly lower ($p\leq0.036$) than the vehicle group starting on day 3 and lasting for all days after (Figure 4.5). PWTs are compiled for each rat in Appendix C.

Despite collagenase inducing immediate and sustained behavioral sensitivity (Figure 4.5), there is no obvious deterioration of structure in the joint ligament or cartilage. Capsular ligament collagen fibers stained with a Picrosirius Red/Alcian Blue stain (Schmitz et al. 2010) were analyzed for the degree to which their orientation is random or

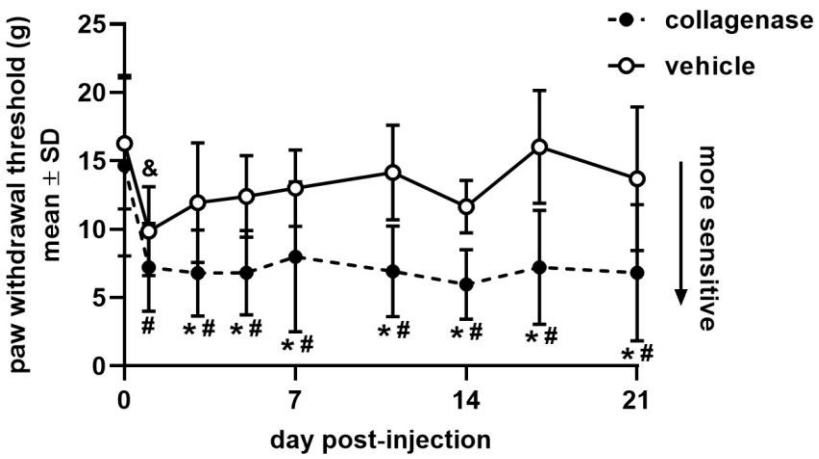

Figure 4.5. Paw withdrawal threshold (PWT) for 21 days after intra-articular injection of collagenase or vehicle. PWTs quantifying mechanically evoked pain-like behavior exhibit a decrease (corresponding to greater sensitivity) after collagenase injection at all days (#$p<0.001$) compared to baseline (day 0). Intra-articular injection of vehicle produces a decrease in PWT from baseline (&$p=0.009$) at day 1 that resolves by day 3. Starting on day 3, intra-articular collagenase induces sensitivity that is significantly lower (*$p\leq0.036$) than vehicle for all days of testing. All p-values are calculated using a repeated-measures ANOVA and post-hoc Tukey HSD tests.

aligned (Sander and Barocas 2009); that analysis reveals no difference ($p=0.731$) in organization of the capsule's collagen fibers between collagenase-and vehicle-injected joints (Figure 4.6A). Both groups exhibit a similar mean anisotropy index showing a mild level of alignment (mean±SD; collagenase 0.45±0.20; vehicle 0.45±0.17) on a scale from 0 (isotropic, random) to 1 (aligned) (Figure 4.6A) (Sander and Barocas 2009). The summary of the stained images and alignment data is provided in Appendix D.

Similarly, Mankin scoring quantification of Safranin O/Fast Green (Schmitz et al. 2010; Xu et al. 2009) stained joints shows no differences ($p=0.444$) in the structure and health of the bone and cartilage between groups (Figure 4.6A), with a few of the collagenase-injected joints exhibiting very mild cartilage degeneration (Figure 4.3B). Collagenase-injected joints exhibit a mean Mankin score of 2.54±1.64 on a scale of 0

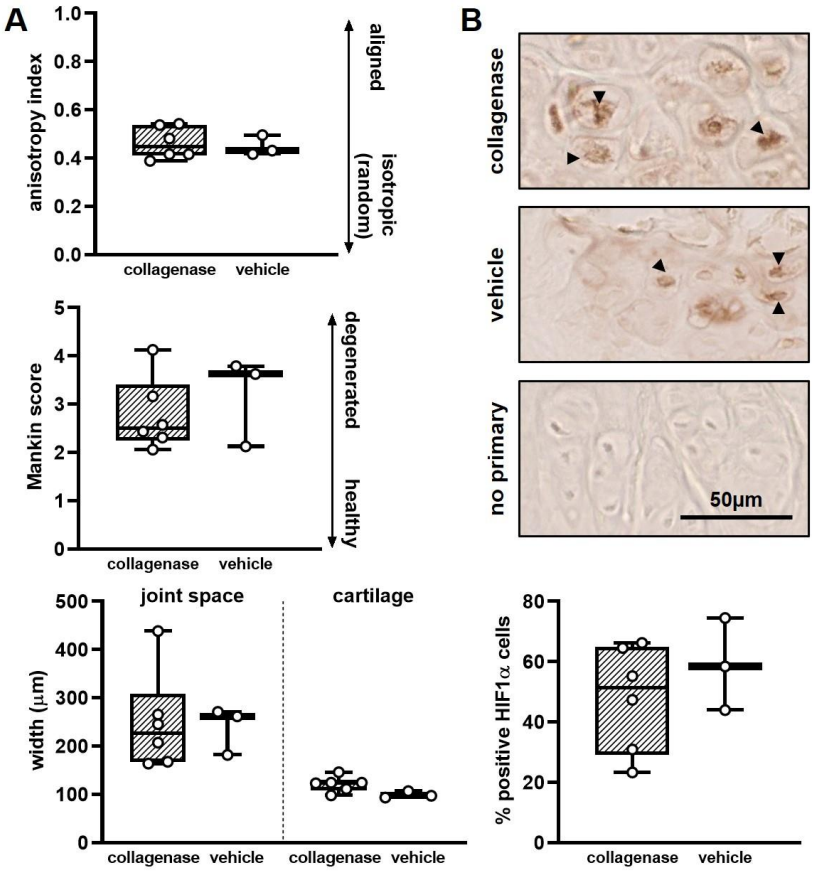

Figure 4.6. Assessment of damage and health in joint tissues at 21 days post-injection. **(A)** Intra-articular collagenase (6 joints) does not change the collagen fiber orientation of collagen networks from vehicle (3 joints) (two-tailed t-test; p=0.731). Bone and cartilage staining with Safranin O/Fast Green reveals no significant difference in Mankin score (Wilcoxon test; p=0.444). Similar to the Mankin score, neither joint space width (two-tailed t-test; p=0.841) nor cartilage width (two-tailed t-test; p=0.111) change after intra-articular collagenase. **(B)** Images show chondrocytes in the articular cartilage immunolabeled with HIF-1α where black arrowheads indicate positive HIF-1α labeling. Chondrocytes exhibit a similar pattern of positive labeling regardless of group that is not different (two-tailed t-test; p=0.423). An image of the no primary, negative control for the HIF-1α label is also shown; scale bar applies to all HIF-1α images. Box-and-whisker plots show horizontal lines representing the first (lower) quartile, median, and third (upper) quartile of the data. Whiskers represent the minimum and maximum of the data set. Data points for individual joints are superimposed on boxplots and show the mean value from 5-6 images/rat and 2-4 ROIs/image for the anisotropy index, 6-8 images/rat for the Mankin score, 3-4 images/rat for the joint space and cartilage width measurements, and 5 images/rat for the HIF-1α labeling.

(healthy) to 10 (maximally degenerate) (Xu et al. 2009) that is within one Mankin point of the vehicle group (3.45±1.92), indicating no change in structure (Figure 4.6A). In addition, neither joint space width (p=0.841) nor cartilage width (p=0.111) is altered by collagenase

(Figure 4.6A). The images, Mankin scores, and width measurements are summarized for each rat in Appendix D. The percentage of HIF-1α-positive cells in collagenase-injected joints (47.9±24.7%) is not different from ($p=0.423$) vehicle (53.31±23.68%) (Figure 4.6B), suggesting collagenase exposure that induces sensitivity (Figure 4.5) is not sufficient to disrupt chondrocyte homeostasis at day 21. Images of chondrocytes with HIF-1α immunolabeling and their quantification are detailed in Appendix D.

Immunolabeling of substance P and pERK in the DRG and spinal cord on day 21 suggests that collagenase may activate neuronal nociceptor and injury pathways in the peripheral and central nervous systems (Figures 4.7 & 4.8). Expression of both substance P and pERK in MAP-2-positive DRG cells significantly increases ($p<0.001$) in samples from collagenase-injected joints (Figure 4.7). Peripheral substance P expression after collagenase (14.95±8.85) is nearly twice that of control (7.66±4.94), and pERK levels increase by approximately 1.4-fold (collagenase 21.42±9.65; vehicle 15.37±6.10) (Figure 4.7A). In the neurons assessed from the collagenase group (n=337 neurons), 14.3% are small, 60.9% are medium, and 24.8% are large; neuron proportions are similar in the vehicle group (n=220 neurons; 13.2% small, 61.8% medium, 25.0% large). The mean size of all neurons tested is 34.8±8.5μm, which is consistent with the reported average cell diameter (~30μm) of the DRG neuronal population in the rat (Bosco et al. 2010). Collagenase elevates both substance P and pERK in small-, medium-, and large-diameter neurons over vehicle ($p\leq0.0295$) (Figure 4.7B). Further, there is a significant and different effect of cell size for substance P ($p<0.001$) and pERK ($p=0.002$) expression in DRG neurons from collagenase-injected, but not vehicle-injected rats ($p\geq0.171$) (Figure 4.7B).

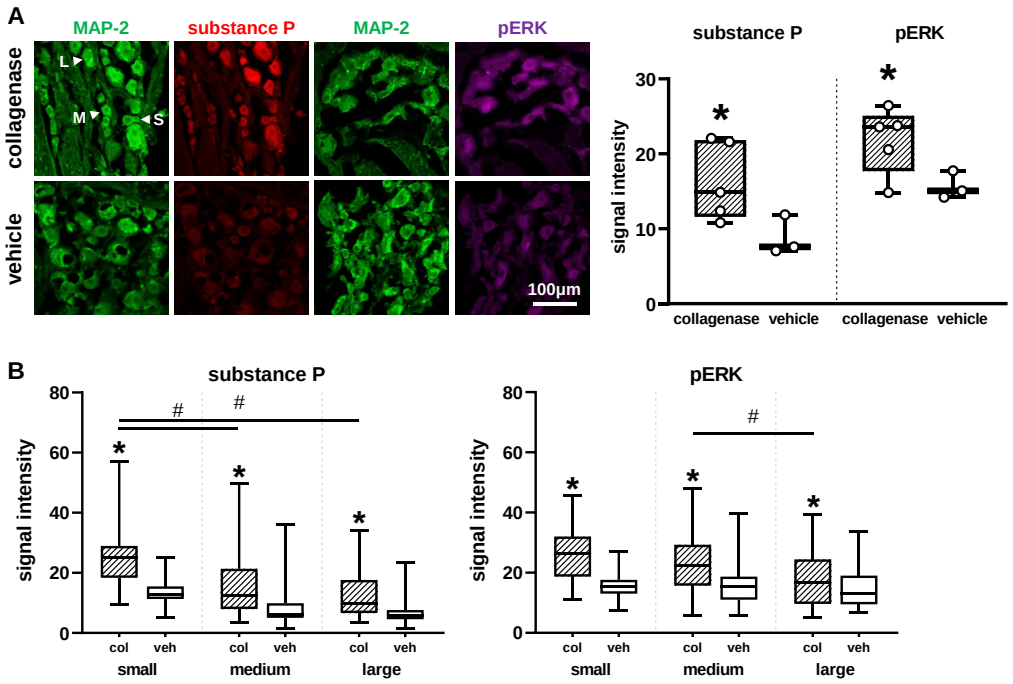

Figure 4.7. Immunolabeling of substance P and phosphorylated ERK in the dorsal root ganglia (DRG) at day 21. **(A)** Quantification of labeling intensity for the neurotransmitter substance P (red) and the MAP kinase pERK (purple) in cells with MAP-2 (green) positive labeling shows elevated expression after collagenase (col) injection relative to vehicle (veh) injection for both substance P (Wilcoxon test; *p<0.001) and pERK (Wilcoxon test; *p<0.001). Data points superimposed on box plots in **(A)** represent the mean for each rat (n=5-7 images/rat; n=10 cells/image). White arrows indicate exemplary neurons identified as small (S), medium (M), or large (L) diameter neurons. Aggregate data from **(A)** separated by neuronal size in **(B)** shows that increases in substance P and pERK after collagenase occur in small (<21µm), medium (21-40µm), and large (>40µm) diameter neurons (Wilcoxon tests; *p≤0.0295). Size has a significant effect on protein expression after collagenase, with small-diameter neurons having greater levels than medium- and large-diameter neurons (Tukey HSD tests; #p≤0.003), and medium-diameter neurons expressing greater levels of pERK than large-diameter neurons (Tukey HSD tests; #p=0.002). Box-and-whisker plots show horizontal lines representing the first (lower) quartile, median, and third (upper) quartile of the data.

After intra-articular collagenase, small-diameter neurons have greater substance P expression than medium- (p=0.003) and large-diameter (p<0.001) neurons (Figure 4.7B). Yet, pERK expression is greatest in medium-diameter neurons, which have elevated expression levels over large-diameter neurons (p=0.002) (Figure 4.7B). Positive labeling for both substance P and pERK is also evident in the superficial spinal dorsal horn (Figure 4.8). Although spinal substance P and pERK increase after intra-articular collagenase over

levels for intra-articular vehicle, the difference is only significant for substance P (p=0.039) (Figure 4.8). Triple-labeled substance P/pERK/MAP-2 images for each rat are itemized with their quantification for each label in Appendix E.

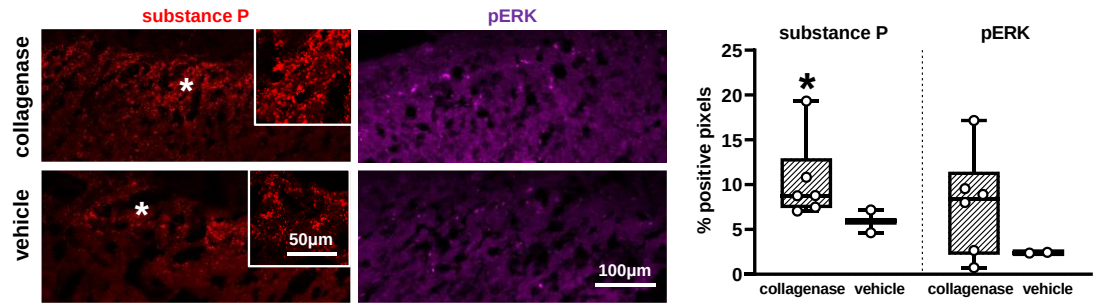

Figure 4.8. Immunolabeling of substance P and phosphorylated ERK in the spinal cord at day 21. Intra-articular collagenase increases positive labeling for substance P (red) and pERK (purple) in the superficial dorsal horn. Spinal substance P (Wilcoxon test; *p=0.039) is significantly greater after collagenase injection than after injection of the vehicle, but the same increase is not detected with pERK expression (Wilcoxon test; p=0.147). Spinal cord images show regions of the superficial dorsal horn (700x300 pixels) where immunolabels were quantified; insets show higher magnification of regions (white stars) to demonstrate positive substance P labeling. Individual data points on boxplots in represent the mean value per rat quantified for 6-8 images/rat. Box-and-whisker plots show horizontal lines representing the first (lower) quartile, median, and third (upper) quartile of the data and whiskers represent the minimum and maximum values of the data set.

Pain-like behavior (Figure 4.5) and elevated substance P and pERK expression (Figures 4.7 & 4.8) are paralleled by changes in MMP-1 expression in the DRG and spinal cord. MMP-1 expression increases both peripherally and spinally after intra-articular collagenase injection (Figure 4.9). The average level of MMP-1 labeling in the DRG neurons of collagenase-injected rats (24.75±22.48%) is significantly greater (p=0.039) at twice that expressed in control rats with vehicle injections (12.50±9.69%) (Figure 4.9). Similarly, there is a significant increase in MMP-1 expression in the superficial dorsal horn (p=0.041) of those rats receiving intra-articular collagenase (Figure 4.9). Appendix E contains the MMP-1 immunolabeled images and their quantification.

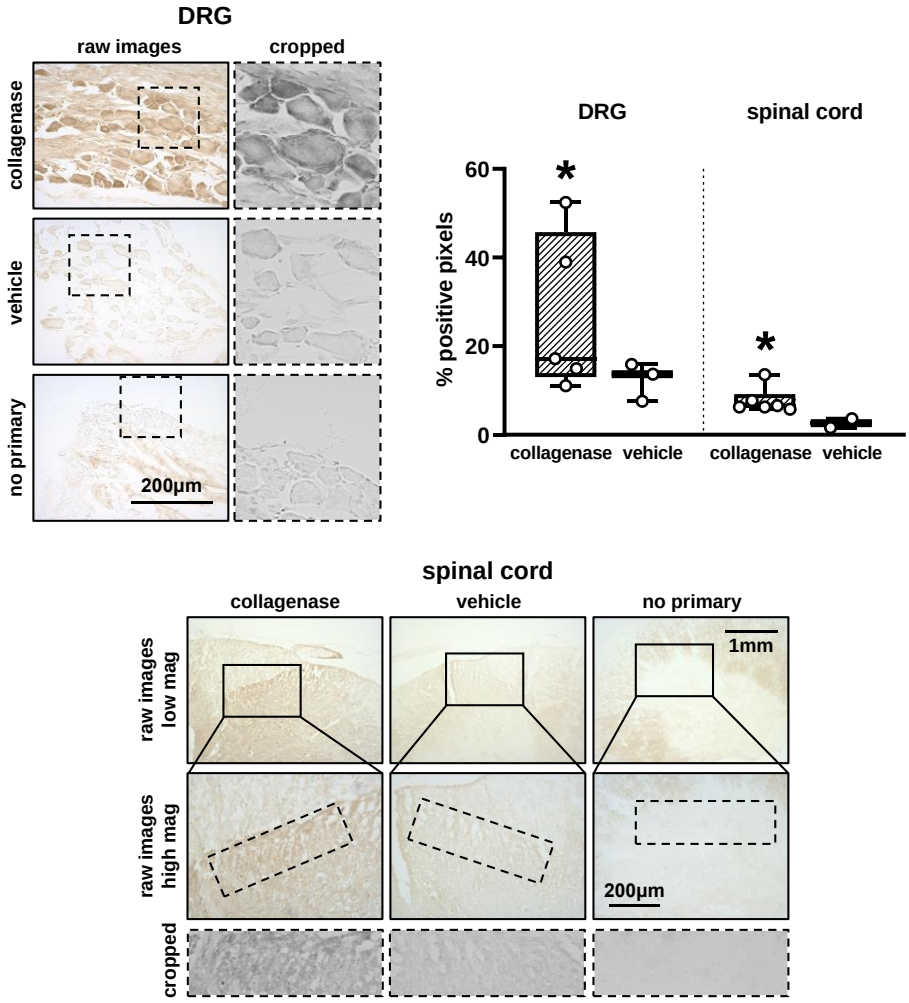

Figure 4.9. Detection of matrix metalloproteinase 1 (MMP-1) expression in the dorsal root ganglia (DRG) and spinal cord at day 21. Collagenase injection in the facet increases MMP-1 protein expression in the DRG (Wilcoxon test; *p=0.039) with pronounced labeling in DRG cells. Dashed insets in the DRG images show representative cropped regions (600x600 pixels) where MMP-1 labeling is quantified in DRG cells. Spinal MMP-1 in the superficial dorsal horn is also greater with intra-articular collagenase (Wilcoxon test; *p=0.041). Low magnification images (top) show the superficial spinal cord, from which high magnification images (middle) were acquired for quantification. Dashed insets in high magnification images show representative cropped (1500x500 pixels) regions where MMP-1 labeling is quantified in the superficial dorsal horn. Images of the no primary, negative controls are shown for both DRG and spinal cord labels. Box-and-whisker plots show horizontal lines representing the first (lower) quartile, median, and third (upper) quartile of the data. Data points for individual rats on boxplots represent the mean of 6-8 images/rat for each of the DRG and spinal cord quantification.

4.5. Discussion

This study demonstrates that introducing intra-articular collagenase in the cervical facet joint alone is enough to induce sustained mechanical hyperalgesia and dysregulation of neuronal mediators in the periphery and spinal cord (Figures 4.5, 4.7-4.9). The increase in known nociceptive and afferent regulators (substance P, pERK) as well as the catabolic and signaling protease MMP-1 in DRG neurons (Figures 4.7 & 4.9) adds to growing evidence that trauma- and osteoarthritis-induced joint sensitivity is regulated by *dysregulation* of a host of neurotransmitters, cell signaling proteins, and matrix-altering proteins in the DRG (Lee and Winkelstein 2009; Loeser et al. 2012; Miller et al. 2018; Sperry et al. 2017). Further, this occurs absent joint space narrowing, cartilage lesions, osseous changes, or chondrocyte disruption (Figure 4.6), all of which are pronounced in loading-induced osteoarthritis (Kartha et al. 2016; Sperry et al. 2020b) and with intra-articular crude collagenase (Adães et al. 2014; Gou et al. 2019; Yeh et al. 2008). Collagenase-induced changes in neural and joint outcomes (Figures 4.5-4.9) occur coincident with mechanical hyperalgesia (Figure 4.5), which is a proxy for peripheral sensitization; since this measurement is mechanically evoked, it does not fully capture the affective components of pain (Loeser et al. 2012). Integrating techniques such as the facial grimace scale in rats (Sperry et al. 2018) into in vivo models of joint pain would provide a measurement of spontaneous pain that is more translatable to the affective components of the pain experience in the human.

The results of this study imply that joint-mediated behavioral sensitivity from purified collagenase may develop and persist (Figure 4.5) by different mechanisms than

those etiologies with considerable joint degeneration. For example, contrary to the finding of elevated substance P in the DRG (Figure 4.7), crude collagenase in the knee decreases substance P expression in DRG neurons at 4 and 6 weeks after injection despite the presence of pain-like behaviors (Adães et al. 2015). The authors of that study infer that the decrease in substance P is due to afferents being injured by the severe articular destruction and subsequent exposure of subchondral bone caused by crude collagenase (Adães et al. 2015). The opposite findings that substance P *decreases* with severe damage (Adães et al. 2015), but *increases* without damage in the current study (Figures 4.6-4.8) are aligned with the disparity of observations related to structural destruction observed between the use of crude or purified collagenase (Adães et al. 2014; Gou et al. 2019; Yeh et al. 2008). The lack of change in chondrocytic HIF1α (Figure 4.6B) also differs from osteoarthritis models reporting HIFs being elevated with pain-like behaviors (Kartha et al. 2016; Sperry et al. 2020b). It is possible that HIF1α may play a role in an earlier, yet transient, chondrocyte response to the intra-articular collagenase (Sperry et al. 2020b). Yet, the lack of other evidence of cartilage damage (Figure 4.6) does not necessarily support such a hypothesis and further highlights that pain-like behavior persists here absent the hallmark cartilage breakdown.

Notwithstanding the lack of tissue-level damage with collagenase-induced hyperalgesia (Figures 4.5 & 4.6), afferent regulators can act peripherally to transmit pain within apparently undamaged joint tissues. The increase in substance P and pERK in the DRG (Figure 4.7) implies that collagenase in the joint induces synthesis of these, and likely other, proteins in neurons and would be available for distribution to peripheral synaptic

terminals in innervated tissues. Moreover, pilot studies demonstrate that collagenase increases substance P and pERK expression in DRG monolayer culture (Sperry et al. 2017), absent a collagen substrate, suggesting that collagenase may increase these proteins independent of its influence on collagen molecules. Although substance P was not probed in joint tissues, its expression has been shown to increase in subchondral bone several weeks after administration of crude intra-articular collagenase (Gou et al. 2019), suggesting substance P could also be transported peripherally in the model used here and contribute to peripheral sensitization (Figure 4.5). The increased phosphorylation of ERK in the DRG that is evident in this model (Figure 4.7) supports the notion of peripheral sensitization since ERK is activated in neurons in response to intense noxious stimulation (Dai et al. 2002).

The finding that collagenase increases pERK and substance P expression in neurons across all sizes (Figure 4.7) suggests that collagenase affects several neuronal populations that are functionally and molecularly heterogeneous (Basbaum et al. 2009). In their most common characterization during non-pathologic states, small-diameter neurons are nociceptors that transmit "slow pain" via unmyelinated C-fibers, medium-diameter neurons are nociceptors that transmit "fast pain" via Aδ myelinated fibers, and large-diameter neurons are mechanoreceptors that relay touch sensation via Aβ myelinated fibers (Basbaum et al. 2009). Since ERK phosphorylation occurs within minutes of a noxious stimulus in small- and medium-diameter neurons (Dai et al. 2002; Obata and Noguchi 2004), its elevation at the late timepoint (day 21) after collagenase (Figure 4.7), but when behavioral sensitivity is still present (Figure 4.5), suggests there may be ongoing noxious

input from the joint. Of note, peripheral noxious input does not appear to involve injury to the joint's chondrocytes since HIF1α levels are unaltered (Figure 4.6B). The phosphorylation of ERK in large-diameter neurons indicates that some degree of tissue injury may be occuring after collagenase injection (Figure 4.7B), since ERK is only phosphorylated in mechanoreceptors after nerve injury (Ji et al. 2009). This widespread ERK phosphorylation across DRG neurons likely contributes to the development of behavioral sensitivity (Figure 4.5).

Collagenase also increases substance P in neurons of all sizes, with the highest intensity of labeling in small- and medium-diameter nociceptors (Figure 4.7), suggesting that the behavioral sensitivity caused by intra-articular collagenase (Figure 4.5) may be transmitted via both the primary and secondary populations of nociceptors. Although this analysis does not distinguish between the peptidergic and nonpeptidergic neurons that make up the small-diameter, C-fiber population, the small-diameter neurons where substance P increases are likely the peptidergic population that release neuropeptides like substance P and calcitonin-gene related peptide (Figure 4.7B) (Basbaum et al. 2009). Furthermore, the hyperalgesia we report in the forepaw is secondary hyperalgesia since it is remote from the C6/C7 injection site. It is possible that abnormal recruitment of mechanoreceptors in nociception contributes to the manifestation of hyperalgesia away from the injury site (Basbaum et al. 2009), since substance P increases in large-diameter neurons (Figure 4.7B). Of note, the percentage of neurons positive for protein expression was not assessed; rather, a semi-quantitative technique was used to determine the level of expression (Kras et al. 2013b; Weisshaar et al. 2010). Further refining assessment of the

population of neurons in which afferent regulators increase could lend deeper insight into how collagenase leads to noxious transmission and the molecular receptors involved.

Central sensitization may also contribute to the manifestation of behavioral sensitivity from elevated spinal substance P (Figures 4.5 & 4.8), but to a different extent than peripheral sensitization since spinal pERK levels are not elevated (Figure 4.8). Increased substance P in the superficial dorsal horn (Figure 4.8), where peptidergic C and Aδ afferent fibers synapse, suggests that collagenase may induce central sensitization by enhancing nociceptive circuits decoupled from peripheral noxious input (Basbaum et al. 2009; Latremoliere and Woolf 2009). Indeed, there is evidence of central pain processing after joint trauma (Crosby et al. 2015), in experimental osteoarthritis models (Rahman and Dickenson 2015), and in patients with osteoarthritis knee pain who exhibit signs of central sensitization using quantitative sensory testing (Finan et al. 2013; Lluch et al. 2014). Although widespread, systemic sensitivity is evident in patients with osteoarthritis (Finan et al. 2013), additional sites further from the forepaw were not probed in this study to assess if there is widespread sensitivity. Despite evidence for central sensitization, the ability of clinical interventions, such as local intra-articular anesthetics and total joint replacement, to alleviate joint pain suggests that ongoing peripheral input from the affected joint, at least in part, may drive joint pain at chronic stages (Malfait and Schnitzer 2013). In fact, the relative contributions of peripheral and central sensitization have been proposed to vary by patient and may explain the disagreement between pain severity and radiographic joint damage whereby patients with little damage exhibit higher physiological evidence of central sensitization, and vice versa (Finan et al. 2013). Although substance P signaling

contributes to neuronal hyperexcitability (Basbaum et al. 2009; Latremoliere and Woolf 2009), electrophysiology data from DRG and spinal neurons are needed to identify if, where, and when, aberrant firing occurs. Furthermore, neuronal protein assays represent a snapshot in time (only at day 21 in this case), and do not inform about the temporal development and/or maintenance of neuronal hypersensitivity.

The collagenase used in this study is from the bacterium *Clostridium histolyticum*, and is a foreign body except during certain bacterial infections (Fields 2013). So, it is devoid of the many other pathophysiological roles of native MMPs (Sbardella et al. 2012; Visse and Nagase 2003) and effectively isolates *only* the collagen catabolism function of native collagenases. As such, intra-articular collagenase is not taken as a model of osteoarthritis, but rather purified bacterial collagenase enables answering questions about the role of collagen *catabolism* in degenerative joint diseases. Because of this "simple" effect, collagenase presumably initiates nociceptive cascades via a microscale degradation of collagenous tissues in the joint and not through non-collagenolytic-dependent pathways such as direct receptor binding on neurons (Conant et al. 2002; Dumin et al. 2001; Lakes and Allen 2016). Although over 90% of the injected collagenase is predicted to leave the joint space immediately (Otterness et al. 2000), and the remainder of the enzyme is likely cleared within several hours (Otterness et al. 2000), neither the volume nor clearance of injectant were directly measured in this study. Notably, this study used only a single dose and did not investigate whether the behavioral sensitivity, joint, and/or neural outcomes vary with the amount of bacterial collagenase. Investigating whether lower and/or more frequent collagenase doses induce transient and/or sustained behavioral sensitivity would

provide insight into how “tunable” collagen catabolism effects are on the extent and duration of pain-like behaviors.

Collagenase-mediated collagen breakdown could initiate nociception by altering the microstructure of the collagen network that surrounds the innervating afferents in the facet capsule leading to aberrant cell-matrix interactions. Indeed, prior studies in knockout mice implicate Type V and Type IX collagen directly in the manifestation of pain-related behaviors (Allen et al. 2009; Syx et al. 2020). Mechanosensitive afferent fibers and fibroblast cells embedded in a collagenous ligament respond to changes in their mechanical microenvironment via adhesive interactions with the ECM (Zhang et al. 2017); such disruption of collagen types involved in ECM cohesion may directly induce several behavioral characteristics of pain (Allen et al. 2009). Collagen breakdown could interfere with transmembrane integrin receptors that mediate collagen-axon adhesions, for example, and regulate substance P-mediated signaling (Zhang et al. 2017).

Although it is well-established that nociceptive signaling is activated in afferents by *stretch-induced* changes to their local matrix (Zarei et al. 2017; Zhang et al. 2016; Zhang et al. 2017), the current study suggests that *degradation-induced* changes alone, absent any stretch, may also affect neuronal signaling. This notion is supported by the dysregulation of neuronal regulators in the DRG and spinal cord (Figures 4.7-4.9) absent any mechanical injury with a collagenase injection. It is also possible that the degradation itself does not initiate nociception, but rather weakens the collagen matrix itself and lowers the neuronal threshold for mechanical activation. In fact, exposing isolated rat facet joints to digestion using this same collagenase also lowers the failure force and stiffness of the capsular

ligament (Singh and Winkelstein 2020). There is also more abnormal microstructural reorganization of fibers in collagenase-treated capsules at strains associated with pERK upregulation (Singh and Winkelstein 2020; Zhang et al. 2016), further supporting that stretch of a degraded ligament could initiate injury and/or nociceptive signals in neurons, transmitting pain from the periphery. This notion is further supported by studies of human classical Ehlers-Danlos syndrome in mice, whereby Type V collagen deficiency compromises joint stability and causes generalized sensitization (Syx et al. 2020). A reduced threshold for mechanical activation of nociceptive afferents in degraded capsules could explain the hyperalgesia detected with collagenase exposure (Figure 4.5), as well as pain symptoms experienced by patients with osteoarthritis during usually non-injurious movements like walking or climbing stairs (Hunter et al. 2013; Loeser et al. 2012).

It is also possible that collagenase produces collagen degradation products that act as signaling peptides in the joint. Collagen fragments produced by MMP-degradation are detectable in synovial fluid, serum, urine, and plasma in patients with painful joint degeneration (Bay-Jensen et al. 2016) and can act as ligands in cell-cell signaling (Siebert et al. 2010). Although the majority of studies characterizing collagen degradation products in humans have measured products of cartilage degradation and bone resorption, like CTX-II and COMP (Bay-Jensen et al. 2016), a few show that the Type I collagen degradation fragment C1M is detectable in serum of patients with symptomatic osteoarthritis (Arendt-Nielsen et al. 2014; Leeming et al. 2011; Siebuhr et al. 2014). C1M levels and hypersensitivity trend towards being positively correlated (Arendt-Nielsen et al. 2014), suggesting a clinically-relevant relationship between Type I collagen degradation and

nociception. Although the initial mechanism of cleavage differs between native interstitial collagenases (the human MMPs) and bacterial collagenases, both kinds of enzymes produce collagen fragments that can be subsequently post-processed into fragments <40kDa (Amar et al. 2017; Fields 2013; Otterness et al. 2000); those fragments are measurable in the synovial fluid within minutes of an MMP-13 intra-articular injection in the hamster (Otterness et al. 2000). Small collagen fragments ranging between 2.7-15.6kDa bind directly to the α2A domain of integrin (Siebert et al. 2010). Since neurons express integrin receptors and integrin-signaling is involved in the transduction of noxious stimuli (Conant et al. 2004; Zhang et al. 2017), it is possible that small collagen fragments may also bind to neuronal receptors, or indirectly influence neuronal signaling through their regulation of integrin. Such collagen fragment-mediated cascades could play a role in the development of the behavioral sensitivity (Figure 4.5) and neuronal dysregulation (Figures 4.7-4.9) observed in our model. Measuring Type I collagen degradation products and their interactions with neurons is a promising direction for future work.

MMP-1 activates several other proteases that directly regulate substance P (Visse and Nagase 2003). So, the increase of substance P and MMP-1 in DRG neurons and the spinal cord suggests their expression could be related to each other in collagenase-induced behavioral sensitivity (Figures 4.5 & 4.7-4.9). In normal non-pathologic tissues, MMP-1 levels are usually low (Sbardella et al. 2012), so the fact that MMP-1 is detectable and elevated over controls in the rat DRG (Figure 4.9) indicates a distressed cellular state. MMPs are regulated in part by fibroblasts and interactions with ECM components, including matrix turnover (Craig et al. 2015; Petersen et al. 2012; Visse and Nagase 2003),

and it is possible that collagenase triggers mechanotransduction cascades in the fibroblast-like synoviocytes that reside in the capsular ligament upon its injection. However, MMP-1 was not quantified in the fibroblast-containing region of the ligaments in this study, although MMP-1 is expected to be produced by, and localized to, fibroblasts in pathologic states (Bartok and Firestein 2010). MMP-1 localization to DRG neurons (Figure 4.9) may directly stimulate action potentials and trigger abnormal firing patterns since there are known relationships between MMP-1, cell surface receptors, and non-matrix substrates involved with nociception (Conant et al. 2002; Dumin et al. 2001; Lakes and Allen 2016; Visse and Nagase 2003). Exogenous MMP-1 increases neuronal excitability (Allen et al. 2016), so MMP-1 may contribute to the peripheral and/or central hyperexcitability in the rat.

Overall, these studies put forth a model of how nociception may occur from an apparently structurally unaffected joint, effectively mimicking the clinical scenario in which symptomatic joint pain patients do not present with hallmark evidence of joint destruction on imaging (van der Donk et al. 1991; Finan et al. 2013; Hunter et al. 2013; Kjaer et al. 2005). Microscale collagen degradation is put forth leading to behavioral sensitivity and some combination of peripheral and/or central alterations to nociceptive processing via altered cell-matrix interactions or production of potent collagen fragment ligands. Changes in the composition of joint tissues, such as a loss of Type I collagen, are posited as an early initiator of degenerative joint disease that precedes “currently detectable” pathology (Hunter et al. 2013). Still, there remain many challenges in detecting microscale collagen damage clinically, as evidenced by a lack of overt changes in joint

structure (Figures 4.3 & 4.6). Advances in MRI and other imaging modalities are beginning to achieve greater sensitivity than the characteristic radiographs used for a clinical joint degeneration diagnosis. MRI features, like bone marrow lesions, synovitis, and effusion, show promise as stronger correlates with pain (Hunter et al. 2013), and support that pain without overt joint destruction could be due to inflammatory changes in joint tissues in concert with, or instead of, microscale collagen degradation (Adães et al. 2017; Arendt-Nielsen et al. 2014; Chakrabarti et al. 2020; Miotla Zarebska et al. 2017). The ability of nonsteroidal anti-inflammatory drugs to attenuate pain-related behaviors after intra-articular collagenase (Adães et al. 2014; Gou et al. 2019), as well as pilot studies showing increased gene expression of cytokines with collagenase both in vivo and in vitro (Ita et al. 2017; Ita et al. 2018), support that inflammation may play a role in hyperalgesia (Figure 4.5). Even so, the associations with inflammatory MRI features and pain are still inconsistent and MRI "abnormalities" are common in otherwise pain-free joints (Hunter et al. 2013). Since substance P, pERK, and MMP-1 appear to be indicators of Type I collagen degradation, these molecular regulators should be considered in diagnostic and therapeutic advances as facilitators of hyperalgesia in joint diseases that involve pathologic Type I collagen degradation.

4.6. Integration & Conclusions

The findings in this chapter demonstrate that exogenous levels of a protease distinctly chosen for its purity of collagenolytic activity can induce immediate and

sustained behavioral sensitivity in the cervical facet joint (Figure 4.5), consistent with the hypothesis in Aim 2. The increases in substance P, pERK, and MMP-1 in neural tissue (Figures 4.7-4.9) further supports the hypothesis that sensitivity results from collagenase mediating nociceptive and/or mitogen-activated kinase (MAPK) signaling pathways (Cheng and Ji 2008; Ji et al. 2009; Obata and Noguchi 2004). Contrary to the original hypothesis put forth in Section 2.2, intra-articular collagenase does *not* result in tissue-level joint degeneration (Figure 4.6), at least as measured by the histological stains, Mankin scoring, and alignment analyses utilized in this study. The evidence of very mild surface fibrillation and slightly decreased Safranin O staining of the articular cartilage (Figure 4.3) suggests the possibility that intra-articular collagenase may mildly compromise structural integrity. Yet, it is very unlikely that such a modest change would qualify, or even be detectable, as "characteristic degeneration" according to current diagnostic criteria (Hunter et al. 2013; Kraus et al. 2015). Thus, results collectively point to a mechanism of collagenolytic-mediated behavioral sensitivity that does not follow clinical etiologies with substantial structural damage.

Although thesis in vivo results are useful in demonstrating that purified collagenase alone is sufficient to induce and sustain pain (Figure 4.5), the underlying mechanism of nociceptive transmission cannot be concluded from the data in this study. Certainly, elevated substance P and pERK in DRG neurons suggests the sensation of noxious and/or injurious stimuli from peripheral nerve endings, but the mechanisms by which collagenase brings about this dysregulation in the joint and its tissues is unknown. It is postulated that microscale collagen degradation induced by collagenase alters the local microenvironment

of innervating nerves in the capsular ligament and triggers aberrant signaling in resident cells. Whether cleavage of collagen fibers acts directly on adhesion sites with neurons, fibroblasts, or via more complicated signaling pathways is also unknown. Furthermore, the cleavage of Type I collagen by collagenase is an assumption, since the studies in this chapter do not quantify collagen fragments nor the relative amount of degraded collagen after injection. In vitro studies described in the next chapter help clarify the mechanisms by which collagenase may induce sensitivity utilizing a neuron-fibroblast co-culture model of the capsular ligament. The in vitro co-culture model enables higher-resolution investigation of the cell and fiber responses with less variability and complexity than in the animal; studies detailed in Chapter 5 assay neuron, fibroblast, and collagen responses to a bacterial collagenase exposure to define such possible mechanisms. Further, mechanisms by which nociceptive signaling is derived from innervated ligaments *under load*, and how such mechanisms may depend on MMPs, are defined using that same co-culture model in Chapters 6 and 8.

Reports of elevated MMP-1 with painful joint trauma and/or degeneration are exclusively in the joint tissues; MMP-1 increases in the joint capsule after elbow trauma (Cohen et al. 2007) and with facet degeneration (Kim et al. 2015), and its concentration increases in synovial fluid after knee trauma (Chockalingam et al. 2013; Haller et al. 2015; Konttinen et al. 1999; Tchetverikov et al. 2005). Findings in this chapter demonstrate that increased MMP-1 expression localizes to neural tissue in the periphery and spinal cord (Figure 4.9), demonstrating that joint-mediated sensitivity is accompanied by elevated MMP-1 in the nervous system as well as in musculoskeletal tissues. Elevated MMP-1

levels in the peripheral and central nervous systems may be a result of increased levels in joint tissues and MMP-1 translocation along axons; yet, this animal study did not evaluate MMP-1 levels in the capsular ligament, synovial fluid, or other joint tissues. However, studies in Chapters 5, 6, and 8 quantify MMP-1 levels in the collagen substrate surrounding peripheral neurons in the co-culture model as a proxy for the capsular ligament in vivo, and provide insight into how mechanical and chemical stimuli might alter MMP-1 levels in joint tissues.

Measuring MMP-1, a human collagenase, after intra-articular bacterial collagenase may appear redundant; yet, bacterial collagenase is not a direct substrate of, or ligand to, MMP-1. MMP-1 is regulated, in part, by neurons (Zhou et al. 2014), fibroblasts (Bartok and Firestein 2010; Petersen et al. 2012), the extracellular matrix (Visse and Nagase 2003), and by other MMPs (Clark et al. 2008; Fields 2013). So, its increase with bacterial collagenase (Figure 4.9) suggests that collagenase alters any one, or all, of these regulatory mechanisms and implicates MMP-1 in joint-mediated sensitivity. Studies in Chapter 7 parallel those from this chapter by using intra-articular MMP-1 to capture the collagenolytic and myriad non-collagenolytic roles of human MMP-1 on pain, joint structure-function, and neuronal dysregulation.

Chapter 5

Development & Characterization of a Neuron-Fibroblast Co-Culture Collagen Gel Model of the Capsular Ligament

This chapter has been adapted from the following abstracts and portions of manuscripts:

Ita ME, Troche HR, Winkelstein BA. Primary synovial fibroblast-collagen gels exhibit unique tensile failure properties & microstructure from 3T3-collagen gels. *Summer Biomechanics, Bioengineering & Biotransport Conference*, Abstract #216, June 2019. Seven Springs, PA.

Leavitt GE, Ita ME, Winkelstein BA. Differential MMP-1 Expression is Induced After Stretch in Neuron-Collagen Co-Cultures Seeded with Either Fibroblast-Like Synoviocytes or 3T3s. *Biomedical Engineering Society Annual Meeting*, Abstract #3973, Oct. 2019. Philadelphia, PA.

Ita ME, Winkelstein BA. Concentration dependent effects of fibroblast-like synoviocytes on collagen gel multiscale biomechanics & neuronal signaling: Implications for modeling human ligamentous tissues. *Journal of Biomechanical Engineering*, 141(9): 091013, 2019.

Ita ME, Winkelstein BA. Collagenase exposure that disrupts collagen microstructure in a co-culture model of ligament also alters neuronal activity & MMP-1 expression. *Summer Biomechanics, Bioengineering & Biotransport Conference,* Abstract #46, June 2020.

Ita ME, Ghimire P, Welch R, Troche HR, Winkelstein BA. Intra-articular collagenase in the spinal facet joint induces pain, neuronal dysregulation, & increased MMP-1, in the absence of joint destruction. *Scientific Reports*, in press.

5.1. Overview

In vitro neuron-seeded three-dimensional (3D) collagen gels replicating the sensory innervation and collagen network microstructures of the ligamentous capsule have helped

to define mechanisms by which mechanical stimuli may activate nociceptive responses in neurons in ligamentous joint capsules (Zhang et al. 2016; Zhang et al. 2017; Zhang et al. 2018). Yet, that work omitted the possible effects of synovial fibroblasts, which are interspersed within the capsule's matrix (Bartok and Firestein 2010; Provenzano et al. 2002; Valencia et al. 2004; Yahia and Garzon 1993; Yamashita et al. 1996). Those cells not only alter local network mechanics (Grinnell 2008; Kural and Billiar 2013; Rhee and Grinnell 2007), but are also known to have myriad roles in regulating MMPs (Bartok and Firestein 2010; Daniels et al. 2003; Petersen et al. 2012). As such, existing models are limited in not being able to define cell-to-cell interactions between fibroblasts and neurons, especially in the context of MMP regulation and/or nociception.

The studies in this chapter describe the development of a co-culture model that integrates fibroblast-like synoviocytes (FLS) into an existing neuron-collagen system to investigate how FLS participate in afferent signaling. To replicate the in vivo environment and preserve the functional role with MMP-1, studies use primary-harvested synovial fibroblasts. The studies in this chapter also directly build off the in vivo study in Chapter 4 by mimicking the collagenase exposure used in the rat in the new co-culture model. Since the co-culture model is able to minimize any confounding factors that may be present in vivo and enables measuring fiber- and cell-level outcomes, it provides helpful insight into possible mechanisms by which intra-articular collagenase alone may induce behavioral sensitivity. Specifically, the effect of collagenase exposure on the amount of collagen, its network microstructure, live-neuronal signaling responses, and neuronal MMP-1 expression are all assessed, matching the in vivo assays (Chapter 4).

A combined background section (Section 5.2) summarizes the neuron-collagen model in the context of the anatomy of capsular ligaments, emphasizing its utility and where it falls shorts in mimicking the in vivo scenario. The existing literature on fibroblast-embedded collagen gels is presented and highlights the need for incorporating fibroblasts derived from the capsular ligament of synovial joints. Section 5.3 details studies performed to develop and optimize the new co-culture model, enumerating methods for cell harvest and isolation, characterization of fibroblast-like synoviocytes cells, and integration of neuronal and fibroblast cell types together. Separate methods, results, and discussion sections are presented for the studies characterizing the co-culture response to a biomechanical stretch to failure (Section 5.4) and to a bacterial collagenase exposure (Section 5.5). A combined conclusion (Section 5.6) integrates outcomes from both of the model development and characterization studies. Collectively, the studies in this chapter address Aim 3 and provide context for studies in Chapters 6 and 8.

5.2. Relevant Background

At each spinal level from the cervical to the lumbar spine, the bilateral synovial facet joints articulate between adjoining vertebrae. In the cervical spine these joints are a common source of neck pain and are susceptible to injury from trauma or during spinal degeneration (Hogg-Johnson et al. 2008; Jaumard et al. 2011; Panjabi et al. 1998; Winkelstein et al. 2000). The abnormal kinematics that are produced in the spine during neck injury or other dynamic spine loading can injure the individual tissues in the facet joint and/or the joint as a whole (Anderst et al. 2014; Pearson et al. 2004). The pathology

associated with those tissue injuries includes microstructural damage to the collagen fibrous matrix of the capsular ligament, synovial fold pinching, and/or degenerative changes to the articular cartilage, which can lead to osteoarthritis (Kim et al. 2015; Pearson et al. 2004; Schofferman et al. 2007). Because the facet joints are innervated by mechanoreceptive and nociceptive afferent fibers (Bogduk and Marsland 1988; Lu et al. 2005b), any abnormal loading of the facet joint can also generate forces that mechanically load those afferents and initiate a host of pathophysiological responses that can lead to pain (Ita et al. 2017b; Kallakuri et al. 2008; Lee et al. 2004; Lee and Winkelstein 2009; Lu et al. 2005a). In particular, injury of the innervated ligament tissue that encapsulates the synovial joint has the potential to act as a pain sensor.

Innervating fibers of the ligamentous capsule of most other peripheral synovial joints, in addition to the spinal facets, have their cell bodies in the dorsal root ganglia (DRG) and synapse with spinal dorsal horn neurons in the spinal cord (Basbaum et al. 2009; Kallakuri et al. 2012). The extracellular matrix (ECM) of the joint capsule is comprised primarily of collagen, with Type I collagen making up 80-99% of the ECM network (Burgeson and Nimni 1992). The capsular network of the facet joints in particular has subregions with parallel and irregular collagen fiber orientations (Ban et al. 2017; Kallakuri et al. 2012; Yahia and Garzon 1993; Yamashita et al. 1996). Along with afferent fibers, fibroblast-like synoviocytes, also known as synovial fibroblasts or type B synoviocytes, reside in the capsule's ECM and in the lining of the synovium of synovial joints (Bartok and Firestein 2010; Kallakuri et al. 2012; Valencia et al. 2004; Yahia and Garzon 1993; Yamashita et al. 1996). For the spinal facet capsules, FLS density is greater

in the inner capsule than the outer capsule (Yahia and Garzon 1993; Yamashita et al. 1996), and collagen network organization also varies, with regions that are randomly aligned and regions that are differentially aligned depending on the anatomical location (Ban et al. 2017; Kallakuri et al. 2012; Yahia and Garzon 1993; Yamashita et al. 1996).

Prior work with collagen gels embed DRGs containing cell bodies of the sensory neurons that innervate the capsule (Basbaum et al. 2009; Kras et al. 2013) in a 3D collagen network with either aligned or randomly oriented fibers (Yahia and Garzon 1993; Yamashita et al. 1996) to mimic the facet capsule anatomy (Zhang et al. 2016; Zhang et al. 2017; Zhang et al. 2018). That neuron-collagen gel model has been especially useful for defining load-induced neuron-collagen interactions in the context of nociception; for example, the strain threshold for collagen fiber realignment is the same as the threshold for elevated expression of phosphorylated extracellular signaling kinase (pERK) (Zhang et al. 2016); pERK indicates the presence of a noxious stimuli and is taken as an indicator of cellular injury (Ji et al. 2009). In addition, regional strains caused by a bulk stretch to the neuron-embedded collagen gel directly relate to increased expression of pERK and expression of the neurotransmitter substance P in DRG axons (Zhang et al. 2017; Zhang et al. 2018). However, that system does not include synovial fibroblasts, which are abundantly interspersed within the capsule's ECM (Bartok and Firestein 2010; Provenzano et al. 2002; Valencia et al. 2004; Yahia and Garzon 1993; Yamashita et al. 1996). As such, afferent-fibroblast interactions are absent in any conclusions. In fact, no culture system has integrated neurons or DRGs together with FLS in a co-culture model to capture the anatomy and physiology of human joint capsules. Accordingly, despite their co-existence

in capsular ligaments, very little is known about the interactions of afferent fibers and FLS with each other and/or their surrounding collagen network.

Fibroblasts are ubiquitous stromal cells that play crucial roles in both normal physiologic and pathological functions, including development, repair, wound healing, and ECM remodeling (Rinn et al. 2006). In healthy and disease states, fibroblasts model and remodel their ECM via mechanotransduction mechanisms that convert mechanical cues into biological events (Dallon and Ehrlich 2008; Grinnell and Petroll 2010; Kural and Billiar 2013; Wang et al. 2007). Although fibroblasts are defined broadly by their morphology, adherence characteristics, and lack of lineage-specific markers (Frank-Bertoncelj et al. 2017; Rinn et al. 2006), they are functionally and phenotypically diverse, with distinct gene expression profiles depending on their anatomical origin in the body (Rinn et al. 2006), even across synovial joints (Frank-Bertoncelj et al. 2017). Therefore, a primary goal in improving the physiological nature of existing neuron-collagen models is not only to integrate fibroblasts, but to integrate fibroblast cells directly from the capsular ligament. Although the role of FLS in inflammation and degradation, particularly in rheumatoid arthritis, has been described (Bartok and Firestein 2010), little is known about the effect of FLS on regulating matrix mechanics, either in an unloaded state or during loading, despite reports that fibroblast-collagen mechanobiological relationships exist for fibroblasts not derived from capsular ligaments (Dallon and Ehrlich 2008; Grinnell and Petroll 2010; Kural and Billiar 2013). Defining if, and how, FLS alter matrix mechanics and/or microstructure is critical to understanding load-induced cell signaling and afferent-FLS interactions in the synovial lining and the capsular ligaments in which FLS reside.

Fibroblasts cultured in 3D collagen gels have been extensively studied to define fibroblast-matrix interactions, with tension and network parameters found to regulate fibroblast mechanobiology (Dallon and Ehrlich 2008; Grinnell and Petroll 2010; Kural and Billiar 2013). The initial seeding concentration of fibroblasts also regulates the biomechanics of the collagen gels in which they are embedded (Evans and Barocas 2009). Fibroblast seeding concentrations in gels range from $5x10^4$ to $2x10^6$ cells/mL, with primary cell lines generally on the lower end of that range due to their lower passage of senescence and less robust proliferation compared to immortalized cell lines like NIH 3T3 cells (Bing et al. 2012; Evans and Barocas 2009; Nobe et al. 2000; Sander et al. 2011; Saravanan et al. 2014; Simon et al. 2012; Thomopoulos et al. 2007). Since capsular ligaments exhibit variable FLS densities in different regions of the capsule (Yamashita et al. 1996), the biomechanics, microstructure, and cell-to-cell interactions between FLS and neurons are also likely to vary regionally within the capsule.

Synovial fibroblasts are elongated, with polygonal morphology and branched cytoplasmic processes, commonly identified by the cytoskeletal proteins vimentin (Varani et al. 2008) or F-actin (Bing et al. 2012), and express several specific membrane proteins (Bartok and Firestein 2010; Rosengren et al. 2007; Valencia et al. 2004). One surface protein that is specific to FLS cells is CD90, also called Thy-1; it mediates adhesion (Ahn et al. 2008; Bartok and Firestein 2010; Neidhart et al. 2003; Rosengren et al. 2007). CD90 has been shown to distinguish synovial fibroblasts from synovial macrophages and is present on greater than 70% of FLS in cell culture (Neidhart et al. 2003; Rosengren et al. 2007; Zimmermann et al. 2001). Synovial fibroblasts contain cell surface receptors to

which MMP-1 can bind and initiate inter- and intra-cellular signaling (Bartok and Firestein 2010; Jenkins et al. 1999), including integrin-triggered cascades and MAPK activation, both of which are implicated in nociception (Ji et al. 2012; Obata and Noguchi 2004; Zhang et al. 2017). Since load stimulates MMP-1 secretion in fibroblasts (Petersen et al. 2012) they are a possible source of the MMP-1 that is found in joints after trauma (Cohen et al. 2007; Haller et al. 2015; Konttinen et al. 1999; Lattermann et al. 2017). As such, including FLS in models that investigate the role of MMPs in joint pain is crucial.

Studies culturing DRGs alone, and with stem cells or keratinocytes, visualize neurite growth by immunocytochemistry (ICC) labeling for βIII tubulin, a microtubule primarily expressed in neurons (Cullen et al. 2012; de Luca et al. 2015; Mehnert et al. 2014; Zhang et al. 2018). Although βIII tubulin can assess healthy axons and neurite outgrowth, technically it can evaluate *only* the end-state at a single point. Genetically engineered calcium indicators (GECI), on the other hand, enable probing temporal functional outcomes in live cells (Chen et al. 2013; Grienberger and Konnerth 2012). GECIs consist of circularly permuted GFP, the calcium-binding protein calmodulin (CaM), and calmodulin-interacting M13 peptide (Chen et al. 2013). Calcium binding to the CaM-M13 peptide causes conformational changes that result in increased brightness of the fluorescent protein (Chen et al. 2013). GECIs, such as GCaMP6f, can be virally transduced by an adeno-associated virus, and upon successful transduction, rapidly and transiently fluoresce with changes in intracellular calcium (Chen et al. 2013). Calcium-induced fluorescence traces can then be mapped to known characteristics of action potentials, like exponential decay, short duration, and timing parameters to identify action potential-induced calcium

transients (Patel et al. 2015; Schultz et al. 2009). Furthermore, dead cells can be identified by the GCaMP6f signal if the nucleus of the cell is fluorescing, since the interaction between calcium and calmodulin that leads to viral-induced fluorescence is *not* expected in the nucleus unless the nuclear membrane has been compromised, indicating cell death. Both βIII tubulin ICC and GCaMP6f viral transduction techniques are utilized in the studies in this chapter to help characterize the neuronal response to FLS integration.

The following studies integrate primary FLS cells into an existing DRG-collagen model (Zhang et al. 2017; Zhang et al. 2018) to more closely mimic the multicellular environment of the capsular ligament of synovial joints (Bartok and Firestein 2010; Kallakuri et al. 2012; Valencia et al. 2004; Yahia and Garzon 1993; Yamashita et al. 1996). Pilot experiments detail the technical aspects of FLS isolation, biological characterization of the FLS phenotype, and optimization of a co-culture media. Viability and morphological assays further test the effects of co-culture integration parameters on the health and viability of both DRG neurons and FLS cells in the model. Biomechanical and physiological responses of the optimized DRG-FLS co-culture collagen gel model are examined in studies utilizing a biomechanical stretch and a bacterial collagenase exposure. Together, these studies begin to elucidate cell-matrix and cell-cell interactions under conditions of loading and degradation in the capsular ligament.

5.3. Neuron-Fibroblast Co-Culture Collagen Gel Model Development

5.3.1. Cell Harvest & Isolation

All cells were harvested from Sprague-Dawley male rats under approved conditions and using sterile procedures. DRGs from all spinal levels were taken from embryonic day 18

Sprague-Dawley rats obtained from the CNS Cell Culture Service Center of the Mahoney Institute of Neuroscience. DRGs were dissected using fine forceps to remove individual DRG explants after exposing the rat's spine and removing the spinal cord according to prior methods (Cullen et al. 2012; Melli and Höke 2009) and established lab protocols (Zhang et al. 2017; Zhang et al. 2018). Following harvest, DRGs were stored in Hibernate-E medium supplemented with 1% GlutaMAX and 2% B-27 at 4°C for up to two weeks before plating. In monocellular, isolated culture, DRG feeding medium consisted of Neurobasal feeding medium supplemented with 1% GlutaMAX, 2% B-27, 1% fetal bovine serum (FBS), 10ng/ml 2.5S nerve growth factor, 2mg/ml glucose, 10mM FdU, and 10mM uridine (Cullen et al. 2012; Zhang et al. 2017).

FLS were harvested from both hind knees of a sexually mature adult rat (384g) by finely dissecting the capsular tissue surrounding the knee joints, dicing the isolated capsular tissue as finely as possible, and incubating the diced tissue from both knee capsules together in Dulbecco's Modified Eagle Medium (DMEM) with 10% FBS, 1% Penicillin-Streptomycin (P-S), and 2mg/mL crude bacterial collagenase (C0130; Sigma-Aldrich) for 6 hours at 37°C under gentle agitation (Saravanan et al. 2014). Digested tissue was filtered with a 70µm cell strainer, spun down at 300g for five minutes, and resuspended in feeding medium made up of DMEM with 10% FBS and 1% P-S. That initial passage was taken as passage 0 (P0). Culture medium was changed every other day, and cells were passaged at 90% confluence.

5.3.2. FLS Characterization

After harvest, the cells harvested from capsular ligaments of synovial joints that adhere at P0 are primarily synovial macrophages and fibroblast-like synoviocytes (Rosengren et al. 2007). Studies show that cultures reach ≥95% purity for synovial fibroblasts by passage 3 and reach senescence by passage 9 or 10 (Bartok and Firestein 2010; Bing et al. 2012; Rosengren et al. 2007; Saravanan et al. 2014; Tanner et al. 2015). To ensure culture purity for the FLS cell type and to visualize the morphology of FLS cells, monolayer FLS cultures on glass plates were immunolabeled for the structural filament vimentin and the FLS-specific protein CD90. Separate FLS cultures at P4, P7, and P9 were labeled for characterization. P4, P7, and P9 cultures that were frozen for long-term storage and then thawed were also included in labeling studies to determine if cell viability is maintained through standard freeze-thaw cell culture protocols.

Cultures were blocked in PBS with 10% normal goat serum (Vector Laboratories) and 0.3% Triton-X100 (Bio-Rad Laboratories) for one hour at room temperature and incubated overnight at 4°C with primary antibodies to vimentin (anti-chicken; 1:500; Novus) and CD90 (anti-mouse; 1:100; Abcam). Cultures were then washed in PBS and incubated with the secondary antibodies goat anti-chicken Alexa Fluor 647 and goat anti-mouse Alexa Fluor 546 for two hours at room temperature (both 1:1000; Life Technologies). Finally, cultures were incubated in DAPI solution (1:200; Thermo Fisher) at room temperature for 15 minutes to stain cell nuclei, washed in PBS, washed in distilled water, and then cover-slipped. Labeled culture plates were imaged using the 20X objective of a Leica TCS SP8 confocal microscope (1024X1024 pixels; Leica Microsystems).

FLS exhibit a dendritic and elongated morphology with a few branched cytoplasmic processes characteristic of the reported FLS phenotype (Figure 5.1) (Rosengren et al. 2007). Notably, no cells appear to exhibit the rounder and smaller macrophage morphology (Figure 5.1) (Rosengren et al. 2007). The FLS "characteristic" morphology is most obvious

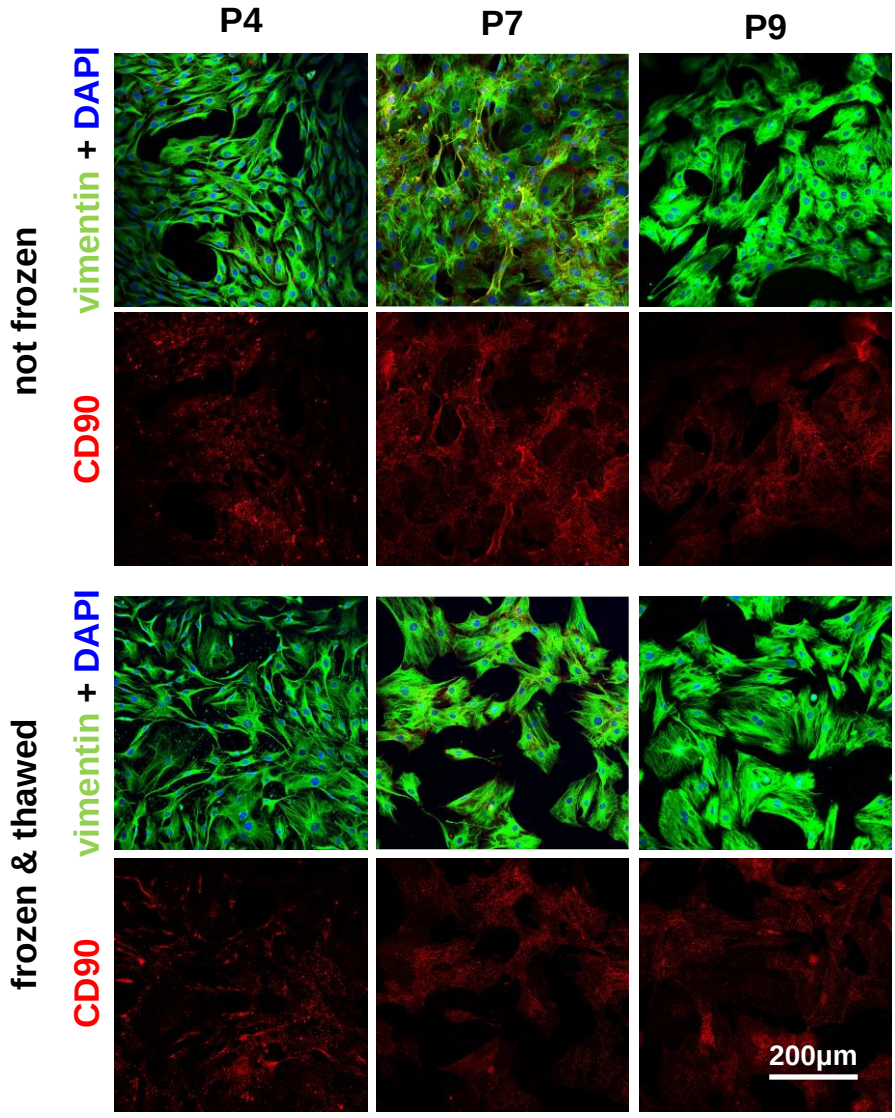

Figure 5.1. Primary-harvested cultures from the rat capsular ligament demonstrate the characteristic FLS morphology by vimentin labeling and express the cell-surface specific protein CD90. Cultures at passages 4, 7, and 9 (P4, P7, P9) are shown both without (top) and with (bottom) freeze-thaw cycles. Scale bar applies to all images.

at P4, with FLS becoming more ovular and exhibiting myofibroblast-type morphology and stress-fibers (Figure 5.1) (Grinnell 2008). All passages exhibit similar morphologies regardless if they underwent freeze-thaw protocols (Figure 5.1), suggesting cells from the same animal harvest could be used over different experiments without altering outcomes due to their long-term storage. FLS label abundantly for CD90 regardless of passage number or freeze-thaw protocol (Figure 5.1), demonstrating that cultures from ligament harvests contain primarily fibroblast-like cells by P4 and all subsequent passages. Based on those findings, future studies utilized FLS from passages 4 and 5 and frozen cells were thawed to achieve the target passage if required.

5.3.2. DRG & FLS Co-Culture Integration

5.3.2.1. Co-Culture Media

Prior to integrating FLS and DRG cell types together, various culture media formulations were investigated to determine the optimal co-culture media for the health and viability of *both* cell types. Since the health of embryonic DRGs depends on growth factors included in the supplemented Neurobasal medium (Melli and Höke 2009), and FLS generally require higher concentrations of FBS than DRGs (10% compared to 1% included in DRG medium) (Rosengren et al. 2007), supplemented Neurobasal medium with higher FBS concentrations was hypothesized to optimize the health of both cell types. Since the lower limit of FBS concentration required for FLS viability is not known, pilot experiments tested FLS viability in response to several media formulations with varying concentration of FBS.

Accordingly, FLS at P3 were cultured in supplemented DMEM (the default medium for monocellular fibroblast cultures) or supplemented Neurobasal medium (the default medium for monocellular DRG cultures) with either 0%, 1%, 2.5%, 5%, or 10% FBS (n=2 wells/group) until 90% confluence. Qualitatively, dead, poorly adhered, and/or floating cells were observed in media formulations with 2.5%, 1%, and 0% FBS, with the number of dead cells increasing with decreasing FBS concentrations. There was no evidence of dead or floating cells in formulations with 5% and 10% FBS. As such, after cultures reached 90% confluence, media supernatants for the 5% and 10% FBS groups were assayed for lactate dehydrogenase (LDH), an enzyme released by cells after damage, using a Pierce Cytotoxicity LDH Assay (Thermo Fisher). The LDH assay was run in triplicate with six wells for each media condition. At 5% FBS concentration, Neurobasal medium released *less* LDH levels (9.7±1.9% of the positive maximum lysis control group) than the 5% FBS DMEM medium formulation (12.4±0.6% cell lysis) (t-test; p=0.015). Percent cell lysis was not different between the formulations with 10% FBS (Neurobasal 17.5±1.5%; DMEM 16.7±0.2%; t-test; p=0.244). Based on these results, a co-culture media formulation of supplemented Neurobasal medium with 5% FBS was chosen.

5.3.2.2. Serum-Starving

The main group of experiments using the co-culture collagen gel model involve measuring MMP levels. However, since serum, including FBS, used in culture media is "messy" and contains unregulated and unknown amounts of proteases including MMPs, serum could confound MMP quantification. Typically, studies account for this effect by "serum-starving" cultures for at least 24 hours prior to assaying MMP levels (Attia et al.

2014; Rogers et al. 2014). As such, pilot studies tested if FLS cells tolerate culture in serum-free conditions or with a 24-hour serum-starvation. Since the experiments assaying MMPs embedded FLS in collagen gels, pilot experiments were performed using FLS-embedded collagen gels.

In order to culture FLS within a 3D collagen environment, P4 FLS cultures were trypsinized, rinsed, and resuspended in rat tail Type I collagen solution (2mg/mL; Corning, Inc) cast in 12-well plates (1mL/well) (Zhang et al. 2018). After 45 minutes allowed for gelation at 37°C, the standard fibroblast DMEM media with 10% FBS and 1% P-S was added to gels. At day-in-vitro (DIV) 1, media was changed to supplemented Neurobasal medium with 5% FBS or 0% FBS (n=3 gels/group); gels underwent a full media change on DIV3 and DIV5. On DIV6, gels underwent three PBS washes for five minutes each, and serum-free supplemented Neurobasal media was added to both groups. On DIV7, gels were fixed with 4% paraformaldehyde for 2-3 hours and blocked in PBS with 10% normal goat serum and 0.3% Triton-X100 for two hours at room temperature. Gels were incubated overnight at 4°C with a primary antibody to vimentin (anti-chicken; 1:250; Novus). Cultures were then washed in PBS and incubated with the secondary antibody goat anti-chicken Alexa Fluor 647 (1:1000; Life Technologies) and DAPI solution (1:200; Thermo Fisher) for two hours at room temperature. Image stacks through a 20μm depth and a 5μm step size were acquired using 10x, 20x, and 40x objectives of a Leica TCS SP8 confocal microscope (1024x1024 pixels; Leica Microsystems).

FLS grown in supplemented Neurobasal media with 5% FBS and a 24-hour serum-free period exhibited healthy morphology and growth in the collagen gel (Figure 5.2). The

FLS morphology was compared to FLS cultured in a 2mg/mL collagen gel cultured in DMEM media with 10% FBS as the "gold-standard" for healthy FLS growth (Figure 5.2). FLS did not appear to grow at all in serum-free conditions for the whole culture period (Figure 5.2). As such, experiments assaying MMP levels using the co-culture model include a 24-hour serum starvation, as opposed to completely serum-free conditions, prior to the DIV on which MMP assays are conducted.

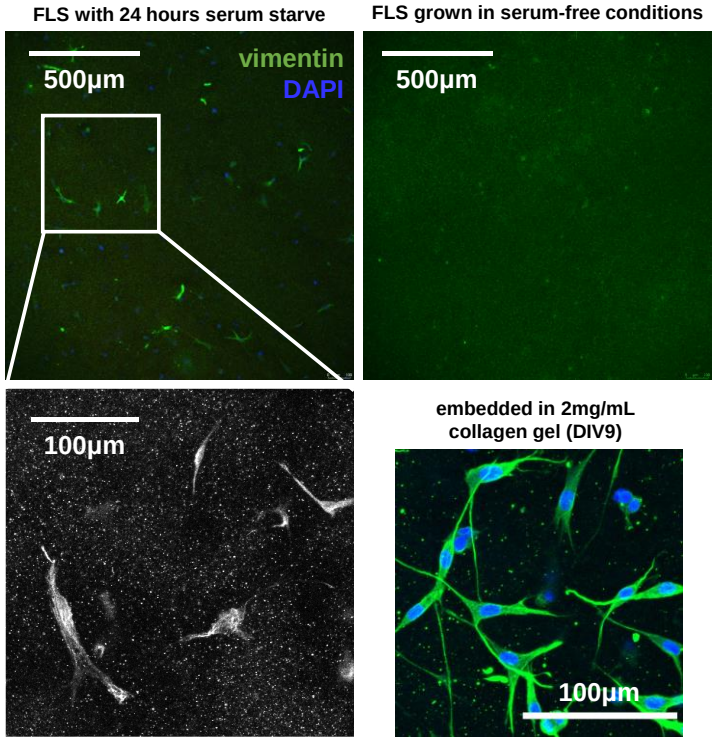

Figure 5.2. Vimentin labeling shows FLS dendritic morphology in a 2mg/mL collagen gel at DIV7 after 24 hours of serum-starving. The inset shows vimentin labeling at high magnification. Vimentin labeling is very faint in FLS grown in serum-free conditions showing a lack of cell survivability in completely serum-free culture conditions. Immunolabeling of vimentin and DAPI in the lower right image demonstrates the "gold-standard" of FLS morphology and health for comparison in a 2mg/mL collagen gel at DIV9 with supplemented DMEM media.

5.3.2.3. Cell Viability & Health Assessment in Co-Culture Protocol

Based on FLS characterization and co-culture media optimization experiments, a protocol was established to integrate FLS and DRGs together in 2mg/mL collagen gels

(Figure 5.3). In that protocol, FLS cultures between P3 and P5 are trypsinized, rinsed, and resuspended in rat tail Type I collagen solution (2mg/mL; Corning, Inc) cast in 12-well plates (1mL/well) (Zhang et al. 2018). After gelation on the day of gel fabrication (DIV0), gels are cultured in the standard fibroblast DMEM media with 10% FBS and 1% P-S. On DIV1, DMEM medium is removed from the top of the gels, and DRGs are seeded on the gel surface for all samples (6-10/gel) in 100µL of Neurobasal feeding medium supplemented with 1% GlutaMAX, 2% B-27, 5% FBS, 10ng/ml 2.5S nerve growth factor, 2mg/ml glucose, 10mM FdU, and 10mM uridine (Cullen et al. 2012; Zhang et al. 2018) (Figure 5.3). After 12-24 hours, fresh Neurobasal feeding medium is added and changed

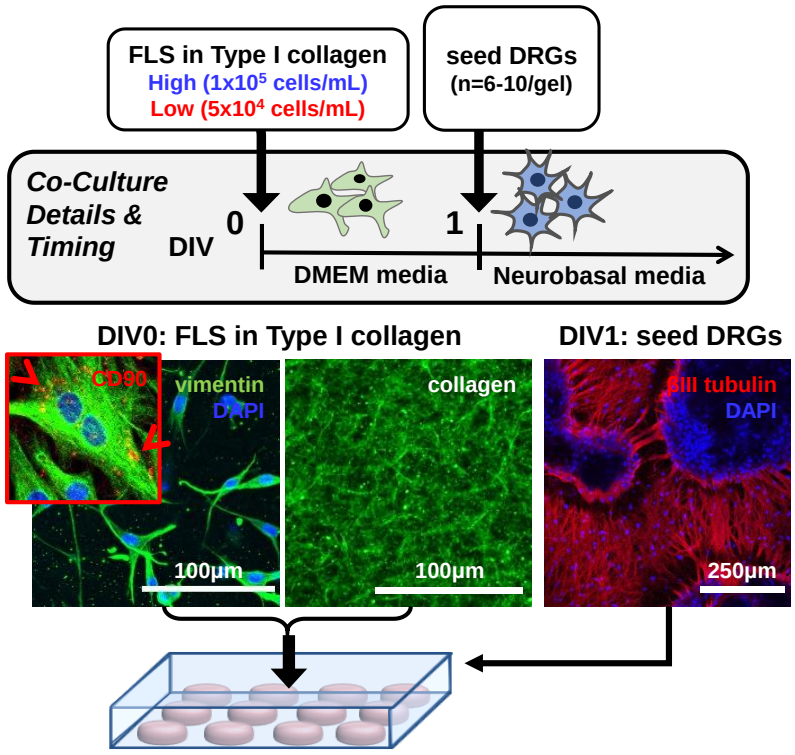

Figure 5.3. Experimental timeline and parameters for co-culture conditions. Fibroblast-like synoviocytes (FLS) are seeded into a Type I collagen gel solution on day-in-vitro (DIV) 0 at either a low or high concentration, followed by DRG seeding at DIV1. Until DRG plating, gels are cultured in supplemented DMEM medium with 10% FBS. After DRG plating, gels are cultured in supplemented Neurobasal medium with 5% FBS until the experimental end point.

every other day. Co-culture gels are cultured seven to 14 days in the studies presented in this thesis, depending on the experimental details and outcomes being measured. Throughout the studies in this thesis, FLS are seeded at concentrations of either $5x10^4$ cells/mL (low) to simulate regions with low FLS cell density or $1x10^5$ cells/mL (high) to simulate regions with high FLS cell density in the capsular ligament (Figure 5.3) (Yamashita et al. 1996).

With an established protocol (Figure 5.3), a live-dead cell assay was performed to verify that integrating the two cell types together does not compromise their viability with co-cultures fabricated at the low and high FLS densities (n=3 co-culture gels/density). A live-dead cell assay using calcein-AM, with green fluorescence indicating live cells, and ethidium homodimer, with red fluorescence indicating dead cells was conducted at the longest anticipated timepoint, DIV14 (Thermo Fisher). Indeed, no evidence of cell death was observed in DRG neurons and negligible cell death was observed in FLS cells (Figure 5.4).

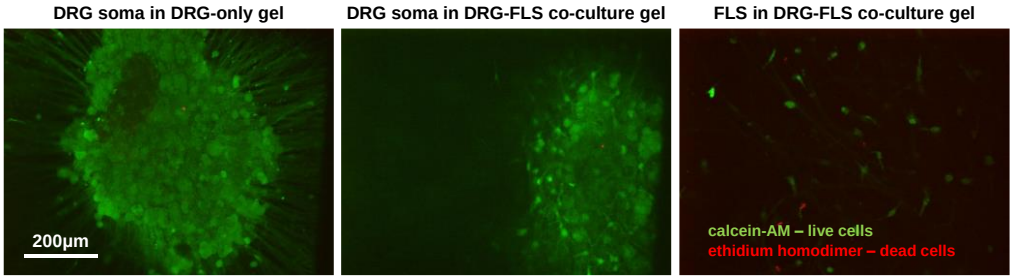

Figure 5.4. Live-dead cell assay assessing cell viability with DRG-FLS co-culture integration at DIV14. There is no evidence of cell death in neurons of the DRG soma with FLS co-culture, as shown by similar green fluorescence in the first image (DRG without co-culture) and the second image (DRG with FLS). Although a few FLS cells show red labeling (dead) with co-culture integration (third image), cells are predominantly alive. The DRG-FLS co-culture collagen gel shown has an FLS concentration of $7.2x10^4$ cells/mL. Scale bar applies to all images.

To ensure that DRG axonal growth was not inhibited by co-culture with FLS cells, neurite outgrowth was quantified by calculating the ratio of the soma diameter to the average axonal length for each DRG in low resolution images where gross DRG morphology can be visualized (Figure 5.5); a neurite outgrowth soma-to-axon length ratio above 0.54 can be taken as healthy and viable DRG neurite growth into the gel (Zhang et al. 2017; Zhang et al. 2018). As such, neurite outgrowth was quantified in DRG cultures in 2mg/mL gels with and without FLS co-culture (n=9/condition) (Figure 5.5). Images from the co-culture model at DIV9 were compared to those from a prior study with no FLS from DIV7 (Figure 5.5) (Zhang et al. 2018). Outgrowth surpasses the threshold for both cases (DIV7 no FLS 0.60±0.16; DIV9 with FLS 0.65±0.12) and is not different (t-test; p=0.45) between the two conditions (Figure 5.5), suggesting that DRG growth is not impeded by FLS co-culture.

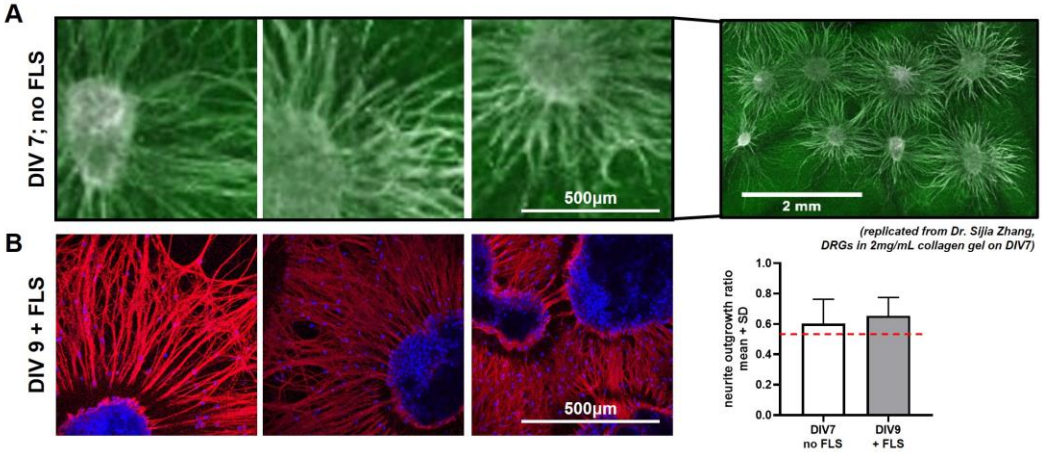

Figure 5.5. DRG neurite outgrowth, quantified as the ratio of the soma diameter to the average axon length is not different between DRGs cultured **(A)** without FLS and DRGs cultured **(B)** with FLS. Images also demonstrate that neurite outgrowth does not differ between DIV7 and DIV9. Data in **(A)** are taken as the healthy control (Zhang et al, *J Orthop Res*, 2018). The outgrowth ratio standard for healthy DRG growth (0.54) is shown (red dashed line) on the bar plot quantification. The low magnification image shows gross DRG morphology at DIV7.

5.4. Distinct Response of Fibroblast-Like Synoviocytes to Stretch

5.4.1 Rationale

Given the functional diversity of fibroblasts derived from different organs and tissues throughout the body (Frank-Bertoncelj et al. 2017), and the lack of studies investigating capsular-ligament derived fibroblasts in the context of load or neuronal signaling, the effect of primary FLS cells on matrix mechanics and microstructure in the 3D collagen gel model stretched to tensile failure was characterized. MMP-1 immunolabeling was assessed in a subset of co-culture collagen gels after stretch to gain insight into how FLS may regulate MMP-1 in the context of stretch and in a shared microenvironment with neuronal cells. All experiments were run in parallel with fibroblasts from the NIH 3T3 immortalized cell line. Since 3T3-collagen interactions in 3D gels are more extensively studied in the literature than FLS, and are known to exert mechanical forces on their surrounding collagen fibers (Mohammadi et al. 2015; Simon et al. 2012), 3T3 outcomes served as a comparison group for better contextualizing the findings with FLS.

To test the effect of cell concentration within the limits of primary FLS growth and to simulate the variable region-dependent concentrations in the capsular ligament (Yamashita et al. 1996), two FLS concentrations of $5x10^4$ and $1x10^5$ cells/mL were used. Although those concentrations are on the low end of the range reported by studies that embed fibroblasts in collagen gels (Bing et al. 2012; Evans and Barocas 2009; Nobe et al. 2000; Sander et al. 2011; Saravanan et al. 2014; Simon et al. 2012; Thomopoulos et al. 2007), $5x10^4$ and $1x10^5$ cells/mL have differential effects on matrix mechanics under

failure (Evans and Barocas 2009). As such, they were expected to be sufficient to reveal any concentration-dependent differences across outcomes.

Macroscopic gel mechanics were quantified using force-displacement curves and stiffness using stretch-to-failure tests. Force and regional strains were compared at several displacement points during loading. Polarized light imaging integrated with the mechanical test setup enabled analysis of network microstructure through high-speed capture of collagen alignment maps at those same displacement points during loading (Quinn and Winkelstein 2009; Tower et al. 2002; Zhang et al. 2016). Collagen fiber orientation was quantified using circular variance (CV), with a lower CV indicating a tighter clustering and a higher degree of fiber alignment (Miller et al. 2012; Zhang et al. 2016). Since the relative expression of MMP-1 in different host cells after capsule stretch is also unknown, separate neuron-fibroblast co-cultures seeded with either FLS or 3T3 cells were loaded in tension until failure and assayed for their MMP-1 expression. MMP-1 expression was quantified in the DRG neurons and the FLS/3T3 fibroblasts to gain insight into relative MMP-1 responses across cell type in the co-culture model.

5.4.2. Methods

5.4.2.1. Mechanical Testing & Data Analyses

FLS and NIH/3T3 fibroblasts were maintained in DMEM with 10% FBS and 1% P-S. On passage 4, cultures were separately passaged and resuspended in a 2mg/mL rat tail Type I collagen solution (Corning) at a concentration of either $5x10^4$ cells/mL (low FLS n=6; low 3T3 n=5) or $1x10^5$ cells/mL (high FLS n=5; high 3T3 n=6) (Figure 5.6A). Collagen gels were cast in 12-well plates (1mL/well) and allowed to gel at 37°C, after

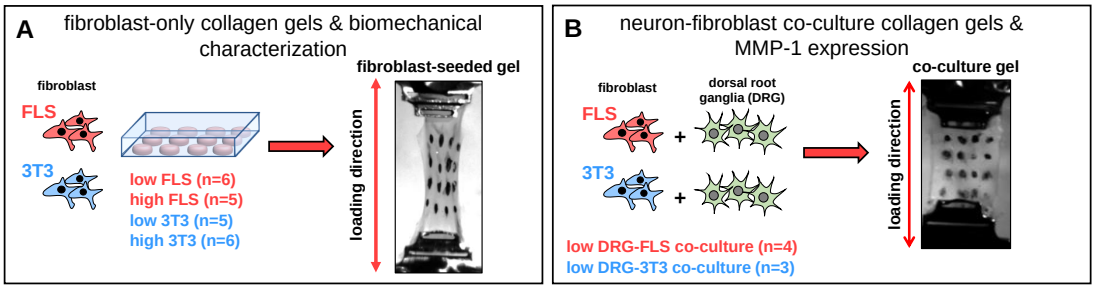

Figure 5.6. Study design for experiments comparing the **(A)** biomechanical behavior and **(B)** MMP-1 expression of FLS fibroblasts to 3T3 fibroblasts after failure stretch. **(A)** The multiscale mechanics of FLS and 3T3 fibroblast-seeded collagen gels are compared under uniaxial tension at a low ($5x10^4$ cells/mL) and high ($1x10^5$ cells/mL) concentration. In **(B)**, FLS and 3T3 cells are co-cultured with DRGs at only a low concentration to investigate MMP-1 expression and its cellular localization after failure in uniaxial tension.

which warm media was added. Fibroblast-seeded gels were cultured until DIV9 in DMEM media.

Fibroblast-only seeded collagen gels (Figure 5.6A) were removed from plates on DIV9 and cut into a vertical strip (21mmx8mm). Using ink, a grid of markers was added to the gel for strain tracking (Zhang et al. 2016). Gels were loaded into the grips of a planar test machine (574LE2; TestResources) and immersed in a 37°C PBS bath (Figure 5.7). Grips were attached to controllable actuators equipped with 500g load cells. The mechanical test setup was integrated with a polarized light imaging system (Quinn and Winkelstein 2009; Tower et al. 2002; Zhang et al. 2016) and two high-speed cameras (Phantom-v9.1; Vision Research) to acquire pixel-wise alignment maps and to track markers during loading (Figure 5.7). Gels underwent uniaxial displacement to failure at 0.5mm/sec, with force and displacement data (200Hz) synchronized with high-speed imaging (500Hz) (Figure 5.7). Immediately after failure, gels were removed from the grips and fixed for two hours in 4% paraformaldehyde.

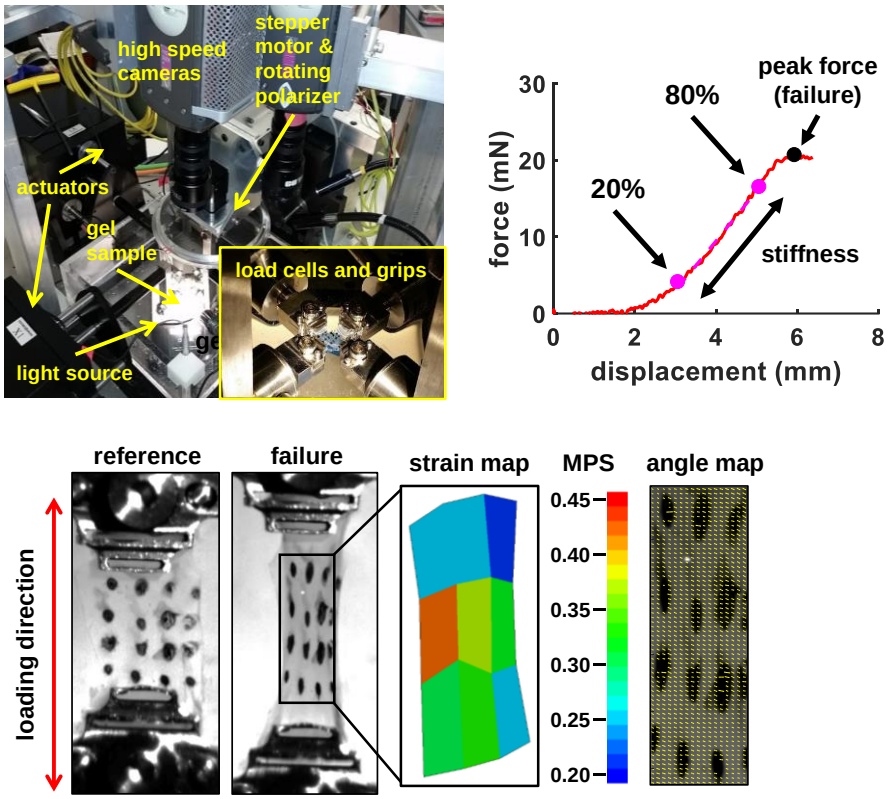

Figure 5.7. Mechanical testing setup with an integrated polarized light imaging system. During loading, each gel is affixed in grips for uniaxial tension to failure and marked with a grid of dots for strain tracking. For each gel, peak force defines the failure and stiffness is calculated as the linear slope of the force-displacement curve between 20% and 80% of the peak force. Maximum principal strain (MPS) and collagen alignment maps are extracted at the displacement points corresponding to 20% of peak force, 80% of peak force, and at failure. Strain and collagen alignment maps are shown for a 3T3-embedded collagen gel at failure.

Force data were filtered using a 10-point moving average filter (Zhang et al. 2016). The maximum force from the force-displacement curve was defined as failure and designated as the peak force (Figure 5.7). Stiffness was calculated as the slope of the loading curve from 20-80% of the peak force (Figure 5.7) (Lee et al. 2006). Marker positions were digitized using Fiji software (NIH) and the high-speed images taken before loading (reference), at 20% of peak force, at 80% of peak force, and at 100% of peak force (failure) (Figure 5.7). LS-DYNA (LSTC) was used to calculate the maximum principal

strain (MPS) for each element defined by the grid and averaged across all elements for each gel (Zhang et al. 2016). Collagen alignment maps were generated at the same points along the loading curve as MPS and used to calculate the circular variance (CV) of the spread of fiber angles (Miller et al. 2012; Zhang et al. 2016); CV at failure was normalized to the reference CV for each gel. Differences in stiffness and reference CV were assessed between gels with different cell types and by concentration with a two-way ANOVA. The effect of cell type on force, MPS, and normalized CV at the points during loading was compared between FLS- and 3T3-seeded gels for each concentration, separately, using a repeated-measures ANOVA.

5.4.2.2. MMP-1 Immunolabeling in Co-Cultures

Separate Type I collagen gels (2mg/mL) were fabricated as co-cultures with DRGs (6-10/gel) and either FLS or NIH/3T3 fibroblasts (low DRG-FLS n=4; low DRG-3T3 n=3) (Figure 5.6B). This experiment probed whether MMP-1 is differentially regulated by FLS compared to 3T3 fibroblasts under load by measuring MMP-1 expression in both fibroblast types in response to the same mechanical stretch. As such, all gels in this subset were fabricated with fibroblasts at the lower $5x10^4$ cells/mL concentration based on biomechanical results from stretch experiments with the fibroblast-only seeded collagen gels (Figure 5.6A) showing FLS and 3T3-seeded gels have the same mechanics at a low, but not high, concentration (details presented in Section 5.4.3.1 following). Gels were fabricated according to the optimized co-culture protocol (Figure 5.3).

On DIV7, co-culture gels containing either DRGs and FLS fibroblasts or DRGs and 3T3 fibroblasts (Figure 5.6B) were prepared for mechanical testing and stretched to failure

in uniaxial tension as described in Section 5.4.2.1. Force, displacement and MPS were quantified at failure as described above (Figure 5.6). Stiffness was calculated as the slope of the force-displacement curve at 20-80% peak force (failure) (Figure 5.6). All mechanical parameters were compared between groups using separate t-tests.

Immediately after failure, gels were fixed in 4% paraformaldehyde and immunolabeled overnight with primary antibodies to MMP-1 (1:250; Proteintech), vimentin as a structural protein for fibroblasts (1:250; Novus) and βIII tubulin as a structural protein for neurons (1:500; Biolegend). Unstretched gels (DRG+FLS n=2; DRG+3T3 n=1) were also labeled. Confocal images were taken of the DRG axons, DRG somas, and fibroblasts (n=1-3/cell type/gel).

The extent of MMP-1 was evaluated overall and by cell-type (Figure 5.8). MMP-1 labeling was rated by five blinded graders as either absent (0) or present (1) (Figure 5.8) (Villasmil et al. 2017), with the determination of MMP-1 taken as the majority rating.

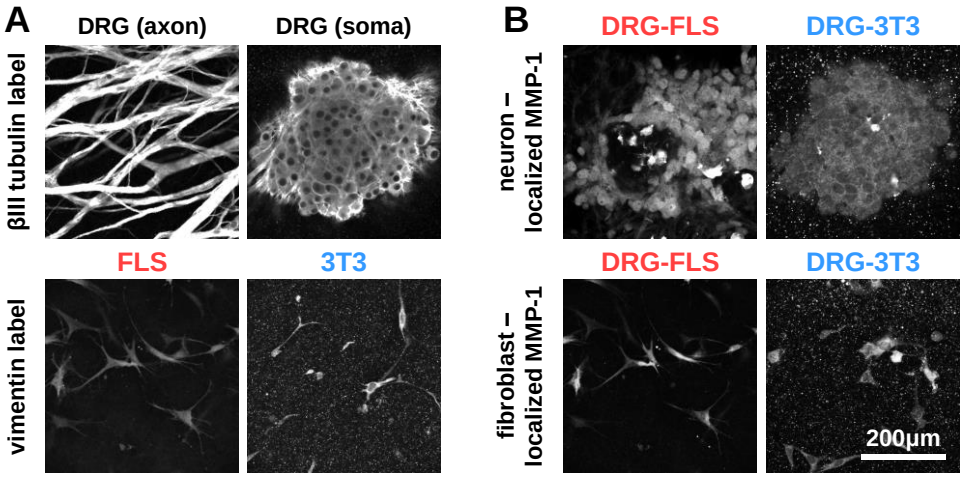

Figure 5.8. (A) βIII tubulin and vimentin immunolabels identify DRG soma/axons and fibroblasts, respectively, in co-culture gels. MMP-1 immunolabeling in **(B)** shows exemplary images with positive labeling in DRG-FLS co-cultures (left) and DRG-3T3 co-cultures (right) in regions localized to DRG neurons (top) and fibroblasts (bottom). The scale bar applies to all images.

MMP-1 ratings in all fibroblasts and DRG images were analyzed in separate contingency tables for stretched and unstretched conditions by co-culture type. Additional contingency tables subdivided the aggregate data for stretched gels to compare MMP-1 ratings between co-culture type for fibroblast images and DRG images, separately. The effect of co-culture type (DRG-FLS vs. DRG-3T3) on contingency table outcomes were tested with two-tailed Fisher's Exact tests.

5.4.3. Results

5.4.3.1. Multiscale Mechanics in FLS & 3T3-Seeded Collagen Gels

In 2D culture, FLS exhibit an elongated, polygonal, and branched morphology, while the 3T3 cells are rounder but still branched (Figure 5.9). A high FLS concentration seems to induce contraction of the gel causing it to pull away from the wall of the well

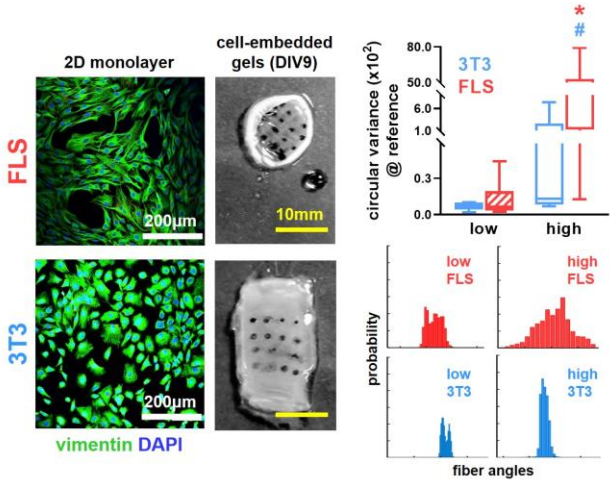

Figure 5.9. Labeling of the intermediate filament vimentin in fibroblasts shows elongated FLS morphology and rounded 3T3s in 2D culture. Macroscale photographs of collagen gels after DIV9 for the $1x10^5$ cells/mL (high) concentration show the gel compaction observed in FLS, but not 3T3, embedded gels. The collagen microstructure after nine days in culture, prior to loading, is significantly more disorganized in FLS-collagen gels at a high concentration. Histograms show the spread of fiber angles for exemplary FLS and 3T3 gels at both concentrations, with the high FLS group exhibiting the widest spread of fiber angles. Quantification of CV reflects this, with high FLS gels exhibiting significantly greater CV than low FLS (*p=0.018) and high 3T3 (#p=0.037).

during culture, producing shrunken gels with a curled circular edge (Figure 5.9). Neither gel contraction nor wall separation were observed for the 3T3 groups, nor consistently for the low concentration FLS group. Before loading, the collagen organization in the high FLS gels is different from its low concentration counterpart (p=0.018) and from the high 3T3 gels (p=0.037), indicating a larger spread of collagen fiber angles (Figure 5.9).

Although force-displacement curves are similar between gels with both cell types at a low concentration, the failure force is consistently higher for 3T3 than for FLS gels made using a high cell concentration (Figure 5.10). Although the forces at both 80% and 100% of the peak force (Figure 5.10) are 4.1-fold higher for gels with 3T3 compared to

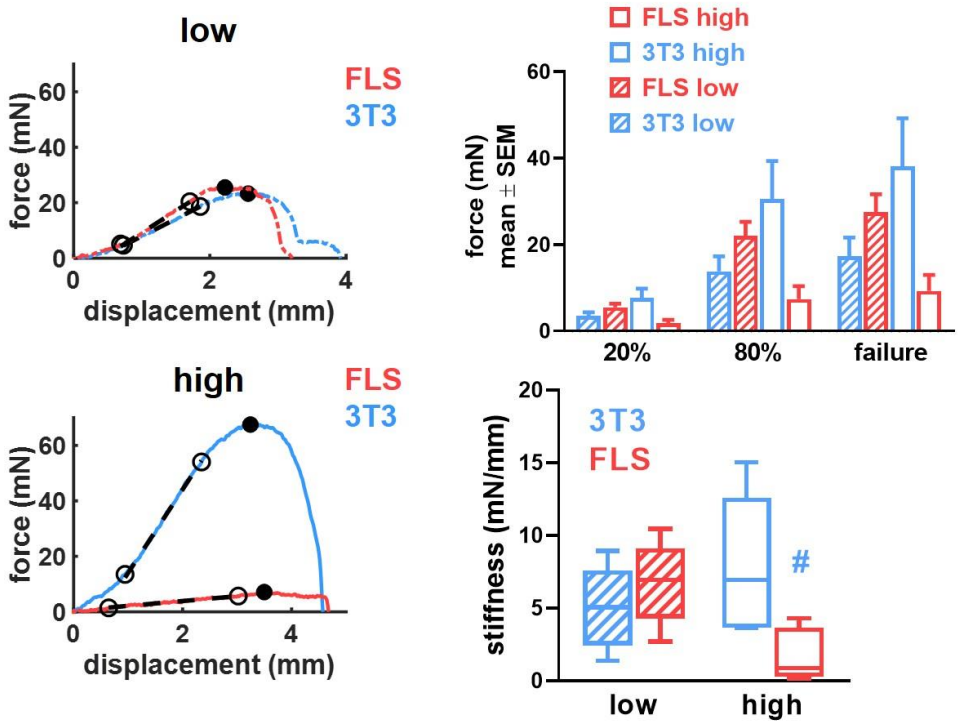

Figure 5.10. Exemplar force-displacement curves show similar biomechanical behavior between cell types at a low concentration, but markedly different curve shapes at a high concentration. FLS and 3T3 gels do not exhibit differences in force at a low or high concentration despite FLS gels having substantially lower peak forces than 3T3 gels. Despite no significant differences in force, the differences in curve shape are captured in stiffness, with the high FLS gels having significantly lower stiffness than 3T3 gels at the same concentration (#p=0.031).

FLS at a high concentration, this difference is not significant. The stiffness of FLS gels at a high concentration, however, is significantly lower than the stiffness of 3T3 gels at the same concentration ($p=0.031$) (Figure 5.10). MPS is significantly different between cell types at the high concentration, only at 80% of loading and at peak force (Figure 5.11). Although peak force is lower in the high FLS group, the MPS sustained in high FLS gels is greater ($p<0.001$) than at a matched concentration of 3T3 cells (Figure 5.11). Average MPS at 80% of peak force is also different between cell types at the high concentration ($p<0.001$).

Cell type does not affect CV at either concentration at any of the displacements investigated (Figure 5.12). Yet, evaluation of the change in CV throughout loading for individual FLS-seeded gels reveals that the low and high concentrations exhibit differential trends. In particular, low FLS gels continue to reorganize throughout loading, as indicated

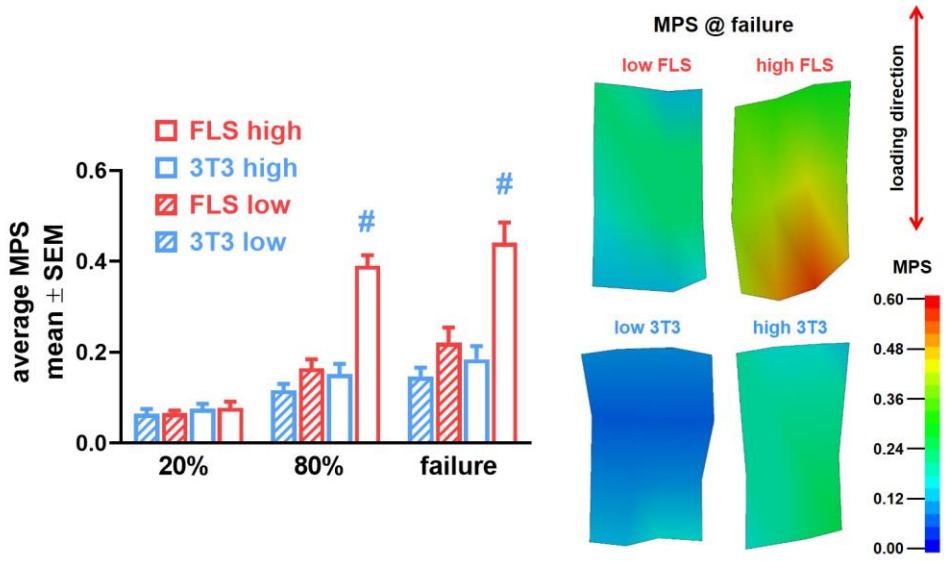

Figure 5.11. Average maximum principal strain (MPS) is the same for both fibroblast types at a low concentration; yet, increases significantly at 80% of failure (#$p<0.001$) and at failure (#$p<0.001$) for high FLS gels compared to high 3T3 gels. Strain maps at failure showing hot spots of high magnitude MPS sustained by a high FLS collagen gel.

by an increase in CV and a greater degree of reorganization (Figure 5.12). High FLS gels, in contrast, sometimes reorganize throughout loading and sometimes become *less* organized at displacements closer to failure, as indicated by a decrease in normalized CV (Figure 5.12). The multiscale mechanical data including force-displacement curves, MPS fields, and CV quantification for each gel in this study are summarized in Appendix G.

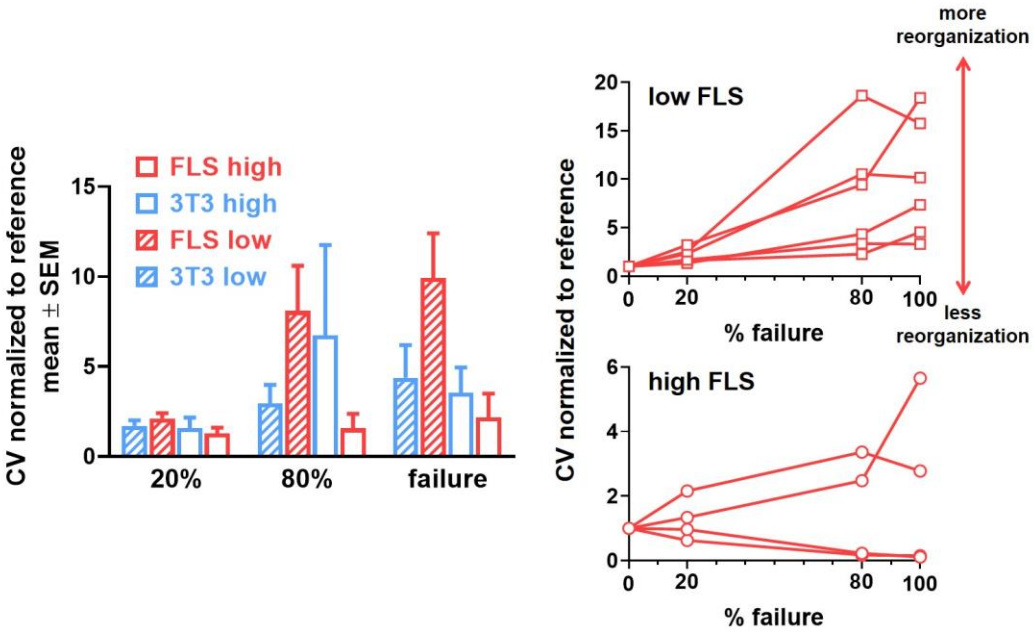

Figure 5.12. Circular variance (CV) normalized to the reference loading state does not vary with concentration or cell type. Despite this, differential microstructural kinematics are observed between individual sample curves in the low and high FLS groups, whereby all low FLS gels disorganize during tensile stretch, but not all high FLS gels follow this behavior.

5.4.3.2. Differential MMP-1 Expression Between FLS & 3T3 Co-Cultures After Stretch

Failure mechanics are the same for both DRG-FLS and DRG-3T3 co-culture collagen gels, with no differences ($p>0.11$) in failure force (34.1±17.3mN), displacement (5.2±1.8mm), MPS (0.25±0.07%), nor stiffness (9.0±4.7mN/mm). All macroscale and strain data are detailed in Appendix G. Despite having the same mechanics, overall MMP-

1 labeling is different (p=0.01) in stretched gels between the different co-culture systems (Table 5.1). The incidence of positive MMP-1 labeling is higher in DRG-FLS stretched gels (18 of 25 images) than in DRG-3T3 stretched gels (7 of 22 images) (Table 5.1). Unstretched levels are not different (p=0.68) between types of co-cultures (Table 5.1). The greater extent of positive MMP-1 labeling that is observed in co-cultures with FLS than in those with 3T3 cells appears to be driven by the FLS fibroblasts, since FLS co-cultures have greater MMP-1-positive images in fibroblast-localized images (11 of 12 images) than 3T3 gels (2 of 8 images) (p<0.01). Conversely, there is no difference (p=0.45) in stretched DRGs (5 of 14 images in FLS+DRG; 7 of 13 images in 3T3+DRG) (Table 5.1). All images and their incidence of positive labeling are summarized in Appendix G.

Table 5.1. Quantification of MMP-1 labeling in stretched DRG-FLS & DRG-3T3 co-culture gels

stretched

	-	+
DRG-FLS	7	18
DRG-3T3	15	7

stretched – fibroblast images

	-	+
DRG-FLS	1	11
DRG-3T3	6	2

unstretched

	-	+
DRG-FLS	6	12
DRG-3T3	2	7

stretched – neuronal images

	-	+
DRG-FLS	6	7
DRG-3T3	9	5

5.4.4. Discussion

At the higher concentration used in this study, FLS-embedded gels exhibit different macroscale mechanical behavior, stiffness, and strain fields than 3T3-embedded gels (Figures 5.10 & 5.11). High FLS gels contract, separating from their boundary wall, an effect not observed by 3T3s (Figure 5.9). Although this study did not investigate the mechanism by which FLS may be shrinking the gel, fibroblast-mediated gel contraction is

postulated to occur by cell contraction, cell traction forces, or initial cell elongation and spreading (Dallon and Ehrlich 2008), any of which may be occurring in this system (Figure 5.9). ECM remodeling or degradation by FLS at a high concentration may also be responsible for gel contraction, the more disorganized matrix at reference, and/or the decreased gel stiffness (Figures 5.9 & 5.10) (Grinnell and Petroll 2010; Hinz 2013). Dermal fibroblasts cultured in a 2mg/mL collagen gel at the same concentrations used in this study have been shown to *increase* the gel modulus by 1.12 and 3 times, respectively, from a no cell control, after only one day in culture (Evans and Barocas 2009). In contrast with that effect, FLS cells *decrease* the gel stiffness at higher concentrations (Figure 5.10). Although strain has been shown to increase with CV in collagen gels without fibroblasts (Zhang et al. 2016), this is not true in the presence of a high concentration of FLS; the MPS for high FLS is greater than high 3T3, but the normalized CV is not different (Figures 5.11 & 5.12). This may be due to FLS exhibiting cell traction forces on the gel (Dallon and Ehrlich 2008), although visualization of cells within the gel is necessary in order to conclude the exact cell-matrix interactions that may be occurring.

This study demonstrates a concentration-dependent effect of FLS comparisons to 3T3 cells on collagen gel stiffness, regional strains, and microstructure, both before and after loading (Figures 5.9-5.12). Since different regions of the synovial lining and capsular ligament have varying densities of embedded FLS (Yamashita et al. 1996), a concentration-dependent effect of FLS could have implications for mechanosensitive cells in regions with varying FLS cell density. For example, in this same collagen gel model, absent fibroblasts, nociceptive related signaling has been found to be triggered in embedded nerve fibers by

strains above 14-40% and concurrent with reorganization of the collagen network (Zhang et al. 2016; Zhang et al. 2018). The results of the current study suggest that under traumatic loading, nerve fibers in FLS-dense regions may be subjected to different regional strain fields *and* microstructural changes than those in FLS-sparse regions (Figures 5.11 & 5.12).

Despite comparable mechanical responses to load, co-cultures with FLS fibroblasts have more MMP-1 than those with 3T3 fibroblasts (Table 5.1), suggesting that FLS and 3T3 fibroblasts may upregulate MMP-1 after stretch by different mechanisms. Furthermore, differential expression in fibroblast-localized regions from neuron-localized regions (Table 5.1) suggests a unique relationship between FLS fibroblasts and MMP-1 in trauma-induced nociception. Notably, only one concentration of fibroblasts was examined here to achieve comparable mechanical insults, and it is possible that FLS show concentration-dependent effects on cellular responses under load. Indeed, this is likely given concentration-dependent biomechanical behavior (Figures 5.10 & 5.11) and variable microstructures during culture (Figure 5.9 & 5.12); concentration-dependent effects are investigated further in the studies in Chapter 6. Collectively, findings demonstrate that FLS cells exhibit a unique phenotype and effect on matrix mechanics and MMP-1 expression after failure stretch that is distinct from NIH/3T3 cells. This work emphasizes the importance of considering FLS in models of the capsular ligament and supports the use of primary FLS, versus fibroblasts from another source, in studies aiming to mimic the capsular ligament of synovial joints.

5.5. Effects of Collagenase Exposure in the Co-Culture Model of Ligament

5.5.1. Rationale

Injecting crude bacterial collagenase in the facet joint and knee leads to degradative changes in the bone and cartilage of those joints and behavioral sensitivity, in part, are attributed to such joint damage (Adães et al. 2014; Gou et al. 2019; Yeh et al. 2008). Yet, the in vivo study detailed in Chapter 4 shows that intra-articular collagenase induces behavioral sensitivity (Figure 4.5) and neuronal dysregulation (Figures 4.7-4.9) without any evidence of substantial joint damage (Figure 4.3 & 4.6). The same severe joint damage is not hypothesized to be detected in the model presented because it used a purified bacterial collagenase, which differs from the crude collagenase used in prior work (Adães et al. 2014; Gou et al. 2019; Yeh et al. 2008). The combination of proteolytic enzymes in crude collagenase catabolize extracellular molecules in addition to collagen, and in doing so, induce severe joint degeneration (Grenier et al. 2014). In contrast, the purified formula consists of two proteases with collagenolytic activity toward the alpha helices that comprise Type I, II, and III collagen and thus act *only* on collagen molecules (Fields 2013). Since bacterial collagenase does not act *directly* on afferent fibers, FLS cells, or other cellular populations in joint tissues, purified collagenase is hypothesized to induce sustained sensitivity (Figure 4.5) and neuronal dysregulation (Figures 4.7-4.9) by acting on the collagen molecules in joint tissues. But, since tissue-level histological changes are not detected after collagenase (Figure 4.3 & 4.6), collagen molecular-level changes in vivo are posited to occur at a smaller scale than is detectable by histological methods. To test

whether purified collagenase changes the collagen microstructure and initiates neuronal dysregulation, the bacterial collagenase exposure was repeated using the in vitro co-culture collagen gel model to enable measure higher-resolution cell and fiber responses.

5.5.2. Methods

5.5.2.1. Bacterial Collagenase Exposure

Type I collagen gels (2mg/mL) were fabricated with FLS (~$5x10^4$ cells/mL) and DRGs (6-10/gel) (Figure 5.3) and cultured until DIV10. On DIV10, co-culture gels were incubated with 60U of purified bacterial collagenase (CLSPANK; Worthington) in DMEM (collagenase) or DMEM only (vehicle) for 20 minutes, since gel mechanics are altered by collagenase exposures for 15-35 minutes (Sperry et al. 2017) and 20 minutes allows enough time to detect changes in neuronal firing patterns (Allen et al. 2016). Separate co-cultures were designated to exposure experiments performed under a physiological, constrained hold (Figure 5.6A) and under free-floating conditions (Figure 5.6B).

5.5.2.2. Constrained Physiological Hold & Mechanical Analysis

To assess the effects of collagenase on multiscale mechanics, a group of gels (collagenase n=3; vehicle n=3) were cut into cruciforms and marked with a grid to track surface strains (Figure 5.13A) (Zhang et al. 2017). Gels were immersed in a 37°C PBS bath and gripped biaxially in a planar test device (Figure 5.13A) (574LE2; TestResources). PBS was aspirated to expose the gel surface to air, and slack in the gel was removed from the arms (<2mN). Collagenase or vehicle solution (600µL) was pipetted onto the gel's center

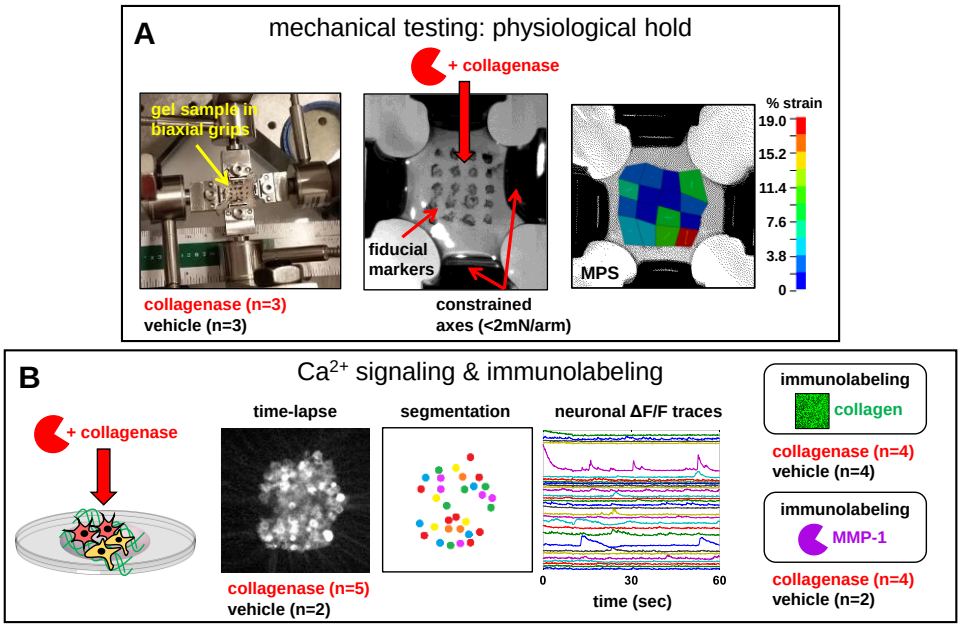

Figure 5.13. Study design for bacterial collagenase exposure experiments in the co-culture model of the capsular ligament. Co-cultures undergo a 60U, 20-minute exposure either during **(A)** a constrained biaxial hold to simulate the boundaries of capsular ligaments in vivo or **(B)** exposure during free-floating conditions. **(A)** Force and high-speed image data were collected during the hold; fiducial markers were used to calculate maximum principal strain (MPS) across the gel surface. An exemplary co-culture gel in biaxial grips shows an overlaid elemental strain field with MPS magnitudes reaching 19%. **(B)** Live-cell calcium (Ca^{2+}) was performed before, and 20 minutes, after collagenase exposure. DRG time-lapse images were manually segmented to delineate neurons and the normalized fluorescence traces ($\Delta F/F$) were computed for each segmented neuron. Colored fluorescence traces match the segmented neuron colors. Co-cultures exposed to collagenase in free-floating conditions were immunolabeled for Type I collagen and MMP-1.

and left for 20 minutes (Figure 5.13A); the solution was observed *not* to evaporate during that time period. The test device was integrated with high-speed cameras (Phantom-v9.1; Vision Research; 200fps) to track the grid of surface markers. Force data (10Hz) were continuously acquired, and high-speed images (500Hz) were taken immediately before (baseline) adding any solution and at 20 minutes after. The change in force from baseline was computed for each arm and averaged for each gel. Marker positions were digitized (Fiji software; NIH) at the same timepoints for elemental strain analyses (Figure 5.13A).

LS-DYNA (LSTC) software was used to calculate the maximum principal strain (MPS) for each gel.

5.5.2.3. GCaMP6f Transduction, Calcium Imaging & Data Analysis

To measure neuronal activity during collagenase exposure, DRG neurons were transduced on DIV2 by adding the adeno-associated virus expressing GCaMP6f (#AAV1.Syn.GCaMP6f.WPRE.SV40; 1:4,000) directly into the culture media. GCaMP6f rapidly and transiently fluoresces with calcium influx (Chen et al. 2013) and enables the visualization of calcium (Ca^{2+}) transient waveforms in real-time. Furthermore, the GCaMP6f used here is under control of the Synapsin promoter that exclusively transduces neurons (Chen et al. 2013; Patel et al. 2015). In a subset of gels incubated in collagenase (n=5) or vehicle (n=2), time-lapse images were acquired (20Hz for 1 minute) at baseline and after 20 minutes with a Nikon Eclipse TE2000U spinning disk confocal microscope (CSU-10b; Solamere Technologies; Salt Lake City, UT) in an environmental chamber held at 37°C and 5% CO_2 (Figure 5.13B) (Patel et al. 2015). For each gel, DRGs (1-2) were imaged, maintaining a constant field of view. The same DRGs were imaged at both baseline and 20 minutes so that time-lapse data tracked the same DRGs over time.

Fluorescence data were analyzed using FluoroSNNAP in MATLAB (MathWorks) (Patel et al. 2015). Individual neurons (n=28-33) were segmented in each DRG (Figure 5.13B); although neurons in the same DRG were segmented at both timepoints, the segmentation of identical neurons could not be maintained due to motion artifact caused by collagenase-induced gel degradation during the exposure. Only neurons with a cell nucleus distinct from the cytosol were selected in order to ensure that only living neurons

were analyzed. The number of Ca^{2+} events was counted using a template-matching algorithm to identify Ca^{2+} waveforms that are known to match those that occur with action potentials (Patel et al. 2015; Schultz et al. 2009). The total Ca^{2+} events across all segmented neurons was calculated for each DRG and concatenated for each group at each timepoint.

5.5.2.4. Immunolabeling & Image Analyses

To assess the effect of collagenase on the amount of collagen and its organization, a subset of gels (collagenase n=4; vehicle n=4) was fixed (4% PFA) after 20 minutes of incubation at 37°C and immunolabeled for Type I collagen using a free-floating protocol. Gels were triple washed in PBS, blocked in PBS with 10% normal goat serum (Vector Laboratories) and 0.3% Triton-X100 (Bio-Rad Laboratories) for two hours at room temperature, and incubated overnight at 4°C with a primary antibody to collagen (mouse; 1:400). Gels were triple-washed and incubated with the Alexa Fluor secondary antibody goat anti-mouse 488 for two hours at room temperature (1:1,000; Thermo Fisher Scientific), triple washed, and then cover-slipped with Fluorogel (Electron Microscopy). Image stacks (n=4/gel) were acquired at 10μm steps over a 50μm depth at 40x with a Leica TCS SP8 confocal microscope. A single maximum projection image from each stack was analyzed to quantify the number of positive pixels (Ita et al. 2017a). Collagen fiber orientations were analyzed using a Fourier transform method to compute the magnitude and direction of the principal orientation axes of the image (Sander and Barocas 2009); the anisotropy index was calculated from the ratio of principal axes on a scale from isotropic (random; 0) to aligned (1) (Sander and Barocas 2009).

Separate gels incubated in collagenase (n=4) or vehicle (n=2) were fixed (4% PFA) after 20 minutes of incubation at 37°C to assess effects of collagenase on MMP-1 expression using immunolabeling. Gels were fluorescently labeled using the same protocol as was used for the collagen immunolabel with primary antibodies to MMP-1 (rabbit; 1:200; Proteintech), βIII tubulin (anti-mouse; 1:300; Biolegend), and vimentin (chicken; 1:400; Novus). After incubation with the Alexa Fluor secondary antibodies goat anti-rabbit 555, goat anti-mouse 488, and goat anti-chicken 633 (all 1:1,000; Thermo Fisher), gels were incubated in DAPI (1:200; Thermo Fisher) at room temperature for 15 minutes to stain cell nuclei. Images were acquired in regions of the DRG axons and somas (n=5/gel) and in regions with only FLS cells (n=2-3/gel), at 40x with a Leica TCS SP8 confocal microscope. Labeling above a threshold for positive MMP-1, βIII tubulin, and vimentin was separately quantified using a custom densitometry script in MATLAB. MMP-1 co-localization to βIII tubulin and vimentin was computed, separately, to quantify neuronal and fibroblast-localized MMP-1, respectively. MMP-1-βIII tubulin co-localized pixels were normalized to total βIII tubulin, and MMP-1-vimentin co-localized pixels to total vimentin as a measure of neuronal and fibroblast-localized MMP-1. The MATLAB scripts for single channel and co-localization are provided in Appendix B.

5.5.2.5. Statistical Analyses

All statistical analyses were performed with $\alpha=0.05$ using JMP Pro v14 (SAS Institute Inc.; Cary, NC). Normality was tested using a Shapiro-Wilk goodness-of-fit test for a normal continuous fit on the residuals of all outcomes. T-tests compared changes in force and MPS from baseline at 20 minutes. Differences between the distribution of

calcium events were tested with a non-parametric Wilcoxon test, separately at each of baseline and 20 minutes. A Wilcoxon test assessed the differences in collagen labeling between groups. A t-test compared anisotropy index between gel exposures. Neuronal and fibroblast-localized MMP-1 labeling was compared using a Wilcoxon test since those data were non-normally distributed.

5.5.3. Results

Collagenase exposure significantly decreases collagen labeling (p=0.008), with collagenase-incubated gels (5.76±7.72%) exhibiting a 6-fold decrease relative to gels held in a control solution (36.28±26.61%) (Figure 5.14), suggesting substantial Type I collagen

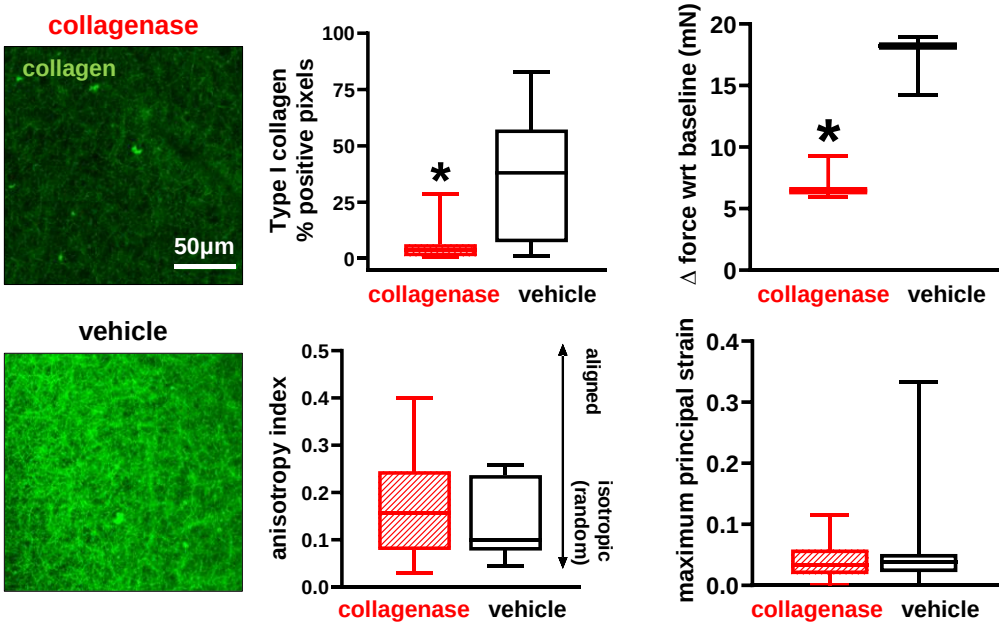

Figure 5.14. Effects of collagenase exposure on the collagen network. Type I collagen labeling (green) after 20 minutes of collagenase incubation is significantly reduced from levels with vehicle exposure (Wilcoxon test; *p=0.008); in contrast, fiber orientation is unchanged with collagenase exposure (two-tailed t-test; p=0.380). Significantly less force is required to maintain a constrained hold with collagenase treatment (t-test; *p=0.005); yet, the maximum principal strain sustained by the gel surface is not affected by collagenase. Box-and-whisker plots show horizontal lines representing the first (lower) quartile, median, and third (upper) quartile of the data; whiskers are the minimum and maximum. Scale bar applies to both collagen labeling panels.

enzyme degradation during the 20-minute incubation. Despite decreased collagen labeling, the organization of the fiber network is not changed by collagenase ($p=0.380$) (Figure 5.14). Since collagen gels were fabricated with a random isotropic orientation, this finding suggests collagenase degrades fibers without preference to fiber orientation. Collagenase exposure also produces a change in force over 20 minutes that is smaller ($p=0.005$) by more than 55% than the change from a vehicle exposure, although there are no differences in the magnitude of elemental MPS after 20 minutes ($p=0.336$) (Figure 5.14). Force, strain, and collagen immunolabeling data and quantification for each gel are detailed in Appendix F.

The pattern of neurons with firing profiles before any exposure is not different ($p=0.562$) (Figure 5.15), indicating that the neuronal populations from the collagenase and vehicle groups exhibit equivalent activity, and any change in firing patterns after the exposure is due to the collagen exposure itself. After 20 minutes, neuronal firing profiles differ by treatment, with the distribution of vehicle-treated neurons exhibiting a greater number of inactive neurons and significantly fewer calcium events compared to those with collagenase exposure ($p=0.002$) (Figure 5.15). The decrease in calcium events detected implies that those neurons quiet over time, whereas neurons exposed to collagenase maintain a heightened level of activity (Figure 5.15). Quantification of calcium events at each timepoint by neuron and DRG are itemized in Appendix F.

Neuronal and FLS-localized MMP-1 are elevated after collagenase (Figure 5.16). Exposure increases neuronal MMP-1 ($p<0.001$) by nearly 15-fold ($25.75\pm10.10\%$) over that measured in co-cultures exposed to vehicle ($1.74\pm1.52\%$) (Figure 5.16). MMP-1

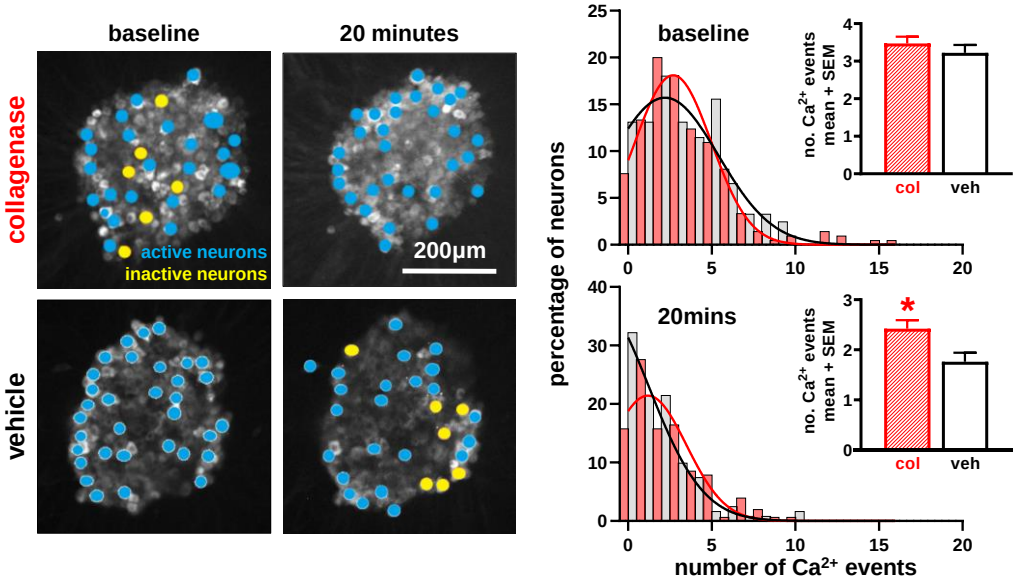

Figure 5.15. Time-lapse captures of fluorescent calcium imaging show DRGs with segmented individual neurons labeled as active (blue; ≥1 calcium events) or inactive (yellow; no calcium events) in images from both before the addition of either collagenase (7 DRGs) or vehicle (4 DRGs) solution and after 20 minutes of exposure. Neuronal firing profiles captured across 28-33 neurons/DRG are the same in both groups at baseline (Wilcoxon test; p=0.562), shown by frequency distributions of the percentage of neurons versus the firing magnitude per minute. Summary data in the bar plot also show no difference in number of calcium events at baseline. However, firing frequency patterns differ with treatment after 20 minutes, with vehicle-exposed neurons quieting as shown by a left-shift of the frequency curve peak toward zero and the summary data detailed in the bar plot (Wilcoxon test; *vs. vehicle p=0.002).

expression in FLS cells increases by nearly 6-fold (collagenase: 31.93±21.27%; vehicle: 5.40±6.34%) after exposure to bacterial collagenase ($p<0.001$) (Figure 5.16). Immunolabeled images and their densitometric quantifications for each co-culture gel are detailed in Appendix F.

5.5.4. Discussion

Less force required to maintain a constrained hold of collagen gels may be due to the degradation of fibers (Figure 5.14) and subsequent change in force distribution at the cruciform-grip interface. Less collagen content with an exposure to an enzyme that degrades collagen is intuitive (Figure 5.14); yet, this finding together with a lack of change

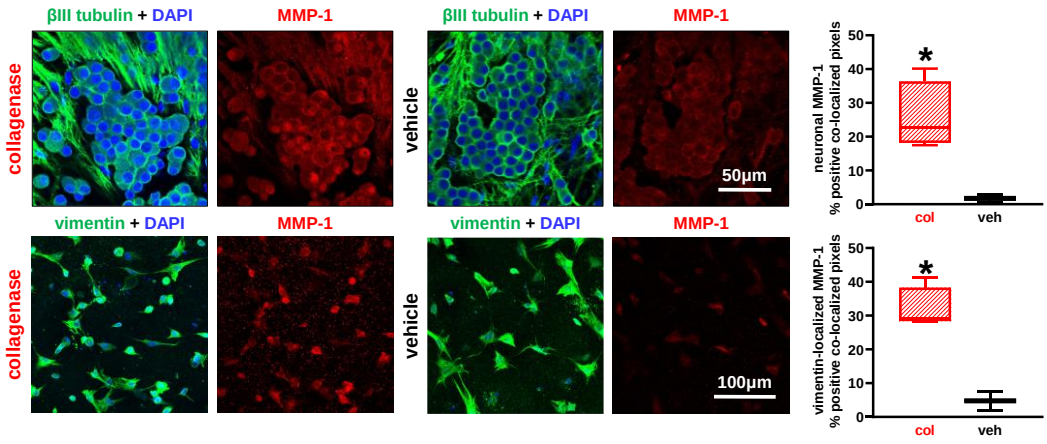

Figure 5.16. Collagenase (col) exposure increases neuronal and fibroblast-localized MMP-1 expression over vehicle (veh) (Wilcoxon tests; *p<0.001) quantified by the co-localization of the neuronal structural protein βIII tubulin (green) and MMP-1 (red) (top panel) or by the co-localization of the fibroblast structural protein vimentin (green) and MMP-1 (red) (bottom panel). A DAPI label for nuclei is also shown (blue). The box-and-whisker plots show horizontal lines representing the first (lower) quartile, median, and third (upper) quartile of the data; whiskers are the minimum and maximum.

in strain suggests that collagenase degrades collagen on a microscale that may not be detected on the macroscopic tissue-level. A lack of effect of collagenase on fiber orientation in vitro is consistent with the observation that the collagen orientation in the rat's capsular ligament is unchanged by intra-articular collagenase administration (Figure 4.6) (Ita et al. 2020). This implies that collagenase does not degrade fibers with any preference for orientation. Moreover, it suggests that probing metrics of *degraded* collagen in addition to, or instead of, metrics of *reorganized* collagen may be more sensitive in detecting collagenase-induced changes in the capsular ligament's microstructure, at least under physiological loads.

Indeed, the detectable signal in the change in force but not strain (Figure 5.14), begs the question of how a collagenase-exposed system would behave *under load*. Here, the mechanical response under a static load was all that was examined, but prior work in vitro has shown that collagenase-degraded collagen gels (Sperry et al. 2017) and rat facet joints

(Singh and Winkelstein 2020) are weaker and restructure differently when loaded to failure. In the rat facet joint, collagenase increases the capsular ligament's fiber disorganization and the occurrence of anomalous realignment in the collagen fibers (Singh and Winkelstein 2020). Collectively, these findings (Figure 5.14) and prior work (Singh and Winkelstein 2020; Sperry et al. 2017) suggest that increases in collagenases in human capsules with disease (Cohen et al. 2007; Kim et al. 2015) or exogenously introduced, may alter the microstructure of the ligament, potentially increasing its vulnerability to stretch-induced injury.

Mechanically-triggered neuronal (Zarei et al. 2017) and fibroblast (Petersen et al. 2012) responses depend on collagen concentration, so a collagenase-induced decrease in collagen (Figure 5.14) could alter how DRG neurons and fibroblasts respond to mechanical cues after exposure. In fact, a collagenase-induced reduction in collagen by nearly 50% compromises the tensile biomechanical responses of gels using the same formulation as presented here (Sperry et al. 2017). Since the collagenase exposure used in the current studies decreases collagen labeling by approximately 87% (Figure 5.14), it is likely that if subjected to load, degraded co-cultures would be weaker, less stiff, and reorganize differently, and as such, alter cell-matrix interactions.

The notion that collagen degradation of the capsular ligament alone is sufficient to evoke neuronal regulation of nociception (and pain in vivo) is supported by the maintained neuronal signaling (Figure 5.15) and elevated neuronal MMP-1 expression (Figure 5.16) after collagenase digestion absent any additional mechanical stimulus. The ability of collagenase to maintain firing profiles in live neurons (Figure 5.15) supports that

collagenase influences neuronal signaling at least very early after exposure and could explain the later increases in substance P observed with intra-articular injection *in vivo* (Figure 4.7) (Ita et al. 2020). The higher number of calcium events in collagenase-exposed neurons (Figure 5.15) suggests a possible mechanism by which degradation-induced changes to the collagen network may regulate neuronal firing; further investigation and electrophysiological studies are needed to more fully define such mechanisms. Further, although collagenase exposure results in a greater number of calcium events than exposure to a vehicle solution (Figure 5.15), this effect is measured across all neurons, since the Synapsin promoter used here does not selectively transduce different types of neurons (Chen et al. 2013; Jackson et al. 2016).

The collagenase-induced increases in MMP-1 observed *in vitro* (Figure 5.16), corroborates a possible causal relationship between intra-articular collagenase and the upregulation of MMP-1 in DRGs in the rat (Figure 4.9) (Ita et al. 2020). MMPs are regulated in part by fibroblasts and interactions with ECM components, including matrix turnover (Craig et al. 2015; Petersen et al. 2012; Visse and Nagase 2003); so, degradation of collagen (Figure 5.14) may be responsible for its elevation (Figure 5.16). As such, an increase in fibroblast-localized MMP-1 (Figure 5.16), at least in joint tissues where degradation is presumably localized, is expected; yet, the MMP-1 localization to neurons in both co-culture gels (Figure 5.16) and DRG tissue (Figure 4.9) (Ita et al. 2020) is surprising. MMP-1 localization to neurons may directly stimulate action potentials and trigger abnormal firing patterns since there are known relationships between MMP-1 and

cell surface receptors and non-matrix substrates involved with nociception (Conant et al. 2002; Dumin et al. 2001; Lakes and Allen 2016; Visse and Nagase 2003).

This study demonstrates that a collagenase-induced loss of collagen (Figure 5.14), absent a mechanical stimulus, influences neuronal firing profiles and increases MMP-1 expression (Figures 5.15 & 5.16). Since the purified collagenase used here is known to only act on collagen molecules, and not on cells, the neuronal dysregulation can be taken to be a result of collagenase's effect on the surrounding collagen fibers, further reinforcing the notion that degradation to surrounding fibers alone, absent a noxious mechanical stimulus, might be able to trigger nociceptive-relevant responses.

5.6. Integration & Conclusions

The studies in this chapter present the development and characterization of a neuron-fibroblast co-culture in vitro model simulating the capsular ligament and provide initial evidence that fibroblast-like synoviocytes regulate the microstructure of their surrounding collagen network during non-constrained culture (Figure 5.9) and under stretch (Figure 5.12). The experiments performed under load (Section 5.4) elucidate a distinct response of FLS compared to 3T3 fibroblasts and emphasize the importance of defining afferent signaling in the ligament in the presence of primary FLS cells. Yet, the statistical comparisons in those stretch experiments (Section 5.4) do not focus on the concentration-dependence of outcomes between FLS at a low and high concentration. Studies detailed in Chapter 6 investigate the concentration-dependence in larger sample sizes and expand outcomes to also evaluate neuropeptide expression in DRGs. Counter to

the hypothesis associated with Aim 3, FLS do not appear to strengthen the biomechanical properties of the bulk matrix, as least not relative to 3T3 fibroblasts (Figure 5.10). Experiments in Aim 3 compare DRG-FLS co-cultures to collagen gels containing only DRGs in order to define FLS effects on collagen multiscale mechanics in parallel with neuronal signaling.

Results of these studies support the hypothesis that FLS regulate the cellular localization of MMPs to peripheral neurons in their local environment. Moreover, these findings establish a role for MMP-1 both due to mechanical (Table 5.1) *and* degradative (Figure 5.16) stimuli, each in isolation; in doing the studies reveal mechanisms by which MMP-1 may participate in aging- and/or trauma-induced joint pain. Yet, the influence of FLS on neuronal expression of nociceptive neuropeptides is not evaluated. Experiments in Chapters 6 and 8 investigate load-induced changes in MMP-1 expression and collagen microstructure in the context of substance P expression.

Chapter 6

Regulation of MMP-1, MMP-9, & Nociceptive Responses In Vitro

This chapter has been adapted from:

Ita ME, Leavitt OME, Winkelstein BA. MMP-1 induces joint pain that may be mediated by increased activity in peripheral neurons. *Orthopaedic Research Society Annual Meeting*, Abstract #2184, March 2018. New Orleans, LA.

Ita ME, Winkelstein BA. Concentration dependent effects of fibroblast-like synoviocytes on collagen gel multiscale biomechanics & neuronal signaling: Implications for modeling human ligamentous tissues. *Journal of Biomechanical Engineering*, 141(9): 091013, 2019.

Ita ME, Winkelstein BA. MMP-1 & MMP-9 increase after tensile stretch: lessons from neuronal-fibroblast co-cultures simulating joint capsules. *Biomedical Engineering Society Annual Meeting*, Abstract #767, October 2019. Philadelphia, PA.

6.1. Overview

The density and shape of fibroblast-like synoviocytes (FLS) in the spinal facet capsular ligament vary with both anatomic region and between healthy and pathologic states. For example, in the outer layer of the facet joint capsule FLS are less dense and have elongated nuclei; in the inner layer, FLS are more dense and exhibit round and ovoid nuclei (Yahia and Garzon 1993; Yamashita et al. 1996). FLS density can also increase with fibroblast infiltration into the capsular tissue which can occur with both inflammation and/or traumatic injury (Bartok and Firestein 2010; Cohen et al. 2007; Provenzano et al.

2002). Since the afferent nerve fibers that innervate the capsule are also found in those same capsular regions that have variable FLS density, any cell-cell interactions between FLS and afferent fibers may depend on the FLS cell density. The studies in Chapter 5 suggest that there are concentration-dependent effects of fibroblasts on the collagen gel stiffness (Figure 5.10) and regional strains sustained during failure stretch (Figure 5.11). Those studies demonstrated the unique functional phenotype of the FLS fibroblasts by comparing FLS-seeded collagen gels to 3T3-seeded collagen gels, and did not investigate concentration-dependent effects of FLS specifically on the multiscale mechanics, or in the context of neuronal physiologic outcomes. The studies in this chapter vary FLS seeding density in the DRG-FLS co-culture model presented in Chapter 5 to define the effects of FLS on stiffness, failure mechanics of the collagen gel and the collagen fibers, and MMP-1 and MMP-9 expression. Studies also assay neuronal substance P to begin to define the effects of FLS concentration on nociception. To accomplish these goals, studies in this chapter utilize uniaxial tensile loading to gel failure to define if, and how, FLS alter macroscopic failure properties. Additionally, experiments integrate polarized light techniques with mechanical testing to quantify mechanics on the microscale and to understand mechanical changes on a multiscale in the context of physiological cellular responses.

Quantitative polarized light imaging (QPLI) exploits the natural birefringence of collagen molecules to quantify the dynamic reorganization of collagen fibers during loading, and has been used to evaluate soft tissue biomechanics and other collagenous tissue equivalents (Lake et al. 2011; Quinn and Winkelstein 2009; Sander et al. 2009b;

Tower et al. 2002). Using that approach, collagen fiber realignment during tensile and posterior retraction loading of isolated human cadaveric facets, and tensile loading of isolated rat facet capsules has been defined by our lab (Quinn and Winkelstein 2009; Quinn and Winkelstein 2010; Quinn et al. 2010; Quinn and Winkelstein 2008; Quinn and Winkelstein 2011). Other groups have used polarized light imaging techniques to define how fibroblasts seeded in collagen regulate their network structure and composition (Chandran and Barocas 2004; Sander et al. 2011). The studies in this chapter integrate QPLI as was introduced in the studies in Chapter 5 (Figure 5.7) to define the effect of FLS concentration on collagen fiber microstructure and kinematics in the gel model. QPLI enables comparisons between changes in the local fiber reorganization and neuronal protein expression to elucidate possible mechanotransduction cascades that are triggered by loading.

Complementary studies are presented in this chapter that: (1) define the effects of FLS concentration on the mechanics of collagen gels and the physiologic responses of cells in the co-culture model under failure loading and (2) interrogate MMP-9 responses in the context of MMP-1 and failure loading, as well as probe neuronal activity in response to MMP-1 exposure. The first study (Section 6.3) defines the multiscale mechanical response to failure loading of collagen gels, and the associated total MMP-1 and neuronal substance P expression in those co-cultures. Experiments test co-cultures using a high FLS concentration and a low FLS concentration to match the experiments with FLS-seeded collagen gels in the studies in Chapter 5, and also include collagen gels without FLS cells (and only DRGs) as a control for the effects of FLS on the collagen matrix and cell

signaling. Based on the outcomes of those studies, a collection of three complementary experiments (Section 6.4) probed the MMP-9 response and neuronal responses. The quantification of MMP-9 in the studies in this chapter provides insight into the mechanistic role of the MMP-9 that was detected in the ligamentous capsule and disc from temporomandibular joints with chronic disorders in Chapter 3 (Ita et al. 2020a). Because those studies provide evidence that MMP-9 expression correlates with both MMP-1 expression (Figure 3.3) and with patient-reported pain scores (Figure 3.4) (Ita et al. 2020a), its expression was probed in co-cultures following the same stretch to failure insult that was found to increase MMP-1 and neuronal substance P expression in the studies in the first portion of this chapter. Furthermore, the effect of exogenous MMP-1 exposure on MMP-9 expression was investigated to test the mechanistic relationship between those two proteases that is suggested by their positive correlation in innervated joint tissues (Figure 3.3) (Ita et al. 2020a). The studies in Chapter 5 demonstrate that an exposure to an enzyme with collagenolytic activity alters neuronal firing profiles in the co-culture model (Figure 5.15) (Ita et al. 2020b); the studies in this chapter build off of that work and test the effect of MMP-1 exposure on DRG monolayer cultures to determine if MMP-1 affects neuronal activity absent a collagen substrate. A combined background section (Section 6.2) sets up both sets of studies, and they are jointly discussed (Section 6.5) to integrate findings that cross both studies together. Collectively, the studies in this chapter address Aim 3 and findings begin to put forth a mechanistic relationship between MMP-1 and MMP-9, and implications for nociception, in the DRG-FLS co-culture model.

6.2. Relevant Background

Joint pain is a leading cause of chronic pain (Institute of Medicine 2011), affecting 27 million adults in the US with an annual cost of $100 billion expected by 2020 (Oliviero et al. 2010). Synovial joints can become painful with aging or from trauma due to repeated and/or supra-physiologic loading, any of which can initiate tissue damage and degeneration (Mow et al. 1993). For example, neck and low back pain are among the most prevalent chronic syndromes (Hogg-Johnson et al. 2008), and can be due to pathology of the spinal facet joints which themselves are susceptible to trauma (Elliott et al. 2009; Manchikanti et al. 2004) and degeneration (Gellhorn et al. 2013; Suri et al. 2013). Abnormal loading of a joint's ligamentous capsule can initiate pathophysiological pain cascades by activating the nociceptive fibers that innervate the capsule (Kallakuri et al. 2008; Lee et al. 2008; Lu et al. 2005).

In vitro models have been developed using either dissociated neurons or DRGs seeded in three-dimensional (3D) collagen gels to replicate both the sensory innervation and network microstructural organization of the ligamentous capsule of the synovial spinal facet joint (Zhang et al. 2016; Zhang et al. 2017; Zhang et al. 2018a). Using that model, the strain threshold for collagen fiber realignment was defined and found to co-exist with the strain threshold for elevated expression of phosphorylated extracellular signaling kinase (pERK) (Ji et al. 1999; Zhang et al. 2016). In addition, regional strains and increased expression of each of pERK and the neurotransmitter substance P are related in DRG axons (Zhang et al. 2017; Zhang et al. 2018a). Collectively, the findings from those studies demonstrate that in collagen networks, non-physiologic loading mediates neuronal

signaling (Zhang et al. 2016; Zhang et al. 2017; Zhang et al. 2018a) and begin to define mechanisms by which traumatic joint loading causes pain (Elliott et al. 2009; Ita et al. 2017). A degradation-induced loss of collagen fibers has also been shown to decrease failure properties and alter network reorganization under tension (Sperry et al. 2017); yet, if, and how, a degradation-induced loss of collagen alters the relationship between load and neuronal signaling is not known.

In vitro fibroblast-collagen gel models have also defined mechanisms by which fibroblasts regulate, and are regulated by, their local microenvironment (Dallon and Ehrlich 2008; Grinnell and Petroll 2010; Kural and Billiar 2013). For example, in free-floating matrices, fibroblasts exist in a "low-tension" environment and reorganize collagen fibers circumferentially around the edge of the gel, if at all (Dallon and Ehrlich 2008; Kural and Billiar 2013); in anchored matrices, fibroblasts exist in a "high-tension" environment and reorganize collagen fibers according to the gel geometry and the direction of applied tension (Grinnell and Petroll 2010; Kural and Billiar 2013; Sander et al. 2011). Although that body of work suggests that fibroblasts alter their local collagen network in a manner that is concentration-dependent, no culture system has integrated neurons or DRGs together with FLS to capture the anatomy and/or physiology of human joint capsules. Accordingly, despite their co-existence in capsular ligaments, very little is known about the interactions of afferent fibers and FLS with each other and their surrounding collagen network.

Matrix-metalloproteinase-1 (MMP-1) is a likely mediator of joint pain given its role in mediating ECM degradation. For example, since collagen degradation alters the

biomechanics and microstructure of joint tissues (Otterness et al. 2000; Varady and Grodzinsky 2016), and MMP-1 can degrade Type I collagen (Visse and Nagase 2003), it is possible that MMP-1 may alter the local microenvironment and initiate mechano-regulated responses in afferent fibers (Zarei et al. 2017; Zhang et al. 2016; Zhang et al. 2018b; Zhang et al. 2018a). Since mechanical loading increases secretion of MMP-1 by dermal fibroblasts and upregulates MMP-1 gene expression in patellar tendon fibroblasts (Petersen et al. 2012; Yang et al. 2005), it is possible that abnormal loading of a joint's ligamentous capsule may modulate FLS regulation of MMP-1.

MMP-1 has also been implicated in pain since it also binds to receptors involved in nociception in both catabolically active and inactive states (Allen et al. 2016; Boire et al. 2005; Conant et al. 2002; Conant et al. 2004); MMP-1 can bind to several non-ECM substrates that are also involved in pain signaling, including substance P, which regulates nociception in culture (Basbaum et al. 2009; Cheng and Ji 2008; Zhang et al. 2017) and in joint pain (Kras et al. 2015). In the extracellular space, MMP-1 also cleaves the bait region of the MMP-9 gelatinase, rendering it active (Visse and Nagase 2003). MMP-9 has an established role in neuropathic pain (Kawasaki et al. 2008) and its activation can further lead to increases in substance P and subsequent nociceptive transmission (Diekmann and Tschesche 1994). MMP-9 is elevated along with MMP-1 in the synovial fluid of post-traumatic and painful knee joints (Haller et al. 2015). Despite this growing body of literature, the responses of MMP-1 and MMP-9 in painful joint disease, and whether MMP-1 regulates MMP-9 in the joint, are unknown.

Regional strains of cell-embedded in vitro constructs directly relate to neuronal nociceptive signaling (Zhang et al. 2016; Zhang et al. 2017; Zhang et al. 2018a) and ECM remodeling by fibroblasts, including collagen synthesis, collagen deposition, and protease secretion (Hsieh et al. 2000; Petersen et al. 2012; Sander et al. 2011). Collagen fiber organization and reorganization also regulate those same load-induced pathological responses in cell-embedded networks (Sander et al. 2011; Zarei et al. 2017; Zhang et al. 2016; Zhang et al. 2018a). Under tension, fibers reorganize in the direction of loading, and the extent of fiber reorganization increases with increasing strain (Abhilash et al. 2014; Hadi et al. 2012; Hadi and Barocas 2013; Munster et al. 2013; Sperry et al. 2017; Vader et al. 2009; Zhang et al. 2016). On the cellular level, a "switch-like" response has been observed for fiber alignment, whereby fibers reorganize *together with* neuronal dysfunction that occurs with loading, with strains above 11.3% being a critical strain above which collagen fibers reorient and neurons express greater levels of pERK (Zhang et al. 2016). However, that work was absent any consideration of the physiologically relevant effects of fibroblasts on either the ECM and/or the neuronal function.

6.3. Effects of FLS Concentration on Collagen Gel Multiscale Biomechanics & Neuronal Signaling

This study used the DRG-FLS co-culture collagen gel model described in Chapter 5 to understand the effects of FLS on multiscale collagen gel mechanics and neuron physiology in response to gel distraction to failure. The overall objectives of this study

were to: (1) determine if FLS alter macroscopic failure properties, regional strains, and/or collagen microstructural kinematics and (2) measure if the presence and extent of FLS in the gel alters MMP-1 expression and/or neuronal nociceptive signaling. Since capsular ligaments exhibit variable FLS densities in different regions of the capsule (Yamashita et al. 1996), and the mechanical properties of fibroblast-embedded collagen gels depend on the initial fibroblast concentration (Evans and Barocas 2009), FLS were seeded in collagen gels at two concentrations to simulate the extremes of the physiologic range (Yahia and Garzon 1993; Yamashita et al. 1996). Further, since active MMP-1 stabilizes by six-eight days in ligament fibroblasts embedded in gels (Attia et al. 2014), the effects of failure loading on MMP-1 expression was tested after seven and nine days of culture. Day-in-vitro (DIV) 7 was chosen because DRGs exhibit neurite outgrowth nearly twice the diameter of their soma by that time (Zhang et al. 2017; Zhang et al. 2018a); DIV9 was selected because *total* active and inactive MMP-1 reaches a steady state before DIV10 (Attia et al. 2014). To determine if the longer time in culture affects FLS-induced gel organization and/or baseline cell responses, expression of MMP-1 or substance P before any gel loading was compared between those two days (DIV7; DIV9). Macroscopic gel mechanics were quantified by failure properties and gel stiffness, and regional strains and collagen alignment and organization were analyzed to assess effects of FLS on regional kinematics. Fiber alignment data were measured during loading by QPLI, which quantifies dynamic fiber reorganization (Lake et al. 2011; Quinn and Winkelstein 2009; Sander et al. 2009b; Tower et al. 2002). Using fiber angle distributions, collagen organization was quantified by the circular variance (CV) of the spread of fiber angles, describing the clustering of

angles, with a lower CV indicating a tighter clustering and a higher degree of fiber alignment (Zhang et al. 2016; Zhang et al. 2018a). After failure, gels were assayed for total MMP-1 and neuronal substance P protein in the context of multiscale mechanical outcomes.

6.3.1. Methods

6.3.1.1. Co-Culture System, Mechanical Testing, & Data Acquisition

All cells were harvested from Sprague-Dawley male rats under approved conditions and using sterile procedures. DRGs were harvested from all spinal levels of embryonic day 18 rats (from the CNS Cell Culture Service Center of the Mahoney Institute of Neuroscience) and stored in Hibernate-E medium supplemented with 1% GlutaMAX and 2% B-27 at 4°C until plating (Cullen et al. 2012; Zhang et al. 2018a). Following the protocols detailed in Chapter 5 (Section 5.3.1), FLS were harvested from both hind knees of a sexually mature adult rat (384g) and resuspended at passages 3 or 4 in two separate groups with different concentrations, based on densities found in the facet capsule (Yamashita et al. 1996): $5x10^4$ cells/mL (low; n=10) to simulate regions with low FLS cell density and $1x10^5$ cells/mL (high; n=9) to simulate denser regions. Collagen gels without any FLS were included as controls (none; n=8) for their effects on mechanics, MMP-1 and/or neuronal substance P.

On DIV1, DMEM medium was removed from the top of the gels, and DRGs were seeded on the gel surface for all samples (6-10/gel) in 100µL of Neurobasal feeding medium supplemented with 1% GlutaMAX, 2% B-27, 5% FBS, 10ng/ml 2.5S nerve growth factor, 2mg/ml glucose, 10mM FdU, and 10mM uridine (Cullen et al. 2012; Zhang

et al. 2018a) (Figure 6.1). After 12-24hrs, fresh Neurobasal feeding medium was added to all gels and then changed every other day; all gels were cultured in the supplemented Neurobasal feeding medium for the remainder of the study. On DIV6, an additional layer of collagen (150µL) was added to encapsulate the DRGs in half of the samples (none n=4; low n=4; high n=3). For the remaining samples (n=4/group), DRGs were encapsulated with collagen using the same protocol but on DIV8 (Figure 6.1).

Gels underwent distraction to failure on DIV7 (none n=4; low n=4; high n=3) or DIV9 (n=4/group) (Figure 6.1). On the day of testing, gels were stamped into a strip (21mmX8mm), and a 4X4 grid of markers was drawn on the surface in the center of each

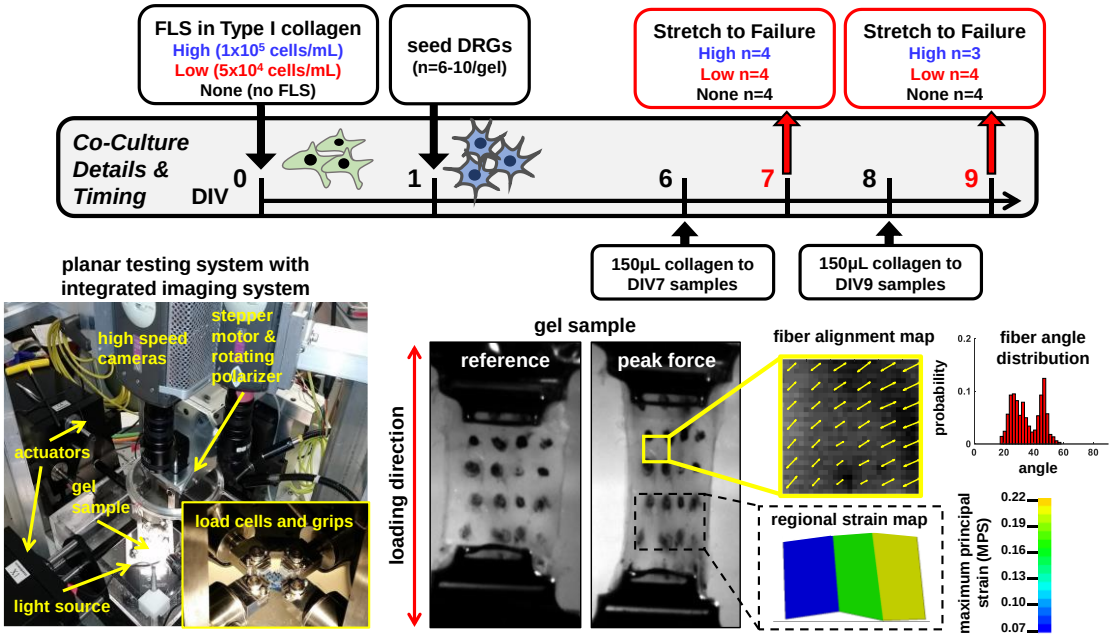

Figure 6.1. Experimental timeline for co-culture conditions, set-up for mechanical testing, and analyses of elemental strain and collagen organization. Fibroblast-like synoviocytes (FLS) were seeded into a collagen gel solution on day-in-vitro (DIV) 0 at either a low or high concentration, or were omitted (none), followed by seeding DRGs onto all gels at DIV1. On either DIV7 or DIV9 gels were loaded in a planar test device with an integrated polarized light imaging system. During loading, each gel was affixed in grips for uniaxial tension to failure and marked with a grid of dots for strain tracking. The corresponding strain map of maximum principal strain (MPS) is shown extracted from three elements on the representative low FLS gel. The corresponding vector map is also shown displaying the raw fiber alignment data for an element, which is used to calculate circular variance (CV).

gel to establish regional elements and enable strain tracking (Zhang et al. 2018a). Using the grid of markers, each group of four nodes was designated as an element (Figure 6.1) and used for data analyses. Using a planar testing machine (574LE2; TestResources; Shakopee, MN), gels were loaded into grips attached to actuators equipped with 500g load cells attached to each grip and immersed in a 37°C PBS bio-bath (Figure 6.1). The mechanical system was integrated with a polarized light imaging system (Quinn et al. 2010; Quinn and Winkelstein 2008; Tower et al. 2002; Zhang et al. 2016) and high-speed cameras (Phantom-v9.1; Vision Research, Inc.; Wayne, NJ) that acquired collagen alignment maps and tracked marker locations and displacements during loading. Force and displacement data (200Hz) were synchronized with high-speed imaging (500Hz). Gels were pre-loaded until slack was removed (less than 2mN) in either arm, and then distracted at 0.5mm/sec to failure. Immediately following the distraction, gels were removed from the grips and fixed for two hours in 4% paraformaldehyde, washed, and stored in 30% sucrose at 4°C. To assess the effect of days in culture and FLS concentration on protein expression, additional gels were fabricated for all three FLS concentrations (none; low; high). Those control gels were not loaded (n=2/group/DIV) and were removed from culture on DIV7 or DIV9 for chemical fixation and storage.

6.3.1.2. Immunolabeling of MMP-1 & Neuronal Substance P

Gels were immunolabeled after loading for MMP-1, substance P, and βIII tubulin to evaluate effects on MMP-1 and neuronal substance P. Gels were blocked in PBS with 10% normal goat serum (Vector Laboratories; Burlingame, CA) and 0.3% Triton-X100 (Bio-Rad Laboratories; Hercules, CA) for two hours at room temperature and incubated

overnight at 4°C with primary antibodies to MMP-1 (anti-rabbit; 1:200; Proteintech; Rosemont, IL), substance P (anti-guinea pig; 1:200; Neuromics Inc.; Minneapolis, MN), and βIII tubulin (anti-mouse; 1:300; Biolegend; San Diego, CA). Gels were then washed in PBS and incubated with the secondary antibodies goat anti-guinea pig Alexa Fluor 633, goat anti-rabbit Alexa Fluor 555, and goat anti-mouse Alexa Fluor 488 for two hours at room temperature (all 1:1000; Life Technologies; Carlsbad, CA). Finally, gels were incubated in DAPI solution (1:200; ThermoFisher; Waltham, MA) at room temperature for 15 minutes to stain cell nuclei, washed in PBS, washed in distilled water, and then cover-slipped. Labeled gels were imaged using the 40X objective of a Leica TCS SP8 confocal microscope (1024X1024 pixels; Leica Microsystems; Wetzlar, Germany). Stacks of six confocal images were acquired for each gel (5 stacks/gel) at 1μm increments up to a depth of 5μm. Since MMP-1 and substance P can localize to DRG axons and cell bodies (somas) (Kallakuri et al. 2004; Lee and Winkelstein 2009; Zhang et al. 2017), images were acquired from both regions, with at least n=2/region of the five stacks acquired for each gel and each stack acquired from a distinct region, with no DRG soma or its axons imaged twice. The location of each image was registered with the regional elements from each gel in order to relate cellular outcomes with the strain and collagen organization data. Image stacks were also acquired for control gels that did not undergo any loading but were fixed at either DIV7 or DIV9 containing either the low or high FLS concentration (n=1/group/day) in order to evaluate whether FLS concentration alters the baseline expression of immunolabeled proteins.

6.3.1.3. Data & Statistical Analyses

Force data were filtered using a 10-point moving average filter (Zhang et al. 2018a) and the maximum force detected was extracted and taken as the failure point (Figure 6.2A). Stiffness was calculated using the force-displacement curves and defined as the slope of the curve at between 20% and 80% of the maximum force (Lee et al. 2006) (Figure 6.2A). The locations of the fiducial markers on the gel captured by high-speed imaging were digitized with FIJI software (NIH) (Schindelin et al. 2012) for the unloaded image before any distraction (reference) and in the image immediately prior to failure. Grid position data were processed in LS-DYNA (Livermore Software Technology Corp.; Livermore, CA) to calculate the maximum principal strain (MPS) for each element for each loaded gel (Figure 6.1). Pixel-wise fiber alignment maps were created using 20 consecutive high-speed images acquired both before distraction (reference) and immediately prior to failure using a custom script based on a harmonic equation in MATLAB (R2018; MathWorks Inc., Natick, MA) (Quinn et al. 2010; Quinn and Winkelstein 2008; Tower et al. 2002). The CV was quantified from the spread of fiber angles detected for each element separately (Figure 6.1) (Zhang et al. 2016); CV at failure was normalized to the reference CV for all elements analyzed.

To quantify the amount of positive protein labeling in the immunolabeled gels, the average intensity projection of each stack was generated using Fiji, and a custom MATLAB script (found in Appendix B) quantified the number of positive pixels above the threshold for positive MMP-1, substance P, and βIII tubulin labeling in naïve controls, separately (Kartha et al. 2018; Zhang et al. 2016). Thresholds were determined from pilot studies with naïve FLS and DRG cultures, and samples with no primary antibodies added

to control for labeling procedures were included as controls to verify the specificity of each antibody. The overall percentage of positive MMP-1 labeling was quantified without discriminating by cell type (neurons and FLS) in order to account for total MMP-1 in the overall culture system, from both cell sources. In order to compare *neuronal* substance P, the co-localization of βIII tubulin and substance P was computed; the co-localization of pixels positive for each was normalized to the total βIII tubulin for each image, separately, to account for differences in neuronal labeling.

All statistical analyses were performed in JMP (Pro 14; SAS Institute; Cary, NC) with $\alpha=0.05$. To test the effect of day-in-vitro on collagen fiber organization, separate t-tests compared CV at reference between DIV7 and DIV9 for each concentration. Further, a one-way analysis of variance (ANOVA) was used to assess the effect of FLS concentration on reference CV separately for each day in vitro. Similarly, the total MMP-1 and neuronal substance P quantification in non-distracted control gels were compared across the two days (DIV7 and DIV9) for each concentration using separate t-tests, to determine if the difference in the length of time in culture alters baseline protein expression. An ANOVA assessed the effect of FLS concentration on baseline expression of total MMP-1 and neuronal substance P quantification. Statistical comparisons between day-in-vitro and across groups for baseline protein expression were calculated with each quantified image as a statistical unit; this justification was rationalized since control gels that were used for baseline protein expression were non-distracted, so there was no variation in the local biomechanical environment as is the case with stretched gels. The effect of FLS concentration on force at failure, displacement at failure, and stiffness was tested with a

one-way ANOVA comparing the different FLS concentration groups (none; low; high). The MPS values and normalized CV quantification for those elements in which confocal images were acquired (n=5/gel) were extracted and compared at failure between gels with different FLS concentrations (none; low; high); the effect of concentration on elemental MPS, elemental CV, total MMP-1, and neuronal substance P was tested with separate one-way ANOVAs and post-hoc Tukey tests for each outcome.

6.3.2. Results

Overall, neither FLS concentration nor time in culture affect collagen microstructure before undergoing distraction. Although gels with FLS at either concentration spontaneously released from the culture plate wall by DIV2; the presence of FLS at either concentration does not change the collagen organization compared to gels without any FLS (Table 6.1). This is true regardless of the length in culture, with the CV at reference not different between no (none), low, and high concentrations at either DIV7 ($p=0.56$) or DIV9 ($p=0.45$) (Table 6.1). Further, the reference CV is also not different *between* DIV7 and DIV9, regardless of group (Table 6.1); there is no difference between the two DIV culture times detected in the microstructure of collagen for gels without any FLS ($p=0.41$), with the low FLS concentration ($p=0.35$), or with the high FLS concentration ($p=0.28$) (Table 6.1).

As with the collagen microstructure, neither the concentration of FLS nor the time in culture alter baseline expression levels of MMP-1 or neuronal substance P in gels. The time in culture from DIV7 to DIV9 does not influence the baseline protein expression of

Table 6.1. Summary of macroscale biomechanics and microstructure before distraction and after failure

Group	Gel ID	Unloaded CV ($\times 10^3$)*	Force (mN)	Displacement (mm)	Stiffness (mN/mm)	Normalized CV*+
			DIV7			
high FLS	28	0.13±0.07	13.60	4.47	4.14	17.48±15.13
	29	N/A	20.43	6.34	3.57	N/A
	31	N/A	16.82	6.06	5.02	N/A
	37	0.39±0.15	11.68	5.97	1.56	2.37±1.35
	Mean	**0.28**	**15.63**	**5.71**	**3.57**	**8.85**
	SD	**0.18**	**3.83**	**0.84**	**1.47**	**11.93**
low FLS	7	0.34±0.08	20.42	2.00	9.82	1.07±1.18
	8	0.31±0.17	37.13	4.63	8.83	2.25±1.08
	13	1.86±2.20	65.61	4.26	18.53	2.83±1.39
	34	0.27±0.22	16.02	5.47	3.78	5.66±2.17
	Mean	**0.62**	**34.79**	**4.09**	**10.24**	**3.15**
	SD	**0.99**	**22.47**	**1.47**	**6.13**	**2.24**
none	3	0.62±0.51	4.74	2.53	2.00	1.37±0.48
	9	0.12	11.70	6.06	2.42	3.59
	11	0.33±0.12	22.40	4.40	4.41	4.97±2.06
	38	0.29±0.28	11.48	5.71	3.64	7.04±7.28
	Mean	**0.37**	**12.58**	**4.68**	**3.12**	**4.14**
	SD	**0.29**	**7.30**	**1.60**	**1.11**	**3.69**
			DIV9			
high FLS	43	1.43±0.27	15.96	6.00	2.92	16.30±17.29
	44	0.20±0.12	15.91	6.08	3.32	43.28±34.12
	46	0.28±0.10	15.20	4.95	3.89	24.10±12.01
	Mean	**0.50**	**15.69**	**5.68**	**3.38**	**30.89**
	SD	**0.54**	**0.42**	**0.63**	**0.48**	**25.64**
low FLS	3	0.13±0.10	6.49	5.36	1.10	13.74±9.60
	4	1.97	11.91	4.26	1.89	1.91
	7	0.13±0.11	20.71	5.92	6.47	7.42±3.34
	11	0.19±0.16	15.84	7.94	4.34	36.33±21.42
	Mean	**0.28**	**13.74**	**8.33**	**2.44**	**25.57**
	SD	**0.52**	**6.03**	**3.41**	**1.22**	**5.96**
none	28	1.04±0.58	72.46	8.09	13.63	9.93±7.54
	29	N/A	12.32	4.43	3.92	N/A
	30	0.41±0.20	21.65	3.42	7.70	2.76±0.86
	33	0.25±0.14	5.12	2.14	2.77	2.45±1.36
	Mean	**0.49**	**27.89**	**4.52**	**7.01**	**4.23**
	SD	**0.42**	**30.48**	**2.56**	**4.89**	**4.56**

*****elemental data are presented as mean ± standard deviation for all elements for that sample
+normalized CV is calculated by dividing raw CV at reference by raw CV at failure
N/A data were not collected due to technical problems with data capture

either MMP-1 or neuronal substance P in unloaded gels. Specifically, the amount of MMP-1 on DIV7 is not different from the quantification of MMP-1 on DIV9 for gels with no FLS (none) ($p=0.62$), low ($p=0.39$) or high ($p=0.15$) FLS concentrations (Table 6.2). The same relationship exists for neuronal substance P between DIV7 and DIV9 for the none

Table 6.2. Summary of protein expression in unloaded controls

Group	Total MMP-1 (% positive pixels)*	Neuronal substance P (% positive pixels)*
	DIV7	
high FLS	0.08±0.15	0.009±0.007
low FLS	0.04±0.03	0.006±0.006
none	0.04±0.02	0.001±0.001
	DIV9	
high FLS	0.01±0.01	0.003±0.003
low FLS	0.08±0.13	0.002±0.002
none	0.05±0.06	0.020±0.036

*****elemental data are presented as mean ± standard deviation for all elements for that sample

(p=0.14), low (p=0.06) and high (p=0.07) FLS concentrations (Table 6.2). Furthermore, MMP-1 expression in gels is not different across groups (none vs. low vs. high) ($p \geq 0.31$), regardless of DIV (Table 6.2); the same is evident for neuronal substance P expression ($p \geq 0.05$), with no difference based on concentration of FLS (Table 6.2). Since the overall time in culture does not influence any outcome of the gel properties between DIV7 and DIV9, those groups were combined for each concentration condition in order to investigate effects of the three different concentrations on the biomechanical and physiological responses during and after failure.

Neither the presence nor amount of FLS in the culture system alters the macromechanical responses of gels at failure (Table 6.1 & Figure 6.2). None of the force or displacement at failure, or gel stiffness ($p \geq 0.30$) are different across the three concentration groups (none; low; high) (Figure 6.2B). In contrast, there are differences in the elemental responses; there are FLS concentration-dependent differences in both elemental MPS and collagen organization (Figure 6.3). Despite undergoing similar deformations and forces at failure (Figure 6.2), the gels that incorporate FLS experience

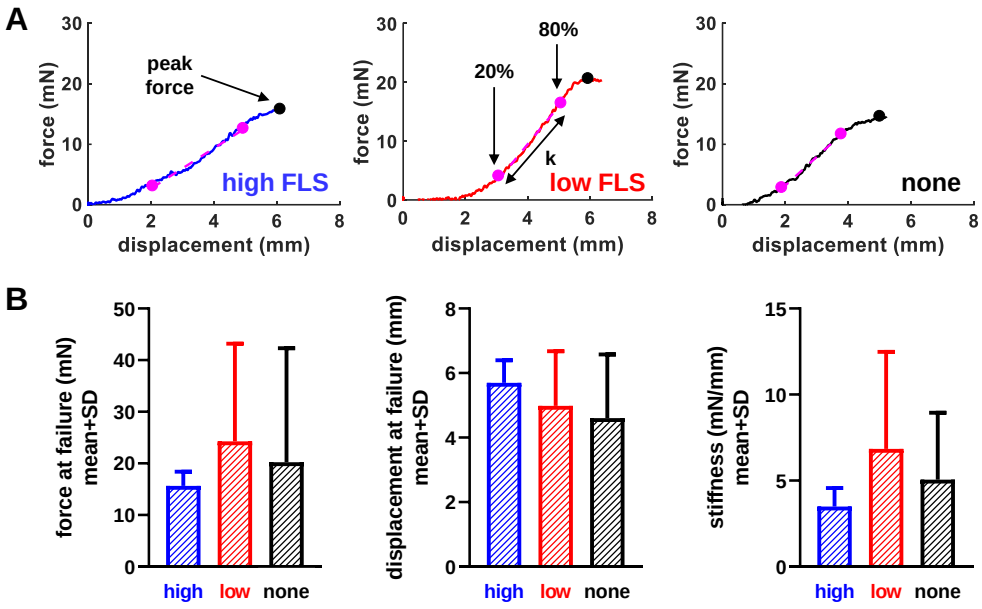

Figure 6.2. Analysis of macromechanics after tensile distraction to failure show no differences between FLS concentration groups. **(A)** Force-displacement data for representative gels with high (Gel 44; DIV9), low (Gel 7; DIV9), and no (none; Gel 30; DIV9) FLS included. For each gel, peak force defines the failure; stiffness (k) is calculated as the linear slope of the force-displacement curve between 20% and 80% of the peak force. **(B)** There are no differences between the FLS concentration groups for any of force at failure (p=0.63), displacement at failure (p=0.42), or stiffness (p=0.30). DIV7 and DIV9 data are pooled in bar plots.

higher strains at failure than gels without any FLS, with both the low ($p<0.01$) and the high ($p=0.01$) FLS concentration gels sustaining strains that are nearly twice the strains sustained in gels with no FLS (Figure 6.3). Further, for the greater FLS concentration (high FLS group), the collagen network shows a higher degree of reorganization at failure, with a graded normalized CV increasing with increasing FLS concentration (Figure 6.3). However, the difference in normalized CV at failure is only significant ($p<0.01$) between the high FLS concentration (21.2±23.1) and the group with no FLS (none; 4.3±4.2) (Figure 6.3). The force-displacement curves and strain fields for all gels in this study are summarized in Appendix H.

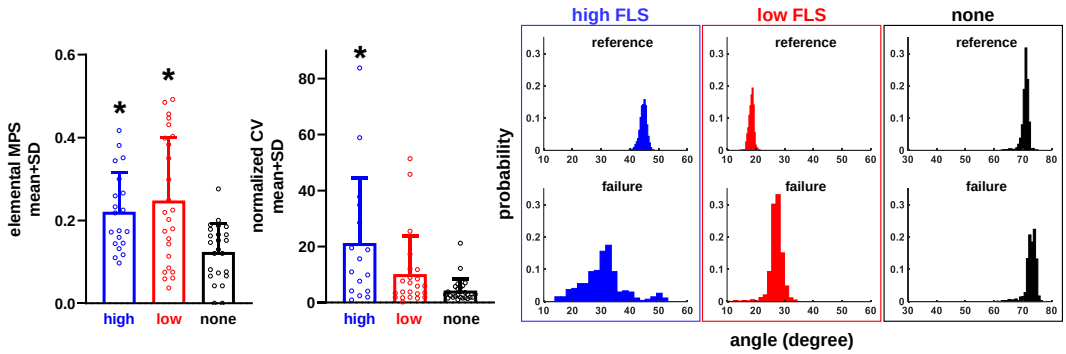

Figure 6.3. Regional strain and collagen microstructure at failure are FLS concentration-dependent. Stretch-induced maximum principal strain (MPS) in gels with FLS at both concentrations (low; high) are significantly higher than the MPS at failure in gels without FLS (*p≤0.01). Circular variance (CV) normalized to the corresponding reference CV is also significantly greater (*p≤0.01) in gels with high FLS concentration than in those without FLS (none). Bar graphs show summary data with DIV7 and DIV9 pooled and overlaid with individual data points, each representing an element (open circles). Histograms show the probability that collagen will orient at a given angle for reference and at failure for representative elements from each of the high (Gel 44; DIV9), low (Gel 7; DIV9), and no FLS (Gel 33; DIV9). A larger spread of angles is evident with the high FLS gel element at failure and corresponds to a larger CV value, indicating a large degree of fiber reorganization relative to the network microstructure prior to loading.

As with the regional micromechanics outcomes (Figure 6.3), the physiological effects of the presence, and amount, of FLS cells after tensile gel failure are differentially altered (Figure 6.4). In fact, the stretch-induced expression of both total MMP-1 in the culture system and neuronal substance P generally follow each other with the low concentration of FLS having the greatest expression, at either DIV7 or DIV9 (Figure 6.4). MMP-1 expression is observed in both the DRG somas and axons and appears to label in concentrated or compacted masses in contrast to a more diffuse label (Figure 6.4A); there is little MMP-1 in gels with only DRGs (Figure 6.4A). Despite positive labeling in gels with either concentration of FLS, those with a low FLS concentration (35.4±27.4%) express significantly greater levels ($p<0.01$) of MMP-1 after stretch to failure than gels without FLS (none; 13.1±16.3%) (Figure 6.4A). In addition, neuronal substance P in the

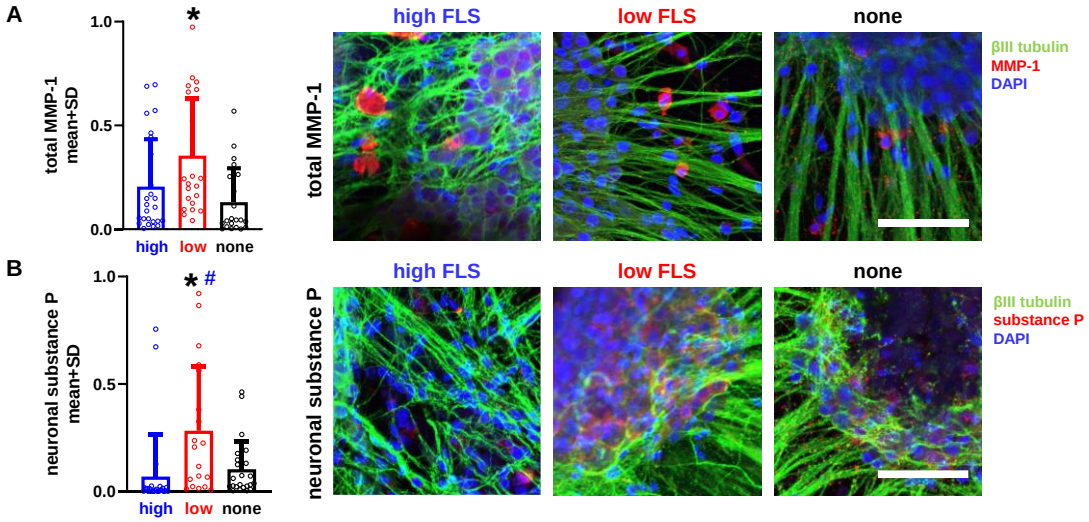

Figure 6.4. Stretched gels with a low FLS concentration exhibit the greatest expression of total MMP-1 and neuronal substance P, with representative images from gels in all three groups including regions with soma and/or axons. Images are shown for high FLS (Gel 44; DIV9), low FLS (Gel 11; DIV9), and none (Gel 11; DIV7), respectively, for MMP-1 images. Neuronal substance P images are of Gels 31 (DIV7), 7 (DIV9), and 11 (DIV7) for high FLS, low FLS, and none, respectively. **(A)** Total MMP-1 labeling is greatest in gels with the low FLS concentration, but is only significantly higher than the expression in gels with no FLS (*$p<0.01$). **(B)** Neuronal substance P labeling is also observed in both DRG soma and axons, but is more diffuse than MMP-1 labeling. The co-localization (yellow) of positive substance P labeling (red) with the marker βIII tubulin (green), for neurons is significantly greater in the low FLS group than in the other two groups (*$p=0.02$ vs. none; #$p<0.01$ vs. high FLS). The scale bar is 100μm in both panels and applies to all images. Bar graphs show summary data for each group with DIV7 and DIV9 pooled, overlaid with individual data points, each representing confocal images from a single element (open circle). Y-axes indicate percent positive pixels from 0 (0%) to 1.0 (100%).

low FLS group is higher than expression in gels with no FLS and only DRGs (none; $p=0.02$) and those with the high FLS concentration ($p<0.01$) (Figure 6.4B). Neuronal substance P appears to be more evident in the soma and surrounding many cell bodies (Figure 6.4B). Immunolabeled images and quantification for MMP-1 and neuronal substance P are detailed in Appendix I for both the stretched and unstretched control gels from this study.

6.4. Investigating Relationships between Load-Induced MMP-1, MMP-9 & Neuronal Firing

Since total MMP-1 increases with gel distraction to failure (Figure 6.4A), and MMP-1 regulates MMP-9 (Conant et al. 2002; Visse and Nagase 2003), it was hypothesized that MMP-9 also increases in parallel with MMP-1 in response to gel failure. To test that hypothesis, a subset of gels were assayed for MMP-1 *and* MMP-9 protein expression in the low FLS concentration group ($5x10^4$ cells/mL), since MMP-1 increases significantly with low FLS concentration over co-cultures without FLS (Figure 6.4A). Since the primary goal with this set of experiments was to evaluate the effect of distraction to failure on MMP-1 and MMP-9 expression, no stretch controls were also included.

Parallel increases in MMP-1 and substance P may indicate substance P mediation via MMP-1 by two possible mechanisms; MMP-1 can increase neuronal firing via ligand-substrate interactions with cell surface receptors on DRG somas or axons, and subsequently trigger neurotransmitter release (Allen et al. 2016; Conant et al. 2002; Dumin et al. 2001), and/or extracellular MMP-1 may activate any MMP-9 present in the co-culture environment and lead to downstream regulation of substance P by MMP-9 (Diekmann and Tschesche 1994; Visse and Nagase 2003). Further, although assaying MMP-9 after failure loading addresses the unknown of how load regulates MMP-9 expression, coincident with MMP-1 (Figure 6.4A), it does not elucidate whether MMP-1 *causes* any change detected in MMP-9 expression.

Two sets of experiments were conducted to investigate if MMP-1 directly regulates neuronal activity and/or increases MMP-9 expression in neurons. Separate experiments

exposed monolayer cultures containing only DRGs to exogenous MMP-1 and measured calcium signaling fluorescence traces as a proxy for action potentials or MMP-9 expression (Figure 6.5). To first define the temporal effects of exogenous MMP-1 on neuronal firing, calcium imaging time-lapse images were captured immediately, at one hour, and at 24 hours after the application of exogenous MMP-1 (Figure 6.5). Based on outcomes from the calcium imaging data, a second set of experiments probed MMP-9 expression at 24 hours after the addition of MMP-1 into the DRG culture media. Because MMP-1 exposure alone has also been shown to be cytotoxic to cortical neurons (Vos et al. 2000), cytotoxicity assays were also conducted on culture media.

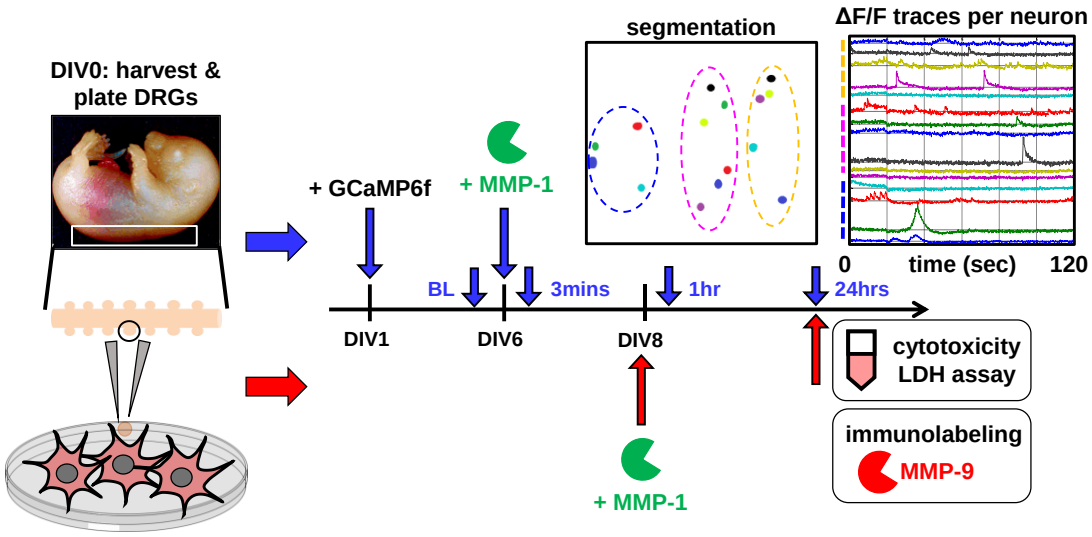

Figure 6.5. Study design for experiments testing the effect of exogenous MMP-1 on neuronal responses. In one set of experiments (timeline on top; blue arrows), dissociated DRG cultures were transduced with GCaMP6f to visualize calcium transients. Time-lapse images were acquired prior to MMP-1 application (baseline; BL), immediately after application (3mins), and at 1hr and 24hrs. Time-lapse images were manually segmented to delineate neurons and the normalized fluorescence traces (ΔF/F) were computed for each segmented neuron. Colored regions and neuron colors in the segmentation panel correspond to the y-axis colors and neuronal traces in the ΔF/F traces panel, respectively. In a second set of experiments (timeline on bottom; red arrows), cytotoxicity and MMP-9 expression were assayed at 24hrs after the application of exogenous MMP-1.

6.4.1. Immunolabeling of MMP-1 & MMP-9 in Co-Culture Gels After Failure Loading

6.4.1.1. Methods

A subset of co-culture collagen gels from DIV7 with a low concentration of FLS (n=3; $5x10^4$ cells/mL) (Figure 6.1) were prepared for immunolabeling immediately following distraction to failure as described earlier (Section 6.3.1). Gels were blocked and incubated overnight at 4°C with antibodies to MMP-1 (1:300; Proteintech) and MMP-9 (1:300; ThermoFisher). Gels were then washed in PBS and incubated at room temperature with the secondary antibodies goat anti-rabbit 633, goat anti-mouse 555 (1:1000; Alexa Fluor Life Technologies), and DAPI (1:200; ThermoFisher) to stain cell nuclei. Gels were imaged using a Leica confocal microscope focusing on FLS- and DRG-rich regions (n=7-8/each). A control gel with no stretch was also included. The number of pixels positive for each MMP immunolabel above levels in naïve cultures was quantified using MATLAB (code provided in Appendix B) and compared to the number in unstretched control using t-tests.

6.4.1.2. Results

The subset of gels immunolabeled for MMP-1 and MMP-9 fail at a peak force of 35±22mN at 4.1±1.5mm; this failure stretch increases expression of both MMP-1 ($p<0.01$) and MMP-9 ($p=0.04$) (Figure 6.6). Positive MMP-1 and MMP-9 labeling is observed in both the FLS- and DRG-rich regions of gels (Figure 6.6). Although MMP-1 labeling is more pronounced in DRG-rich regions, MMP-9 labeling appears equally distributed

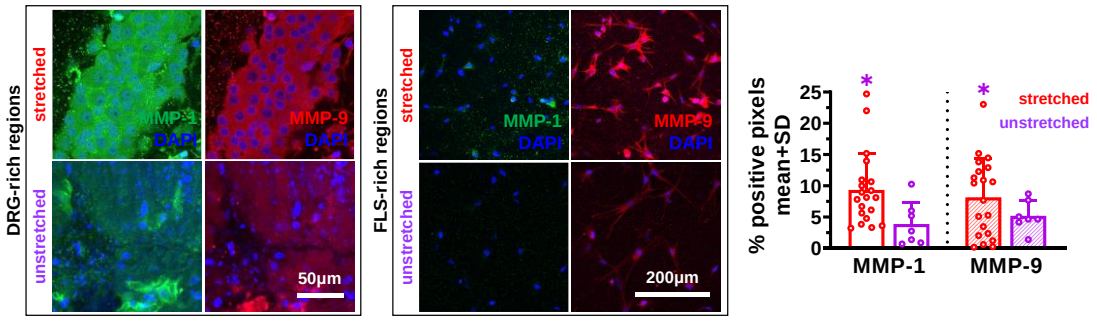

Figure 6.6. Expression of MMP-1 and MMP-9 in stretched gels with a low FLS concentration. Total MMP-1 and MMP-9 expression increase after stretch compared to expression in unstretched control gels (*p≤0.04). Images show MMP-1 and MMP-9 labeling in DRG-rich and FLS-rich regions of co-cultures. MMP-1 is primarily localized to DRGs, whereas elevated MMP-9 may be expressed by both DRG and FLS cells. The scale bars apply to all other images within their panel. Bar graphs show summary data overlaid with individual data points, each representing confocal images from a single gel element (open circle).

between the two types of regions of the gel (Figure 6.6). The confocal images and their densitometric quantification for this study are summarized in Appendix I.

6.4.2. Calcium Imaging with Exogenous MMP-1 in Neuronal Cultures

6.4.2.1. Methods

DRGs were harvested from day 18 embryonic rats, dissociated, and plated at $3.0x10^5$ cells/mL (Figure 6.5) (Cullen et al. 2012). One day after plating, neurons were transduced with the adeno-associated virus GCaMP6f (#AAV1.Syn. GCaMP6f.WPRE.SV40; 1:6000) that fluoresces with increases in intracellular calcium using protocols described in Chapter 5 (Section 5.5.2.3) (Chen et al. 2013). After five days to allow for viral expression (Chen et al. 2013; Patel et al. 2015), separate dishes were treated with MMP-1 in deionized water (100µL; 30µg/mL; Worthington; n=5) or water alone (control; n=2) (Figure 6.5). Fields of view containing the same neurons in each dish were imaged using a spinning disk confocal microscope (Nikon Eclipse TE2000U; 20Hz for one minute) before the addition of MMP-1 and then immediately and at one and 24

hours after the addition of activated human MMP-1 enzyme in order to define the temporal neuronal activity (Figure 6.5) (Patel et al. 2015). The MATLAB software script FluoroSNNAP was used to analyze images by segmenting neurons, normalizing their fluorescence, and using a template-matching algorithm to count calcium events in 60 second periods (Patel et al. 2015; Schultz et al. 2009). Neurons with no calcium activity at any time were omitted from analyses. Changes in the number of events for each neuron over time and across groups were compared by a multivariate analysis of variance (MANOVA) with matched pairs. A repeated-measures ANOVA compared the magnitude of events over time within groups.

6.4.2.2. Results

Of the total 159 neurons imaged, calcium activity was detected in 18 neurons from controls and 52 neurons exposed to MMP-1. In matched comparisons with neurons across groups, there is no difference ($p>0.05$) in activity from baseline detected immediately in either group, or in the controls from baseline to one hour (-0.78±1.99 events) or to 24 hours (-0.28±2.93 events) (Figure 6.7). MMP-1 increases calcium activity from baseline ($p<0.01$) at both one hour (+0.74±1.65 events) and 24 hours (+2.13±2.73 events) (Figure 6.7), which is significantly different from the response of control neurons ($p<0.01$). The number of calcium events does not change over time for the control or MMP-1 group immediately or after one hour, but does change ($p<0.01$) at 24 hours after MMP-1 exposure, with increased activity in over 60% of the neurons (n=36/52) (Figure 6.7).

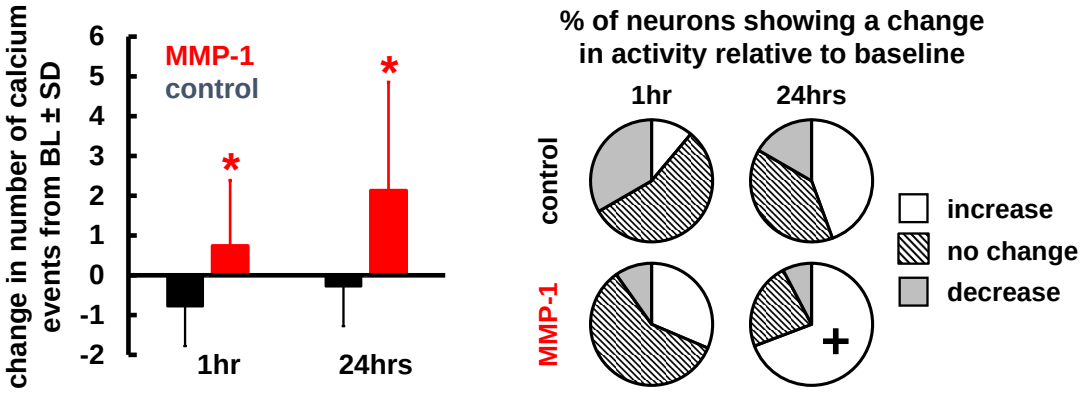

Figure 6.7. Neuronal firing with exposure to exogenous MMP-1. Neurons treated with MMP-1 exhibit significant increases in activity at 1 hour (1hr) and 24 hours (24hrs) (*p<0.01) compared to changes in control neurons. Over time, the magnitude of the number of event changes is significant only for MMP-1 at 24hrs (+p<0.01), with most neurons increasing their activity.

6.4.3. Neuronal MMP-9 Expression & Viability with Exogenous MMP-1

6.4.3.1. Methods

DRGs were harvested from day 18 embryonic rats, dissociated, and plated as full explants (6-10) on PDL-laminin treated glass in Neurobasal media (Figure 6.5) (Cullen et al. 2012). On DIV8, dishes were treated with MMP-1 (100µL; 30µg/mL; Worthington; n=4) or left untreated (n=2) for 24 hours since neuronal calcium signaling peaks at that time after MMP-1 exposure (Figure 6.7). After 24 hours, media aliquots were sampled and stored at -20°C for the viability assay. Cultures were fixed in 4% PFA for 15 minutes and stored in 1XPBS for immunolabeling. Cultures were incubated overnight at 4°C with an MMP-9 antibody (1:200; ThermoFisher), washed, and incubated at room temperature with goat anti-mouse Alexa Fluor 555 (1:1000) and DAPI (1:200). Confocal images (n=5-6/plate) were taken. The number of pixels positive for MMP-9 immunolabeling above levels in naïve cultures was quantified using densitometry analyses in MATLAB

(Appendix B). MMP-9 labeling in treated cultures was compared to that in controls using a t-test.

Cell viability was assessed by an LDH assay (Kartha et al. 2017). Matched untreated cultures were included as assay controls. The percent cell death between treated and untreated cultures was compared using a t-test.

6.4.3.2. Results

An exposure to exogenous MMP-1 for 24 hours increases MMP-9 protein expression in DRG cultures compared to naïve DRG cultures (Figure 6.8). LDH assayed in cell culture media that same time (24 hours) shows an increase in cell death, indicating a potentially cytotoxic effect of MMP-1 accompanying that elevated MMP-9 (Figure 6.8). MMP-9 labeled images and their quantifications, as well as LDH data, are detailed in Appendix I.

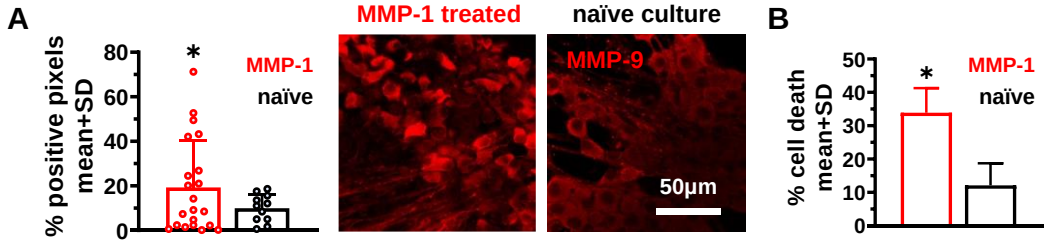

Figure 6.8. MMP-9 expression and cellular cytotoxicity after 24 hours of exogenous MMP-1 exposure. **(A)** Exogenous MMP-1 increases MMP-9 in DRG cells after 24 hours (*p=0.03), paralleled by an increase in cell death (*****p=0.02) **(B)**. The scale bar applies to both images; bar graphs show summary data overlaid with individual data points, each representing confocal images from an element (open circle) in **(A)**.

6.5. Discussion

Given that human ligamentous joint capsules include fibroblast-like synoviocytes and afferent nerve fibers in a collagenous matrix (Burgeson and Nimni 1992; Kallakuri et al. 2012; Yahia and Garzon 1993; Yamashita et al. 1996), the DRG-FLS co-culture collagen gel system used here provides a novel platform to better mimic the human anatomy, biomechanics, and physiology. Not surprisingly, because fibroblasts exert mechanical forces on their surrounding microenvironment (Dallon and Ehrlich 2008; Grinnell and Petroll 2010; Sander et al. 2011), including FLS in the DRG-collagen gel model increases the regional strains and the extent of microstructural reorganization at failure (Figure 6.3), despite not altering fiber organization *before* loading nor changing the macroscale failure properties (Table 6.1 & Figure 6.2). Although total MMP-1 and neuronal substance P are the same regardless of FLS concentration before any load (Table 6.1), both of those proteins are mediated after gel failure by FLS concentration (Figure 6.4). In fact, the increased protein expression exhibits differential patterns from both the strain responses and the fiber reorganization (Figures 6.3 & 6.4), which suggests that either or both cell types (FLS, DRG) is sensitive to the local surroundings in this system during failure loading.

The behavior of fibroblasts in fibrous networks and their subsequent effect on gel mechanics varies with the culture conditions (i.e. free-floating or constrained boundary conditions) (Grinnell 2003; Kural and Billiar 2013; Mohammadi et al. 2015). Fibroblasts in anchored collagen gels weaken the gel under tension after six days (Saddiq et al. 2009); whereas fibroblasts in free-floating collagen gels strengthen it under tension after one day

(Evans and Barocas 2009). In the current study, gels were cultured in 12-well plastic non-treated tissue-culture plates and could freely contract on their own. Indeed, gels with either the low or the high FLS concentrations contracted over the culture period, spontaneously detaching from the well wall and demonstrating contractile function throughout their time in culture. In fact, in pilot studies using low and high FLS concentrations and the same culture conditions as used in this study, gels decreased their diameter by approximately 46-50% after seven days in culture (Figure 6.9). In addition, although FLS were not visualized explicitly in each individual gel in this study, separate pilot studies confirmed the presence, phenotypic morphology, and viability of low and high FLS embedded in 2mg/mL collagen gels with immunolabeling and live-dead cell assays presented in Chapter 5.

Dermal fibroblasts cultured with the same collagen concentration (2mg/mL) and seeded at the same concentrations as used here, increase the gel modulus by between 1.12- and 3-times depending on the concentration (Evans and Barocas 2009). Although that

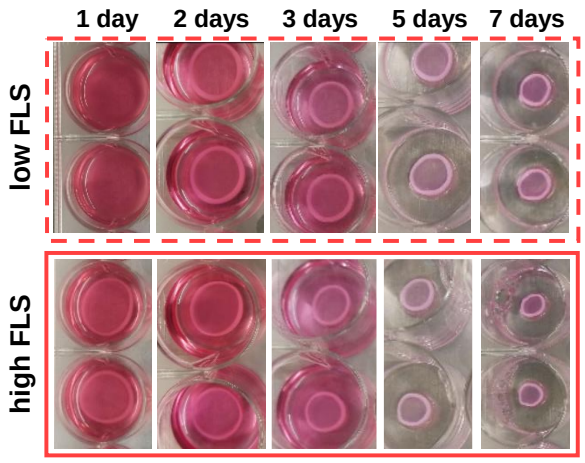

Figure 6.9. Collagen gel compaction by FLS cells over one week in culture. Although collagen gel compaction was consistently observed with a high concentration of FLS (target density of $1x10^5$ cells/mL), compaction was not always observed in gels with a low concentration of FLS (target density of $5x10^4$ cells/mL).

finding does not corroborate the lack of effect on stiffness observed for the same FLS concentrations (Figure 6.2), the difference may be due to functional differences between FLS and dermal or 3T3 fibroblasts, as well as the different culture times since the short culture time of one day used in the dermal fibroblast study has been hypothesized to not allow for collagen synthesis or degradation (Evans and Barocas 2009). In contrast, in gels seeded separately with either human dermal or mouse 3T3 fibroblasts, the failure force under uniaxial tension is decreased (Saddiq et al. 2009), for a similar loading rate (~0.16mm/sec) and time in culture (six days) but a lower cellular concentration ($2.5x10^4$ cells/mL). Since in that study the dermal and 3T3 fibroblast-seeded gels were anchored in culture (Saddiq et al. 2009) and the cell-mediated gel contraction would be minimal, any decrease in failure properties would likely be due to fibroblast-mediated remodeling via enzyme degradation (Saddiq et al. 2009). Although the gels in the current study with the higher FLS concentration do exhibit a lower failure force and stiffness than gels without FLS, those differences are not significant (Figure 6.2). Taken together, these studies suggest that early in culture strengthening of free-floating gels may be driven by cell contraction (Evans and Barocas 2009), and the weakening of stretched gels at later times in culture may be due to degradation (Saddiq et al. 2009). It is possible that by the time of mechanical testing (DIV7, DIV9), FLS-mediated collagen degradation may have occurred, which would explain why the FLS do not change the macroscale biomechanics (Figure 6.2). Further, despite the similar morphology and ability to synthesize and degrade ECM components across FLS, dermal, and 3T3 fibroblasts (Rinn et al. 2006), their differences in contractile behavior may differentially regulate their surrounding local microstructure.

Both experimental (Vader et al. 2009; Zhang et al. 2016) and computational (Abhilash et al. 2014; Hadi and Barocas 2013) investigations of collagen networks under tension demonstrate fiber realignment in the direction of loading, with load redistributed as fibers parallel to the applied tension align and those perpendicular to it buckle, facilitating a transition from a bending-dominated to a stretching-dominated response. The distribution of fibers in all groups regardless of the amount of FLS exhibit a distribution with more variance at failure than at reference (Figure 6.3), which likely captures the redistribution as fibers reorient towards the direction of loading (Figure 6.3). Reorganization of collagen fibers along the loading direction likely also reorients the DRGs embedded in that network. Since neurons are more compliant than collagen fibers, any change in collagen fiber kinematics can compress and/or stretch the neurons (Cullen et al. 2007; Sander et al. 2009a; Zhang et al. 2016). In fact, for this same neuron-collagen gel system under tension, the greatest extent of fiber alignment and elongation corresponds to the largest reorientation of neurons towards the loading direction *and* increased neuronal expression of pERK, an indicator of signal transduction caused by a noxious stimuli (Obata and Noguchi 2004; Zhang et al. 2016). That finding also suggests that DRGs in all of the gel constructs used here are likely being deformed since all gels exhibit some extent of fiber reorganization, with the greatest being in the high FLS gels (Figure 6.3). However, the protein expression is *not* increased in the gels with high FLS in which the fibers reorganize the most (Figures 6.3 & 6.4). This observation is contrary to the finding that pERK *increases* when fibers reorganize the most in the collagen gels with neurons only (Zhang et al. 2016). Although fiber reorganization may be responsible for some degree of

the increases in MMP-1 and substance P that are evident in all gels (Figure 6.4), the disconnect between fiber reorganization and protein increases brings to the forefront the notion that the different concentrations of FLS are likely interacting with their collagen microstructure differently.

FLS do not alter the organization of the collagen network during culture at the concentrations and days-in-vitro tested here (Table 6.1); but, under tension the collagen matrix reorganizes to different extents in a concentration-dependent manner (Figure 6.3). This may be due to the FLS contracting the network by different mechanisms depending on their concentration, leading to differential load distribution and fiber reorganization. For free-floating circular gels, fibroblasts contract their matrix either by tractional-force locomotion during cell migration, in which the fibers become aligned parallel to the fibroblasts around the circumference of the gel, and not in its center, or by elongation/spreading, which has no effect on the fiber organization (Dallon and Ehrlich 2008; Grinnell and Petroll 2010; Kural and Billiar 2013). During tractional-force locomotion, cytoplasmic microfilaments in fibroblasts contract, and pull on cell surface integrin-collagen fibril complexes through a myosin ATPase dependent mechanism (Dallon and Ehrlich 2008). In the cell elongation/spreading mechanism, fibroblasts reach out in all directions as they are introduced into a collagen matrix and pull collagen fibrils towards them (Dallon and Ehrlich 2008). Since at a low, but not high, fibroblast concentration, cells transition from the elongation/spreading to the locomotion mechanism (Dallon and Ehrlich 2008; Kural and Billiar 2013), it is likely that above a critical cell concentration threshold, fibroblasts start to reorganize collagen fibers circumferentially.

Although that concentration threshold is not defined for FLS, it is possible that the same mechanisms are at play and that the high FLS concentration is orienting collagen via the elongation and spreading mechanism. If this is the case, it may explain the graded reorganization response at failure that is concentration-dependent (Figure 6.3) and it would imply that the distribution of forces across fibers and the embedded cells also differs between groups. Differential force distribution could affect the soft embedded DRGs differently, and it is even possible that the greater fiber recruitment in the high FLS gels might *lower* the loads experienced by the DRGs. Although this could explain the disconnect between fiber reorganization and MMP-1 and neuronal substance P increases (Figures 6.3 & 6.4), quantifying gel contracture and the microstructure across the entire gel is needed to more fully elucidate the FLS-collagen fiber interactions that may also directly and/or indirectly affect neurons.

MMP-1 is expressed by both FLS and neurons in response to mechanical stimuli (Petersen et al. 2012; Yang et al. 2005; Zhou et al. 2014) and by FLS in inflammatory states (Bartok and Firestein 2010; Saravanan et al. 2014). Yet, since total MMP-1 was measured here (Figures 6.4 & 6.6), it is not known which proportion is attributable solely to FLS or to DRGs. Since MMP-1 was quantified only in regions containing DRG somas and/or axons in the first study presented in this chapter (Figure 6.4), it is probable that positive MMP-1 immunolabeling represents extracellular MMP-1 that is co-localized to DRG cells, or that MMP-1 that is sequestered in the cytosol of DRG cells (Craig et al. 2015; Murphy 2017). However, MMP-1 is also detected in FLS-rich regions of the gels after stretch (Figure 6.6), suggesting its increase could be driven by FLS. Ultimately, it is likely that

load regulates MMP-1 in both DRG and FLS cells since both have been found to express MMP-1 when they are mechanically stimulated (Ghasemi et al. 2018; Yang et al. 2005; Zhou et al. 2014).

Given the quick fixation of cells after stretch, it is likely that differences in MMP-1 protein between groups indicate differential MMP-1 regulation via cellular localization, cell sequestration, endocytic/exocytotic processes, or even stretch-induced cell rupture (Craig et al. 2015; Murphy 2017; Visse and Nagase 2003), not regulation on the transcriptional or post-translational levels which take hours to days (Petersen et al. 2012; Yang et al. 2005). Although MMP-1 is quantified in DRG-biased images (Figure 6.4), it may be FLS-secreted (Figure 6.6) and could depend on FLS proliferation throughout the gel (Evans and Barocas 2009; Petersen et al. 2012). In fact, pilot studies co-labeling MMP-1 either with the intermediate filament vimentin, which structurally identifies fibroblasts, or with the neuronal microtubule βIII tubulin, show that MMP-1 co-localizes with *both* FLS and neurons (Figure 6.10), supporting the notion that stretch increases FLS-produced MMP-1 in addition to the MMP-1 that co-localizes to DRGs (Figures 6.4 & 6.6).

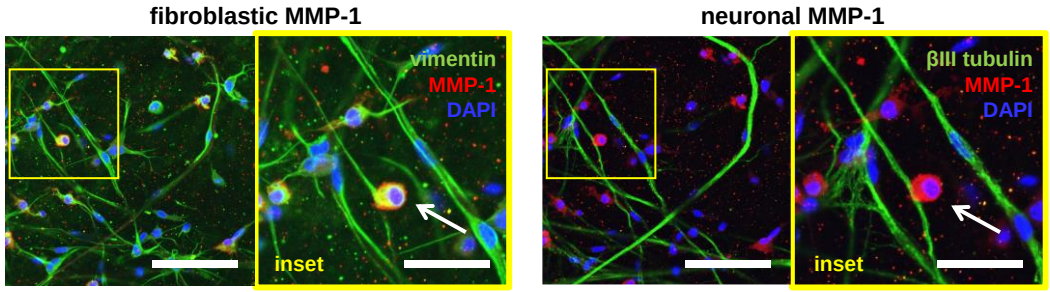

Figure 6.10. The co-localization (yellow) of vimentin or βIII tubulin (green) and MMP-1 (red) shows MMP-1 co-localized with FLS and DRG axons in a co-culture gel from DIV9. The insets show a cell labeled positively (white arrows) for MMP-1 that is clearly co-localized with vimentin, not βIII tubulin, suggesting MMP-1 is from the FLS cell type in this specific cell. The scale bar for the low magnification images is 100μm and is 50μm in the insets.

Although neither cell-specific MMP-1 nor FLS proliferation analyses were included in the present study since the primary goal was to investigate neuronal outcomes in the context of nociception, those findings highlight the need to evaluate MMP-1 expression by cell type in order to understand if it is being secreted by FLS (Petersen et al. 2012) and/or neurons (Zhou et al. 2014). Furthermore, along with neurons, DRG somas may contain Schwann cells, microglia, and resident macrophages (Melli and Höke 2009), which may contribute to stretch-induced changes in cell physiology, although these cell populations were not investigated in this study.

Although MMP-1 is elevated after failure in the presence of FLS, it is only different from gels with no FLS at the lower ($5x10^4$ cells/mL) FLS concentration (Figure 6.4), despite similar force and strains at failure in both groups with FLS (Figures 6.2 & 6.3). This disconnect between the biomechanical and MMP-1 outcomes in the low and high FLS gels supports the assertion that the force distribution and deformations on the embedded cells are concentration-dependent and contribute to differential MMP-1 expression (Figure 6.4). An alternative hypothesis is that FLS-mediated degradation occurs by the time of the mechanical testing (Saddiq et al. 2009), resulting in a less dense collagen network at the time of gel stretch; such an altered gel composition could lead to cell-secreted MMP-1 that is trapped in the collagen matrix to be released to the gel surface where the DRGs are, making the MMP-1 more available for antibody detection via immunolabeling; it could also be released out of the gel into the testing bath, making it non-detectable via immunolabeling (Attia et al. 2014). If either or both mechanisms occur then the levels of secreted and/or trapped MMP-1 would depend on the degree of matrix degradation, an

effect which might be FLS concentration-dependent since fibroblasts model and remodel their surrounding ECM (Dallon and Ehrlich 2008; Grinnell and Petroll 2010; Kural and Billiar 2013; Wang et al. 2007). Assaying secreted MMP-1 in the culture medium, together with quantifying MMP-1 proximal to cells (Figure 6.4), would provide insight(s) into the effects of such factors on the local biochemical environment of joint tissues. Finally, although neither overall time in culture nor FLS concentration influence the baseline protein levels (Table 6.1), assessing cell-localized, gel entrapped, and secreted proteins, and in larger sample sizes, would provide a more complete understanding of the cellular environment in the resting state before stretch.

Elevated total MMP-1, regardless of the cellular source, can increase neuronal excitability (Figure 6.7) (Allen et al. 2016) and/or contribute to receptor- or cytokine-mediated nociceptive signaling (Boire et al. 2005; Conant et al. 2002; Conant et al. 2004; Miller et al. 2014; Visse and Nagase 2003). Exposure to exogenous MMP-1 alone causes an influx of intracellular calcium in DRG neurons (Figure 6.7) and also has a cytotoxic effect (Figure 6.8), an effect that has also been demonstrated in cortical neurons (Allen et al. 2016; Chen et al. 2013; Patel et al. 2015; Vos et al. 2000). The ability of exogenous MMP-1 to increase neuronal firing (Figure 6.7) indicates more action potentials and increased neuronal excitability, and suggests that MMP-1 that is increased by stretch (Figure 6.4) may also excite DRG neurons independent of the stretch itself and may even have an excitotoxic effect (Figure 6.8). Since increased afferent activity and neuronal hyperexcitability are characteristic of pain from joint trauma (Crosby et al. 2015), it is possible that MMP-1 may have a role in vivo by potentiating afferent hyperexcitability.

Further, both pro-MMP-1 and MMP-1 bind to the $\alpha_2\beta_1$-integrin complex (Conant et al. 2004) and the PAR-1 receptor (Allen et al. 2016; Conant et al. 2002) on neurons, which are both involved in nociception and painful facet joint injury (Dong et al. 2013; Smith and Winkelstein 2017; Zhang et al. 2017). This suggests that elevated MMP-1 (Figures 6.4 & 6.6) in the low FLS concentration gels may increase neuronal excitability or propagate nociceptive signaling (via increased substance P) through an $\alpha_2\beta_1$-integrin and/or PAR-1 receptor mediated mechanism. In fact, inhibiting the $\alpha_2\beta_1$-integrin complex has been shown to prevent the strain-induced increases in axonal substance P in this same DRG-collagen model under equibiaxial stretch injury (~20% strain) (Zhang et al. 2017). Since total MMP-1 and neuronal substance P together increase in low FLS concentration gels (Figure 6.4), it is possible that the increase in neuronal substance P may be due to the concomitant increase in MMP-1 via integrin interactions. Probing MMP-1 co-expression with other pain-related neuronal receptors to which MMP-1 can bind (Boire et al. 2005; Conant et al. 2002; Conant et al. 2004; Visse and Nagase 2003) would provide important physiological insight.

The higher neuronal substance P expression that is evident in the low FLS gels (Figure 6.4) provides a proxy for indicators of a heightened state of nociceptive signaling (Lee and Winkelstein 2009; Zhang et al. 2017; Zhang et al. 2018a) and may also contribute to a further upstream neuronal signaling role of MMP-1 (Conant et al. 2002; Visse and Nagase 2003). In addition to its ability to bind to the $\alpha_2\beta_1$-integrin complex and to affect downstream signaling cascades (Conant et al. 2004), MMP-1 stimulation of release and/or activation of other MMPs is also directly involved in substance P signaling (Conant et al.

2002; Visse and Nagase 2003). Most notably, MMP-1 stimulates neuronal MMP-9 secretion (Conant et al. 2002) and activates pro-MMP-9 (Visse and Nagase 2003). Indeed, the ability of MMP-1 exposure alone to increase MMP-9 in DRG cultures (Figure 6.8) suggests that MMP-1 may be directly responsible for the simultaneous increase in MMP-9 along with MMP-1 that is evident after failure (Figure 6.6). Since MMP-9 directly cleaves substance P (Diekmann and Tschesche 1994), it may also contribute to neural regulation in vivo (Mitchell et al. 2013). MMP-9, like MMP-1, can sensitize peripheral neurons (Kawasaki et al. 2008), and is necessary for early-phase acute pain (Kawasaki et al. 2008). Whether the increased neuronal substance P (Figure 6.4) is MMP-1-independent or MMP-1-dependent, that finding implies incorporating FLS not only better mimics the anatomy and physiology of ligaments in a culture system but also alters cell-cell interactions to dysregulate neuronal signaling.

Although MMP-1 may act independent of regulating the ECM, it is also possible that MMP-1 alters the microstructural environment via collagen degradation much like bacterial collagenase (Figures 5.14 & 5.15) (Visse and Nagase 2003), and by doing so, it triggers afferent signaling, including upregulation of substance P (Chan et al. 2018; Zarei et al. 2017; Zhang et al. 2016; Zhang et al. 2018a). However, MMP-1-mediated degradation depends on MMP-1 enzyme kinetics and diffusion (Flynn et al. 2010), which likely occurs over longer time scales than does MMP-1 signaling. Since cellular assays were made within minutes of the mechanical stimulus in this study, it is more likely that if MMP-1 mediates neuronal substance P, it is through an ECM-independent mechanism.

The finding that the mechanical effect of FLS on the collagen network is not resolved at the macroscale (Figure 6.2) and varies with FLS concentration on smaller scales (Figure 6.3) has implications for injury thresholds. This is further complicated for DRGs in a stretched heterogeneous network, since the microenvironment in capsular ligaments can vary with anatomical location (Kallakuri et al. 2012; Yahia and Garzon 1993; Yamashita et al. 1996). Even in simple cases, uniaxial tension produces spatial variability in strain fields and fiber organization (Zhang et al. 2016); as such, the local microenvironment of the embedded cells, and subsequently their mechano-regulated responses, also varies. In fact, computational models of the ligamentous capsule report altered strains and fiber kinematics experienced by neurons in a stretched fibrous network that are not predicted by macroscale mechanics (Chan et al. 2018; Zarei et al. 2017). Furthermore, those models find that embedded cells can sustain strains much greater than the bulk gel stretch (Chan et al. 2018), and that "strain amplification" depends on the direction and angle of loading, cell geometry and orientation, and fiber volume and organization (Chan et al. 2018; Zarei et al. 2017). Of note, effects of FLS have not been considered in those models.

The current finding that FLS have differential effects on regional strains and microstructure (Figure 6.3) supports the need to include FLS or other contractile cells into computational models to fully capture their physiological effects, improve model fidelity, and perhaps help elucidate FLS-fiber interactions that are not yet able to be probed experimentally. The concentration-dependent effect of FLS on collagen gel microstructure is particularly relevant since the ligamentous capsule regions have different FLS densities

and show regional variability (Yamashita et al. 1996). Together, these findings imply there is a high likelihood that variable mechanosensitive properties may be conferred to innervating fibers based on the regional anatomical FLS cell density. Since microstructure reorganization at failure and loading-induced protein expression are both concentration-dependent (Figures 6.3 & 6.4), it is likely that the nerve fibers in FLS-dense regions of the ligament reside in a microstructural and cellular environment that is unique from than those in FLS-sparse regions.

In summary, this study presents considerations for in vitro modeling of the complex biomechanical and physiological anatomic structures to better understand their multiscale behavior. Addition of FLS into an existing DRG-collagen gel model (Zhang et al. 2017; Zhang et al. 2018a) not only alters the regional microenvironment in a concentration-dependent manner but also modulates the physiologic cellular responses (Figures 6.3 & 6.4). Load-induced increases in MMP-1 may act upstream of MMP-9 (Figure 6.8) and/or directly influence neuronal firing (Figure 6.7). Certainly, there are also cell-specific variations that must be considered when incorporating fibroblasts with neurons and an ECM. The biomechanical and physiological effects of cell-cell and cell-fiber interactions are themselves mediated by the presence, and extent of, FLS present. Nevertheless, this study demonstrates that FLS mechanically alter the local DRG microenvironment and affect load-induced protein expression in neurons, and are thus critical in understanding nociceptive mechanisms in capsular ligaments. Certainly, expanding experimental techniques and applications to better visualize both the collagen microstructure *and* the cells within the matrix, along with quantifying bulk gel contracture is needed to fully

describe the FLS-collagen fiber interactions and how they relate to cellular and microstructural function and dysfunction, especially under load. Nevertheless, this study provides important information about mechanical and physiological interactions between afferent fibers and FLS, with each other, and their surrounding collagenous network, emphasizing the importance of considering the FLS cell type in modeling ligamentous capsules.

6.6. Integration & Conclusions

The studies in this chapter support the hypothesis that FLS regulate the microstructure of their surrounding collagen network under stretch (Figure 6.3). Moreover, the outcomes presented here demonstrate that FLS-regulation of collagen network kinematics under load is concentration dependent. Similar to the result that FLS-seeded collagen gels are not biomechanically stronger than 3T3-seeded gels (Figure 5.10), DRG-FLS gels do not have stronger biomechanical properties than collagen gels with only DRGs (Table 6.1 & Figure 6.2). The similar macroscale biomechanics of gels with and without FLS could be due to the ECM remodeling by FLS cells (Saddiq et al. 2009). Yet, the effect of FLS on network composition is not assayed in this study. Nonetheless, differential effects of the presence and extent of FLS on collagen microstructure and neuronal physiology, and *not* on macroscale gel biomechanics, strengthens the assertion that interactions on a *local* cell- and fiber- level drive neuronal increases in substance P and MMP-1 localized to DRG soma and axons (Figure 6.4). Nociceptive regulation by MMP-

1 is further supported by the finding that exogenous MMP-1 exposure increases neuronal firing in DRG cultures (Figure 6.7).

The results presented in this chapter demonstrate that FLS cells influence neuronal expression of the nociceptive neuropeptide substance P (Figure 6.4B), supporting the hypothesis for Aim 3. Together with the evidence in Chapter 5 supporting a distinct functional role of FLS as a fibroblast phenotype, increased substance P in the presence of fibroblasts underscores the importance of including FLS in models of the capsular ligament, especially in the context of nociception and understanding MMP-related signaling pathways.

MMP-1 is detectable at baseline in gels with and without FLS (Table 6.2), with no difference in MMP-1 levels assayed by immunolabeling. That finding supports the hypothesis in Aim 3 that fibroblasts secrete low levels of MMPs at baseline, but does not suggest that MMP levels are any different than cultures without FLS, at least for protein localized to DRG somas and axons. FLS are known to secrete MMPs in normal and healthy remodeling processes (Bartok and Firestein 2010), and it is very likely that MMP-1 expression may be elevated in gels with FLS but that the MMP-1 is localized to the FLS cells, trapped within the matrix but distant from DRGs, or in the culture media (Attia et al. 2014). Indeed, elevated MMP-1 in regions not probed in this study (FLS-localized or in culture media) could explain why more MMP-1 is localized to DRG soma and axons immediately after stretch (Figures 6.4 & 6.6).

The findings in this chapter that an exposure to exogenous MMP-1 alone increases neuronal activity (Figure 6.7) and neuronal MMP-9 expression (Figure 6.8) were

conducted in DRG-only monolayer cultures absent a collagen substrate and FLS cells. As such, those findings support that MMP-1 directly regulates neuronal responses, at least in part, via pathways that are independent of the surrounding collagen network. Taken together with the findings from Chapter 5 that bacterial collagenase decreases collagen density in concert with altered neuronal signaling (Figures 5.14 & 5.15) and the fact that bacterial collagenase and MMP-1 have similar collagenolytic functionality (Fields 2013), it is likely that MMP-1 mediates neuronal responses via collagen-independent *and* collagen-dependent pathways. The studies that are presented in Chapter 7 test the effect of exogenous intra-articular MMP-1 in the rat and assay both the biomechanical effect of MMP-1 on the collagen network of the capsular ligament and the physiological effect of MMP-1 on substance P expression in DRG neurons and the spinal cord. Studies in the rat quantify behavioral sensitivity in order to determine if any effects of MMP-1 on ligament biomechanics and/or neuronal physiology are relevant to the manifestation of pain. The ability of MMP-1 to directly alter MMP-9 levels and firing patterns in neurons (Figures 6.7 & 6.8) also has implications for the MMP-1 that is detected in tissues from patients with painful TMJ disorders (Chapter 3) (Ita et al. 2020a), and supports that the correlations between MMP-1 with MMP-9 (Figure 3.3) and pain scores (Figure 3.4) may indeed be driven by mechanistic relationships between MMP-1 and MMP-9, and between MMP-1 and nociceptive signaling, respectively.

The studies in the chapter assay MMP-1 and MMP-9 immediately after distraction to failure. Given the fixation of co-cultures which minutes, differences in MMP-1 and MMP-9 expression (Figures 6.4 & 6.6) are almost certainly due to rapid cellular re-

localization of MMPs via endocytosis, exocytosis, or cell rupture (Craig et al. 2015; Murphy 2017; Visse and Nagase 2003). Although the rapid re-localization of MMPs in response to stretch, especially to neuronal-rich regions (Figures 6.4 & 6.6) may have implications on downstream nociceptive signaling (Allen et al. 2016; Conant et al. 2002; Dumin et al. 2001; Vos et al. 2000), any load-induced changes at the MMP transcriptional and/or post-translational level cannot occur in the matter of minutes (Petersen et al. 2012; Yang et al. 2005). Studies in Chapter 8 assay MMP-1, MMP-9, and substance P protein expression at 24 hours after a painful stretch to allow for MMP regulatory mechanisms to take place. Further, failure loading in uniaxial tension was imposed in the studies in this chapter, yet imposing *sub-failure* stretch to this co-culture model will provide further quantitative measures of how FLS may modulate biomechanical thresholds for nociceptive signaling previously defined in the DRG-collagen gel model absent FLS (Zhang et al. 2017; Zhang et al. 2018a). Moreover, imposing sub-failure loading in a *biaxial* configuration better mimics the bony boundaries of the capsular ligament in situ. Accordingly, studies in Chapter 8 utilize a sub-failure painful stretch in equibiaxial tension.

Chapter 7

Effects of Intra-Articular MMP-1 on Pain, Facet Joint Tissue Structure-Function, & Neuronal Dysregulation

This chapter has been adapted from:

Ita ME, Winkelstein BA. Intraarticular MMP-1 is sufficient to induce pain & substance P regulation in DRG afferents absent any structural damage. *Cervical Spine Research Society Annual Meeting*, Abstract #40, November 2019. New York, NY.

Ita ME, Leavitt OME, Winkelstein BA. MMP-1 induces joint pain that may be mediated by increased activity in peripheral neurons. *Orthopaedic Research Society Annual Meeting*, Abstract #2184, March 2018. New Orleans, LA.

Ita ME, Singh S, Welch RL, Troche HR, Ghimire P, Winkelstein BA. Intra-articular MMP-1 induces long-lasting pain accompanied by altered capsular structure, biomechanical function, & nociceptive responses. *Osteoarthritis & Cartilage*, submitted.

7.1. Overview

Although the studies presented in this thesis demonstrate that MMP-1 levels track with patient-reported pain in human patients (Chapter 3) and increase in response to both biomechanical and biochemical stimuli coincident with the nociceptive neurotransmitter substance P in vitro and in vivo (Chapters 4-6), they do not enable answering the question of whether MMP-1 *alone* is sufficient to initiate nociception from the joint. The studies presented in this chapter align with parts of Aim 2 and define the effect of exogenous intra-articular MMP-1, absent other painful exogenous stimuli, on pain-like behaviors in the rat

as well as begin to test the hypothesis that MMP-1 may be implicated in trauma and/or degenerative joint pain (Cohen et al. 2007; Elliott et al. 2009; Haller et al. 2015; Ita et al. 2017; Kim et al. 2015; Loeser et al. 2012). The studies in this chapter use the same behavioral, histological, and immunohistochemical assays that are reported with intra-articular bacterial collagenase in Chapter 4 (Ita et al. 2020b), including evaluating the expression of substance P and MMP-9 protein in peripheral neurons. Substance P and MMP-9 expression were also evaluated in the spinal cord since changes in central processing are also associated with joint-mediated chronic pain (Finan et al. 2013; Lluch et al. 2014). These studies also expand prior work with collagenase to augment evaluation of C6/C7 capsular ligament functional and structural responses to mechanical testing with integrated polarized light imaging. Fiber alignment maps and the corresponding dihedral angles of the fibers are extracted from polarized light images and quantified using the circular variance (CV), which measures the heterogeneity of fiber directions, where a lower CV indicates the alignment of many collagen fibers in a common direction and a higher CV indicates that the angles of collagen fibers have a larger spread (Ita and Winkelstein 2019; Miller et al. 2012; Zhang et al. 2016). By integrating these techniques, studies provide more comprehensive insight into how exogenous MMP-1 affects the joint structure-function relationships at both the whole joint macroscale and at the microstructural level of the collagenous capsular fiber network.

Studies using polarized light collectively demonstrate that areas of the facet capsule with the highest fiber reorganization correspond to those regions that exhibit microstructural damage to the collagen matrix (Quinn and Winkelstein 2008; Quinn and

Winkelstein 2009; Quinn and Winkelstein 2010; Quinn et al. 2010a; Quinn and Winkelstein 2011). Furthermore, regions with the greatest fiber realignment are correlated with subsequent tissue rupture (Quinn and Winkelstein 2009; Quinn et al. 2010a), but do not necessarily correspond to the regions with the greatest maximum principal or shear strain (Quinn and Winkelstein 2008). That work also defines how the microstructure of the capsular ligament contributes to the biomechanical function and potential for injury in the context of loading known to be painful in otherwise unaltered ligaments (Quinn and Winkelstein 2009; Quinn et al. 2010a). Although there are substantial and growing studies that describe the potential for injury and/or altered local mechanics, little is known about what factors may predispose the capsular ligament to altered biomechanical responses during loading. In the current study, polarized light techniques are integrated with mechanical loading to define how intra-articular exposure to exogeneous MMP-1 alters the microstructure of the capsular ligament in situ and in response to loading. A particular focus is placed on assessing the macro- and microstructural kinematics at the first occurrence of anomalous fiber realignment, ligament yield, ligament failure, and ultimate rupture of the tissue since those events collectively represent mechanical events both above and below the strain threshold for painful loading. The studies in this chapter begin to elucidate mechanisms by which MMP-1-induced alterations to the ligament's microstructure compromises integrity of the collagen network. Furthermore, the implications of intra-articular MMP-1 on the ligament's microstructure are contextualized with MMP-1's effects on behavioral sensitivity and nociceptive dysregulation in the peripheral and central nervous systems.

7.2. Relevant Background

Musculoskeletal pain is the most common single type of chronic pain and reported cause of disability, with neck and low back pain being among the most prevalent sources of pain (Institute of Medicine 2011). Over 15% of adults report neck pain in a three-month span, and it is estimated that the cervical facet joints are the source of pain in 28% of neck-pain cases (Manchikanti et al. 2004; Manchikanti et al. 2015; Schofferman et al. 2007). The facet joints of the spine act as movement and pain sensors owing to their innervation by mechanoreceptors and nociceptors, respectively (Bogduk and Marsland 1988; Kallakuri et al. 2012; McLain 1994).

The ligamentous facet capsule is one of the innervated facet joint tissues and is capable of transmitting pain sensation under pathologic conditions (Cavanaugh et al. 2006; Ita et al. 2017; Jaumard et al. 2011; Manchikanti et al. 2004). For example, excess stretch of the capsular ligament resulting from either direct trauma to the facet joint or its mechanical injury due to altered spine kinematics can initiate physiological cascades that induce sensitivity and modifications in neuronal signaling (Crosby et al. 2014; Crosby et al. 2015; Ita et al. 2017; Lu et al. 2005; Sperry et al. 2017). In addition to injury, joint-mediated pain occurs with tissue degeneration that is characteristic of diseases like osteoarthritis (Neogi 2013; Torrie and Adams 2012). Joint pain can also manifest seemingly spontaneously in the absence of injury and degeneration (Hunter et al. 2013; Sharma 2016). Both molecular mechanisms that cause joint-mediated pain across etiologies including injury, non-injurious degeneration, or by other mechanisms, and the degree of involvement of the capsular ligament across etiologies, are not well defined.

Degeneration is caused by a complex combination of biomechanical and biological cascades that initiate nociception in innervated joint tissues (Loeser et al. 2012; Malfait and Miller 2016; Varady and Grodzinsky 2016), and there is evidence that neuropathic and inflammatory cascades accompany degeneration to maintain pain (Malfait et al. 2013). Yet, if, and which, biologic mediators regulate the pathophysiological cascades that transmit nociceptive signals in joint-mediated pain etiologies is unknown.

Matrix metalloproteinases (MMPs) are ubiquitous proteases with roles in healthy and disease states that may regulate the mechanical, structural, and/or cellular responses of resident nerves and/or fibroblasts in the capsular ligament in painful joint pathology (Agrawal et al. 2008; Huntley 2012; Rosenberg 2002; Sbardella et al. 2012). The interstitial collagenase MMP-1 is a likely mediator of pathophysiological cascades in joint tissues since it is in the joint synovium, fluid, and capsule after trauma (Cohen et al. 2007; Haller et al. 2015; Konttinen et al. 1999) and with degeneration (Kim et al. 2015; Loeser et al. 2012). Moreover, MMP-1 functions as a direct regulator of structure and cell-signaling, and as an indirect regulator of joint mechanics. For example, MMP-1 degrades extracellular matrix (ECM) components of innervated joint tissues, including the synovium and capsular ligament (Visse and Nagase 2003), and in doing so can alter the biomechanics of the overall joint (Grenier et al. 2014; Otterness et al. 2000). In addition to catabolism of the ECM and independent of its proteolytic activation, MMP-1 acts on several neuronal receptors involved in nociception (Allen et al. 2016; Dumin et al. 2001) and has substrates to neuropeptides and cytokines that mediate pain (Visse and Nagase 2003). However, despite growing evidence of increased MMP-1 in painful diseases, its role in *joint* pain is

not defined. Moreover, it is unknown if MMP-1 *alone*, absent trauma or degeneration, is enough to induce pain.

As such, an in vivo study tested whether intra-articular MMP-1 induces pain when introduced in the rat C6/C7 facet joint. This study tests the hypothesis that exogenous intra-articular MMP-1 in the facet joint induces behavioral sensitivity via its mediation of the capsular ligament's collagen network and its regulation of both substance P and MMP-9. Behavioral sensitivity was measured using mechanical hyperalgesia for 28 days after its injection. After 28 days, the cartilage, bone, and capsular ligament of the injected joints were assessed using histology to evaluate the extent of structural degradation. The macroscale biomechanics, surface strain fields, and microstructural kinematics of the capsular ligament under tensile load were also tested in isolated joints. Quantitative polarized light imaging (QPLI) was integrated with that testing to quantify microstructural changes in the collagen fiber kinematics prior to, and at relevant mechanical events during, tensile loading (Quinn and Winkelstein 2009; Quinn et al. 2010a; Tower et al. 2002). To evaluate effects of intra-articular MMP-1 on unwound collagen chains in the capsular ligament, a collagen hybridizing peptide (CHP) was used to detect degraded triple-helical collagen in capsular ligament tissue homogenates from samples taken at day 28 (Lin et al. 2019). Substance P, a neurotransmitter involved in nociception (Basbaum et al. 2009; Zhang et al. 2017), and MMP-9, a gelatinase implicated in neuropathic pain and regulated by MMP-1 (Conant et al. 2002; Kawasaki et al. 2008), were both assayed in dorsal root ganglia neurons (DRG) and the spinal cord at the same time point (day 28).

7.3. Methods

7.3.1. Intra-Articular Injection, Mechanical Hyperalgesia & Tissue Harvest

All procedures were approved by the University of Pennsylvania IACUC and performed under the Committee for Research and Ethical Issues of the IASP guidelines (Zimmermann 1983). Studies used Male Holtzman rats (Envigo; Indianapolis) with surgeries performed under inhalation isoflurane anesthesia (4% induction; 2.5% maintenance). To expose the cervical facet joints, a midline incision was made over the C4-T2 vertebrae and the paraspinal musculature was cleared as described in Section 4.3.2 (Figure 4.2). The bilateral C6/C7 facet joints were further finely cleared of musculature and injected bilaterally with either 10μL of human recombinant MMP-1 (n=18) dissolved in sterile water (30μg/mL; SRP3117; Sigma; St. Louis, MO) or only sterile water (10μL; vehicle n=13) (Figure 7.1). Immediately after injection, wounds were sutured and stapled, and rats were recovered in room air. Weight gain and animal welfare were monitored daily, and the surgical staples were removed after 14 days.

To measure pain responses, behavioral sensitivity was assessed by measuring mechanical hyperalgesia in the bilateral forepaws of each rat before surgery (baseline) and at post-operative days 1, 3, 5, 7, 11, 14, 17, 21, 25, and 28 (Figure 7.1). A tester blinded to procedures measured the paw withdrawal threshold (PWT) in the bilateral forepaws in response to stimulation using a series of von Frey filaments (Stoelting; Wood Dale, IL) of increasing strength (1.4, 2, 4, 6, 8, 10, 15, and 26 grams) (Figure 7.1) (Crosby et al. 2014; Crosby et al. 2015; Ita et al. 2020b; Kras et al. 2015; Quinn et al. 2010b). Each filament was separately applied five times to each forepaw, and a positive response was recorded if

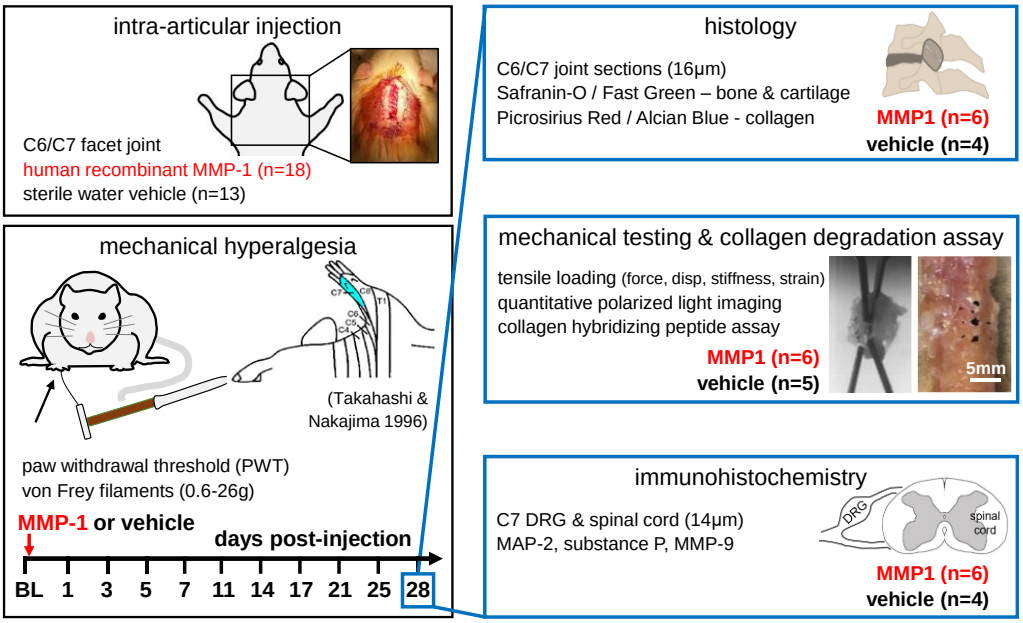

Figure 7.1. Schematic depicting the study design and specifics for each outcome measure. Rats underwent an intra-articular injection of either MMP-1 or vehicle at baseline (BL); the photograph shows a rat with its wound sutured immediately after injection. Mechanical hyperalgesia quantified behavioral sensitivity for 28 days. On day 28, tissue was harvested from separate groups of rats for: joint histology, mechanical testing of isolated joint tissue, a collagen degradation assay, or immunohistochemical assays of neural tissues.

the rat exhibited licking, shaking, or withdrawing the forepaw in response to stimulation. Once a positive response was recorded for two consecutive filaments, the lower strength filament was taken as the PWT for that testing session. Three rounds of testing were completed on each designated day, separated by at least 10 minutes; all rounds were averaged across rats for both the left and right PWTs on each day.

On day 28, immediately after behavior testing, rats were anesthetized with sodium pentobarbital (65mg/kg; i.p.) and underwent transcardial perfusion with phosphate-buffered saline (PBS; 250ml) followed by 4% paraformaldehyde (PFA; 250ml) (MMP-1 n=12; vehicle n=8), or PBS only (n=6 MMP-1; n=5 vehicle). Spinal columns from the occiput to T2 (MMP-1 n=6; vehicle n=4) or cervical DRG and spinal cord tissues (MMP-

1 n=6; vehicle: n=4) were harvested from separate groups of rats after perfusion with PFA (Figure 7.1). Fixed spinal columns were post-fixed in 4% PFA for 24 hours, held in sucrose (Sigma; St. Louis, MO) dissolved in PBS (30%) for seven days, and decalcified in 10% EDTA (Thermo Fisher; Waltham, MA) for three weeks (Ita et al. 2020b; Kras et al. 2015). The C6/C7 facet joint segment was embedded in Tissue-Tek OCT Compound (Fisher Scientific; Waltham, MA), coronally cryosectioned (16μm), and thaw-mounted onto Superfrost Plus slides (Fisher Scientific). Fixed DRGs and spinal cord tissues were post-fixed in PFA for 24 hours, held in 30% sucrose for seven days, and embedded in OCT. Axial cryosections (14μm; 6-8/rat) of DRG and spinal cord sections were thaw-mounted onto Superfrost Plus slides. Joint and neural tissue sections from naïve rats (n=2) were included in all analyses in order to provide un-operated tissues as control samples.

Fresh, unfixed matched spinal columns from occiput to T2 (MMP-1 n=6; vehicle n=5) were separately harvested from rats that received perfusion with only PBS for biomechanical testing and the CHP assay (Figure 7.1). Fresh cervical spinal columns were wrapped in saline-soaked gauze and stored at -20ºC; a fresh spinal column from a naïve rat was also processed for biomechanical testing and the CHP assay and served as a normal comparison for an un-operated facet joint.

7.3.2. Histological Assessment of Joint Tissues

Separate C6/C7 coronal joint tissue sections were stained with Safranin O/Fast Green to visualize cartilage and bone and Picrosirius Red/Alcian Blue to visualize collagen fibers (Schmitz et al. 2010); stained sections were imaged with the 20x objective of an EVOS FL Auto Imaging microscope as described in Chapter 4 (Ita et al. 2020b). Stained

Safranin O/Fast Green articular surfaces (n=3-6/rat) were scored by blinded graders using the modified Mankin score (Table 4.1) (Xu et al. 2009; Yeh et al. 2007); in the case that the inferior and superior articular surfaces could not be imaged simultaneously with the 20x objective, the superior and inferior articular surfaces were imaged and graded separately. Regions of interest (ROIs; n=2-4/image) throughout the Picrosirius Red/Alcian Blue stained images (n=3-9 images/rat) were analyzed using the Fourier transform method to calculate anisotropy index detailed in Section 4.3.3 (Figure 4.3) (Ita et al. 2020b; Sander and Barocas 2009).

7.3.3. Tensile Testing of Isolated Facet Capsules & Analyses of Mechanical & Optical Data

To prepare samples for mechanical testing, harvested spines from the occiput to T2 were dissected en bloc and the facet joints were isolated by finely dissecting them and removing the superficial musculature (Quinn and Winkelstein 2007; Singh and Winkelstein 2020). The in situ length across the C6/C7 motion segment was measured from the rostral-caudal midpoint of each vertebra's laminae using micro-calipers (Figure 7.2A & Table 7.1) (Singh and Winkelstein 2020). Dissected spines were carefully bisected, with one side prepared to undergo biomechanical testing and the other side prepared for the biochemical CHP assay; left and right sides were assigned to assays at random. The capsular ligament of the isolated C6/C7 facet joint was marked with fiducial markers to enable strain tracking during loading. The unilateral C6/C7 facet was then mounted in an Instron 5865 (Instron; Norwood, MA) by gripping each of the laminae and transverse processes of the C6 and C7 vertebrae with micro-forceps (Figure 7.2A) (Quinn and

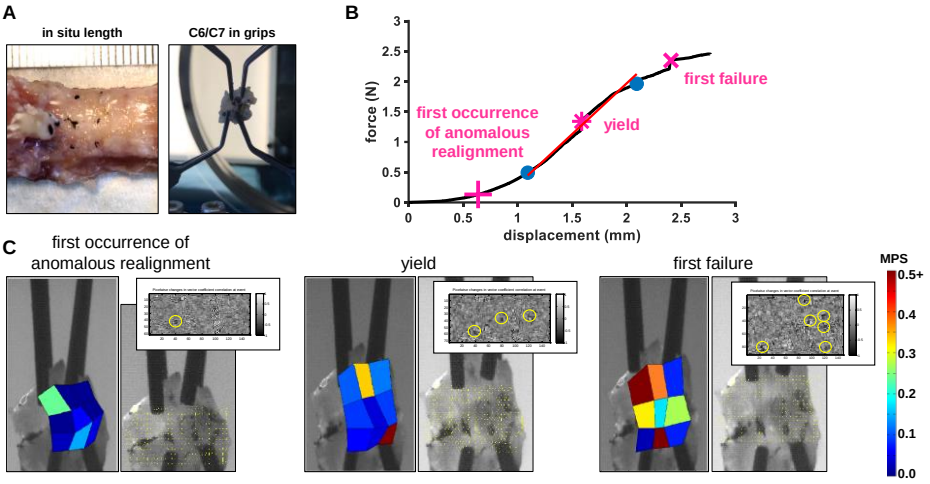

Figure 7.2. Specimen preparation, mechanical testing, and analysis of biomechanical and optical data. **(A)** Harvested spines were finely dissected and the in situ length across the C6/C7 motion segment was measured; that length was set as the unloaded reference position during grip-mounting in the Instron. **(B)** An exemplary force-displacement response of a ligament from a vehicle-injected joint (Rat #54) showing the identification of the first occurrence of anomalous realignment (+), yield (*), and first failure (x). Stiffness was calculated as a linear fit from 20% to 80% of first failure (blue circles); the line fit to calculate stiffness is shown by the red line. **(C)** Exemplary high-speed images with corresponding maximum principal strain (MPS) maps, collagen fiber alignment maps, and the detection of anomalous fiber reorganization events (yellow circles in insets) at first occurrence of anomalous realignment, yield, and first failure for the specimen curve depicted in **(B)**.

Winkelstein 2007; Singh and Winkelstein 2020). The in situ length was re-established in the Instron loading device and taken as the unloaded reference position (Figure 7.2A).

Isolated ligament specimens underwent tensile loading at 0.08mm/sec to failure. Force and displacement data were collected at 500Hz during loading, along with high-speed imaging by a Phantom v9.1 camera (500Hz; 40pixels/mm; Vision Research; Wayne, NJ). The Instron mechanical testing setup was equipped with a QPLI imaging system that acquired pixel-wise collagen fiber alignment maps both prior to, and during, loading (Quinn and Winkelstein 2009; Quinn and Winkelstein 2011; Singh and Winkelstein 2020; Tower et al. 2002; Zhang et al. 2016).

Table 7.1. Summary of in situ length, degraded collagen, macroscale biomechanics, maximum principal strain, microstructure, and anomalous events at mechanical events during tensile failure

		reference			first anomalous fiber realignment					yield				
Rat		**CV**	**CHP/mg**	**length**	**force**	**disp**	**MPS**	**CV**	**#Ev**	**force**	**disp**	**MPS**	**CV**	**#Ev**
14	**MMP-1**	0.127	1191.7	2.25	0.177	0.771	0.082	0.141	1	1.255	1.648	0.165	0.163	2
15		0.063	450.0	2.82	0.478	1.664	0.126	0.115	1	2.589	2.622	0.254	0.147	5
19		0.083	747.4	3.34	0.490	0.889	0.104	0.139	1	0.910	2.355	0.154	0.147	3
55		0.119	796.3	2.66	0.065	0.738	0.105	0.157	1	1.161	1.783	0.210	0.148	4
56		0.149	1225.0	2.45	0.244	1.054	0.092	0.177	1	0.755	1.366	0.118	0.163	2
59		0.136	1437.2	2.27	0.546	1.069	0.117	0.216	1	2.521	2.918	0.380	0.195	4
	avg	**0.113**	**974.6**	**2.63**	**0.333**	**1.031**	**0.104**	**0.158**	**1.00**	**1.532**	**2.115**	**0.213**	**0.161**	**3.33**
	SD	**0.033**	**369.5**	**0.41**	**0.198**	**0.339**	**0.016**	**0.035**	**0.00**	**0.813**	**0.608**	**0.094**	**0.019**	**1.21**
54	**vehicle**	0.126	1710.0	3.13	0.132	0.637	0.110	0.188	1	1.341	1.587	0.224	0.202	3
57		0.102	560.7	2.66	2.208	0.750	0.138	0.122	2	2.791	1.088	0.197	0.189	8
58		0.098	963.6	2.88	1.449	0.844	0.071	0.159	1	2.006	1.374	0.121	0.188	2
61		0.093	574.2	2.33	0.462	1.881	0.194	0.143	1	0.539	1.934	0.287	0.138	2
62		0.156	786.3	2.74	0.823	0.551	0.188	0.179	2	1.441	0.789	0.269	0.205	1
	avg	**0.115**	**918.9**	**2.75**	**1.015**	**0.933**	**0.140**	**0.158**	**1.40**	**1.624**	**1.354**	**0.220**	**0.184**	**3.20**
	SD	**0.026**	**472.4**	**0.29**	**0.827**	**0.542**	**0.052**	**0.027**	**0.54**	**0.836**	**0.442**	**0.066**	**0.027**	**2.77**
65	**naive**	0.143	358.2	2.91	0.852	1.047	0.188	0.213	2	1.549	1.422	0.367	0.228	4

		first failure					ultimate rupture					
Rat		**force**	**disp**	**MPS**	**CV**	**#Ev**	**force**	**disp**	**MPS**	**CV**	**#Ev**	**stiffness**
14	**MMP-1**	2.153	2.047	0.230	0.243	11	2.153	2.047	0.230	0.243	11	1.880
15		2.674	2.918	0.379	0.154	7	2.674	2.918	0.379	0.154	7	2.553
19		2.662	3.152	0.182	0.272	9	2.662	3.152	0.182	0.272	9	0.335
55		1.874	2.314	0.206	0.287	6	1.874	2.314	0.206	0.287	6	1.452
56		2.805	2.187	0.278	0.259	8	2.825	2.191	0.287	0.263	8	2.382
59		2.735	3.396	0.366	0.265	7	2.735	3.396	0.366	0.265	7	0.797
	avg	**2.484**	**2.669**	**0.273**	**0.247**	**8.00**	**2.487**	**2.670**	**0.275**	**0.247**	**8.00**	**1.566**
	SD	**0.378**	**0.560**	**0.083**	**0.048**	**1.78**	**0.382**	**0.560**	**0.083**	**0.048**	**1.78**	**0.879**
54	**vehicle**	2.348	2.406	0.263	0.266	6	2.451	2.770	0.609	0.281	11	1.740
57		2.791	1.088	0.197	0.189	8	2.966	1.165	0.312	0.206	9	4.424
58		2.958	2.951	0.251	0.254	8	2.958	2.951	0.251	0.254	8	1.255
61		2.044	2.587	0.225	0.263	9	2.301	2.859	0.273	0.282	7	1.519
62		1.536	0.835	0.289	0.248	6	1.730	1.158	0.305	0.255	8	2.584
	avg	**2.335**	**1.973**	**0.245**	**0.244**	**7.40**	**2.481**	**2.181**	**0.350**	**0.256**	**8.60**	**2.304**
	SD	**0.574**	**0.949**	**0.035**	**0.032**	**1.34**	**0.515**	**0.933**	**0.147**	**0.031**	**1.51**	**1.285**
65	**naive**	1.701	1.738	0.532	0.238	8	1.728	1.795	0.415	0.238	8	1.231

CV: circular variance; CHP: collagen hybridizing peptide; length is in situ reference in mm: force is in N; disp: displacement in mm
MPS: maximum principal strain; #Ev: number of anomalous events; stiffness is in N/mm
shaded cells in ultimate rupture indicate capsules with first failure and ultimate rupture as the same event

Force, displacement, and optical data were used to define several events of interest throughout the stretch to failure: the first occurrence of anomalous collagen fiber realignment, yield, the first failure, and ultimate rupture of the ligament (Figure 7.2B). Force data were digitally filtered using a ten-point moving average (Ita and Winkelstein 2019; Quinn et al. 2010a). Ultimate rupture, first failure, and yield were defined using the mechanical data. First failure was defined by a decrease in force with increasing displacement between any two data points prior to ultimate rupture (Figure 7.2B). Ultimate rupture was defined as the maximum force sustained during loading (Figure 7.2B). For

some specimens, first failure and ultimate rupture occurred at the same point (Table 7.1). Yield was defined by the first occurrence of a decrease in the maximum tangent stiffness of at least 10% (Figure 7.2B) (Quinn et al. 2010a; Quinn and Winkelstein 2008). Ligament stiffness was calculated as a linear slope of the force-displacement curve fit from 20% to 80% of the force value at first failure (Figure 7.2B) (Ita and Winkelstein 2019; Lee et al. 2006).

Collagen fiber alignment maps were generated during loading and used to determine the first occurrence of anomalous realignment (Quinn and Winkelstein 2009; Quinn et al. 2010a). Briefly, vector correlations were generated for every acquired alignment map in order to identify changes in the fiber alignment maps immediately preceding and following the alignment map based on pixel-by-pixel correlation calculations (Quinn et al. 2010a). Anomalous collagen realignment was defined by a decrease of 0.35 or more in the alignment vector correlation between maps, and a single region was defined as sustaining anomalous realignment when at least nine pixels were connected to one another (Figure 7.2C) (Quinn et al. 2010a). Alignment maps were also generated in the unloaded reference state in order to measure microstructural organization of each ligament prior to loading.

Force, displacement, collagen fiber alignment, and high-speed images were extracted at the first occurrence of anomalous fiber realignment, yield, first failure, and ultimate rupture. At the unloaded reference state and each of those events, fiducial markers were digitized from the high-speed images using the centroid of each capsule marker. Marker coordinates were transformed into x-y coordinates using ProAnalyst (Xcitex, Inc.;

Cambridge, MA) and maximum principal strains were computed relative to the unloaded reference at each event using a customized mapping program in MATLAB (Matlab 7.2; Mathworks Inc., Natick, MA) (Figure 7.2C) (Quinn and Winkelstein 2010; Quinn et al. 2007). The number of anomalous events (Quinn et al. 2010a; Singh and Winkelstein 2020) and the circular variance (CV) was calculated at each event, as well as at the unloaded reference state (Miller et al. 2012; Zhang et al. 2016). Circular variance quantified the spread of collagen fiber angles, with a lower CV indicating a tighter clustering and a higher degree of fiber alignment (Miller et al. 2012; Zhang et al. 2016).

7.3.4. CHP Assessment for Degraded Collagen

To quantify the amount of degraded collagen, the capsular ligament of the isolated C6/C7 facet joint from the other side was finely dissected away from the surrounding bone. The wet weight of each isolated capsular ligament was taken as the average of three measurements. Ligaments were lyophilized overnight and then incubated in 15μM of 5-FAM conjugate of CHP (3Helix; Salt Lake City, UT) overnight, triple-washed in PBS for 30 minutes for each wash, then incubated in 1mg/mL Proteinase K for 3 hours at 60ºC (Lin et al. 2019). After homogenization, the fluorescence of 200μL duplicates of the homogenate solution were measured using a microplate reader (Lin et al. 2019); fluorescence measurements were normalized to the wet weight of the sample as a metric of degraded collagen per ligament weight.

7.3.5. Substance P & MMP-9 Immunohistochemistry in Neural Tissue

To assess substance P and MMP-9 expression in DRG neurons and the spinal cord, cryosections of C7 DRGs and spinal cord (n=6/rat) were co-labeled with a primary antibody to MAP-2 (chicken; 1:400; Abcam; Cambridge, MA) and either a primary antibody to substance P (guinea pig; 1:400; Neuromics; Edina, MN) or MMP-9 (mouse; 1:200; Thermo Fisher). Immunolabeling protocols were performed as described in Section 4.3.5 with Alexa Fluor goat anti-chicken 488 and goat anti-guinea pig 633 secondary antibodies used for the MAP-2-substance P co-label, and Alexa Fluor goat anti-chicken 647 and goat anti-mouse 488 secondary antibodies used for the MAP-2-MMP-9 co-label (all secondary antibodies at 1:1,000; Thermo Fisher).

Fluorescently labeled tissue sections were imaged with the 20x objective of a Leica TCS SP8 confocal microscope (n=6-8 images/rat). The mean signal pixel intensity of substance P (n=6-8 images/rat) and MMP-9 (n=2 images/rat) was separately quantified in MAP-2-positive neurons (n=10 neurons/image) identified by a blinded scorer as described in Chapter 4 (Figure 4.4). Neurons were categorized as small- (<21μm), medium- (21-40μm), or large- (>40μm) diameter neurons (Kras et al. 2014; Weisshaar et al. 2010) to enable comparing protein expression by neuron size. Spinal cord images were cropped to isolate the superficial dorsal horn (700x300 pixels); substance P and MMP-9 were quantified, separately, by counting the number of pixels above the threshold for expression in naïve tissue using the custom MATLAB densitometry script found in Appendix B (Lee and Winkelstein 2009).

7.3.6. Statistical Analyses

All statistical analyses were performed with $\alpha=0.05$ using JMP Prov14 (SAS Institute Inc.; Cary, NC). Normality was tested using a Shapiro-Wilk goodness-of-fit test for a normal continuous fit on the residuals of all outcomes. The average paw withdrawal thresholds per rat were compared between groups of rats receiving either intra-articular MMP-1 or vehicle using a repeated-measures ANOVA with post-hoc Tukey HSD tests. Differences between Mankin score and anisotropy index in groups were assessed with Wilcoxon tests. Separate repeated-measures ANOVA with post-hoc Tukey tests assessed differences in force, displacement, strain, CV, and the number of anomalous events across events *within* the MMP-1 and vehicle injection groups, separately; comparisons for those same outcomes *between* groups were tested with Wilcoxon Rank Sum tests. A t-test compared stiffness and CHP fluorescence between the two groups. Correlations between CHP and CV at reference, first occurrence of anomalous fiber realignment, and yield were separately analyzed using linear regressions and an ANOVA to assess the goodness of fit. Differences in the signal intensity of substance P and MMP-9 labeling were tested using Wilcoxon tests between groups. The effect of neuronal size on DRG immunolabeling was analyzed within groups, separately, using a one-way ANOVA with an effect of size and post-hoc Tukey HSD tests. Separate t-tests assessed differences in each protein expression outcome in the spinal cord between groups.

7.4. Results

MMP-1 decreases PWT within one day of injection that lasts for at least 28 days ($p<0.001$) (Figure 7.3). That MMP-1-induced increase in sensitivity (decrease in PWT) is

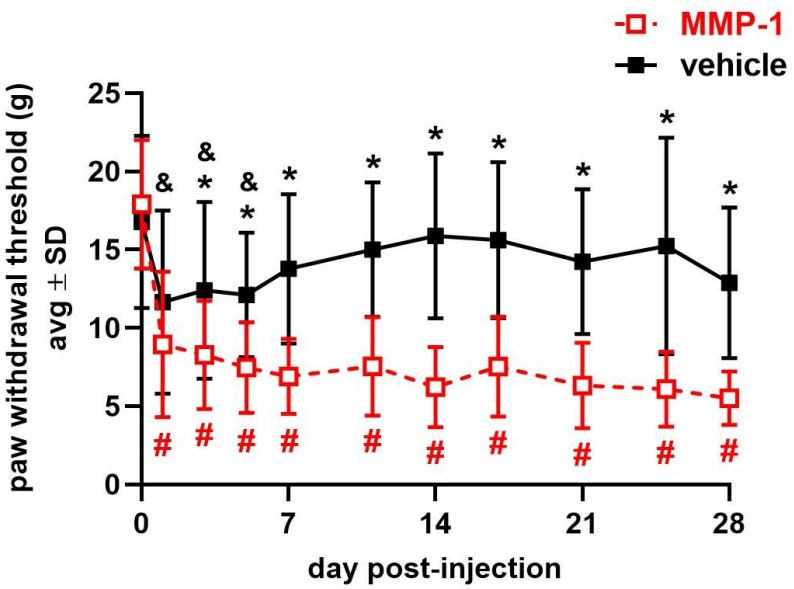

Figure 7.3. Paw withdrawal thresholds for 28 days after intra-articular injection of MMP-1 or vehicle with a decrease in threshold indicating greater sensitivity in the forepaw. MMP-1 significantly decreases the threshold from baseline (day 0) for all days (#$p<0.001$) and decreases from vehicle responses beginning on day 3 (*$p\leq0.025$). Rats initially show sensitivity after a vehicle injection (&$p\leq0.027$) but it resolves by day 7. Withdrawal thresholds at baseline (day 0) is not different between MMP-1 and vehicle groups ($p=1.00$).

significantly different from the response to a vehicle injection beginning at day 3 ($p\leq0.025$), an effect which is sustained through day 28 (Figure 7.3). Although rats initially show sensitivity after injection of the vehicle ($p\leq0.027$), that sensitivity resolves by day 7. The PWTs between rats injected with MMP-1 and those injected with vehicle are not different at baseline ($p=1.00$), prior to injection, so any differences between groups after day 0 (baseline) are due to the injection itself (Figure 7.3). PWTs are itemized for each rat in Appendix C.

Despite significant effects on sensitivity thresholds, the effects of intra-articular MMP-1 on the structure of joint tissues are not as evident. Joints injected with the vehicle appear healthy with normal pericellular and background Safranin O labeling and no

evidence of cartilage fibrillation (Figure 7.4). Although there are occasional occurrences of lighter Safranin O labeling in the articular cartilage and mild surface fibrillations in joint injected with MMP-1 (Figure 7.4), such observations are not consistent across the MMP-1 group. In fact, the large variability in Mankin score after MMP-1 illustrates this inconsistency; there is no significant difference between MMP-1 and vehicle groups ($p=0.105$) (Figure 7.4). Like the Mankin score, the primary alignment of the collagen microstructure is unchanged in the capsular ligament ($p=0.448$), with anisotropy indices being the same between the MMP-1 (0.45 ± 0.18) and vehicle (0.47 ± 0.20) groups (Figure 7.5). The detailed histology-stained images, Mankin score, and anisotropy index measurements for each sample are summarized for each rat in Appendix D.

The force-displacement response of capsular ligaments that received a vehicle injection appear like the response of the C6/C7 ligament from a naïve rat, with the force-displacement responses of the naïve ligament fully within the range of curves for the

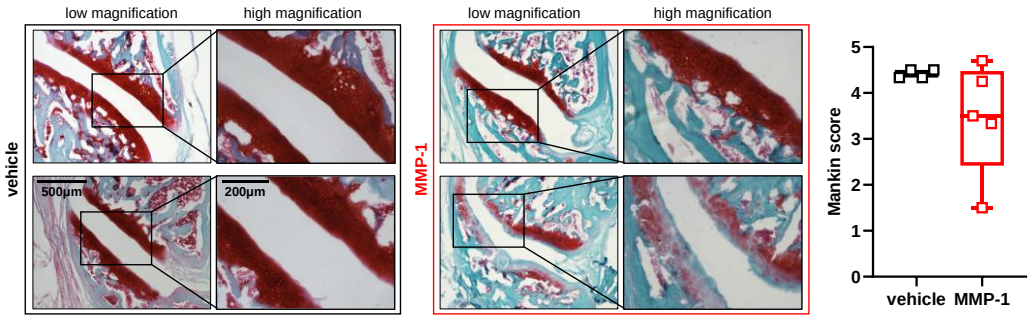

Figure 7.4. Structural assessment of the facet joint cartilage and bone at 28 days after intra-articular injection. Low and high magnification images show overall healthy and non-degraded cartilage. The bottom panel of the MMP-1-injected joint shows lighter Safranin O staining and surface defects and has a 4.25 Mankin score. Degenerative features are not observed consistently across joints with MMP-1; as such, there is no difference in Mankin score between groups ($p=0.105$). Box-and-whisker plot shows horizontal lines representing the first (lower) quartile, median, and third (upper) quartile of the scores. Whiskers represent the minimum and maximum of the data set. Data points showing the mean value from individual joints are superimposed on boxplots. The scale bars on the low and high magnification images apply to all images with the corresponding magnification.

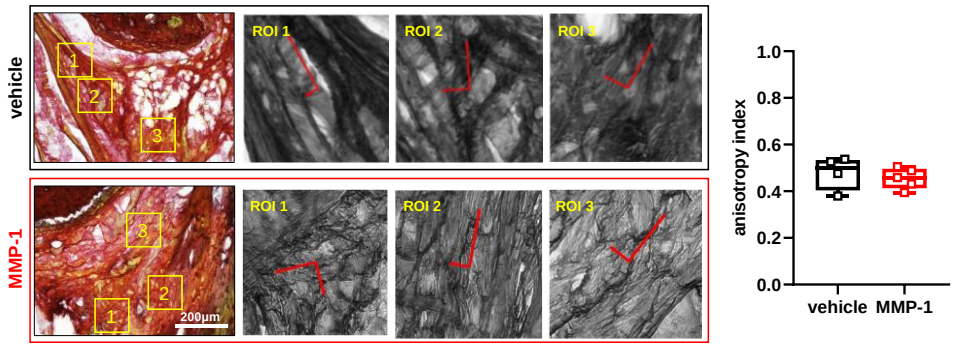

Figure 7.5. Evaluation of the collagen microstructure of the capsular ligament. Images show Picrosirius Red-stained collagen fibers in the ligament. Yellow boxes show three regions of interest (ROIs) throughout each tissue section. ROIs next to each stained image are overlaid with the principal orientation axes of the stained collagen fibers and are used to calculate the anisotropy index, with 1 indicating aligned orientation and 0 indicating isotropic orientation. The anisotropy index is unchanged with MMP-1 (p=0.448). Box-and-whisker plots show horizontal lines representing the first (lower) quartile, median, and third (upper) quartile of the data. Whiskers represent the minimum and maximum of the data set. Data points showing the mean value from individual joints are superimposed on boxplots. The scale bar applies to both Picrosirius Red stained images.

vehicle injected capsules (Figure 7.6). The loading curves of ligaments after an intra-articular MMP-1 injection have forces at rupture similar to the forces at rupture in loading curves of ligaments after vehicle injection, but displacements that are lower in magnitude (Figure 7.6). Indeed, the force-displacement curves for the joints with MMP-1 injection are shifted to the right compared to vehicle responses (Figure 7.6). The displacement at yield is significantly greater for intra-articular MMP-1 than for vehicle (p=0.040) (Table 7.1 & Figure 7.7). Despite the different displacements at yield and nearly a 1.5-fold decrease in stiffness between the MMP-1 (1.56±0.87) and vehicle (2.30±1.28) groups, a statistically significant difference in stiffness is not detected (p=0.312) (Figure 7.7 & Table 7.1). The occurrence of first failure and ultimate rupture are coincident for five of the six ligaments that received MMP-1 and were loaded to failure, but for only one of the five ligaments with vehicle treatment (Table 7.1).

Ligaments from joints with a vehicle injection exhibit a smooth increase in force, displacement, and strain with the progression of the different mechanical events (Figure 7.7). Intra-articular MMP-1, however, appears to induce a "step-like" change around the events of first anomalous fiber realignment and yield (Figure 7.7). For example, the force sustained at yield with an MMP-1 injection is significantly different from the force at every other mechanical event ($p \leq 0.008$); this is also true for displacements for intra-articular

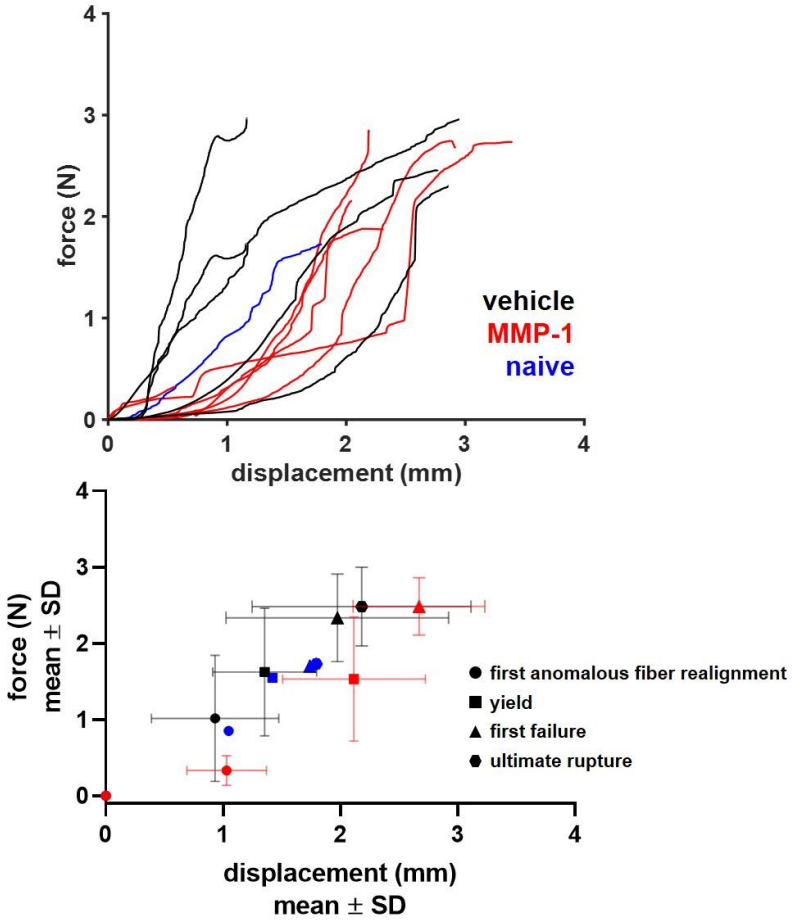

Figure 7.6. Force-displacement curves of C6/C7 facet capsular ligaments failed in tension, showing the response through the ultimate rupture. The bottom panel shows the mean and standard deviation of the force and displacement by group at each event: first anomalous fiber realignment (circles), yield (squares), first failure (triangles), and ultimate rupture (hexagons). Note that for MMP-1 injected ligaments, the first failure and ultimate rupture occur at very similar forces and displacements, so only the event of first failure is shown.

MMP-1 at the first occurrence of anomalous fiber realignment ($p \leq 0.007$) (Figure 7.7). That step-like behavior is also observed in the maximum principal strain response with strain being significantly different between first anomalous realignment and first failure after an MMP-1 injection ($p=0.001$) (Figure 7.7). For all outcomes with intra-articular vehicle treatment, no event is significantly different from any of the others for any of force, displacement, or maximum principal strain (Figure 7.7). The full-field strain maps for each tested ligament are summarized in Appendix J.

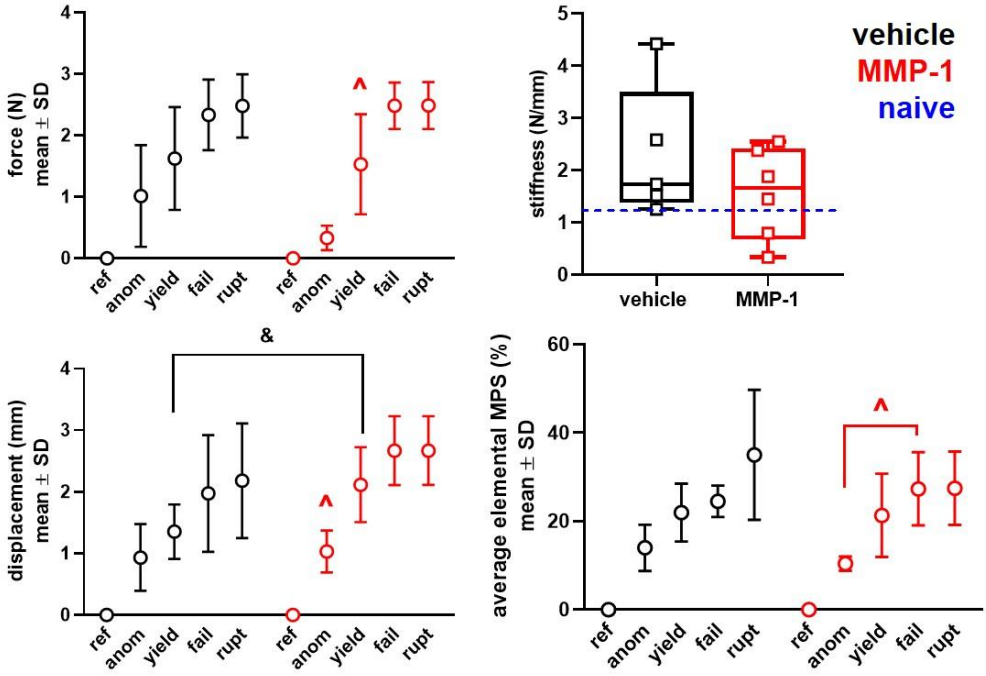

Figure 7.7. Force, displacement, and average maximum principal strain (MPS) at each mechanical event by group show smooth patterns with the intra-articular vehicle injection and a step-like response for the intra-articular MMP-1 (ref: reference; anom: first anomalous fiber realignment; yield; fail: first failure; rupt: ultimate rupture). The force at yield ($^p \leq 0.008$) and the displacement at first anomalous realignment ($^p \leq 0.007$) are significantly different than that at every other event with intra-articular MMP-1. Average MPS increases from first anomalous realignment to first failure with MMP-1 ($^p=0.001$). Stiffness is not different between the MMP-1 and vehicle group ($p=0.312$), although ligaments in the MMP-1 group have greater displacements at yield ($\&p=0.040$) than ligaments in the vehicle group at that same event. The blue dashed line on the stiffness plot shows the stiffness of a ligament from an un-operated rat. Box-and-whisker plots show horizontal lines representing the first (lower) quartile, median, and third (upper) quartile of the data with whiskers as the minimum and maximum. Superimposed data points show the mean value from individual ligaments on boxplots.

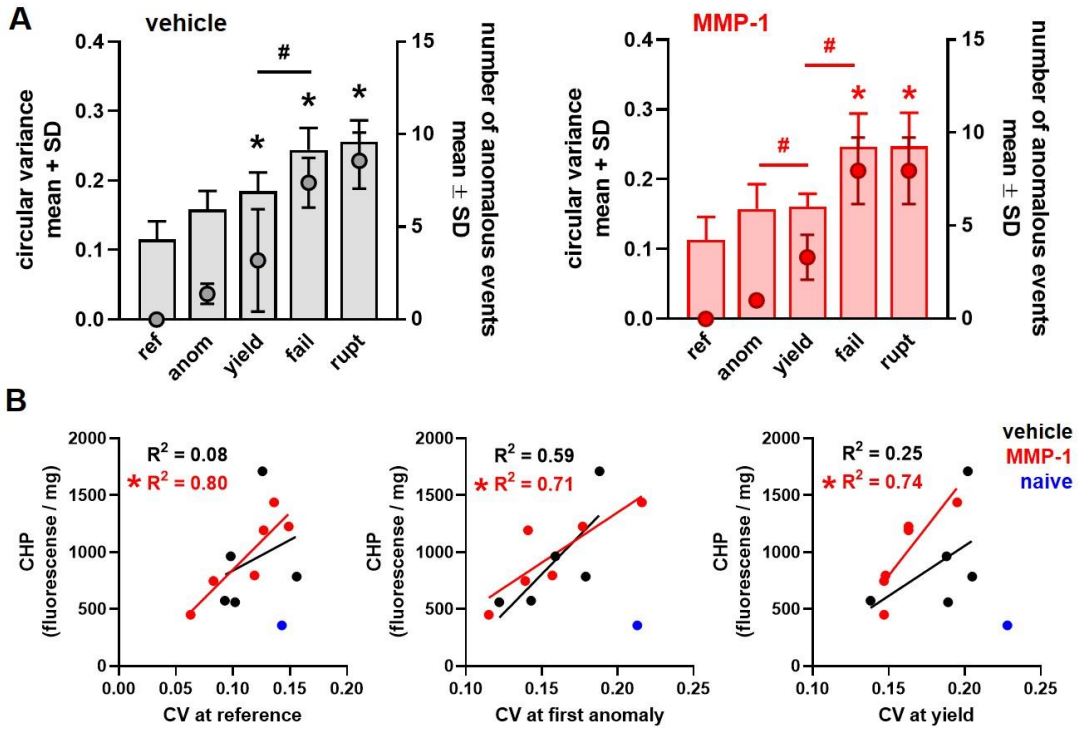

Figure 7.8. Collagen microstructural kinematics and relationships to the extent of degraded collagen at different mechanical events (ref: reference; anom: first anomalous fiber realignment; yield; fail: first failure; rupt: ultimate rupture). **(A)** Circular variance (bar plots; left axis) is different from reference at yield, failure, and ultimate rupture with the vehicle group (*p≤0.026 vs. ref), and at failure and ultimate rupture relative to reference for the MMP-1 group (*p≤0.001). The number of anomalous events (mean ± standard deviation; right axis) is significantly different between yield and failure with vehicle (#p=0.003) and MMP-1 (#p=0.026) treatment and also between the first occurrence of anomalous fiber realignment and yield only in the MMP-1 group (#p<0.001). **(B)** The correlations between collagen hybridizing peptide (CHP) and circular variance (CV) show significant associations between CHP and CV with intra-articular MMP-1 at reference before loading (*p=0.015), at the first occurrence of anomalous fiber realignment (*p=0.035), and at yield (*p=0.027). However, those relationships are not significant for vehicle treatment (reference: p=0.626; first anomalous realignment: p=0.125; yield: p=0.387). R^2 values show goodness-of-fit on each correlation plot and the blue data point represents data from an un-operated naïve rat.

There are also subtle, but detectable differences between groups in the microstructural kinematics across the mechanical events. For intra-articular vehicle treatment, the circular variance at ligament yield and reference are significantly different from each other (p≤0.026) (Figure 7.8A). However, for an MMP-1 injection, the collagen fibers do not reorganize until the first failure (p≤0.001) (Figure 7.8A). Despite this, the

number of anomalous events increases significantly from the first occurrence of anomalous realignment to yield after an MMP-1 injection ($p=0.026$) (Figure 7.8A). In contrast, the number of anomalous events within the fibers of vehicle-injected ligament capsules is not different between the first occurrence of anomalous realignment and yield, but differs between yield and first failure ($p=0.003$) (Figure 7.8A). The MMP-1-injected capsules also experience more anomalous events at failure than at yield ($p<0.001$) (Figure 7.8A).

Before loading, in the reference configuration, neither the amount of degraded collagen measured by CHP fluorescence (MMP-1 974.6±369.4; vehicle 918.9±472.3; $p=0.835$) nor the microstructural organization of the capsule quantified by CV (MMP-1 0.112±0.033; vehicle 0.115±0.026; $p=1.000$) are different. Yet, the relationships between the magnitude of damaged collagen before loading and the microstructural kinematics depend on whether the ligament had been exposed to MMP-1 or vehicle (Figure 7.8B). The relationship between CHP and CV at reference is significant for all ligaments, regardless of what the injected solution was ($p=0.048$); yet, this relationship is driven by a significant association between CHP and reference CV *only* with intra-articular MMP-1 ($p=0.015$; $R^2=0.80$) and not with intra-articular vehicle ($p=0.626$; $R^2=0.08$) (Figure 7.8B). That significant positive association between CHP and CV in the unloaded state with intra-articular MMP-1 is maintained at both the first occurrence of anomalous fiber realignment ($p=0.035$; $R^2=0.71$) and yield ($p=0.027$; $R^2=0.74$) (Figure 7.8B).

Intra-articular MMP-1 significantly increases substance P expression that is localized to peripheral neurons in the DRG ($p<0.001$) (Figure 7.9). Moreover, substance P increases in neurons of all sizes ($p<0.001$) (Figure 7.9). Across the different sizes of the

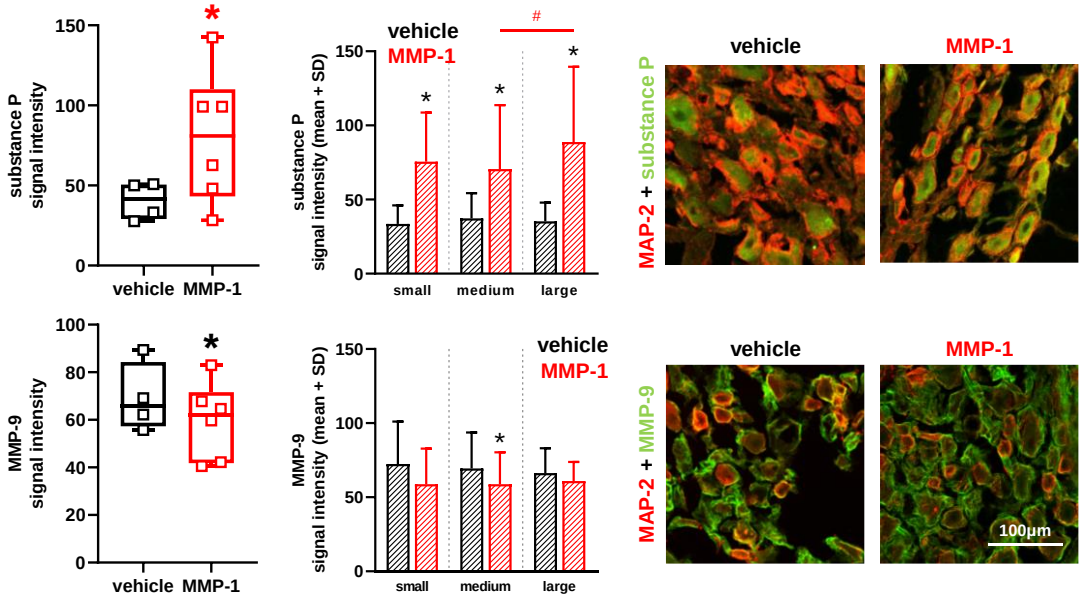

Figure 7.9. Substance P and MMP-9 labeling in dorsal root ganglia (DRG) neurons at day 28 after intra-articular vehicle or MMP-1. Images show immunolabeled DRG tissue sections with channels for the neuronal marker MAP-2 (red) and the protein of interest (substance P or MMP-9; green) merged. Intra-articular MMP-1 significantly increases total substance P (*p<0.001) and significantly decreases total MMP-9 (*p=0.014) compared to vehicle treatment. The MMP-1-induced increase in substance P is evident in neurons of all sizes (*p<0.001); yet, the decrease in MMP-9 is detected only in medium-diameter neurons (*p=0.029). Neuronal size has a significant effect on substance P expression with MMP-1 injection, with large-diameter neurons expressing significantly more substance P than medium-diameter neurons (#p=0.001). Box-and-whisker plots show horizontal lines representing the first (lower) quartile, median, and third (upper) quartile of the data. Whiskers represent the minimum and maximum of the data set. Data points showing the mean value from each rat are superimposed. The scale bar applies to all images.

neurons from MMP-1-injected rats, neuron size has a significant effect on substance P expression, with large-diameter neurons having significantly more expression than medium-diameter neurons (p=0.001) (Figure 7.9). Neuronal MMP-9 expression follows a different pattern, with expression levels significantly lower for DRGs exposed to MMP-1 treatment compared to vehicle (p=0.014) (Figure 7.9). The difference in MMP-9 labeling between injection groups is only evident in medium-sized neurons (p=0.029) (Figure 7.9).

The effect of intra-articular MMP-1 on spinal substance P expression is different than the effect of intra-articular MMP-1 on spinal MMP-9 expression (Figure 7.10). MMP-

1 injection in the facet increases substance P in the superficial dorsal horn at day 28 (p=0.002) and has no effect on MMP-9 expression in the spinal cord (p=0.333) (Figure 7.10). Substance P labeling in the dorsal horn is punctate in the most superficial layers and MMP-9 labeling is more diffuse, with labeling extending into the deeper laminae than substance P (Figure 7.10). Immunolabeled images and their quantifications for each label are itemized for each rat in Appendix E.

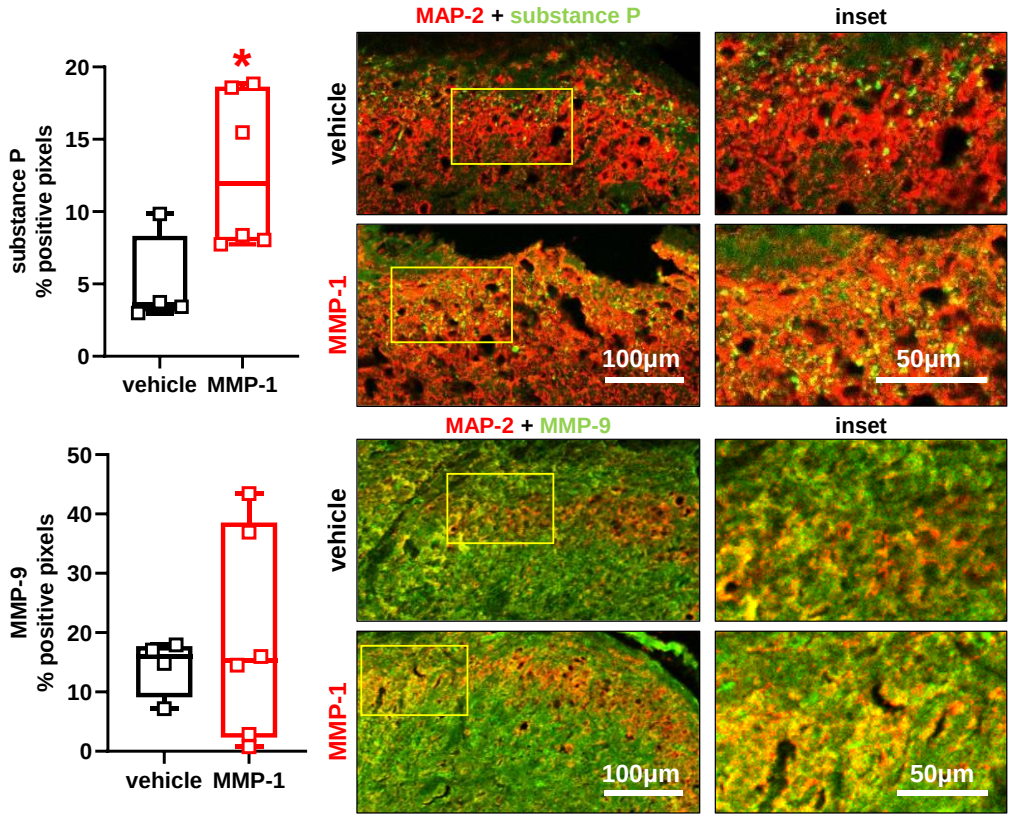

Figure 7.10. Immunohistochemical labeling of substance P and MMP-9 in the superficial dorsal horn of the spinal cord at day 28. Substance P labeling appears punctate and increases with intra-articular MMP-1 (*p=0.002) compared to vehicle. MMP-9 labeling is evident as a more diffuse label but is not changed from vehicle (p=0.333). The insets are magnified regions of the yellow boxes on the merged images. Box-and-whisker plots show horizontal lines representing the first (lower) quartile, median, and third (upper) quartile of the data. Whiskers represent the minimum and maximum of the data set. Data points showing the mean value from each rat. The scale bars also apply to the image directly above it.

7.5. Discussion

This study demonstrates that intra-articular MMP-1 alone is sufficient to induce immediate and sustained behavioral sensitivity in the rat (Figure 7.3), and that the mechanism of MMP-1-induced sensitivity may involve altered microstructural kinematics of the capsular ligament (Figure 7.8) and/or sensitization of the embedded neurons in the capsule, the periphery, and/or spinal cord (Figures 7.9 & 7.10). The result that sensitivity (Figure 7.3) and elevated substance P (Figures 7.9 & 7.10) occur in the absence of any significant modifications in the joint structure and/or function (Figures 7.4 & 7.5) mirror the results observed with intra-articular bacterial collagenase (Figures 4.5 & 4.6) (Ita et al. 2020b). Together, these similarities suggest that exogenous proteases with collagenolytic functions have similar effects on tissue structure regardless of the protease source. Bacterial collagenase is hypothesized to induce sensitivity by degrading the collagen fibers in the capsular ligament and subsequently triggering afferent signaling via altering the microenvironment of the afferents in the ligament (Ita et al. 2020b). The current study provides additional evidence supporting that hypothesis by demonstrating that MMP-1, likely via its collagenolytic capabilities, alters the collagen organization and reorganization during loading (Figure 7.8). The decreased peripheral MMP-9 (Figure 7.9) and unchanged MMP-9 in the spinal cord (Figure 7.10), however, counter the hypothesis that pain from MMP-1 involves MMP-9 upregulation, at least at 28 days following injection. However, the finding that MMP-9 expression decreases in medium-sized DRG neurons (Figure 7.9) suggests that MMP-1 may downregulate MMP-9 in nociceptors that transmit “fast pain” via Aδ myelinated fibers (Basbaum et al. 2009).

MMP-1 may degrade collagen in several regions of the capsule and in doing so predispose ligaments to altered kinematics on both the macroscale and microscale (Figures 7.6-7.8). For example, it is possible that MMP-1 localizes to Type I collagen in its local vicinity (near the injection site), cleaves triple-helical collagen strands, and those local regions respond differently to load than their surrounding unaffected neighboring regions of the capsular ligament. That conjecture is supported by the correlation between CHP, a metric of degraded and/or partially unwound collagen (Lin et al. 2019) and the spread of collagen fibers (i.e. CV), observed for joints in the unloaded state after intra-articular MMP-1 (Figure 7.8B). That positive correlation suggests that more damaged collagen fibers correlate to more disorganized (less-aligned) fibers even in the unloaded state. Of course, whether less-aligned fibers indicate a deviation from normal depends on the region of the capsule since the collagen fiber orientation has been shown to vary across capsule layers and anatomic regions (Ban et al. 2017; Yahia and Garzon 1993; Yamashita et al. 1996). Of note, the CHP measurements are made using whole capsular tissue homogenates and so lack the resolution to define regional variations. Nonetheless, the significant relationship between CHP and CV holds at both the first detection of anomalous fiber realignment and yield (Figure 7.8B), supporting that the microstructural state of the facet capsule is different after MMP-1 exposure and remains as such during its loading.

The proposed schema that the ligament is predisposed by MMP-1 degradation with "hot-spots" of anomalous collagen fiber reorganization may also explain the differential responses to loading between ligaments exposed to MMP-1 and ligaments exposed to vehicle (Figures 7.6-7.8), particularly at the first occurrence of anomalous realignment and

yield. A greater displacement at yield for MMP-1 ligaments may indicate the development of laxity in those ligaments (Figure 7.3) (Quinn and Winkelstein 2011). Although laxity is not quantified is this study, greater laxity in ligaments could explain the decreased paw withdrawal threshold in rats treated with MMP-1 (Figure 7.3), since ligaments with greater laxity may be more prone to injury during physiologic movements. This assertion is supported by prior work with a rat model of facet capsule stretch-induced pain that found that facet joint displacements that produce persistent pain symptoms also induce laxity and collagen fiber disorganization in the capsular ligament (Lee et al. 2008; Lee and Winkelstein 2009; Quinn et al. 2007). It is also expected that the MMP-1-injected ligaments would exhibit decreased stiffness compared to those receiving a vehicle; however, this was not the case here. Since the average ligament stiffness with MMP-1 treatment is nearly 50% lower than with vehicle treatment (Figure 7.7), a power analysis was conducted to test the required sample size needed for statistical significance. Power analyses shows the least significant number for significance as twice that of the current sample size (n=6 MMP-1; n=5 vehicle), suggesting that a meaningful difference could be detected with more samples.

It is possible that the MMP-1 injection produces partial collagen degradation across regions of the capsule and those may result in the anomalous realignment that is observed earlier, or at severe conditions during tensile loading. This is supported by the significant jump in the number of anomalous events at yield for MMP-1-injected samples (Figure 7.8); in contrast, a significant increase in the number of anomalous events is not evident until failure in the vehicle samples (Figure 7.8). The first occurrence of anomalous realignment

of the collagen fibers has been associated with ligament yield in otherwise unaltered native ligaments (Quinn et al. 2010a). Although the CV differs between yield and reference with vehicle treatment, the CV is not different between yield and reference with MMP-1 treatment (Figure 7.8). In other words, vehicle-injected ligaments experience a reorganization of the collagen network at yield and that response is the same as the response of unaltered native ligaments (Quinn et al. 2010a). Thus, the finding that collagen in the MMP-1-injected ligaments does not reorganize until failure (Figure 7.8) differs from the response of healthy ligaments (Quinn et al. 2010a). That finding suggests that the collagen fibers of ligaments exposed to MMP-1 may abruptly reorganize at failure and raises the question of which regions or properties of the capsule's collagen network drive this response.

In fact, the number of collagen anomalous reorganization events may be a more sensitive indicator of the ligament's kinematic response under load than either CV or strain. Maximum principal strain quantifies the greatest relative deformation at the resolution of fiducial-marked elements (~0.1mm). Optical data are acquired at a greater resolution of ~25μm; yet, CV quantifies the spread of fiber angles at that resolution over the entire surface area of the imaging field of view and through the tissue thickness (Quinn and Winkelstein 2009; Tower et al. 2002). Therefore, both strain and CV are coarser measurements than the number of anomalous events, which resolves anomalous realignment to nine connected pixels corresponding to ~75x75μm regions (Quinn and Winkelstein 2009; Quinn et al. 2010a). As such, it is conceivable that the total surface areal CV measurements may not differ between the two treatment groups at any mechanical

event, because the resolution for single occurrences of anomalous realignment is much smaller than the resolution for the CV measured over the visible surface area. Since the microstructure of the capsular ligament dictates its biomechanical function and potential for injury (Ita et al. 2017; Quinn et al. 2010a; Quinn and Winkelstein 2011; Zhang et al. 2018), any variation in the tissue's microstructure will likely correspond to its ability to guide, function, and/or limit motions of the overall joint (Jaumard et al. 2011). Taken together with the current results, the occurrence of isolated, yet frequent, anomalous events that is observed with MMP-1 treatment (Figure 7.8) highlights the possibility that afferent fibers embedded in those regions may be more susceptible to activation if they are located in regions where the collagenous matrix undergoes abnormal kinematics.

Intra-articular bacterial collagenase is hypothesized to generate small collagen fragments via microscale collagen degradation of the Type I collagen network (Ita et al. 2020b); it is also possible that intra-articular MMP-1 may generate small collagen fragments when injected into the joint space. This notion is supported by evidence of collagen degradation products in the synovial fluid that has been observed within 15 minutes of the injection of MMP-13 into the hamster knee joint (Otterness et al. 2000). Collagen fragments generated by MMP-1-mediated degradation can act as cell signaling agents on both fibroblasts and afferent nerves that reside in the ligament (Leeming et al. 2011; Siebert et al. 2010). For example, the collagen fragment known as C1M binds to integrin receptors that are expressed by fibroblast-like synoviocyte cells and afferent nerves in the capsular ligament (Leeming et al. 2011; Siebert et al. 2010). Integrin interactions at the cell surface can trigger intracellular signaling cascades, such as the activation of MAPK

signaling pathways (Campos et al. 2004) and the dysregulation of neuropeptides (Zhang et al. 2017). Since both neurotransmitters and MAPK signaling are implicated in nociception (Basbaum et al. 2009; Chen et al. 2015; Ji et al. 2009; Zieglgänsberger 2019), the activation of those pathways by collagen degradation products may contribute to the development of pain from intra-articular MMP-1.

Furthermore, load is known to mediate the rate of enzymatic breakdown of collagen by protecting strained fibers from degradation (Bhole et al. 2009; Camp et al. 2011; Flynn et al. 2010; Ruberti and Hallab 2005; Wyatt et al. 2009; Zareian et al. 2010). Since the collagen network of the fibers in the facet capsule has varied orientations and undergoes heterogeneous strains under load (Ban et al. 2017), regions with collagen fibers that are *less* strained may be preferentially degraded by MMP-1. The preferential degradation of collagen fibers that are unstrained, and likewise, bear less load, could explain the simultaneous absence of overt structural damage (Figures 7.4 & 7.5), with subtle, but measurable effects of intra-articular MMP-1 on multiscale kinematics (Figures 7.6-7.8).

In addition to the possibility that MMP-1 may initiate afferent signaling via its role as a biomechanical regulator of the capsule's collagenous network, it may also induce nociception by initiating extracellular cell-signaling and/or intracellular protein regulatory pathways that are independent of collagen regulated mechanotransduction pathways (Bartok and Firestein 2010; Chakrabarti et al. 2020; Miller et al. 2014). For example, MMP-1 cleaves the pro-inflammatory cytokines tumor necrosis factor α (TNFα) and interleukin-1β (IL-1β) into their bioactive forms that can function as messengers in the extracellular space (Visse and Nagase 2003). Both of those cytokines can potentiate

nociceptive signaling by interacting with neurons (Basbaum et al. 2009); for example, TNFα stimulation increases the amount of spontaneous firing in peripheral neurons (Chakrabarti et al. 2020). Furthermore, there are positive feedback loops between MMPs (including MMP-1) and cytokines that are regulated by the fibroblast-like synoviocytes that are embedded in the capsular ligament (Bartok and Firestein 2010). Those feedback loops lead to cytokine-initiated production of MMPs by fibroblasts, recruitment of new fibroblasts to the synovial lining, and increases in the production of inflammatory mediators, including cytokines (Bartok and Firestein 2010; Bottini and Firestein 2013; Sluzalska et al. 2017). As such, it is possible that exogenous MMP-1 localizes to fibroblasts in the capsular ligament and can initiate the synthesis and activation of cytokines and/or other MMPs, like the collagenase MMP-13 and the stromelysin MMP-3 (Bartok and Firestein 2010). The possibility that cytokines are involved in MMP-1-induced pain is supported by their detection in the synovial fluid of patients with painful osteoarthritis (Miller et al. 2014).

Notably, both intra-articular MMP-1 and intra-articular bacterial collagenase increase the expression of peripheral and spinal neuronal substance P (Figures 4.7-4.8 & 7.9-7.10) (Ita et al. 2020b). Both MMP-1 and bacterial collagenase share collagenolytic activity, and *not* ECM-independent functional roles in cell signaling. Taken together, those findings suggest that the mechanism by which MMP-1 induces and mediates behavioral sensitivity is not completely independent of the ECM. In fact, it is possible that aberrant recruitment of mechanoreceptors in nociception may contribute to the behavioral sensitivity since substance P increases in large-diameter neurons (Figure 7.9). The

recruitment of mechanoreceptors in pain processing only occurs in the presence of tissue injury (Basbaum et al. 2009; Obata and Noguchi 2004). So, it is possible that the altered microstructural kinematics (Figure 7.8) injure proprioceptive fibers embedded in the collagen network. In fact, a loss of proprioception, and a corresponding *increase* in pain symptoms, is observed in patients with knee osteoarthritis (Malfait and Schnitzer 2013), suggesting that mechanoreceptors may adopt nociceptive roles in states of degenerated pathology.

Although MMP-1 may mediate MMP-9 early after intra-articular administration or within the capsular tissue itself, neither early times nor tissue-localized MMP-9 were investigated in the current study. It is well-established that MMP-9 is required only for the initiation, and not the maintenance, of neuropathic pain induced by nerve injury in the rat (Ji et al. 2008; Kawasaki et al. 2008). So, it is not surprising that a strong regulatory role of MMP-1 on MMP-9 is not supported at this late time after a single injection (Figures 7.9 & 7.10). Contrary to findings in the rat, MMP-9 levels in the capsular ligament tissue from patients with late-stage chronic joint disease do correlate with pain symptoms (Chapter 3) (Ita et al. 2020a), suggesting that MMP-9 may play a regulatory role in pain maintenance in at least some patient populations. So, it is possible that MMP-9 protein may indeed be elevated in capsular tissue at day 28; the distribution of MMP-9 from peripheral neurons to axonal projections in the capsular tissue may even explain the decrease in substance P that is observed with intra-articular MMP-1 in medium-sized DRG neurons (Figure 7.9). MMP-1 likely regulates MMP-9 at least early after its injection, since MMP-1 has been shown to activate and stimulate the release of MMP-9 (Conant et al. 2002), and MMP-9

subsequently cleaves substance P (Diekmann and Tschesche 1994). Ultimately, it is likely that the mechanisms by which MMP-1 *initiates* sensitivity are different than those that *maintain* sensitivity.

7.6. Integration & Conclusions

The studies in this chapter demonstrate that intra-articular MMP-1 alone is sufficient to induce immediate and sustained pain-like behaviors (Figure 7.3), altered microstructural ligament kinematics (Figure 7.8), and dysregulation of substance P in peripheral and spinal neurons (Figures 7.9 & 7.10). In the parallel study from Aim 2 (Chapter 4), the assertion that microscale degradation drives bacterial collagenase-induced sensitivity is largely speculative (Ita et al. 2020b); yet, the findings presented in this chapter demonstrate an effect of MMP-1 on the multiscale kinematics of the ligament under tension (Figures 7.6-7.8). Since both intra-articular bacterial and human collagenases induce behavioral sensitivity absent overt tissue degradation, the collective findings from both of those studies implicate collagenases, and more specifically their collagenolytic function, as a regulator of the ligament's collagen network and support the hypothesis of Aim 2. These studies also reveal collagenase involvement in a joint structure-function relationship, whereby structural alterations may only be detectable on a microscopic level.

The experiments in this chapter demonstrate that intra-articular MMP-1 increases substance P and decreases MMP-9 in peripheral neurons (Figure 7.9), providing support for the hypothesis that MMP-1 regulates nociceptive mediators but lacking support for the hypothesis that MMP-1 does this via MMP-9. Although MMP-9 and MMP-1 do not appear

mechanistically related at day 28 in this in vivo study, both increase in parallel with each other and with pain in the innervated soft tissues from patients (Figure 3.3) and in response to load (Figure 6.6) (Ita et al. 2020a; Ita and Winkelstein 2019). Whether the decrease in MMP-9 at day 28 observed here (Figure 7.9) is a result of MMP-9 accumulation in a region other than peripheral neurons is unknown. The studies in Chapter 8 expand this work by defining the effects of MMP-1-targeted inhibition on MMP-9 and begin to explore the mechanistic relationship between MMP-1 and MMP-9 in nociception that is derived from the innervated ligament.

Chapter 8

Effects of Sub-Failure Stretch & MMP Inhibition on MMP-1, MMP-9, & Substance P

Portions of this chapter have been adapted from the following abstract:

Ita ME, Winkelstein BA. MMP-regulation is dependent on the presence of fibroblasts in a ligament model of sub-failure, painful stretch. *Orthopaedic Research Society Annual Meeting*, February 2021, *accepted.*

8.1. Overview

Matrix metalloproteinases (MMPs) are involved in a wide range of pathologies across many organ systems (Sbardella et al. 2012; Vandenbroucke and Libert 2014). Owing to this ubiquity, over 50 MMP inhibitors have been investigated in clinical trials (Vandenbroucke and Libert 2014), with the majority targeting MMPs as catalysts of tumor growth in cancer progression (Coussens et al. 2002). Unfortunately, most of those clinical trials have been unsuccessful, with their failure explained in part by poor metabolic stability and bioavailability, poor substrate specificity between inhibitors and their intended MMP targets, and unwanted side effects due to the role of MMPs in healthy processes (Vandenbroucke and Libert 2014). Yet, the growing understanding of the role of MMPs in physiology *and* disease, primarily with respect to their non-tissue remodeling functions, has led to recent successes of MMP inhibition in inflammatory diseases (Vandenbroucke and Libert 2014). Moreover, small molecule MMP inhibitors selective to

MMP-13 show promise in their ability to interfere with inflammatory and degenerative milieu in animal models of both rheumatoid arthritis and osteoarthritis (Baragi et al. 2009; Gege et al. 2012; Jüngel et al. 2010). For example, small molecule MMP-13 inhibitors have been shown to decrease the extent of cartilage erosion and to reduce the release of matrix degradation products both in human cartilage explant cultures and in rodent models of knee degeneration (Baragi et al. 2009; Jüngel et al. 2010).

Hydroxamate-based inhibitors are a class of MMP inhibitors that competitively inhibit substrate binding at the Zn^{2+}-containing catalytic domain (Galardy et al. 1994; Grobelny et al. 1992; Vandenbroucke and Libert 2014). This class of inhibitors is designed with the basic chemical backbone of collagen and a hydroxamate group (-CONHOH) (Vandenbroucke and Libert 2014). To inhibit MMP activity, the hydroxamate group binds to the catalytic Zn^{2+} site and creates a distorted 3D geometry around the Zn^{2+} ion. Then, the –NH group forms a short, strong hydrogen bond with the neighboring carbonyl oxygen, and hydrophobically stabilizes the inhibitor-enzyme complex (Vandenbroucke and Libert 2014). Examples of hydroxamate-based inhibitors include marimastat, batimastat, and ilomastat, also known as GM6001 (Galardy et al. 1994; Grobelny et al. 1992; Vandenbroucke and Libert 2014). Studies in this chapter use the hydroxamate-based inhibitor ilomastat to target inhibition of MMP-1 in the co-culture model described in Chapters 5 and 6 to determine if, and how, MMP-1 inhibition may alter neuronal expression of substance P and/or MMP-9 expression.

Since the Zn^{2+}-containing catalytic domain is preserved across many MMPs (Visse and Nagase 2003), hydroxamate-based inhibitors act on several MMPs depending on their

chemical structure; as such, they are considered to be broad-spectrum inhibitors (Galardy et al. 1994; Grobelny et al. 1992; Vandenbroucke and Libert 2014). However, the K_i inhibitor dissociation constant, an indication of inhibitor potency for a given enzyme, varies for different MMPs (Galardy et al. 1994). As such, the concentration can be tuned to make the inhibitors more selective and less broad-spectrum. For example, ilomastat inhibits MMP-8, MMP-9, MMP-1, MMP-2, and MMP-3 with K_i values ranging from 0.1nM for MMP-8 (most potent) to 27nM for MMP-3 (least potent) (Grobelny et al. 1992). The studies presented in this chapter utilize a 25nM ilomastat dose, which was intentionally chosen to optimize MMP-1 inhibition while preventing unnecessary inhibition of other MMPs with higher K_i values. Unfortunately, ilomastat also inhibits MMP-9 since that has a lower (more potent) K_i than MMP-1 (Grobelny et al. 1992), so the 25nM concentration of ilomastat is also expected to interact with the Zn^{2+} catalytic site on MMP-9. Accordingly, any changes in MMP-9 expression that may be observed could be attributed to direct MMP-9 inhibition *or* be due to indirect effects of MMP-1-ilomastat inhibition and the resulting less bioavailable MMP-1 that would normally activate MMP-9 in normal environments absent ilomastat (Conant et al. 2002; Visse and Nagase 2003). Despite the difficulties in selectively inhibiting MMP-1 and the caveat that both MMP-1 and MMP-9 could be directly impacted by ilomastat, the pilot studies in this chapter are helpful in beginning to identify putative effects of MMP inhibition, albeit broadly, on stretch-induced substance P expression.

Collectively, the studies in this chapter address Aim 4. A combined background section (Section 8.2) motivates the use of a sub-failure equibiaxial mechanical stretch. The

three sub-aims of Aim 4 are all addressed in the studies which are then presented in order with separate methods and results sections for each sub-aim. The studies in Section 8.3 (Aim 4a) define whether sub-failure strains that induce nociceptive signaling in the previous neuron-collagen gel model (Zhang et al. 2017; Zhang et al. 2018) also increase substance P in the co-culture model (Ita and Winkelstein 2019b). That study also characterizes the expression of both MMP-1 and MMP-9 resulting from a sub-failure equibiaxial stretch of a magnitude that induces facet-mediated behavioral sensitivity in the rat (Dong et al. 2012; Lee et al. 2006). The equibiaxial stretch studies in this chapter assay protein expression and/or MMP-1 activity at 24 hours after the stretch is imposed, unlike the failure stretch studies in Chapters 5 and 6 that assayed outcomes *immediately* following stretch. The later timepoint was chosen to allow for the MMP transcriptional and/or post-translational regulation that occurs on the scale of hours to days (Petersen et al. 2012; Yang et al. 2005). Section 8.4 includes studies that utilize the MMP inhibitor ilomastat. Studies in Section 8.4.1 (Aim 4b) test the effect of several ilomastat dosing regimens on MMP expression using a biochemical exposure to bacterial collagenase; studies in Section 8.4.2 (Aim 4c) utilize the stretch and dosing parameters defined from the earlier sections to define if, and how, ilomastat inhibition alters MMP expression and/or prevents increases in substance P in the sub-failure painful loading regime. A combined discussion (Section 8.5) integrates the outcomes from all of these studies collectively and elaborates on how these findings can be expanded to strengthen conclusions about the regulatory roles of MMP-1 and MMP-9 in stretch-induced nociceptive signaling and about how those MMP regulatory roles differ between cell types.

8.2. Relevant Background

Studies of facet capsule stretch in vivo and in vitro support that aspects, and consequences, of sub-failure biomechanical loading to the intact facet capsule have critical contributions to the development of pain and nociceptive transmission that depend on the magnitude of strain. For example, the extent of pain is directly related to the magnitude of strain across the facet capsular ligament (Dong et al. 2012; Panjabi et al. 1998; Pearson et al. 2004), as are neuronal expression of substance P and activated signaling kinase phosphorylated ERK (pERK) (Zhang et al. 2016; Zhang et al. 2017), and neuronal activity (Chen et al. 2006; Crosby et al. 2015; Lu et al. 2005; Quinn et al. 2010). Strains during ligament stretch that induce pain (8-31% at 500%/sec) (Dong et al. 2012) align with those measured in painful neck injury scenarios (29-40%) (Panjabi et al. 1998; Pearson et al. 2004). Similarly, a strain threshold of 11-40% (at 1%-7%/sec) has been identified in neuron-collagen gels for generating an increase in pERK and substance P expression (Zhang et al. 2016; Zhang et al. 2017; Zhang et al. 2018). Although capsular stretch-induced pain symptoms in the rat depend on capsular strain magnitude (Dong et al. 2012; Dong and Winkelstein 2010; Lee and Winkelstein 2009), pain is not further increased if the capsule is stretched until it fails (Lee et al. 2008; Winkelstein and Santos 2008). Despite the counterintuitive finding that a more severe injury (i.e. failure) is less detrimental than a sub-failure mechanical injury (Lee et al. 2008; Winkelstein and Santos 2008), those behavioral studies further amplify that afferent fiber signaling is requisite for mechanotransduction in the capsular ligament and necessary for both the development and maintenance of injury-induced pain.

Stretching the facet capsule beyond its physiologic limit can alter a variety of responses in the afferent neurons that innervate the ligamentous capsule, like hyperexcitability and persistent firing, altered expression of neurotransmitters and nociceptive molecules, and morphological changes, all of which can contribute to the transmission of pain (Cavanaugh et al. 2006; Crosby et al. 2014; Dong et al. 2012; Kallakuri et al. 2008; Lu et al. 2005; Quinn et al. 2010). In characterizing neuronal changes in the supraphysiologic regime, that body of work collectively presents possible mechanisms by which sub-failure facet capsule stretch may induce pain. Prior studies have demonstrated that MMP-1 and MMP-9 increase with the nociceptive-related neuropeptide substance P in a co-culture system mimicking the innervated facet capsule stretched in tension to failure (Chapter 6) (Ita and Winkelstein 2019a; Ita and Winkelstein 2019b). Although failure stretch induces strains across the gel that are sufficient to modulate MMP-1 and MMP-9 (Ita and Winkelstein 2019a; Ita and Winkelstein 2019b), whether a sub-failure stretch affects MMPs and/or substance P in the co-culture model is unknown despite that regime being relevant for pain.

8.3. Sub-Failure Biaxial Stretch in the Co-Culture Model

A sub-failure equibiaxial stretch that has been defined to be painful in DRG-collagen gels (Zhang et al. 2017; Zhang et al. 2018) is imposed on the new DRG-FLS co-culture collagen gel model. Although uniaxial tension is a simple loading modality with utility of defining the effects of tissue mechanics on the cellular and fiber-level responses (Lake and Barocas 2011; Roeder et al. 2002; Vader et al. 2009), biaxial loading

configurations better mimic the physiological boundaries and constraints of the ligament-bone complex and simulate the complex loading profiles of the facet capsular ligament in vivo (Dong et al. 2012; Ita et al. 2017; Jaumard et al. 2011). Sub-failure stretch was hypothesized to increase MMP-9 and substance P expression in parallel, since MMP-9 cleaves substance P and both are involved in neuronal transmission of noxious stimuli (Diekmann and Tschesche 1994; Kawasaki et al. 2008). Sub-failure stretch was also expected to elevate MMP-1 in gels containing FLS more than those without FLS since FLS secrete MMP-1 during culture and in response to failure (Attia et al. 2014; Ita and Winkelstein 2019b).

8.3.1. Methods

Type I collagen gels (2mg/mL) were fabricated as co-cultures with passage four rat FLS (~$5x10^4$ cells/mL) and DRGs (6-10/gel) (co-culture; n=12) or with DRGs only (DRG-only; n=10), as previously detailed (Figures 5.3 & 6.1) (Ita and Winkelstein 2019b). On DIV6, gels were triple-rinsed with 1XPBS, and an additional layer of collagen (125μL) was added to encapsulate the DRGs (Figure 6.1). After the PBS washes, media was changed to supplemented Neurobasal media without serum (Attia et al. 2014). On DIV7, gels were cut into a cruciform shape with each arm having the dimensions of 6.25mm by 8mm (Zhang et al. 2017) and marked with grid of fiducial markers using black India ink (Koh-I-Noor). The arms of the gels were loaded into grips attached to actuators with 500g load cells immersed in a 37°C 1XPBS bio-bath (Figure 6.1). Gels were pre-loaded until taut (less than 2mN/arm) and then stretched in equibiaxial tension at 4mm/sec to 1.5mm/arm (co-culture n=6; DRG-only n=5) in a planar testing machine (574LE2;

TestResources) to impose strains that induce pain in vivo and also increase nociceptive modulators in vitro (Dong et al. 2012; Zhang et al. 2017).

Force data were acquired at 200Hz from each arm and high-speed cameras (Phantom-v9.1; 500Hz) tracked the grid of fiducial markers to enable strain calculations (Ita and Winkelstein 2019b). Immediately after loading, gels were released from the grips, washed with 1XPBS with 1% Pen-Strep, and transferred to pre-warmed serum-free supplemented Neurobasal culture media with 1% Pen-Strep (Zhang et al. 2017). After 24 hours, gels were washed, and half of each gel was frozen at -80°C for homogenization and the other half was fixed in 4% PFA for immunolabeling. The post-stretch culture media (1mL) was stored at -80°C for an MMP-1 ELISA. Matched gels for each type (co-culture n=6; DRG-only n=5) underwent the same protocol but did not undergo any stretch and served as unloaded controls. The maximum magnitude of force during a gel stretch recorded by any of the four load cells was taken as the peak force for that gel. The marker locations in the unloaded reference image and the image immediately after the maximum force were digitized with FIJI software (NIH) and position data were processed in LS-DYNA (LSTC) to calculate the maximum principal strain (MPS) for each element of each gel (Ita and Winkelstein 2019b). The largest magnitude MPS sustained out of all elements within a gel was taken as the peak MPS for that gel.

Fixed gels were blocked in 1XPBS with 10% goat serum and 0.03% Triton-X and incubated overnight at 4°C with primary antibodies to substance P (anti-guinea pig, 1:250, Neuromics), MMP-1 (anti-rabbit, 1:400, Proteintech), and MMP-9 (anti-mouse, 1:250, Invitrogen). Gels were then washed and incubated with the secondary antibodies goat anti-

guinea pig 633, goat anti-rabbit 488, and goat anti-mouse 568 (all Alexa Fluor 1:1000; Invitrogen) and DAPI (1:750, ThermoFisher). Confocal images were acquired for each gel (6 images/gel) in regions containing DRG soma and/or axons (Ita and Winkelstein 2019b). In a subset of the co-cultures (n=4 stretched; n=4 unstretched), 6-image confocal stacks were acquired at 5μm steps throughout a 20μm depth in regions manually selected to contain only FLS cells; no DRG soma or axons were visualized in those regions. The amount of positive labeling was quantified using densitometry and a custom MATLAB script (Appendix B) in each image; for the FLS-localized images, the maximum intensity projection of each stack was generated prior to quantification with densitometry. For each image, substance P, MMP-1, and MMP-9 were normalized to DAPI to account for different cell densities in each image, and then normalized to the unloaded control gel, separately for each label.

Since secreted MMP-1 can be retained in the gel or released into the culture media (Attia et al. 2014), MMP-1 was measured in both the gel homogenate and media by ELISA. Gels were homogenized and their supernatants and the media were spun down (15 minutes, 10kg, 4°C) according to the kit protocol from the manufacturer (Sensolyte Plus 520 MMP-1 Assay Kit; Anaspec). MMP-1 values were quantified using a standard curve ranging from 20-0.625ng that was optimized for the range of MMP-1 concentrations expected in cell culture media. An APMA-activation step was used to activate any pro-MMP-1 in the samples so that total MMP-1 was assayed (Attia et al. 2014).

Separate two-tail t-tests compared the peak force and the peak MPS between the stretched culture types. Differences in substance P labeling, MMP-1 labeling, and MMP-9

labeling in DRG-localized images were tested using a two-way ANOVA by stretch (sub-failure; unstretched control) and culture type, and post-hoc Tukey HSD tests; differences in labeling in the FLS-localized images were analyzed between stretched and unstretched co-cultures with t-tests. A two-way ANOVA by stretch and culture type tested MMP-1 levels separately in media supernatant and gel homogenate.

8.3.2. Results

There is no evidence of visible tears or macroscopic gel rupture for any gel during the 1.5mm/arm equibiaxial stretch imposed here. Equibiaxial stretch generates greater peak forces in the co-culture (11.17±4.79mN) than DRG-only (4.22±2.35mN) gels (p=0.015); yet, similar peak maximum principal strains are sustained across the gel surface (co-cultures 18.64±6.57%; DRG-only 23.08±7.85%; p=0.387) (Figure 8.1). Force-displacement curves, strain maps, and quantification of the mechanical data are summarized for each gel in Appendix K.

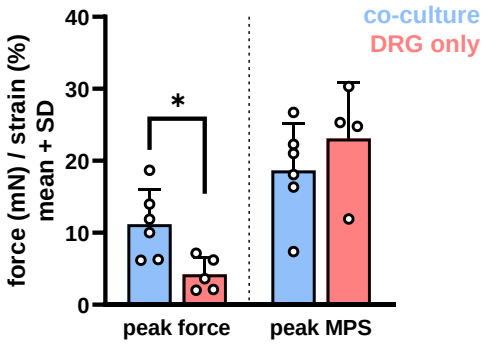

Figure 8.1. Peak force and maximum principal strain (MPS) with a sub-failure equibiaxial stretch of 1.5mm/arm at 4mm/sec. Peak forces are lower in the DRG-only gels that lack FLS (*p=0.015); yet, peak MPS does not differ by culture type (p=0.387).

Sub-failure stretch increases substance P labeling (p=0.005) in both culture types (Figure 8.2), with substance P levels in DRGs 2.5-fold over levels in unstretched control gels in DRGs. Substance P labeling is primarily evident in the cell bodies of the DRG soma (Figure 8.2). There is almost no detectable substance P labeling in the FLS cells, with less than 0.5% of pixels detected as positive in all images taken in the FLS regions (Figure 8.2). As such, substance P was not assessed in FLS cells in subsequent inhibitor studies (Section 8.4).

The average percentage of positive MMP-1 labeling in all co-culture gels, regardless of stretch condition, is 25.8% positive pixels, which is nearly 1.7-fold greater than the average positive labeling in all DRG-only gels (15.3%). Abundant MMP-1 labeling is observed in the DRG soma of gels with both cell types and is also prevalent in cells surrounding the DRG axons in the co-culture gels (Figure 8.3). Despite more overall

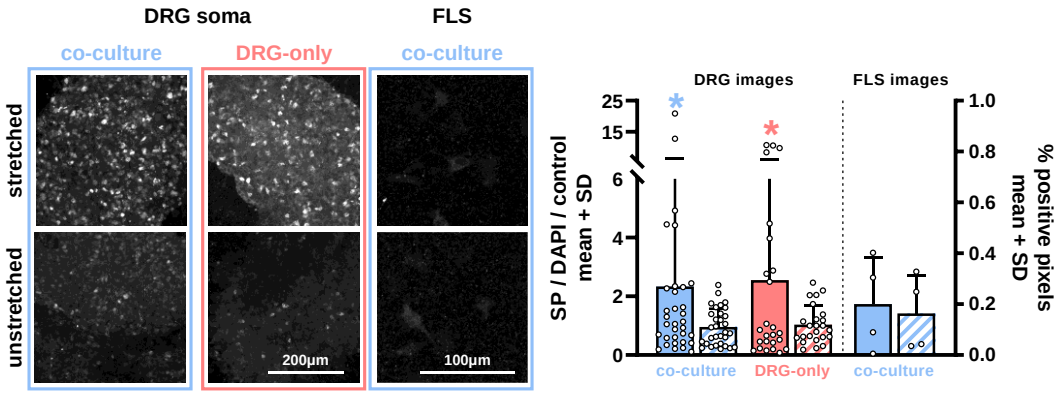

Figure 8.2. Substance P protein expression in co-culture and DRG-only collagen gels at 24 hours after a sub-failure equibiaxial stretch. Images show regions of most abundant labeling with substance P in the soma of both culture types. Stretch elevates substance P in the co-cultures and DRG-only collagen gels (*p=0.005). Essentially no positive substance P labeling is observed in FLS; protein quantification in the FLS cells is quantified as percent of positive pixels (on the right y-axis) instead of normalized to the unstretched control because labeling magnitudes near zero in the FLS resulted in artificially high fold changes. Superimposed data points represent quantification in each confocal image acquired. Solid bars=stretched; hashed bars= unstretched control. The scale bar in the DRG soma image applies to all images of DRG soma; the scale bar in the FLS image applies to both sets images with FLS.

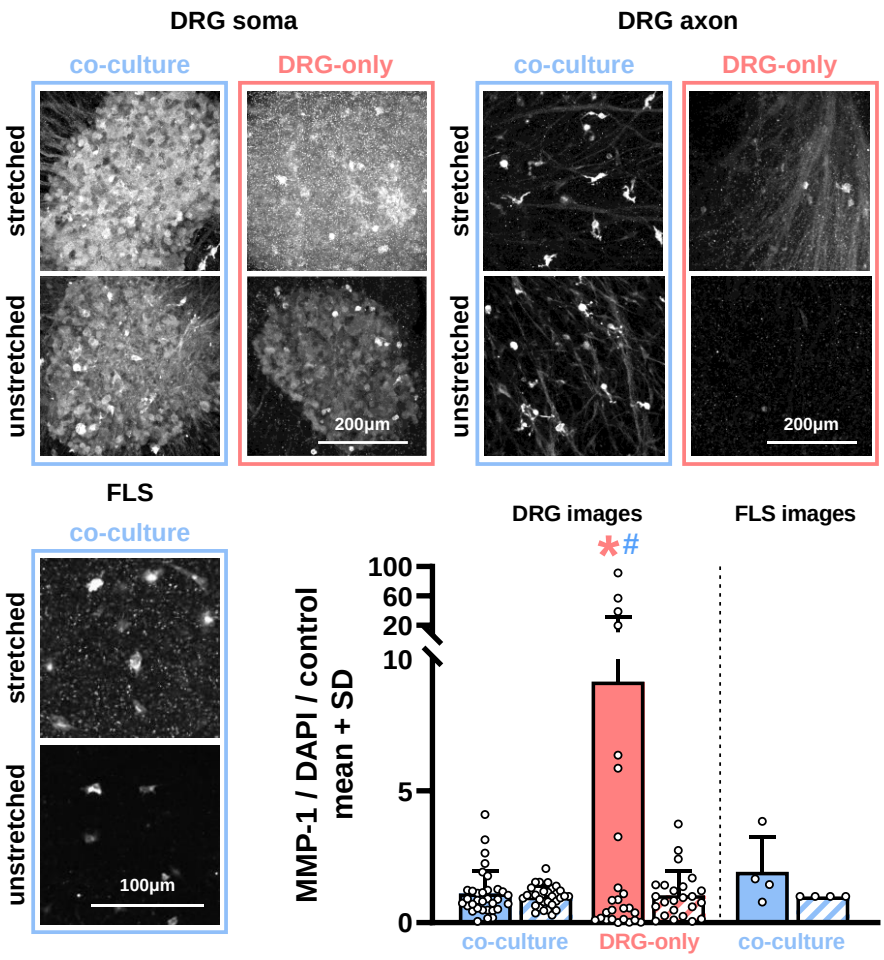

Figure 8.3. MMP-1 protein expression in co-culture and DRG-only collagen gels at 24 hours after a sub-failure equibiaxial stretch. Images show regions with positive labeling in DRG soma, DRG axons, and FLS cells. MMP-1 levels in the stretched DRG-only gels are greater than the levels in the unstretched DRG-only gels (*p=0.035) and greater than the levels in the stretched co-cultures (#p=0.024). Sub-failure stretch increases MMP-1 by 1.9-fold in FLS. Superimposed data points represent quantification in each confocal image acquired. Solid bars=stretched; hashed bars= unstretched control. The scale bar in the DRG soma image applies to all images of DRG soma or axons; the scale bar in the FLS image applies to both images of FLS.

labeling in the co-culture than the DRG-only gels, stretch only significantly elevates MMP-1 in the DRG-only group (p=0.035) (Figure 8.3). Furthermore, the increase in MMP-1 labeling in DRG-only gels with stretch is greater than that caused by stretch to co-cultures (p=0.024) (Figure 8.3). The average positive MMP-9 labeling, unlike MMP-1, is similar

between the co-culture (13.7%) and the DRG-only (15.2%) groups (Figure 8.4). Yet, the effect of stretch is the same for MMP-1 as MMP-9, with stretch significantly elevating MMP-9 in gels that only have DRGs (p=0.003), and that stretch-induced MMP-9 increase over unstretched controls is greater than what is observed in the co-cultures (p=0.002) (Figure 8.4).

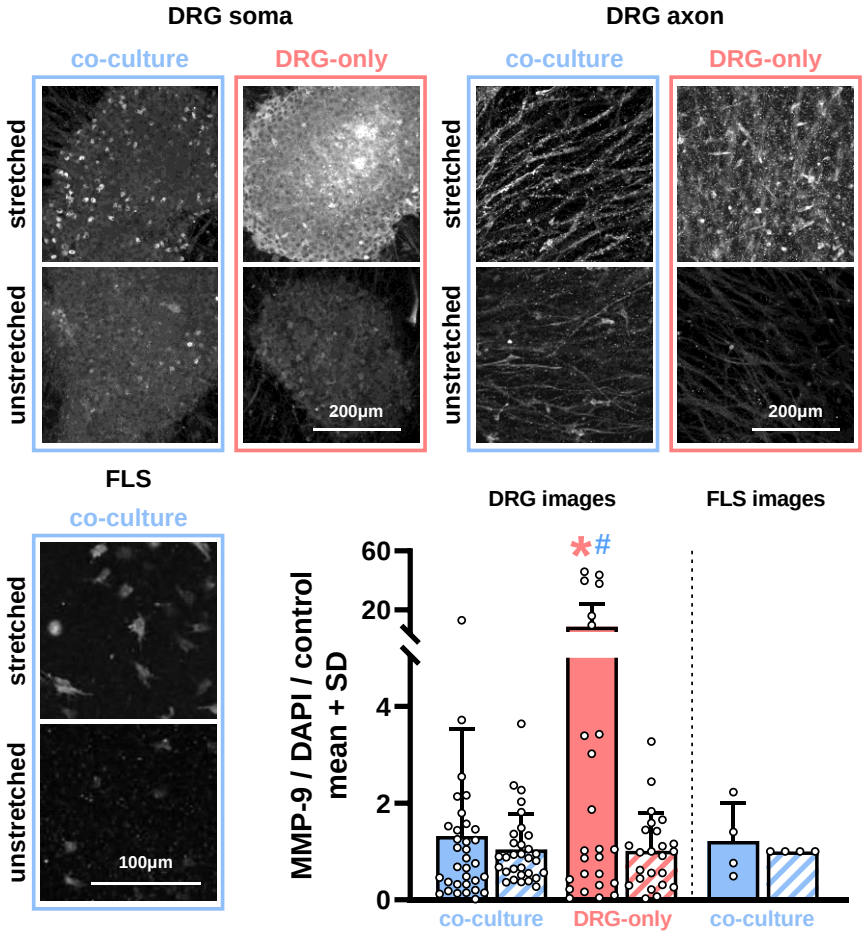

Figure 8.4. MMP-9 protein expression in co-culture and DRG-only collagen gels at 24 hours after a sub-failure equibiaxial stretch. The images show regions with positive labeling in DRG soma, DRG axons, and FLS cells. MMP-9 levels in the stretched DRG-only gels are greater than levels in the unstretched DRG-only gels (*p=0.003) and greater than the levels in the stretched co-cultures (#p=0.002). Sub-failure stretch increases MMP-9 by 1.2-fold in FLS. Superimposed data points represent quantification in each confocal image acquired. Solid bars=stretched; hashed bars= unstretched control. The scale bar in the DRG soma image applies to all images of DRG soma or axons; the scale bar in the FLS image applies to both images of FLS.

MMP-1 and MMP-9 immunolabeling is evident in FLS-rich regions after a sub-failure stretch in the co-cultures (Figures 8.3 & 8.4). Although MMP-1 increases 1.9-fold over the unstretched control level (Figure 8.3), and MMP-9 increases 1.2-fold (Figure 8.4), the sample size (n=4 images/group) is too small to detect meaningful differences between culture type and/or stretch condition. Power analyses indicate that a total sample size of 18 gels is required to detect significant differences in MMP-1, and a sample size of 98 gels is needed for MMP- 9. The concentration of MMP-1 levels within the gel homogenate are not different with stretch or culture conditions (Figure 8.5); yet, the MMP-1 concentration is lower (p=0.027) in the culture media after stretch for the DRG-only group (Figure 8.5). Immunolabeled images and their quantification, as well as the quantification for MMP-1 measured by ELISA, are summarized in Appendix L.

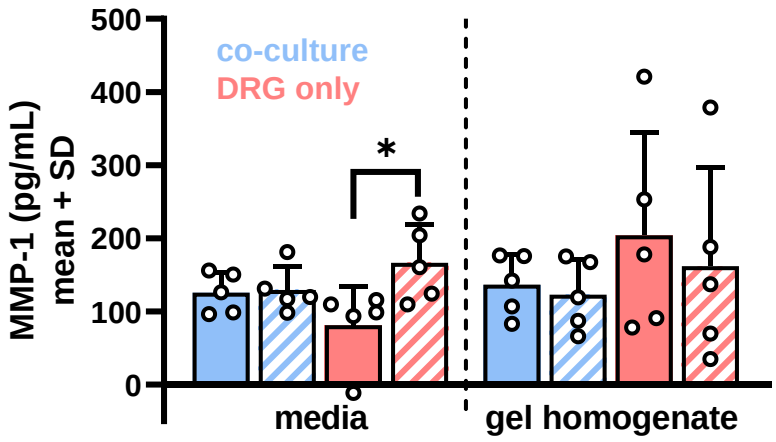

Figure 8.5. Concentration of MMP-1 in cell culture media and captured within the gel homogenate at 24 hours after sub-failure stretch. Superimposed data points represent quantification for each gel. There is a significant effect of stretch in the DRG-only gels in the culture media, with stretch decreasing MMP-1 concentration (*p=0.027). Neither culture nor stretch type alter MMP-1 levels in gel homogenate (p=0.620). Solid bars=stretched; hashed bars= unstretched control.

8.4. MMP-1 Inhibition

8.4.1. Optimization of Inhibitor Dosing Using Bacterial Collagenase Exposure

8.4.1.1. Methods

Type I collagen gels (2mg/mL) were fabricated as co-cultures with rat FLS (~$5x10^4$ cells/mL) from passages three to five and DRGs (6-10/gel) for all experiments as described earlier (Figures 5.3 & 6.1) (Ita and Winkelstein 2019b). On DIV6, all gels were triple-rinsed with 1XPBS and media was changed to supplemented Neurobasal media without serum (Attia et al. 2014). On DIV7, all gels underwent an incubation with 60U of purified bacterial collagenase (CLSPANK; Worthington) in DMEM for 20 minutes at 37°C since that exposure increases MMP-1 in DRG and FLS cells when exposed in co-cultures (Figure 5.16) (Ita et al. 2020b). Immediately following the exposure, gels were washed in 1XPBS, and half of each gel was frozen at -80°C for homogenization and the other half was fixed in 4% PFA for immunolabeling. The culture media was also saved and stored at -80°C for future assays.

In two separate experiments, co-cultures underwent different ilomastat dosing regimens prior to bacterial collagenase exposure on DIV7 (Table 8.1). In the first experiment, the co-culture media was treated from DIV3 until DIV7 with either a 25nM dose of the MMP inhibitor ilomastat, an equal volume dose of sterile H_2O vehicle, or a combination of each at different days in vitro (Table 8.1). A 25nM ilomastat dose (GM6001; Millipore Sigma) was prepared from a 2.5mM stock solution in dimethyl sulfoxide (DMSO) (5µL) dissolved into sterile cell culture H_2O to a concentration of 0.5µM (Conant et al. 2004; Rogers et al. 2014); 25µL of the 0.5µM dilution was then added to the

media to achieve a final concentration of 25nM. Accordingly, the H_2O vehicle dose consisted of 25µL of sterile H_2O. Separate co-cultures received either: ilomastat daily and one hour before exposure (daily), with every media change and one hour before exposure (media Δ), only one hour before exposure (1hr before), or not at all (H_2O veh) (n=4/group) (Table 8.1). Water vehicle doses were added to media whenever a dosing regimen did not call for ilomastat (Table 8.1).

A second experiment utilized the dosing regimen with ilomastat given at every media change (media Δ) and a matched vehicle group with DMSO instead of water (DMSO veh), since the purchased stock ilomastat was stored in DMSO. The 25nM ilomastat dose was prepared as described above for the first experiment, and the DMSO vehicle was prepared identically to the ilomastat with sterile DMSO (Invitrogen) dissolved in sterile H_2O to a concentration of 25nM (n=2/group) (Table 8.1).

In order to determine how various treatments of this MMP inhibitor effect MMP-1 and MMP-9 expression after an exposure previously shown to increase MMP-1 (Figure 5.16) (Ita et al. 2020b), gels were immunolabeled after 20 minutes of exposure to bacterial collagenase for MMP-1 (anti-rabbit, 1:400, Proteintech), MMP-9 (anti-mouse, 1:250, Invitrogen), and substance P (anti-guinea pig, 1:250, Neuromics) as described in Section 8.3.1. Although the primary goal of this study was to optimize the inhibitor regimen to attenuate and/or abolish MMP-1, substance P was also labeled to track the neuronal nociceptive-signaling response in parallel with any effect of exposure and/or treatment on MMP expression. Confocal images were acquired for each gel in regions containing DRG soma and/or axons (n=5-6 images/gel) (Ita and Winkelstein 2019b). Confocal image stacks

(6X 5μm steps through a 20μm depth) were also acquired in regions containing FLS cells and no DRGs (n=2 images/gel). The amount of positive protein labeling was quantified using densitometry and a custom MATLAB script (Appendix B) for each image; for the FLS-localized images, the maximum intensity projection of each stack was generated prior to quantification by densitometry. Positive labeling across all images (DRGs & FLS) was compared for MMP-1 and MMP-9 to quantify total MMP in the system; substance P was only compared in the DRG images since FLS do not show positive labeling for substance P (Figure 8.2). Student's t-tests compared the percentage of positive pixels of each protein between groups, separately for each of the first and second experiments (Table 8.1).

8.4.1.2. Results

Total MMP-1 protein expression is significantly attenuated in co-cultures receiving ilomastat at every media change compared to co-cultures with only one dose at one hour before the exposure ($p=0.031$) and compared to co-cultures with matched volume H_2O doses ($p=0.044$) (Figure 8.6). Despite that difference in MMP-1 levels between ilomastat with media changes and H_2O vehicle, ilomastat with media changes does not change MMP-1 levels from those treated with the DMSO vehicle (Figure 8.6). Administration of daily ilomastat doses increases MMP-9 expression relative to its expression in co-cultures receiving doses only on DIV3, DIV6, and prior to exposure ($p=0.009$) (Figure 8.6). Yet, results from the second experiment show that inhibitor doses with every media change significantly decrease MMP-9 expression from expression in the co-cultures with DMSO

Table 8.1. Ilomastat dosing regimens with bacterial collagenase exposure on day-in-vitro (DIV) 7

Group	Description	Regimen
Experiment 1		
daily	25nM ilomastat dose given daily starting on DIV3 & 1 hour before exposure on DIV7	DIV3 - ilomastat DIV4 - ilomastat DIV5 - ilomastat DIV6 - ilomastat DIV7 - ilomastat
media Δ	25nM ilomastat dose given during every media change beginning on DIV3 & 1 hour before exposure on DIV7; an H_2O vehicle dose given on DIV4 & DIV5	DIV3 - ilomastat DIV4 - H_2O DIV5 - H_2O DIV6 - ilomastat DIV7 - ilomastat
1hr before	H_20 vehicle dose given on DIV3 through DIV6; 25nM ilomastat dose given 1 hour before exposure on DIV7	DIV3 - H_2O DIV4 - H_2O DIV5 - H_2O DIV6 - H_2O DIV7 - ilomastat
H_20 veh	H_20 vehicle dose given daily starting on DIV3 & 1 hour before exposure on DIV7	DIV3 - H_2O DIV4 - H_2O DIV5 - H_2O DIV6 - H_2O DIV7 - H_2O
Experiment 2		
media Δ	25nM ilomastat dose given during every media change beginning on DIV3 & 1 hour before exposure on DIV7	DIV3 - ilomastat DIV4 - none DIV5 - none DIV6 - ilomastat DIV7 - ilomastat
DMSO veh	25nM DMSO vehicle dose given during every media change beginning on DIV3 & 1 hour before exposure on DIV7	DIV3 - DMSO DIV4 - none DIV5 - none DIV6 - DMSO DIV7 - DMSO

vehicle (p=0.023) (Figure 8.6). Substance P expression follows the same trends as MMP-1 expression (Figures 8.6 & 8.7); co-cultures treated with ilomastat at every media change have lower levels of substance P than those receiving only one dose of ilomastat prior to exposure (p=0.038) and those receiving H_2O vehicle (p=0.019) (Figure 8.7). Ilomastat does

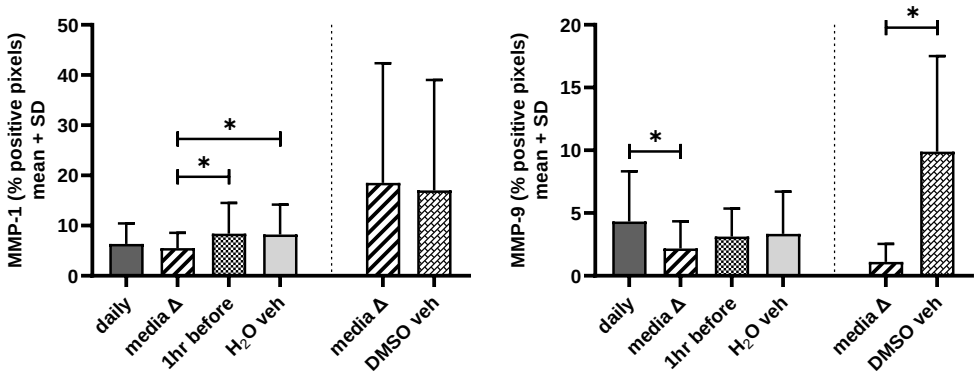

Figure 8.6. Level of positive immunolabeling for MMP-1 and MMP-9 with dosing regimens of the MMP inhibitor ilomastat after 20 minutes of exposure to bacterial collagenase. The dotted line demarcates protein outcomes that are quantified from the two separate experiments. Co-cultures with the "media Δ" regimen have less MMP-1 expression than co-cultures receiving the "1hr before" and "H_2O veh" regimens (*p≤0.044). MMP-9 is greater in co-cultures with daily inhibitor administration than with doses every media change (*p=0.009). MMP-9 expression is lower with ilomastat treatment than with the DMSO vehicle in the second study (*p=0.023).

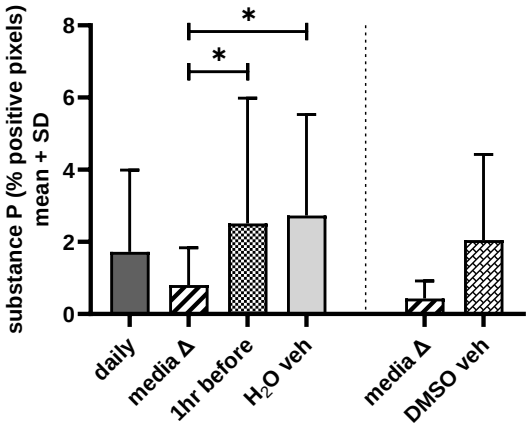

Figure 8.7. Positive immunolabeling for substance P with dosing regimens of ilomastat after 20 minutes of bacterial collagenase exposure. The dotted line demarcates protein outcomes that are quantified from two separate experiments. The "media Δ" regimen decreases substance P expression from co-cultures receiving the "1hr before" and "H_2O veh" regimens (*p≤0.038).

not change substance P expression from levels with the matched DMSO vehicle treatment (Figure 8.7). Immunolabeled images and their quantification are summarized in Appendix L.

8.4.2. Sub-Failure Biaxial Stretch with MMP Inhibition

8.4.2.1. Methods

The primary goal of this study was to impose a sub-failure painful stretch in the presence of MMP inhibition and characterizing effects on MMP-1, MMP-9, and substance P protein expression. Since a 1.5mm/arm equibiaxial stretch increases substance P expression by 2.5-fold in co-cultures (Figure 8.2), that same mechanical insult was imposed in this study. The ilomastat dosing regimens used in stretch experiments most closely followed the regimen of dosing on every media change, that is on day-in-vitro (DIV) 3, 6, and one hour before the stimulus (Table 8.1). Although the effectiveness of ilomastat dosing to reduce total MMP-1 is not evident in comparisons with the DMSO vehicle (Figure 8.6), the "media Δ" dosing regimen decreases total MMP-1 compared to a matched H_2O vehicle (Figure 8.6). Furthermore, dosing at every media change decreases total MMP-9 from DMSO vehicle (Figure 8.6) and substance P from H_2O vehicle (Figure 8.7). Therefore, the "media Δ" dosing regimen was chosen as the most promising inhibitor treatment procedure to reduce MMP levels in the current study. Further, to determine if such an inhibitor intervention after a painful sub-failure stretch affects protein outcomes, groups were included with and without an inhibitor dose immediately following the painful stretch.

Therefore, co-cultures were fabricated with rat FLS (~$5x10^4$ cells/mL) from passages three to five and DRGs (6-10/gel) (Figures 5.3 & 6.1) (Ita and Winkelstein 2019b), and underwent one of four different dosing regimens with ilomastat and/or DMSO vehicle (Figure 8.8). Ilomastat and DMSO vehicle doses were prepared for a final

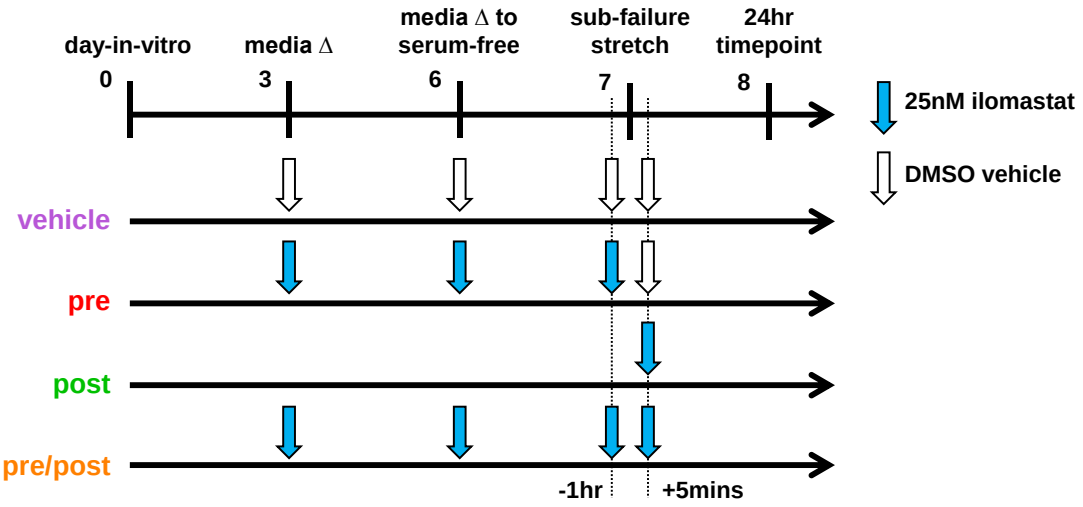

Figure 8.8. Study design of the dosing regimens for MMP inhibition with sub-failure equibiaxial stretch experiments. Co-cultures either received DMSO vehicle at every timepoint (vehicle; n=10), ilomastat leading up to the stretch and DMSO after the stretch (pre; n=16), ilomastat only after the stretch (post; n=12), or ilomastat at every dose (pre/post; n=14). All ilomastat and DMSO vehicle doses were given at 25nM concentration. Co-culture doses prior to stretch on DIV7 were given one hour before stretch, and doses after the stretch were given after five minutes.

concentration of 25nM as described in Section 8.4.1.1. Doses added to the culture media on DIV7 before the sub-failure stretch were given one hour prior to the stretch, and post-stretch doses were added to media five minutes after the stretch (Figure 8.8). Separate co-cultures received either: DMSO vehicle at every dosing time (vehicle; n=10), ilomastat leading up to the stretch and DMSO after the stretch (pre; n=16), ilomastat only after the stretch (post; n=12), or ilomastat at every dosing time (pre/post; n=14) (Figure 8.8). All co-culture gels were prepared for mechanical testing as described in section 8.3.1 (Zhang et al. 2017); half of the gels in each group were stretched in equibiaxial tension at 4mm/sec to 1.5mm/arm (Section 8.3.1), and the other half underwent the same protocol without any imposed stretch, serving as unstretched controls.

Force and high-speed imaging data were acquired as described in Section 8.3.1 (Figure 6.1) (Ita and Winkelstein 2019b). Immediately after loading, gels were released

from the grips, washed with 1XPBS with 1% Pen-Strep, and transferred to pre-warmed serum-free supplemented Neurobasal culture media with 1% Pen-Strep (Zhang et al. 2017); all post-stretch ilomastat and/or DMSO vehicle doses were added directly into the fresh media (Figure 8.8). After 24 hours, gels were washed, and half of each gel was stored at -80°C and the other half was fixed in 4% PFA for immunolabeling. The post-stretch culture media (1mL) was also saved and stored at -80°C for future use. The peak force and peak maximum principal strain were computed per gel as described earlier (Section 8.3.1).

Fixed gels were blocked in 1XPBS with 10% goat serum and 0.03% Triton-X and incubated overnight at 4°C with primary antibodies to substance P (anti-guinea pig, 1:250, Neuromics), MMP-1 (anti-rabbit, 1:400, Proteintech), and MMP-9 (anti-mouse, 1:250, Invitrogen). Gels were then washed and incubated with the secondary antibodies goat anti-guinea pig 633, goat anti-rabbit 488, and goat anti-mouse 568 (all Alexa Fluor 1:1000; Invitrogen) and DAPI (1:750, ThermoFisher). Labeled gels were imaged using the 20x objective of a Leica TCS SP8 confocal microscope (1024x1024 pixels, Leica Microsystems). Images were acquired for each gel (6 images/gel) in regions containing DRG soma and/or axons (Ita and Winkelstein 2019b). In a subset of the co-cultures (n=3-4/group/stretch condition), 6-image confocal stacks (1-2 images/gel) were acquired at 5μm steps throughout a 20μm depth in regions manually selected to contain only FLS cells. The location of each image was registered with the elements from each gel to relate cellular outcomes to the elemental strain. The amount of positive protein labeling was quantified using densitometry (Appendix B); for the FLS-localized images, the maximum intensity projection of each stack was generated prior to quantification with densitometry. For each

image, substance P, MMP-1, and MMP-9 were normalized to DAPI to account for different cell densities, and then normalized to the unloaded control gel, separately for each label.

One-way ANOVAs by dosing group with post-hoc Tukey HSD tests compared peak force, peak MPS, and the fold-change in protein expression over unstretched controls. Differences in MMP-1, MMP-9, and substance P were tested separately for images taken in the DRG regions and for MMP-1 and MMP-9 in images taken in the FLS regions. Protein outcomes in the neuronal images were further binarized based on whether they were acquired in elements that sustained MPS below or above 11.7% strain, the threshold for increasing phosphorylated ERK and collagen matrix reorganization in stretched neuron-collagen cultures (Zhang et al. 2016). Neuronal protein expression below and above that 11.7% strain threshold was compared for each protein label in each group separately using t-tests.

8.4.2.2. Results

Neither the force ($p=0.439$) nor the maximum principal strain ($p=0.229$) is different across groups (Figure 8.9). The average peak force (15.1±9.0mN) and MPS (23.3±12.3%) across all groups are similar to those detected in co-cultures receiving the same sub-failure stretch (force 15.8±4.2mN; MPS 18.6±6.5%) in the earlier study (Figure 8.1). Force-displacement curves, strain maps, and quantification of mechanical data are summarized for each gel in these experiments Appendix K.

In neuronal regions, there is a significant effect of inhibitor treatment on MMP-1 labeling, with the post group having significantly *more* expression after sub-failure stretch than the vehicle ($p=0.004$), pre ($p=0.002$), and pre/post ($p=0.025$) groups (Figure 8.10).

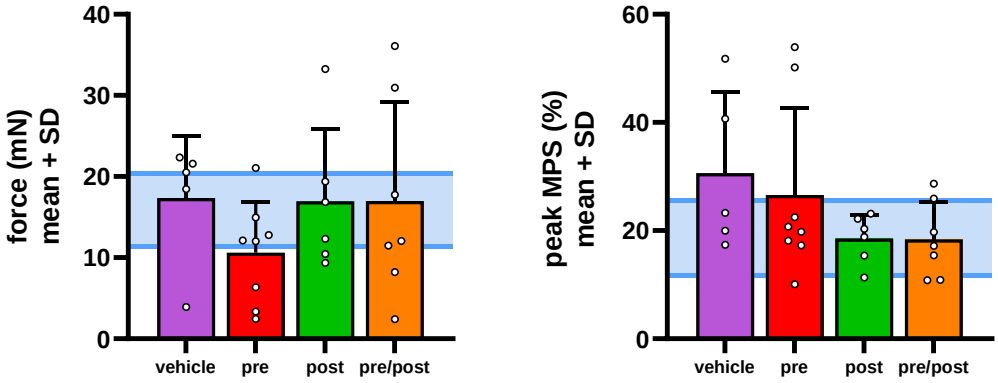

Figure 8.9. Peak force and maximum principal strain (MPS) with sub-failure equibiaxial stretch. Neither peak force (p=0.439) nor peak MPS (p=0.229) differs across treatment groups. Superimposed data points represent quantification in each gel; blue corridors represent 95% confidence intervals around the mean of stretched co-cultures from the study in Section 8.3 for reference.

Despite elevated MMP-1 with post-exposure inhibition, there are no differences in the fold-change of MMP-9 expression (p=0.130) across any of the inhibitor regimens (Figure 8.10). As with MMP-1, neuronal regions in the group with post treatment also have the highest levels of substance P, with expression levels significantly greater expression than in co-cultures with pre treatment only (p=0.005) (Figure 8.10). MMP-1 and MMP-9 expression

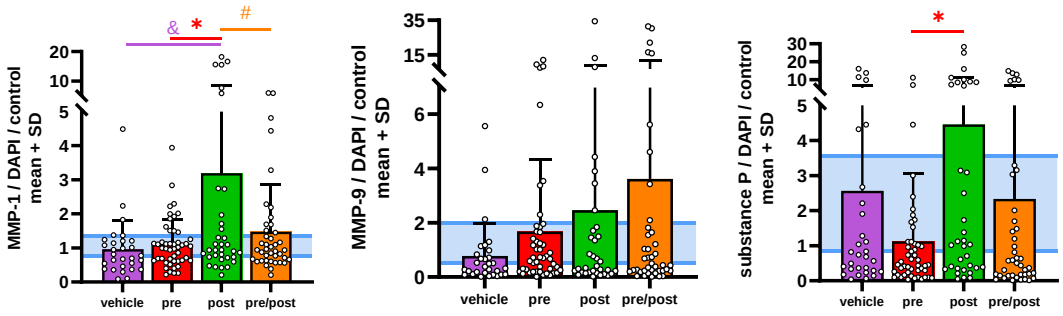

Figure 8.10. Protein expression over unstretched controls for MMP-1, MMP-9, and substance P in DRG soma and axons 24 hours after a sub-failure equibiaxial stretch. DRGs in co-cultures receiving the post inhibitor regimen have significantly more MMP-1 than those with vehicle (&p=0.004), pre inhibition (*p=0.002), and pre/post inhibition (#p=0.025). Stretch does not cause differential MMP-9 expression across groups (p=0.130). The post inhibition group has increased substance P with sub-failure stretch compared to the pre inhibition only (p=0.005). Superimposed data points represent quantification in each confocal image acquired; blue corridors represent 95% confidence intervals around the mean of stretched co-cultures from the study in Section 8.3 for reference.

in FLS cells are not different between the different inhibitor regimens (MMP-1 p=0.524; MMP-9 p=0.722) (Figure 8.11), although power analyses indicate that increasing the sample of confocal images to 3 images/gel and 6 images/gel are sufficient to reveal differences in MMP-1 and MMP-9 expression across groups, respectively. Immunolabeled images and their quantification are summarized in Appendix L.

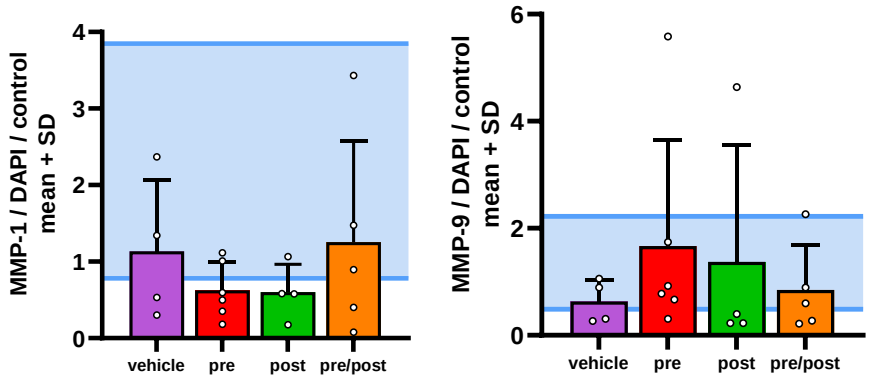

Figure 8.11. Protein expression over unstretched controls for MMP-1 and MMP-9 in FLS cells at 24 hours after a sub-failure equibiaxial stretch. No differences are detected across groups for MMP-1 (p=0.524) nor for MMP-9 (p=0.722). Superimposed data points represent quantification in each confocal image acquired; blue corridors represent the maximum and minimum of protein expression quantified in stretched co-cultures from the study in Section 8.3 for reference.

There are no differences in protein expression between DRGs that sustain strains below 11.7% and DRGs that sustained strains above that threshold with the DMSO vehicle ($p \geq 0.292$) (Figure 8.12). Yet, each of the inhibitor treatment groups have some differential expression based on analyses by the strain threshold. The most significant differential expression across the 11.7% strain threshold is observed in the post group, with *lower* protein expression in the DRGs located in the elements with strains *above* 11.7% for MMP-1 (p=0.017), MMP-9 (p=0.046), and substance P (p=0.008). With the pre inhibition only

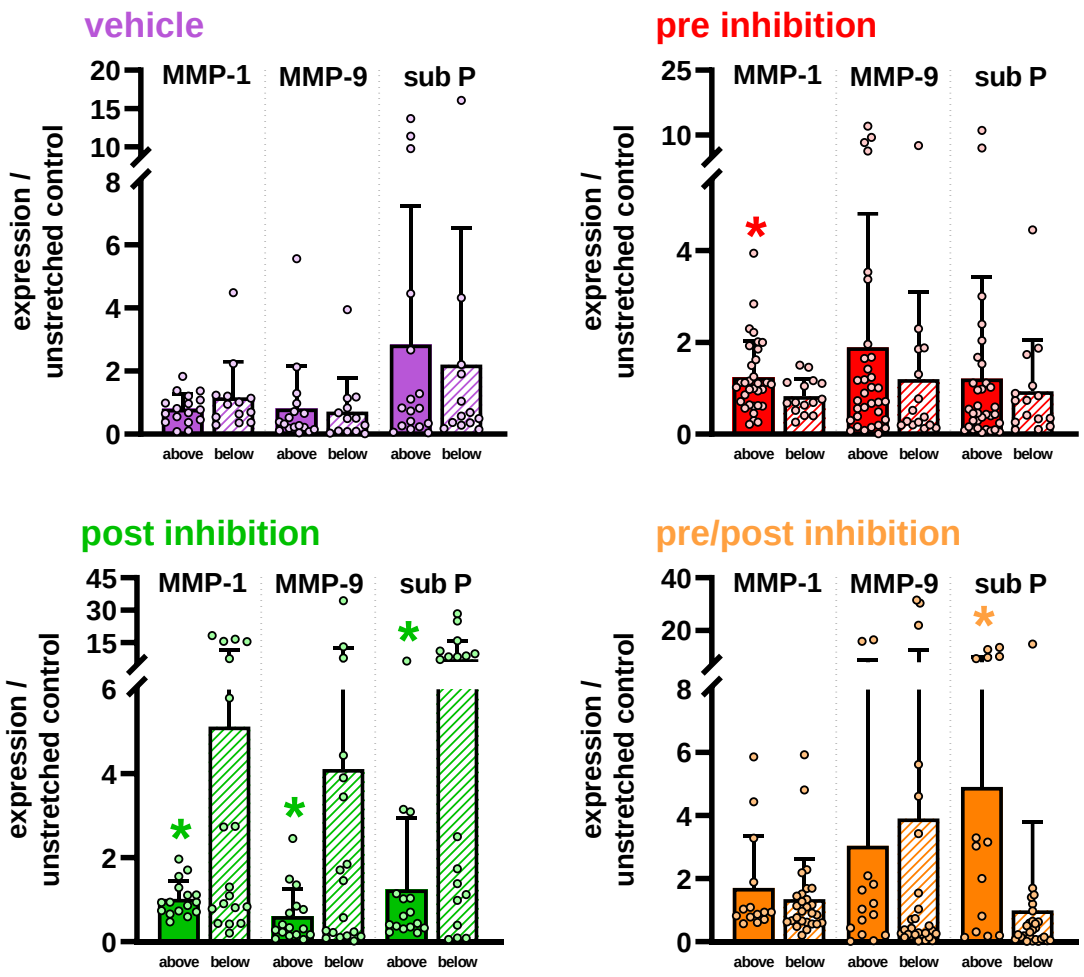

Figure 8.12. Protein expression by group binarized by whether DRGs reside in elements sustaining maximum principal strain above or below 11.7%. Protein expression does not vary across the threshold groups with vehicle ($p \geq 0.292$). In the pre group, MMP-1 is elevated for strains above the threshold (*$p=0.020$). In the post group, MMP-1 ($p=0.017$), MMP-9 ($p=0.046$), and substance P (sub P) ($p=0.008$) are decreased with strains above the threshold. In the pre/post group, substance P is greater with strains above the threshold ($p=0.015$). Superimposed data points represent quantification in each confocal image acquired.

regimen, MMP-1 is significantly elevated in elements above the strain threshold ($p=0.026$) (Figure 8.12). Strains above the threshold also have more substance P labeling in co-cultures receiving the pre/post treatment ($p=0.015$) (Figure 8.12).

8.5. Discussion

This study demonstrates that a sub-failure, biaxial stretch is sufficient to induce nociceptive signaling in a co-culture model of the capsular ligament (Figure 8.2). Increased substance P coincident with peak maximum principal strains of 18-23% for DRG-FLS co-cultures and DRG-only cultures is consistent with prior reports that strain magnitudes from 8-40% relate to pain and substance P protein expression (Dong et al. 2012; Zhang et al. 2017). The peak forces induced by sub-failure biaxial stretch range from 2.0-18.6mN and are lower in magnitude than the peak forces reported with the same sub-failure uniaxial distraction (21.1±6.5mN) (Zhang et al. 2018), demonstrating that uniaxial and equibiaxial distractions can impose similar strains yet differential force. That finding suggests that any force-regulated cellular responses may be different between uniaxial and biaxial stretch modalities and emphasizes the importance of modeling the in-situ ligament boundaries in defining cellular responses to stretch.

In response to a sub-failure stretch, DRG-only gels express more MMP-1 and MMP-9 (Figures 8.3 & 8.4) and experience lower peak forces than co-culture gels (Figure 8.1). In contrast, co-culture gels sustain higher peak forces than DRG-only gels (Figure 8.1), but stretch does not alter MMP expression (Figures 8.3 & 8.4); it is possible that the *higher* peak forces sustained by co-culture gels is related to the finding that stretch does *not* alter MMP expression in DRGs. Moreover, MMP-1 and MMP-9 appear to increase in neurons only when FLS are not present (Figure 8.4). Since force regulates signaling pathways in ligament fibroblasts (Kook et al. 2009), it is possible that FLS regulate MMPs in the co-culture group via MMP sequestration and/or retention (Bartok and Firestein 2010;

Bottini and Firestein 2013); but, altered MMP expression is not detected in the neuronal regions where images are taken. The possibility that FLS retain MMPs is supported by the fact that MMP-1 and MMP-9 localize to FLS cells after failure stretch in this same co-culture model (Figure 6.6) (Ita and Winkelstein 2019a). Although stretch does not increase either MMP-1 or MMP-9 in FLS (Figures 8.3 & 8.4), if more images and larger sample sizes were used then differences in MMP expression with stretch may be revealed. For example, increasing image sampling to n=5 images/gel for MMP-1 expression may enable detecting differences as indicated by power analyses. Similarly, power analyses show that increasing the sample size to 12 gels for each stretch condition may reveal differences in MMP-9 expression between the FLS cells in stretched and unstretched co-culture gels.

The lack of changes in MMP-1 in co-culture media with stretch (Figure 8.5) could also be explained by FLS retention of MMPs or differences in the relative amounts of the pro- and active forms of MMP-1. For example, the proportion of MMP-1 that is retained within the gel relative to the amount secreted into the culture media changes over time with normal growth in culture secreted by ligament fibroblasts seeded in collagen gels (Attia et al. 2014). Furthermore, the proportion of pro- and active MMP-1 in both gel homogenate and media varies over time (Attia et al. 2014; Daniels et al. 2003). Since the ELISA assay utilized in these studies includes an APMA-activation step to activate any latent MMP-1, total MMP-1 in the system is quantified. Since that measurement does not distinguish between pro- and active forms of MMP-1, there may be effects on MMP-1 activation with stretch and/or culture type that are not detected. Of note, pilot studies were run to use the ELISA assay without the APMA-activation step, but MMP-1 signals were below the noise

threshold and not detected; pooling samples by group and/or densifying protein with additional extraction protocols could address this technical difficulty. Nonetheless, stretch appears to modulate MMP-1 in the media in gels in which MMP-1, MMP-9, and substance P expression are elevated (Figures 8.2-8.6), suggesting all of these proteins to be related in stretch-induced neuronal signaling.

The lack of robust effects of ilomastat on MMP expression with bacterial collagenase exposure (Figure 8.6) may be due to technical details of the immunolabeling assays or the 25nM dose of ilomastat. The primary antibodies used to visualize MMP-1 and MMP-9 bind to the pro- and active forms of the enzyme; further, the antibody interaction is not expected to be altered if the MMP is in a bound state with the ilomastat inhibitor. As such, MMP expression levels measured by immunolabeling cannot distinguish between inhibitor bound MMP nor between pro- and active forms. Nonetheless, ilomastat inhibition may lower the *total* MMP levels in the system, regardless of their state, especially in the regimens with multiple ilomastat doses during time in culture (Table 8.1). This notion is supported by the decreased MMP-1 and MMP-9 observed with ilomastat for every media change (Figure 8.6). Although a 25nM ilomastat dose was chosen as the minimum dose expected to inhibit MMP-1 (Galardy et al. 1994; Grobelny et al. 1992), it is possible that this concentration is too low to consistently lower expression of MMPs. Concentrations of ilomastat between 1μM and 100μM reduce the contractile function and collagen production of smooth muscle cells and fibroblasts in a dose-dependent manner (Daniels et al. 2003; Rogers et al. 2014). So, it is possible that higher doses of ilomastat may have more robust effects on MMP expression levels.

Despite those challenges, ilomastat treatment differentially alters MMP-1 and substance P expression induced by a painful sub-failure stretch (Figure 8.10). Since neither the peak force nor the peak maximum principal strain differ between groups (Figure 8.9), changes in the proteins can be attributed to the presence or absence of ilomastat. A single dose of ilomastat produces the most prominent differences in proteins, with that group (post) having significantly more MMP-1 than all other groups (Figure 8.10) and greater levels of all proteins with strains *below* a threshold for the increase of pERK (Figure 8.12). The fact that MMP-1, MMP-9, and substance P increase with lower strains when co-cultures receive one dose of ilomastat after stretch (Figure 8.12) is unexpected since 11.7% strain is considered as the threshold for noxious stimuli in neurons and coincident with reorganization of the local collagen matrix that can trigger nociceptive responses (Zhang et al. 2016).

The counterintuitive finding that MMP and substance P expression increases with strains *below* 11.7% in the post-treatment co-cultures (Figure 8.12) may be explained by that group having higher amounts of total MMP-1 at the time of stretch that lead to altered collagen-neuron adhesion sites and/or result in the post-stretch ilomastat dose incompletely blocking MMP-1 activity. FLS cells synthesize and secrete MMP-1 during normal culture that plateaus after 7-10 days (Attia et al. 2014). As such, it is likely that baseline synthesis and secretion of MMP-1 leading up to DIV7 is inhibited by the earlier ilomastat doses (on DIV3, DIV6, and DIV7) that are given to the "pre" and "pre/post" co-cultures (Daniels et al. 2003), which corresponds to less total MMP-1 in "pre" and "pre/post" than in "post" and vehicle co-cultures. More MMP-1 activity in the "post" and vehicle groups may mean

that collagen networks of those groups have a different microstructure than the networks of the groups that received ilomastat prior to the sub-failure stretch, since MMP-1 has a role in remodeling the collagen structure and matrix composition (Sbardella et al. 2012; Visse and Nagase 2003). As such, it is possible that the collagen-neuron adhesion sites that transduce local deformations in to nociceptive signals (Zarei et al. 2017; Zhang et al. 2017; Zhang et al. 2018) are altered in the "post" group and may explain why there is less MMP and substance P expression with higher magnitude strains (Figure 8.12). Furthermore, a post-stretch 25nM ilomastat dose may be able to inhibit all active MMP-1 in the "pre" and "pre/post" co-cultures, but not in the "post" and vehicle co-cultures. So, it is possible that active MMP-1 is only partially inhibited in the "post" co-cultures, or at least to a lesser extent than in the "pre" and "pre/post" co-culture groups. A different extent of post-stretch MMP-1 inhibition in the "post" co-cultures from the "pre" and "pre/post" co-cultures might mean that there are differential ratios of pro-MMP-1 to active MMP-1 across groups. Consequences of this could be that non-mechanotransduction compensatory and/or feedback pathways, such as FLS-regulated cytokine "storms" (Bartok and Firestein 2010; Chakrabarti et al. 2020; Sluzalska et al. 2017), may be triggered in the "post" co-cultures. However, the fact that the protein expression with vehicle does not follow the same patterns as the post-treatment group suggests that treating with ilomastat after a stretch may actually have a detrimental effect, causing increases in MMP-1 and substance P expression, as opposed to the "pre" and "pre/post" ilomastat dosing regimens attenuating protein expression (Figure 8.10).

To further explore the relationships between MMP-1 and each of MMP-9 and substance P after sub-failure stretch, linear regressions and strength of correlations were separately tested within each dosing regimen group; stretched co-cultures from the first study in this chapter (Section 8.3) were included in this analysis as a comparator "naïve" group not receiving any vehicle and/or ilomastat. A significant correlation exists between MMP-1 and MMP-9 *only* in the naïve co-cultures 24 hours after sub-failure stretch ($p<0.001$) (Figure 8.13). That finding is consistent with the positive correlation between active MMP-1 and active MMP-9 detected in innervated soft tissues from patients with painful TMJ disorders (Figure 3.3) (Ita et al. 2020a) and further supports a possible mechanistic relationship between those two proteases. Significant correlations are detected between MMP-1 and substance P only in the groups with no pre-inhibition dosing (Figure 8.13), supporting the notion that ilomastat may regulate MMP-1 during normal co-culture growth (Attia et al. 2014; Daniels et al. 2003; Rogers et al. 2014). That is, substance P increases with MMP-1 in the vehicle ($p=0.012$) and post ($p<0.001$) groups (Figure 8.13). Although that positive trend is also evident in naïve stretched gels, the relationship is not significant ($p=0.058$) (Figure 8.13). The stretch-induced increase in MMP-1 coincident with substance P expression in the vehicle and post groups is consistent with parallel increases in MMP-1 and substance P immediately after failure stretch (Figure 6.4) (Ita and Winkelstein 2019b) and with bacterial collagenase exposure in groups with no ilomastat or with only one ilomastat dose preceding exposure (Figures 8.6 & 8.7). Collectively, those findings show that the expression level of substance P follows the expression of MMP-1 immediately after a biomechanical stretch to gel failure, at 24 hours after a sub-failure

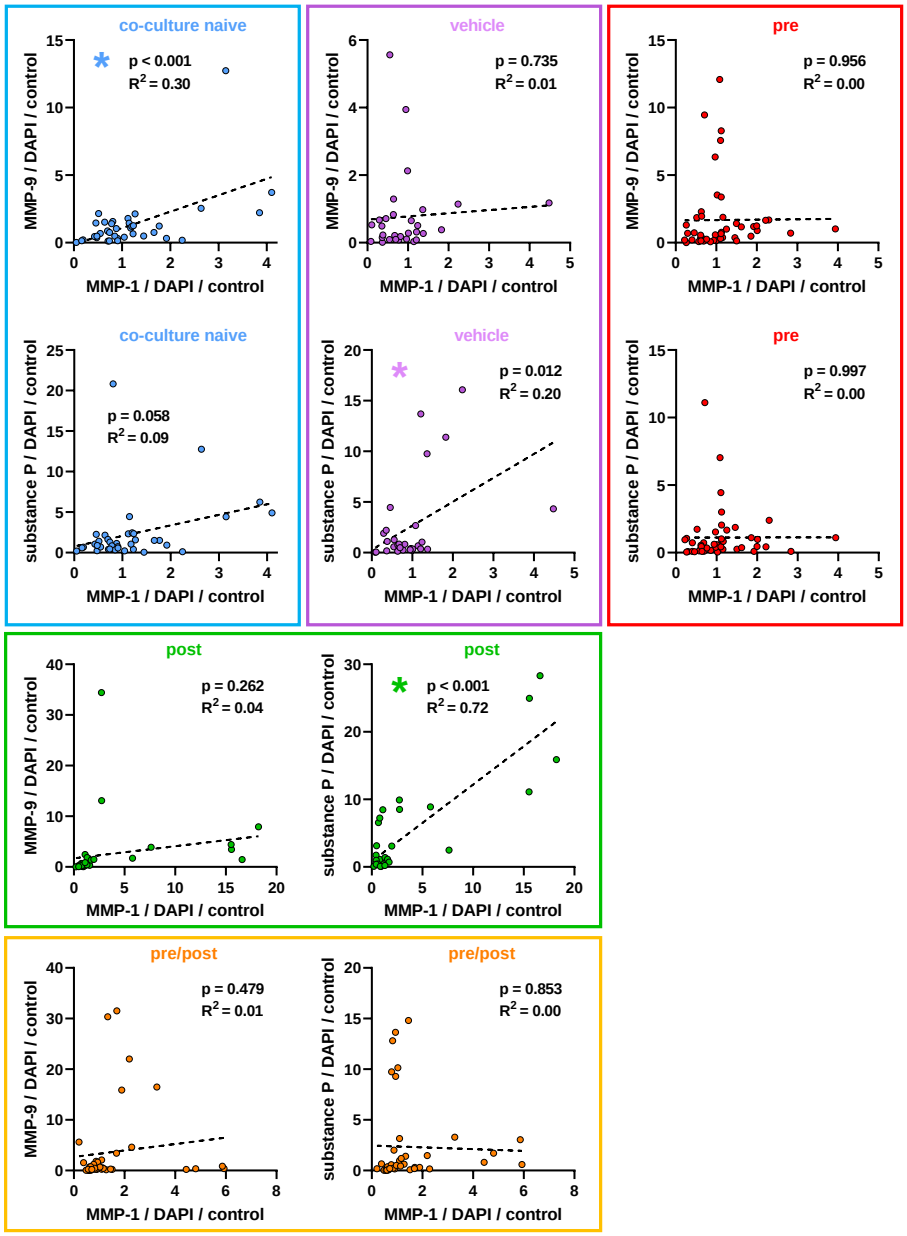

Figure 8.13. Linear regressions between MMP-1 and MMP-9 and between MMP-1 and substance P; all protein outcomes represent measurements in stretched co-cultures normalized to unstretched controls. Samples included in the co-culture naïve group (top left) are the cohort of gels tested in studies comparing co-cultures to DRG-only gels in Section 8.3; samples in all boxes are the cohort of gels tested in ilomastat inhibition studies in Section 8.4.2. There is a significant correlation between MMP-1 and MMP-9 only in the naïve co-culture gels after sub-failure stretch ($p<0.001$; $R^2=0.30$). Significant correlations are detected between MMP-1 and substance P in co-cultures with vehicle ($p=0.012$; $R^2=0.20$) and post ($p<0.001$; $R^2=0.72$) treatment regimens.

biomechanical stretch, and after 20 minutes of biochemical degradation. Taken together

with the lack of association between MMP-1 and substance P in cultures that were given ilomastat at DIV3, DIV6, and DIV7 during culture (Figure 8.13), those findings suggest that broad spectrum inhibition of MMPs (including MMP-1 and MMP-9) suppresses an interaction between MMP-1 and substance P that is triggered by noxious stimuli.

The protein expression outcomes in this study must be considered with the supposition that any inhibitory effect of ilomastat is likely only acting on the *collagenolytic* functionality of MMP-1, suggesting that the myriad cell signaling roles of MMP-1 (Allen et al. 2016; Boire et al. 2005; Conant et al. 2002; Conant et al. 2004; Dumin et al. 2001; Visse and Nagase 2003; Vos et al. 2000) are not altered. This supposition is due to the fact that hydroxamate-based inhibitors like ilomastat bind to the Zn^{2+}-containing catalytic domain of MMPs, and so, can presumably only bind to MMPs in its active form, when the Zn^{2+} site is biochemically available to the inhibitor (Grobelny et al. 1992; Visse and Nagase 2003; Yong et al. 2001). As such, the inhibitor theoretically only interferes with MMP functionality that requires the Zn^{2+} binding site. For the case of an MMP-1-ilomastat enzyme-inhibitor complex, the collagenolytic activity of MMP-1 would be inhibited; yet, any functional role of MMP-1 *not* requiring the Zn^{2+} binding site may still biochemically occur in the presence of the ilomastat inhibitor. So, the finding that none of the ilomastat dosing regimens significantly attenuate stretch-induced substance P expression (Figure 8.10) could indicate that the non-Zn^{2+}-dependent functions of MMP-1 are sufficient alone to trigger stretch-induced nociceptive signaling. Although there is no evidence that ilomastat alters the force and/or regional strains due to sub-failure stretch (Figure 8.9), the collagen organization and kinematics of the fiber network were not evaluated in this study.

Yet, it is possible that ilomastat treatment alters the collagen network's response to stretch by suppressing MMP-mediated collagen degradation that occurs during normal culture or that is induced by the sub-failure stretch. Assaying the composition and structure of the collagen matrix before and after stretch would help determine if the ilomastat dose used here influences collagenolytic effects on the collagen fibers and define if those effects occur in parallel with elevated nociceptive signaling in DRGs.

Experiments testing the ability of ilomastat to reduce MMP expression levels were optimized using a biochemical exposure to bacterial collagenase intentionally used because of its ability to robustly increase MMP-1 in the same co-culture model used here (Figure 5.16) (Ita et al. 2020b). Although biomechanical and biochemical stimuli increase MMP-1 (see Chapter 5), the magnitude of change in MMP-1 expression depends on the type of noxious stimuli and the length of time after the stimuli (Allen et al. 2016; Ita et al. 2020b; Ita and Winkelstein 2019b). As such, it is possible that an equivalent ilomastat dosing regimen has different effects on MMP expression immediately after a bacterial collagenase exposure than 24 hours after a sub-failure equibiaxial stretch. For example, a collagenase-induced increase in MMP-1 within minutes (Ita et al. 2020b) may occur via FLS-mediated secretion of sequestered MMP-1 in response to positive MMP feedback loops (Aghvami et al. 2016; Craig et al. 2015; Murphy 2017; Visse and Nagase 2003), whereas a stretch-induced increase in MMP-1 after one day may occur as a result of transcriptional regulatory mechanisms in FLS cells and/or peripheral neurons (Bartok and Firestein 2010; Bottini and Firestein 2013; Nishida et al. 2008; Zhou et al. 2014). As such, a dose of ilomastat given one hour before collagenase exposure is presumed to effectively reduce MMP-1 activity

and/or expression. However, there may have different, or no, effect on any transcriptional regulatory mechanisms induced by a sub-failure stretch. Thus, an ilomastat dose and frequency of dosing regimen should be optimized for reducing MMP-1 expression and/or activity specifically for a sub-failure stretch for the purpose of defining the effect of MMP-1 inhibition on stretch-induced nociceptive signaling.

Overall, the studies in this chapter show that MMP-1 and MMP-9 are involved in nociceptive signaling from sub-failure ligament injury in a fibroblast-dependent manner (Figures 8.2-8.5). Further, 25nM of ilomastat likely partially inhibits MMP-1 and MMP-9 (Figures 8.6 & 8.8), and the frequency of that dose alters stretch-regulation of MMPs and substance P in the painful and sub-failure regime (Figures 8.9-8.13). The immunolabeling data presented in this chapter do not completely capture FLS-localized expression responses for MMP-1 and MMP-9 (Figures 8.3, 8.4 & 8.11); studies should quantify MMP expression localized to fibroblasts to determine if the effects of ilomastat inhibition on FLS cells are similar to the effects on peripheral neurons (Figure 8.10) and to elucidate if MMP expression in FLS cells is regulated by strain magnitude (Figure 8.12). Study designs should also explore more selective inhibition of MMP-1 by methodologies such as siRNA silencing (Rogers et al. 2014) in order to block the translation of active MMP-1 *and* pro-MMP-1, thus providing a means to interfere in Zn^{2+} binding site-dependent *and* independent pathways. MMP-1 inhibition via siRNA techniques would also enable answering questions about MMP-1's regulation of MMP-9 that is not possible with the broad-spectrum ilomastat inhibitor. Investigating techniques that selectively inhibit MMP-1 is particularly important if inhibition studies are pursued in vivo, since broad-spectrum

MMP inhibitors like ilomastat are known to cause side effects like widespread musculoskeletal pain due to off-target effects of the ilomastat intervention (Fingleton 2008). Indeed, off-target side effects of ilomastat are a primary reason that clinical trials of MMP inhibitors have failed (Coussens et al. 2002; Vandenbroucke and Libert 2014). Of note, musculoskeletal pain induced by hydroxamate-based inhibitors has since been determined to be caused by off-target interactions with a disintegrin and metalloproteinases with thrombospondin motifs (ADAMTS) in human trials, and not MMPs (Fingleton 2008). The widespread musculoskeletal pain in cancer trials attributed to ilomastat-ADAMTS interactions is hypothesized to be due to systemic administration of the ilomastat drug (Fingleton 2008), and those mechanisms are not expected to be at play in the co-culture model here given the less complex nature of the in vitro model relative to a whole organism. Nonetheless, ilomastat may also have off-target effects in the co-culture model like binding to non-MMP enzymes that contain metals or interfering with ADAMTS released by fibroblasts (Bottini and Firestein 2013; Ernberg 2017; Fingleton 2008). Although no selective inhibitors for MMP-1 exist currently, selective inhibition of MMP-13 has been successfully achieved without evidence of musculoskeletal pain by targeting regions other than the preserved Zn^{2+} binding site (Baragi et al. 2009; Gege et al. 2012; Jüngel et al. 2010). Pursuing MMP-1 inhibition by this same selective approach may provide a fruitful opportunity to define the effect of isolated blocking of MMP-1 activity on other MMPs, like MMP-9, and to determine if selective MMP-1 inhibition in vivo has the potential to reduce pain without clinical side effects.

8.6. Integration & Conclusions

The studies in this chapter support the hypothesis that sub-failure stretch of the DRG-FLS co-culture collagen gel model above the magnitude of strain that increases substance P in peripheral neurons also regulates MMP-1 and MMP-9 expression in peripheral neurons (Figures 8.2-8.4). The presence of FLS, however, *prevents* the increase in MMP expression compared to DRG-only cultures (Figures 8.2-8.4); that is the opposite regulatory pattern than what was expected. This may be explained by incompletely captured measurements of MMPs in the culture media and/or gel homogenate (Figure 8.5) or by localization of MMP-1 and MMP-9 to the fibroblast-like synoviocyte cells in the co-cultures which were not fully assessed. Although larger group sizes are needed, pilot data suggest that sub-failure stretch regulates MMP-1 and MMP-9 expression in fibroblast-like synoviocytes, as well as in neurons (Figures 8.3-8.4). Despite the fact that sub-failure stretch does not increase MMP-1 nor MMP-9 in co-cultures (Figures 8.3 & 8.4), MMP-1 and MMP-9 are positively correlated in stretched DRGs (Figure 8.13), corroborating the notion put forth in Chapters 3 and 6 that those two MMPs are mechanistically related. Collectively, the studies assaying protein expression immediately after failure stretch (Chapter 6) and those presented here assaying proteins at 24 hours after sub-failure stretch implicate MMP-1 and MMP-9 in the rapid nociceptive response to severe injury and in a delayed response to sub-failure injury.

Because ilomastat inhibits MMP-9 in addition to MMP-1 at the concentrations used in these studies (Galardy et al. 1994; Grobelny et al. 1992; Vandenbroucke and Libert 2014), whether MMP-1 mediates stretch-induced nociceptive responses via its regulation

of MMP-9 cannot be determined. Furthermore, experiments with ilomastat treatment do not support the hypothesis that MMP-1 inhibition decreases stretch-induced MMP-9 and/or substance P. Instead, results demonstrate an interesting effect of ilomastat timing on protein expression and strain-dependence of those protein outcomes (Figures 8.10 & 8.12), whereby a single ilomastat dose following a painful sub-failure stretch appears to increase MMP-1 and substance P in DRGs that experience lower magnitude strains during the stretch. The finding that a post-stretch dose of ilomastat results in *greater* MMP-1, MMP-9, and substance P expression in neurons that underwent a strain *below* a threshold for noxious stimuli (Figure 8.12) (Zhang et al. 2016) suggests that blocking MMP activity after a painful stretch may disrupt the collagen-neuron adhesion sites that transduce biomechanical stimuli to physiological signals in neurons. Together these findings are integrated with those from studies in the co-culture model (Chapters 5 & 6), in the rat (Chapters 4 & 7), and in the human (Chapter 3) in the final chapter to put forth a mechanistic role for MMP-1 in nociceptive transmission from the capsular ligament, with suggestions for future directions.

Chapter 9

Synthesis & Future Work

9.1. Introduction

Chronic joint pain presents an enormous healthcare challenge affecting the daily lives of nearly one-fifth of Americans and costing the United States hundreds of billions of dollars annually (IBM Corporation 2019; Institute of Medicine 2011; National Academies of Sciences, Engineering, and Medicine 2020). Although matrix metalloproteinases (MMPs) are present in the tissues of joints with painful disorders, either due to trauma (Cohen et al. 2007; Haller et al. 2015; Konttinen et al. 1999; Lattermann et al. 2017) or degeneration (Kim et al. 2015; Loeser et al. 2012), whether their presence is relevant to pain transmission from those joints is unknown. Early studies of MMPs elucidated their role in regulating constituent components of the extracellular matrix (ECM) (Evanson et al. 1967; Sellers et al. 1977); in the context of degenerative joint disease, MMPs play a large role in the transition of ECM turnover from healthy to pathological (Freedman et al. 2015a; Kraus et al. 2015; Murphy and Nagase 2009). In the last few decades, a myriad of ECM-independent roles for MMPs in cellular interactions with the external microenvironment have emerged (Murphy 2017; Sbardella et al. 2012), many of which include cellular interactions in and across the peripheral and central nervous systems (Agrawal et al. 2008; Huntley 2012; Rosenberg 2002). MMP-1, for example, has

defined roles in degrading triple helical collagen (Evanson et al. 1967; Visse and Nagase 2003) and interactions with neurons and their receptors have emerged recently (Allen et al. 2016; Boire et al. 2005; Conant et al. 2002; Conant et al. 2004; Dumin et al. 2001; Vos et al. 2000). However, despite evidence that MMP-1 is involved in tissue degradation and neuronal signaling cascades, whether MMP-1 has a *mechanistic* role in nociceptive transmission from innervated peripheral joint tissues, or what functional roles of MMP-1 may be involved, has not been defined.

Therefore, the goal of this thesis was to define the biomechanical and biochemical actions of MMP-1 in the nociceptive transmission that causes pain with joint diseases. To accomplish this goal, the studies in this thesis establish the clinical relevance of MMP-1 in association with pain symptoms, define possible stimuli that may lead to increased levels of MMP-1 in capsular ligament tissue, and quantify the behavioral, biomechanical, and physiological consequences of excess MMP-1 in the joint space (Figure 9.1). The major findings are summarized in this chapter and discussed in the context of the broader literature related to chronic joint pain (Section 9.2). Broadly, the integrated findings across studies support the hypothesis that MMP-1 mediates collagen-neuron interactions in the capsular ligament by changing the biomechanical environment of the ligament and by acting as a biochemical mediator of MMP-9. MMP-1 was also hypothesized to mediate fibroblast-neuron interactions in the capsular ligament in the context of tissue loading. Although outcomes indirectly support this claim, findings more strongly support that the fibroblast-like synoviocytes (FLS) themselves found in capsular ligaments mediate the extent of load-induced MMP-1 in the ligament; as such, any consequences of MMP-1 on

peripheral neurons depend on FLS functionality. This chapter also discusses the limitations across the collection of studies presented here and elaborates on areas for future work that would build upon these current findings (Section 9.3).

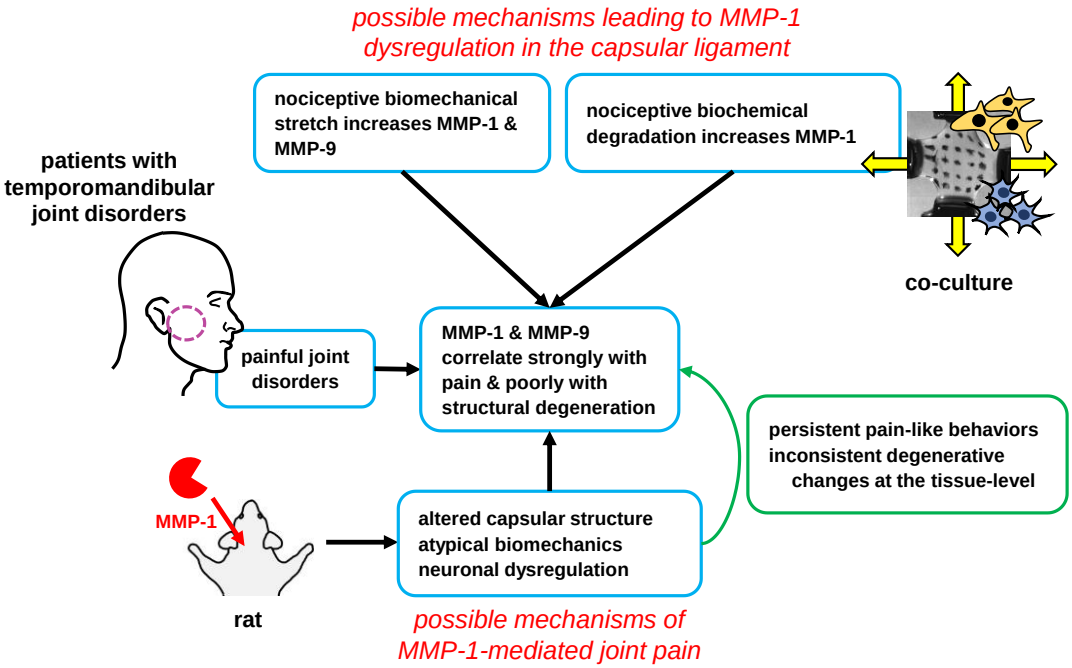

Figure 9.1. Integration of findings across studies. Characterization of MMPs in innervated capsular tissue from patients with painful temporomandibular joint disorders implicate MMP-1 and MMP-9 as positive correlates with pain symptoms. Studies in the co-culture collagen gel model of the capsular ligament reveal that biomechanical stretch and biochemical degradation are both mechanisms that increase MMP-1 expression in parallel with increased expression of the nociceptive neurotransmitter substance P. Studies that introduce exogenous intra-articular MMP-1 in the rat demonstrate that MMP-1 is sufficient alone to induce pain-like behaviors without degenerated joint structure that is reminiscent of findings in the patient population. Studies in the rat further define the implications of pathologically increased levels of MMP-1 on the structure and biomechanical function of the capsular ligament, as well as on neuronal dysfunction.

9.2. Summary & Synthesis of Major Findings

Intra-articular purified bacterial collagenase and MMP-1 both induce immediate and sustained behavioral sensitivity and increases in the neurotransmitter substance P in

peripheral neurons and the spinal dorsal horn (Chapters 4 & 7) (Ita et al. 2020b); together, those findings suggest that the collagenolytic function of MMP-1 *alone* is sufficient to cause pain from the peripheral synovial facet joint. This reasoning is supported by the fact that the *only* theoretical function of purified bacterial collagenase in the capsular ligament is to act on collagen molecules, directly influencing the Type I collagen network of the capsular ligament (Fields 2013). Despite that assumed role of collagenase in the joint space, there is no obvious effect on the tissue-level structure of either the cartilage or the capsular ligament, for either intra-articular bacterial collagenase (Chapter 4) or MMP-1 (Chapter 7). Although the lack of overt structural changes in joint tissues might initially lend more weight to mechanisms not related to the ECM components as being important in pain signaling, the detectable alterations in the collagen fiber kinematics and biomechanical responses of ligaments with MMP-1 treatment suggest that, indeed, collagen structure is altered on a scale that is undetectable by histological assays (Chapter 7).

Those findings suggest that the elevated MMP-1 in the joints of patients after traumatic injury or with age-related degeneration may also function in the joint space to initiate and/or mediate pain (Chapter 3) (Cohen et al. 2007; Haller et al. 2015; Ita et al. 2020a; Kim et al. 2015; Konttinen et al. 1999; Lattermann et al. 2017; Loeser et al. 2012). In fact, MMP-1 correlates with clinical pain symptoms (Chapter 3) and neuronal levels of substance P expression in response to stretch and degradation (Chapters 5 & 6), further implicating MMP-1 in nociception on a clinical and molecular level.

Placing the findings of this thesis in the context of previous studies begins to suggest mechanisms by which MMP-1 may be involved in the transmission of pain from

the capsular ligament due to noxious stretch and/or pathological collagen degradation (Figures 9.2-9.5). Within minutes of a stretch in the supraphysiologic regime, MMP-1 and MMP-9 expression increases in regions localized to both FLS and peripheral neurons (Figures 6.4 & 6.6) (Ita and Winkelstein 2019c) that is likely due to rapid cellular re-localization of MMPs via endocytosis, exocytosis, or cell rupture (Figure 9.3) (Craig et al. 2015; Murphy 2017; Visse and Nagase 2003). Increased MMP-1 in the presence of neurons can co-localize with $\alpha_2\beta_1$-integrin in its pro- and active forms (Conant et al. 2004; Dumin et al. 2001). The trimeric complex formed by $\alpha_2\beta_1$-integrin, pro-MMP-1, and type I collagen spatially confines proteolysis to promote migratory mechanisms in keratinocytes (Figures 9.2 & 9.3) (Dumin et al. 2001).

The formation of this trimeric complex on peripheral neurons could initiative nociceptive-related cascades directly via integrin interactions or indirectly via collagen

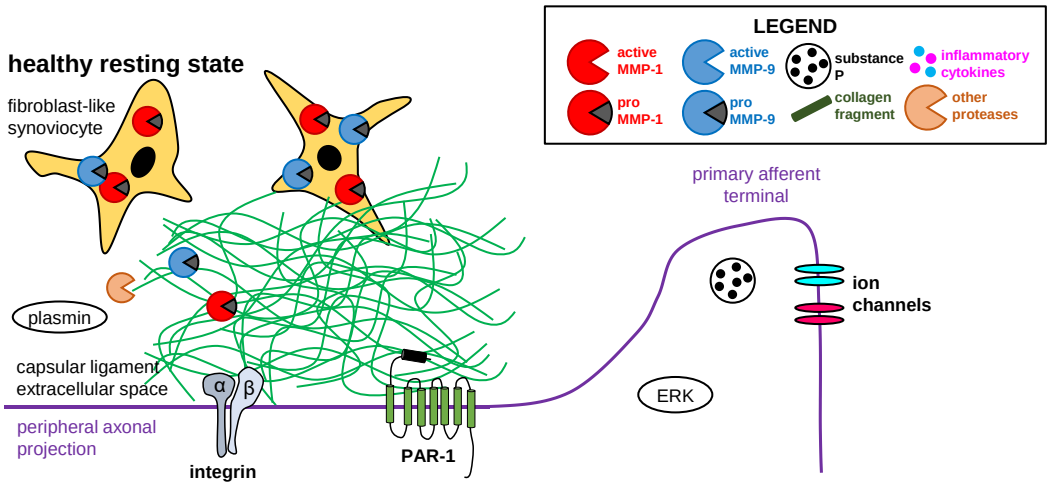

Figure 9.2. Schematic showing possible partial mechanisms for MMP-1 protein regulation in the capsular ligament during the resting state. A peripheral axonal terminal is depicted in a network of collagen fibers (green fibers) and fibroblast-like synoviocytes (not to scale). In healthy states, levels of active MMP-1 are very low. In response to stimuli of the local environment, plasmin and/or other proteases can activate pro-MMP-1 and trigger signaling and/or catabolic cascades.

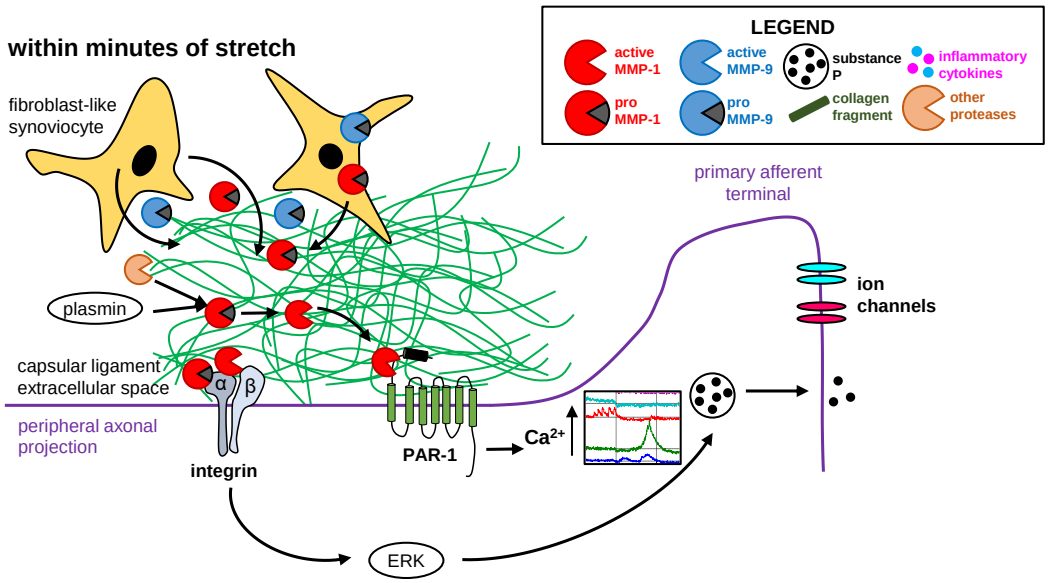

Figure 9.3. Schematic showing possible partial mechanisms for MMP-1 protein regulation in the capsular ligament immediately after a biomechanical stretch. Severe capsular stretch increases MMP-1 protein expression that may be regulated by fibroblast-like synoviocytes and act on neuronal surface receptors to transmit nociceptive signals. Plasmin and/or other proteases such as MMP-3 activate pro-MMP-1 in the extracellular space.

catabolism (Figure 9.3). For example, localization of pro-MMP-1 to $\alpha_2\beta_1$-integrin receptors on peripheral neurons may function to directly trigger intracellular integrin-dependent cascades, such as activation of the ERK pathway (Campos et al. 2004). Furthermore, MMP-1 proteolysis localized at the binding sites of collagen with peripheral axon terminals, like in keratinocytes (Dumin et al. 2001), could *indirectly* disrupt neuronal adhesion sites with collagen by first catabolizing the collagen molecules focal to neuronal receptors. Integrin-collagen binding sites have been directly implicated in strain-induced increases in substance P in a DRG-collagen gel model (Zhang et al. 2017); so, MMP-1 interaction with integrin could lead to nociceptive transmission. Moreover, inhibiting the α_2-integrin blocks the intracellular cascades initiated by the integrin-MMP-1-collagen complex, but inhibiting MMPs with an hydroxamate-based inhibitor does not (Conant et

al. 2004). That finding suggests that integrin-MMP-1-collagen mechanisms depend on the availability of the α_2-integrin binding site but not on collagenolytic activity of MMP-1. That finding further supports that the hydroxamate-based MMP inhibitor ilomastat used in the studies in Chapter 8 may not inhibit the functional ability of MMP-1 to bind to and/or act on cell surface receptors.

MMP-1 leads to increases in intracellular calcium within minutes of its introduction into the extracellular space via cleavage of the protease-activated receptor-1 (PAR-1) (Allen et al. 2016; Conant et al. 2002). Since PAR-1 is expressed on nociceptive neurons (Vellani et al. 2010), increased MMP-1 in the capsular ligament (Figures 6.4 & 6.6) may cleave PAR-1 on afferent fibers and increase intracellular calcium concentrations in peripheral neurons (Figure 9.3). This mechanism could lead to increased neuronal signaling and contribute to peripheral sensitization (Basbaum et al. 2009); indeed, PAR-1 activation by MMP-1 could explain the finding observed that exogenous MMP-1 exposure to DRG cultures increases their calcium firing (Figure 6.7) (Ita et al. 2018a). Notably, MMP-1's interaction with PAR-1 has only been demonstrated with the active form of the enzyme (Allen et al. 2016; Conant et al. 2002), suggesting that inhibiting the Zn^{2+} active site of MMP-1, like with ilomastat, may intervene in PAR-1 interactions. PAR-1 is also expressed on dorsal horn neurons in the spinal cord and is required for the development of neuropathic pain from a nerve root compression injury (Smith and Winkelstein 2017), so any MMP-1 that is transported on axonal terminals to spinal synapses may also have similar consequences on PAR-1 receptors on dorsal horn neurons.

At 24 hours after a noxious stretch, the gene and protein expression levels of MMP-1 and MMP-9 may increase from transcriptional and/or post-translational regulation of MMPs (Bartok and Firestein 2010; Murphy and Nagase 2009; Petersen et al. 2012; Yang et al. 2005). Although an increase in MMP-1 protein could amplify any of MMP-1's interactions with cell surface receptors on afferent fibers as described above (Figure 9.4), stretch in the painful sub-failure regime does not appear to increase MMP-1 or MMP-9 on the cell surface of peripheral neurons when FLS are present in the microenvironment (Figures 8.3 & 8.4). Therefore, it is likely that mechanisms other than those between MMP-1 and neuronal receptors may dominate nociceptive transmission 24 hours after capsular stretch. For example, active MMP-1 activates the zymogen form of pro-MMP-9 into active MMP-9 (Visse and Nagase 2003), and even if MMP-1 is not elevated on peripheral neurons (Figure 8.3), its extracellular activity may activate any latent MMP-9 within the collagen

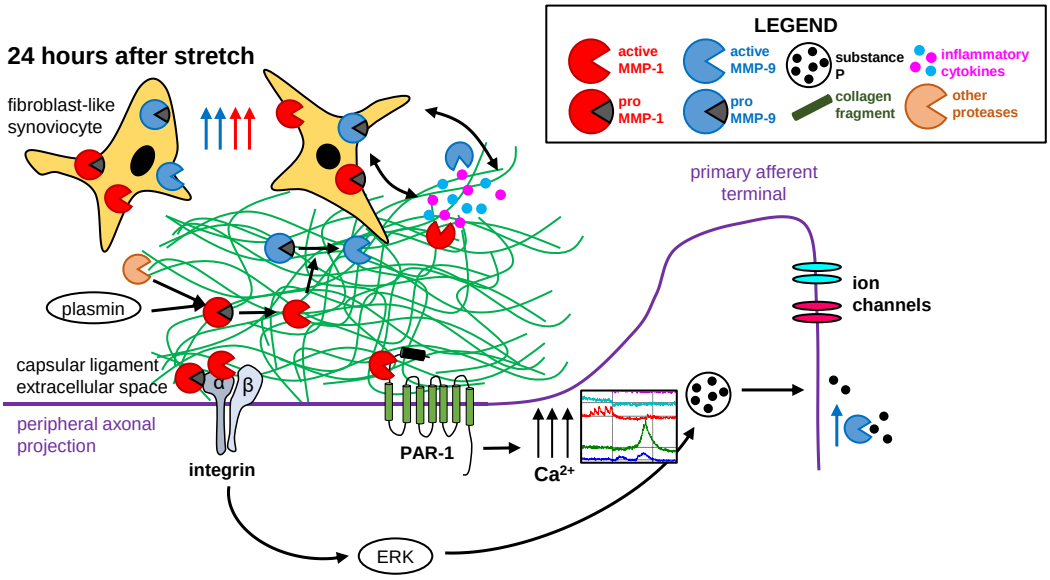

Figure 9.4. Schematic showing possible partial mechanisms for MMP-1 protein regulation in the capsular ligament 24 hours after a biomechanical stretch. One day after a painful stretch, MMP-1 may regulate pain transmission via MMP-9 and its downstream effects on substance P and/or via feedback mechanisms with inflammatory cytokines.

network surrounding the resident cells (Figure 9.4). This notion is supported by the positive correlations between active MMP-1 and active MMP-9 in innervated soft tissues from painful joint disorders (Figure 3.3) and after a sub-failure stretch in the DRG-FLS co-culture model (Figure 8.13). Moreover, direct stimulation with active MMP-1 increases MMP-9 expression in DRG cultures (Figure 6.8), an effect that corroborates previous findings in cortical neurons (Conant et al. 2002). Elevated active MMP-9 has many implications for pain signaling, including downstream interactions with substance P (Diekmann and Tschesche 1994) and subsequent propagation of excitatory signaling that contributes to nociceptive transmission from facet capsular stretch injury (Crosby et al. 2014).

If transported centrally, MMP-9 can impair the integrity of the blood brain barrier (BBB) and/or blood spinal cord barrier (BSCB) by degrading matrix components of the basement membrane and inducing abnormal vascular permeability (Lee et al. 2014; Noble et al. 2002; Rosenberg 2002). Increased permeability of the BSCB allows for the extravasation of serum molecules into the spinal cord, including leakage of the circulating cytokines that promote inflammation into the central nervous system (Ren and Dubner 2008). Cytokines can facilitate excitatory glutamate signaling by activating kinases that phosphorylate ion channels, and separately induce aberrant signaling between spinal neurons and glia (Ren and Dubner 2008); both of those mechanisms can amplify neuronal outputs when activated and can lead to central sensitization and persistent pain (Ji et al. 2018; Latremoliere and Woolf 2009). Moreover, even a *transient* breakdown of the BSCB is sufficient to induce behavioral sensitivity via cytokine trafficking into the spinal cord

(Smith et al. 2016). As such, even a transient increase in MMP-9 in peripheral DRGs may induce neuroinflammatory cascades and sensitize spinal neurons if that MMP-9 is transported to the central terminals of the afferent fibers. Indeed, MMP-9 may play a role in the central sensitization that is evident with joint pain from stretch injury (Crosby et al. 2013; Crosby et al. 2014; Crosby et al. 2015; Van Oosterwijck et al. 2013) and with non-traumatic degenerative disorders (Lluch Girbés et al. 2016; Perrot 2015). Together, the finding that MMP-9 is detectable in the innervated soft tissue from TMJ patients (Figures 3.2 & 3.3), and the fact that it is correlated with patient-reported pain (Figure 3.4), further support this notion.

MMP-1 and MMP-9 in the capsular space may also regulate, or be regulated by, pro-inflammatory cytokines (Bartok and Firestein 2010; Rosenberg 2002; Schonbeck et al. 1998; Visse and Nagase 2003). Neuronal injury promotes the release of numerous cytokines that may interact directly with nociceptors and/or increase cellular production of algesic agents (Basbaum et al. 2009); although microglia are the primary producers of cytokines in the nervous system (Basbaum et al. 2009), fibroblast-like synoviocytes have a key role in producing inflammatory cytokines that perpetuate inflammation in the synovial membrane tissues (Bartok and Firestein 2010). Indeed, inflammatory cytokines are regulated in the spinal cord by painful stretch after seven days (Lee et al. 2008), contribute to synovial inflammation within the first few days after intra-articular crude bacterial collagenase (Adães et al. 2014; Yeh et al. 2008), and are abundant in the synovial fluid of patients with painful degenerative joint disorders (Miller et al. 2014). Tumor necrosis factor α (TNFα) and interleukin 1β (IL-1β) are both substrates to MMP-1 and

MMP-9 (Schonbeck et al. 1998; Visse and Nagase 2003) and can convert those two cytokines into their biologically active forms, further promoting inflammatory damage and/or positive feedback loops that promote additional synthesis of MMPs by FLS cells (Figure 9.4).

Exposure of the capsular ligament to exogenous collagenolytic enzyme (purified bacterial collagenase) in the rat (Chapter 4) and in the DRG-FLS co-culture model (Chapter 5) leads to increased expression levels of the human collagenase MMP-1 localized to peripheral neurons. Because MMP-1 has no known direct interactions with purified bacterial collagenase, it is most likely that MMP-1 increases as a result of collagen molecule catabolism in the peripheral joint tissues (Figure 9.5). Homeostatic and pathological remodeling of the extracellular matrix regulates the production and secretion of MMPs by fibroblasts (Bartok and Firestein 2010; Camelliti et al. 2005; Hsieh et al. 2000;

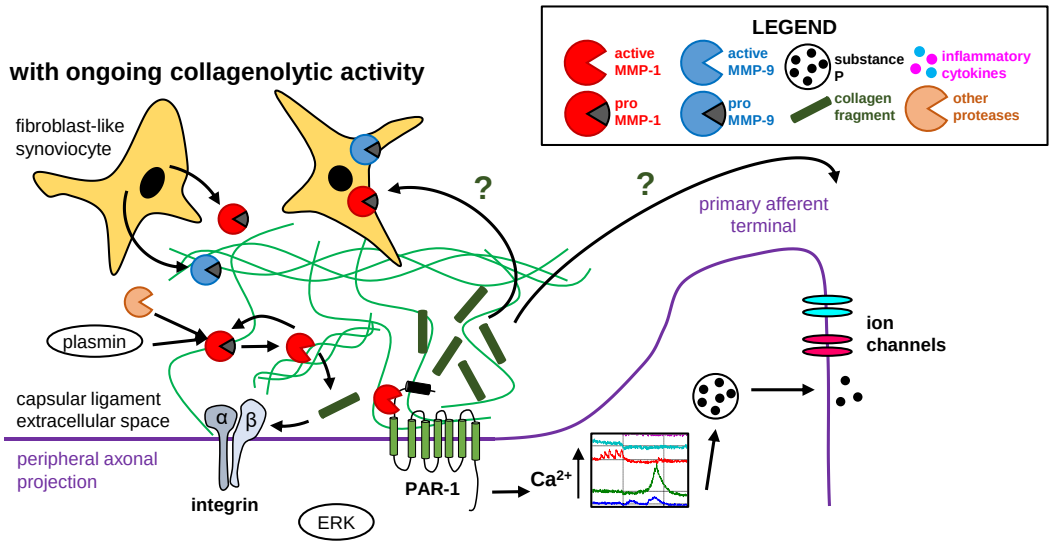

Figure 9.5. Schematic showing possible partial mechanisms for MMP-1 protein regulation in the capsular ligament in the presence of biochemical degradation of the collagen fibers. Collagenolytic activity in the capsular ligament, even absent a macroscale biomechanical stimulus, increases MMP-1 that may contribute to neuronal dysregulation via collagen degradation fragments.

Kim et al. 2002; Provenzano and Vanderby 2006; Wang et al. 2007), so collagen breakdown by bacterial collagenase presumably also leads to increases in MMP-1 production by fibroblast-like synoviocytes.

Although the mechanism by which bacterial collagenase increases MMP-1 expression is not completely clear, the resulting elevation in MMP-1 protein may act in the peripheral space by any one of the mechanisms described for stretch injury (Figures 9.3 & 9.4). Furthermore, it is possible that collagen catabolism results in small collagen fragments that may be involved in cellular signaling (Figure 9.5). Upon the initial cleavage of collagen molecules, human collagenases produce one-quarter (~100-116kDa) and three-quarter (~23-38kDa) collagen fragments (Amar et al. 2017; Fields 2013), and those collagen fragments are often subsequently cleaved in vivo to produce even smaller fragments (Otterness et al. 2000). Bacterial collagenases produce 35kDa and 62kDa collagen fragments. So, although native interstitial collagenases initially produce larger collagen fragments than bacterial ones, native post-processing likely produces collagen fragments that are similar in size to those produced by bacterial collagenases.

Whether collagen fragments interact directly with neurons is not known, although prior work indicates that collagen fragment-to-neuron interactions are possible (Figure 9.5) (Siebert et al. 2010; Zhang et al. 2017). Studies have measured collagen fragments in serum and synovial fluid *coincident* with evidence of nociceptive responses, including elevated substance P (Gou et al. 2019), and more severe disease progression in patients with painful degeneration (Arendt-Nielsen et al. 2014; Siebuhr et al. 2014). Small collagen fragments ranging between 2.7-15.6kDa bind directly to the α2A-domain of integrin, depending on if

they are single or triple-stranded (Siebert et al. 2010). Since peripheral neurons express this receptor (Zhang et al. 2017), it is possible that small collagen fragments may also bind to neuronal receptors, or indirectly influence neuronal signaling through their regulation of integrin (Figure 9.5). In fact, the most specific collagen fragment to measure collagen breakdown in the capsular ligament is C01-764, also known as C1M, and has a very small size of 10 amino acids and 0.93kDa (Leeming et al. 2011). C1M is a Type I collagen fragment that is specific for connective tissue and produced natively by MMPs (Leeming et al. 2011). It is possible that C1M interacts with neuronal integrins (Siebert et al. 2010) and is involved in integrin-mediated nociception.

The MMP-1-dependent mechanisms described here are put forth as local interactions between peripheral neurons, fibroblast-like synoviocytes, and collagen molecules that provide possible explanations of how biomechanical and/or biochemical stimuli, in the form of loading on, or degradation of, collagen molecules can trigger nociceptive signaling. Yet, the proposed mechanisms have implications for capsular ligaments where MMP-1 protein is detected (Cohen et al. 2007; Haller et al. 2015; Ita et al. 2020a; Kim et al. 2015; Konttinen et al. 1999; Lattermann et al. 2017; Loeser et al. 2012), regardless of the mechanism underlying its increase. For example, exogenous MMP-1 in the capsular ligament may initiate pain by the mechanisms posited to occur after stretch (Figures 7.3 & 9.2-9.5), even though a supraphysiologic stretch is not involved in the injection of exogenous MMP-1. MMP-1 binds to neuronal surface receptors (Allen et al. 2016), increases expression of active MMP-9 (Figure 6.8) (Conant et al. 2002; Vos et al. 2000), and increases calcium signaling in neurons (Figure 6.7) (Allen et al. 2016) within

minutes to hours. Because of this, it is likely that each or all of these interactions are at play in the initiation of pain at one day after MMP-1 injection (Figure 7.3). Initial degradation at the site of MMP-1 localization (Figure 9.5) may trigger pathological ECM remodeling by FLS and/or synthesis of MMPs, including more MMP-1 and/or MMP-9 (Bartok and Firestein 2010; Freedman et al. 2015b; Petersen et al. 2012). Pathological ECM remodeling likely contributes to the atypical biomechanical responses of ligaments at 28 days after their treatment with MMP-1 (Figures 7.6-7.8); as such, abnormal biomechanics may have more of a prominent role in maintaining pain at later times than in initiating pain early. Collectively, these findings support the assertion that increased MMP-1 in the joint space, over time, may predispose the collagen network to altered biomechanics that *may* alter the threshold for mechanically evoked pain.

The findings presented in this thesis establish MMP-1 as a biologic mediator in the nociceptive, inflammatory, and neuropathic cascades known to play a role in pain related to degenerative joint diseases (Fu et al. 2018; Gellhorn et al. 2013; Malfait et al. 2013; Zhang et al. 2013). These studies also implicate MMP-1-mediated mechanisms in the understudied painful and degenerative conditions of the spinal facet and temporomandibular joints (relative to the knee and hip) (Gellhorn et al. 2013; Zhang et al. 2013). OA-pain presents with several phenotypes defined by symptom frequency and severity, the extent and progression of joint destruction, and co-morbidities that vary temporally with disease progression (Pan and Jones 2018). Furthermore, different pain phenotypes are almost certainly mediated by the relative extents of contributions of inflammation, degeneration, and neural injury since patients with different phenotypes

respond differently to analgesic therapeutics, like NSAIDs and opioids, which target inflammatory and neuropathic pathways, differentially (Fu et al. 2018). The many animal models used to study osteoarthritis of joints mirror the varied pain phenotypes and have begun to define the molecular cascades that drive the signs and symptoms of OA (Hong et al. 2020; Malfait et al. 2013). For example, intra-articular chemical injections of monosodium iodoacetate induces rapid joint degeneration and immediate mechanical allodynia in rats and mice that is mediated by pro-inflammatory cytokines and chemokines that flood joint tissues within days and diminish after two weeks when neuropathic mechanisms appear to dominate (Hong et al. 2020; Kim et al. 2011; Rahman and Dickenson 2015). In contrast, surgical destabilization models, such as meniscal destabilization and ligament transection, show time-dependent cartilage lesions that take two to 12 weeks to develop, with pain symptoms not being consistently evident until after 12 weeks, mirroring a more progressive onset of OA-pain than the chemically induced OA (Inglis et al. 2008; Miotla Zarebska et al. 2017; Syx et al. 2020). In destabilization models, the onset of pain is paralleled by the sensitization of DRG neurons (Miller et al. 2020; Obeidat et al. 2019), suggesting that neuropathic mechanisms occur coincident with the onset of cartilage lesions.

The schema for MMP-1 that is proposed based on the findings in this thesis does align with the clinical presentation of degenerative joint pain whereby pain is experienced during normal activities and evidence of structural degeneration is subtle or absent (Hunter et al. 2013; Kraus et al. 2015; Pan and Jones 2018). As such, intervening in the MMP-1-mediated pathways defined in this thesis - local collagen degradation and/or MMP-9

activation - may be particularly relevant for patients with that clinical presentation of OA pain. Furthermore, although it is unknown if the microscale evidence of biomechanical changes that are observed after intra-articular MMP-1 injection (Figures 7.6-7.8) leads to more evident cartilage lesions at later times after 28 days, as occurs with destabilization OA models (Hong et al. 2020), the upregulation of substance P both peripherally and centrally at 28 days after intra-articular injection in the rodent (Figures 7.9 & 7.10) suggests that neuropathic pain mechanisms contribute to the maintenance of pain.

9.3. Limitations & Future Work

Together, the studies in this thesis demonstrate a role for MMP-1 in nociceptive signaling from the capsular ligament of joints. The in vitro studies presented here show that the co-localization of MMP-1 to peripheral neurons, as well the kinematic behavior of collagen fibers in response to loading, both depend on the presence of fibroblast-like synoviocytes. Yet, even the DRG-FLS co-culture model, which is simpler than the in vivo milieu, does not fully recapitulate the heterogenous in vivo cellular environment nor capture how cell-cell and cell-matrix interactions in the co-culture translate to a whole organism. The in vivo and clinical studies that were presented also have limitations and considerations that must be considered in order to contextualize their outcomes within the broader literature about pain mechanisms in degenerative joint diseases. This section highlights important limitations of the studies utilizing the DRG-FLS co-culture model and the intra-articular injections in vivo, and identifies additional studies that would both

expand the utility for clinically relevant translation and also further clarify the mechanistic role of MMP-1 in nociceptive signaling.

Including fibroblast-like synoviocytes in the co-culture model enabled defining the relative effects of FLS on neuronal signaling and collagen reorganization under load (Chapters 5 & 6). Yet, how FLS interact locally with their surrounding collagen network remains undefined in this system. For example, failure stretch of the co-culture collagen gels in the studies in Chapter 6 elicits concentration-dependent increases in collagen fiber reorganization under load (Figure 6.3). But, the greatest amount of load-induced protein expression in DRG neurons does *not* correspond to the greatest extent of fiber reorganization in the fiducial-marked elements where those same DRG neurons reside (Figure 6.4) (Ita and Winkelstein 2019c). The lack of association between the extent of collagen network reorganization and the greatest neuronal protein expression (Figure 6.4) contradicts prior results observed in neuron-collagen gels absent any fibroblasts in which the greatest extent of fiber alignment under sub-failure uniaxial tension corresponds to the largest increase in neuronal expression of pERK (Zhang et al. 2016). The disconnect between load-induced network reorganization and protein expression observed here (Figures 6.3 & 6.4) may be due to the concentration-dependent restructuring of the collagen network even *before* it undergoes any loading (Figure 9.6A) (Dallon and Ehrlich 2008; Grinnell and Petroll 2010; Kural and Billiar 2013). For example, above a critical density threshold, fibroblasts compact their surrounding matrix via a tractional-force locomotion mechanism that results in fibers that are aligned circumferentially around the periphery of free-floating gels (Dallon and Ehrlich 2008; Grinnell and Petroll 2010; Kural and Billiar

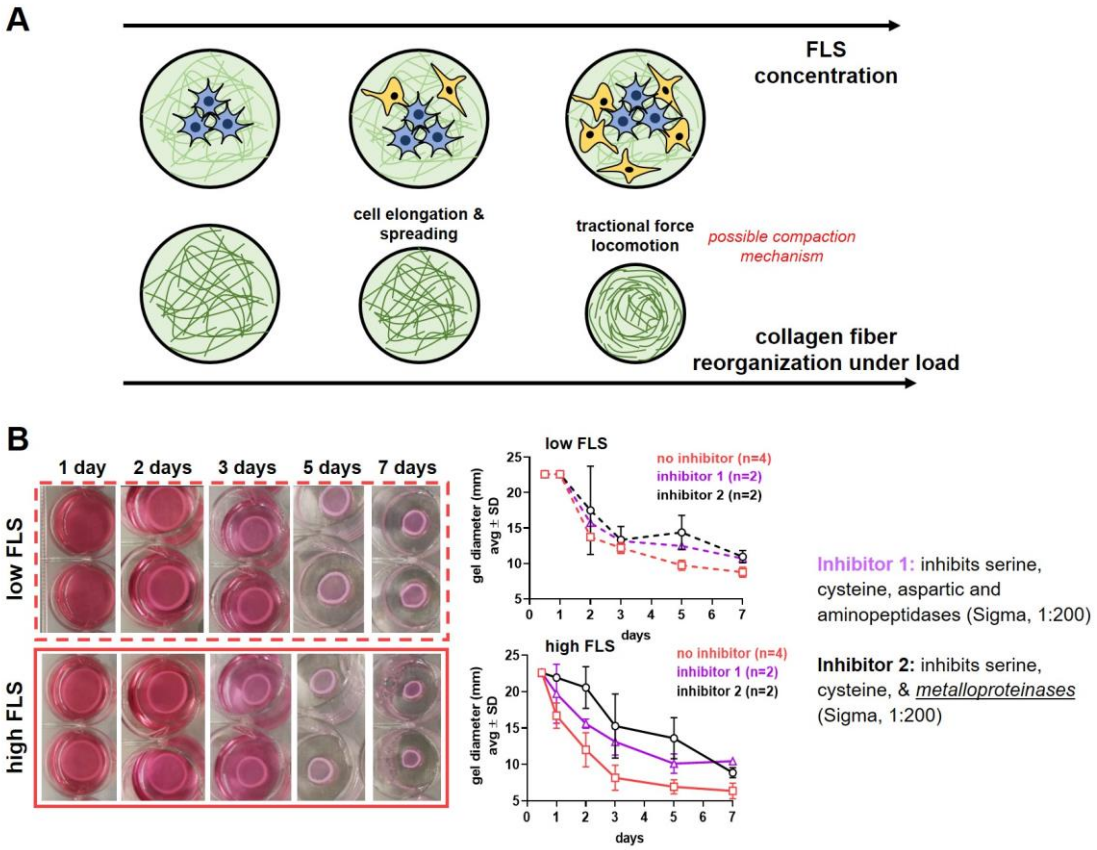

Figure 9.6. Concentration-dependent effects of fibroblast-like synoviocytes (FLS) on collagen fiber microstructure, gel compaction, and extracellular matrix remodeling. **(A)** Higher concentrations of FLS in the collagen gel can produce greater microstructural reorganization of the collagen matrix under load. Differential collagen fiber kinematics in the gel center following a stretch to failure may be due to low and high FLS organizing their matrix via different mechanisms; low FLS may compact the network and leave it isotropic in orientation and high FLS may align fibers circumferentially. **(B)** Photographs of free-floating FLS-seeded collagen gels with low ($5x10^4$ cells/mL) or high ($1x10^5$ cells/mL) FLS concentration show the compaction of gels induced by the FLS over seven days in culture. A pilot study using two different broad-spectrum protease inhibitors (1:200) in culture media suggests compaction is attenuated with blocking protease activity.

2013); below that density threshold, fibroblasts compact their surrounding matrix via an elongation-and-spreading mechanism that has no effect on the original fiber reorganization (Dallon and Ehrlich 2008; Grinnell and Petroll 2010; Kural and Billiar 2013). Although the concentration threshold for the transition from an elongation-and-spreading mechanism to a tractional-force locomotion mechanism is not defined for the FLS cell type,

it is possible that the threshold lies between the low (target density of $5x10^4$ cells/mL) and high (target density of $1x10^5$ cells/mL) concentrations used in the studies in this thesis, and that the low FLS- and high FLS-seeded gels reorganize their surrounding networks differentially.

Despite the proposition that low and high densities of FLS may reorganize their local collagen network differently, the in vitro stretch-to-failure studies in Chapter 6 did not detect differences in collagen microstructure before loading with the polarized light techniques (Table 6.1), suggesting that the low or high densities of FLS do *not* reorganize their collagen network differentially during free-floating culture. However, the polarized light measurements in those experiments were acquired at the center of the collagen gel (Figure 6.1) (Ita and Winkelstein 2019c). The tractional-force locomotion mechanism posited to occur in high concentration FLS-seeded gels produces circumferential collagen fiber alignment at the outer radius of the gel and *not* in the center of the gel (Figure 9.6A) (Dallon and Ehrlich 2008; Grinnell and Petroll 2010; Kural and Billiar 2013). As such, the imaging approach used here may not have captured appropriate regional measures of the collagen microstructure in the FLS-seeded gels even if compaction was occurring via differential concentration-dependent mechanisms. Imaging gels around the edges and/or taking high-resolution confocal tile scans would help determine whether FLS align collagen fibers circumferentially. Further, techniques like scanning electron microscopy could also be used to capture high resolution images of the collagen fibers within and throughout the network (Lake and Barocas 2011; Yang and Kaufman 2009). Indeed, free-floating fibroblast-populated collagen gels using NIH/3T3 immortalized fibroblasts from

mice have been to found to align collagen fibers circumferentially, with robust circumferential alignment at the outer edge of the gel and no realignment in the gel's center (Kural and Billiar 2013; Simon et al. 2012). If concentration-specific FLS compaction mechanisms were occurring in this DRG-FLS co-culture model, it may explain the graded fiber reorganization response that is observed at failure and appears to be concentration-dependent (Figure 6.3). If this conjecture is true it would imply that the force distribution during loading across embedded cells also varies with FLS concentration. Differential force distribution could affect the very weak and compliant embedded DRGs differently and could explain the disconnect between the regions of greatest stretch-induced fiber reorganization and those regions of greatest MMP-1 and substance P protein expression (Figure 6.4) (Ban et al. 2017; Vader et al. 2009; Zhang et al. 2018b).

The mechanisms by which FLS are hypothesized to restructure their collagen network during culture also produce compaction of the collagen gel (Figure 9.6). Although collagen gel compaction was consistently observed in gels with the high concentration of FLS (target density of $1x10^5$ cells/mL), it was not always observed in the gels with a low concentration of FLS (target density of $5x10^4$ cells/mL) (Ita and Winkelstein 2019c). Importantly, the absence of collagen gel compaction is not believed to be attributable to decreased cell viability (Figure 5.5), further supporting that there might be a density threshold above which FLS-collagen interactions switch from tractional-force locomotion to elongation-and-spreading (Dallon and Ehrlich 2008; Grinnell and Petroll 2010; Kural and Billiar 2013). Moreover, since MMP-1 inhibition has been reported in fibroblast- and smooth muscle-seeded collagen gels to decrease the radial compaction of free-floating

collagen gels over time (Daniels et al. 2003; Rogers et al. 2014), MMP-1 is likely involved in the mechanism of FLS-mediated collagen gel compaction. The finding that MMP-1 inhibition decreases fibroblast-mediated collagen gel compaction in free-floating collagen gels (Daniels et al. 2003; Rogers et al. 2014) suggests that MMP-1 is a likely mediator of the collagen microstructure absent any external biomechanical stimuli and supports the notion that MMP-1 regulates interactions between fibroblasts and collagen fibers in the local environment of the FLS cells.

Pilot studies using broad-spectrum protease inhibitors also suggest that proteases, in general, are involved in collagen gel compaction. Experiments used two broad spectrum protease inhibitor cocktails in the media of FLS-seeded collagen gels (a 1:200 daily dose) and tracked compaction over seven days in culture by quantifying the change in gel diameter (Figure 9.6B); one inhibitor cocktail (Inhibitor 1) had broad specificity to serine, cysteine, aspartic and aminopeptidases, and the other inhibitor cocktail (Inhibitor 2) had broad specificity to serine, cysteine, and metalloproteinases, including the MMPs (Figure 9.6B). Both broad-spectrum inhibitor cocktails attenuated collagen gel compaction over one week in culture (Figure 9.6B). Furthermore, protease inhibitors attenuated the magnitude of gel compaction in collagen gels made using both the low and high FLS concentrations (Figure 9.6B). Those pilot data suggest that FLS remodel the composition of their surrounding matrix and that FLS remodeling mechanisms depend on proteases. Therefore, the DRG-FLS co-culture collagen gel likely has a different matrix composition than a gel made only with DRGs. For example, FLS may secrete Type I and Type III collagen (Kim et al. 2002; Wang et al. 2007), resulting in different proportions of

constituent matrix components than in gels where FLS are absent. Indeed, there is evidence in the literature supporting that fibroblast-seeded gels have different compositions than collagen gels without fibroblasts (Bartok and Firestein 2010; Dallon and Ehrlich 2008; Grinnell and Petroll 2010; Kural and Billiar 2013; Petersen et al. 2012; Wang et al. 2007; Yang et al. 2005). An altered gel composition from the original Type I collagen formulation in which the co-cultures are cast (Figure 5.3) could also alter neuronal signaling, since the outgrowth and receptor expression of neurons varies with their matrix substrate (Cullen et al. 2007). Moreover, since matrix composition affects the local and global mechanical properties of collagen gels (Kural and Billiar 2013; Lake and Barocas 2011; Lake et al. 2011), FLS-mediated remodeling could explain why collagen gels with FLS exhibit higher forces than collagen gels without FLS in response to an equibiaxial sub-failure stretch (Figure 8.1). Consequently, since the compositional variation depends on the distribution and/or proliferation of FLS throughout the gel, any effect of altered composition on neuronal signaling would also exhibit regional variability.

The implications of FLS-dependent network restructuring, collagen gel compaction, and ECM remodeling on the function of peripheral neurons when they are cultured in the same microenvironment as FLS were not fully investigated in this thesis. However, ongoing studies are exploiting the ability of computational modeling to manipulate network parameters that are acquired experimentally in order to probe cell-cell and cell-matrix interactions (Figure 9.7). Those studies build off of a computational neuron-in-gel model (Zarei et al. 2017), and are further developed using parameters

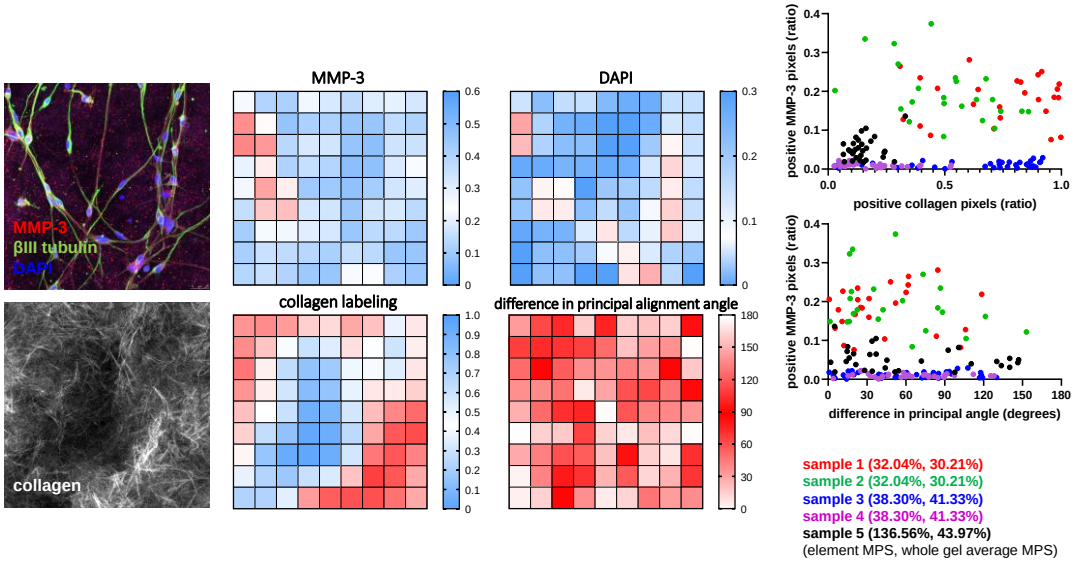

Figure 9.7. Collagen and MMP-3 protein expression data from co-culture collagen gel stretch experiments are integrated in computational studies to investigate relationships between the heterogenous properties of the collagen network and MMP expression. The top image on the left shows dorsal root ganglia axonal projections (green) with expression of the matrix metalloproteinase-3 (MMP-3) (red) and cell nuclei (blue). The bottom image shows the collagen fiber network in which the axons are embedded. Each of the axonal and collagen labeled images are divided into 9x9 higher resolution regions, from which MMP-3 expression, DAPI quantification, collagen labeling intensity, and axonal and/or fiber alignment data are extracted; the difference in primary alignment of axons from that of collagen fibers matched by region is computed as the difference in principal alignment angle. Scatter plots on the right show relationships from five such images between MMP-3 labeling and collagen density (top) and between MMP-3 labeling and the difference in alignment between axons and collagen fibers (bottom). Colored data points show regions from different images; the maximum principal strain (MPS) sustained by the axons and network varies across images from 32.04-136.56%. Ongoing studies are use computational models that replicate the range of collagen network parameters (collagen density and fiber organization) and the imposed strains to elucidate relationships between local collagen network heterogeneities and MMP-3 expression.

informed by collagen and MMP-3 protein expression after co-culture failure stretch (Figure 9.7) to simulate the stretch experiments presented in Chapter 6. Although these computational studies investigate MMP-3 for its role in regulating the activation of other MMPs, including MMP-1 and MMP-9 (Visse and Nagase 2003), and because it is upregulated with painful facet capsular stretch in vivo (Singh et al. 2017), findings will help inform about mechanistic relationships between the collagen network and the MMPs (-1 and -9) investigated in this thesis. More specifically, results from those experimentally-

informed simulations will provide additional insight into how FLS- and/or collagenase-induced changes to the collagen microstructure and density may alter collagen-neuron mechanotransduction responses.

The studies in this thesis could be expanded to define the cell source of MMP and the localization of MMPs to relevant cell types. Indeed, those effects would inform about cellular mechanotransduction in this system and would help guide design of studies probing, and even intervening in, cell signaling pathways. For example, if FLS secrete the majority of MMP-1 in this system, then silencing the translation of MMP-1 in FLS or blocking vesicular secretion of MMP-1 may be most effective in understanding the mechanistic role of MMP-1 in nociceptive signaling. In fabricating the co-culture model, FLS are seeded throughout the gel and DRGs are plated on a monolayer surface near the gel's center; as such, confocal imaging was focused to capture immunolabeling in regions with only DRG soma and/or axons or only FLS cells. Although DRGs and FLS cells can be easily distinguished to enable assessment by cell type under the microscope to acquire expression data by cell type, co-labeling for cell-specific proteins along with MMP-1 and/or MMP-9 would determine with which cell(s) MMPs localize (Figure 6.10). For DRG neurons, βIII tubulin is a robust protein and is often used to achieve this goal (Cullen et al. 2012; Ita et al. 2020b; Ita and Winkelstein 2019c; de Luca et al. 2015; Mehnert et al. 2014; Zhang et al. 2018a). The studies in Chapter 5 that co-localized MMP-1 to FLS used the cytoskeletal protein vimentin since it is a matrix protein expressed by FLS cells (Figure 5.16) (Varani et al. 2008). However, other non-fibroblast cells, like glial cells, also express vimentin and may remain in the culture due to the methods of DRG harvest and may also

therefore be present in the co-culture model (Pekny and Nilsson 2005). As such, localizing proteins of interest to vimentin does not necessarily imply that proteins co-localize to FLS cells. Utilizing a protein that is expressed exclusively by FLS cells, like CD90 (Figure 5.1) (Ahn et al. 2008; Bartok and Firestein 2010; Neidhart et al. 2003; Rosengren et al. 2007), would more specifically distinguish FLS-localized proteins from those localized to other vimentin-expressing cell types, like glial cells. Since there is evidence that fibroblasts produce and secrete MMP-1 during healthy states (Attia et al. 2014), in response to inflammatory stimuli (Bartok and Firestein 2010; Bottini and Firestein 2013), and in response to external loading (Petersen et al. 2012), it is anticipated that FLS cells are the primary cell *source* of MMP-1 in the studies in this thesis. Furthermore, since the findings in this thesis demonstrate that MMP-1 clearly *localizes to* peripheral neurons in vivo (Figure 4.9) and in vitro (Figures 5.8, 5.16, 6.4, & 6.6), it is expected that much of that MMP-1 in neuronal-rich regions is produced by FLS and localizes to peripheral neurons in response to noxious stimuli. Assays utilizing the co-localization of immunolabels to cell-specific proteins and MMPs would help test this hypothesis.

Indeed, the multicellular environment of the co-culture model contains more cell types than only peripheral DRG neurons and FLS, since DRG somas may contain Schwann cells, microglia, and resident macrophages (Melli and Höke 2009). This heterogenous cell population should be considered in the context of MMP synthesis and regulation under load and in degenerative states because cells other than the FLS and DRG neurons can also interact with MMPs (Kobayashi et al. 2008; Muir et al. 2002; Sbardella et al. 2012; Schurigt et al. 2008). Furthermore, although the FLS cultures were intentionally optimized

to contain over 95% purity for the FLS cell type (Figure 5.1), with passages high enough (greater than 3 passages) to eliminate macrophages from the culture, fluorescence-activated cell sorting (FACS) could be used to characterize the population of cells harvested directly from the capsular ligament (Ahn et al. 2008). Using FACS also with cells derived from the capsular ligament of human patients, like in the specimens characterized from patients with painful temporomandibular joint disorders in Chapter 3, would define the population of cells expressed in capsular ligaments to which innervating fibers of the ligament are exposed during degenerative and painful joint states.

Collectively, characterizing the population of primary-harvested cells, and their secreted factors, would provide information about the cellular environment in pathologic joint tissues, and offer insight into how to better recapitulate that pathogenesis in the DRG-FLS co-culture model. Furthermore, primary-harvested cells from the capsular ligament of human patients with joint diseases could be harnessed in studies with DRG cultures in vitro to investigate how FLS from a pathogenic and/or degenerated ligament influence neuronal regulation and/or dysregulation in vitro. For example, FLS cells derived from patients with inflammatory rheumatoid arthritis have unique phenotypes and secrete disease-specific inflammatory and immune regulators (Ahn et al. 2008; Bartok and Firestein 2010; Bottini and Firestein 2013). FLS derived from capsules of joints with inflammation or degenerative pathology, and conditioned-media from those FLS cultures, increase spontaneous action potential firing and enhance the function of transient receptor potential vanilloid 1 (TRPV1) ion channels in DRG cultures (Chakrabarti et al. 2020). As such, studies integrating patient-derived FLS cells in co-cultures would recapitulate the in vivo

pathological multicellular environment and enable measuring how peripheral neurons respond to that environment. It is expected that those experiments would define a distinct population of MMP proteases (including MMP-1, -9, and -3) and inflammatory cytokines (including TNFα and IL-1β) secreted by cells from the capsular ligament of degenerated joints, and that action potential firing and neurotransmitter expression would increase in peripheral neurons in response to an exposure to those secreted proteases and cytokines.

The studies in Chapter 3 using human tissues separately quantify the pro- and active forms of MMPs (Figures 3.2 & 3.3) (Ita et al. 2020a); yet, MMP quantification in the other studies in this thesis do not distinguish between those pro- and active forms of MMP-1 and MMP-9. The inability to distinguish pro- and active MMPs in the in vivo and in vitro studies is due to technical limitations. The antibodies used in both rat tissue and in cells in those studies bind to amino acid sequences on both enzyme forms. This limitation hampers conclusions about the mechanistic roles of the latent and catabolically active forms of the proteases since only the total MMP expression (including both latent (pro-) and catabolically active enzyme states) can be measured. Since pro- and active forms of MMPs have different roles in mediating cell-cell and cell-matrix interactions (Sbardella et al. 2012; Visse and Nagase 2003), it is not possible to attribute changes in MMP expression to *specific* mechanistic pathways - for example, degrading ECM proteins or acting on cell-surface receptors. For example, the catabolic degradation of Type I collagen and cleavage of the PAR-1 cell-surface receptor can be performed exclusively by active MMP-1 (Boire et al. 2005; Conant et al. 2002); in contrast, both pro- and active MMP-1 can interact with integrin receptors (Conant et al. 2004; Dumin et al. 2001). For MMP-9, only the active

form of the enzyme is able to degrade basement membrane proteins required for breakdown of the BSCB (Visse and Nagase 2003). Furthermore, antibodies that lack the ability to distinguish between the pro- and active MMP forms are also used to assess the efficacy of MMP inhibition by the ilomastat inhibitor in the studies in Chapter 8; so while ilomastat-induced changes in *total* MMP were determined, the immunolabeling assays cannot conclude whether the *activity* of MMP-1 and/or MMP-9 is altered by ilomastat. Since ilomastat inhibits MMP activity by binding to the Zn^{2+} binding site of MMP-1 and MMP-9 (Galardy et al. 1994; Grobelny et al. 1992), it is expected that ilomastat decreases the amount of *active* enzyme forms and does not affect the amount of *pro*-enzymes.

Assaying MMPs using zymography Western Blot techniques and/or ELISA-based methods could be used in parallel with immunolabels to quantify the relative amounts of pro- and active MMPs, separately (Attia et al. 2014; Nascimento et al. 2013). For example, the ELISA-based assay used in the studies in Chapter 8 (Figure 8.5) quantifies active MMP-1 by quantifying the fluorescence signal excited upon active MMP-1 cleavage of a FRET substrate (Attia et al. 2014). If wells are included in that assay to both include APMA-activation steps (quantifies total MMP-1) in one set of samples and separate wells are included in that assay to *exclude* APMA-activation steps (quantifies only active MMP-1) in a second replicate set of the same samples, then the relative amount of pro-MMP-1 can be determined by subtracting the amount of active MMP-1 from the total MMP-1 (Attia et al. 2014). In the studies in this thesis that quantified MMP-1 in gels by ELISA after the sub-failure stretch (Figure 8.5), the APMA-activation step was always included due to low signal-to-noise ratios with the gel homogenate and media supernatant samples used in that

experiment. However, that same ELISA was successfully utilized in pilot studies to validate the activity of the human recombinant MMP-1 that was used in the intra-articular studies in the rat; because the results from that study demonstrated that the ELISA can unequivocally distinguish between latent pro-MMP-1 and active MMP-1, that approach has utility for future assays for higher-concentration samples. Further, optimizing a protocol for consistent and reliable quantification of MMP-1 by ELISA would be beneficial to assess gel-entrapped and secreted proteins. Complementing that approach with localizing MMPs to cell type by immunolabeling would provide a more complete understanding of where MMPs localize and how they are altered by stimuli in the cellular microenvironment. The immunolabeling studies in this thesis demonstrate that MMPs localize to neurons in response to stimuli; yet, additional quantification of MMPs in co-culture media would provide information about whether secreted MMPs are also altered in response to stimuli. Quantifying secreted MMPs would also help determine whether those secreted MMPs might be available for transport along axonal stalks and/or to innervated joint tissues other than the capsular ligament, such as the synovium or bone. Moreover, quantifying the regional localization of gel-entrapped MMPs would reveal if matrix sites undergo MMP-mediated remodeling and/or degradation. Areas with MMP-mediated alterations could have consequences on the bulk mechanics of the collagen gel and change microstructural collagen fiber kinematics under load. Indeed, such experiments would be useful for probing both the collagen gel of the DRG-FLS co-culture model or the capsular ligament tissue following intra-articular injection of collagenase.

The ilomastat inhibitor used in the gel studies in Chapter 8 does not selectively inhibit MMP-1 nor does it interfere with functions of MMP-1 that do not depend on the Zn^{2+} binding site (Galardy et al. 1994; Grobelny et al. 1992). Since ilomastat also inhibits MMP-9 at a higher affinity than MMP-1 (Galardy et al. 1994; Grobelny et al. 1992), ilomastat is not the optimal inhibition tool to use to evaluate and define mechanistic relationships between MMP-1 and MMP-9. One obstacle in developing an effective and specific MMP-1 inhibitor is the 53-63% homology between interstitial collagenase in the human and the rodent (Balbín et al. 2001). Although interstitial collagenases in the rodent exhibit structural features characteristic of human archetypal MMPs, those sequence differences from the human have hindered development of MMP-1 knockout mice and present difficulties in confidently testing MMP-1 inhibition in mouse and/or rat models (Löffek et al. 2011; Vandenbroucke and Libert 2014). However, studies utilizing siRNA silencing techniques in cell cultures could be exploited to target MMP-1 synthesis (Rogers et al. 2014). siRNA-induced post transcriptional silencing would suppress the translation of MMP-1 (Agrawal et al. 2003), selectively removing MMP-1 production by cells without the off-target effects on other MMPs that occurs with the ilomastat synthetic inhibitor. A beneficial study design could separately silence MMP-1 synthesis in FLS cultures and/or DRG cultures before their co-culture in order to fully define the role of cell-specific MMP-1 in nociceptive responses. Those studies would also be able to directly determine if the complete obliteration of MMP-1 affects the pro- and/or active levels of MMP-9. That proposed approach would answer the question of whether MMP-1 *is required* for the increase in substance P expression that is observed after stretch (Figures 6.4 & 8.2),

maintenance of neuronal firing with a degradative stimulus (Figure 5.15), and/or for the initiation and maintenance of mechanical hyperalgesia after intra-articular bacterial collagenase (Figure 4.5).

Collectively, the studies in this thesis begin to define a role for MMP-1 at different times following a biomechanical or biochemical stimulus, including immediately after a noxious stimulus in the studies utilizing the co-culture model (Chapter 6) (Ita and Winkelstein 2019c), weeks after exogenous intra-articular MMP-1 exposure in the rat facet joint (Chapter 7), and very late in disease progression with painful joint disorders in humans (Chapter 3) (Ita et al. 2020a). However, each study reports on findings from only one timepoint and provides limited information about the temporal regulation of MMPs. Examining MMP-9 in the DRG early after exogenous injection in the rat is needed because MMP-9 is required for the initiation of behavioral sensitivity (i.e. pain) from nerve root injury (Kawasaki et al. 2008). Since the increase in MMP-9 in the DRG is transient, returning to baseline values three days after the nerve injury (Kawasaki et al. 2008), it is likely that the assessment at day 28 after intra-articular MMP-1 (Figure 7.9) is too late to detect MMP-1-induced changes in MMP-9 expression in DRG neurons. As such, it is hypothesized that MMP-9 increases early, but transiently, after MMP-1 is introduced in the intra-articular space (Figures 9.3 & 9.4). Furthermore, since MMP-1 and MMP-9 are significantly correlated in the innervated soft tissue very late in disease progression (Figure 3.3) (Ita et al. 2020a), exogenous MMP-1 may actually increase MMP-9 in *peripheral tissues* early after injection; MMP-9 distribution from DRG neurons to peripheral tissues may, in fact, explain the later (day 28) decrease in MMP-9 in the DRG neurons after MMP-

1 treatment (Figure 7.9). If this transport of MMP-9 from DRG neurons to the periphery occurs, then MMP-9 may be available to sensitize afferent nerve terminals embedded within the capsular ligament (Jiang et al. 2017) or to interact with inflammatory cytokines in signaling pathways in the joint tissues (Muir et al. 2002; Visse and Nagase 2003). Indeed, clinical studies have shown that there is ongoing nociceptive input from the joint tissues even in late-stage chronic joint disease (Malfait and Schnitzer 2013), so elucidating either of these roles for MMP-9 in peripheral joint tissues would support targeting MMP-9 locally in the joint.

The studies in this thesis measure changes in the protein expression of substance P and phosphorylated ERK, and/or alterations in intracellular calcium levels as indicators of neuronal dysregulation that have a known role in pain mechanisms. However, those outcomes represent only a subset of mechanisms by which pain can be transmitted from the periphery and sensed in the brain. For example, substance P is expressed only in peptidergic nociceptors and not in nonpeptidergic nociceptors (Basbaum et al. 2009). Peptidergic and nonpeptidergic nociceptors terminate in distinct regions of the spinal cord (Basbaum et al. 2009) and engage different and independent ascending pathways to the brain (Braz et al. 2005). So, although the increases in neuronal substance P detected after intra-articular collagenase (Figures 4.7 & 4.8), intra-articular MMP-1 (Figures 7.9 & 7.10), and mechanical stretch in vitro (Figures 6.4 & 8.2) suggest that peptidergic circuits are involved in nociception in all of those studies, any pain processing occurring via nonpeptidergic circuitry is not captured. Probing neurotrophic factors that target nonpeptidergic nociceptors, such as glial-derived neurotrophic factor (GDNF), neurturin,

and artemin (Basbaum et al. 2009; Skaper 2012), would reveal if MMPs also engage nonpeptidergic nociceptive circuits along with the peptidergic circuits identified in this thesis. In addition, probing responses in the brain would inform about whether such circuits that are known to be modulated in painful chronic joint disorders (Sperry et al. 2020) also play a role in the development and/or maintenance of pain in the clinical and/or rat studies in this thesis. Indeed, since several MMPs, including MMP-1, MMP-9, and MMP-2, are implicated in pathologies of the nervous system that involve the brain (Rosenberg 2002; Sbardella et al. 2012), it is likely that any mechanistic role of MMPs in mediating the pain experience also extend to brain circuits.

Substance P is only one of the neurotransmitters released by peptidergic neurons in response to stimuli and/or neuronal injury (Basbaum et al. 2009; Zieglgänsberger 2019). Defining responses of other neurotransmitters involved in pain, like calcitonin-gene related peptide (CGRP), glutamate, and adenosine triphosphate (ATP), would further inform the breadth of interaction of MMPs with the full pain axis. Indeed, studies inducing OA via monosodium iodoacetate injection in the rat report an increase in CGRP in primary neurons innervating the injected knee (Fernihough et al. 2005; Hong et al. 2020). Further, CGRP is upregulated in the capsular ligament of the hip joint in patients with painful OA (Saxler et al. 2007). Together, these studies suggest that the neuropeptide CGRP also facilitates nociception from peripheral degenerated tissues.

The phosphorylation of ERK (pERK), a mitogen-activated protein kinase (MAPK), in the spinal cord has been shown to play a critical role in the development of central sensitization by regulating the activity of glutamate receptors and potassium channels (Ji

et al. 1999; Ji et al. 2009). As such, the increase in pERK in DRG neurons observed 21 days after injection of intra-articular bacterial collagenase (Figure 4.7) (Ita et al. 2020b) suggests that ERK at least partially facilitates nociceptive input from joint tissues to the DRG and may alter expression of receptors and/or ion channels of DRG neurons. However, pERK does *not* increase in the spinal cord at that same time (day 28) (Figure 4.8) (Ita et al. 2020b), suggesting that ERK signaling may not alter the central processing induced by bacterial collagenase injection in that study. However, it is possible that the other MAPKs, p38 and c-Jun N-terminal kinase (JNK), may contribute to nociceptive signaling peripherally and/or centrally, since in addition to ERK, both p38 and JNK are also modulated by nerve injury (Chen et al. 2016; Ji et al. 2002; Ji et al. 2009; Obata and Noguchi 2004). Indeed, inhibiting all three MAPK signaling pathways attenuates behavioral sensitivity from inflammatory stimuli and neuronal injury in animal models (Ji et al. 2009), so it is expected that p38 and JNK may also be upregulated after MMP-1 and bacterial collagenase injection in the rat facet joint (Chapters 4 & 7) (Ita et al. 2020b).

Studies in this thesis measure changes in intracellular calcium using the adeno-associated virus GCaMP6f (Figures 5.5 & 6.7) (Ita et al. 2018a; Ita et al. 2020b), and analyze GCaMP6f-regulated fluorescence with a technique that is optimized to detect action potentials (Patel et al. 2015; Schultz et al. 2009). Since the mechanisms of calcium influx from the extracellular space that result in GCaMP6f-regulated fluorescence in neurons are associated with the exocytosis of neurotransmitter-containing synaptic vesicles and the subsequent action potentials (Grienberger and Konnerth 2012), calcium imaging outcomes represent the extent to which neurons are excitable. Changes in neuronal

excitability *within* a population of neurons, and/or the recruitment of *new* excitable neurons, occur by several mechanisms with pain, including the sensitization of neurons peripherally and centrally (Basbaum et al. 2009; Latremoliere and Woolf 2009). As such, calcium imaging is a useful tool to determine whether neurons are sensitized to an extent that is applicable broadly to known pain mechanisms. Yet, calcium imaging cannot necessarily resolve the mechanism by which the neurons become or remain sensitized. Integrating immunolabeling with proteins specific to nociceptor type, cell surface receptors, and/or MMPs with live-cell calcium imaging could harness the broad utility of GCaMP6f-transduction to answer mechanism-specific questions. For example, one mechanism by which MMP-1 exposure increases MMP-9 expression and calcium signaling in DRG neurons (Figures 6.7 & 6.8) could be via cleavage of the PAR-1 receptor (Boire et al. 2005; Conant et al. 2002); if calcium imaging outcomes were matched by neuron with immunolabeling of PAR-1 and MMP-9, then that hypothesis could be directly tested. Furthermore, using analyses of neuronal synchronization, interspike interval computation, and stochastic point processes (Broussard et al. 2014; Tomar 2019) that expand on the spike detection and template-matching algorithms (Patel et al. 2015) could provide insight about how MMPs influence the connectivity and firing patterns across entire neural networks. Indeed, synchronization analyses have been employed to detect changes in functional connectivity between neurons using GCaMP6f data (Broussard et al. 2014; Patel et al. 2015), and so those techniques would enable expanding analyses from the individual neuron to the network scale.

Evidence across studies of FLS-DRG co-cultures (Chakrabarti et al. 2020), joint degeneration in vivo (Adães et al. 2017; Miotla Zarebska et al. 2017), and biomarker and imaging characterization of joint disease in human patients (Arendt-Nielsen et al. 2014; Siebuhr et al. 2014) all point to a prominent role of inflammation in degenerative joint pain. Furthermore, the regulation of MMPs and inflammatory cascades are tightly interconnected (Bartok and Firestein 2010; Murphy and Nagase 2009; Rosenberg 2002). As such, it is likely that inflammatory cascades play a role in nociceptive transmission from the capsular ligament in painful joint disorders. Indeed, there is evidence that inflammatory changes in the joints of patients with painful joint disorders, such as synovitis and effusion, correlate more strongly with reported pain than do structural changes like joint space narrowing and cartilage thinning (Emshoff et al. 2003; Hunter et al. 2013; Torres et al. 2006). As such, it is possible that the discordance between tissue-level evidence of degeneration and pain symptoms observed with intra-articular bacterial collagenase (Chapter 4) and with intra-articular MMP-1 (Chapter 7) may be explained by inflammatory changes in the joint (Wang et al. 2017). Remarks on whether there was evidence of inflammation were limited in the MRI reports scored in the clinical study in Chapter 3 (Table 3.1); yet, this does not preclude the possibility that synovitis and/or effusion may contribute to the pain reported by patients in that study (Table 3.1). Indeed, that notion could explain the lack of association between osseous damage scores and patient reported pain (Figure 3.5).

Although inflammatory cascades were not examined in the studies in this thesis, pilot studies in cells and in the rat collectively begin to suggest that collagenases induce an

immediate inflammatory response that may last for at least one week in the rat. For example, the astrocytic protein glial fibrillary acidic protein (GFAP) does not increase in the spinal cord at 28 days after intra-articular MMP-1 (Figure 9.8A), suggesting that at that timepoint, MMP-1 does not induce astrocyte infiltration or proliferation. However, other cells in the nervous system, such as microglia, also drive neuroinflammation in the peripheral and central nervous systems (Ji et al. 2018), so the fact that spinal GFAP is unchanged does not preclude the possibility that inflammation has a role in DRG neurons, within innervated joint tissues, or at earlier timepoints. Indeed, separate pilot data support that seven days after administration of intra-articular purified bacterial collagenase, mRNA

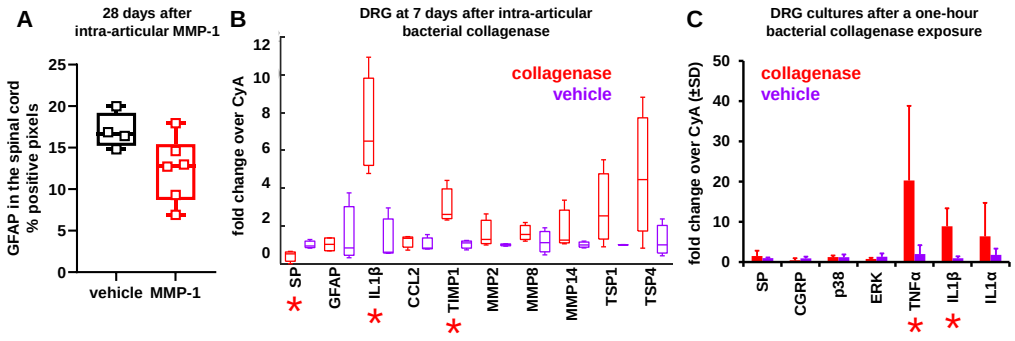

Figure 9.8. Studies investigating a possible role for inflammation with intra-articular MMP-1 in the spinal cord **(A)** and testing changes in mRNA for pro-inflammatory, degenerative, and nociceptive regulators with intra-articular bacterial collagenase in the dorsal root ganglia (DRG) **(B)**, or with bacterial collagenase exposure in DRG neurons **(C)**. **(A)** Glial fibrillary acidic protein (GFAP), an intermediate filament expressed primarily by astrocytes, is unchanged in the spinal dorsal horn with intra-articular MMP-1 (vehicle n=4; MMP-1 n=6). **(B)** Gene expression for substance P (SP), GFAP, pro-inflammatory cytokines (IL-1β, CCL2), the tissue inhibitor of metalloproteinase (TIMP) 1, matrix metalloproteinases (MMP) 2, 8, and 14, and the extracellular matrix proteins thrombospondins (TSP) 1 and 4 in the DRG seven days after a single 60U injection of purified bacterial collagenase into the C6/C7 cervical facet joint (collagenase n=3; vehicle n=3). At day 7 after collagenase injection, gene expression of substance P in the DRG is lower than vehicle, and IL-1β and TIMP-1 expression are higher in rats that receive collagenase than those receiving vehicle (*p≤0.04). **(C)** Gene expression for the neuropeptides SP and calcitonin gene-related peptide (CGRP), signaling kinases p38 and ERK, and pro-inflammatory cytokines TNFα, IL-1β, and IL-1α in DRG cultures after a one hour exposure to 60U of purified bacterial collagenase (collagenase n=5; vehicle n=5). Only mRNA for TNFα (p=0.046) and IL-1β (p=0.016) increases immediately after one hour of collagenase exposure. Gene levels in **(B)** and **(C)** are calculated as the fold change over the housekeeping gene CyA.

levels of the pro-inflammatory cytokine IL-1β increase in the C7 DRG ($p=0.039$) (Figure 9.8B) (Ita et al. 2018b). Notably, that study also found increases in the tissue inhibitor of metalloproteinase 1 (TIMP-1) ($p<0.010$) (Figure 9.8B) (Ita et al. 2018b), one of the endogenously expressed MMP inhibitors, which may be an early indicator of degeneration since TIMPs regulate ECM degradation (Loeser et al. 2012; Visse and Nagase 2003). Yet, degradation as a cause for upregulated TIMP-1 is not supported by the absence of changes in joint structure at day 21 (Figure 4.6). Since TIMP-1 also protects neurons from toxic injury (Tan et al. 2003), its increase may reflect an injurious neuronal stimulus. Levels of mRNA for TNFα ($p=0.046$) and IL-1β ($p=0.016$) are also elevated immediately in dissociated DRG cultures after a one hour exposure to 60U of purified bacterial collagenase (Figure 9.8C) (Ita et al. 2017). Collectively, those two pilot studies (Figures 9.8B & 9.8C) suggest that intra-articular collagenase, and thus the collagenolytic function of MMP-1, may initiate at least an early inflammatory response in peripheral neurons.

Inflammation after intra-articular collagenase may also affect the central nervous system, in addition to the periphery (Kras et al. 2014; Lee et al. 2008). This notion is supported by the finding that painful facet joint injury in the rat increases the pro-inflammatory markers IL-1α and prostaglandin E2 in the spinal cord after one day (Kras et al. 2014), and increases mRNA levels of TNFα and IL-1β in the spinal cord after seven days (Lee et al. 2008). Yet, it is likely that the profile of inflammatory cytokines and chemokines varies with the progression of degeneration in painful joint diseases, since different types of painful injuries initiate differential cytokine profiles (Rothman and Winkelstein 2010). Nonetheless, these pilot data provide evidence that inflammatory

cytokines, and their interactions with MMPs, may play a role in nociceptive transmission from the capsular ligament (Figure 9.4).

9.4. Summary

Together, the studies in this thesis begin to provide a schema by which MMP-1 is a biomechanical and biochemical regulator in painful joint disorders. Findings in the rat demonstrate that exogenous MMP-1 in the joint space is sufficient alone to induce behavioral sensitivity that is immediate and long-lasting (Ita and Winkelstein 2019a). Parallel studies using intra-articular bacterial collagenase in the rat support that the behavioral sensitivity and neuronal dysregulation induced by intra-articular MMP-1 is due, at least in part, to the collagenolytic function of MMP-1 (Ita et al. 2020b). Indeed, MMP-1 alters how the collagen fiber network of the capsular ligament responds to load, despite not inducing degradation of the cartilage or bone (Ita and Winkelstein 2019a). Those alterations of the collagen microenvironment can trigger nociceptive signaling in peripheral neurons and the dysregulation of MMP-9 that leads to the initiation and development of behavioral sensitivity (Ita et al. 2020b; Ita and Winkelstein 2019b).

Studies in the neuron-fibroblast co-culture model of the capsular ligament support that both painful loading in the supraphysiologic regime and biochemical degradation of the collagen fibers in which neurons are embedded are possible mechanisms that increase MMP-1 in the capsular ligament (Ita et al. 2020b; Ita and Winkelstein 2019c). Moreover, fibroblast-like synoviocytes appear to regulate the extent of MMP-1 induced by biomechanical and biochemical stimuli. Analyses of MMP levels in the innervated tissues

from temporomandibular joints from patients with chronic and painful joint disorders implicate MMP-1 and MMP-9 in the clinical presentation of joint pain without radiographic evidence of structural damage (Ita et al. 2020a). Indeed, the fact that intra-articular MMP-1 in the rat induces persistent pain and inconsistent degenerative changes at the tissue-level mirrors clinical reports in that patients with chronic pain have inconsistent structural degeneration (Bedson and Croft 2008; Finan et al. 2013); that similarity, together with a strong correlation between MMP-1 levels and patient-reported pain, supports a role for MMP-1 in clinically relevant joint pain.

Collectively, the findings in this thesis support that MMP-1-mediated cascades contribute to both the initial transmission of noxious stimuli from the periphery and the late-stage mechanisms that maintain pain with severe disease progression. With the advent of more selective MMP inhibitors, especially for the interstitial collagenases, MMP-1 inhibitors could have potential as a therapeutic intervention for degenerative joint pain, since the local abrogation of MMP-1 could provide effective interference in the neuronal signaling that mediates nociceptive transmission. Indeed, blocking MMP-1-mediated extracellular signaling pathways and the collagenolytic functions of MMP-1 could mitigate both the immediate transmission of external noxious stimuli in the capsular ligament and also the long-term deficits in joint structure and function, respectively. Furthermore, the findings in this body of research emphasize that both treatment and diagnostic tools for degenerative joint pain could have improved utility by targeting the microscopic anatomic damage in parallel with pain symptoms.

APPENDIX A

Clinical Data, Imaging Reports & MMP Quantification in Soft Tissue from Studies of TMJs with Painful Joint Disorders

This appendix contains human subjects information, clinical and imaging data, and MMP quantification for the clinical studies presented in Chapter 3 of this thesis. The collection of the information contained in this appendix was approved by the Institutional Review Board (IRB; protocol #828997) of the University of Pennsylvania.

Table A.1 details the data collected during patient consent at the time of study enrollment, which was the same day as the scheduled surgery and prior to the start of surgery. Data include the patient age, patient sex, surgery details, and tissue type(s) collected during surgery. The Wilkes stage assigned by the surgeon (Wilkes 1989) and the pain score reported by the patient at the time of consent on a Likert scale (Wolford et al. 2015) are also included. The maximal incisal opening (MIO) measured was also collected prior to surgery and represents the greatest distance between the incisal edge on the maxillary and mandibular central incisors (Leonardi et al. 2016). The medical history and list of medications reported by the patient are listed in the last columns of Table A.1; a "simple" description of the medications is also listed and designates any group of

medications (i.e. NSAID, opioid, analgesic) that are used to mitigate pain symptoms (National Academies of Sciences, Engineering, and Medicine 2020).

Table A.2 contains the information from the magnetic resonance imaging (MRI) reports that were available from five of the patients in the study cohort. The clinical impression and scan type from the MRI reports is directly transcribed in the second and third columns of Table A.2, respectively. The last column contains the side (left, right, or both) that was taken for MMP quantification and is included so that the clinical impressions from the matching side can be compared with MMP levels. The damage scores that were assigned to the report details in Table A.2 are listed in Table 3.1 in Chapter 3.

Table A.3 details the protein expression quantified by Western Blots of pro-MMP-1, active MMP-1, active MMP-9, pro-MMP-2, and active MMP-2 normalized to the housekeeping protein β-actin for each sample. The quantification of MMPs normalized to β-actin and β-actin levels are separately tabulated.

Table A.1. Clinical data by subject collected during IRB consent

Subject ID	Age (yrs)	Sex	Surgery type	Surgery date	Tissue type	Wilkes stage	Pain score	MIO (mm)	Medical history	Medications all	Medications simple
S01	53	M	TJR	01/08/ 2018	disc	5	10	20	high blood pressure, previous disc	amlodipine-benazepril	none
S02	52	F	ART	01/09/ 2018	lig	4	9	48	asthma, depression, OA	albuterol, escitalopram, percocet,senna, singulair	NSAID opioid
S03	61	F	TJR	02/12/ 2018	disc	5	6	40	anemia, depression, scoliosis, TMJ OA	bupropion, clonazepam, escitalopram, ibuprofen, omega-3 (fish-oil), tylenol, vitamin A	NSAID, analgesic
S04	39	F	ART	02/27/ 2018	disc & lig	5	8	26	anemia, anxiety, chronic lower back pain, chronic pain, depression, glomerulonephritis, lumbar stenosis, substance abuse	amitriptyline, fentanyl, gabapentin, oxycodone, tylenol, senna, zofran	analgesic, opioid, anti-convulsant
S06	33	F	TJR	04/02/ 2018	lig	5	10	28	TMJ OA	etodulac	NSAID
S09	29	F	ART	10/29/ 2018	disc & lig	3	6	28	irritable bowel, TMJ OA	meclizine, nuva ring, voltaren gel	NSAID
S10	66	F	TJR	12/03/ 2018	lig	5	6	35	anosmia, anxiety, arthralgia, cervicalgia, degenerated lumbosacral disc, depression, hyperthyroidism, osteopenia, radiculopathy,	baclofen, buproprion, buspirone, citalopram, compazine, ibuprofen, levothyroxine, lorezopam, oxycodone, senna, tylenol, vitamin D	NSAID, analgesic, opioid
S12	44	F	TJR	08/05/ 2019	disc	5	8	33	depression, OA	fluoxetine, meloxicam	NSAID
S13	29	F	TJR	09/30/ 2019	disc & lig	5	9	44	maxillary sinusitis, TMJ OA	flagyl, naproxen, nuva ring	NSAID

M, male; F, female; TJR, total joint replacement; ART, arthroplasty; MIO, maximal incisal opening.
lig, ligament; TMJ, temporomandibular joint; OA, osteoarthritis.
NSAID, nonsteroidal anti-inflammatory drug.

Table A.2. Transcribed clinical impression reports for patients with MR imaging

ID	transcription from MR imaging report	scan type	side taken
S01	RIGHT *articular disc mouth closed: mild displacement anteriorly. disc has dysmorphic appearance with the normal bioconcave appearance not seen; *articular disc mouth open: normal position consistent with recapture; *rotation: normal rotation and translation of the mandibular condyle with respect to the articular eminence; *bone: there is susceptibility at the lateral aspect of the mandibular condyle consistent with reported surgery. there is mild to moderate flattening of the mandibular condylar head, no fracture seen; *effusion; there is none evident. LEFT *articular disc mouth closed: normal position, disc has dysmorphic appearance with the normal bioconcave appearance not seen; *articular disc mouth open: normal position; *rotation: normal rotation and translation of the mandibular condyle with respect to the articular eminence; *bone: there is susceptibility at the lateral aspect of the mandibular condyle consistent with reported surgery. there is mild to moderate flattening of the mandibular condylar head, no fracture seen; *effusion; there is none evident. SUMMARY 1. On the R, mild displacement of the disc anteriorly with recapture on open mouth positioning. 2. Postsurgical changes involving both mandibular condyles consistent with prior surgery. 3. Mild-to-moderate flattening of both mandibular condyles consistent with degenerative changes.	MR OF THE TMJS WO CONTRAST. Multiplanar, multisequence MR on 1.5T. Patient was unable to tolerate the open-mouth sagittal T2-weighted sequence and was therefore not obtained. also CT available	samples from the LEFT side
S03	Prominent soft tissue in both condylar fossas and there is marked flattening of both condylar articular surfaces visible on the sequences. There is also remodeling of the skull base in the region of the mandibular fossa at the joints. The articular discs are not well-seen bilaterally and presumably are degenerated. There is also increased fluid in doth TMJs, especially the left. There is debris or synovial proliferation in both joints. There is minimal, if any, condylar translation. Markedly abnormal bilateral TMJs with sclerosis and remodeling of the joints, flattening of the condyles, increased joint fluid and debris or synovial proliferation in both joints, along with poor depiction of the articular discs and minimal, if any, condylar translation.	TMJ MRI acquired on a 3T scanner. Angled sagittal and angled coronal T1 and T2 sequences were acquired with the mouth closed and open. A cine sequence was then acquired in the angled sagittal plane.	tissue samples from the LEFT and RIGHT sides
S06	RIGHT The articular disc is within normal position with the mouth open and closed with intermediate zone positioned between the mandibular condyle and articular eminence. Normal anterior translation with mouth opening. No degenerative changes or fluid in the joint. LEFT Flattening and spurring of the mandibular condyle with mild joint space loss. With the mouth closed, the posterior band of the disc appears thin and atrophic. There is mild partial anterior displacement of the disc. With the mouth open the disc is no longer displaced however there is incomplete anterior translation of the mandibular condyle. Impression 1. ID of the left with partial anterior displacement of the disc with reduction and incomplete anterior translation of the left mandibular condyle. Degenerative changes in left TMJ. 2. Normal right TMJ.	Bilateral MR of the TMJs with 1.5T. also CT available	tissue sample from the LEFT side
S09	Impression Markedly limited mouth opening without appropriate translocation of the mandibular condyles. In the closed mouth position, the right meniscus is deformed and anterior inferiorly subluxed. No evidence of recapture of the disc with attempted mouth opening. The left meniscus appears mildly distorted but is normally located in the closed mouth position. Narrative In closed mouth, left meniscus somewhat distorted but normally located; On the right, closed mouth, the meniscus is deformed and anteriorly and inferiorly subluxed; Only very limited mouth opening occurred without appropriate translocation of the mandibular condyles and without evidence of disc recapture on the right; Mandibular condyles normal in appearance; Scattered intraparotid lymph nodes are seen. There are multiple bilateral top normal sized cervical lymph nodes are present, likely reactive in a patient of this age.	MR TMJ WO IV CONTRAST; MRI at 1.5T, oblique sagittal and axial and coronal T1-weighted images of the TMJs obtained with closed mouth positions. Subsequently oblique sagittal T2-weighted images obtained in the open and closed mouth position and coronal T1-weighted images in the open mouth position. also NM bone spect available	tissue sample from the RIGHT side

Note: Table is continued on the next page.

S13	1. Advanced OA and severe ID in the right TMJ; 2. Moderate OA with articular disc degeneration but w/o disc displacement in the left TMJ; RIGHT With the mouth closed, the R mandibular condyle is seated in fossa. The articular disc is fragmented and anteriorly displaced. The condyle is abnormal with the articular surface irregularity. There is subchondral sclerosis of the eminence. With the mouth opening, the condyle translates minimally, and the articular disc remains anteriorly displaced with recapture and translates in normal relation to the condyle. LEFT With the mouth closed, the left mandibular condyle is seated in the fossa. The articular disc is attenuated and heterogeneous in signal in keeping with degeneration but is not anteriorly displaced. The condyle is abnormal with articular surface irregularity. With the mouth opening, the condyle translates minimally, and the articular disc remains in normal anatomic relationship to the condyle. There is moderate osteosclerosis with articular disc in the left TMJ.	MR TMJ WO IV CONTRAST; MR imaging of the TMJ performed at 1.5T. Oblique sagittal T1, proton-density- and heavily T2-weighted images and coronal T1-weighted images were obtained with the mouth closed. With the mouth open, additional oblique sagittal T1-weighted images were obtained.	tissue sample from the RIGHT side

Table A.3. Western Blot quantification of MMPs normalized to the housekeeping protein β-actin

		MMP-1			MMP-9		MMP-2		
Subject ID	**Tissue**	**pro MMP-1 /β-actin**	**active MMP-1 /β-actin**	**β-actin**	**active MMP-9 /β-actin**	**β-actin**	**pro MMP-2 / β-actin**	**active MMP-2 /β-actin**	**β-actin**
S01	disc	0.920	10.120	25.000	0.000	0.000			
S02	retro	128.500	180.250	4.000	4.227	485.000	9.777	0.262	359.000
S03 left	disc	0.795	2.055	1460.000	1.444	2500.000	13.060	1.700	1466.000
S03 right	disc	0.363	0.423	2810.000	1.103	2710.000	6.017	1.739	1150.000
S03	disc average	0.579	1.239	2135.000	1.274	2605.000	9.539	1.720	1308.000
S04	disc	5.915	35.775	71.000	23.032	155.000	50.976	0.366	123.000
S04	ligament	1.543	1.914	700.000	1.822	1740.000	13.852	1.469	488.000
S06	ligament	1.541	3.941	85.000	6.894	264.000	2.737	0.249	811.000
S09	ligament	0.377	0.892	1300.000	1.377	1460.000	1.867	0.164	1960.000
S09	disc	0.654	0.447	7490.000	1.569	2760.000	4.000	0.160	2050.000
S10	ligament	0.157	1.113	2560.000	5.465	904.000	4.775	1.018	1110.000
S12	disc	1.757	2.057	734.000	2.328	1890.000	2.520	0.009	1980.000
S13	ligament	1.568	0.585	1690.000	0.936	5170.000	3.043	0.106	3680.000
S13	retro	0.831	3.677	189.000	6.215	428.000	6.802	0.091	494.000
S13	ligament average	1.199	2.131	939.500	3.576	2799.000	4.923	0.099	2087.000
S13	disc	-0.099	-0.890	182.000	8.923	455.000	22.308	0.638	520.000

Retro, retrodiscal ligament: retrodiscal ligaments make up a portion of the entire capsular ligament; since there were not enough retrodiscal ligament samples to justify its own tissue type subgroup, retrodiscal samples were grouped with the ligament tissue type for all analyses.

Yellow shading indicates samples for which no housekeeping protein β-actin was detected.

Red shading indicates samples for which the β-actin protein was detected but no MMP-1 protein was detected.

Blue shading indicates the patients (S03 and S13) for which MMP levels were averaged; for S03, since discs from both sides were assayed, MMP levels were averaged for all analyses *except* for analyses with MR damage scores since separate damage scores were assigned from side-specific clinical impressions from the MRI reports. For S13, a ligament sample and retrodiscal ligament sample were assayed; since retrodiscal ligaments were grouped with the ligament subgroup, MMP levels for the ligament and retrodiscal ligament were averaged for patient S13.

APPENDIX B

MATLAB Code for Densitometry and Co-Localization

This appendix contains the MATLAB scripts that perform the automated densitometry analyses on immunolabeled images. The first script titled "Single Channel Densitometry" inputs .tif images that are uniformly cropped to the same pixel size and contain an immunolabel for a single wavelength channel (e.g. 488nm, 568nm, etc.). Users of this script must specify the following variables: *D*, the file directory indicating the images to analyze as designated by filename; *pos_thresh*, the threshold for positive pixels from 0-250 determined from no primary controls and naïve animal tissue and/or in vitro controls, depending on the experiment; and *whiteSpace*, the parameter that determines the amount of background defined in an image. The main output variables of this script are *percpos* and *percpos_nobackg*; *percpos* subtracts out pixels defined as background and *percpos_nobackg* does not account for background subtraction. The Single Channel Densitometry script was used to quantify substance P, pERK, and MMP-1 immunolabels in the rat spinal cord in the studies in Chapter 4, as well as used to calculate the positive labeling for MMP-1 in the rat DRG in the studies in Chapter 4. Spinal substance P and MMP-9 labeling in the Chapter 7 rat studies was also quantified using the Single Channel Densitometry script. Finally, the Single Channel script was used in the analyses of MMP-

1, MMP-9, and substance P immunolabels in the in vitro studies described in Chapters 6 and 8.

The second script in this Appendix titled "Co-localization Densitometry" calculates the percent positive pixels for two separate wavelength channels from the same multi-channel image (e.g. a 488nm and 568nm co-labeled sample) and then computes the regional co-localization of positive pixels between the two channels. Users of this script must specify separate directories for the two channels (*D1, D2*) with corresponding names (*D1_name, D2_name*), thresholds for positive labeling (*D1_thresh, D2_thresh*) and whiteSpace parameters (*y_background_D1, y_background_D2*). The channel designated as D1 should be the structural marker (e.g. a neuronal or fibroblast structural protein) and the channel designated as D2 should be the protein of interest. The primary output variables of this script are *per_co*, the total percent of co-localized pixels using the number of positive pixels in D1 for the percentage calculation, and *col_per_area*, which divides per_co by the number of positive pixels in the D1 channel. The Co-localization Densitometry script was used to quantify the amount of neuronal MMP-1 (βIII tubulin and MMP-1 co-localized pixels) and the amount of fibroblastic MMP-1 (vimentin and MMP-1 co-localized pixels) in the studies in Chapter 5.

Single Channel Densitometry

This script was written to calculate and visualize percent positive pixels per image. To run the file, you want to create an excel file that has the detailed information about the images to be analyzed, then number those images with a common name that has an ordered numerical (1, 2...) ending. NOTE: for the excel file, please have the following columns (in order): rat #, tissue type, injury type, image no., threshold, raw results, normalized results. Number normals last.

```
% requires MATLAB 7.0 (or higher) and imaging toolbox.

% Written by Ling Dong (modified from K. Quinn) on Feb 2, 2009.
% Modified by Kristen Nicholson December 2009
% Nate - no background subtraction
% Modified by Meagan Ita 06/19/18
```

Begin script

```
clear all;
close all;
clc

D = dir('*.tif'); % specify which images to analyze (* = wildcard character)
i=1;
intensity = zeros(1, length(D));

for k=1:length(D)  % all do 1:length(D);


    % reads file in
    file=D(k).name;

    % load the image
    imag_orig = imread(file);
    % converts to grayscale
    % imag_orig = imag_orig(:,:,1);%grab the red labeled image (doesn't
    % apply to single channel)
    % imag_orig = imag_orig(:,:,1);%grab the green labeled image (doesn't
    % apply to single channel
    % imag_orig = rgb2gray(imag_orig);
    imag = imag_orig;
    intensity(k) = mean(mean(imag));
    invImag = 255-imag;
    imag = invImag;

    % Calc number of pixels
```

```
[a, b]=size(imag);
tsize=a*b;
low=double(min(imag(:)));
high=double(max(imag(:)));
% INPUTS REQUIRED HERE - whiteSpace is the parameter that will affect the
% background, and pos_thresh is your parameter that will defines the
% threshold at which pixels are considered positively labeled
whiteSpace = 0.985*high; % usually .985*high
pos_thresh = 240; % input based on normal run, remember for DAB staining
% higher value corresponds to a higher positive threshold.

backg=sum(sum(imag>whiteSpace));
posp=sum(sum(imag<pos_thresh));

% Calc percent of positive pixels in tissue
percpos(k) = posp/(tsize-backg)
percpos_nobackg(k) = posp/(tsize)
tpost(k) = posp;
Iname(k) = {file};

% Map out pos and neg pixels
pmap=(imag<pos_thresh);
nmap=(imag>whiteSpace);

% Make figure for each image, if you are processing a bunch of images, you
% may want to comment this part out

% Make positive pixels more green, and background pixels less blue
imag1(:,:,1)=double(imag)/255;
imag1(:,:,2)=(1-pmap).*double(imag)/255+pmap;
imag1(:,:,3)=double(imag)/255.*(1-nmap);

h = figure(i);
subplot(1,3,3);
subimage(imag);
title('Inverted Image')
axis image
axis off
subplot(1,3,2);
subimage(imag1);
title('Positive Pixels Green')
axis image
axis off
colormap gray
subplot(1,3,1);
subimage(imag_orig)
title('Original Image')
axis image
axis off
drawnow
```

```
    i=i+1;

    % Save the gray-scale, inverted, and pos/neg images as a new figure
    % Uncomment below if you want to save each image
    % saveas(h, ['dens-' D(k).name], 'jpg')

    % clear imag imag1
    % clf
end

percpos=percpos'
percpos_nobackg=percpos_nobackg'
avg=mean(percpos)
```

Published with MATLAB® R2018b

Co-localization Densitometry

This script was written to calculate the positive pixels per image in two separate channels and then to calculate and visualize the co-localization of the positive pixels between the two channels.

```
% requires MATLAB 7.0 (or higher) and imaging toolbox.

% Written by Ling Dong (modified from K. Quinn) on Feb 2, 2009.
% Modified 06/21/2018 by MEI

clear all;
close all;
clc;
```

Load files and input thresholds and write file

```
% file1 should be the "reference" label (a structural marker, like MAP2, or
% beta III tubulin, something you don't expect would change across groups)
% file2 should be the label that you would consider your "protein of
% interest" or in other words you might expect this to change across groups

D1 = dir('B*.tif'); %common prefix for all images
D2 = dir('MMP*.tif'); %common prefix for all images
%D3 = dir('R*.tif'); %common prefix for all UNMERGED images (this is only to display in
the subplot at the end)
D1_name = 'betaIII';
D2_name = 'MMP1';

% input thresholds here - should be based on normal run
% higher value corresponds to MORE positive pixels
D1_thresh = 170;
D2_thresh = 220;

% input whitespace parameter here - multiplier of high will affect background
% detection, a higher multiplier (e.g. 0.99) will result in LESS pixels
% labeled as background, a lower multiplier (e.g. 0.85) will result in MANY
% pixels being labeled as background
y_background_D1 = 0.930;
y_background_D2 = 0.982;

% name the excel output file
IPfname = 'E4_betaIII_MMP1_colocal';
OPfile = strcat(IPfname, '.xls');
fid = fopen(OPfile, 'w'); % opens the excel file to write
```

```
h1 = waitbar(0,'Please wait...');
```

Calculate percent positive pixels for each image

```
for k=1:length(D1);
    % D1 and D2 should be the same length
    % reads both D1 and D2 files in
     file1 = D1(k).name;
     file2 = D2(k).name;

     imag_D2 = imread(file2);
%      imag_D2 = rgb2gray(imag_D2);
     imag_D1 = imread(file1);
%      imag_D1 = rgb2gray(imag_D1);

    % take the inverse of the image
    % imag_red = uint8(-double(imag_red) + 255);
    % imag_green = uint8(-double(imag_green) + 255);
     invImag_D2 = 255-imag_D2;
     imag_D2 = invImag_D2;
     invImag_D1 = 255-imag_D1;
     imag_D1 = invImag_D1;

    % calculate number of pixels of the D1 image
     [a b] = size(imag_D1);
     tsize = a*b;
     %low = double(min(imag_D1(:)));
     high_D1 = double(max(imag_D1(:)));
     high_D2 = double(max(imag_D2(:)));
     whiteSpace_D1 = y_background_D1*high_D1;
     whiteSpace_D2 = y_background_D2*high_D2;

    % calculate the background in D1, then D2
     backg_D1 = sum(sum(imag_D1 > whiteSpace_D1));
     backg_D2 = sum(sum(imag_D2 > whiteSpace_D2));
    % calculate the positive pixels in D1, then D2
     posp_D1 = sum(sum(imag_D1 < D1_thresh));
     posp_D2 = sum(sum(imag_D2 < D2_thresh));
    % calculate percent of positive pixels in D1, then D2
     percpos_D1(k) = posp_D1/(tsize-backg_D1)
     percpos_D2(k) = posp_D2/(tsize-backg_D2)

    % map out pos and neg pixels
    pmap_D2 = (imag_D2 < D2_thresh);
    nmap = (imag_D1 > whiteSpace_D1);
    pmap_D1 = (imag_D1 < D1_thresh);
```

```
    % make positive pixels green, and background pixels black
    % D1 image
    imag1(:,:,1) = zeros(a,b);
    imag1(:,:,2) = pmap_D1;
    imag1(:,:,3) = zeros(a,b);
    % D2 image
    imag2(:,:,1) = zeros(a,b);
    imag2(:,:,2) = pmap_D2;
    imag2(:,:,3) = zeros(a,b);
```

Set all non-D1/D2-positive-labeled pixels in the D1 image to zero and create a new image for the co-localization

```
    [R, C] = find(pmap_D2 == 0);% finds all pixels not positive in D2
    imag_co = imag1;
    for ind = 1:length(R)
        imag_co(R(ind),C(ind),2) = 0; %imag_co(:,:,2) is map of D1 positive pixels so
finds all such pixels not also positive in D2 to 0
    end
```

Calculate the number of colocalized positive pixels

```
    tot_co(k) = length(find(imag_co(:,:,2) == 1));
    perc_co(k) = tot_co(k)/(tsize-backg_D1); % percent colocalized, using D1 background
for total pixels
    col_per_area(k) = tot_co(k)/posp_D1; % amount colocalized per D1 POSITIVE pixels
```

Save data and make plots

```
    fprintf(fid, '%s \n', D1(k).name); % D1 file names
    fprintf(fid, 'percent+ D1 : \t\t%7.4d\n', percpos_D1(k));
    fprintf(fid, 'percent+ D2 : \t\t%7.4d\n', percpos_D2(k));
    fprintf(fid, 'percent colocalized : \t\t%7.4d\n', perc_co(k));
    fprintf(fid, 'percent colocalized per D1+ label : \t\t%7.4d\n', col_per_area(k));

    h = figure(k);
    subplot(3,2,1); % D1 in gray scale
      subimage(imag_D1);
      axis image; axis off
      title(D1_name)
    subplot(3,2,2); % D2 in gray scale
      subimage(imag_D2);
      axis image; axis off
```

```
      title(D2_name)
    subplot(3,2,3); % D1 positive pixels
       subimage(imag1);
       axis image; axis off;
       title('D1 positive')
    subplot(3,2,4); % D2 positive pixels
       subimage(imag2);
       axis image; axis off;
       title('D2 positive')
%     subplot(3,2,5);
%        file3 = D3(k).name;
%        imag_orig = imread(file3);
%        subimage(imag_orig);
%        axis image; axis off
%        title('original image - all channels')
    subplot(3,2,6);
       subimage(imag_co)
       axis image; axis off
       title('colocalized pixels')
       drawnow

    %saveas(h, ['colocalize-' D1(k).name], 'jpg')
    waitbar(k/length(D1))
    clear imag imag1 imag2 R C
end

close(h1)
status = fclose(fid);
```

Published with MATLAB® R2018b

APPENDIX C

Mechanical Hyperalgesia

This appendix summarizes the behavioral responses for each rat included in the studies presented in Chapters 4 and 7. In those in vivo studies, behavioral sensitivity was quantified using mechanical hyperalgesia which was measured by the paw withdrawal threshold of each rat's bilateral forepaws in response to von Frey filament stimulation (Crosby and Smith 2015; Kras et al. 2015; Lee et al. 2006). Table C.1 details withdrawal thresholds for the studies in Chapter 4 for rats injected bilaterally in the C6/C7 facet joint with either purified bacterial collagenase (collagenase) or a saline vehicle (vehicle). Thresholds were measured before (day 0) intra-articular administration of collagenase or the vehicle solution and on days 1, 3, 5, 7, 11, 14, 17, and 21 after the injection. Withdrawal thresholds for the studies in Chapter 7 are summarized in Table C.2 and include thresholds measured before (day 0) the intra-articular injection of exogenous MMP-1 (MMP-1) or a sterile H_2O vehicle (vehicle) into the bilateral C6/C7 facet joints and on days 1, 3, 5, 7, 11, 14, 17, 21, 25, and 28 after the injection. For both studies, withdrawal thresholds are listed separately for the left and the right forepaw and represent the average of three rounds of testing conducted 10 minutes apart for each timepoint.

Table C.1. Forepaw withdrawal thresholds for rats with intra-articular injection of bacterial collagenase or vehicle (Chapter 4)

		baseline (day 0)		day 1		day 3		day 5		day 7	
Rat #	Group	right	left	right	left	right	left	right	left	right	left
10	collagenase	20.67	22.33	20.00	4.67	4.67	3.33	6.00	4.00	4.67	3.33
11		13.33	11.67	4.67	7.33	7.33	6.00	4.67	5.33	7.33	7.33
12		5.33	4.67	1.40	1.40	1.13	0.60	1.80	1.80	1.60	1.60
22		20.67	26.00	14.00	8.33	15.67	13.33	15.00	15.00	26.00	22.33
23		22.33	20.67	9.67	3.80	6.67	7.33	6.67	7.33	9.67	8.00
25		26.00	20.00	8.00	9.33	8.67	8.00	7.33	6.00	7.33	8.67
28		20.67	17.00	7.33	6.67	6.00	6.67	8.00	6.67	6.67	7.33
29		10.33	13.33	5.33	4.67	8.67	7.33	4.67	4.67	8.67	8.67
30		11.00	10.33	9.00	9.67	7.33	6.00	6.00	8.00	7.33	5.33
33		14.00	11.00	13.33	6.67	7.33	3.33	8.00	6.67	6.67	8.00
34		8.00	7.33	6.00	4.67	7.33	5.33	6.67	7.33	6.67	6.67
36		8.00	7.33	4.00	3.33	8.00	7.33	8.00	8.00	6.67	5.33
24	vehicle	22.33	12.67	13.33	7.33	11.00	6.67	9.33	7.33	18.67	6.67
26		26.00	15.33	22.33	9.00	18.67	10.00	8.00	11.00	13.33	22.33
27		17.00	20.67	8.67	8.00	17.00	17.00	13.33	16.33	12.67	12.67
31		26.00	13.33	12.67	8.00	17.00	15.33	15.00	10.00	15.00	9.33
32		12.67	12.67	6.00	6.00	7.33	8.67	10.33	16.33	7.33	11.00
35		8.00	8.67	9.67	7.33	7.33	7.33	17.00	15.00	10.00	17.00

		day 11		day 14		day 17		day 21	
Rat #	Group	right	left	right	left	right	left	right	left
10	collagenase	7.33	6.67	1.80	8.00	2.67	6.00	4.00	6.00
11		7.33	5.33	1.80	5.33	4.00	7.33	8.00	2.47
12		1.13	1.33	1.60	1.33	2.47	2.47	2.00	2.47
22		14.00	15.00	11.00	11.67	20.00	17.00	20.67	22.33
23		7.33	8.00	6.67	7.33	6.67	10.33	6.67	5.33
25		11.67	9.00	7.67	6.00	6.67	7.33	7.33	8.67
28		7.33	5.33	7.33	6.67	10.00	9.33	8.67	8.00
29		10.00	6.67	9.00	8.00	10.33	7.33	7.33	8.00
30		4.67	5.33	5.33	6.00	4.67	7.33	6.00	6.00
33		5.33	8.67	6.00	6.00	6.00	4.67	3.33	4.00
34		5.33	6.00	7.33	4.00	7.33	6.67	5.33	4.67
36		4.00	3.33	4.67	2.67	3.33	3.33	4.00	2.67
24	vehicle	13.33	7.33	11.00	6.67	11.67	8.00	15.33	8.00
26		26.00	12.67	14.67	9.33	17.00	18.67	26.00	22.33
27		20.00	14.00	8.00	13.33	22.33	22.33	11.67	11.67
31		18.67	8.00	11.67	15.33	18.67	14.67	11.00	11.67
32		11.00	17.00	7.33	20.67	8.00	20.67	8.67	11.00
35		8.67	13.33	11.00	11.00	10.33	20.00	11.67	15.33

Table C.2. Forepaw withdrawal thresholds for rats with intra-articular MMP-1 or vehicle (Chapter 7)

		baseline (day 0)		day 1		day 3		day 5		day 7	
Rat #	Group	right	left	right	left	right	left	right	left	right	left
13	MMP-1	14.67	26.00	26.00	11.00	12.67	9.67	9.33	6.00	9.67	6.00
14		15.67	16.33	14.00	6.67	15.33	10.00	10.00	8.33	6.67	11.00
15		22.33	20.67	5.33	7.33	14.67	17.00	14.00	11.00	8.67	11.00
16		14.67	26.00	3.33	7.33	6.00	9.00	3.33	5.33	10.33	8.00
17		20.67	22.33	6.67	9.67	10.33	8.00	7.33	20.67	9.33	11.67
18		17.00	16.33	6.00	8.67	5.33	6.67	9.00	7.33	5.33	7.00
19		26.00	26.00	14.67	13.33	17.00	12.67	14.67	7.33	8.67	10.00
20		9.33	18.67	2.67	5.33	5.33	7.33	5.33	4.67	4.67	6.67
21		14.00	17.00	4.00	4.67	4.67	7.33	6.00	6.00	4.00	6.67
37		1.40	1.40	2.67	1.33	0.87	0.60	1.60	1.60	1.60	1.13
38		11.67	13.33	8.67	6.67	4.67	6.67	4.67	6.67	2.00	4.00
43		22.33	22.33	26.00	8.00	8.67	7.33	8.67	8.00	7.00	6.00
44		11.00	22.33	11.00	9.00	8.67	3.33	6.67	4.00	5.33	4.67
46		17.00	20.67	3.33	8.67	5.33	6.00	4.67	3.33	3.13	4.67
47		11.00	11.67	6.67	4.00	5.33	6.00	4.67	6.00	7.33	5.33
55		22.33	22.33	26.00	6.00	14.00	6.00	6.00	4.00	16.33	4.67
56		20.67	9.00	9.00	3.80	7.33	2.67	8.67	8.00	4.67	3.33
59		16.33	11.00	7.33	3.33	7.33	3.33	8.00	6.67	4.67	7.33
42	vehicle	22.33	16.33	5.33	4.67	8.00	4.67	7.33	6.00	8.00	8.00
45		20.67	17.00	8.00	6.67	8.67	10.33	13.33	11.33	9.00	17.00
48		18.67	17.00	6.67	26.00	20.67	14.67	9.67	13.33	20.67	10.33
49		15.00	11.00	15.00	7.00	8.00	11.00	10.67	16.33	11.00	12.67
50		12.67	14.67	11.00	6.67	7.33	7.33	8.67	7.33	10.33	8.67
51		9.33	8.67	8.67	8.00	14.00	8.00	10.00	8.00	16.33	14.67
52		10.00	8.67	7.33	5.33	11.00	6.00	10.33	7.33	6.67	5.67
53		11.67	11.67	13.33	8.67	16.33	9.33	11.67	11.00	13.33	11.00
54		26.00	26.00	20.50	8.00	14.00	20.67	20.67	14.67	22.33	8.67
57		26.00	20.00	22.33	12.67	18.67	12.67	18.67	13.33	26.00	20.00
58		15.00	13.33	6.00	6.67	6.00	6.67	8.67	7.33	9.33	12.67
61		22.33	26.00	26.00	26.00	26.00	26.00	22.33	9.33	16.33	22.33
62		22.33	14.00	9.67	17.00	9.67	17.00	22.33	15.33	17.00	20.67

		day 11		day 14		day 17		day 21		day 25		day 28	
Rat #	Group	right	left	right	left	right	left	right	left	right	left	right	left
13	MMP-1	6.00	6.67	4.67	4.67	4.00	4.67	7.33	3.33	6.00	7.33	5.33	3.33
14		8.00	9.67	5.13	5.33	8.00	11.00	6.67	5.33	4.67	6.67	3.33	3.33
15		6.67	10.33	8.67	8.67	6.67	11.67	8.67	14.67	9.67	8.00	8.00	4.67
16		6.00	6.00	8.67	9.67	6.67	6.67	7.33	8.67	6.00	6.00	6.00	3.13
17		8.00	9.00	4.67	5.33	6.67	8.67	6.00	6.67	5.33	5.33	6.67	6.00
18		6.00	13.33	6.00	7.33	4.00	7.33	2.67	5.33	6.67	3.13	8.00	8.00
19		18.67	12.67	15.67	10.33	9.33	17.00	7.33	6.67	6.67	8.00	10.33	5.33
20		7.33	8.67	3.33	6.00	7.33	7.33	4.00	6.00	5.33	8.67	6.67	6.67
21		10.33	15.00	6.00	8.67	10.33	17.00	4.67	5.33	6.67	13.33	3.33	6.67
37		1.60	1.40	2.47	1.60	1.40	1.13	1.33	1.60	1.80	1.13	1.40	0.60
38		4.00	3.33	4.00	4.00	1.40	2.67	1.40	2.00	2.67	1.80	3.33	2.67
43		9.33	8.00	11.67	5.33	8.67	16.33	8.00	12.67	11.67	10.33	8.67	5.33
44		7.00	2.00	8.00	6.00	8.00	5.33	14.67	7.33	6.67	3.80	6.00	9.33
46		2.00	6.00	2.67	2.67	4.67	8.00	2.27	4.67	1.60	6.67	7.33	5.33
47		6.67	6.00	7.33	6.00	7.33	6.67	8.00	7.33	8.67	7.33	6.00	2.67
55		6.00	9.00	4.67	4.47	8.00	4.00	8.00	4.67	4.00	2.47	2.47	2.47
56		6.00	3.33	4.67	3.33	8.00	4.00	4.67	2.47	6.67	2.47	6.67	2.47
59		4.67	5.33	4.67	3.13	4.00	4.67	6.67	4.00	4.47	2.67	6.67	5.13
42	vehicle	8.00	22.33	15.00	8.00	10.33	8.67	20.67	11.67	11.00	11.67	13.33	8.67
45		8.67	22.33	14.67	11.00	7.33	22.33	7.33	16.33	9.33	14.67	6.67	16.33
48		20.67	20.67	18.67	11.00	22.33	20.67	15.00	13.33	18.67	16.33	16.33	8.67
49		15.67	7.33	20.67	18.67	22.33	17.00	17.00	8.67	8.67	8.00	9.67	8.67
50		11.67	8.67	6.67	6.67	6.67	9.33	11.67	8.00	5.33	8.00	7.33	10.33
51		14.67	26.00	14.67	17.00	20.67	22.33	26.00	15.00	22.33	18.67	9.33	20.00
52		12.67	13.33	15.33	11.00	15.33	22.33	11.00	11.00	17.00	10.33	17.00	10.00
53		14.67	6.00	22.33	15.00	17.00	12.67	8.67	7.33	10.33	9.00	13.33	7.33
54		17.00	26.00	22.33	26.00	20.67	18.67	14.67	26.00	22.33	20.67	11.67	12.67
57		10.00	9.00	22.33	8.00	20.67	9.67	22.33	15.33	26.00	26.00	18.67	22.33
58		5.33	20.67	14.67	5.33	8.00	4.67	6.67	6.67	6.00	5.33	6.00	6.00
61		19.67	20.00	26.00	14.00	11.67	22.33	14.67	22.33	22.33	26.00	26.00	22.33

APPENDIX D

Joint Histology & HIF-1α Immunolabeling in the Facet Joint for Intra-Articular Rat Studies

This appendix summarizes the histological and immunohistochemical assays performed on facet joint tissues from the in vivo rat studies that are detailed in Chapters 4 and 7. All assays of tissues exposed to bacterial collagenase, MMP-1, and/or the matched vehicle were performed using the injected C6/C7 facet joints; data from naïve rats are also included and are from un-injected C6/C7 facet joints. In each of the tables and figures detailed in this appendix, data are identified by their injection group and rat number. Labels above each image within the figures list the rat number followed by the image number (e.g. "R10 – 01" indicates image 1 from rat 10); the image number in the labels matches the image numbers listed in the corresponding data table.

Table D.1 details the anisotropy index that was calculated from each Picrosirius Red/Alcian Blue stained image of the capsular ligament (detailed in Figure D.1) for the in vivo studies detailed in Chapter 4 that utilized intra-articular injection of bacterial collagenase or a saline vehicle. Tissue sections were stained with Picrosirius Red/Alcian Blue (Schmitz et al. 2010) to visualize collagen fibers in the capsular ligament. Separate regions of interest (ROIs) containing only the ligament were randomly selected from each image of the stained ligament (2-4 ROIs/image); the number of ROIs selected for each

image in Figure D.1 are detailed in Table D.1. Fiber orientation was quantified by computing the anisotropy index as the ratio of the principal axes to describe orientation on a continuous scale from isotropic (random; 0) to aligned (1) (Sander and Barocas 2009). In addition to anisotropy (ani) index, Table D.1 also details the estimated depth into the joint at which the section was taken, measured from the posterior surface of the spinous process, in microns.

Table D.2 details the Mankin scores for each Safranin O/Fast Green image (Figure D.2) taken of the articular cartilage and surrounding bone for the in vivo studies detailed in Chapter 4. The Safranin O/Fast Green stain visualizes cartilage and bone (Schmitz et al. 2010). The Mankin score assesses cartilage degradation based on cellular and background staining, chondrocyte arrangement, and structural surface condition, with scores ranging from normal (0) to maximally degenerate (10) (Xu et al. 2009). The Mankin score was assigned by two blinded graders, also detailed in Table D.2. Since Safranin O/Fast Green images in Figure D.2 may contain only the top articular surface, only the bottom articular surface, or both, Table D.2 details the articular surface (top or bottom) for which the Mankin score corresponds.

Data acquired from the immunohistochemical label of HIF-1α in chondrocytes are detailed in Table D.3 and Figure D.3 for the in vivo studies using intra-articular bacterial collagenase that are detailed in Chapter 4. Immunolabeling for HIF-1α expression was used to evaluate the health of chondrocytes in the C6/C7 articular cartilage (Kartha et al. 2016; Sperry et al. 2020b). An assessor blinded to groups counted both the number of cells positive for HIF-1α and the total number of cells in each image, using images shown in

Figure D.3 (Sperry et al. 2020b); the percentage of HIF-1α-positive cells based on that analysis is summarized in Table D.3.

Table D.4 and Figure D.4 summarize the anisotropy index that was calculated for each Picrosirius Red/Alcian Blue stained capsular ligament for the in vivo rat studies using intra-articular MMP-1 or its vehicle that are detailed in Chapter 7. Similarly, Table D.5 and Figure D.5 summarize the Mankin scoring and Safranin O/Fast Green images of the articular cartilage and surrounding bones from those intra-articular MMP-1 rat studies found in Chapter 7. The data analyses and summary of data in figures and tables for anisotropy index and Mankin score for the Chapter 7 studies in this appendix match those outlined above for the Chapter 4 studies.

Table D.1. Anisotropy (ani) indices computed from Picrosirius Red/Alcian Blue stained capsular ligaments injected with bacterial collagenase or vehicle (Chapter 4)

Rat	Group	image no.	ROI	depth (μm)	ani index
R10	collagenase	1	1	240	0.050
R10		1	2	240	0.154
R10		2	1	240	0.891
R10		2	2	240	0.438
R10		2	3	240	0.221
R10		3	1	240	0.115
R10		3	2	240	0.454
R10		4	1	240	0.747
R10		4	2	240	0.265
R10		5	1	240	0.122
R10		5	2	240	0.314
R10		6	1	464	0.358
R10		6	2	464	0.549
R10		7	1	464	0.239
R10		7	2	464	0.399
R10		8	1	464	0.524
R10		8	2	464	0.415
R10		9	1	656	0.272
R10		9	2	656	0.557
R10		10	1	656	0.227
R10		10	2	656	0.335
R10		11	1	1072	0.299
R10		12	1	1072	0.382
R10		12	2	1072	0.681
R10		13	1	1072	0.719
R11	collagenase	1	1	112	0.089
R11		1	2	112	0.145
R11		2	1	112	0.758
R11		2	2	112	0.677
R11		2	3	112	0.409
R11		3	1	112	0.583
R11		3	2	112	0.703
R11		4	1	432	0.687
R11		4	2	432	0.504
R11		4	3	432	0.704
R11		5	1	432	0.486
R11		5	2	432	0.499
R11		5	3	432	0.338
R11		6	1	672	0.814
R11		6	2	672	0.878
R11		7	1	672	0.185
R11		7	2	672	0.486
R11		8	1	1024	0.743
R11		9	1	1024	0.571
R11		10	1	1024	0.485
R12	collagenase	1	1	1056	0.544
R12		1	2	1056	0.723
R12		2	1	1056	0.546
R12		2	2	1056	0.215
R12		2	3	1056	0.367
R12		3	1	1056	0.541
R12		3	2	1056	0.582
R12		3	3	1056	0.661
R12		4	1	1216	0.516
R12		4	2	1216	0.081
R12		5	1	1392	0.367
R12		5	2	1392	0.424
R12		6	1	1392	0.484
R12		6	2	1392	0.517
R12		6	3	1392	0.534
R12		7	1	1392	0.577
R12		7	2	1392	0.411
R12		8	1	1712	0.411
R12		8	2	1712	0.429
R12		9	1	1712	0.419
R12		9	2	1712	0.209
R12		10	1	2032	0.742
R12		11	1	2528	0.757
R22	collagenase	1	1	512	0.422
R22		1	2	512	0.316
R22		2	1	512	0.434
R22		2	2	512	0.511
R22		3	1	512	0.296
R22		3	2	512	0.554
R22		3	3	512	0.774
R22		3	4	512	0.509
R22		4	1	512	0.140
R22		4	2	512	0.418
R22		5	1	864	0.340
R22		5	2	864	0.282
R24	vehicle	1	1	144	0.273
R24		1	2	144	0.371
R24		2	1	144	0.225
R24		2	2	144	0.488
R24		2	3	144	0.713
R24		3	1	368	0.501
R24		3	2	368	0.718
R24		4	1	368	0.286
R24		4	2	368	0.355
R24		5	1	368	0.401

Note: Table is continued on the next page.

Table D.1. continued

Rat	Group	image no.	ROI	depth (μm)	ani index
R24	vehicle	5	2	368	0.408
R24		6	1	560	0.652
R24		6	2	560	0.416
R24		7	1	1360	0.211
R24		7	2	1360	0.275
R24		8	1	944	0.562
R24		8	2	944	0.570
R24		9	1	944	0.120
R24		9	2	944	0.649
R27	vehicle	1	1	288	0.659
R27		1	2	288	0.452
R27		1	3	288	0.235
R27		2	1	288	0.526
R27		2	2	288	0.330
R27		2	3	288	0.521
R27		3	1	288	0.329
R27		3	2	288	0.485
R27		3	3	288	0.506
R27		4	1	640	0.227
R27		5	1	640	0.451
R27		6	1	944	0.366
R27		6	2	944	0.527
R27		6	3	944	0.542
R27		7	1	944	0.641
R27		7	2	944	0.589
R27		8	1	1184	0.835
R27		8	2	1184	0.697
R27		9	1	1184	0.781
R27		9	2	1184	0.547
R27		10	1	1792	0.155
R32	vehicle	1	1	256	0.786
R32		1	2	256	0.470
R32		1	3	256	0.605
R32		2	1	256	0.434
R32		2	2	256	0.230
R32		3	1	464	0.426
R32		3	2	464	0.233
R32		4	1	464	0.438
R32		4	2	464	0.428
R32		5	1	704	0.644
R32		6	1	704	0.309
R32		6	2	704	0.495
R32		6	3	704	0.284
R32		7	1	1056	0.322
R32		7	2	1056	0.157

Rat	Group	image no.	ROI	depth (μm)	ani index
R33	collagenase	1	1	64	0.574
R33		1	2	64	0.385
R33		1	3	64	0.747
R33		2	1	64	0.107
R33		2	2	64	0.561
R33		3	1	336	0.282
R33		3	2	336	0.419
R33		4	1	336	0.673
R33		4	2	336	0.557
R33		4	3	336	0.654
R33		5	1	624	0.500
R33		5	2	624	0.338
R33		6	1	624	0.403
R33		6	2	624	0.343
R33		6	3	624	0.245
R33		7	1	624	0.213
R33		7	2	624	0.254
R33		8	1	784	0.503
R33		8	2	784	0.510
R33		9	1	784	0.716
R33		9	2	784	0.723
R33		10	1	784	0.331
R33		10	2	784	0.240
R33		10	3	784	0.319
R33		11	1	944	0.077
R33		11	2	944	0.212
R33		12	1	944	0.621
R33		12	2	944	0.625
R33		13	1	1104	0.308
R33		13	2	1104	0.029
R34	collagenase	1	1	400	0.780
R34		1	2	400	0.212
R34		2	1	400	0.457
R34		2	2	400	0.761
R34		2	3	400	0.364
R34		2	4	400	0.724
R34		3	1	400	0.405
R34		3	2	400	0.818
R34		3	3	400	0.634
R34		4	1	864	0.139
R34		4	2	864	0.907
R34		5	1	864	0.384
R34		5	2	864	0.501
R34		5	3	864	0.461
R34		6	1	1296	0.603

Note: Table is continued on the next page.

Table D.1. continued

Rat	Group	image no.	ROI	depth (μm)	ani index
R34	collagenase	6	2	1296	0.523
R443	naïve	1	1	1264	0.520
R443		1	2	1264	0.329
R443		1	3	1264	0.433
R443		2	1	1280	0.584
R443		2	2	1280	0.786
R443		3	1	1296	0.561
R443		3	2	1296	0.501
R444	naive	1	1	1312	0.662
R444		1	2	1312	0.726
R444		1	3	1312	0.533
R444		2	1	1328	0.245
R444		2	2	1328	0.091
R444		3	1	1376	0.344
R444		3	2	1376	0.169

Figure D.1. Picrosirius Red/Alcian Blue stained capsular ligaments injected with bacterial collagenase or vehicle as designated in Table D.1 (Chapter 4)

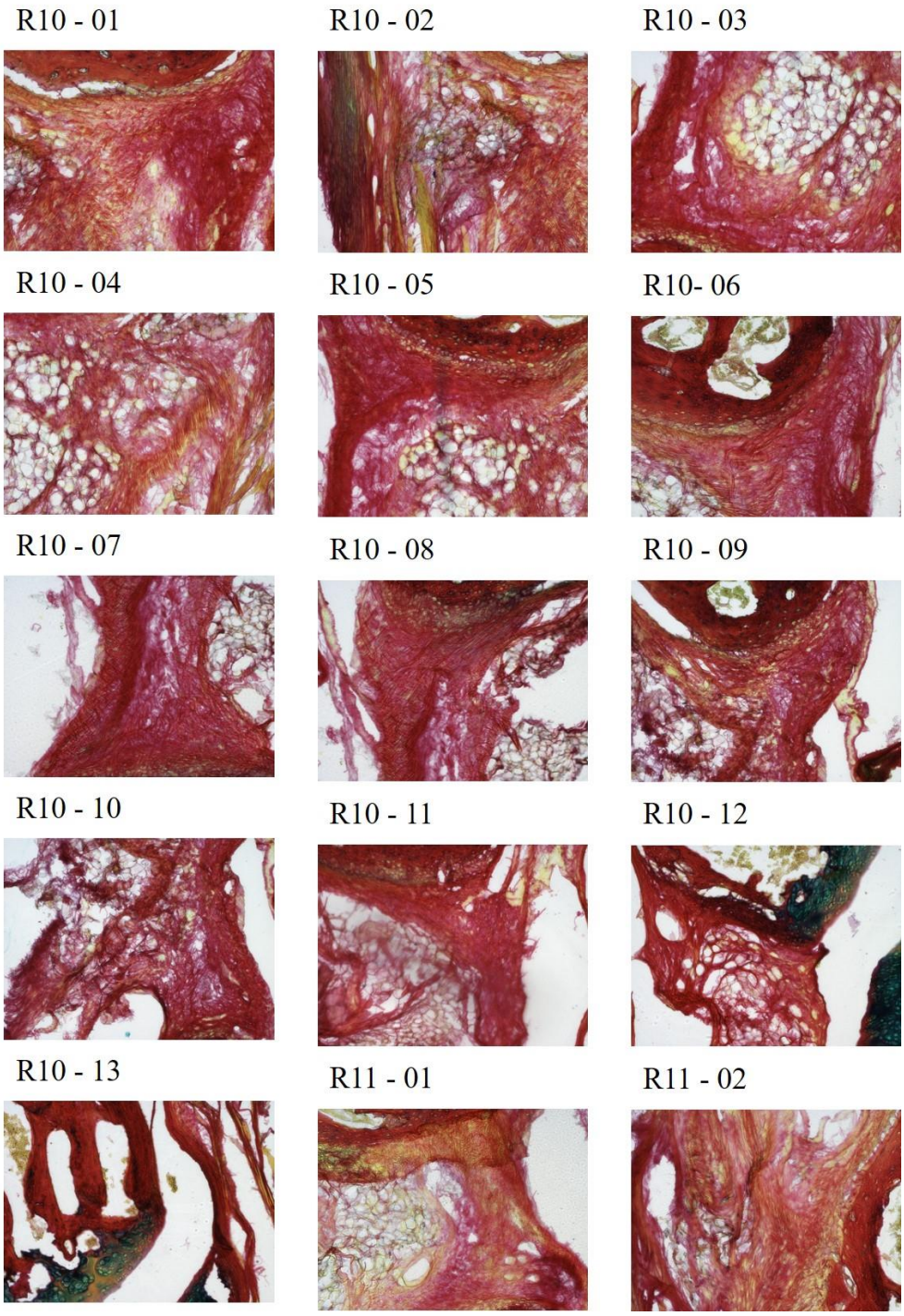

Note: Figure is continued on the next page.

Figure D.1. continued

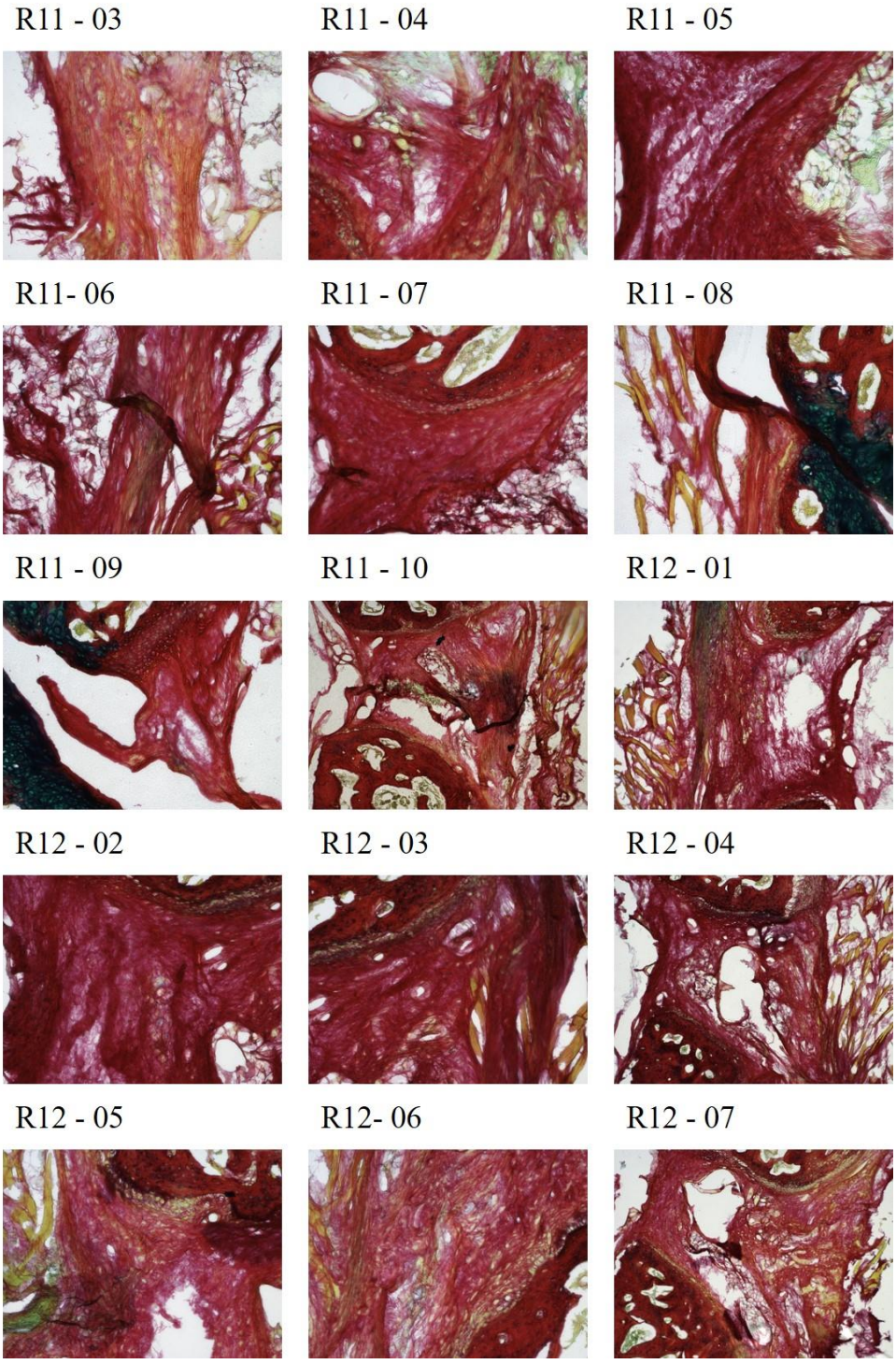

Note: Figure is continued on the next page.

Figure D.1. continued

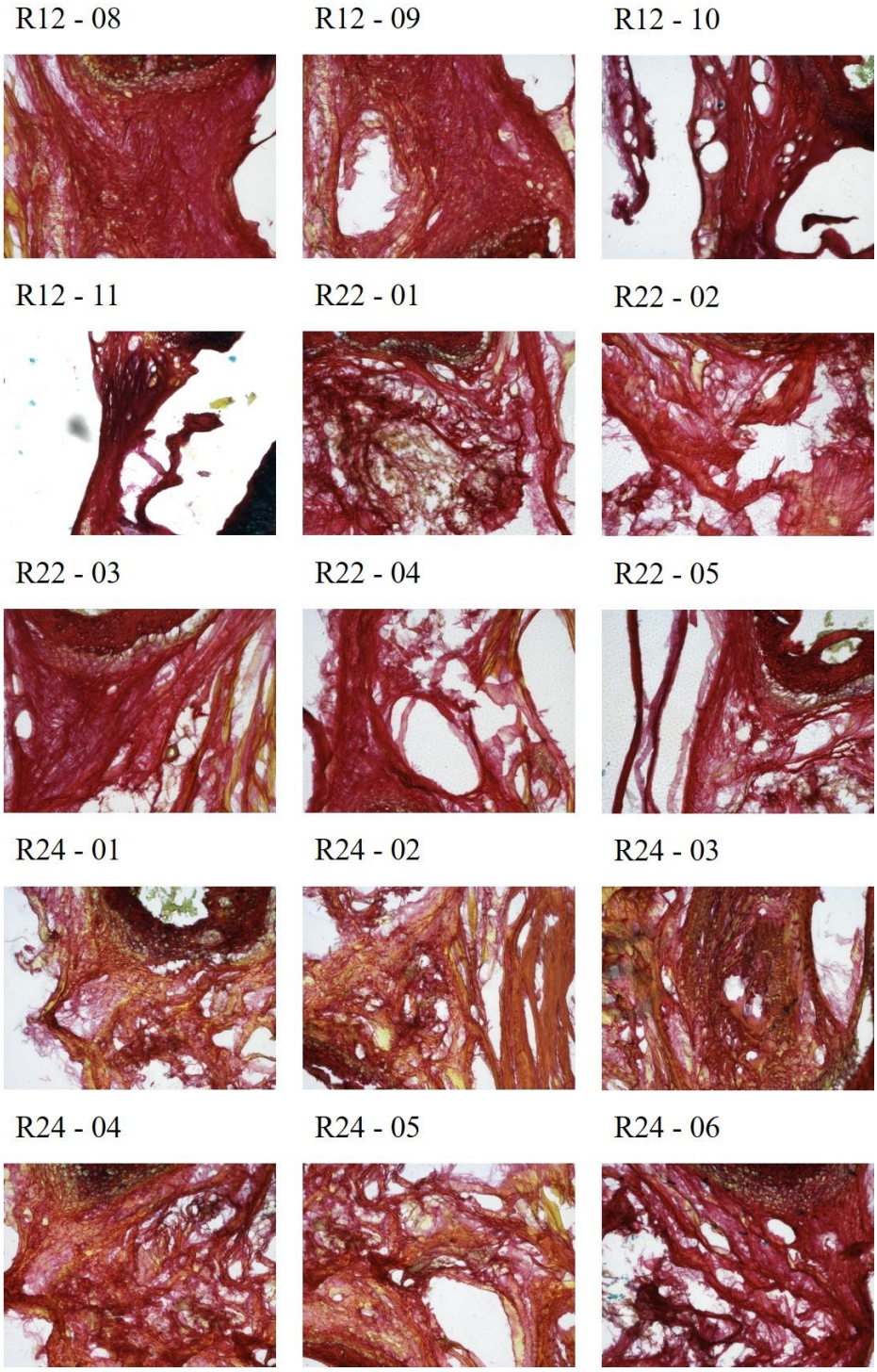

Note: Figure is continued on the next page.

Figure D.1. continued

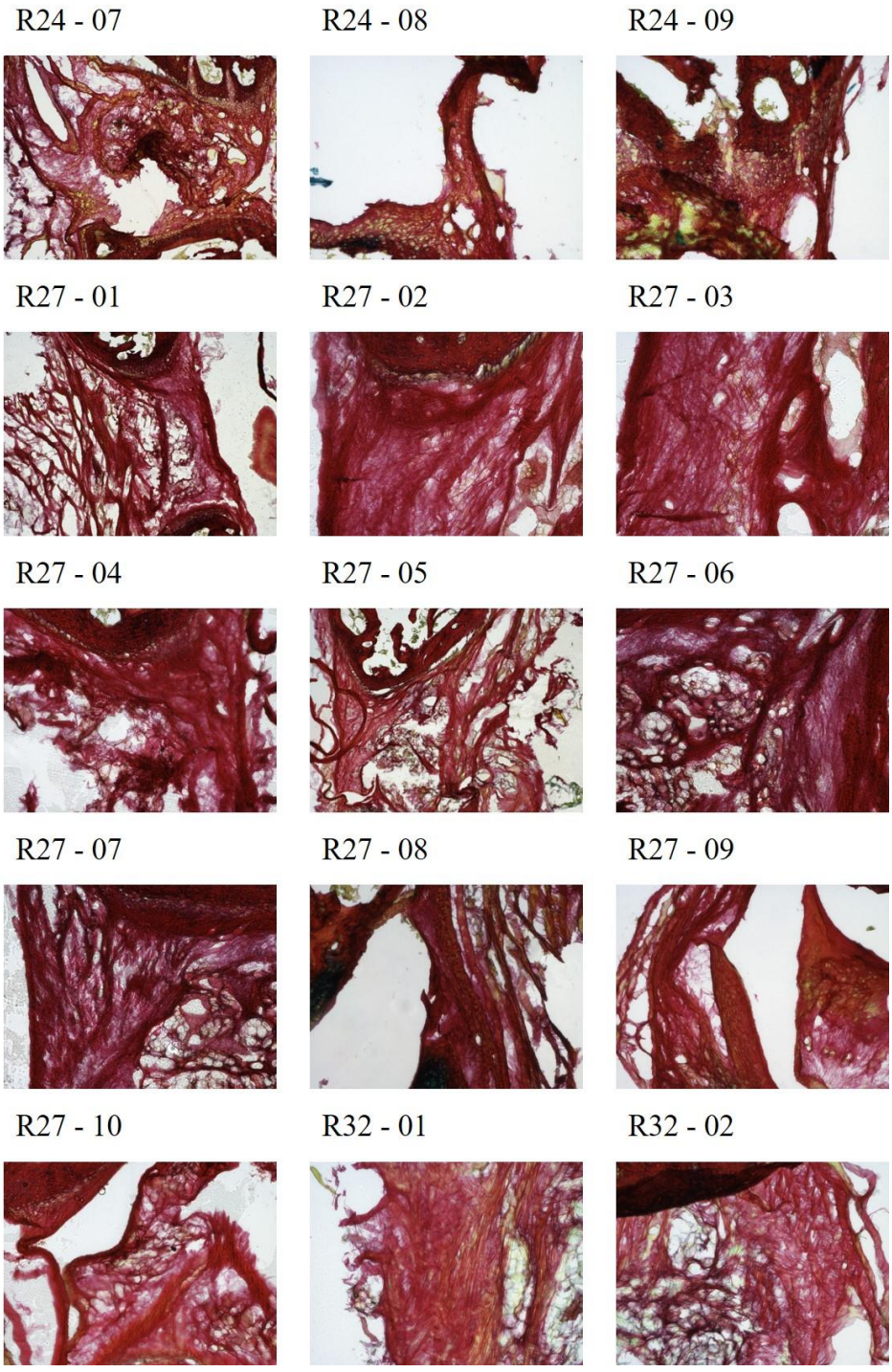

Note: Figure is continued on the next page.

Figure D.1. continued

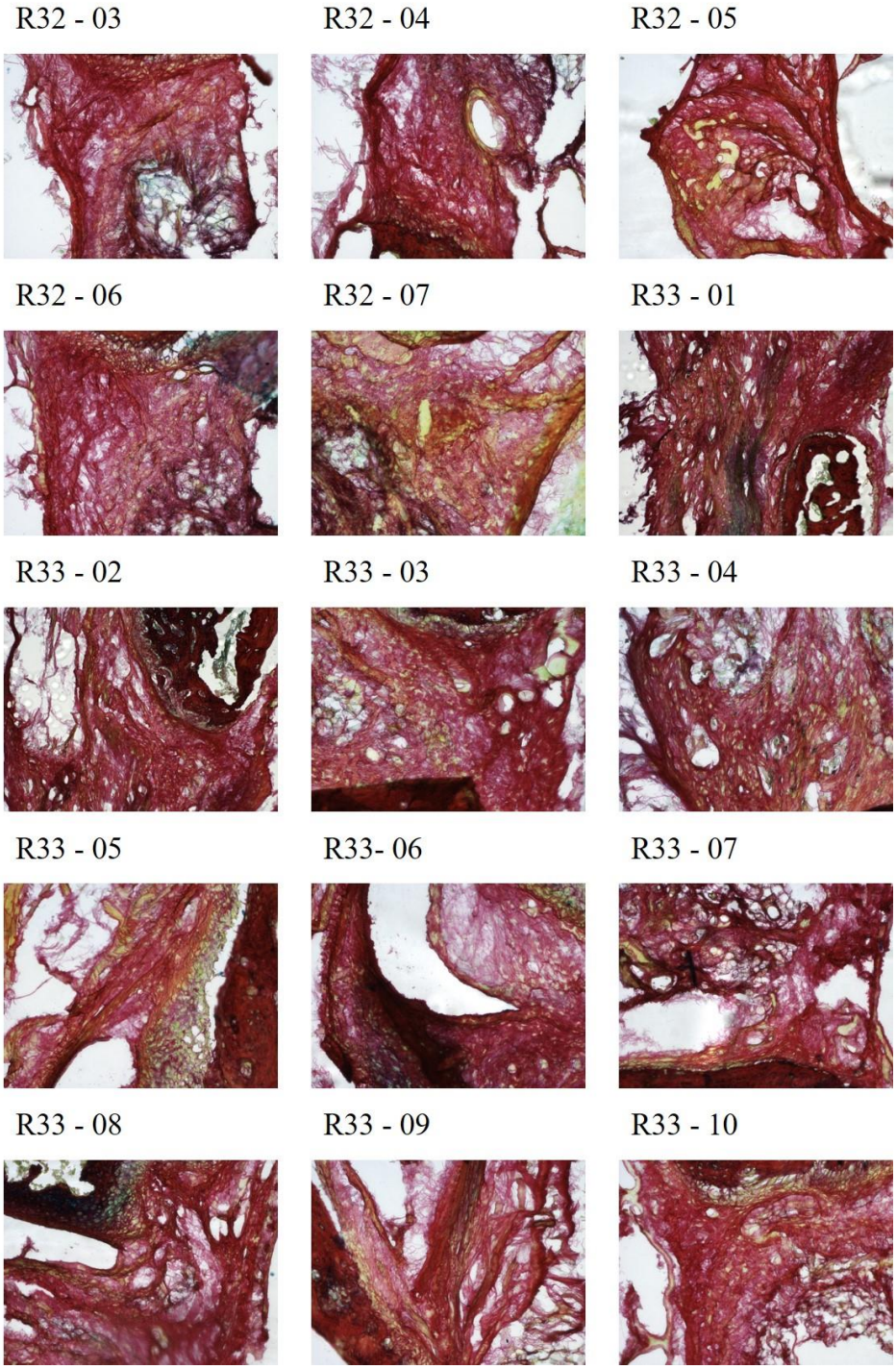

Note: Figure is continued on the next page.

Figure D.1. continued

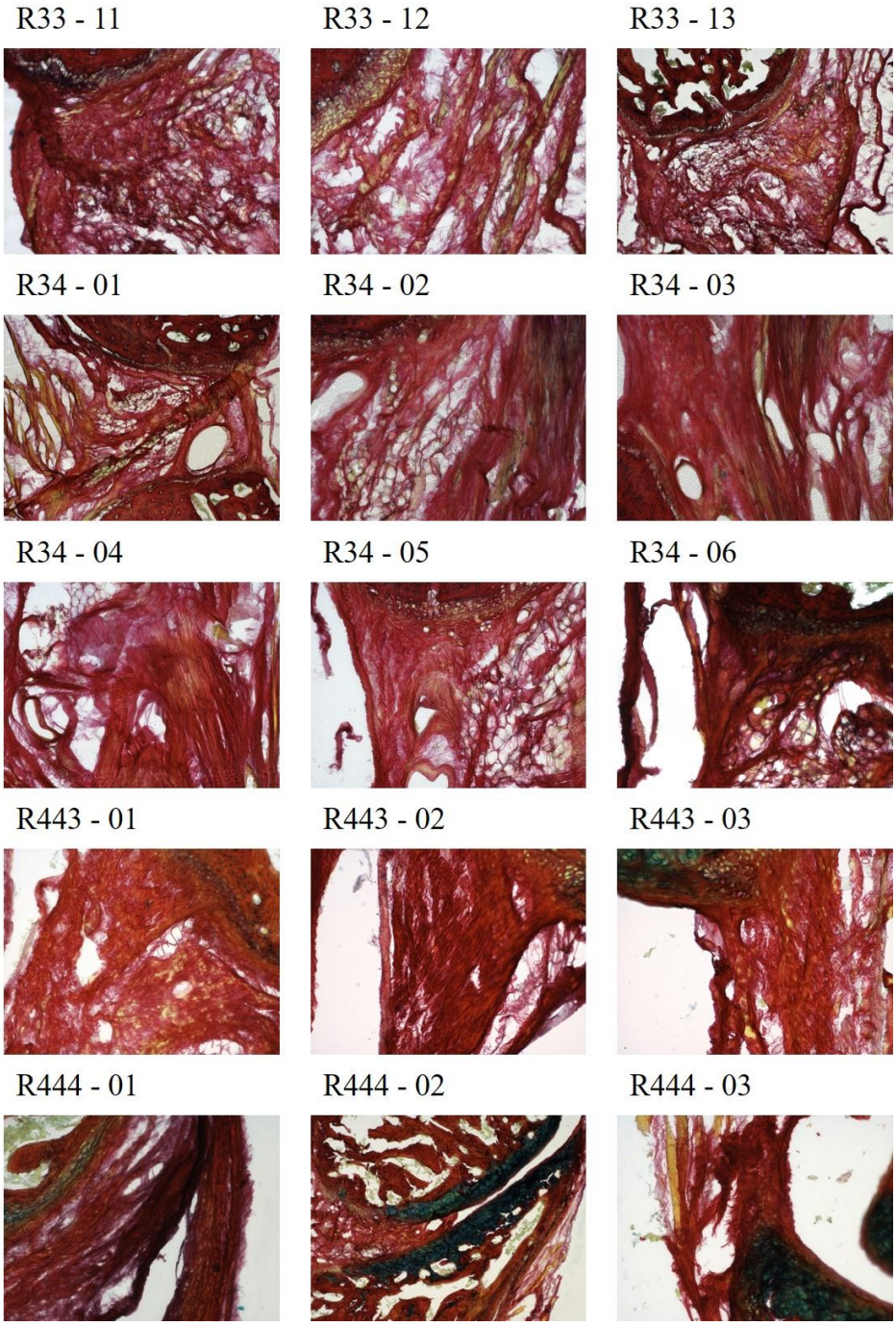

Table D.2. Mankin score assigned from Safranin O/Fast Green stained facet joints injected with bacterial collagenase or vehicle (Chapter 4)

Rat	Group	image no.	Mankin score	articular surface	grader
R10	collagenase	1	3	bottom	PG
R10		1	5	top	PG
R10		1	1	bottom	RW
R10		1	2	top	RW
R10		2	4	bottom	PG
R10		2	4	top	PG
R10		2	1	bottom	RW
R10		2	4	top	RW
R10		3	2	bottom	PG
R10		3	2	top	PG
R10		3	1	bottom	RW
R10		3	0	top	RW
R10		4	2	bottom	PG
R10		4	4	top	PG
R10		4	0	bottom	RW
R10		4	4	top	RW
R11	collagenase	1	4	bottom	PG
R11		1	4	top	PG
R11		1	0	bottom	RW
R11		1	5	top	RW
R11		2	5	bottom	PG
R11		2	5	top	PG
R11		2	1	bottom	RW
R11		2	2	top	RW
R11		3	2	bottom	PG
R11		3	6	top	PG
R11		3	1	bottom	RW
R11		3	3	top	RW
R12	collagenase	1	6	top	PG
R12		1	4	top	RW
R12		2	2	bottom	PG
R12		2	2	top	PG
R12		2	1	bottom	RW
R12		2	0	top	RW
R12		3	5	bottom	PG
R12		3	3	top	PG
R12		3	1	bottom	RW
R12		3	2	top	RW
R12		4	2	bottom	PG
R12		4	4	top	PG
R12		4	1	bottom	RW
R12		4	3	top	RW
R22	collagenase	1	6	top	PG
R22		1	2	top	RW
R22		2	5	top	PG
R22		2	3	bottom	RW
R22		3	5	top	PG
R22		3	3	top	RW
R24	vehicle	1	7	bottom	PG
R24		1	7	top	PG
R24		1	3	bottom	RW
R24		1	3	top	RW
R24		2	6	bottom	PG
R24		2	7	bottom	RW
R24		3	6	top	PG
R24		3	2	top	RW
R24		4	2	bottom	PG
R24		4	2	top	PG
R24		4	3	bottom	RW
R24		4	3	top	RW
R24	vehicle	5	6	bottom	PG
R24		5	6	top	PG
R24		5	1	bottom	RW
R24		5	4	top	RW
R24		6	4	bottom	PG
R24		6	4	top	PG
R24		6	2	bottom	RW
R24		6	1	top	RW
R24		7	4	bottom	PG
R24		7	4	top	PG
R24		7	1	bottom	RW
R24		7	3	top	RW
R27	vehicle	1	3	bottom	PG
R27		1	0	top	PG
R27		1	3	bottom	RW
R27		1	1	top	RW
R27		2	5	bottom	PG
R27		2	1	bottom	RW
R32	vehicle	1	5	bottom	PG
R32		1	6	top	PG
R32		1	1	bottom	RW
R32		1	3	top	RW
R32		2	5	bottom	PG
R32		2	4	top	PG
R32		2	5	bottom	RW
R32		2	6	top	RW
R32		3	6	bottom	PG
R32		3	5	top	PG
R32		3	2	bottom	RW
R32		3	1	top	RW
R32		4	2	bottom	PG
R32		4	3	top	PG
R32		4	2	bottom	RW
R32		4	2	top	RW
R33	collagenase	1	4	bottom	PG
R33		1	4	top	PG
R33		1	0	bottom	RW
R33		1	3	top	RW
R33		2	4	bottom	PG
R33		2	4	top	PG

RW: Rachel Welch; PG: Prabesh Ghimire

Note: Table is continued on the next page.

Table D.2. continued

Rat	Group	image no.	Mankin score	articular surface	grader
R33	collagenase	2	2	bottom	RW
R33		2	2	top	RW
R33		3	2	bottom	PG
R33		3	4	top	PG
R33		3	0	bottom	RW
R33		3	3	top	RW
R33		4	2	bottom	PG
R33		4	2	top	PG
R33		4	0	bottom	RW
R33		4	3	top	RW
R33		5	2	bottom	PG
R33		5	2	top	PG
R33		5	0	bottom	RW
R33		5	1	top	RW
R33		6	2	bottom	PG
R33		6	2	top	PG
R33		6	2	bottom	RW
R33		6	3	top	RW
R33		7	1	bottom	PG
R33		7	2	top	PG
R33		7	0	bottom	RW
R33		7	2	top	RW
R33		8	2	bottom	PG
R33		8	2	top	PG
R33		8	2	bottom	RW
R33		8	2	top	RW
R34	collagenase	1	2	bottom	PG
R34		1	2	top	PG
R34		1	2	bottom	RW
R34		1	2	top	RW
R34		2	2	top	PG
R34		2	1	bottom	RW
R34		3	6	top	PG
R34		3	1	top	RW
R34		4	2	bottom	PG
R34		4	2	top	PG
R34		4	0	bottom	RW
R34		4	4	top	RW
R34		5	4	bottom	PG
R34		5	6	top	PG
R34		5	0	bottom	RW
R34		5	1	top	RW
R443	naive	1	2	bottom	PG
R443		1	2	top	PG
R443		1	3	bottom	RW
R443		1	2	top	RW
R443		2	1	bottom	PG
R443		2	1	top	PG
R443		2	2	bottom	RW
R443		2	2	top	RW
R443	naive	3	2	bottom	PG
R443		3	2	top	PG
R443		3	2	bottom	RW
R443		3	3	top	RW
R443		4	3	bottom	PG
R443		4	3	top	PG
R443		4	2	bottom	RW
R443		4	2	top	RW
R444	naive	1	1	bottom	PG
R444		1	1	top	PG
R444		1	2	bottom	RW
R444		1	3	top	RW
R444		2	3	bottom	PG
R444		2	3	top	PG
R444		2	1	bottom	RW
R444		2	1	top	RW
R444		3	4	bottom	PG
R444		3	4	top	PG
R444		3	1	bottom	RW
R444		3	2	top	RW
R444		4	4	bottom	PG
R444		4	4	top	PG
R444		4	2	bottom	RW
R444		4	5	top	RW

RW: Rachel Welch; PG: Prabesh Ghimire

Figure D.2. Safranin O/Fast Green stained facet joints injected with bacterial collagenase or vehicle as designated in Table D.2 (Chapter 4)

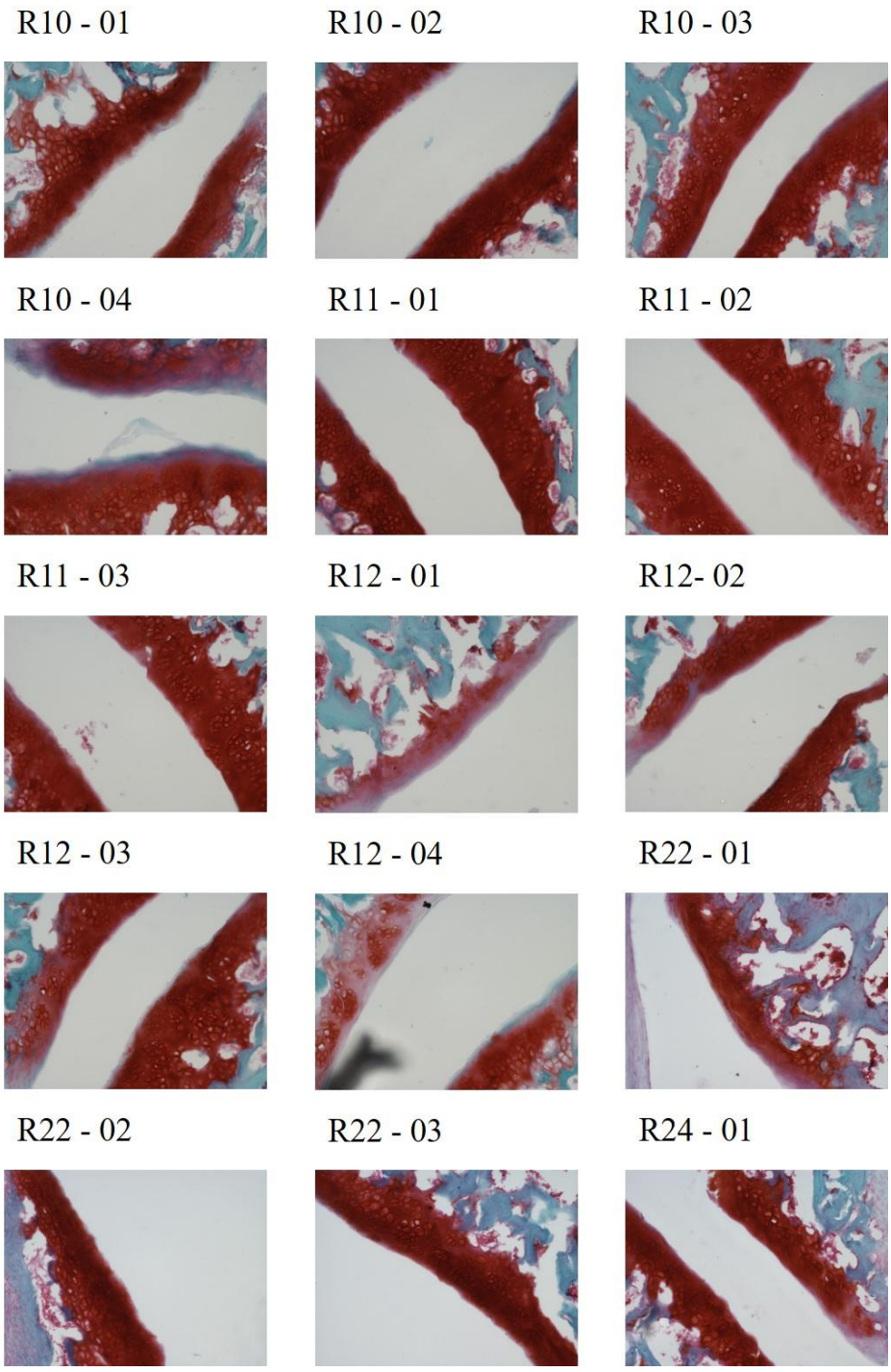

Note: Figure is continued on the next page.

Figure D.2. continued

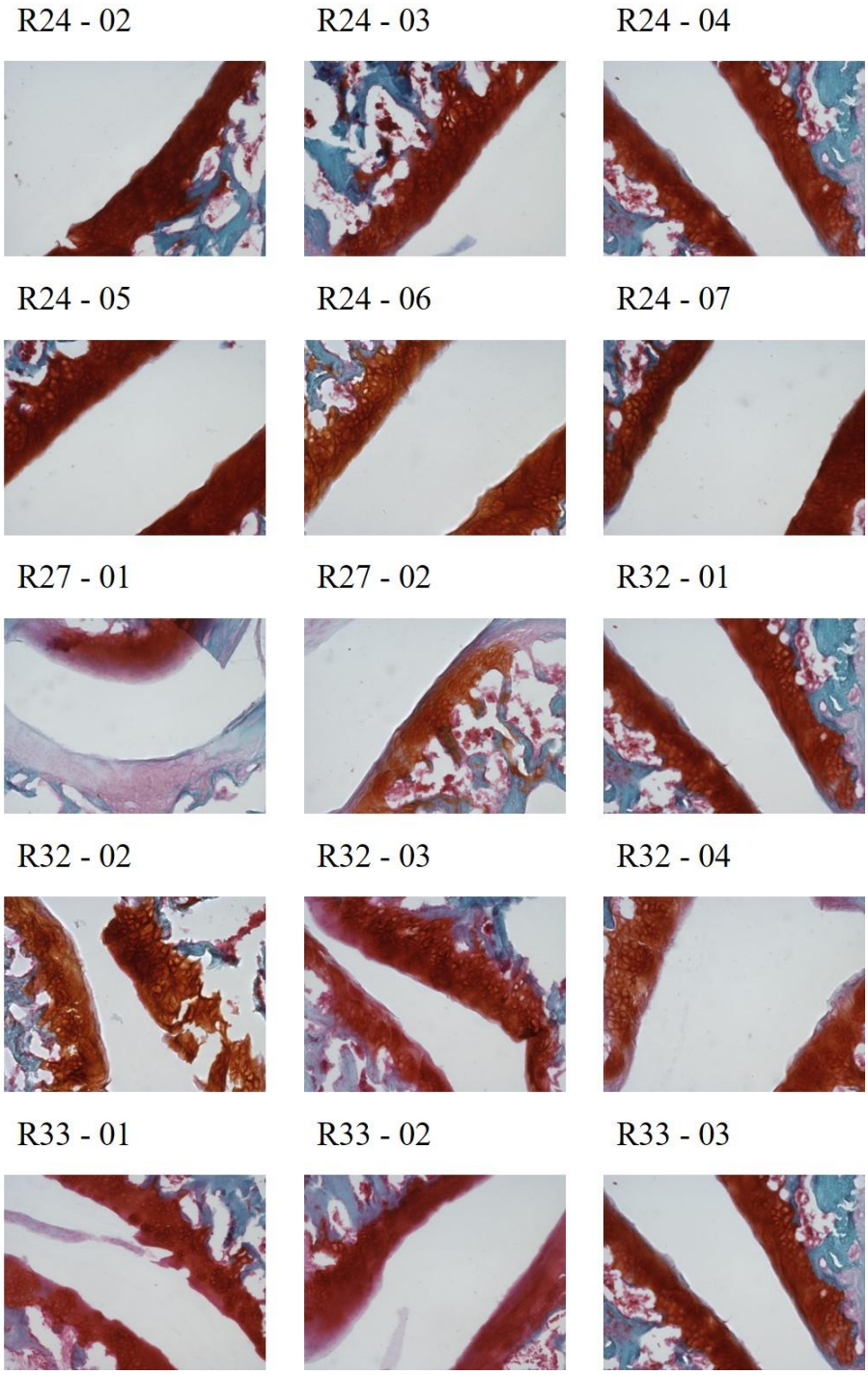

Note: Figure is continued on the next page.

Figure D.2. continued

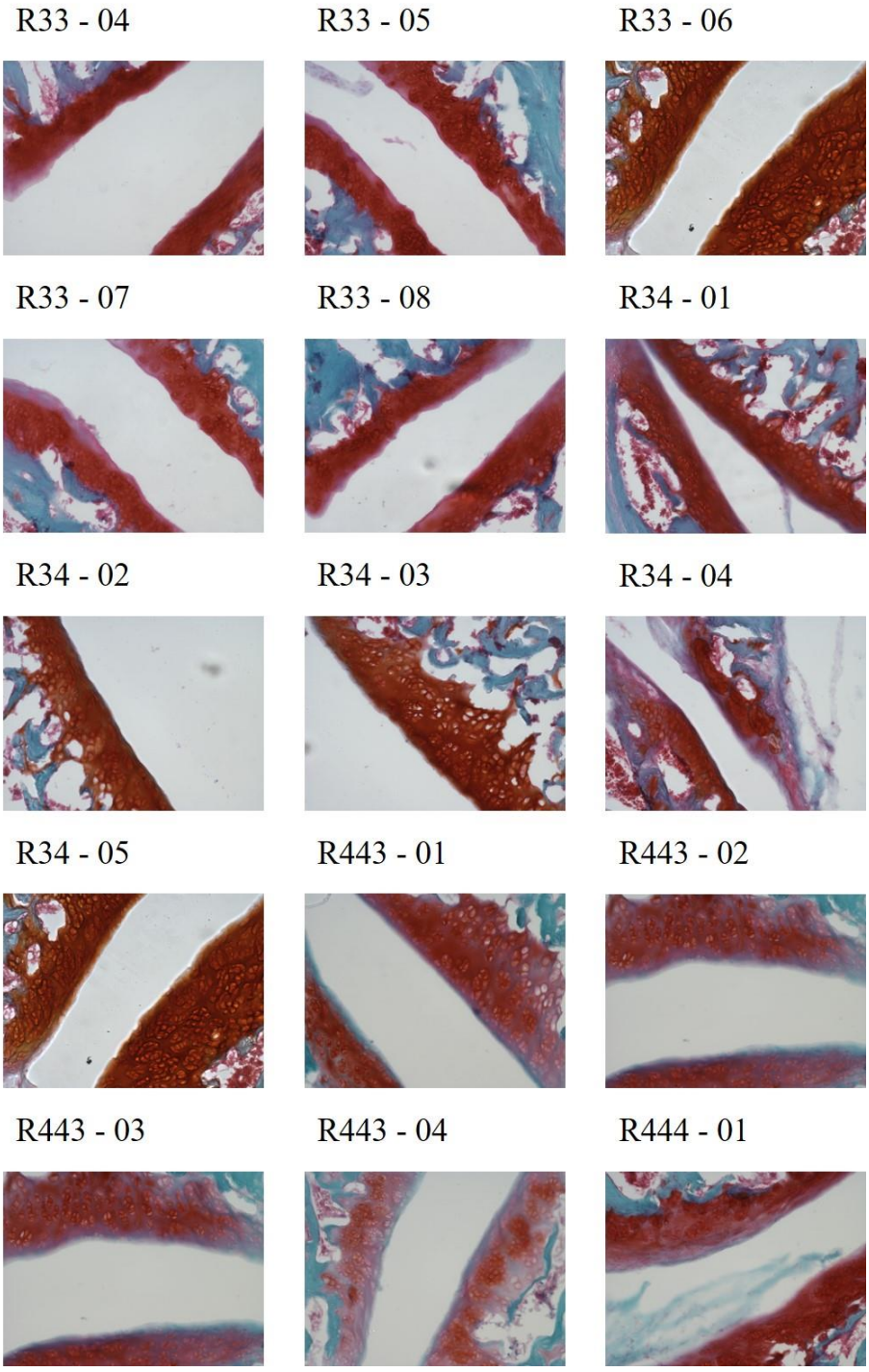

Note: Figure is continued on the next page.

Figure D.2. continued

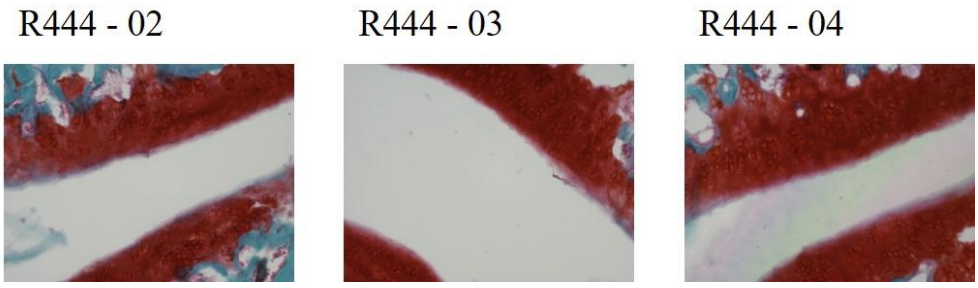

Table D.3. Percent positive chondrocytes for HIF-1α expression in bacterial collagenase or vehicle-injected facet joints (Chapter 4)

Rat	Group	image no.	% positive cells
R10	collagenase	1	90.48%
R10		2	61.11%
R10		3	45.95%
R10		4	65.38%
R10		5	60.00%
R11	collagenase	1	44.09%
R11		2	48.45%
R11		3	63.64%
R11		4	91.26%
R11		5	83.81%
R12	collagenase	1	55.65%
R12		2	59.12%
R12		3	2.56%
R12		4	70.19%
R12		5	49.38%
R22	collagenase	1	10.29%
R22		2	59.29%
R22		3	14.68%
R22		4	36.84%
R22		5	33.33%
R24	collagenase	1	74.50%
R27	collagenase	1	89.19%
R27		2	80.49%
R27		3	31.34%
R27		4	20.95%
R27		5	70.11%
R32	vehicle	1	57.00%
R32		2	59.30%
R32		3	40.19%
R32		4	40.78%
R32		5	22.62%
R33	collagenase	1	63.33%
R33		2	70.27%
R33		3	52.80%
R33		4	38.64%
R33		5	51.12%
R34	collagenase	1	25.20%
R34		2	61.47%
R34		3	8.11%
R34		4	21.67%
R34		5	0.00%
R41	naive	1	18.63%
R41		2	0.00%
R41		3	0.00%
R41		4	61.36%
R41		5	16.53%
R41A	naive	1	51.82%
R41A		2	30.46%
R41A		3	57.28%
R41A		4	18.02%
R41A	naive	5	24.14%
R64	naive	1	43.93%
R64		2	35.96%
R64		3	3.25%
R64		4	11.86%
R64		5	0.00%

Figure D.3. HIF-1α immunolabeling in chondrocytes of the articular cartilage of bacterial collagenase or vehicle-injected facet joints as designated in Table D.3 (Chapter 4)

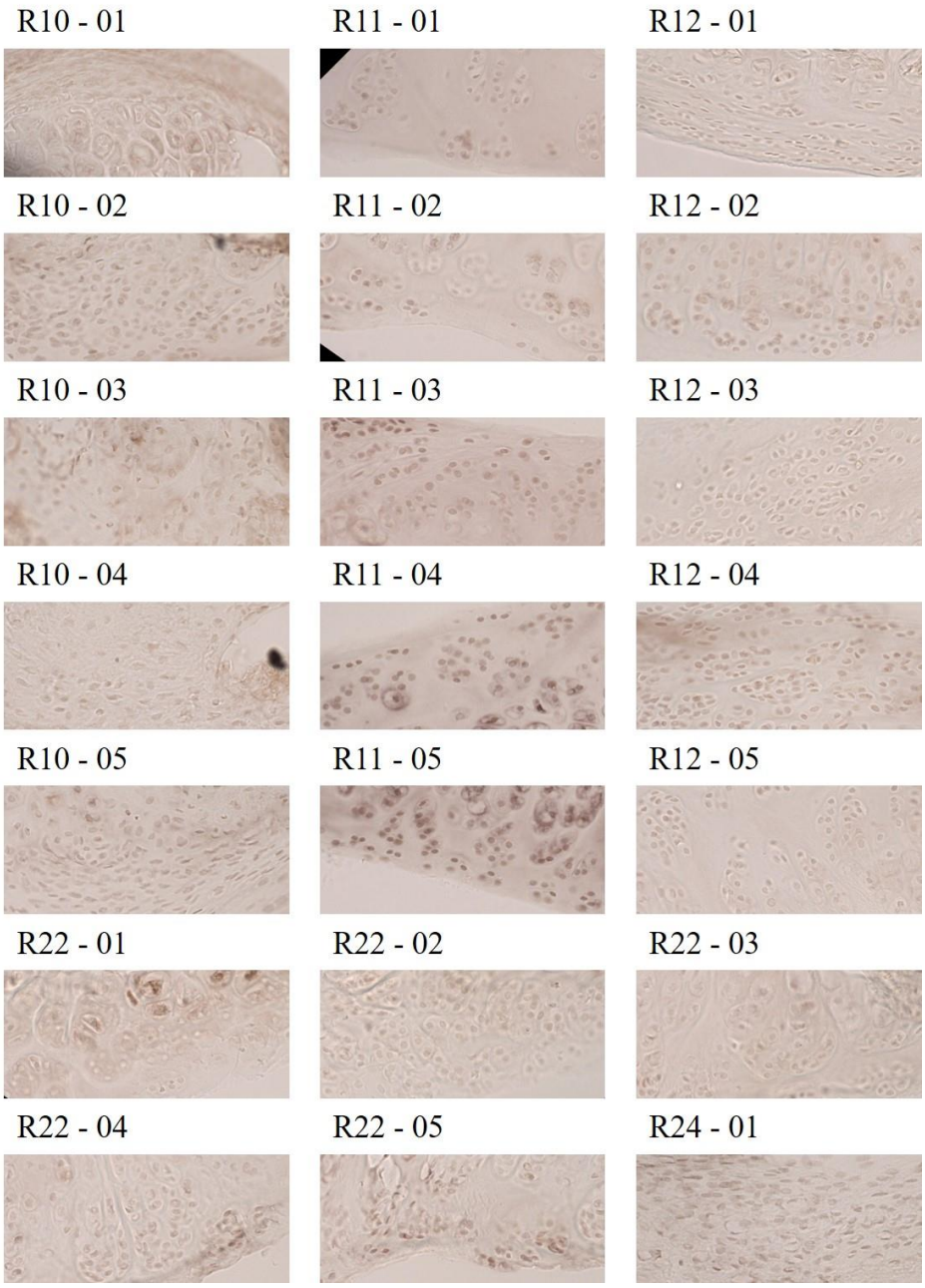

Note: Figure is continued on the next page.

Figure D.3. continued

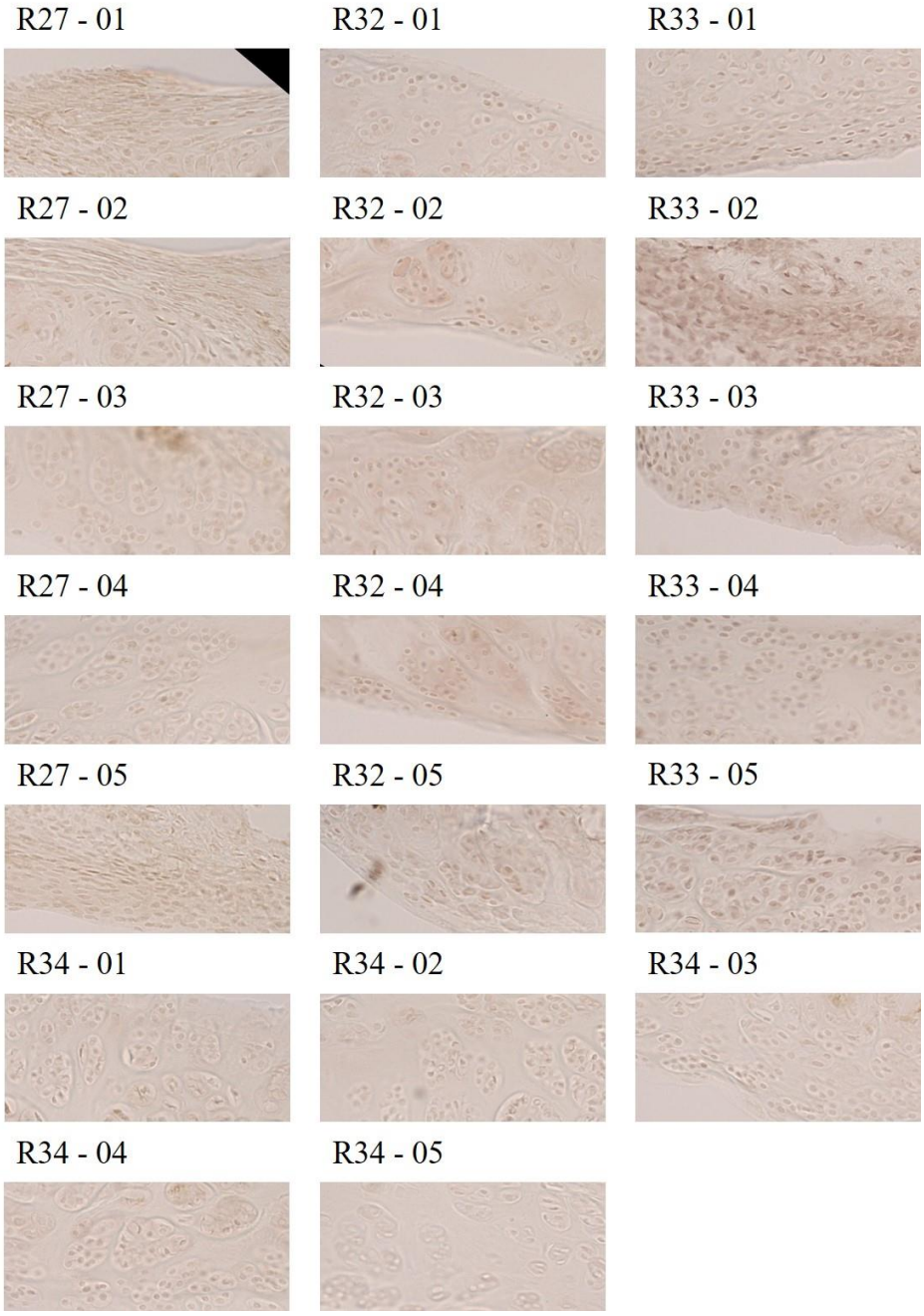

Note: Figure is continued on the next page.

Figure D.3. continued

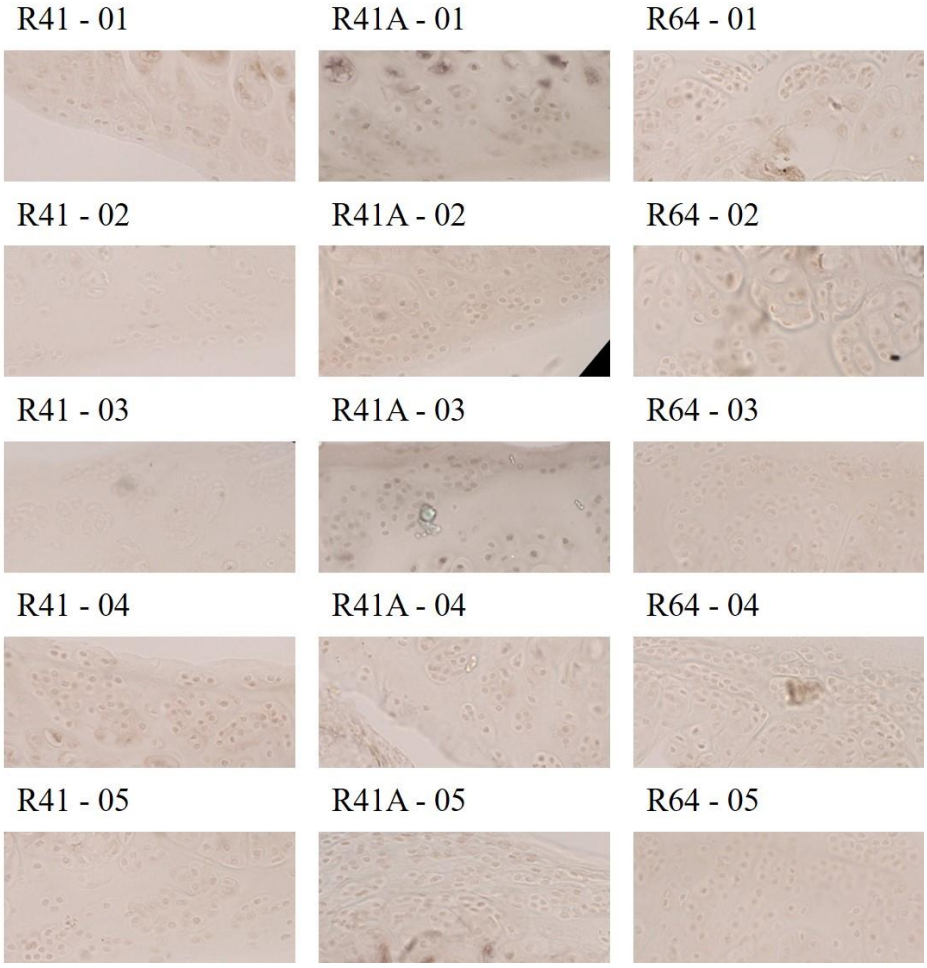

Table D.4. Anisotropy (ani) indices computed from Picrosirius Red/Alcian Blue stained capsular ligaments injected with MMP-1 or vehicle (Chapter 7)

Rat	Group	image no.	ROI	depth (μm)	ani index
R20	MMP-1	1	1	368	0.768
R20		1	2	368	0.756
R20		1	3	368	0.546
R20		2	1	624	0.143
R20		2	2	624	0.463
R20		2	3	624	0.456
R20		3	1	992	0.324
R20		3	2	992	0.534
R20		3	3	992	0.401
R21	MMP-1	1	1	112	0.391
R21		1	2	112	0.214
R21		1	3	112	0.131
R21		2	1	112	0.756
R21		2	2	112	0.647
R21		3	1	750	0.360
R21		3	2	750	0.176
R21		3	3	750	0.711
R21		4	1	1624	0.376
R21		4	2	1624	0.418
R21		5	1	1624	0.689
R21		5	2	1624	0.630
R37	MMP-1	1	1	464	0.349
R37		1	2	464	0.412
R37		1	3	464	0.510
R37		2	1	720	0.177
R37		2	2	720	0.668
R37		2	3	720	0.611
R37		3	1	944	0.191
R37		3	2	944	0.320
R37		3	3	944	0.362
R37		4	1	1504	0.345
R37		4	2	1504	0.803
R38	MMP-1	1	1	176	0.030
R38		1	2	176	0.441
R38		1	3	176	0.396
R38		1	4	176	0.056
R38		2	1	176	0.447
R38		2	2	176	0.335
R38		2	3	176	0.410
R38		3	1	176	0.360
R38		3	2	176	0.583
R38		4	1	724	0.404
R38		4	2	724	0.384
R38		4	3	724	0.422
R38		5	1	724	0.469
R38		5	2	724	0.346
R38		6	1	1602	0.702
R38		6	2	1602	0.529
R42	vehicle	1	1	192	0.331
R42		1	2	192	0.649
R42		1	3	192	0.442
R42		2	1	192	0.780
R42		2	2	192	0.421
R42		2	3	192	0.506
R42		2	4	192	0.304
R42		3	1	400	0.654
R42		3	2	400	0.223
R42		4	1	400	0.372
R42		4	2	400	0.669
R42		4	3	400	0.847
R42		5	1	400	0.435
R42		5	2	400	0.719
R42		6	1	592	0.291
R42		6	2	592	0.140
R42		6	3	592	0.579
R42		7	1	592	0.146
R42		7	2	592	0.645
R42		7	3	592	0.608
R42		8	1	848	0.100
R42		8	2	848	0.221
R42		9	1	848	0.824
R42		9	2	848	0.525
R43	vehicle	1	1	144	0.692
R43		1	2	144	0.720
R43		2	1	144	0.728
R43		2	2	144	0.414
R43		3	1	144	0.724
R43		3	2	144	0.530
R43		3	3	144	0.394
R43		4	1	400	0.579
R43		4	2	400	0.245
R43		4	3	400	0.429
R43		5	1	400	0.565
R43		5	2	400	0.418
R43		5	3	400	0.334
R43		6	1	1040	0.495
R43		6	2	1040	0.496
R43		7	1	1264	0.323
R45	vehicle	1	1	192	0.651
R45		1	2	192	0.433
R45		1	3	192	0.417
R45		1	4	192	0.464
R45		2	1	192	0.542
R45		2	2	192	0.255
R45		2	3	192	0.095
R45		2	4	192	0.143
R45		3	1	192	0.267
R45		3	2	192	0.487
R45		3	3	192	0.213
R45		4	1	444	0.472

Note: Table is continued on the next page.

Table D.4. continued

Rat	Group	image no.	ROI	depth (μm)	ani index
R45	vehicle	4	2	444	0.675
R45		4	3	444	0.222
R45		5	1	444	0.500
R45		5	2	444	0.199
R45		5	3	444	0.279
R45		5	4	444	0.496
R45		6	1	864	0.383
R45		6	2	864	0.311
R45		6	3	864	0.557
R45		7	1	864	0.407
R45		7	2	864	0.449
R45		7	3	864	0.191
R52	vehicle	1	1	384	0.721
R52		1	2	384	0.717
R52		1	3	384	0.707
R52		1	4	384	0.178
R52		2	1	384	0.678
R52		2	2	384	0.540
R52		2	3	384	0.396
R52		3	1	384	0.246
R52		3	2	384	0.369
R52		3	3	384	0.445
R52		3	4	384	0.248
R52		4	1	640	0.730
R52		4	2	640	0.330
R52		4	3	640	0.544
R52		4	4	640	0.563
R52		5	1	640	0.165
R52		5	2	640	0.706
R52		5	3	640	0.564
R52		6	1	640	0.686
R52		7	1	992	0.385
R52		7	2	992	0.726
R52		8	1	1424	0.723
R52		8	2	1424	0.736
R53	vehicle	1	1	160	0.406
R53		1	2	160	0.672
R53		1	3	160	0.525
R53		2	1	160	0.712
R53		2	2	160	0.368
R53		2	3	160	0.239
R53		3	1	432	0.366
R53		4	1	432	0.761
R53		4	2	432	0.221
R53		4	3	432	0.718
R53		5	1	432	0.200
R53		5	2	432	0.352
R53		5	3	432	0.703
R53		6	1	432	0.676
R53		6	2	432	0.727

Rat	Group	image no.	ROI	depth (μm)	ani index
R53	vehicle	6	3	432	0.643
R53		7	1	912	0.359
R53		7	2	912	0.588
R53		7	3	912	0.702
R53		8	1	1120	0.603
R53		8	1	1120	0.712
R53		8	2	1120	0.556
R443	naive	1	1	1264	0.520
R443		1	2	1264	0.329
R443		1	3	1264	0.433
R443		2	1	1280	0.584
R443		2	2	1280	0.786
R443		3	1	1296	0.561
R443		3	2	1296	0.501
R444	naive	1	1	1312	0.662
R444		1	2	1312	0.726
R444		1	3	1312	0.533
R444		2	1	1328	0.245
R444		2	2	1328	0.091
R444		3	1	1376	0.344
R444		3	2	1376	0.169

Figure D.4. Picrosirius Red/Alcian Blue stained capsular ligaments injected with MMP-1 or vehicle as designated in Table D.4 (Chapter 7)

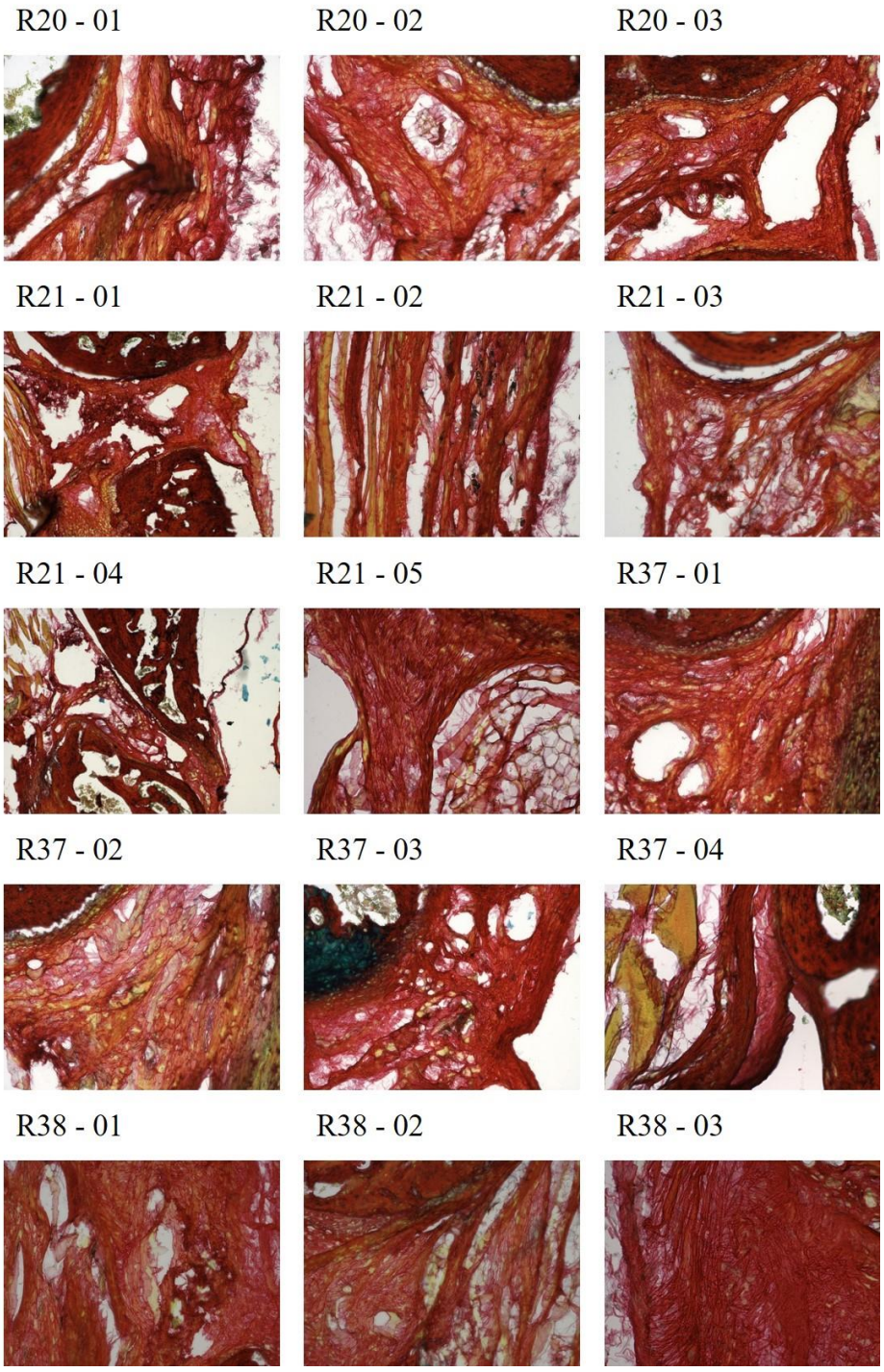

Note: Figure is continued on the next page.

Figure D.4. continued

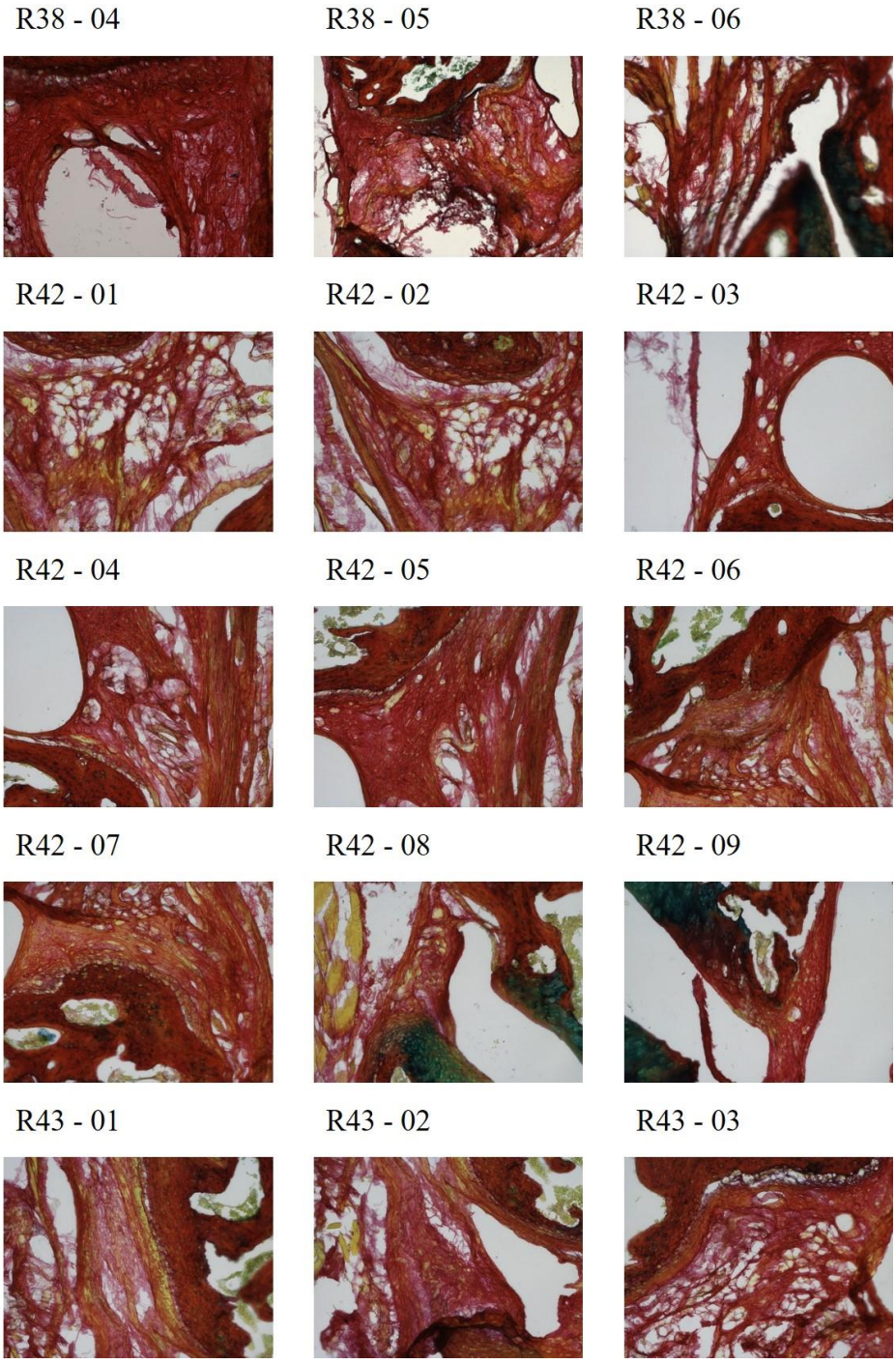

Note: Figure is continued on the next page.

Figure D.4. continued

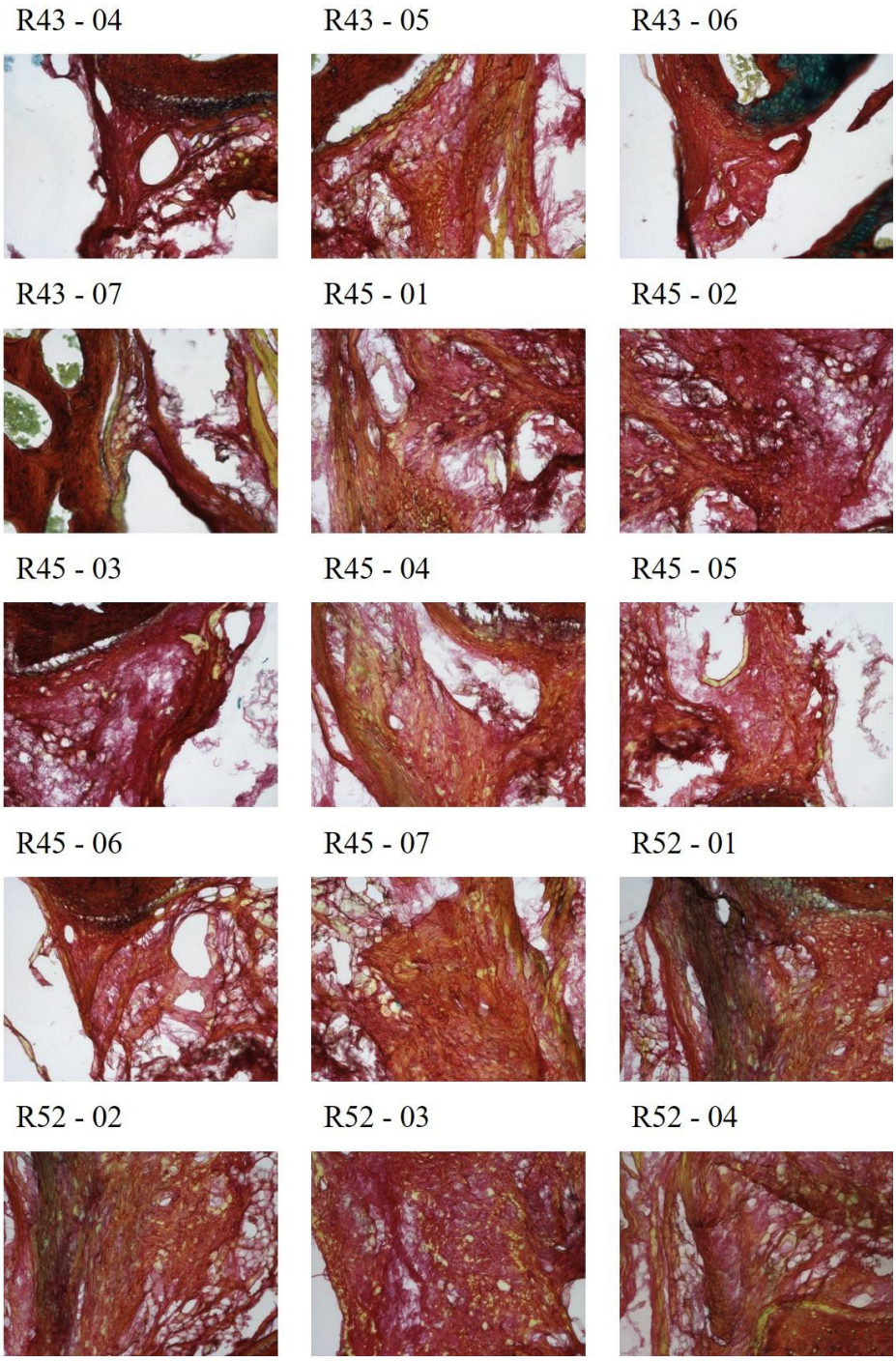

Note: Figure is continued on the next page.

Figure D.4. continued

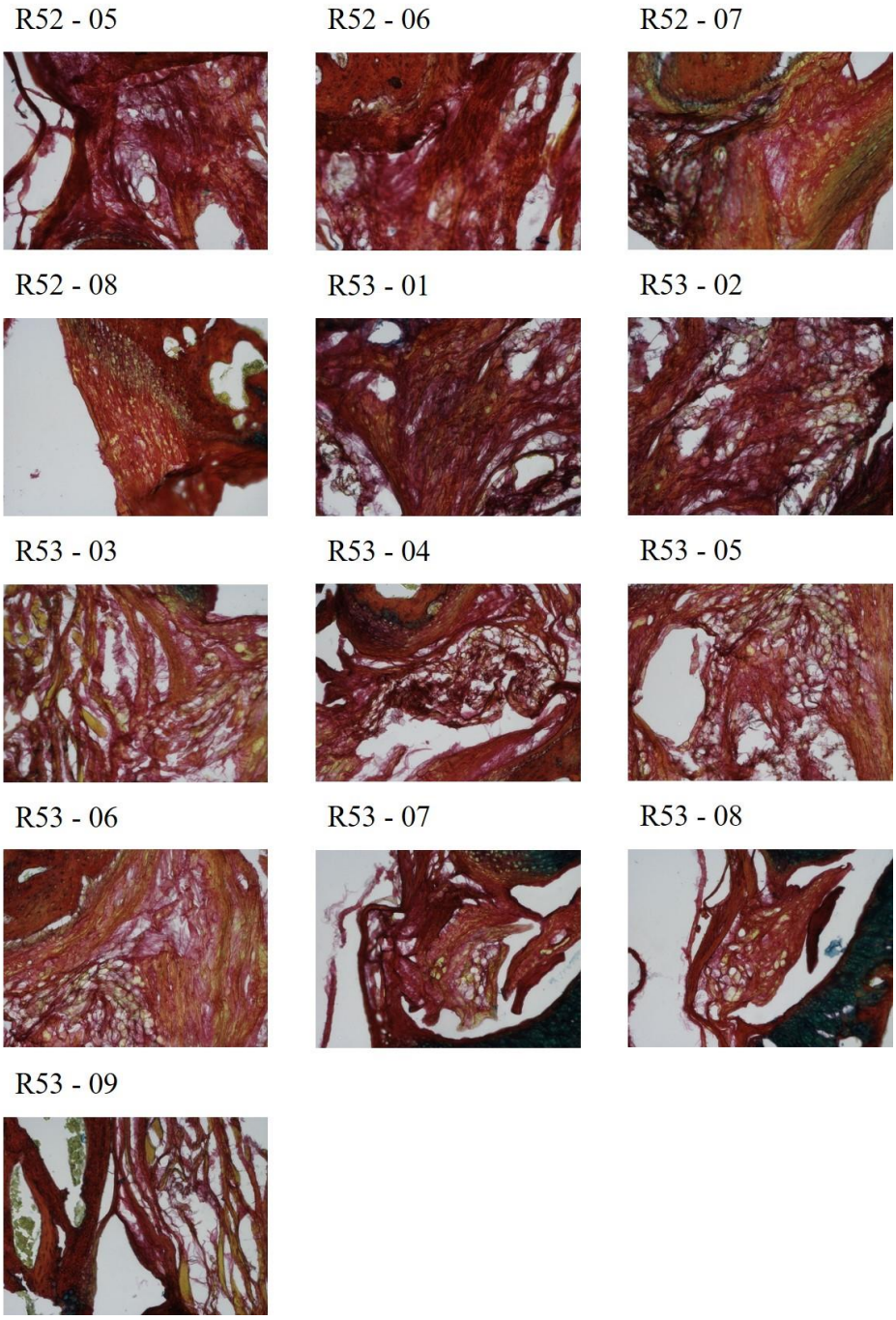

Note: Figure is continued on the next page.

Figure D.4. continued

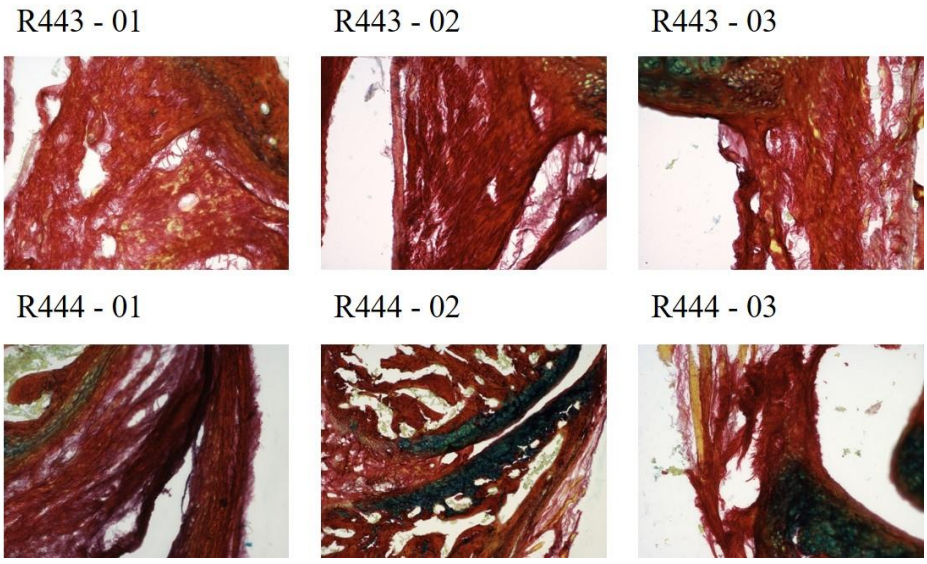

Table D.5. Mankin score assigned from Safranin O/Fast Green stained facet joints injected with MMP-1 or vehicle (Chapter 7)

Rat	Group	image no.	Mankin score	articular surface
R20	MMP-1	1	3	top
R20		2	4	top
R20		3	3	bottom
R21		1	2	top
R21	MMP-1	2	0	bottom
R21		3	1	bottom
R37		1	5	bottom
R37	MMP-1	1	5	top
R37		2	3	bottom
R37		2	4	top
R38		1	4	bottom
R38	MMP-1	2	1	bottom
R38		2	3	top
R38		3	6	top
R42		1	5	bottom
R42		1	5	top
R42		2	3	bottom
R42	vehicle	2	4	top
R42		3	6	top
R42		3	6	bottom
R42		4	3	bottom
R42		4	4	top
R43		1	5	bottom
R43		2	5	top
R43		3	5	bottom
R43		3	6	top
R43	MMP-1	4	4	bottom
R43		5	4	top
R43		6	6	bottom
R43		6	5	top
R43		7	2	bottom
R43		7	5	top
R45		1	3	bottom
R45		1	3	top
R45		2	6	top
R45	vehicle	2	7	bottom
R45		3	3	bottom
R45		3	4	top
R45		4	4	bottom
R45		4	6	top
R52		1	4	bottom
R52		1	6	top
R52	vehicle	2	4	top
R52		2	6	bottom
R52		3	3	bottom
R52		3	3	top
R53		1	3	bottom
R53	vehicle	2	6	top
R53		3	6	bottom
R53		4	5	top

Rat	Group	image no.	Mankin score	articular surface
R53		5	3	top
R53		6	3	bottom
R53		7	7	bottom
R53	vehicle	8	3	top
R53		9	6	top
R53		10	5	bottom
R53		11	1	bottom
R53		12	4	top
R443		1	3	top
R433		2	2	bottom
R443	naive	3	2	bottom
R443		3	2	top
R433		4	3	top
R443		5	4	bottom
R444		1	3	bottom
R444		2	5	bottom
R444	naive	3	2	top
R444		4	2	bottom
R444		4	3	top

Figure D.5. Safranin O/Fast Green stained facet joints injected with MMP-1 or vehicle as designated in Table D.5 (Chapter 7)

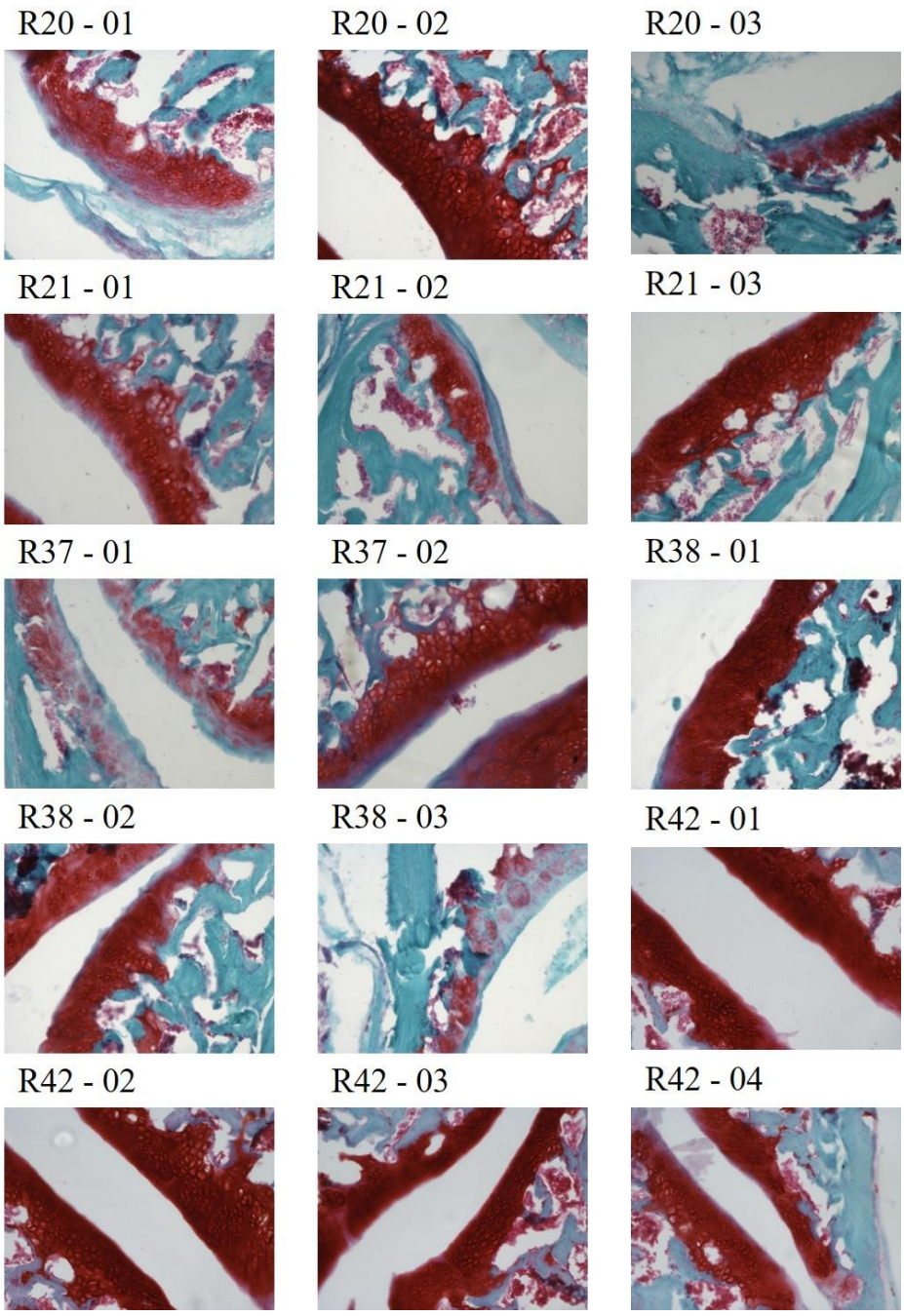

Note: Figure is continued on the next page.

Figure D.5. continued

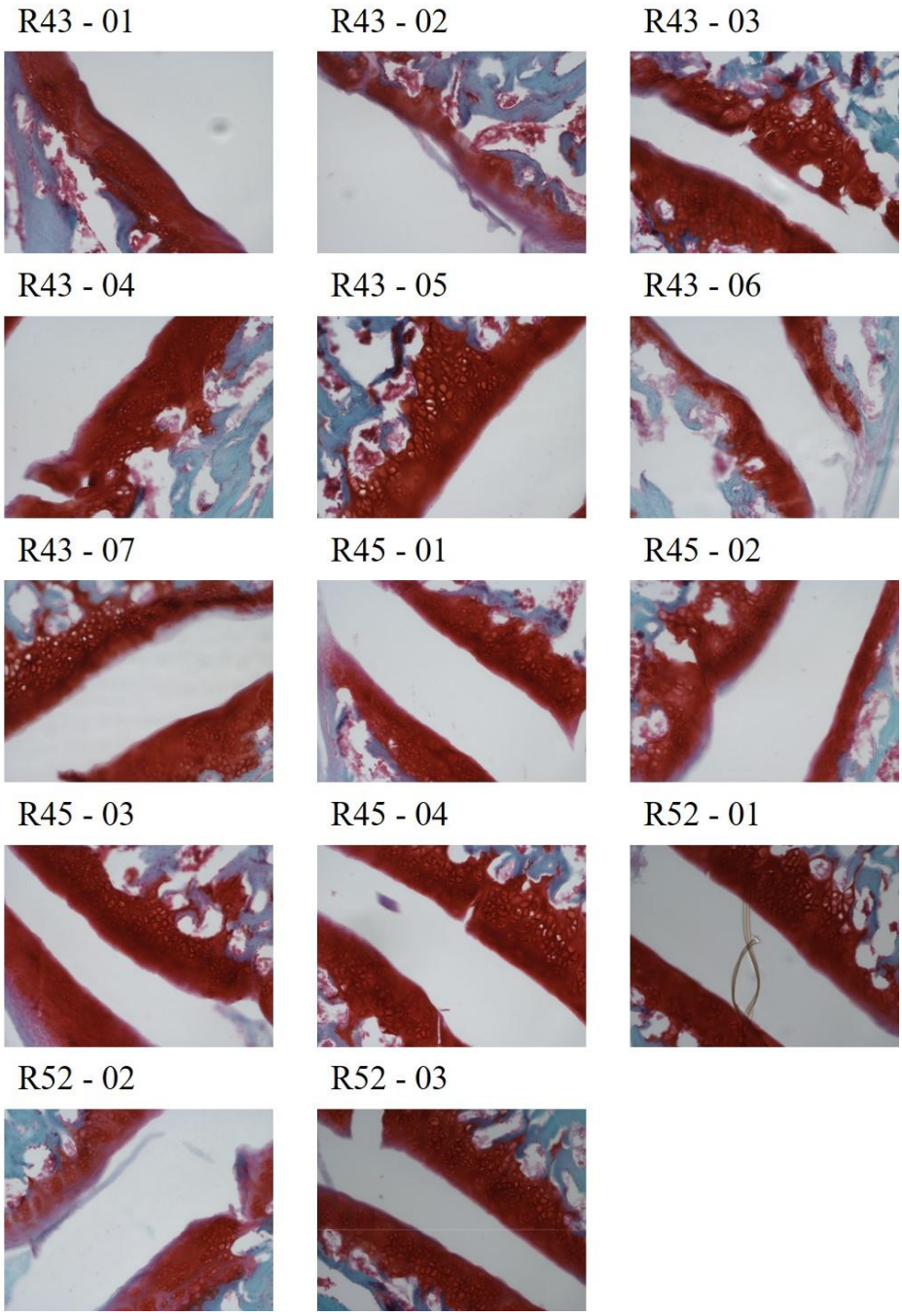

Note: Figure is continued on the next page.

Figure D.5. continued

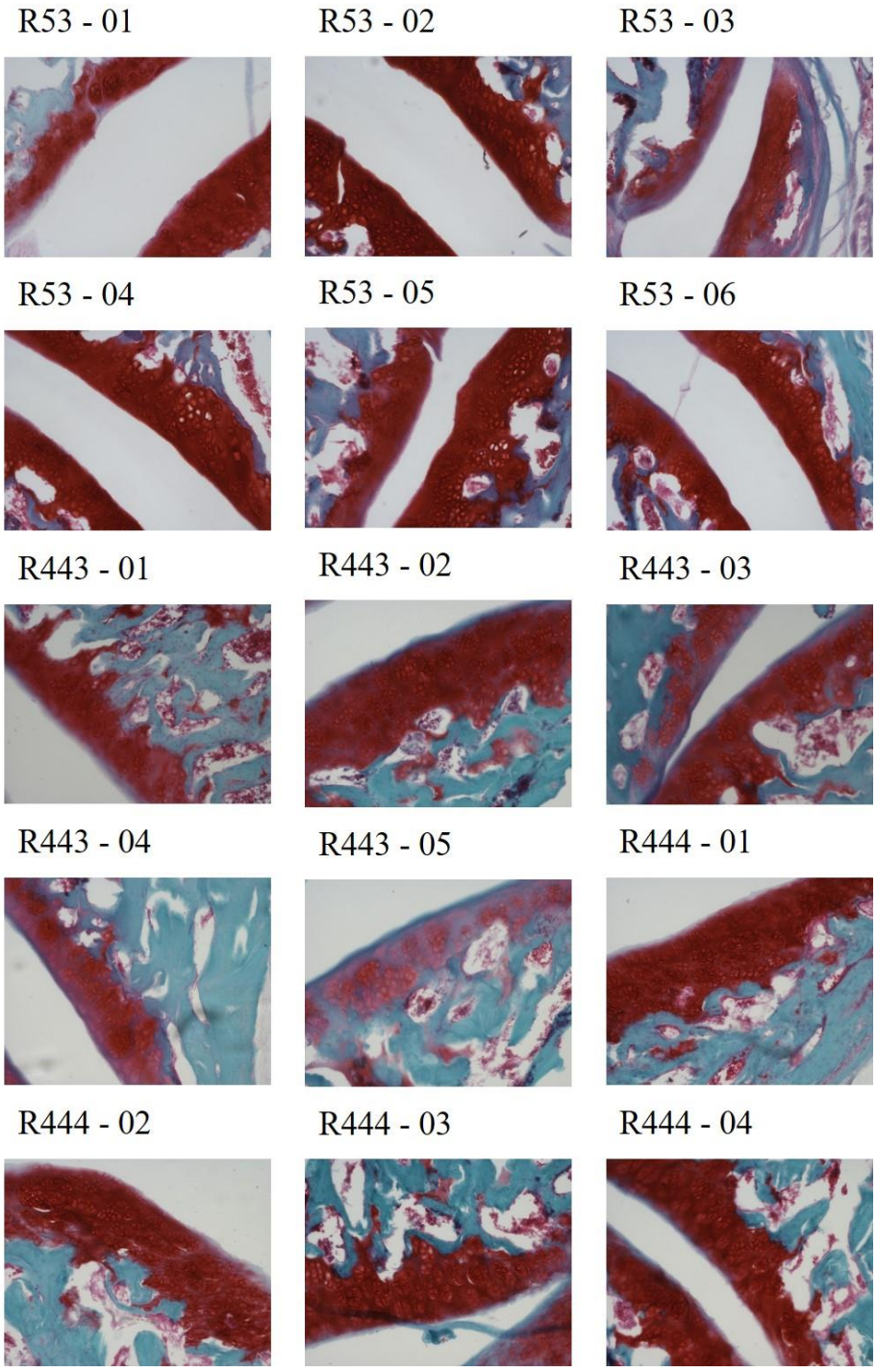

APPENDIX E

Immunohistochemistry in the DRG and Spinal Cord for Intra-Articular Rat Studies

This appendix summarizes the immunohistochemical assays performed on DRG and spinal cord tissues from the in vivo rat studies that are detailed in Chapters 4 and 7. All assays of neural tissues from rats exposed to bacterial collagenase, MMP-1, and/or the matched vehicle were performed using DRG and/or spinal cord tissue from the C7 level; data in the naïve group are also included and are also from the C7 level of an un-injected rat. In each of the tables and figures detailed in this appendix, data are identified by their injection group and rat number. Labels above each image within the figures list the rat number followed by the image number (e.g. "R10 – 01" indicates image 1 from rat 10); the image number in the labels matches the image numbers listed in the corresponding data table.

The in vivo studies that are detailed in Chapter 4 assayed substance P, phosphorylated ERK (pERK), and MMP-1 in the DRG and spinal cord of rats injected with bacterial collagenase or a matched vehicle. To assess substance P and pERK, a triple immunolabel was performed with substance P, pERK, and microtubule-associated protein 2 (MAP-2); MAP-2 was used to visualize neuronal somata and dendrites in parallel with the proteins of interest. Figure E.1 contains confocal images of the triple-label in the DRG;

green fluorescence is MAP-2, red is substance P, and blue is pERK. Figure E.2 contains confocal images of that same triple-label in the superficial dorsal horn of the spinal cord. MMP-1 was assessed in separate tissue sections using 3,3'-diaminobenzidine (DAB) development and imaged using a bright-field microscope; images of the MMP-1 labeling in the DRG and the superficial dorsal horn of the spinal cord are summarized in Figures E.3 and E.4, respectively.

To quantify substance P and pERK labeling intensity in neurons, MAP-2 positive cells were identified by a blinded grader to select neurons; then, the signal intensity of substance P and pERK labeling in the MAP-2 selected neurons was separately quantified by manually outlining the neurons and quantifying the average pixel brightness, using FIJI (NIH; Bethesda, MD). Expression data in DRG neurons were further assessed by neuronal size by calculating the cell diameter as the average of the length and width of each selected cell using FIJI. Neurons were categorized (by bin) as small- (S; <21μm), medium- (M; 21-40μm), and large- (L; >40μm) diameter (φ) neurons (Kras et al. 2014; Weisshaar et al. 2010), based on the known different functional roles across neurons of different sizes (Basbaum et al. 2009; Dai et al. 2002). Pixel intensity and neuronal size quantifications are detailed for substance P and pERK in Tables E.1 and E.2, respectively.

To quantify substance P and pERK in the superficial dorsal horn where nociceptive afferent fibers synapse (Basbaum et al. 2009), spinal cord images were cropped to include only the superficial dorsal horn. Substance P and pERK were quantified, separately, by counting the number of pixels above the threshold for expression in naïve tissue using the custom MATLAB densitometry script that is detailed in Appendix B. The densitometric

analysis of substance P and pERK labeling in the spinal cord is detailed in Table E.3 for the studies in Chapter 4. MMP-1 labeling in the DRG and spinal cord was also quantified using densitometry, and that quantification is summarized in Table E.4 for the DRG and in Table E.5 for the spinal cord.

The in vivo studies that are detailed in Chapter 7 assayed substance P and MMP-9 in the DRG and spinal cord of rats injected with MMP-1 or a matched vehicle. Fluorescent labeling was performed in separate sections for substance P and MMP-9. As such, confocal images of labeling in the DRG are summarized separately for the two labels in Figure E.5 for substance P and in Figure E.6 for MMP-9. The signal intensity of substance P and MMP-9 labeling was performed as described above for the studies in Chapter 4. The quantification of pixel intensity and cell size are detailed in Tables E.6 and E.7 for substance P and MMP-9, respectively. Likewise, Figures E.7 and E.8 contain confocal images of substance P and MMP-9 in the superficial dorsal horn of the spinal cord, respectively. Densitometry was used to quantify the percentage of pixels positive for labeling with both proteins, separately; Table E.7 summarizes that quantification for substance P and Table E.8 contains densitometric analysis for MMP-9.

Table E.1. Pixel intensity of substance P labeling in DRG neurons by size from rats injected with bacterial collagenase or vehicle (Chapter 4)

Rat	Group	image no.	cell no.	intensity	φ (μm)	bin	Rat	Group	image no.	cell no.	intensity	φ (μm)	bin
R03	naive	1	1	10.28	37.59	M	R03	naive	9	1	20.46	25.02	M
R03	naive	1	2	21.95	39.52	M	R03	naive	9	2	13.42	21.12	M
R03	naive	1	3	25.58	26.54	M	R03	naive	9	3	25.42	28.27	M
R03	naive	1	4	12.14	28.85	M	R03	naive	9	4	13.66	20.29	S
R03	naive	1	5	7.15	51.17	L	R03	naive	9	5	17.53	33.94	M
R03	naive	1	6	8.94	36.85	M	R03	naive	9	6	15.14	29.72	M
R03	naive	2	1	11.77	30.89	M	R03	naive	10	1	14.65	29.44	M
R03	naive	2	2	7.26	45.48	L	R03	naive	10	2	25.32	27.30	M
R03	naive	2	3	17.62	39.22	M	R03	naive	10	3	27.70	29.64	M
R03	naive	2	4	10.79	25.42	M	R03	naive	10	4	17.68	23.40	M
R03	naive	2	5	12.70	33.64	M	R03	naive	10	5	9.76	27.52	M
R03	naive	2	6	13.25	29.49	M	R03	naive	10	6	15.48	38.55	M
R03	naive	3	1	13.17	32.77	M	R03	naive	8	4	22.57	30.28	M
R03	naive	3	2	12.20	38.59	M	R03	naive	8	5	10.09	42.48	L
R03	naive	3	3	18.89	36.31	M	R03	naive	8	6	14.60	27.67	M
R03	naive	3	4	13.06	30.45	M	R03	naive	9	1	20.46	25.02	M
R03	naive	3	5	8.40	25.77	M	R23	col	1	1	10.31	40.80	L
R03	naive	3	6	11.89	43.13	L	R23	col	1	2	11.67	38.03	M
R03	naive	4	1	13.12	31.30	M	R23	col	1	3	8.98	39.24	M
R03	naive	4	2	13.83	35.09	M	R23	col	1	4	9.82	23.94	M
R03	naive	4	3	14.96	23.26	M	R23	col	1	5	6.41	36.68	M
R03	naive	4	4	13.24	32.39	M	R23	col	1	6	5.57	47.73	L
R03	naive	4	5	8.56	32.88	M	R23	col	1	7	9.36	40.51	L
R03	naive	4	6	12.88	39.87	M	R23	col	1	8	12.91	32.89	M
R03	naive	5	1	13.90	31.03	M	R23	col	2	1	8.02	36.15	M
R03	naive	5	2	12.22	25.82	M	R23	col	2	2	16.95	26.91	M
R03	naive	5	3	16.25	18.42	S	R23	col	2	3	6.46	43.07	L
R03	naive	5	4	11.81	61.83	L	R23	col	2	4	19.11	41.47	L
R03	naive	5	5	10.52	32.65	M	R23	col	2	5	6.09	22.42	M
R03	naive	5	6	9.50	44.41	L	R23	col	2	6	6.32	37.94	M
R03	naive	6	1	12.95	33.24	M	R23	col	2	7	11.42	36.74	M
R03	naive	6	2	10.67	19.46	S	R23	col	2	8	11.81	33.07	M
R03	naive	6	3	18.41	30.08	M	R23	col	3	1	9.34	39.90	M
R03	naive	6	4	10.55	42.30	L	R23	col	3	2	10.39	32.08	M
R03	naive	6	5	9.17	37.96	M	R23	col	3	3	7.83	33.34	M
R03	naive	6	6	10.24	41.49	L	R23	col	3	4	9.06	41.08	L
R03	naive	7	1	13.51	30.66	M	R23	col	3	5	7.36	37.16	M
R03	naive	7	2	15.51	16.05	S	R23	col	3	6	7.03	38.57	M
R03	naive	7	3	17.85	34.57	M	R23	col	3	7	13.78	29.98	M
R03	naive	7	4	25.93	32.93	M	R23	col	3	8	12.91	41.68	L
R03	naive	7	5	11.16	36.17	M	R23	col	4	1	9.23	38.34	M
R03	naive	7	6	15.20	27.89	M	R23	col	4	2	11.09	29.20	M
R03	naive	8	1	17.62	39.06	M	R23	col	4	3	8.32	37.99	M
R03	naive	8	2	17.27	36.45	M	R23	col	4	4	9.73	46.10	L
R03	naive	8	3	20.79	35.64	M	R23	col	4	5	6.98	26.72	M
R03	naive	8	4	22.57	30.28	M	R23	col	4	6	5.71	22.65	M
R03	naive	8	5	10.09	42.48	L	R23	col	4	7	8.59	38.38	M
R03	naive	8	6	14.60	27.67	M	R23	col	4	8	23.53	34.99	M

φ: diameter; col: collagenase; S: small; M: medium; L: large

Note: Table is continued on the next page.

Table E.1. continued

Rat	Group	image no.	cell no.	intensity	φ (μm)	bin	Rat	Group	image no.	cell no.	intensity	φ (μm)	bin
R23	col	5	1	9.19	47.19	L	R25	col	1	3	8.76	30.56	M
R23	col	5	2	11.66	42.64	L	R25	col	1	4	12.20	42.91	L
R23	col	5	3	6.08	23.29	M	R25	col	1	5	11.45	35.08	M
R23	col	5	4	9.36	40.47	L	R25	col	1	6	9.65	21.67	M
R23	col	5	5	6.64	44.46	L	R25	col	2	1	5.58	41.33	L
R23	col	5	6	7.97	21.93	M	R25	col	2	2	15.83	40.19	L
R23	col	5	7	8.48	31.67	M	R25	col	2	3	7.56	21.43	M
R23	col	5	8	11.55	29.20	M	R25	col	2	4	12.72	39.17	M
R23	col	6	1	11.03	30.21	M	R25	col	2	5	15.74	26.16	M
R23	col	6	2	12.07	34.94	M	R25	col	2	6	5.82	37.60	M
R23	col	6	3	8.62	27.34	M	R25	col	3	1	6.20	43.23	L
R23	col	6	4	12.07	37.16	M	R25	col	3	2	11.40	54.30	L
R23	col	6	5	8.51	32.98	M	R25	col	3	3	5.79	23.45	M
R23	col	6	6	6.56	35.35	M	R25	col	3	4	12.93	32.27	M
R23	col	6	7	10.93	37.77	M	R25	col	3	5	10.20	39.42	M
R23	col	6	8	12.34	33.27	M	R25	col	3	6	5.07	42.26	L
R23	col	7	1	9.15	36.75	M	R25	col	4	1	6.66	42.30	L
R23	col	7	2	11.54	35.88	M	R25	col	4	2	15.38	38.74	M
R23	col	7	3	6.35	37.12	M	R25	col	4	3	9.75	20.40	S
R23	col	7	4	11.83	40.18	L	R25	col	4	4	14.38	25.66	M
R23	col	7	5	6.61	26.68	M	R25	col	4	5	11.86	30.66	M
R23	col	7	6	7.81	25.66	M	R25	col	4	6	7.28	47.70	L
R23	col	7	7	8.71	30.49	M	R25	col	5	1	6.34	24.67	M
R23	col	7	8	16.61	31.20	M	R25	col	5	2	19.32	24.14	M
R23	col	8	1	9.32	28.83	M	R25	col	5	3	7.86	39.66	M
R23	col	8	2	12.09	37.49	M	R25	col	5	4	12.89	27.98	M
R23	col	8	3	6.07	42.10	L	R25	col	5	5	15.86	39.67	M
R23	col	8	4	10.38	37.55	M	R25	col	5	6	7.06	40.08	L
R23	col	8	5	6.77	33.68	M	R25	col	6	1	7.24	44.40	L
R23	col	8	6	8.09	25.65	M	R25	col	6	2	21.17	25.80	M
R23	col	8	7	8.91	21.45	M	R25	col	6	3	7.85	23.19	M
R23	col	8	8	9.84	24.71	M	R25	col	6	4	18.57	28.17	M
R23	col	9	1	13.15	44.19	L	R25	col	6	5	17.97	25.95	M
R23	col	9	2	10.78	41.49	L	R25	col	6	6	6.97	37.69	M
R23	col	9	3	7.49	33.37	M	R25	col	7	1	7.72	35.53	M
R23	col	9	4	9.27	35.12	M	R25	col	7	2	23.82	21.54	M
R23	col	9	5	9.20	27.06	M	R25	col	7	3	8.30	39.99	M
R23	col	9	6	7.59	28.30	M	R25	col	7	4	13.08	31.97	M
R23	col	9	7	9.12	47.28	L	R25	col	7	5	9.30	32.34	M
R23	col	9	8	12.06	18.74	S	R25	col	7	6	7.20	29.80	M
R23	col	10	1	7.88	37.45	M	R25	col	8	1	5.39	39.73	M
R23	col	10	2	9.67	30.93	M	R25	col	8	2	19.37	20.16	S
R23	col	10	3	8.53	44.41	L	R25	col	8	3	7.44	26.49	M
R23	col	10	4	10.92	39.46	M	R25	col	8	4	12.43	43.13	L
R23	col	10	5	5.62	23.22	M	R25	col	8	5	21.23	28.63	M
R23	col	10	6	5.94	45.51	L	R25	col	8	6	8.51	32.45	M
R23	col	10	7	8.27	47.10	L	R25	col	9	1	6.24	45.44	L
R23	col	10	8	11.17	22.51	M	R25	col	9	2	14.26	33.55	M
R25	col	1	1	3.50	61.60	L	R25	col	9	3	9.83	43.52	L
R25	col	1	2	18.41	60.10	L	R25	col	9	4	14.01	38.05	M

φ: diameter; col: collagenase; S: small; M: medium; L: large

Note: Table is continued on the next page.

Table E.1. continued

Rat	Group	image no.	cell no.	intensity	φ (μm)	bin	Rat	Group	image no.	cell no.	intensity	φ (μm)	bin
R25	col	9	5	10.72	28.98	M	R26	vehicle	6	3	5.77	42.26	L
R25	col	9	6	10.32	34.08	M	R26	vehicle	6	4	4.97	36.96	M
R25	col	10	1	7.46	45.04	L	R26	vehicle	6	5	4.55	34.87	M
R25	col	10	2	14.00	33.13	M	R26	vehicle	6	6	7.09	30.40	M
R25	col	10	3	8.46	40.79	L	R26	vehicle	6	7	8.63	36.45	M
R25	col	10	4	14.17	31.07	M	R26	vehicle	6	8	5.72	25.99	M
R25	col	10	5	11.67	25.96	M	R26	vehicle	7	1	5.12	42.81	L
R25	col	10	6	20.01	39.88	M	R26	vehicle	7	2	8.43	29.80	M
R26	vehicle	1	1	5.62	29.75	M	R26	vehicle	7	3	12.59	38.15	M
R26	vehicle	1	2	5.22	46.08	L	R26	vehicle	7	4	6.60	39.06	M
R26	vehicle	1	3	5.41	28.78	M	R26	vehicle	7	5	4.21	36.97	M
R26	vehicle	1	4	6.33	44.57	L	R26	vehicle	7	6	9.68	33.65	M
R26	vehicle	1	5	3.36	32.74	M	R26	vehicle	7	7	4.95	46.89	L
R26	vehicle	1	6	5.34	32.39	M	R26	vehicle	7	8	5.92	29.86	M
R26	vehicle	1	7	6.29	37.96	M	R26	vehicle	8	1	7.09	35.97	M
R26	vehicle	1	8	6.74	29.54	M	R26	vehicle	8	2	4.68	24.95	M
R26	vehicle	2	1	4.52	50.01	L	R26	vehicle	8	3	5.06	18.15	S
R26	vehicle	2	2	4.42	50.75	L	R26	vehicle	8	4	5.96	39.80	M
R26	vehicle	2	3	4.57	34.16	M	R26	vehicle	8	5	5.44	40.63	L
R26	vehicle	2	4	5.51	32.80	M	R26	vehicle	8	6	10.83	34.73	M
R26	vehicle	2	5	3.81	43.68	L	R26	vehicle	8	7	5.74	34.23	M
R26	vehicle	2	6	5.95	30.44	M	R26	vehicle	8	8	8.41	28.18	M
R26	vehicle	2	7	7.13	33.73	M	R26	vehicle	9	1	4.88	38.93	M
R26	vehicle	2	8	6.05	43.12	L	R26	vehicle	9	2	6.35	47.62	L
R26	vehicle	3	1	5.42	30.78	M	R26	vehicle	9	3	5.58	29.01	M
R26	vehicle	3	2	5.55	61.31	L	R26	vehicle	9	4	4.99	36.11	M
R26	vehicle	3	3	3.68	25.93	M	R26	vehicle	9	5	5.60	33.73	M
R26	vehicle	3	4	5.74	30.97	M	R26	vehicle	9	6	10.80	29.28	M
R26	vehicle	3	5	3.84	37.10	M	R26	vehicle	9	7	7.18	29.53	M
R26	vehicle	3	6	6.33	23.35	M	R26	vehicle	9	8	6.77	33.88	M
R26	vehicle	3	7	4.82	41.76	L	R26	vehicle	10	1	6.14	27.97	M
R26	vehicle	3	8	6.04	36.04	M	R26	vehicle	10	2	7.17	53.96	L
R26	vehicle	4	1	5.14	34.23	M	R26	vehicle	10	3	4.96	24.64	M
R26	vehicle	4	2	6.12	40.65	L	R26	vehicle	10	4	5.63	41.80	L
R26	vehicle	4	3	7.43	33.00	M	R26	vehicle	10	5	5.64	29.38	M
R26	vehicle	4	4	6.70	36.92	M	R26	vehicle	10	6	12.85	32.10	M
R26	vehicle	4	5	3.84	49.25	L	R26	vehicle	10	7	15.06	25.40	M
R26	vehicle	4	6	6.57	30.88	M	R26	vehicle	10	8	7.90	33.42	M
R26	vehicle	4	7	5.20	33.36	M	R28	col	1	1	27.99	34.77	M
R26	vehicle	4	8	6.82	42.87	L	R28	col	1	2	34.60	31.45	M
R26	vehicle	5	1	5.60	46.15	L	R28	col	1	3	27.19	38.67	M
R26	vehicle	5	2	3.96	48.07	L	R28	col	1	4	17.58	39.18	M
R26	vehicle	5	3	9.25	28.01	M	R28	col	1	5	15.75	23.31	M
R26	vehicle	5	4	4.89	40.44	L	R28	col	1	6	20.35	43.89	L
R26	vehicle	5	5	5.30	42.06	L	R28	col	1	7	27.49	39.81	M
R26	vehicle	5	6	5.10	23.87	M	R28	col	1	8	9.97	27.82	M
R26	vehicle	5	7	7.45	34.36	M	R28	col	2	1	18.99	33.26	M
R26	vehicle	5	8	6.57	46.76	L	R28	col	2	2	36.00	33.38	M
R26	vehicle	6	1	5.82	40.11	L	R28	col	2	3	25.63	37.53	M
R26	vehicle	6	2	6.23	40.97	L	R28	col	2	4	16.59	34.29	M

φ: diameter; col: collagenase; S: small; M: medium; L: large

Note: Table is continued on the next page.

Table E.1. continued

Rat	Group	image no.	cell no.	intensity	φ (µm)	bin	Rat	Group	image no.	cell no.	intensity	φ (µm)	bin
R28	col	2	5	15.11	22.51	M	R28	col	8	7	32.61	22.59	M
R28	col	2	6	22.67	30.85	M	R28	col	8	8	7.01	31.21	M
R28	col	2	7	30.16	31.11	M	R28	col	9	1	17.31	15.61	S
R28	col	2	8	8.66	25.85	M	R28	col	9	2	28.65	14.40	S
R28	col	3	1	16.81	41.83	L	R28	col	9	3	25.72	25.06	M
R28	col	3	2	29.39	24.15	M	R28	col	9	4	24.42	24.13	M
R28	col	3	3	21.33	43.89	L	R28	col	9	5	20.19	40.78	L
R28	col	3	4	14.01	37.06	M	R28	col	9	6	20.00	22.91	M
R28	col	3	5	11.69	36.92	M	R28	col	9	7	22.46	40.60	L
R28	col	3	6	19.13	29.42	M	R28	col	9	8	8.60	29.83	M
R28	col	3	7	27.04	41.34	L	R28	col	10	1	18.36	20.20	S
R28	col	3	8	9.29	35.98	M	R28	col	10	2	34.04	33.26	M
R28	col	4	1	26.66	25.54	M	R28	col	10	3	26.79	25.42	M
R28	col	4	2	30.23	34.98	M	R28	col	10	4	19.37	28.15	M
R28	col	4	3	29.74	36.36	M	R28	col	10	5	18.28	36.51	M
R28	col	4	4	13.57	33.83	M	R28	col	10	6	27.18	33.36	M
R28	col	4	5	18.02	32.93	M	R28	col	10	7	30.66	29.27	M
R28	col	4	6	17.06	54.88	L	R28	col	10	8	10.01	28.88	M
R28	col	4	7	26.22	42.25	L	R30	col	1	1	7.77	33.54	M
R28	col	4	8	10.05	31.80	M	R30	col	1	2	6.07	42.20	L
R28	col	5	1	18.45	40.03	L	R30	col	1	3	5.60	49.18	L
R28	col	5	2	32.56	25.57	M	R30	col	1	4	5.81	37.41	M
R28	col	5	3	21.53	32.97	M	R30	col	1	5	7.16	55.89	L
R28	col	5	4	14.59	23.04	M	R30	col	1	6	8.17	38.35	M
R28	col	5	5	19.81	44.80	L	R30	col	1	7	16.85	39.03	M
R28	col	5	6	20.18	27.63	M	R30	col	1	8	19.75	29.92	M
R28	col	5	7	26.89	17.53	S	R30	col	2	1	7.47	32.96	M
R28	col	5	8	7.17	37.05	M	R30	col	2	2	7.11	35.54	M
R28	col	6	1	18.71	27.16	M	R30	col	2	3	5.60	51.99	L
R28	col	6	2	31.63	17.22	S	R30	col	2	4	6.23	31.06	M
R28	col	6	3	20.17	24.27	M	R30	col	2	5	6.82	49.03	L
R28	col	6	4	14.62	32.04	M	R30	col	2	6	8.47	43.68	L
R28	col	6	5	17.27	35.03	M	R30	col	2	7	14.61	22.27	M
R28	col	6	6	26.35	38.43	M	R30	col	2	8	22.95	27.11	M
R28	col	6	7	34.02	41.54	L	R30	col	3	1	6.81	30.31	M
R28	col	6	8	7.93	37.02	M	R30	col	3	2	6.83	50.12	L
R28	col	7	1	21.76	24.47	M	R30	col	3	3	5.01	25.02	M
R28	col	7	2	32.30	26.02	M	R30	col	3	4	5.83	52.07	L
R28	col	7	3	18.34	40.88	L	R30	col	3	5	16.90	26.07	M
R28	col	7	4	15.51	34.37	M	R30	col	3	6	6.47	26.66	M
R28	col	7	5	21.25	21.17	M	R30	col	3	7	15.33	18.20	S
R28	col	7	6	19.38	22.06	M	R30	col	3	8	20.28	25.49	M
R28	col	7	7	36.31	28.90	M	R30	col	4	1	9.04	26.31	M
R28	col	7	8	28.88	36.69	M	R30	col	4	2	5.91	36.55	M
R28	col	8	1	20.65	23.43	M	R30	col	4	3	4.91	50.18	L
R28	col	8	2	27.23	27.14	M	R30	col	4	4	4.78	44.46	L
R28	col	8	3	27.51	27.89	M	R30	col	4	5	10.82	35.00	M
R28	col	8	4	19.43	25.37	M	R30	col	4	6	9.73	30.15	M
R28	col	8	5	21.83	31.87	M	R30	col	4	7	16.88	35.98	M
R28	col	8	6	20.57	25.65	M	R30	col	4	8	21.52	45.38	L

φ: diameter; col: collagenase; S: small; M: medium; L: large

Note: Table is continued on the next page.

Table E.1. continued

Rat	Group	image no.	cell no.	intensity	φ (μm)	bin	Rat	Group	image no.	cell no.	intensity	φ (μm)	bin
R30	col	5	1	5.94	22.87	M	R31	vehicle	1	3	3.97	37.51	M
R30	col	5	2	6.91	26.41	M	R31	vehicle	1	4	11.15	37.52	M
R30	col	5	3	4.43	50.62	L	R31	vehicle	1	5	1.39	46.01	L
R30	col	5	4	4.81	30.84	M	R31	vehicle	1	6	6.30	42.09	L
R30	col	5	5	57.18	20.79	S	R31	vehicle	1	7	7.73	47.48	L
R30	col	5	6	6.14	35.11	M	R31	vehicle	2	1	3.73	28.42	M
R30	col	5	7	18.93	18.61	S	R31	vehicle	2	2	4.07	32.38	M
R30	col	5	8	28.29	20.58	S	R31	vehicle	2	3	3.57	33.52	M
R30	col	6	1	8.50	36.85	M	R31	vehicle	2	4	12.72	49.75	L
R30	col	6	2	5.20	30.98	M	R31	vehicle	2	5	2.18	35.39	M
R30	col	6	3	6.55	36.32	M	R31	vehicle	2	6	5.50	34.87	M
R30	col	6	4	4.09	44.62	L	R31	vehicle	2	7	8.33	50.23	L
R30	col	6	5	49.71	22.11	M	R31	vehicle	3	1	4.64	27.21	M
R30	col	6	6	11.66	39.09	M	R31	vehicle	3	2	3.81	45.21	L
R30	col	6	7	16.98	38.61	M	R31	vehicle	3	3	3.52	36.73	M
R30	col	6	8	15.28	37.37	M	R31	vehicle	3	4	14.55	38.46	M
R30	col	7	1	6.35	41.80	L	R31	vehicle	3	5	2.98	31.45	M
R30	col	7	2	6.24	39.71	M	R31	vehicle	3	6	7.85	34.84	M
R30	col	7	3	5.13	48.28	L	R31	vehicle	3	7	5.95	28.34	M
R30	col	7	4	3.84	38.12	M	R31	vehicle	4	1	5.80	23.23	M
R30	col	7	5	10.07	24.90	M	R31	vehicle	4	2	5.37	35.03	M
R30	col	7	6	7.91	47.42	L	R31	vehicle	4	3	3.01	40.43	L
R30	col	7	7	10.70	47.06	L	R31	vehicle	4	4	10.59	49.94	L
R30	col	7	8	25.13	38.05	M	R31	vehicle	4	5	1.88	46.14	L
R30	col	8	1	10.31	25.58	M	R31	vehicle	4	6	7.73	53.11	L
R30	col	8	2	4.63	38.07	M	R31	vehicle	4	7	8.92	36.10	M
R30	col	8	3	6.21	36.44	M	R31	vehicle	5	1	4.58	32.54	M
R30	col	8	4	5.05	35.79	M	R31	vehicle	5	2	5.75	32.29	M
R30	col	8	5	7.49	23.16	M	R31	vehicle	5	3	5.63	32.84	M
R30	col	8	6	5.68	21.13	M	R31	vehicle	5	4	14.05	40.60	L
R30	col	8	7	10.12	50.57	L	R31	vehicle	5	5	1.98	28.01	M
R30	col	8	8	23.75	45.36	L	R31	vehicle	5	6	5.28	46.63	L
R30	col	9	1	9.97	24.26	M	R31	vehicle	5	7	7.11	42.03	L
R30	col	9	2	5.80	41.39	L	R31	vehicle	6	1	7.50	34.37	M
R30	col	9	3	9.22	23.95	M	R31	vehicle	6	2	8.53	23.77	M
R30	col	9	4	4.03	37.29	M	R31	vehicle	6	3	5.34	35.67	M
R30	col	9	5	5.86	22.13	M	R31	vehicle	6	4	11.01	46.92	L
R30	col	9	6	5.77	53.79	L	R31	vehicle	6	5	2.04	42.45	L
R30	col	9	7	18.29	20.66	S	R31	vehicle	6	6	7.93	26.19	M
R30	col	9	8	17.80	42.96	L	R31	vehicle	6	7	9.04	40.20	L
R30	col	10	1	6.27	29.48	M	R31	vehicle	7	1	5.97	36.74	M
R30	col	10	2	5.10	26.85	M	R31	vehicle	7	2	5.82	38.10	M
R30	col	10	3	4.07	47.87	L	R31	vehicle	7	3	4.47	34.48	M
R30	col	10	4	3.40	39.79	M	R31	vehicle	7	4	17.41	26.89	M
R30	col	10	5	9.73	44.56	L	R31	vehicle	7	5	2.57	37.95	M
R30	col	10	6	8.32	33.19	M	R31	vehicle	7	6	4.58	46.79	L
R30	col	10	7	14.60	43.92	L	R31	vehicle	7	7	7.50	37.88	M
R30	col	10	8	14.28	28.65	M	R31	vehicle	8	1	6.83	39.16	M
R31	vehicle	1	1	7.06	34.14	M	R31	vehicle	8	2	8.02	41.13	L
R31	vehicle	1	2	7.23	28.63	M	R31	vehicle	8	3	3.64	41.57	L

φ: diameter; col: collagenase; S: small; M: medium; L: large

Note: Table is continued on the next page.

Table E.1. continued

Rat	Group	image no.	cell no.	intensity	φ (µm)	bin	Rat	Group	image no.	cell no.	intensity	φ (µm)	bin
R31	vehicle	8	4	13.42	17.98	S	R35	vehicle	5	5	10.62	41.85	L
R31	vehicle	8	5	2.47	41.67	L	R35	vehicle	5	6	4.07	37.92	M
R31	vehicle	8	6	6.70	42.27	L	R35	vehicle	5	7	20.87	23.33	M
R31	vehicle	8	7	8.92	23.93	M	R35	vehicle	6	1	19.59	28.54	M
R31	vehicle	9	1	9.41	27.96	M	R35	vehicle	6	2	5.25	31.21	M
R31	vehicle	9	2	5.36	41.17	L	R35	vehicle	6	3	3.03	30.60	M
R31	vehicle	9	3	5.47	29.69	M	R35	vehicle	6	4	10.66	36.60	M
R31	vehicle	9	4	14.40	21.04	M	R35	vehicle	6	5	36.00	27.12	M
R31	vehicle	9	5	3.37	36.02	M	R35	vehicle	6	6	6.54	37.82	M
R31	vehicle	9	6	6.35	29.57	M	R35	vehicle	6	7	17.02	37.00	M
R31	vehicle	9	7	7.55	43.12	L	R35	vehicle	7	1	23.50	47.90	L
R31	vehicle	10	1	8.38	22.00	M	R35	vehicle	7	2	6.69	29.93	M
R31	vehicle	10	2	9.07	25.65	M	R35	vehicle	7	3	4.47	21.75	M
R31	vehicle	10	3	1.48	37.96	M	R35	vehicle	7	4	3.56	22.40	M
R31	vehicle	10	4	23.00	23.06	M	R35	vehicle	7	5	5.65	46.66	L
R31	vehicle	10	5	2.44	32.45	M	R35	vehicle	7	6	4.15	43.99	L
R31	vehicle	10	6	5.12	47.13	L	R35	vehicle	7	7	17.69	37.13	M
R31	vehicle	10	7	8.04	38.05	M	R35	vehicle	8	1	20.47	33.24	M
R35	vehicle	1	1	22.22	46.13	L	R35	vehicle	8	2	7.44	38.80	M
R35	vehicle	1	2	6.62	55.88	L	R35	vehicle	8	3	3.68	27.06	M
R35	vehicle	1	3	4.51	37.88	M	R35	vehicle	8	4	5.02	25.52	M
R35	vehicle	1	4	5.86	36.11	M	R35	vehicle	8	5	5.91	37.53	M
R35	vehicle	1	5	15.39	32.89	M	R35	vehicle	8	6	4.88	24.43	M
R35	vehicle	1	6	6.94	34.84	M	R35	vehicle	8	7	12.56	29.29	M
R35	vehicle	1	7	18.24	37.18	M	R35	vehicle	9	1	22.81	45.65	L
R35	vehicle	2	1	23.72	27.47	M	R35	vehicle	9	2	7.49	44.15	L
R35	vehicle	2	2	5.23	36.63	M	R35	vehicle	9	3	3.91	44.38	L
R35	vehicle	2	3	4.06	35.14	M	R35	vehicle	9	4	4.68	22.39	M
R35	vehicle	2	4	7.45	39.30	M	R35	vehicle	9	5	6.82	20.90	S
R35	vehicle	2	5	5.83	38.41	M	R35	vehicle	9	6	13.26	30.52	M
R35	vehicle	2	6	5.94	41.21	L	R35	vehicle	9	7	13.06	32.08	M
R35	vehicle	2	7	14.60	36.98	M	R35	vehicle	10	1	20.37	44.61	L
R35	vehicle	3	1	21.09	39.72	M	R35	vehicle	10	2	6.54	26.71	M
R35	vehicle	3	2	6.08	35.23	M	R35	vehicle	10	3	4.05	27.45	M
R35	vehicle	3	3	5.69	30.43	M	R35	vehicle	10	4	7.11	43.65	L
R35	vehicle	3	4	6.26	42.58	L	R35	vehicle	10	5	8.07	32.98	M
R35	vehicle	3	5	7.49	37.44	M	R35	vehicle	10	6	5.99	37.24	M
R35	vehicle	3	6	5.94	46.67	L	R35	vehicle	10	7	13.11	35.66	M
R35	vehicle	3	7	15.97	43.02	L	R36	col	1	1	14.12	47.08	L
R35	vehicle	4	1	18.13	34.72	M	R36	col	1	2	37.64	27.36	M
R35	vehicle	4	2	6.79	33.53	M	R36	col	1	3	16.57	35.53	M
R35	vehicle	4	3	5.35	32.68	M	R36	col	1	4	34.73	21.71	M
R35	vehicle	4	4	6.37	39.26	M	R36	col	1	5	24.66	37.44	M
R35	vehicle	4	5	5.74	29.29	M	R36	col	1	6	21.23	50.08	L
R35	vehicle	4	6	4.40	43.06	L	R36	col	1	7	7.28	62.12	L
R35	vehicle	4	7	15.14	30.38	M	R36	col	1	8	11.61	41.35	L
R35	vehicle	5	1	19.48	23.84	M	R36	col	2	1	22.28	34.74	M
R35	vehicle	5	2	6.57	31.43	M	R36	col	2	2	32.51	28.00	M
R35	vehicle	5	3	3.14	29.18	M	R36	col	2	3	27.08	37.89	M
R35	vehicle	5	4	8.42	35.47	M	R36	col	2	4	24.57	19.77	S

φ: diameter; col: collagenase; S: small; M: medium; L: large

Note: Table is continued on the next page.

Table E.1. continued

Rat	Group	image no.	cell no.	intensity	φ (µm)	bin	Rat	Group	image no.	cell no.	intensity	φ (µm)	bin
R36	col	2	5	19.77	27.45	M	R36	z	8	7	7.68	30.60	M
R36	col	2	6	20.36	37.17	M	R36	col	8	8	13.09	22.97	M
R36	col	2	7	8.73	44.30	L	R36	col	9	1	15.94	31.10	M
R36	col	2	8	11.41	41.77	L	R36	col	9	2	24.13	28.81	M
R36	col	3	1	20.99	32.68	M	R36	col	9	3	31.47	34.45	M
R36	col	3	2	29.00	32.63	M	R36	col	9	4	32.22	26.04	M
R36	col	3	3	14.30	26.85	M	R36	col	9	5	29.51	36.88	M
R36	col	3	4	21.64	21.15	M	R36	col	9	6	14.27	31.57	M
R36	col	3	5	18.82	57.09	L	R36	col	9	7	10.34	43.26	L
R36	col	3	6	26.06	21.09	M	R36	col	9	8	11.14	33.80	M
R36	col	3	7	9.73	42.24	L	R36	col	10	1	13.12	31.22	M
R36	col	3	8	10.39	60.39	L	R36	col	10	2	28.03	33.47	M
R36	col	4	1	21.70	27.73	M	R36	col	10	3	24.69	34.29	M
R36	col	4	2	42.87	34.06	M	R36	col	10	4	28.93	30.90	M
R36	col	4	3	25.64	32.21	M	R36	col	10	5	23.01	32.17	M
R36	col	4	4	36.61	19.15	S	R36	col	10	6	11.63	20.14	S
R36	col	4	5	20.92	48.63	L	R36	col	10	7	7.62	29.96	M
R36	col	4	6	14.51	19.03	S	R36	col	10	8	12.38	21.81	M
R36	col	4	7	8.74	60.88	L	R40	naive	1	1	15.48	42.46	L
R36	col	4	8	14.54	40.67	L	R40	naive	1	2	17.85	37.48	M
R36	col	5	1	21.65	31.50	M	R40	naive	1	3	17.44	33.34	M
R36	col	5	2	27.01	32.14	M	R40	naive	1	4	12.40	25.47	M
R36	col	5	3	20.55	37.87	M	R40	naive	1	5	12.13	38.73	M
R36	col	5	4	33.70	28.85	M	R40	naive	1	6	4.92	47.63	L
R36	col	5	5	21.08	40.07	L	R40	naive	2	1	13.57	32.05	M
R36	col	5	6	13.75	43.79	L	R40	naive	2	2	11.88	27.24	M
R36	col	5	7	6.28	43.57	L	R40	naive	2	3	27.47	41.98	L
R36	col	5	8	11.53	22.78	M	R40	naive	2	4	21.24	29.00	M
R36	col	6	1	17.08	31.57	M	R40	naive	2	5	13.24	35.37	M
R36	col	6	2	38.68	27.66	M	R40	naive	2	6	6.84	39.00	M
R36	col	6	3	18.71	33.66	M	R40	naive	3	1	20.32	24.06	M
R36	col	6	4	28.81	26.04	M	R40	naive	3	2	10.70	31.89	M
R36	col	6	5	20.30	50.20	L	R40	naive	3	3	19.79	30.59	M
R36	col	6	6	19.12	18.15	S	R40	naive	3	4	19.73	35.94	M
R36	col	6	7	5.65	27.28	M	R40	naive	3	5	7.76	27.92	M
R36	col	6	8	10.97	20.60	S	R40	naive	3	6	5.46	59.13	L
R36	col	7	1	15.82	34.99	M	R40	naive	4	1	18.81	32.68	M
R36	col	7	2	35.99	35.40	M	R40	naive	4	2	11.44	26.66	M
R36	col	7	3	20.28	39.25	M	R40	naive	4	3	28.30	32.32	M
R36	col	7	4	29.79	21.92	M	R40	naive	4	4	11.97	24.32	M
R36	col	7	5	22.23	42.84	L	R40	naive	4	5	13.46	41.13	L
R36	col	7	6	15.45	24.08	M	R40	naive	4	6	8.00	38.05	M
R36	col	7	7	7.60	29.43	M	R40	naive	5	1	15.87	38.30	M
R36	col	7	8	12.54	35.30	M	R40	naive	5	2	15.62	26.71	M
R36	col	8	1	16.61	39.53	M	R40	naive	5	3	23.31	44.29	L
R36	col	8	2	37.25	35.46	M	R40	naive	5	4	26.48	43.25	L
R36	col	8	3	33.95	40.69	L	R40	naive	5	5	19.03	36.99	M
R36	col	8	4	23.06	33.51	M	R40	naive	5	6	9.96	25.45	M
R36	col	8	5	27.93	50.14	L	R40	naive	6	1	19.11	34.57	M
R36	col	8	6	13.64	37.27	M	R40	naive	6	2	15.92	31.97	M

φ: diameter; col: collagenase; S: small; M: medium; L: large

Note: Table is continued on the next page.

Table E.1. continued

Rat	Group	image no.	cell no.	intensity	φ (μm)	bin
R40	naive	6	3	25.00	28.92	M
R40	naive	6	4	29.25	28.01	M
R40	naive	6	5	6.77	46.14	L
R40	naive	6	6	5.99	40.58	L
R40	naive	7	1	12.54	29.77	M
R40	naive	7	2	18.46	41.98	L
R40	naive	7	3	27.49	38.62	M
R40	naive	7	4	32.76	42.93	L
R40	naive	7	5	11.22	54.11	L
R40	naive	7	6	3.96	55.52	L
R40	naive	8	1	16.49	44.41	L
R40	naive	8	2	13.87	35.87	M
R40	naive	8	3	22.44	43.32	L
R40	naive	8	4	25.22	30.64	M
R40	naive	8	5	14.13	40.25	L
R40	naive	8	6	6.24	40.89	L
R40	naive	9	1	14.31	44.68	L
R40	naive	9	2	34.09	31.20	M
R40	naive	9	3	25.76	38.73	M
R40	naive	9	4	11.96	31.77	M
R40	naive	9	5	18.67	38.11	M
R40	naive	9	6	5.12	31.26	M
R40	naive	10	1	17.25	37.41	M
R40	naive	10	2	11.83	65.86	L
R40	naive	10	3	24.56	43.32	L
R40	naive	10	4	18.28	52.94	L
R40	naive	10	5	12.78	31.42	M
R40	naive	10	6	6.01	50.50	L

φ: diameter; col: collagenase; S: small; M: medium; L: large

Table E.2. Pixel intensity of pERK labeling in DRG neurons by size from rats injected with bacterial collagenase or vehicle (Chapter 4)

Rat	Group	image no.	cell no.	intensity	φ (μm)	bin	Rat	Group	image no.	cell no.	intensity	φ (μm)	bin
R03	naive	1	1	26.34	41.23	L	R03	naive	5	9	27.96	30.46	M
R03	naive	1	2	37.69	29.25	M	R03	naive	5	10	21.63	26.06	M
R03	naive	1	3	36.63	27.91	M	R03	naive	6	1	26.95	35.43	M
R03	naive	1	4	34.37	26.13	M	R03	naive	6	2	32.67	30.24	M
R03	naive	1	5	38.04	31.22	M	R03	naive	6	3	34.69	38.91	M
R03	naive	1	6	35.48	30.18	M	R03	naive	6	4	32.77	36.67	M
R03	naive	1	7	36.01	31.37	M	R03	naive	6	5	25.60	41.04	L
R03	naive	1	8	43.69	34.60	M	R03	naive	6	6	33.98	32.02	M
R03	naive	1	9	46.15	23.66	M	R03	naive	6	7	37.08	26.37	M
R03	naive	1	10	39.43	22.15	M	R03	naive	6	8	33.51	27.95	M
R03	naive	2	1	29.59	39.88	M	R03	naive	6	9	37.59	28.31	M
R03	naive	2	2	10.86	44.05	L	R03	naive	6	10	33.88	38.79	M
R03	naive	2	3	27.19	39.09	M	R23	col	1	1	32.07	41.64	L
R03	naive	2	4	37.45	35.17	M	R23	col	1	2	23.61	35.62	M
R03	naive	2	5	23.23	24.46	M	R23	col	1	3	30.90	36.59	M
R03	naive	2	6	15.69	18.20	S	R23	col	1	4	26.65	40.13	L
R03	naive	2	7	16.21	20.77	S	R23	col	1	5	32.96	46.21	L
R03	naive	2	8	28.09	39.55	M	R23	col	1	6	30.71	29.00	M
R03	naive	2	9	14.39	20.72	S	R23	col	1	7	33.48	33.91	M
R03	naive	2	10	37.85	27.86	M	R23	col	1	8	32.89	28.15	M
R03	naive	3	1	32.64	30.03	M	R23	col	1	9	35.44	42.09	L
R03	naive	3	2	43.79	34.09	M	R23	col	1	10	23.23	36.75	M
R03	naive	3	3	43.81	32.98	M	R23	col	2	1	28.40	39.12	M
R03	naive	3	4	28.88	22.30	M	R23	col	2	2	28.39	29.08	M
R03	naive	3	5	28.21	15.56	S	R23	col	2	3	28.89	27.86	M
R03	naive	3	6	38.11	30.01	M	R23	col	2	4	31.61	27.01	M
R03	naive	3	7	40.25	32.68	M	R23	col	2	5	34.79	40.69	L
R03	naive	3	8	36.64	36.96	M	R23	col	2	6	25.87	41.05	L
R03	naive	3	9	40.65	27.03	M	R23	col	2	7	30.97	34.03	M
R03	naive	3	10	39.79	29.50	M	R23	col	2	8	32.59	34.30	M
R03	naive	4	1	30.64	27.83	M	R23	col	2	9	32.74	37.52	M
R03	naive	4	2	27.70	21.03	M	R23	col	2	10	29.53	33.69	M
R03	naive	4	3	34.71	29.86	M	R23	col	3	1	33.98	38.60	M
R03	naive	4	4	33.17	31.16	M	R23	col	3	2	30.26	42.53	L
R03	naive	4	5	36.34	57.92	L	R23	col	3	3	26.55	33.69	M
R03	naive	4	6	29.72	41.87	L	R23	col	3	4	24.43	44.87	L
R03	naive	4	7	45.68	33.47	M	R23	col	3	5	21.36	21.71	M
R03	naive	4	8	44.04	30.29	M	R23	col	3	6	26.52	27.82	M
R03	naive	4	9	29.80	20.29	S	R23	col	3	7	26.25	33.72	M
R03	naive	4	10	30.83	24.05	M	R23	col	3	8	24.46	45.90	L
R03	naive	5	1	19.34	47.02	L	R23	col	3	9	23.31	35.94	M
R03	naive	5	2	29.41	32.36	M	R23	col	3	10	30.92	41.96	L
R03	naive	5	3	12.55	23.40	M	R23	col	4	1	17.31	24.95	M
R03	naive	5	4	12.69	31.56	M	R23	col	4	2	26.62	39.32	M
R03	naive	5	5	20.24	32.81	M	R23	col	4	3	22.77	39.33	M
R03	naive	5	6	15.86	39.12	M	R23	col	4	4	27.32	39.06	M
R03	naive	5	7	21.81	37.07	M	R23	col	4	5	23.12	40.73	L
R03	naive	5	8	18.15	39.11	M	R23	col	4	6	30.12	35.76	M

φ: diameter; col: collagenase; S: small; M: medium; L: large

Note: Table is continued on the next page.

Table E.2. continued

Rat	Group	image no.	cell no.	intensity	φ (μm)	bin	Rat	Group	image no.	cell no.	intensity	φ (μm)	bin
R23	col	4	7	29.60	39.86	M	R23	col	5	3	10.22	28.51	M
R23	col	4	8	35.53	36.63	M	R23	col	5	4	9.47	31.11	M
R23	col	4	9	23.38	29.91	M	R23	col	5	5	9.54	43.78	L
R23	col	4	10	26.21	38.32	M	R23	col	5	6	12.18	35.76	M
R23	col	5	1	9.01	39.33	M	R23	col	5	7	8.16	30.74	M
R23	col	5	2	7.09	26.13	M	R23	col	5	8	12.29	35.01	M
R23	col	5	3	10.22	28.51	M	R23	col	5	9	20.09	34.61	M
R23	col	5	4	9.47	31.11	M	R23	col	5	10	7.45	29.29	M
R23	col	5	5	9.54	43.78	L	R23	col	6	1	15.99	42.34	L
R23	col	5	6	12.18	35.76	M	R23	col	6	2	17.11	39.21	M
R23	col	5	7	8.16	30.74	M	R23	col	6	3	17.05	39.29	M
R23	col	5	8	12.29	35.01	M	R23	col	6	4	7.09	27.92	M
R23	col	5	9	20.09	34.61	M	R23	col	6	5	12.64	21.21	M
R23	col	5	10	7.45	29.29	M	R23	col	6	6	12.91	38.72	M
R23	col	6	1	15.99	42.34	L	R23	col	6	7	22.84	22.19	M
R23	col	6	2	17.11	39.21	M	R23	col	6	8	23.07	21.21	M
R23	col	6	3	17.05	39.29	M	R23	col	6	9	20.46	27.10	M
R23	col	6	4	7.09	27.92	M	R23	col	6	10	19.27	40.63	L
R23	col	6	5	12.64	21.21	M	R23	col	7	1	22.35	39.74	M
R23	col	6	6	12.91	38.72	M	R23	col	7	2	22.11	40.83	L
R23	col	6	7	22.84	22.19	M	R23	col	7	3	27.67	31.09	M
R23	col	6	8	23.07	21.21	M	R23	col	7	4	27.87	36.72	M
R23	col	6	9	20.46	27.10	M	R23	col	7	5	19.57	32.69	M
R23	col	6	10	19.27	40.63	L	R23	col	7	6	28.99	34.61	M
R23	col	7	1	22.35	39.74	M	R23	col	7	7	19.60	35.40	M
R23	col	7	2	22.11	40.83	L	R23	col	7	8	17.24	23.36	M
R23	col	7	3	27.67	31.09	M	R23	col	7	9	26.90	42.99	L
R23	col	7	4	27.87	36.72	M	R23	col	7	10	23.81	42.49	L
R23	col	7	5	19.57	32.69	M	R23	col	8	1	22.39	36.66	M
R23	col	7	6	28.99	34.61	M	R23	col	8	2	22.68	30.17	M
R23	col	7	7	19.60	35.40	M	R23	col	8	3	23.55	40.55	L
R23	col	7	8	17.24	23.36	M	R23	col	8	4	27.81	35.96	M
R23	col	7	9	26.90	42.99	L	R23	col	8	5	22.16	32.33	M
R23	col	7	10	23.81	42.49	L	R23	col	8	6	18.88	31.98	M
R23	col	8	1	22.39	36.66	M	R23	col	8	7	28.28	31.58	M
R23	col	8	2	22.68	30.17	M	R23	col	8	8	12.95	26.25	M
R23	col	8	3	23.55	40.55	L	R23	col	8	9	11.49	23.20	M
R23	col	8	4	27.81	35.96	M	R23	col	8	10	15.37	22.23	M
R23	col	8	5	22.16	32.33	M	R25	col	1	1	7.41	57.63	L
R23	col	8	6	18.88	31.98	M	R25	col	1	2	11.10	42.99	L
R23	col	8	7	28.28	31.58	M	R25	col	1	3	14.76	43.22	L
R23	col	8	8	12.95	26.25	M	R25	col	1	4	15.44	45.95	L
R23	col	8	9	11.49	23.20	M	R25	col	1	5	15.86	28.91	M
R23	col	8	10	15.37	22.23	M	R25	col	1	6	16.30	45.62	L
R23	col	4	7	29.60	39.86	M	R25	col	1	7	16.58	36.89	M
R23	col	4	8	35.53	36.63	M	R25	col	1	8	11.41	34.82	M
R23	col	4	9	23.38	29.91	M	R25	col	1	9	16.76	41.60	L
R23	col	4	10	26.21	38.32	M	R25	col	1	10	18.05	47.11	L
R23	col	5	1	9.01	39.33	M	R25	col	2	1	16.80	48.33	L
R23	col	5	2	7.09	26.13	M	R25	col	2	2	14.81	32.81	M

φ: diameter; col: collagenase; S: small; M: medium; L: large

Note: Table is continued on the next page.

Table E.2. continued

Rat	Group	image no.	cell no.	intensity	φ (μm)	bin	Rat	Group	image no.	cell no.	intensity	φ (μm)	bin
R25	col	2	3	8.01	55.29	L	R26	vehicle	1	3	9.38	35.39	M
R25	col	2	4	10.89	38.11	M	R26	vehicle	1	4	11.15	33.26	M
R25	col	2	5	11.34	23.28	M	R26	vehicle	1	5	17.67	38.56	M
R25	col	2	6	9.42	33.77	M	R26	vehicle	1	6	13.64	37.67	M
R25	col	2	7	13.67	22.54	M	R26	vehicle	1	7	9.11	47.53	L
R25	col	2	8	13.23	30.01	M	R26	vehicle	1	8	16.01	34.13	M
R25	col	2	9	13.22	31.68	M	R26	vehicle	1	9	11.89	31.76	M
R25	col	2	10	10.74	33.39	M	R26	vehicle	1	10	10.57	29.78	M
R25	col	3	1	27.25	28.96	M	R26	vehicle	2	1	18.91	46.20	L
R25	col	3	2	12.63	23.14	M	R26	vehicle	2	2	15.05	49.23	L
R25	col	3	3	10.21	21.04	M	R26	vehicle	2	3	21.20	59.65	L
R25	col	3	4	17.51	23.37	M	R26	vehicle	2	4	26.93	39.40	M
R25	col	3	5	13.36	41.80	L	R26	vehicle	2	5	11.30	29.63	M
R25	col	3	6	10.21	26.64	M	R26	vehicle	2	6	23.98	38.83	M
R25	col	3	7	20.71	38.91	M	R26	vehicle	2	7	30.08	30.20	M
R25	col	3	8	11.38	23.95	M	R26	vehicle	2	8	13.41	24.80	M
R25	col	3	9	21.90	40.68	L	R26	vehicle	2	9	24.31	44.28	L
R25	col	3	10	16.92	39.74	M	R26	vehicle	2	10	23.16	55.04	L
R25	col	4	1	30.10	37.55	M	R26	vehicle	3	1	13.00	29.03	M
R25	col	4	2	27.00	39.67	M	R26	vehicle	3	2	8.80	32.43	M
R25	col	4	3	29.28	27.24	M	R26	vehicle	3	3	6.45	30.57	M
R25	col	4	4	25.85	27.98	M	R26	vehicle	3	4	25.60	34.88	M
R25	col	4	5	27.59	24.06	M	R26	vehicle	3	5	25.52	26.66	M
R25	col	4	6	29.40	28.74	M	R26	vehicle	3	6	26.54	37.12	M
R25	col	4	7	26.69	34.23	M	R26	vehicle	3	7	33.08	36.21	M
R25	col	4	8	26.75	40.14	L	R26	vehicle	3	8	8.35	22.06	M
R25	col	4	9	31.94	39.05	M	R26	vehicle	3	9	15.76	26.44	M
R25	col	4	10	18.49	34.37	M	R26	vehicle	3	10	15.64	23.74	M
R25	col	5	1	20.61	32.96	M	R26	vehicle	4	1	12.97	40.08	L
R25	col	5	2	24.21	22.69	M	R26	vehicle	4	2	8.90	31.83	M
R25	col	5	3	19.97	35.61	M	R26	vehicle	4	3	11.40	29.32	M
R25	col	5	4	21.80	28.02	M	R26	vehicle	4	4	13.45	36.99	M
R25	col	5	5	24.25	39.51	M	R26	vehicle	4	5	9.93	38.00	M
R25	col	5	6	26.05	23.83	M	R26	vehicle	4	6	11.11	35.25	M
R25	col	5	7	14.53	26.83	M	R26	vehicle	4	7	17.75	38.61	M
R25	col	5	8	27.60	23.68	M	R26	vehicle	4	8	15.74	39.32	M
R25	col	5	9	18.82	26.75	M	R26	vehicle	4	9	9.84	47.54	L
R25	col	5	10	23.15	30.47	M	R26	vehicle	4	10	14.92	39.74	M
R25	col	6	1	12.11	22.43	M	R26	vehicle	5	1	5.69	34.55	M
R25	col	6	2	9.90	35.76	M	R26	vehicle	5	2	6.93	41.88	L
R25	col	6	3	11.98	30.35	M	R26	vehicle	5	3	9.21	32.58	M
R25	col	6	4	15.41	43.83	L	R26	vehicle	5	4	9.25	36.93	M
R25	col	6	5	17.98	37.46	M	R26	vehicle	5	5	10.00	38.62	M
R25	col	6	6	15.36	34.46	M	R26	vehicle	5	6	8.02	35.99	M
R25	col	6	7	11.68	24.12	M	R26	vehicle	5	7	6.77	44.46	L
R25	col	6	8	16.53	29.93	M	R26	vehicle	5	8	10.24	41.76	L
R25	col	6	9	18.24	32.94	M	R26	vehicle	5	9	12.65	38.78	M
R25	col	6	10	23.96	40.04	L	R26	vehicle	5	10	10.07	26.42	M
R26	vehicle	1	1	13.28	29.71	M	R26	vehicle	6	1	14.93	32.82	M
R26	vehicle	1	2	9.32	51.02	L	R26	vehicle	6	2	18.25	27.88	M

φ: diameter; col: collagenase; S: small; M: medium; L: large

Note: Table is continued on the next page.

Table E.2. continued

Rat	Group	image no.	cell no.	intensity	φ (μm)	bin	Rat	Group	image no.	cell no.	intensity	φ (μm)	bin
R26	vehicle	6	3	13.84	26.14	M	R28	col	3	3	25.61	45.33	L
R26	vehicle	6	4	16.94	31.58	M	R28	col	3	4	36.84	32.16	M
R26	vehicle	6	5	12.03	22.02	M	R28	col	3	5	29.59	32.96	M
R26	vehicle	6	6	18.68	28.12	M	R28	col	3	6	26.69	24.24	M
R26	vehicle	6	7	27.29	38.03	M	R28	col	3	7	27.06	35.78	M
R26	vehicle	6	8	25.21	33.11	M	R28	col	3	8	30.96	29.36	M
R26	vehicle	6	9	25.59	27.76	M	R28	col	3	9	32.37	21.95	M
R26	vehicle	6	10	31.78	27.91	M	R28	col	3	10	27.52	21.24	M
R26	vehicle	7	1	11.50	35.41	M	R28	col	4	1	30.94	36.73	M
R26	vehicle	7	2	12.57	28.83	M	R28	col	4	2	27.34	37.45	M
R26	vehicle	7	3	6.61	43.22	L	R28	col	4	3	23.95	38.38	M
R26	vehicle	7	4	8.27	29.67	M	R28	col	4	4	16.81	33.18	M
R26	vehicle	7	5	8.22	33.11	M	R28	col	4	5	19.88	23.60	M
R26	vehicle	7	6	16.81	33.10	M	R28	col	4	6	26.21	26.91	M
R26	vehicle	7	7	10.22	35.78	M	R28	col	4	7	20.42	32.30	M
R26	vehicle	7	8	15.30	29.66	M	R28	col	4	8	28.77	22.95	M
R26	vehicle	7	9	18.59	34.38	M	R28	col	4	9	25.54	28.33	M
R26	vehicle	7	10	10.03	24.81	M	R28	col	4	10	21.91	27.49	M
R26	vehicle	8	1	21.75	29.04	M	R28	col	5	1	17.91	24.71	M
R26	vehicle	8	2	17.66	41.36	L	R28	col	5	2	15.79	22.51	M
R26	vehicle	8	3	11.18	36.79	M	R28	col	5	3	13.08	37.77	M
R26	vehicle	8	4	15.80	40.00	L	R28	col	5	4	22.92	31.12	M
R26	vehicle	8	5	19.15	42.98	L	R28	col	5	5	30.27	36.42	M
R26	vehicle	8	6	9.97	24.72	M	R28	col	5	6	26.50	33.40	M
R26	vehicle	8	7	9.55	29.54	M	R28	col	5	7	27.39	21.12	M
R26	vehicle	8	8	16.24	27.60	M	R28	col	5	8	26.89	33.57	M
R26	vehicle	8	9	13.96	33.91	M	R28	col	5	9	33.58	36.93	M
R26	vehicle	8	10	16.05	34.11	M	R28	col	5	10	26.67	36.02	M
R28	col	1	1	25.50	34.11	M	R28	col	6	1	27.03	41.46	L
R28	col	1	2	15.86	33.05	M	R28	col	6	2	26.61	29.39	M
R28	col	1	3	19.00	40.71	L	R28	col	6	3	24.00	28.47	M
R28	col	1	4	30.55	24.40	M	R28	col	6	4	29.45	40.47	L
R28	col	1	5	16.62	39.68	M	R28	col	6	5	22.97	31.41	M
R28	col	1	6	17.00	26.14	M	R28	col	6	6	33.31	35.64	M
R28	col	1	7	15.94	22.61	M	R28	col	6	7	18.10	20.24	S
R28	col	1	8	17.02	22.99	M	R28	col	6	8	24.97	26.40	M
R28	col	1	9	12.49	15.56	S	R28	col	6	9	21.72	22.99	M
R28	col	1	10	11.95	17.31	S	R28	col	6	10	37.43	32.29	M
R28	col	2	1	33.45	33.62	M	R28	col	7	1	35.52	38.22	M
R28	col	2	2	39.98	33.86	M	R28	col	7	2	37.54	26.65	M
R28	col	2	3	35.62	23.10	M	R28	col	7	3	30.77	29.54	M
R28	col	2	4	32.21	35.32	M	R28	col	7	4	31.88	40.31	L
R28	col	2	5	33.27	23.81	M	R28	col	7	5	24.45	16.65	S
R28	col	2	6	29.91	16.34	S	R28	col	7	6	40.62	38.78	M
R28	col	2	7	38.19	22.57	M	R28	col	7	7	41.78	29.52	M
R28	col	2	8	34.18	22.07	M	R28	col	7	8	37.41	21.58	M
R28	col	2	9	25.16	12.87	S	R28	col	7	9	25.54	36.05	M
R28	col	2	10	32.12	36.90	M	R28	col	7	10	38.08	25.55	M
R28	col	3	1	38.24	36.48	M	R28	col	8	1	20.85	28.12	M
R28	col	3	2	34.25	34.62	M	R28	col	8	2	15.88	27.31	M

φ: diameter; col: collagenase; S: small; M: medium; L: large

Note: Table is continued on the next page.

Table E.2. continued

Rat	Group	image no.	cell no.	intensity	φ (μm)	bin	Rat	Group	image no.	cell no.	intensity	φ (μm)	bin
R28	col	8	3	23.75	32.95	M	R30	col	5	3	17.06	27.44	M
R28	col	8	4	22.48	30.42	M	R30	col	5	4	12.59	40.24	L
R28	col	8	5	15.54	36.97	M	R30	col	5	5	15.20	19.81	S
R28	col	8	6	19.13	28.53	M	R30	col	5	6	13.29	30.78	M
R28	col	8	7	26.20	36.28	M	R30	col	5	7	16.71	26.87	M
R28	col	8	8	16.09	30.42	M	R30	col	5	8	11.94	23.08	M
R28	col	8	9	18.35	27.92	M	R30	col	5	9	11.18	19.81	S
R28	col	8	10	19.34	25.02	M	R30	col	5	10	17.64	47.06	L
R30	col	1	1	8.12	37.15	M	R30	col	6	1	23.17	39.80	M
R30	col	1	2	8.73	30.34	M	R30	col	6	2	23.65	46.51	L
R30	col	1	3	6.18	33.94	M	R30	col	6	3	18.13	28.61	M
R30	col	1	4	13.31	30.70	M	R30	col	6	4	24.11	31.36	M
R30	col	1	5	5.72	25.73	M	R30	col	6	5	17.39	44.98	L
R30	col	1	6	7.47	48.82	L	R30	col	6	6	20.87	43.03	L
R30	col	1	7	6.37	49.02	L	R30	col	6	7	22.72	47.46	L
R30	col	1	8	7.55	29.86	M	R30	col	6	8	18.30	24.05	M
R30	col	1	9	15.21	25.19	M	R30	col	6	9	22.07	48.96	L
R30	col	1	10	5.62	46.08	L	R30	col	6	10	24.54	34.95	M
R30	col	2	1	9.20	41.58	L	R30	col	7	1	21.96	40.95	L
R30	col	2	2	10.69	39.16	M	R30	col	7	2	16.37	23.06	M
R30	col	2	3	9.87	54.47	L	R30	col	7	3	16.82	18.36	S
R30	col	2	4	13.94	38.45	M	R30	col	7	4	25.03	35.12	M
R30	col	2	5	11.62	28.58	M	R30	col	7	5	17.36	20.33	S
R30	col	2	6	9.04	32.34	M	R30	col	7	6	24.24	39.24	M
R30	col	2	7	10.34	37.63	M	R30	col	7	7	13.46	54.33	L
R30	col	2	8	9.22	41.22	L	R30	col	7	8	12.64	52.25	L
R30	col	2	9	10.50	44.54	L	R30	col	7	9	16.49	24.30	M
R30	col	2	10	8.79	27.23	M	R30	col	7	10	18.40	43.85	L
R30	col	3	1	8.72	48.54	L	R30	col	8	1	23.59	30.82	M
R30	col	3	2	9.50	49.18	L	R30	col	8	2	37.02	30.79	M
R30	col	3	3	6.07	26.93	M	R30	col	8	3	25.60	31.68	M
R30	col	3	4	6.86	44.86	L	R30	col	8	4	38.84	42.18	L
R30	col	3	5	5.92	55.45	L	R30	col	8	5	29.74	21.06	M
R30	col	3	6	8.48	41.03	L	R30	col	8	6	25.48	40.31	L
R30	col	3	7	6.49	59.96	L	R30	col	8	7	48.03	35.74	M
R30	col	3	8	7.70	38.12	M	R30	col	8	8	39.50	44.56	L
R30	col	3	9	11.07	24.23	M	R30	col	8	9	26.29	45.02	L
R30	col	3	10	6.69	47.53	L	R30	col	8	10	22.20	29.24	M
R30	col	4	1	8.94	36.75	M	R31	vehicle	1	1	10.60	37.71	M
R30	col	4	2	7.97	33.46	M	R31	vehicle	1	2	8.18	28.68	M
R30	col	4	3	7.14	56.65	L	R31	vehicle	1	3	8.33	30.91	M
R30	col	4	4	6.54	53.44	L	R31	vehicle	1	4	7.92	25.51	M
R30	col	4	5	7.78	37.39	M	R31	vehicle	1	5	8.80	27.96	M
R30	col	4	6	5.39	47.95	L	R31	vehicle	1	6	14.93	30.52	M
R30	col	4	7	6.51	42.81	L	R31	vehicle	1	7	10.73	33.14	M
R30	col	4	8	9.40	39.76	M	R31	vehicle	1	8	12.16	40.15	L
R30	col	4	9	5.65	39.60	M	R31	vehicle	1	9	15.09	23.03	M
R30	col	4	10	5.17	40.85	L	R31	vehicle	1	10	15.51	18.91	S
R30	col	5	1	11.07	72.25	L	R31	vehicle	2	1	15.88	26.20	M
R30	col	5	2	10.40	57.15	L	R31	vehicle	2	2	6.13	32.01	M

φ: diameter; col: collagenase; S: small; M: medium; L: large

Note: Table is continued on the next page.

Table E.2. continued

Rat	Group	image no.	cell no.	intensity	φ (μm)	bin	Rat	Group	image no.	cell no.	intensity	φ (μm)	bin
R31	vehicle	2	3	7.24	43.86	L	R31	vehicle	7	3	10.33	24.49	M
R31	vehicle	2	4	9.54	36.39	M	R31	vehicle	7	4	22.99	33.68	M
R31	vehicle	2	5	10.42	31.65	M	R31	vehicle	7	5	15.11	40.50	L
R31	vehicle	2	6	18.18	24.71	M	R31	vehicle	7	6	24.92	37.32	M
R31	vehicle	2	7	12.07	36.24	M	R31	vehicle	7	7	17.67	33.78	M
R31	vehicle	2	8	19.56	40.05	L	R31	vehicle	7	8	17.00	21.88	M
R31	vehicle	2	9	13.14	39.98	M	R31	vehicle	7	9	16.43	40.82	L
R31	vehicle	2	10	17.97	25.98	M	R31	vehicle	7	10	17.20	35.03	M
R31	vehicle	3	1	19.40	29.40	M	R35	vehicle	1	1	27.51	42.11	L
R31	vehicle	3	2	14.33	34.68	M	R35	vehicle	1	2	22.55	27.56	M
R31	vehicle	3	3	18.49	32.99	M	R35	vehicle	1	3	21.12	39.86	M
R31	vehicle	3	4	19.09	34.92	M	R35	vehicle	1	4	15.19	29.88	M
R31	vehicle	3	5	20.69	28.09	M	R35	vehicle	1	5	12.50	25.36	M
R31	vehicle	3	6	19.16	33.62	M	R35	vehicle	1	6	13.41	29.94	M
R31	vehicle	3	7	18.62	31.80	M	R35	vehicle	1	7	19.33	46.33	L
R31	vehicle	3	8	19.03	38.94	M	R35	vehicle	1	8	17.86	25.64	M
R31	vehicle	3	9	23.67	28.75	M	R35	vehicle	1	9	16.68	41.84	L
R31	vehicle	3	10	9.67	40.09	L	R35	vehicle	1	10	15.65	36.44	M
R31	vehicle	4	1	8.77	40.78	L	R35	vehicle	2	1	12.41	54.83	L
R31	vehicle	4	2	15.01	47.79	L	R35	vehicle	2	2	7.71	43.60	L
R31	vehicle	4	3	15.64	38.71	M	R35	vehicle	2	3	10.81	33.87	M
R31	vehicle	4	4	13.21	47.48	L	R35	vehicle	2	4	12.21	35.50	M
R31	vehicle	4	5	14.03	40.27	L	R35	vehicle	2	5	11.82	30.43	M
R31	vehicle	4	6	11.03	42.30	L	R35	vehicle	2	6	8.03	27.74	M
R31	vehicle	4	7	20.25	26.27	M	R35	vehicle	2	7	10.09	29.26	M
R31	vehicle	4	8	10.54	24.87	M	R35	vehicle	2	8	12.35	38.71	M
R31	vehicle	4	9	9.40	19.54	S	R35	vehicle	2	9	14.96	43.57	L
R31	vehicle	4	10	22.25	27.18	M	R35	vehicle	2	10	9.33	29.47	M
R31	vehicle	5	1	7.03	47.28	L	R35	vehicle	3	1	20.90	40.39	L
R31	vehicle	5	2	10.76	32.03	M	R35	vehicle	3	2	20.65	39.15	M
R31	vehicle	5	3	10.27	36.22	M	R35	vehicle	3	3	25.60	32.60	M
R31	vehicle	5	4	9.29	47.57	L	R35	vehicle	3	4	28.28	30.21	M
R31	vehicle	5	5	7.32	33.97	M	R35	vehicle	3	5	15.55	27.63	M
R31	vehicle	5	6	9.08	40.94	L	R35	vehicle	3	6	15.07	34.77	M
R31	vehicle	5	7	11.00	35.09	M	R35	vehicle	3	7	26.01	22.76	M
R31	vehicle	5	8	11.20	43.50	L	R35	vehicle	3	8	16.34	29.22	M
R31	vehicle	5	9	12.45	34.77	M	R35	vehicle	3	9	25.16	32.83	M
R31	vehicle	5	10	10.80	32.18	M	R35	vehicle	3	10	22.73	27.30	M
R31	vehicle	6	1	10.72	41.38	L	R35	vehicle	4	1	13.12	34.88	M
R31	vehicle	6	2	11.80	27.80	M	R35	vehicle	4	2	16.83	37.81	M
R31	vehicle	6	3	10.47	37.64	M	R35	vehicle	4	3	17.41	39.44	M
R31	vehicle	6	4	15.23	39.85	M	R35	vehicle	4	4	16.94	38.97	M
R31	vehicle	6	5	9.16	46.95	L	R35	vehicle	4	5	23.93	34.32	M
R31	vehicle	6	6	16.01	27.60	M	R35	vehicle	4	6	20.85	35.13	M
R31	vehicle	6	7	9.71	46.40	L	R35	vehicle	4	7	7.30	20.72	S
R31	vehicle	6	8	15.04	44.12	L	R35	vehicle	4	8	9.65	27.18	M
R31	vehicle	6	9	11.72	31.65	M	R35	vehicle	4	9	9.89	23.41	M
R31	vehicle	6	10	11.80	46.30	L	R35	vehicle	4	10	20.88	37.74	M
R31	vehicle	7	1	25.40	37.12	M	R35	vehicle	5	1	14.94	29.48	M
R31	vehicle	7	2	21.94	49.92	L	R35	vehicle	5	2	22.85	32.92	M

φ: diameter; col: collagenase; S: small; M: medium; L: large

Note: Table is continued on the next page.

Table E.2. continued

Rat	Group	image no.	cell no.	intensity	φ (μm)	bin	Rat	Group	image no.	cell no.	intensity	φ (μm)	bin
R35	vehicle	5	3	24.27	34.05	M	R36	col	3	3	35.74	32.28	M
R35	vehicle	5	4	17.04	29.82	M	R36	col	3	4	39.27	35.12	M
R35	vehicle	5	5	33.84	42.65	L	R36	col	3	5	39.44	44.64	L
R35	vehicle	5	6	39.57	22.31	M	R36	col	3	6	37.32	26.72	M
R35	vehicle	5	7	23.89	47.95	L	R36	col	3	7	37.69	36.97	M
R35	vehicle	5	8	25.37	38.10	M	R36	col	3	8	39.11	39.90	M
R35	vehicle	5	9	15.67	23.31	M	R36	col	3	9	40.41	36.93	M
R35	vehicle	5	10	27.78	33.48	M	R36	col	3	10	37.65	40.19	L
R35	vehicle	6	1	15.81	33.44	M	R36	col	4	1	25.30	23.01	M
R35	vehicle	6	2	17.40	37.35	M	R36	col	4	2	37.41	29.69	M
R35	vehicle	6	3	19.11	41.48	L	R36	col	4	3	43.32	34.14	M
R35	vehicle	6	4	13.96	33.76	M	R36	col	4	4	15.09	27.12	M
R35	vehicle	6	5	11.02	32.54	M	R36	col	4	5	34.56	44.47	L
R35	vehicle	6	6	17.97	38.28	M	R36	col	4	6	41.24	30.81	M
R35	vehicle	6	7	10.72	41.57	L	R36	col	4	7	37.10	44.59	L
R35	vehicle	6	8	11.96	24.82	M	R36	col	4	8	39.48	31.99	M
R35	vehicle	6	9	28.22	30.46	M	R36	col	4	9	30.74	33.68	M
R35	vehicle	6	10	16.41	34.59	M	R36	col	4	10	39.27	50.27	L
R35	vehicle	7	1	16.42	33.99	M	R36	col	5	1	15.72	33.69	M
R35	vehicle	7	2	13.53	34.04	M	R36	col	5	2	15.87	31.81	M
R35	vehicle	7	3	15.23	47.77	L	R36	col	5	3	15.47	26.06	M
R35	vehicle	7	4	11.80	26.16	M	R36	col	5	4	14.98	44.34	L
R35	vehicle	7	5	19.21	22.97	M	R36	col	5	5	17.41	44.81	L
R35	vehicle	7	6	16.03	37.87	M	R36	col	5	6	12.84	47.83	L
R35	vehicle	7	7	13.70	32.31	M	R36	col	5	7	12.78	57.22	L
R35	vehicle	7	8	9.87	28.26	M	R36	col	5	8	14.73	41.45	L
R35	vehicle	7	9	11.57	31.87	M	R36	col	5	9	21.39	37.41	M
R35	vehicle	7	10	10.54	33.86	M	R36	col	5	10	18.02	34.90	M
R36	col	1	1	39.58	39.16	M	R36	col	6	1	9.30	58.06	L
R36	col	1	2	29.47	31.41	M	R36	col	6	2	10.03	38.58	M
R36	col	1	3	36.21	22.61	M	R36	col	6	3	9.65	57.46	L
R36	col	1	4	45.97	30.46	M	R36	col	6	4	10.89	35.07	M
R36	col	1	5	32.42	39.73	M	R36	col	6	5	12.50	32.90	M
R36	col	1	6	42.27	34.58	M	R36	col	6	6	9.12	51.22	L
R36	col	1	7	25.60	27.52	M	R36	col	6	7	6.64	56.29	L
R36	col	1	8	37.02	44.13	L	R36	col	6	8	8.71	44.53	L
R36	col	1	9	36.04	43.13	L	R36	col	6	9	6.29	39.29	M
R36	col	1	10	35.37	35.36	M	R36	col	6	10	7.68	54.02	L
R36	col	2	1	31.36	34.90	M	R36	col	3	3	35.74	32.28	M
R36	col	2	2	18.03	35.29	M	R36	col	3	4	39.27	35.12	M
R36	col	2	3	21.54	31.30	M	R36	col	3	5	39.44	44.64	L
R36	col	2	4	21.28	30.18	M	R36	col	3	6	37.32	26.72	M
R36	col	2	5	24.79	25.17	M	R36	col	3	7	37.69	36.97	M
R36	col	2	6	32.79	32.35	M	R36	col	3	8	39.11	39.90	M
R36	col	2	7	28.38	41.30	L	R36	col	3	9	40.41	36.93	M
R36	col	2	8	22.15	33.60	M	R36	col	3	10	37.65	40.19	L
R36	col	2	9	35.75	32.20	M	R36	col	4	1	25.30	23.01	M
R36	col	2	10	22.99	66.83	L	R36	col	4	2	37.41	29.69	M
R36	col	3	1	39.37	32.10	M	R36	col	4	3	43.32	34.14	M
R36	col	3	2	39.11	41.39	L	R36	col	4	4	15.09	27.12	M

φ: diameter; col: collagenase; S: small; M: medium; L: large

Note: Table is continued on the next page.

Table E.2. continued

Rat	Group	image no.	cell no.	intensity	φ (μm)	bin	Rat	Group	image no.	cell no.	intensity	φ (μm)	bin
R35	vehicle	5	3	24.27	34.05	M	R36	col	3	3	35.74	32.28	M
R35	vehicle	5	4	17.04	29.82	M	R36	col	3	4	39.27	35.12	M
R35	vehicle	5	5	33.84	42.65	L	R36	col	3	5	39.44	44.64	L
R35	vehicle	5	6	39.57	22.31	M	R36	col	3	6	37.32	26.72	M
R35	vehicle	5	7	23.89	47.95	L	R36	col	3	7	37.69	36.97	M
R35	vehicle	5	8	25.37	38.10	M	R36	col	3	8	39.11	39.90	M
R35	vehicle	5	9	15.67	23.31	M	R36	col	3	9	40.41	36.93	M
R35	vehicle	5	10	27.78	33.48	M	R36	col	3	10	37.65	40.19	L
R35	vehicle	6	1	15.81	33.44	M	R36	col	4	1	25.30	23.01	M
R35	vehicle	6	2	17.40	37.35	M	R36	col	4	2	37.41	29.69	M
R35	vehicle	6	3	19.11	41.48	L	R36	col	4	3	43.32	34.14	M
R35	vehicle	6	4	13.96	33.76	M	R36	col	4	4	15.09	27.12	M
R35	vehicle	6	5	11.02	32.54	M	R36	col	4	5	34.56	44.47	L
R35	vehicle	6	6	17.97	38.28	M	R36	col	4	6	41.24	30.81	M
R35	vehicle	6	7	10.72	41.57	L	R36	col	4	7	37.10	44.59	L
R35	vehicle	6	8	11.96	24.82	M	R36	col	4	8	39.48	31.99	M
R35	vehicle	6	9	28.22	30.46	M	R36	col	4	9	30.74	33.68	M
R35	vehicle	6	10	16.41	34.59	M	R36	col	4	10	39.27	50.27	L
R35	vehicle	7	1	16.42	33.99	M	R36	col	5	1	15.72	33.69	M
R35	vehicle	7	2	13.53	34.04	M	R36	col	5	2	15.87	31.81	M
R35	vehicle	7	3	15.23	47.77	L	R36	col	5	3	15.47	26.06	M
R35	vehicle	7	4	11.80	26.16	M	R36	col	5	4	14.98	44.34	L
R35	vehicle	7	5	19.21	22.97	M	R36	col	5	5	17.41	44.81	L
R35	vehicle	7	6	16.03	37.87	M	R36	col	5	6	12.84	47.83	L
R35	vehicle	7	7	13.70	32.31	M	R36	col	5	7	12.78	57.22	L
R35	vehicle	7	8	9.87	28.26	M	R36	col	5	8	14.73	41.45	L
R35	vehicle	7	9	11.57	31.87	M	R36	col	5	9	21.39	37.41	M
R35	vehicle	7	10	10.54	33.86	M	R36	col	5	10	18.02	34.90	M
R36	col	1	1	39.58	39.16	M	R36	col	6	1	9.30	58.06	L
R36	col	1	2	29.47	31.41	M	R36	col	6	2	10.03	38.58	M
R36	col	1	3	36.21	22.61	M	R36	col	6	3	9.65	57.46	L
R36	col	1	4	45.97	30.46	M	R36	col	6	4	10.89	35.07	M
R36	col	1	5	32.42	39.73	M	R36	col	6	5	12.50	32.90	M
R36	col	1	6	42.27	34.58	M	R36	col	6	6	9.12	51.22	L
R36	col	1	7	25.60	27.52	M	R36	col	6	7	6.64	56.29	L
R36	col	1	8	37.02	44.13	L	R36	col	6	8	8.71	44.53	L
R36	col	1	9	36.04	43.13	L	R36	col	6	9	6.29	39.29	M
R36	col	1	10	35.37	35.36	M	R36	col	6	10	7.68	54.02	L
R36	col	2	1	31.36	34.90	M	R36	col	3	3	35.74	32.28	M
R36	col	2	2	18.03	35.29	M	R36	col	3	4	39.27	35.12	M
R36	col	2	3	21.54	31.30	M	R36	col	3	5	39.44	44.64	L
R36	col	2	4	21.28	30.18	M	R36	col	3	6	37.32	26.72	M
R36	col	2	5	24.79	25.17	M	R36	col	3	7	37.69	36.97	M
R36	col	2	6	32.79	32.35	M	R36	col	3	8	39.11	39.90	M
R36	col	2	7	28.38	41.30	L	R36	col	3	9	40.41	36.93	M
R36	col	2	8	22.15	33.60	M	R36	col	3	10	37.65	40.19	L
R36	col	2	9	35.75	32.20	M	R36	col	4	1	25.30	23.01	M
R36	col	2	10	22.99	66.83	L	R36	col	4	2	37.41	29.69	M
R36	col	3	1	39.37	32.10	M	R36	col	4	3	43.32	34.14	M
R36	col	3	2	39.11	41.39	L	R36	col	4	4	15.09	27.12	M

φ: diameter; col: collagenase; S: small; M: medium; L: large

Note: Table is continued on the next page.

Table E.2. continued

Rat	Group	image no.	cell no.	intensity	φ (μm)	bin
R36	col	4	5	34.56	44.47	L
R36	col	4	6	41.24	30.81	M
R36	col	4	7	37.10	44.59	L
R36	col	4	8	39.48	31.99	M
R36	col	4	9	30.74	33.68	M
R36	col	4	10	39.27	50.27	L
R36	col	5	1	15.72	33.69	M
R36	col	5	2	15.87	31.81	M
R36	col	5	3	15.47	26.06	M
R36	col	5	4	14.98	44.34	L
R36	col	5	5	17.41	44.81	L
R36	col	5	6	12.84	47.83	L
R36	col	5	7	12.78	57.22	L
R36	col	5	8	14.73	41.45	L
R36	col	5	9	21.39	37.41	M
R36	col	5	10	18.02	34.90	M
R36	col	6	1	9.30	58.06	L
R36	col	6	2	10.03	38.58	M
R36	col	6	3	9.65	57.46	L
R36	col	6	4	10.89	35.07	M
R36	col	6	5	12.50	32.90	M
R36	col	6	6	9.12	51.22	L
R36	col	6	7	6.64	56.29	L
R36	col	6	8	8.71	44.53	L
R36	col	6	9	6.29	39.29	M
R36	col	6	10	7.68	54.02	L
R36	col	7	1	15.35	62.06	L
R36	col	7	2	15.22	46.08	L
R36	col	7	3	16.57	46.13	L
R36	col	7	4	17.32	45.82	L
R36	col	7	5	11.40	47.80	L
R36	col	7	6	7.89	33.59	M
R36	col	7	7	13.22	30.81	M
R36	col	7	8	12.33	28.74	M
R36	col	7	9	16.93	45.10	L
R36	col	7	10	12.09	36.88	M
R36	col	8	1	18.57	44.61	L
R36	col	8	2	21.03	32.84	M
R36	col	8	3	20.88	50.20	L
R36	col	8	4	19.20	41.46	L
R36	col	8	5	14.79	28.83	M
R36	col	8	6	15.74	19.99	S
R36	col	8	7	17.52	34.97	M
R36	col	8	8	16.25	23.68	M
R36	col	8	9	14.51	33.33	M
R36	col	8	10	19.54	27.55	M
R40	naive	1	1	19.82	48.94	L
R40	naive	1	2	31.43	37.26	M
R40	naive	1	3	29.94	31.92	M
R40	naive	1	4	27.44	27.54	M
R40	naive	4	2	28.39	20.21	S
R40	naive	4	3	32.83	21.48	M
R40	naive	4	4	38.64	23.28	M
R40	naive	4	5	44.41	29.62	M
R40	naive	4	6	39.64	28.76	M
R40	naive	4	7	26.95	19.54	S
R40	naive	4	8	35.18	31.05	M
R40	naive	4	9	30.35	27.29	M
R40	naive	4	10	37.94	31.82	M
R40	naive	5	1	37.47	34.40	M
R40	naive	5	2	35.70	24.68	M
R40	naive	5	3	36.14	49.44	L
R40	naive	5	4	36.03	46.86	L
R40	naive	5	5	39.31	36.52	M
R40	naive	5	6	34.79	45.68	L
R40	naive	5	7	33.32	37.94	M
R40	naive	5	8	42.40	44.88	L
R40	naive	5	9	35.33	37.32	M
R40	naive	5	10	29.21	31.98	M
R40	naive	6	1	25.66	45.94	L
R40	naive	6	2	31.69	34.13	M
R40	naive	6	3	26.64	21.18	M
R40	naive	6	4	15.80	17.07	S
R40	naive	6	5	17.32	40.46	L
R40	naive	6	6	26.92	21.60	M
R40	naive	6	7	18.95	20.75	S
R40	naive	6	8	19.64	36.30	M
R40	naive	6	9	21.74	31.35	M
R40	naive	6	10	19.13	19.87	S

φ: diameter; col: collagenase; S: small; M: medium; L: large

Figure E.1. Immunolabeling of substance P (red), pERK (blue), and MAP-2 (green) in DRG neurons as designated in Table E.1 (substance P) and Table E.2 (pERK) (Chapter 4)

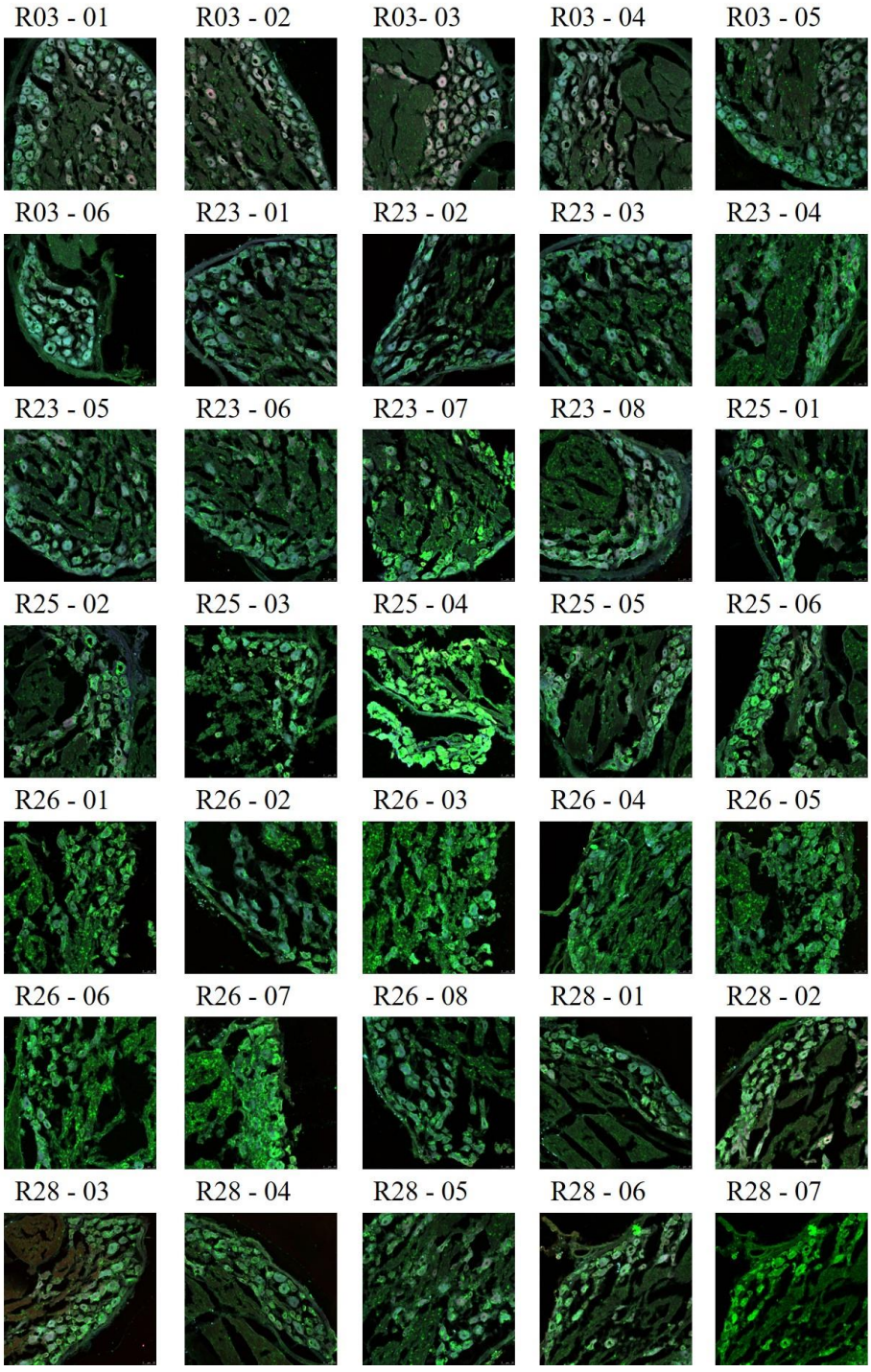

Note: Figure is continued on the next page.

Figure E.1. continued

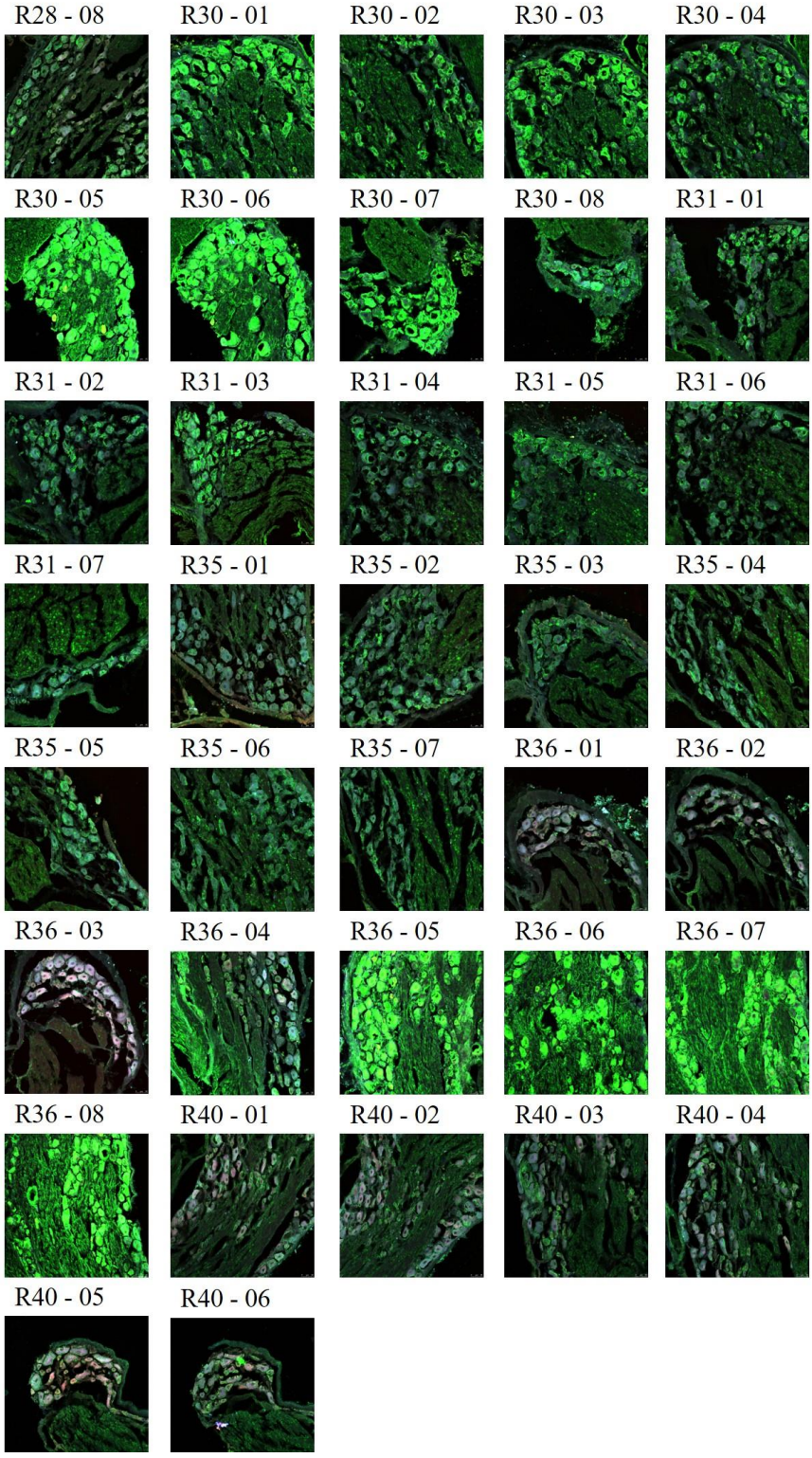

Table E.3. Densitometry of substance P and pERK in the superficial dorsal horn of the spinal cord from rats injected with bacterial collagenase or vehicle (Chapter 4)

Rat	Group	image no.	substance P (% positive)	pERK (% positive)
R03	naive	1	1.88%	5.36%
R03	naive	2	4.30%	5.78%
R03	naive	3	24.07%	10.52%
R03	naive	4	3.25%	23.19%
R03	naive	5	1.98%	0.13%
R03	naive	6	7.29%	5.84%
R23	col	1	19.75%	40.83%
R23	col	2	5.45%	21.24%
R23	col	3	2.80%	22.12%
R23	col	4	15.35%	10.61%
R23	col	5	8.61%	13.78%
R23	col	6	5.47%	14.15%
R23	col	7	5.22%	11.17%
R23	col	8	8.36%	12.94%
R23	col	9	7.88%	7.51%
R25	col	1	36.46%	28.45%
R25	col	2	19.76%	11.89%
R25	col	3	16.08%	0.19%
R25	col	4	11.43%	1.38%
R25	col	5	12.86%	5.83%
R26	vehicle	1	2.40%	0.29%
R26	vehicle	2	2.49%	3.76%
R26	vehicle	3	4.94%	1.62%
R26	vehicle	4	13.19%	3.51%
R26	vehicle	5	12.90%	2.62%
R28	col	1	10.94%	0.24%
R28	col	2	8.52%	0.06%
R28	col	3	9.43%	0.58%
R28	col	4	9.18%	0.13%
R28	col	5	6.60%	0.11%
R28	col	6	10.63%	0.28%
R28	col	7	6.21%	4.12%
R29	col	1	17.69%	0.34%
R29	col	2	9.73%	8.28%
R29	col	3	13.27%	9.36%
R29	col	4	11.56%	18.48%
R29	col	5	3.41%	19.27%
R29	col	6	6.80%	22.77%
R29	col	7	6.13%	1.79%
R29	col	8	13.73%	0.66%
R29	col	8	6.55%	1.40%
R29	col	9	22.33%	5.10%
R29	col	10	7.76%	1.82%
R30	col	1	7.37%	0.43%
R30	col	2	6.54%	12.81%
R30	col	3	10.57%	0.78%
R30	col	4	15.79%	0.54%
R30	col	5	0.43%	0.21%
R30	col	6	4.24%	1.17%
R35	vehicle	1	2.76%	0.25%
R35	vehicle	2	0.76%	0.16%
R35	vehicle	3	2.28%	0.54%
R35	vehicle	4	5.89%	3.42%
R35	vehicle	5	4.26%	2.07%
R35	vehicle	6	11.87%	8.25%
R36	col	1	3.28%	2.97%
R36	col	2	28.40%	17.68%
R36	col	3	4.02%	9.54%
R36	col	4	0.71%	1.77%
R36	col	5	14.66%	32.10%
R36	col	6	2.56%	1.50%
R36	col	7	5.78%	1.01%
R36	col	8	2.64%	4.11%
R36	col	9	1.52%	1.30%
R40	naive	1	11.25%	0.14%
R40	naive	2	3.26%	0.18%
R40	naive	3	3.79%	0.19%
R40	naive	4	5.70%	0.13%
R40	naive	5	5.93%	0.25%
R40	naive	6	6.02%	0.15%
R40	naive	7	12.43%	0.47%
R40	naive	8	11.37%	1.10%
R40	naive	9	13.86%	2.86%
R40	naive	10	24.57%	6.10%

col: collagenase

Figure E.2. Immunolabeling of substance P (red), pERK (blue), and MAP-2 (green) in the superficial dorsal horn of the spinal cord as designated in Table E.3 (Chapter 4)

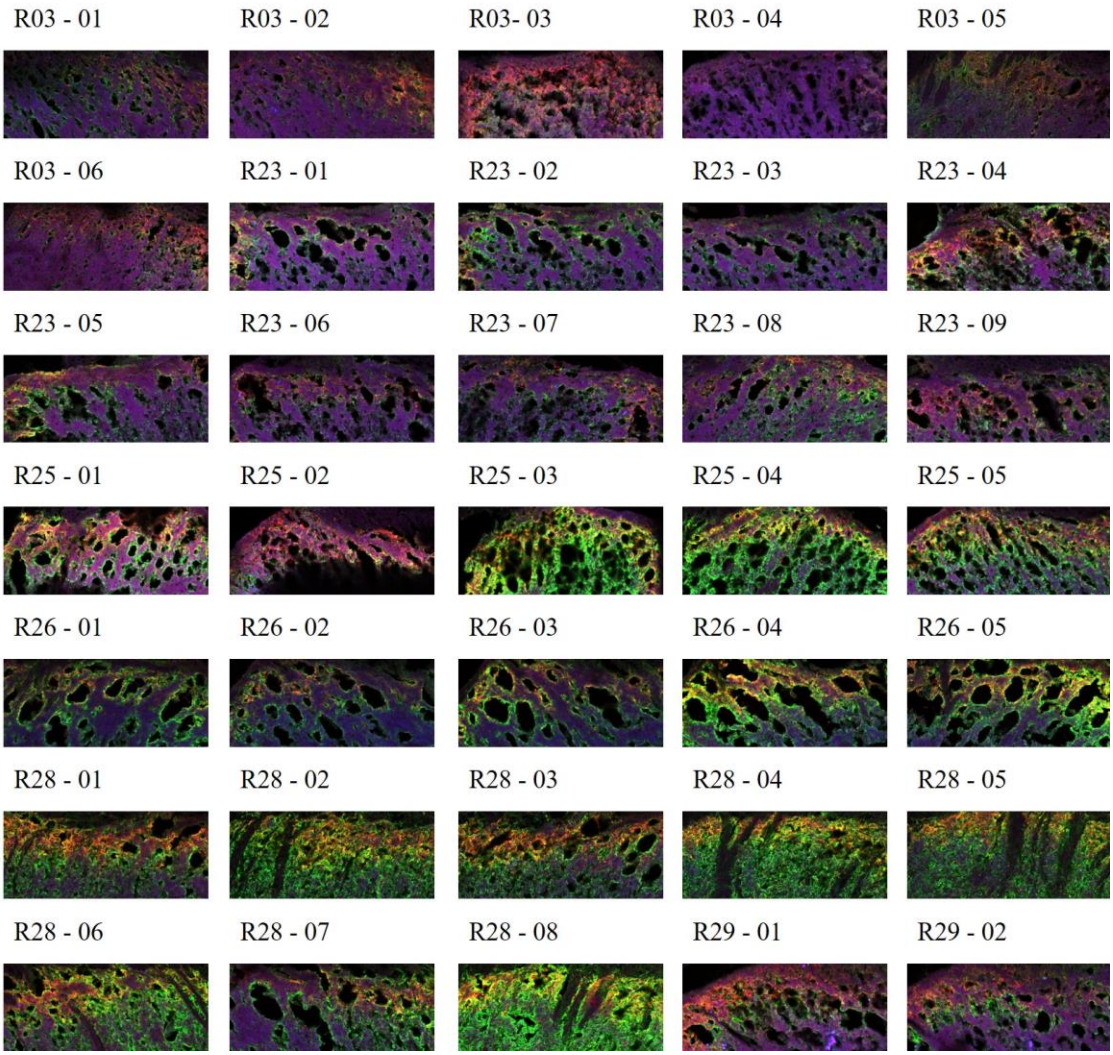

Note: Figure is continued on the next page.

Figure E.2. continued

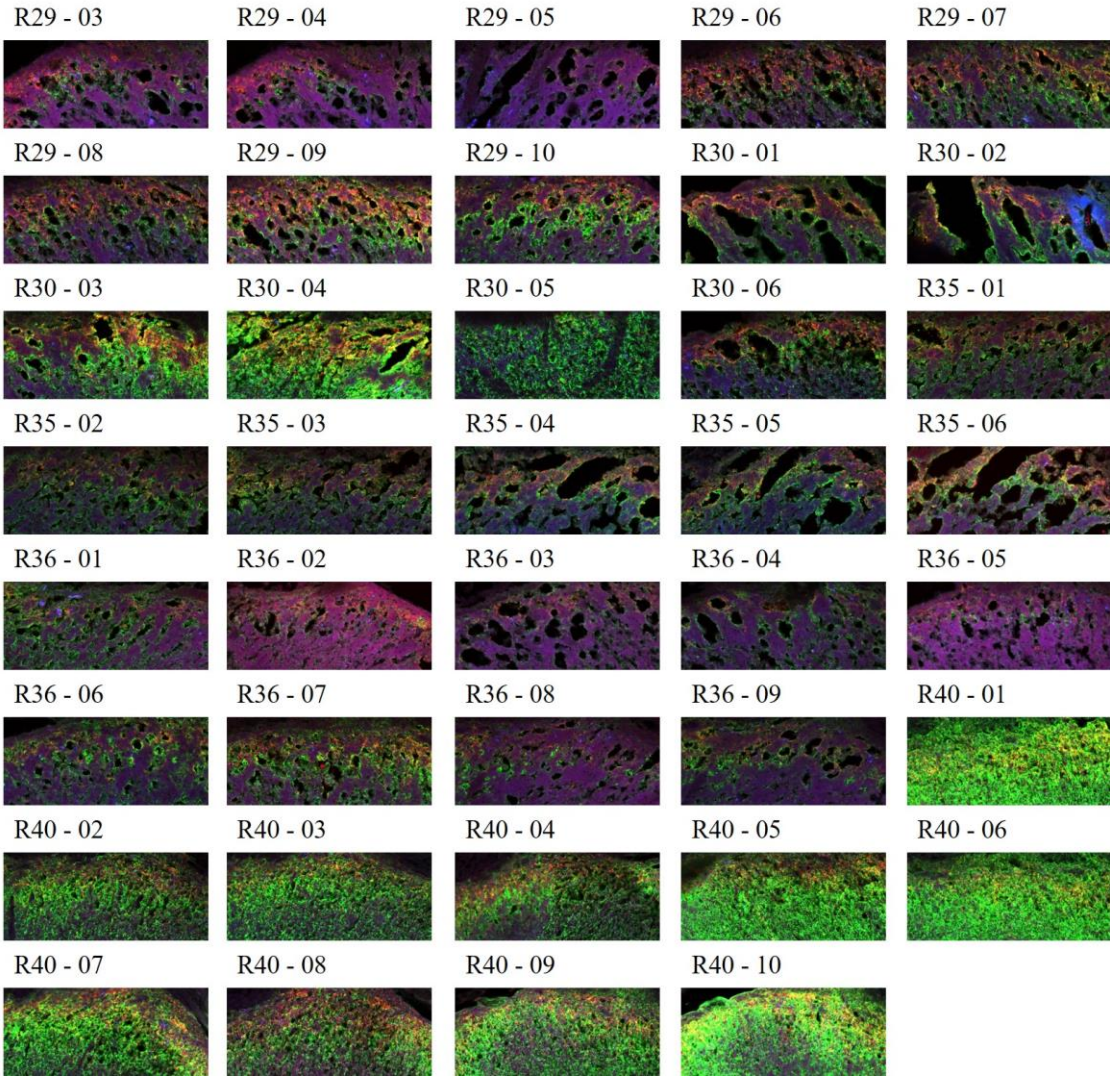

Table E.4. Densitometry of MMP-1 immunolabeling in DRGs from rats injected with bacterial collagenase or vehicle (Chapter 4)

Rat	Group	image no.	MMP-1 (% positive)
R03	naïve	1	12.89%
R03	naïve	2	15.15%
R03	naïve	3	8.39%
R03	naïve	4	2.38%
R03	naïve	5	8.22%
R03	naïve	6	8.25%
R23	col	1	2.85%
R23	col	2	22.34%
R23	col	3	7.85%
R23	col	4	11.07%
R23	col	5	14.18%
R23	col	6	8.18%
R25	col	1	11.00%
R25	col	2	37.57%
R25	col	3	8.25%
R25	col	4	14.48%
R25	col	5	13.79%
R25	col	6	8.87%
R25	col	7	10.58%
R26	vehicle	1	7.14%
R26	vehicle	2	22.51%
R26	vehicle	3	2.15%
R26	vehicle	4	6.59%
R26	vehicle	5	3.22%
R26	vehicle	6	3.86%
R28	col	1	4.38%
R28	col	2	18.61%
R28	col	3	19.70%
R28	col	4	22.68%
R28	col	5	12.36%
R28	col	6	9.15%
R28	col	7	19.92%
R28	col	8	30.73%
R30	col	1	44.89%
R30	col	2	77.11%
R30	col	3	35.28%
R30	col	4	118.54%
R30	col	5	230.98%
R31	vehicle	1	13.20%
R31	vehicle	2	12.74%
R31	vehicle	3	31.70%
R31	vehicle	4	1.46%
R31	vehicle	5	9.21%
R35	vehicle	1	5.94%
R35	vehicle	2	16.18%
R35	vehicle	3	22.57%
R35	vehicle	4	27.88%
R35	vehicle	5	8.76%
R35	vehicle	6	25.94%
R35	vehicle	7	4.01%
R36	col	1	6.08%
R36	col	2	18.53%
R36	col	3	2.51%
R36	col	4	10.75%
R36	col	5	72.49%
R36	col	6	77.37%
R36	col	7	66.18%
R36	col	8	35.01%
R36	col	9	62.00%
R40	naïve	1	5.08%
R40	naïve	2	4.19%
R40	naïve	3	12.91%
R40	naïve	4	12.94%
R40	naïve	5	7.58%
R40	naïve	6	19.56%

col: collagenase

Figure E.3. Immunolabeling of MMP-1 in the DRG as designated in Table E.4 (Chapter 4)

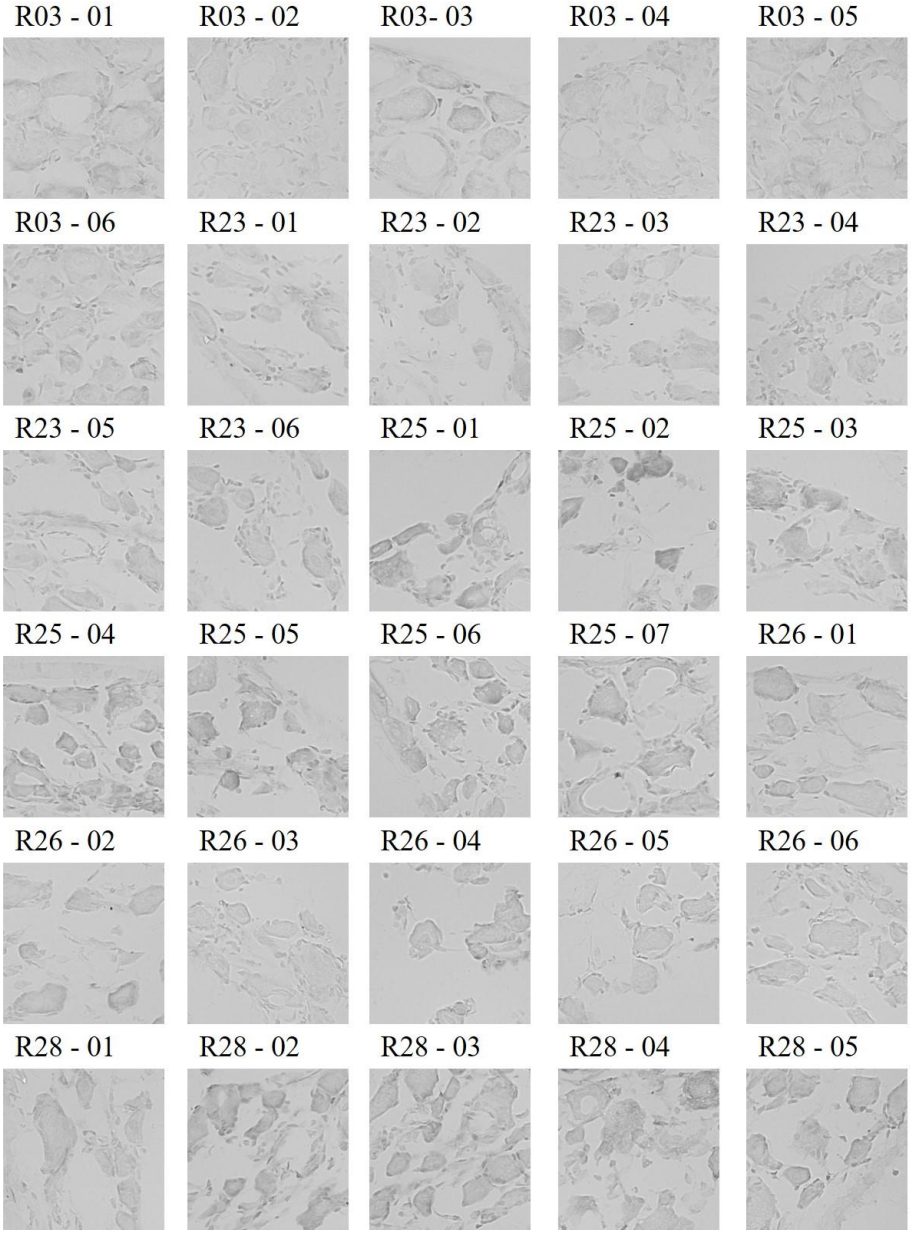

Note: Figure is continued on the next page.

Figure E.3. continued

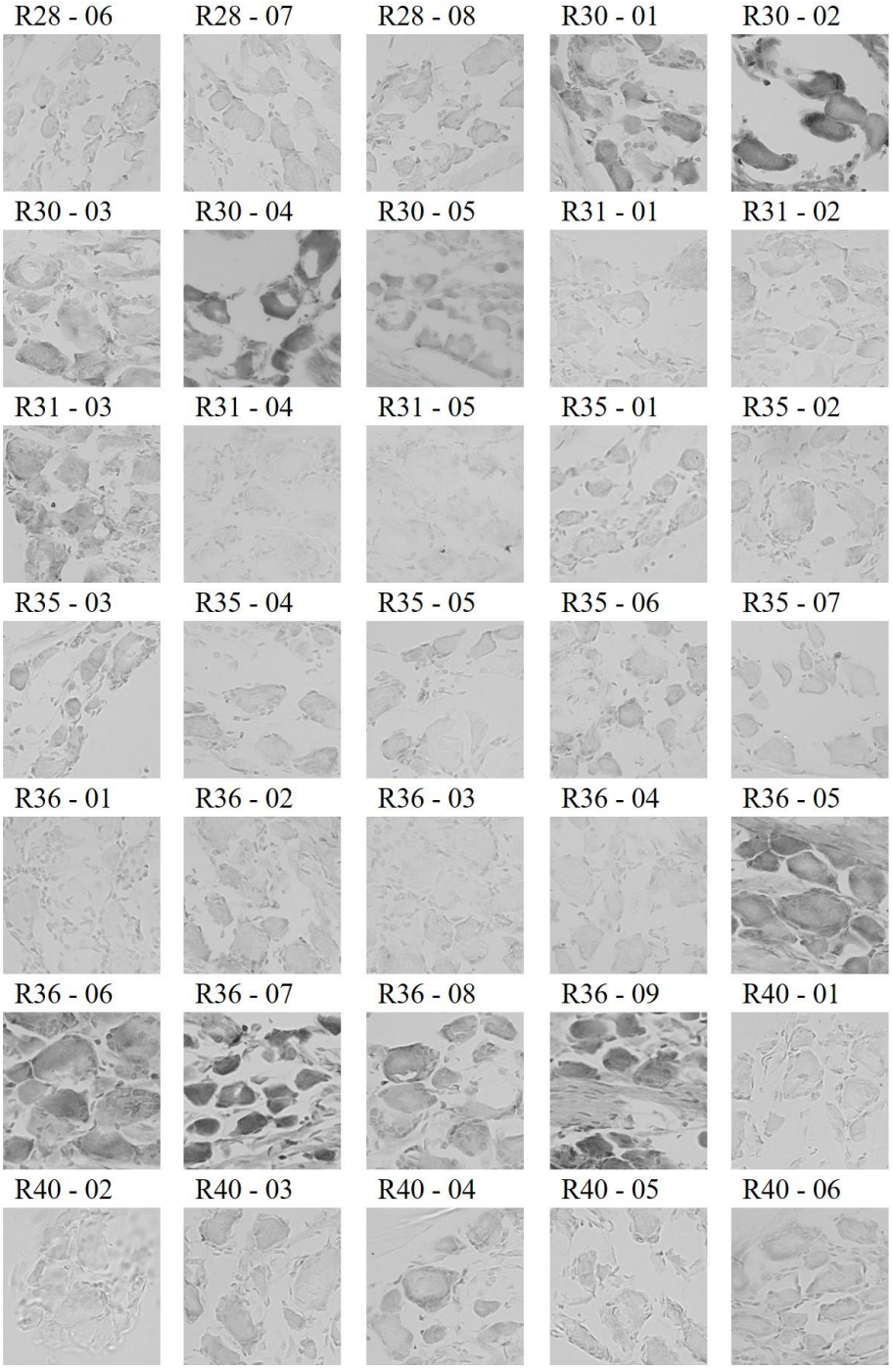

Table E.5. Densitometry of MMP-1 immunolabeling in the superficial dorsal horn of the spinal cord from rats injected with bacterial collagenase or vehicle (Chapter 4)

Rat	Group	image no.	MMP-1 (% positive)	Rat	Group	image no.	MMP-1 (% positive)
R03	naïve	1	5.62%	R29	col	1	0.16%
R03	naïve	2	1.51%	R29	col	2	0.07%
R03	naïve	3	9.18%	R29	col	3	0.94%
R03	naïve	4	14.87%	R29	col	4	5.56%
R03	naïve	5	34.25%	R29	col	5	1.37%
R03	naïve	6	20.84%	R29	col	6	0.05%
R23	col	1	13.05%	R29	col	7	28.36%
R23	col	2	0.58%	R29	col	8	13.56%
R23	col	3	1.34%	R30	col	1	11.82%
R23	col	4	0.34%	R30	col	2	1.47%
R23	col	5	22.51%	R30	col	3	4.08%
R23	col	6	1.64%	R30	col	4	7.91%
R25	col	1	6.18%	R35	vehicle	1	0.54%
R25	col	2	8.67%	R35	vehicle	2	3.45%
R25	col	3	2.07%	R35	vehicle	3	6.32%
R25	col	4	19.14%	R35	vehicle	4	5.34%
R25	col	5	2.02%	R35	vehicle	5	0.30%
R25	col	6	8.40%	R35	vehicle	6	1.97%
R26	vehicle	1	3.54%	R35	vehicle	7	9.22%
R26	vehicle	2	0.30%	R36	col	1	5.76%
R26	vehicle	3	2.28%	R36	col	2	5.00%
R26	vehicle	4	0.16%	R36	col	3	3.25%
R26	vehicle	5	2.91%	R36	col	4	4.33%
R26	vehicle	6	2.33%	R36	col	5	0.78%
R26	vehicle	7	0.00%	R36	col	6	1.49%
R28	col	1	30.61%	R36	col	7	20.27%
R28	col	2	13.06%	R40	naïve	1	21.33%
R28	col	3	23.87%	R40	naïve	2	20.73%
R28	col	4	9.34%	R40	naïve	3	44.82%
R28	col	5	13.32%	R40	naïve	4	2.53%
R28	col	6	4.42%	R40	naïve	5	7.48%
R28	col	7	0.52%	R40	naïve	6	7.80%

col: collagenase

Figure E.4. Immunolabeling of MMP-1 in the superficial dorsal horn of the spinal cord as designated in Table E.5 (Chapter 4)

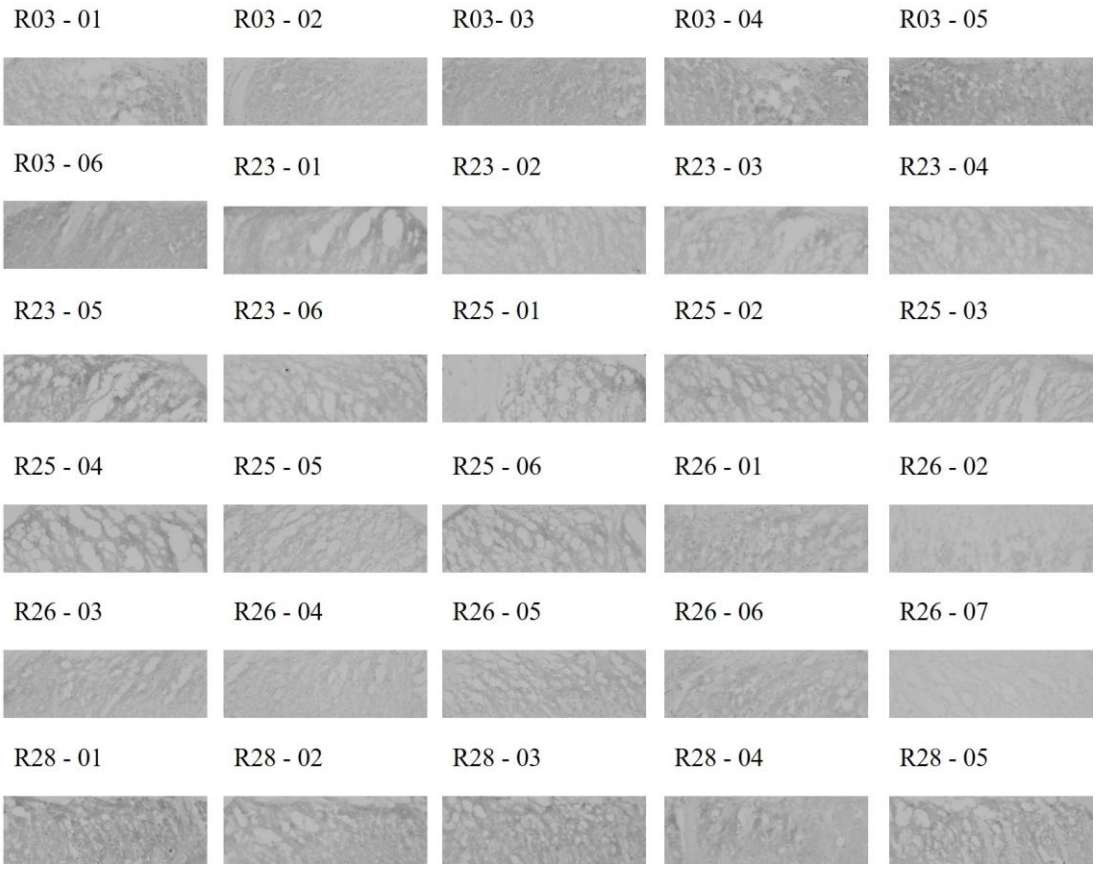

Note: Figure is continued on the next page.

Figure E.4. continued

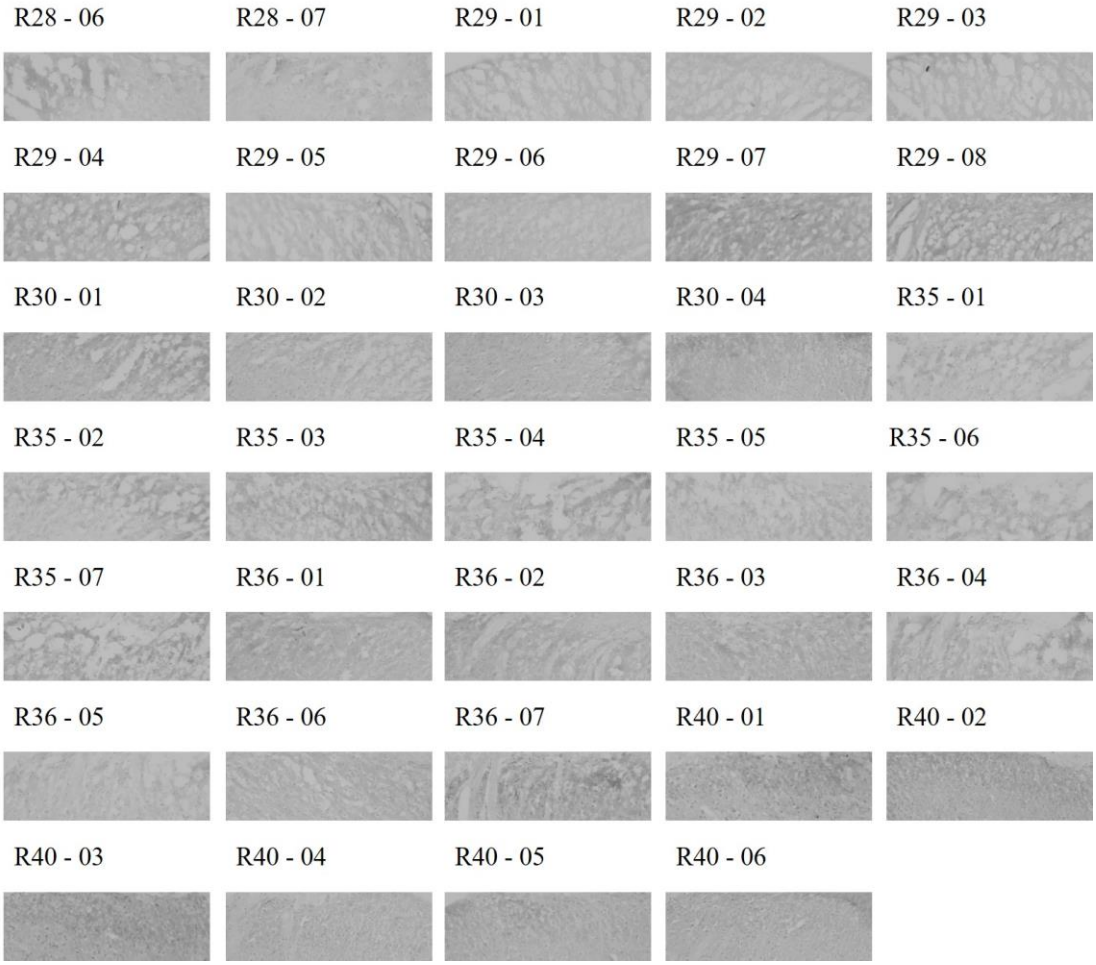

Table E.6. Pixel intensity of substance P labeling in DRG neurons by size from rats injected with MMP-1 or vehicle (Chapter 7)

Rat	Group	image no.	cell no.	intensity	φ (μm)	bin	Rat	Group	image no.	cell no.	intensity	φ (μm)	bin
R03	naïve	1	1	84.57	35.09	M	R03	naïve	5	9	49.70	34.22	M
R03	naïve	1	2	52.15	35.52	M	R03	naïve	5	10	34.73	34.00	M
R03	naïve	1	3	55.59	29.61	M	R13	MMP-1	1	1	73.75	33.35	M
R03	naïve	1	4	52.62	33.87	M	R13	MMP-1	1	2	47.17	34.47	M
R03	naïve	1	5	56.07	25.45	M	R13	MMP-1	1	3	31.43	21.81	M
R03	naïve	1	6	59.96	24.05	M	R13	MMP-1	1	4	73.78	25.89	M
R03	naïve	1	7	62.07	41.89	L	R13	MMP-1	1	5	122.46	29.58	M
R03	naïve	1	8	66.09	30.39	M	R13	MMP-1	1	6	107.42	31.52	M
R03	naïve	1	9	72.99	36.19	M	R13	MMP-1	1	7	74.68	32.58	M
R03	naïve	1	10	58.62	31.88	M	R13	MMP-1	1	8	72.97	37.02	M
R03	naïve	2	1	52.18	28.62	M	R13	MMP-1	1	9	55.27	20.05	S
R03	naïve	2	2	93.47	38.96	M	R13	MMP-1	1	10	60.96	34.03	M
R03	naïve	2	3	73.78	40.16	L	R13	MMP-1	2	1	77.83	34.83	M
R03	naïve	2	4	105.21	28.41	M	R13	MMP-1	2	2	67.55	38.92	M
R03	naïve	2	5	89.54	43.76	L	R13	MMP-1	2	3	57.01	30.65	M
R03	naïve	2	6	76.14	38.88	M	R13	MMP-1	2	4	65.93	25.45	M
R03	naïve	2	7	69.94	26.80	M	R13	MMP-1	2	5	75.55	33.64	M
R03	naïve	2	8	41.10	40.27	L	R13	MMP-1	2	6	64.30	29.64	M
R03	naïve	2	9	65.37	36.92	M	R13	MMP-1	2	7	52.95	29.88	M
R03	naïve	2	10	78.01	40.71	L	R13	MMP-1	2	8	48.47	36.44	M
R03	naïve	3	1	50.12	19.51	S	R13	MMP-1	2	9	44.80	26.08	M
R03	naïve	3	2	77.89	27.06	M	R13	MMP-1	2	10	47.31	30.90	M
R03	naïve	3	3	116.24	44.39	L	R13	MMP-1	3	1	52.87	34.82	M
R03	naïve	3	4	102.38	37.64	M	R13	MMP-1	3	2	60.75	43.37	L
R03	naïve	3	5	72.94	26.31	M	R13	MMP-1	3	3	48.54	37.83	M
R03	naïve	3	6	94.03	43.15	L	R13	MMP-1	3	4	43.76	22.21	M
R03	naïve	3	7	105.16	39.97	M	R13	MMP-1	3	5	52.95	26.36	M
R03	naïve	3	8	83.21	30.66	M	R13	MMP-1	3	6	46.27	26.21	M
R03	naïve	3	9	91.65	27.41	M	R13	MMP-1	3	7	44.65	21.64	M
R03	naïve	3	10	96.99	42.00	L	R13	MMP-1	3	8	41.16	28.66	M
R03	naïve	4	1	58.72	31.72	M	R13	MMP-1	3	9	34.48	26.09	M
R03	naïve	4	2	69.96	42.98	L	R13	MMP-1	3	10	53.65	21.35	M
R03	naïve	4	3	65.67	39.77	M	R13	MMP-1	4	1	82.47	33.22	M
R03	naïve	4	4	49.37	33.96	M	R13	MMP-1	4	2	74.63	36.32	M
R03	naïve	4	5	50.79	22.38	M	R13	MMP-1	4	3	55.09	35.58	M
R03	naïve	4	6	75.40	33.37	M	R13	MMP-1	4	4	53.19	46.70	L
R03	naïve	4	7	60.83	37.06	M	R13	MMP-1	4	5	99.53	27.71	M
R03	naïve	4	8	46.43	24.07	M	R13	MMP-1	4	6	76.62	42.50	L
R03	naïve	4	9	48.65	21.32	M	R13	MMP-1	4	7	65.14	37.85	M
R03	naïve	4	10	59.48	45.39	L	R13	MMP-1	4	8	50.09	24.16	M
R03	naïve	5	1	16.97	31.43	M	R13	MMP-1	4	9	46.47	44.99	L
R03	naïve	5	2	24.99	34.61	M	R13	MMP-1	4	10	62.29	30.38	M
R03	naïve	5	3	32.07	26.08	M	R13	MMP-1	5	1	72.06	34.41	M
R03	naïve	5	4	48.22	32.05	M	R13	MMP-1	5	2	73.30	39.89	M
R03	naïve	5	5	23.20	31.63	M	R13	MMP-1	5	3	77.99	16.54	S
R03	naïve	5	6	30.28	34.72	M	R13	MMP-1	5	4	66.52	43.21	L
R03	naïve	5	7	28.41	32.67	M	R13	MMP-1	5	5	70.81	25.97	M
R03	naïve	5	8	17.31	22.19	M	R13	MMP-1	5	6	74.42	35.93	M

φ: diameter; S: small; M: medium; L: large

Note: Table is continued on the next page.

Table E.6. continued

Rat	Group	image no.	cell no.	intensity	φ (μm)	bin	Rat	Group	image no.	cell no.	intensity	φ (μm)	bin
R13	MMP-1	5	7	71.06	26.43	M	R13	MMP-1	6	3	51.88	41.24	L
R13	MMP-1	5	8	61.87	32.69	M	R13	MMP-1	6	4	67.27	20.76	S
R13	MMP-1	5	9	62.33	32.54	M	R13	MMP-1	6	5	49.07	22.79	M
R13	MMP-1	5	10	87.46	36.80	M	R13	MMP-1	6	6	53.41	18.05	S
R13	MMP-1	6	1	50.07	19.63	S	R13	MMP-1	6	7	56.57	36.70	M
R13	MMP-1	6	2	61.76	32.48	M	R13	MMP-1	6	8	54.31	34.59	M
R13	MMP-1	6	3	51.88	41.24	L	R13	MMP-1	6	9	72.39	29.59	M
R13	MMP-1	6	4	67.27	20.76	S	R13	MMP-1	6	10	61.85	31.95	M
R13	MMP-1	6	5	49.07	22.79	M	R13	MMP-1	7	1	54.16	37.11	M
R13	MMP-1	6	6	53.41	18.05	S	R13	MMP-1	7	2	52.27	37.98	M
R13	MMP-1	6	7	56.57	36.70	M	R13	MMP-1	7	3	49.12	23.13	M
R13	MMP-1	6	8	54.31	34.59	M	R13	MMP-1	7	4	85.38	30.39	M
R13	MMP-1	6	9	72.39	29.59	M	R13	MMP-1	7	5	80.97	35.94	M
R13	MMP-1	6	10	61.85	31.95	M	R13	MMP-1	7	6	59.04	36.51	M
R13	MMP-1	7	1	54.16	37.11	M	R13	MMP-1	7	7	51.17	22.41	M
R13	MMP-1	7	2	52.27	37.98	M	R13	MMP-1	7	8	67.40	47.92	L
R13	MMP-1	7	3	49.12	23.13	M	R13	MMP-1	7	9	67.83	30.98	M
R13	MMP-1	7	4	85.38	30.39	M	R13	MMP-1	7	10	56.42	38.96	M
R13	MMP-1	7	5	80.97	35.94	M	R16	MMP-1	1	1	56.81	31.49	M
R13	MMP-1	7	6	59.04	36.51	M	R16	MMP-1	1	2	81.08	23.10	M
R13	MMP-1	7	7	51.17	22.41	M	R16	MMP-1	1	3	85.05	37.26	M
R13	MMP-1	7	8	67.40	47.92	L	R16	MMP-1	1	4	161.73	30.64	M
R13	MMP-1	7	9	67.83	30.98	M	R16	MMP-1	1	5	84.85	30.64	M
R13	MMP-1	7	10	56.42	38.96	M	R16	MMP-1	1	6	71.65	23.72	M
R16	MMP-1	1	1	56.81	31.49	M	R16	MMP-1	1	7	123.25	33.44	M
R16	MMP-1	1	2	81.08	23.10	M	R16	MMP-1	1	8	112.64	25.27	M
R16	MMP-1	1	3	85.05	37.26	M	R16	MMP-1	1	9	102.63	43.51	L
R16	MMP-1	1	4	161.73	30.64	M	R16	MMP-1	1	10	113.79	25.21	M
R16	MMP-1	1	5	84.85	30.64	M	R16	MMP-1	2	1	94.54	17.42	S
R16	MMP-1	1	6	71.65	23.72	M	R16	MMP-1	2	2	110.68	29.95	M
R16	MMP-1	1	7	123.25	33.44	M	R16	MMP-1	2	3	80.68	24.00	M
R16	MMP-1	1	8	112.64	25.27	M	R16	MMP-1	2	4	116.58	30.47	M
R16	MMP-1	1	9	102.63	43.51	L	R16	MMP-1	2	5	105.78	42.71	L
R16	MMP-1	1	10	113.79	25.21	M	R16	MMP-1	2	6	86.84	30.35	M
R16	MMP-1	2	1	94.54	17.42	S	R16	MMP-1	2	7	108.51	24.60	M
R16	MMP-1	2	2	110.68	29.95	M	R16	MMP-1	2	8	85.53	32.06	M
R16	MMP-1	2	3	80.68	24.00	M	R16	MMP-1	2	9	93.96	27.07	M
R16	MMP-1	2	4	116.58	30.47	M	R16	MMP-1	2	10	91.14	40.89	L
R16	MMP-1	2	5	105.78	42.71	L	R16	MMP-1	3	1	119.68	31.75	M
R16	MMP-1	2	6	86.84	30.35	M	R16	MMP-1	3	2	173.19	23.40	M
R16	MMP-1	2	7	108.51	24.60	M	R16	MMP-1	3	3	129.80	37.81	M
R16	MMP-1	2	8	85.53	32.06	M	R16	MMP-1	3	4	113.68	30.27	M
R16	MMP-1	2	9	93.96	27.07	M	R16	MMP-1	3	5	163.61	35.01	M
R16	MMP-1	2	10	91.14	40.89	L	R16	MMP-1	3	6	139.47	24.54	M
R13	MMP-1	5	7	71.06	26.43	M	R16	MMP-1	3	7	178.36	34.04	M
R13	MMP-1	5	8	61.87	32.69	M	R16	MMP-1	3	8	167.60	38.92	M
R13	MMP-1	5	9	62.33	32.54	M	R16	MMP-1	3	9	111.83	27.05	M
R13	MMP-1	5	10	87.46	36.80	M	R16	MMP-1	3	10	134.33	41.16	L
R13	MMP-1	6	1	50.07	19.63	S	R16	MMP-1	4	1	90.35	39.53	M
R13	MMP-1	6	2	61.76	32.48	M	R16	MMP-1	4	2	100.74	30.73	M

φ: diameter; S: small; M: medium; L: large

Note: Table is continued on the next page.

Table E.6. continued

Rat	Group	image no.	cell no.	intensity	φ (μm)	bin	Rat	Group	image no.	cell no.	intensity	φ (μm)	bin
R16	MMP-1	4	3	80.12	22.81	M	R17	MMP-1	3	3	55.75	18.47	S
R16	MMP-1	4	4	69.65	41.38	L	R17	MMP-1	3	4	71.02	40.27	L
R16	MMP-1	4	5	85.82	31.06	M	R17	MMP-1	3	5	73.84	36.13	M
R16	MMP-1	4	6	106.26	25.76	M	R17	MMP-1	3	6	107.18	21.59	M
R16	MMP-1	4	7	60.12	38.77	M	R17	MMP-1	3	7	42.93	38.46	M
R16	MMP-1	4	8	79.33	33.15	M	R17	MMP-1	3	8	40.31	43.46	L
R16	MMP-1	4	9	65.55	26.67	M	R17	MMP-1	3	9	77.64	32.97	M
R16	MMP-1	4	10	99.51	35.25	M	R17	MMP-1	3	10	75.32	24.46	M
R16	MMP-1	5	1	59.58	45.07	L	R17	MMP-1	4	1	58.23	25.03	M
R16	MMP-1	5	2	87.78	31.22	M	R17	MMP-1	4	2	65.60	48.50	L
R16	MMP-1	5	3	76.61	29.88	M	R17	MMP-1	4	3	50.44	25.73	M
R16	MMP-1	5	4	55.91	38.80	M	R17	MMP-1	4	4	77.13	36.92	M
R16	MMP-1	5	5	69.29	40.99	L	R17	MMP-1	4	5	76.82	28.35	M
R16	MMP-1	5	6	58.97	28.37	M	R17	MMP-1	4	6	72.45	40.91	L
R16	MMP-1	5	7	69.23	34.32	M	R17	MMP-1	4	7	77.15	29.95	M
R16	MMP-1	5	8	74.36	30.80	M	R17	MMP-1	4	8	91.37	40.48	L
R16	MMP-1	5	9	85.81	26.22	M	R17	MMP-1	4	9	66.98	27.90	M
R16	MMP-1	5	10	60.14	36.59	M	R17	MMP-1	4	10	83.95	37.24	M
R16	MMP-1	6	1	142.31	28.19	M	R17	MMP-1	5	1	88.36	41.26	L
R16	MMP-1	6	2	105.28	29.82	M	R17	MMP-1	5	2	56.36	20.82	S
R16	MMP-1	6	3	117.95	34.71	M	R17	MMP-1	5	3	129.16	40.22	L
R16	MMP-1	6	4	95.32	38.66	M	R17	MMP-1	5	4	131.05	38.62	M
R16	MMP-1	6	5	82.72	46.55	L	R17	MMP-1	5	5	155.42	22.70	M
R16	MMP-1	6	6	100.71	40.94	L	R17	MMP-1	5	6	138.80	21.65	M
R16	MMP-1	6	7	86.38	39.49	M	R17	MMP-1	5	7	128.66	40.04	L
R16	MMP-1	6	8	69.23	44.99	L	R17	MMP-1	5	8	129.67	37.23	M
R16	MMP-1	6	9	86.04	37.05	M	R17	MMP-1	5	9	116.68	18.51	S
R16	MMP-1	6	10	130.14	26.37	M	R17	MMP-1	5	10	153.16	34.28	M
R17	MMP-1	1	1	117.68	19.41	S	R17	MMP-1	6	1	140.80	40.56	L
R17	MMP-1	1	2	88.95	42.47	L	R17	MMP-1	6	2	183.07	35.13	M
R17	MMP-1	1	3	106.12	32.80	M	R17	MMP-1	6	3	113.41	26.29	M
R17	MMP-1	1	4	177.67	30.96	M	R17	MMP-1	6	4	67.87	54.39	L
R17	MMP-1	1	5	116.14	20.90	S	R17	MMP-1	6	5	144.54	29.09	M
R17	MMP-1	1	6	81.43	22.98	M	R17	MMP-1	6	6	174.90	37.72	M
R17	MMP-1	1	7	105.27	52.80	L	R17	MMP-1	6	7	92.81	22.44	M
R17	MMP-1	1	8	88.14	18.80	S	R17	MMP-1	6	8	71.12	24.81	M
R17	MMP-1	1	9	76.94	28.42	M	R17	MMP-1	6	9	88.17	46.87	L
R17	MMP-1	1	10	82.92	32.76	M	R17	MMP-1	6	10	165.87	44.45	L
R17	MMP-1	2	1	57.56	26.13	M	R40	naïve	1	1	25.78	21.00	M
R17	MMP-1	2	2	85.63	23.11	M	R40	naïve	1	1	102.81	35.26	M
R17	MMP-1	2	3	61.72	33.47	M	R40	naïve	1	2	45.67	24.87	M
R17	MMP-1	2	4	127.16	43.74	L	R40	naïve	1	2	93.49	32.47	M
R17	MMP-1	2	5	119.92	44.14	L	R40	naïve	1	3	43.37	44.28	L
R17	MMP-1	2	6	109.84	21.96	M	R40	naïve	1	3	113.39	34.95	M
R17	MMP-1	2	7	98.09	22.80	M	R40	naïve	1	4	59.94	29.57	M
R17	MMP-1	2	8	168.16	35.54	M	R40	naïve	1	4	89.68	31.55	M
R17	MMP-1	2	9	118.55	45.64	L	R40	naïve	1	5	54.97	22.46	M
R17	MMP-1	2	10	94.88	29.14	M	R40	naïve	1	5	71.66	34.74	M
R17	MMP-1	3	1	79.04	29.53	M	R40	naïve	1	6	38.36	40.32	L
R17	MMP-1	3	2	57.77	32.06	M	R40	naïve	1	6	154.48	25.58	M

φ: diameter; S: small; M: medium; L: large

Note: Table is continued on the next page.

Table E.6. continued

Rat	Group	image no.	cell no.	intensity	φ (μm)	bin	Rat	Group	image no.	cell no.	intensity	φ (μm)	bin
R40	naïve	1	7	63.08	40.61	L	R40	naïve	4	2	54.29	29.15	M
R40	naïve	1	7	109.63	35.71	M	R40	naïve	4	2	85.05	33.48	M
R40	naïve	1	8	71.41	29.26	M	R40	naïve	4	3	105.96	22.56	M
R40	naïve	1	8	69.54	31.14	M	R40	naïve	4	3	58.94	26.59	M
R40	naïve	1	9	32.55	25.49	M	R40	naïve	4	4	63.84	22.75	M
R40	naïve	1	9	60.74	37.17	M	R40	naïve	4	4	143.38	29.59	M
R40	naïve	1	10	61.14	41.10	L	R40	naïve	4	5	62.94	25.87	M
R40	naïve	1	10	28.35	29.29	M	R40	naïve	4	5	52.31	36.39	M
R40	naïve	2	1	61.77	36.53	M	R40	naïve	4	6	46.13	40.36	L
R40	naïve	2	1	66.64	19.39	S	R40	naïve	4	6	72.64	34.54	M
R40	naïve	2	2	60.81	25.04	M	R40	naïve	4	7	41.55	28.20	M
R40	naïve	2	2	55.34	27.16	M	R40	naïve	4	7	149.05	29.13	M
R40	naïve	2	3	47.55	24.99	M	R40	naïve	4	8	80.37	40.59	L
R40	naïve	2	3	42.15	28.53	M	R40	naïve	4	8	76.32	41.33	L
R40	naïve	2	4	41.93	25.86	M	R40	naïve	4	9	46.65	29.78	M
R40	naïve	2	4	65.18	27.23	M	R40	naïve	4	9	87.80	18.36	S
R40	naïve	2	5	32.39	26.73	M	R40	naïve	4	10	74.66	22.56	M
R40	naïve	2	5	64.17	30.48	M	R40	naïve	4	10	51.02	28.96	M
R40	naïve	2	6	79.15	35.49	M	R40	naïve	5	1	32.11	18.67	S
R40	naïve	2	6	46.92	18.59	S	R40	naïve	5	2	43.16	25.12	M
R40	naïve	2	7	45.65	27.24	M	R40	naïve	5	3	37.48	23.79	M
R40	naïve	2	7	71.86	14.49	S	R40	naïve	5	4	37.87	24.88	M
R40	naïve	2	8	31.82	25.35	M	R40	naïve	5	5	38.07	32.43	M
R40	naïve	2	8	71.95	25.81	M	R40	naïve	5	6	35.07	36.07	M
R40	naïve	2	9	68.95	26.90	M	R40	naïve	5	7	30.10	27.13	M
R40	naïve	2	9	50.71	15.86	S	R40	naïve	5	8	34.61	25.71	M
R40	naïve	2	10	46.94	49.39	L	R40	naïve	5	9	30.31	21.11	M
R40	naïve	2	10	76.88	31.30	M	R40	naïve	5	10	40.04	35.87	M
R40	naïve	3	1	59.63	23.98	M	R40	naïve	6	1	58.12	30.59	M
R40	naïve	3	1	54.37	18.82	S	R40	naïve	6	2	50.82	19.24	S
R40	naïve	3	2	45.03	27.30	M	R40	naïve	6	3	70.12	29.95	M
R40	naïve	3	2	46.92	18.37	S	R40	naïve	6	4	55.91	35.78	M
R40	naïve	3	3	44.87	31.75	M	R40	naïve	6	5	42.68	25.45	M
R40	naïve	3	3	50.37	20.28	S	R40	naïve	6	6	43.03	31.27	M
R40	naïve	3	4	70.21	38.86	M	R40	naïve	6	7	39.80	24.12	M
R40	naïve	3	4	41.79	17.13	S	R40	naïve	6	8	50.04	22.97	M
R40	naïve	3	5	76.93	32.56	M	R40	naïve	6	9	47.91	23.10	M
R40	naïve	3	5	58.44	35.23	M	R40	naïve	6	10	39.11	25.74	M
R40	naïve	3	6	35.67	18.27	S	R40_S2	naïve	1	1	107.94	20.23	S
R40	naïve	3	6	48.95	20.59	S	R40_S2	naïve	1	2	160.76	19.13	S
R40	naïve	3	7	45.87	26.08	M	R40_S2	naïve	1	3	77.74	20.18	S
R40	naïve	3	7	79.25	19.71	S	R40_S2	naïve	1	4	101.60	36.38	M
R40	naïve	3	8	60.24	35.00	M	R40_S2	naïve	1	5	161.88	18.75	S
R40	naïve	3	8	58.95	36.32	M	R40_S2	naïve	1	6	97.45	37.14	M
R40	naïve	3	9	47.15	41.56	L	R40_S2	naïve	1	7	161.51	30.59	M
R40	naïve	3	9	31.30	19.18	S	R40_S2	naïve	1	8	94.39	18.18	S
R40	naïve	3	10	51.41	27.38	M	R40_S2	naïve	1	9	76.93	34.63	M
R40	naïve	3	10	70.74	18.80	S	R40_S2	naïve	1	10	101.72	36.92	M
R40	naïve	4	1	73.37	27.50	M	R40_S2	naïve	2	1	104.24	27.71	M
R40	naïve	4	1	74.59	35.87	M	R40_S2	naïve	2	2	89.93	18.42	S

φ: diameter; S: small; M: medium; L: large

Note: Table is continued on the next page.

Table E.6. continued

Rat	Group	image no.	cell no.	intensity	φ (μm)	bin	Rat	Group	image no.	cell no.	intensity	φ (μm)	bin
R40_S2	naïve	2	3	159.10	34.56	M	R44	MMP-1	3	3	137.95	44.04	L
R40_S2	naïve	2	4	67.48	44.21	L	R44	MMP-1	3	4	109.64	46.12	L
R40_S2	naïve	2	5	102.08	26.52	M	R44	MMP-1	3	5	142.92	30.53	M
R40_S2	naïve	2	6	57.80	45.51	L	R44	MMP-1	3	6	115.43	21.47	M
R40_S2	naïve	2	7	100.43	26.46	M	R44	MMP-1	3	7	130.94	42.03	L
R40_S2	naïve	2	8	121.35	22.58	M	R44	MMP-1	3	8	135.14	33.56	M
R40_S2	naïve	2	9	68.69	30.46	M	R44	MMP-1	3	9	159.19	48.77	L
R40_S2	naïve	2	10	68.28	43.36	L	R44	MMP-1	3	10	99.48	38.63	M
R40_S2	naïve	3	1	84.35	22.18	M	R44	MMP-1	4	1	223.39	23.85	M
R40_S2	naïve	3	2	108.46	19.65	S	R44	MMP-1	4	2	202.41	31.32	M
R40_S2	naïve	3	3	132.08	36.31	M	R44	MMP-1	4	3	217.80	39.99	M
R40_S2	naïve	3	4	127.54	24.34	M	R44	MMP-1	4	4	168.32	29.15	M
R40_S2	naïve	3	5	148.04	45.35	L	R44	MMP-1	4	5	194.03	29.93	M
R40_S2	naïve	3	6	61.67	27.89	M	R44	MMP-1	4	6	184.29	46.80	L
R40_S2	naïve	3	7	121.05	34.23	M	R44	MMP-1	4	7	206.72	27.13	M
R40_S2	naïve	3	8	95.87	23.25	M	R44	MMP-1	4	8	204.67	39.89	M
R40_S2	naïve	3	9	69.93	28.53	M	R44	MMP-1	4	9	225.59	45.08	L
R40_S2	naïve	3	10	133.45	36.45	M	R44	MMP-1	4	10	123.65	51.35	L
R40_S2	naïve	4	1	46.84	19.04	S	R44	MMP-1	5	1	146.04	18.07	S
R40_S2	naïve	4	2	70.49	36.53	M	R44	MMP-1	5	2	100.98	18.98	S
R40_S2	naïve	4	3	104.32	20.85	S	R44	MMP-1	5	3	168.88	34.89	M
R40_S2	naïve	4	4	81.53	32.11	M	R44	MMP-1	5	4	135.88	29.27	M
R40_S2	naïve	4	5	91.81	36.59	M	R44	MMP-1	5	5	180.63	21.38	M
R40_S2	naïve	4	6	104.81	31.09	M	R44	MMP-1	5	6	109.88	27.78	M
R40_S2	naïve	4	7	106.01	40.08	L	R44	MMP-1	5	7	111.11	31.36	M
R40_S2	naïve	4	8	73.37	45.21	L	R44	MMP-1	5	8	141.80	46.54	L
R40_S2	naïve	4	9	57.80	21.58	M	R44	MMP-1	5	9	135.46	36.86	M
R40_S2	naïve	4	10	86.96	19.48	S	R44	MMP-1	5	10	73.83	27.53	M
R44	MMP-1	1	1	96.55	28.74	M	R44	MMP-1	6	1	83.84	27.42	M
R44	MMP-1	1	2	135.43	45.28	L	R44	MMP-1	6	2	73.91	26.80	M
R44	MMP-1	1	3	141.92	37.02	M	R44	MMP-1	6	3	106.27	35.36	M
R44	MMP-1	1	4	196.87	47.25	L	R44	MMP-1	6	4	61.08	31.81	M
R44	MMP-1	1	5	205.65	53.10	L	R44	MMP-1	6	5	119.84	30.52	M
R44	MMP-1	1	6	191.65	44.19	L	R44	MMP-1	6	6	114.01	31.26	M
R44	MMP-1	1	7	201.44	46.15	L	R44	MMP-1	6	7	90.85	24.70	M
R44	MMP-1	1	8	161.20	44.44	L	R44	MMP-1	6	8	76.21	40.02	L
R44	MMP-1	1	9	179.85	49.80	L	R44	MMP-1	6	9	92.38	22.90	M
R44	MMP-1	1	10	135.78	46.38	L	R44	MMP-1	6	10	76.01	42.31	L
R44	MMP-1	2	1	88.64	36.66	M	R46	MMP-1	1	1	29.10	19.36	S
R44	MMP-1	2	2	181.25	43.89	L	R46	MMP-1	1	2	28.15	29.65	M
R44	MMP-1	2	3	211.47	37.50	M	R46	MMP-1	1	3	40.61	30.09	M
R44	MMP-1	2	4	119.09	35.98	M	R46	MMP-1	1	4	38.05	33.18	M
R44	MMP-1	2	5	178.87	37.07	M	R46	MMP-1	1	5	33.81	31.63	M
R44	MMP-1	2	6	175.98	47.47	L	R46	MMP-1	1	6	32.12	22.49	M
R44	MMP-1	2	7	154.68	39.96	M	R46	MMP-1	1	7	26.45	27.91	M
R44	MMP-1	2	8	156.49	36.90	M	R46	MMP-1	1	8	23.57	28.81	M
R44	MMP-1	2	9	60.30	39.60	M	R46	MMP-1	1	9	23.51	27.25	M
R44	MMP-1	2	10	100.84	37.80	M	R46	MMP-1	1	10	31.13	34.98	M
R44	MMP-1	3	1	153.20	24.64	M	R46	MMP-1	2	1	19.87	26.84	M
R44	MMP-1	3	2	142.13	28.21	M	R46	MMP-1	2	2	20.94	29.08	M

φ: diameter; S: small; M: medium; L: large

Note: Table is continued on the next page.

Table E.6. continued

Rat	Group	image no.	cell no.	intensity	φ (μm)	bin	Rat	Group	image no.	cell no.	intensity	φ (μm)	bin
R46	MMP-1	2	3	22.45	32.16	M	R47	MMP-1	1	3	66.95	21.35	M
R46	MMP-1	2	4	20.71	27.61	M	R47	MMP-1	1	4	64.81	36.94	M
R46	MMP-1	2	5	25.06	29.53	M	R47	MMP-1	1	5	50.83	32.72	M
R46	MMP-1	2	6	13.19	30.19	M	R47	MMP-1	1	6	59.44	46.89	L
R46	MMP-1	2	7	24.78	41.42	L	R47	MMP-1	1	7	76.94	34.14	M
R46	MMP-1	2	8	34.75	35.24	M	R47	MMP-1	1	8	62.13	40.90	L
R46	MMP-1	2	9	17.09	34.71	M	R47	MMP-1	1	9	52.23	36.01	M
R46	MMP-1	2	10	22.30	31.63	M	R47	MMP-1	1	10	53.04	22.89	M
R46	MMP-1	3	1	22.01	31.03	M	R47	MMP-1	2	1	50.46	32.55	M
R46	MMP-1	3	2	28.90	23.28	M	R47	MMP-1	2	2	62.05	31.32	M
R46	MMP-1	3	3	29.94	41.11	L	R47	MMP-1	2	3	51.37	47.98	L
R46	MMP-1	3	4	27.98	28.98	M	R47	MMP-1	2	4	50.73	26.69	M
R46	MMP-1	3	5	22.29	32.78	M	R47	MMP-1	2	5	40.49	38.09	M
R46	MMP-1	3	6	35.61	45.50	L	R47	MMP-1	2	6	71.55	38.69	M
R46	MMP-1	3	7	23.72	31.01	M	R47	MMP-1	2	7	41.78	29.63	M
R46	MMP-1	3	8	19.48	33.51	M	R47	MMP-1	2	8	48.94	31.48	M
R46	MMP-1	3	9	34.38	39.94	M	R47	MMP-1	2	9	40.34	27.10	M
R46	MMP-1	3	10	30.44	34.43	M	R47	MMP-1	2	10	55.10	46.09	L
R46	MMP-1	4	1	23.64	36.31	M	R47	MMP-1	3	1	24.32	22.23	M
R46	MMP-1	4	2	29.11	35.03	M	R47	MMP-1	3	2	20.07	29.30	M
R46	MMP-1	4	3	24.20	44.05	L	R47	MMP-1	3	3	27.66	39.66	M
R46	MMP-1	4	4	20.96	30.08	M	R47	MMP-1	3	4	16.15	33.04	M
R46	MMP-1	4	5	30.32	36.51	M	R47	MMP-1	3	5	23.42	31.43	M
R46	MMP-1	4	6	31.52	41.89	L	R47	MMP-1	3	6	21.87	32.15	M
R46	MMP-1	4	7	40.59	39.07	M	R47	MMP-1	3	7	15.14	48.15	L
R46	MMP-1	4	8	32.58	24.62	M	R47	MMP-1	3	8	31.59	27.53	M
R46	MMP-1	4	9	35.23	41.25	L	R47	MMP-1	3	9	20.83	30.02	M
R46	MMP-1	4	10	26.46	36.43	M	R47	MMP-1	3	10	23.44	42.65	L
R46	MMP-1	5	1	25.99	29.86	M	R47	MMP-1	4	1	40.59	26.25	M
R46	MMP-1	5	2	29.44	32.32	M	R47	MMP-1	4	2	34.69	22.93	M
R46	MMP-1	5	3	27.98	26.55	M	R47	MMP-1	4	3	38.66	36.45	M
R46	MMP-1	5	4	27.86	26.35	M	R47	MMP-1	4	4	50.28	45.25	L
R46	MMP-1	5	5	43.34	34.84	M	R47	MMP-1	4	5	42.44	24.84	M
R46	MMP-1	5	6	28.57	32.58	M	R47	MMP-1	4	6	39.20	44.01	L
R46	MMP-1	5	7	24.53	26.52	M	R47	MMP-1	4	7	42.29	34.72	M
R46	MMP-1	5	8	18.57	34.91	M	R47	MMP-1	4	8	40.02	27.32	M
R46	MMP-1	5	9	44.46	37.07	M	R47	MMP-1	4	9	37.29	25.74	M
R46	MMP-1	5	10	36.72	24.55	M	R47	MMP-1	4	10	35.92	43.37	L
R46	MMP-1	6	1	30.08	29.44	M	R47	MMP-1	5	1	25.62	29.69	M
R46	MMP-1	6	2	41.28	32.71	M	R47	MMP-1	5	2	26.27	29.31	M
R46	MMP-1	6	3	23.75	31.41	M	R47	MMP-1	5	3	25.36	28.83	M
R46	MMP-1	6	4	35.37	36.93	M	R47	MMP-1	5	4	40.80	38.92	M
R46	MMP-1	6	5	24.25	40.50	L	R47	MMP-1	5	5	32.14	24.46	M
R46	MMP-1	6	6	31.73	44.16	L	R47	MMP-1	5	6	29.03	44.54	L
R46	MMP-1	6	7	39.54	41.68	L	R47	MMP-1	5	7	17.72	28.54	M
R46	MMP-1	6	8	28.67	25.89	M	R47	MMP-1	5	8	20.55	32.96	M
R46	MMP-1	6	9	25.06	27.39	M	R47	MMP-1	5	9	23.56	26.71	M
R46	MMP-1	6	10	16.89	30.77	M	R47	MMP-1	5	10	35.52	25.01	M
R47	MMP-1	1	1	53.44	22.69	M	R47	MMP-1	6	1	60.14	45.27	L
R47	MMP-1	1	2	58.05	30.36	M	R47	MMP-1	6	2	38.03	28.65	M

φ: diameter; S: small; M: medium; L: large

Note: Table is continued on the next page.

Table E.6. continued

Rat	Group	image no.	cell no.	intensity	φ (μm)	bin	Rat	Group	image no.	cell no.	intensity	φ (μm)	bin
R47	MMP-1	6	3	94.81	41.54	L	R48	MMP-1	4	3	27.03	22.14	M
R47	MMP-1	6	4	71.27	24.51	M	R48	MMP-1	4	4	43.24	38.29	M
R47	MMP-1	6	5	65.65	35.78	M	R48	MMP-1	4	5	26.71	26.06	M
R47	MMP-1	6	6	79.46	29.81	M	R48	MMP-1	4	6	26.99	33.86	M
R47	MMP-1	6	7	86.57	38.34	M	R48	MMP-1	4	7	30.05	37.63	M
R47	MMP-1	6	8	80.14	27.59	M	R48	MMP-1	4	8	33.75	35.54	M
R47	MMP-1	6	9	124.63	31.95	M	R48	MMP-1	4	9	22.10	32.04	M
R47	MMP-1	6	10	69.12	44.52	L	R48	MMP-1	4	10	27.27	26.28	M
R47	MMP-1	7	1	52.83	25.82	M	R48	MMP-1	5	1	28.97	28.18	M
R47	MMP-1	7	2	54.25	25.97	M	R48	MMP-1	5	2	29.88	32.80	M
R47	MMP-1	7	3	52.81	31.09	M	R48	MMP-1	5	3	20.43	22.03	M
R47	MMP-1	7	4	62.46	40.52	L	R48	MMP-1	5	4	32.92	35.87	M
R47	MMP-1	7	5	57.13	21.78	M	R48	MMP-1	5	5	33.52	41.17	L
R47	MMP-1	7	6	48.23	26.93	M	R48	MMP-1	5	6	21.63	25.97	M
R47	MMP-1	7	7	68.97	44.95	L	R48	MMP-1	5	7	36.66	40.78	L
R47	MMP-1	7	8	64.12	25.67	M	R48	MMP-1	5	8	25.90	27.17	M
R47	MMP-1	7	9	62.43	33.38	M	R48	MMP-1	5	9	39.63	37.19	M
R47	MMP-1	7	10	59.11	41.11	L	R48	MMP-1	5	10	36.37	29.75	M
R48	MMP-1	1	1	64.28	56.40	L	R48	MMP-1	6	1	62.75	36.44	M
R48	MMP-1	1	2	47.87	19.39	S	R48	MMP-1	6	2	57.68	32.16	M
R48	MMP-1	1	3	90.13	31.73	M	R48	MMP-1	6	3	45.00	20.60	S
R48	MMP-1	1	4	52.69	28.22	M	R48	MMP-1	6	4	54.08	25.26	M
R48	MMP-1	1	5	69.71	30.86	M	R48	MMP-1	6	5	46.92	39.17	M
R48	MMP-1	1	6	53.64	22.88	M	R48	MMP-1	6	6	40.96	21.79	M
R48	MMP-1	1	7	48.53	26.63	M	R48	MMP-1	6	7	38.76	28.84	M
R48	MMP-1	1	8	50.68	29.32	M	R48	MMP-1	6	8	46.07	27.69	M
R48	MMP-1	1	9	53.05	38.21	M	R48	MMP-1	6	9	56.55	30.24	M
R48	MMP-1	1	10	57.49	32.40	M	R48	MMP-1	6	10	72.94	37.44	M
R48	MMP-1	2	1	45.42	26.75	M	R48	MMP-1	7	1	45.56	30.47	M
R48	MMP-1	2	2	41.18	20.93	S	R48	MMP-1	7	2	51.18	37.86	M
R48	MMP-1	2	3	71.50	38.70	M	R48	MMP-1	7	3	40.59	25.40	M
R48	MMP-1	2	4	42.75	33.46	M	R48	MMP-1	7	4	88.38	40.37	L
R48	MMP-1	2	5	53.71	52.54	L	R48	MMP-1	7	5	132.86	43.93	L
R48	MMP-1	2	6	55.39	31.66	M	R48	MMP-1	7	6	59.48	29.34	M
R48	MMP-1	2	7	54.41	36.77	M	R48	MMP-1	7	7	33.40	30.97	M
R48	MMP-1	2	8	78.11	37.73	M	R48	MMP-1	7	8	44.16	45.20	L
R48	MMP-1	2	9	41.91	31.70	M	R48	MMP-1	7	9	58.83	31.99	M
R48	MMP-1	2	10	50.21	34.83	M	R48	MMP-1	7	10	43.37	29.09	M
R48	MMP-1	3	1	73.54	27.78	M	R49	vehicle	1	1	21.95	24.67	M
R48	MMP-1	3	2	73.97	28.31	M	R49	vehicle	1	2	18.58	20.85	S
R48	MMP-1	3	3	84.80	28.25	M	R49	vehicle	1	3	21.27	43.64	L
R48	MMP-1	3	4	69.70	27.78	M	R49	vehicle	1	4	30.85	22.25	M
R48	MMP-1	3	5	63.88	26.82	M	R49	vehicle	1	5	20.68	24.04	M
R48	MMP-1	3	6	74.95	44.12	L	R49	vehicle	1	6	34.07	45.12	L
R48	MMP-1	3	7	52.91	25.39	M	R49	vehicle	1	7	18.34	31.80	M
R48	MMP-1	3	8	72.62	37.84	M	R49	vehicle	1	8	27.35	28.33	M
R48	MMP-1	3	9	57.13	22.13	M	R49	vehicle	1	9	19.72	23.56	M
R48	MMP-1	3	10	67.50	47.76	L	R49	vehicle	1	10	35.06	40.05	L
R48	MMP-1	4	1	29.86	22.09	M	R49	vehicle	2	1	24.99	28.26	M
R48	MMP-1	4	2	50.09	40.80	L	R49	vehicle	2	2	33.00	34.56	M

φ: diameter; S: small; M: medium; L: large

Note: Table is continued on the next page.

Table E.6. continued

Rat	Group	image no.	cell no.	intensity	φ (μm)	bin	Rat	Group	image no.	cell no.	intensity	φ (μm)	bin
R49	vehicle	2	3	35.56	43.07	L	R50	vehicle	1	3	33.18	25.95	M
R49	vehicle	2	4	31.27	24.17	M	R50	vehicle	1	4	26.94	24.00	M
R49	vehicle	2	5	26.84	32.13	M	R50	vehicle	1	5	34.38	26.79	M
R49	vehicle	2	6	30.57	38.75	M	R50	vehicle	1	6	19.11	27.29	M
R49	vehicle	2	7	15.10	27.63	M	R50	vehicle	1	7	38.48	27.57	M
R49	vehicle	2	8	23.36	25.41	M	R50	vehicle	1	8	39.30	42.08	L
R49	vehicle	2	9	24.04	35.16	M	R50	vehicle	1	9	39.30	50.56	L
R49	vehicle	2	10	24.07	23.66	M	R50	vehicle	1	10	47.22	23.72	M
R49	vehicle	3	1	33.76	19.34	S	R50	vehicle	2	1	22.06	26.79	M
R49	vehicle	3	2	16.44	23.30	M	R50	vehicle	2	2	27.41	49.62	L
R49	vehicle	3	3	20.87	32.10	M	R50	vehicle	2	3	27.82	43.72	L
R49	vehicle	3	4	20.84	27.17	M	R50	vehicle	2	4	29.89	30.89	M
R49	vehicle	3	5	37.51	31.09	M	R50	vehicle	2	5	21.30	39.42	M
R49	vehicle	3	6	20.84	35.46	M	R50	vehicle	2	6	31.50	25.26	M
R49	vehicle	3	7	22.51	39.37	M	R50	vehicle	2	7	20.36	39.95	M
R49	vehicle	3	8	15.61	23.67	M	R50	vehicle	2	8	17.47	28.46	M
R49	vehicle	3	9	14.70	26.24	M	R50	vehicle	2	9	18.21	34.81	M
R49	vehicle	3	10	24.82	26.54	M	R50	vehicle	2	10	29.39	37.77	M
R49	vehicle	4	1	21.33	47.49	L	R50	vehicle	3	1	28.52	33.41	M
R49	vehicle	4	2	29.59	34.31	M	R50	vehicle	3	2	25.69	48.04	L
R49	vehicle	4	3	19.52	28.63	M	R50	vehicle	3	3	24.25	30.16	M
R49	vehicle	4	4	24.89	34.52	M	R50	vehicle	3	4	30.33	32.59	M
R49	vehicle	4	5	27.80	16.23	S	R50	vehicle	3	5	28.02	26.73	M
R49	vehicle	4	6	20.50	39.45	M	R50	vehicle	3	6	14.94	26.37	M
R49	vehicle	4	7	16.59	33.51	M	R50	vehicle	3	7	29.64	36.03	M
R49	vehicle	4	8	32.69	30.20	M	R50	vehicle	3	8	20.11	25.98	M
R49	vehicle	4	9	21.80	28.42	M	R50	vehicle	3	9	18.96	35.19	M
R49	vehicle	4	10	13.47	30.56	M	R50	vehicle	3	10	26.58	36.55	M
R49	vehicle	5	1	26.23	20.09	S	R50	vehicle	4	1	34.43	36.90	M
R49	vehicle	5	2	23.46	21.32	M	R50	vehicle	4	2	44.25	29.54	M
R49	vehicle	5	3	32.49	33.04	M	R50	vehicle	4	3	43.59	30.47	M
R49	vehicle	5	4	32.00	32.86	M	R50	vehicle	4	4	47.89	35.45	M
R49	vehicle	5	5	21.32	32.97	M	R50	vehicle	4	5	33.19	30.10	M
R49	vehicle	5	6	34.88	33.98	M	R50	vehicle	4	6	21.14	26.30	M
R49	vehicle	5	7	18.37	24.20	M	R50	vehicle	4	7	39.92	33.96	M
R49	vehicle	5	8	26.89	33.12	M	R50	vehicle	4	8	26.82	39.19	M
R49	vehicle	5	9	19.29	38.13	M	R50	vehicle	4	9	30.30	39.50	M
R49	vehicle	5	10	21.29	43.59	L	R50	vehicle	4	10	12.82	42.24	L
R49	vehicle	6	1	51.93	26.77	M	R50	vehicle	5	1	53.21	26.06	M
R49	vehicle	6	2	46.15	28.20	M	R50	vehicle	5	2	34.79	28.08	M
R49	vehicle	6	3	61.78	38.26	M	R50	vehicle	5	3	42.75	25.32	M
R49	vehicle	6	4	26.50	25.27	M	R50	vehicle	5	4	49.61	38.27	M
R49	vehicle	6	5	47.40	38.85	M	R50	vehicle	5	5	46.40	45.59	L
R49	vehicle	6	6	45.58	37.11	M	R50	vehicle	5	6	37.37	28.55	M
R49	vehicle	6	7	31.85	27.86	M	R50	vehicle	5	7	28.42	37.24	M
R49	vehicle	6	8	38.95	33.91	M	R50	vehicle	5	8	35.29	25.25	M
R49	vehicle	6	9	41.13	24.57	M	R50	vehicle	5	9	26.49	29.28	M
R49	vehicle	6	10	43.59	35.71	M	R50	vehicle	5	10	35.62	33.59	M
R50	vehicle	1	1	30.69	30.09	M	R50	vehicle	6	1	45.15	21.76	M
R50	vehicle	1	2	38.91	25.47	M	R50	vehicle	6	2	55.48	20.45	S

φ: diameter; S: small; M: medium; L: large

Note: Table is continued on the next page.

Table E.6. continued

Rat	Group	image no.	cell no.	intensity	φ (μm)	bin
R50	vehicle	6	3	27.42	30.42	M
R50	vehicle	6	4	47.44	27.57	M
R50	vehicle	6	5	52.08	40.81	L
R50	vehicle	6	6	41.11	29.76	M
R50	vehicle	6	7	41.86	49.75	L
R50	vehicle	6	8	50.89	40.50	L
R50	vehicle	6	9	32.97	33.00	M
R50	vehicle	6	10	29.73	26.35	M
R51	vehicle	1	1	42.07	29.48	M
R51	vehicle	1	2	26.61	20.84	S
R51	vehicle	1	3	37.62	27.91	M
R51	vehicle	1	4	47.98	24.60	M
R51	vehicle	1	5	34.82	26.38	M
R51	vehicle	1	6	39.99	35.70	M
R51	vehicle	1	7	72.43	32.80	M
R51	vehicle	1	8	40.30	31.04	M
R51	vehicle	1	9	42.90	25.00	M
R51	vehicle	1	10	19.93	33.41	M
R51	vehicle	2	1	60.81	27.89	M
R51	vehicle	2	2	61.96	33.80	M
R51	vehicle	2	3	38.53	27.00	M
R51	vehicle	2	4	70.75	32.09	M
R51	vehicle	2	5	43.28	24.65	M
R51	vehicle	2	6	71.87	32.76	M
R51	vehicle	2	7	25.13	22.25	M
R51	vehicle	2	8	38.83	29.74	M
R51	vehicle	2	9	46.13	43.19	L
R51	vehicle	2	10	51.87	25.00	M
R51	vehicle	3	1	28.75	24.94	M
R51	vehicle	3	2	34.59	28.62	M
R51	vehicle	3	3	26.80	24.10	M
R51	vehicle	3	4	54.93	31.01	M
R51	vehicle	3	5	41.73	24.10	M
R51	vehicle	3	6	49.44	26.22	M
R51	vehicle	3	7	21.27	26.34	M
R51	vehicle	3	8	35.48	32.18	M
R51	vehicle	3	9	53.64	32.56	M
R51	vehicle	3	10	51.66	34.09	M
R51	vehicle	4	1	31.07	18.96	S
R51	vehicle	4	2	58.67	36.73	M
R51	vehicle	4	3	60.91	21.91	M
R51	vehicle	4	4	41.29	25.48	M
R51	vehicle	4	5	67.68	37.60	M
R51	vehicle	4	6	76.91	28.02	M
R51	vehicle	4	7	54.19	24.49	M
R51	vehicle	4	8	26.02	30.06	M
R51	vehicle	4	9	31.52	34.53	M
R51	vehicle	4	10	72.08	33.68	M
R51	vehicle	5	1	37.29	21.89	M
R51	vehicle	5	2	80.55	33.25	M
R51	vehicle	5	3	117.79	32.67	M
R51	vehicle	5	4	82.11	35.48	M
R51	vehicle	5	5	50.71	38.48	M
R51	vehicle	5	6	43.36	34.57	M
R51	vehicle	5	7	49.19	29.37	M
R51	vehicle	5	8	74.07	37.93	M
R51	vehicle	5	9	38.63	33.54	M
R51	vehicle	5	10	64.04	33.16	M
R51	vehicle	6	1	70.95	22.31	M
R51	vehicle	6	2	32.06	23.08	M
R51	vehicle	6	3	75.01	32.01	M
R51	vehicle	6	4	52.41	35.31	M
R51	vehicle	6	5	49.12	20.78	S
R51	vehicle	6	6	57.39	34.15	M
R51	vehicle	6	7	58.40	43.39	L
R51	vehicle	6	8	46.97	33.08	M
R51	vehicle	6	9	39.22	26.13	M
R51	vehicle	6	10	53.91	32.42	M

φ: diameter; S: small; M: medium; L: large

Figure E.5. Immunolabeling of substance in DRG neurons as designated in Table E.6 (Chapter 7)

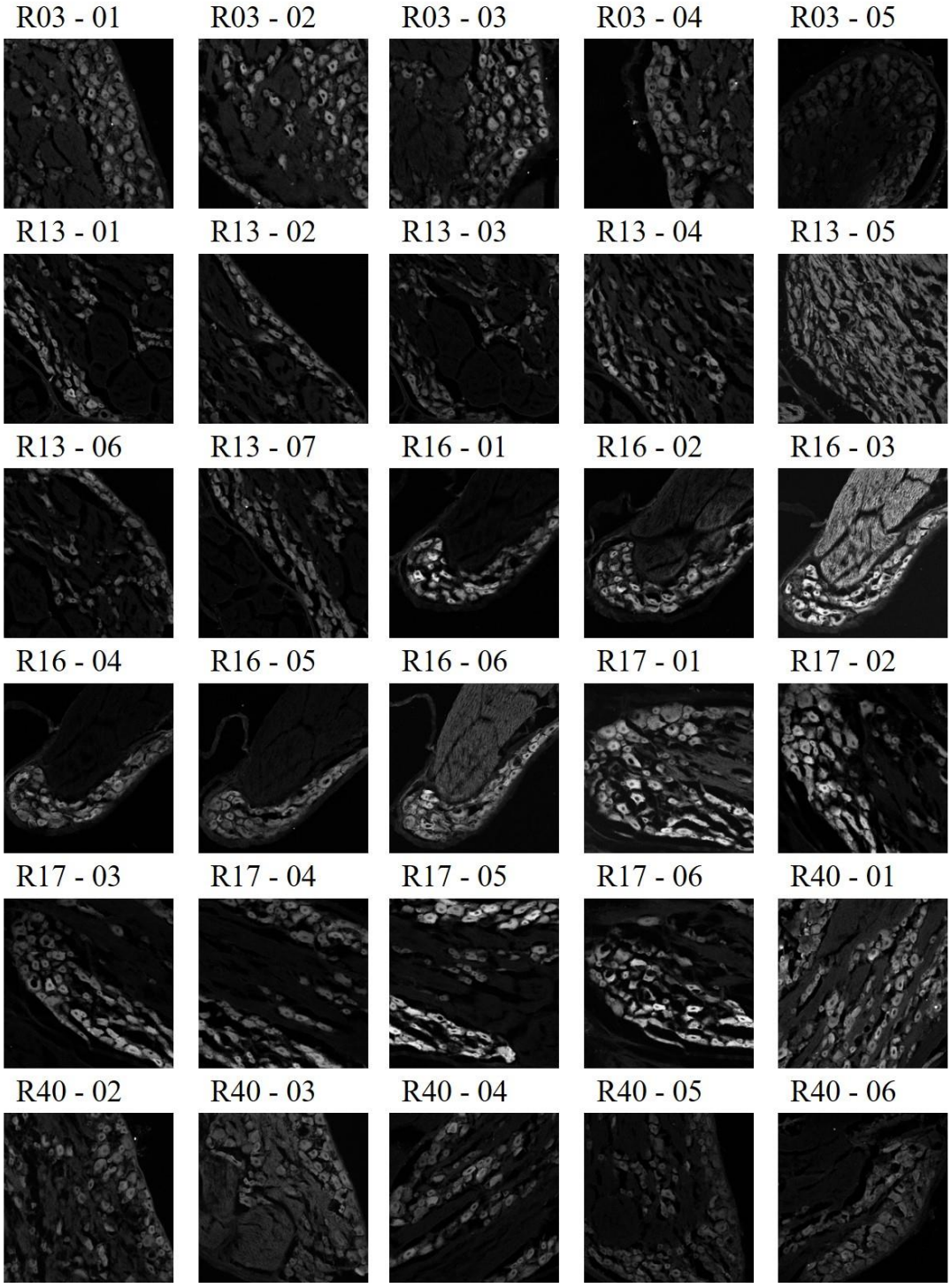

Note: Figure is continued on the next page.

Figure E.5. continued

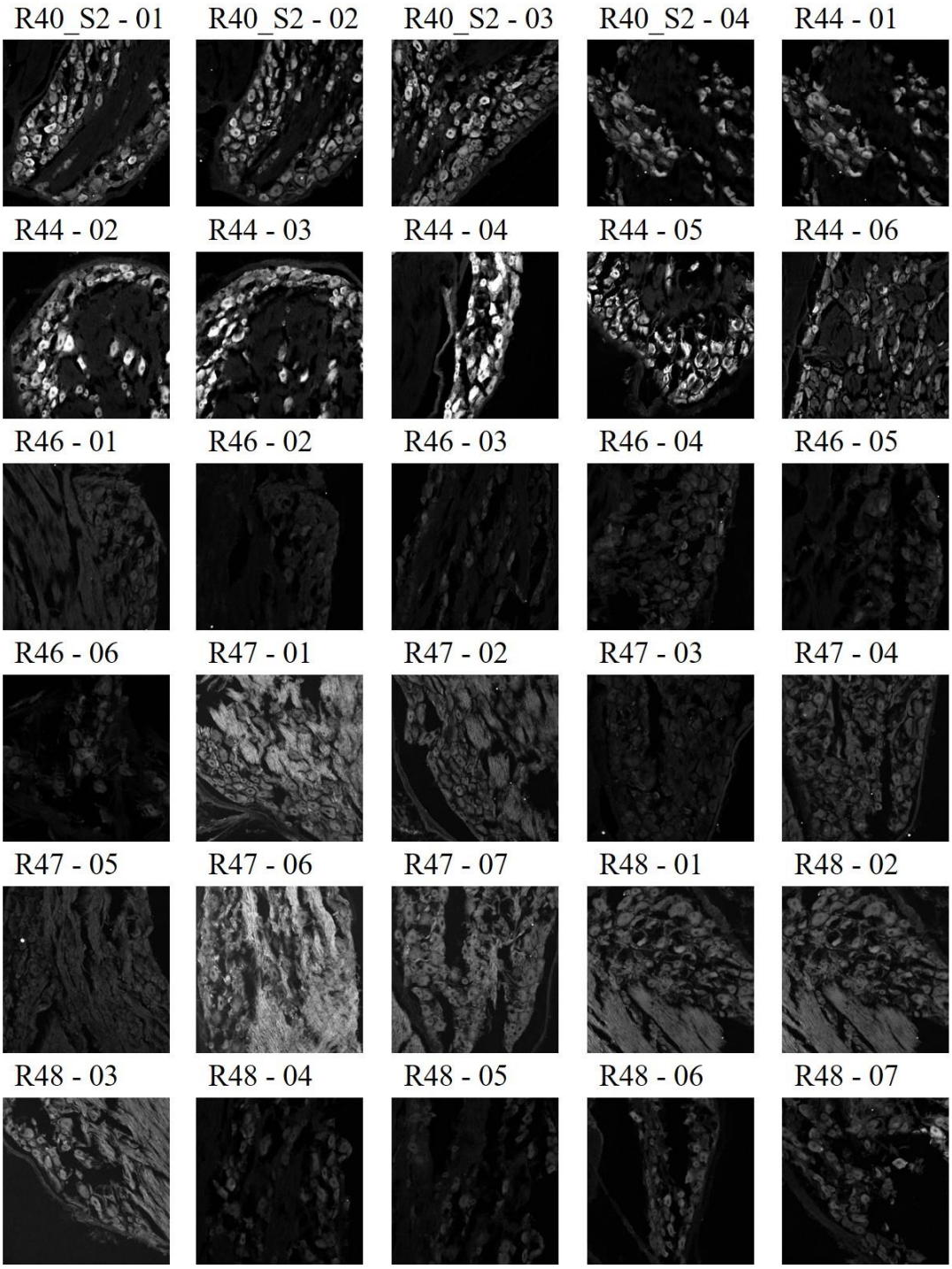

Note: Figure is continued on the next page.

Figure E.5. continued

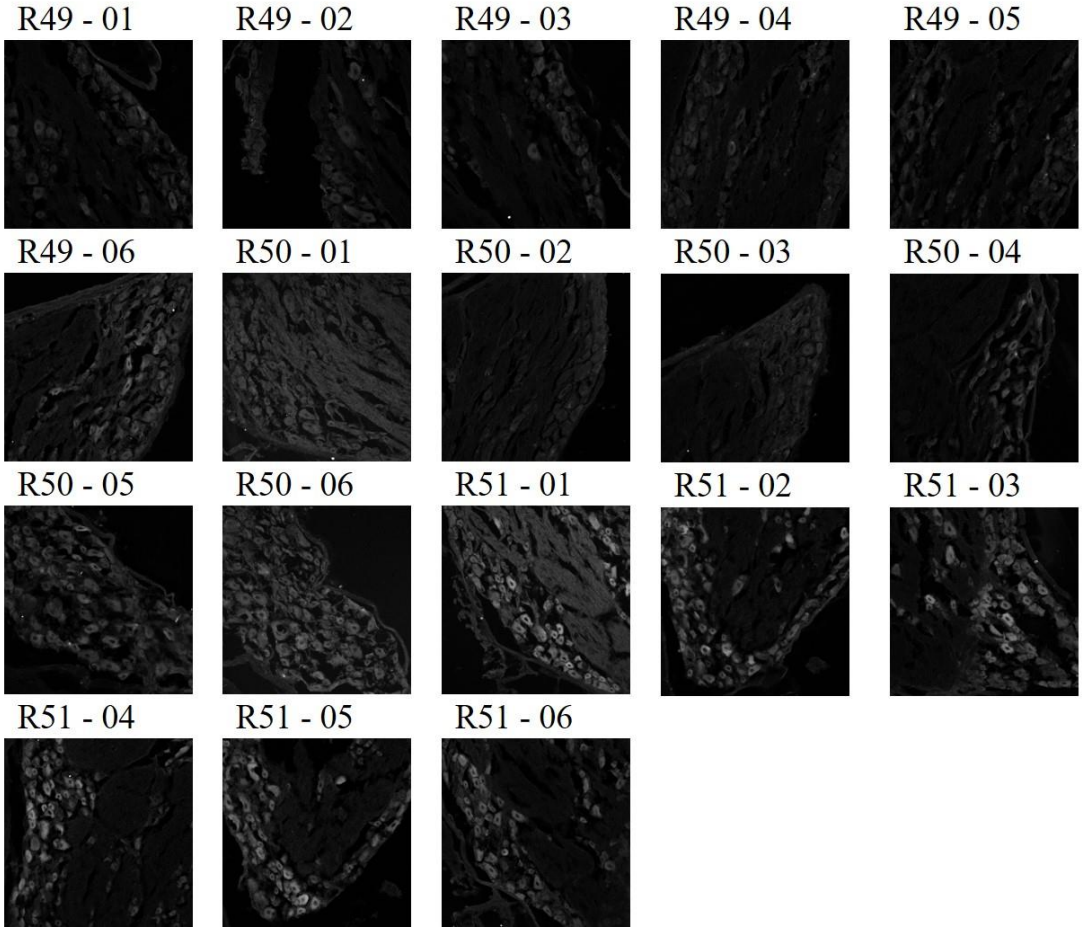

Table E.7. Pixel intensity of MMP-9 labeling in DRG neurons by size from rats injected with MMP-1 or vehicle (Chapter 7)

Rat	Group	image no.	cell no.	intensity	φ (μm)	bin	Rat	Group	image no.	cell no.	intensity	φ (μm)	bin
R13	MMP-1	5	1	41.60	24.48	M	R17	MMP-1	4	9	50.07	21.11	M
R13	MMP-1	5	2	30.23	40.48	L	R17	MMP-1	4	10	61.99	38.88	M
R13	MMP-1	5	3	23.92	27.65	M	R17	MMP-1	5	1	55.72	20.40	S
R13	MMP-1	5	4	28.26	27.16	M	R17	MMP-1	5	2	47.58	25.31	M
R13	MMP-1	5	5	35.29	25.47	M	R17	MMP-1	5	3	44.42	26.60	M
R13	MMP-1	5	6	41.98	33.21	M	R17	MMP-1	5	4	62.45	22.76	M
R13	MMP-1	5	7	27.67	29.54	M	R17	MMP-1	5	5	66.23	17.81	S
R13	MMP-1	5	8	37.03	39.03	M	R17	MMP-1	5	6	90.22	24.08	M
R13	MMP-1	5	9	49.23	26.96	M	R17	MMP-1	5	7	68.61	22.89	M
R13	MMP-1	5	10	31.88	34.50	M	R17	MMP-1	5	8	74.43	26.35	M
R13	MMP-1	6	1	44.31	23.28	M	R17	MMP-1	5	9	59.93	38.65	M
R13	MMP-1	6	2	41.09	23.28	M	R17	MMP-1	5	10	62.97	30.00	M
R13	MMP-1	6	3	46.87	25.03	M	R40	naïve	5	1	49.27	21.61	M
R13	MMP-1	6	4	62.96	22.79	M	R40	naïve	5	2	45.88	17.88	S
R13	MMP-1	6	5	65.12	25.31	M	R40	naïve	5	3	43.36	15.13	S
R13	MMP-1	6	6	49.72	25.74	M	R40	naïve	5	4	60.88	31.19	M
R13	MMP-1	6	7	49.87	21.71	M	R40	naïve	5	5	49.13	28.43	M
R13	MMP-1	6	8	37.99	19.94	S	R40	naïve	5	6	60.14	18.36	S
R13	MMP-1	6	9	26.11	18.18	S	R40	naïve	5	7	54.61	22.36	M
R13	MMP-1	6	10	40.07	25.06	M	R40	naïve	5	8	34.74	22.07	M
R16	MMP-1	3	1	77.35	21.75	M	R40	naïve	5	9	42.25	25.35	M
R16	MMP-1	3	2	66.48	26.84	M	R40	naïve	5	10	63.31	22.11	M
R16	MMP-1	3	3	61.54	48.20	L	R40-S9	naïve	4	1	23.32	18.18	S
R16	MMP-1	3	4	105.42	37.66	M	R40-S9	naïve	4	2	24.12	17.59	S
R16	MMP-1	3	5	85.72	25.18	M	R40-S9	naïve	4	3	25.34	18.18	S
R16	MMP-1	3	6	58.24	25.14	M	R40-S9	naïve	4	4	24.21	18.56	S
R16	MMP-1	3	7	64.78	27.79	M	R40-S9	naïve	4	5	14.47	26.87	M
R16	MMP-1	3	8	94.20	23.01	M	R40-S9	naïve	4	6	19.63	22.78	M
R16	MMP-1	3	9	87.54	37.95	M	R40-S9	naïve	4	7	23.09	21.44	M
R16	MMP-1	3	10	118.35	26.08	M	R40-S9	naïve	4	8	19.69	26.77	M
R16	MMP-1	6	1	46.07	29.97	M	R40-S9	naïve	4	9	20.53	14.75	S
R16	MMP-1	6	2	35.71	17.72	S	R40-S9	naïve	4	10	26.40	21.62	M
R16	MMP-1	6	3	62.95	20.66	S	R44	MMP-1	4	1	62.38	28.23	M
R16	MMP-1	6	4	48.38	20.94	S	R44	MMP-1	4	2	51.79	20.14	S
R16	MMP-1	6	5	50.21	13.32	S	R44	MMP-1	4	3	95.27	18.62	S
R16	MMP-1	6	6	60.50	34.67	M	R44	MMP-1	4	4	44.20	22.58	M
R16	MMP-1	6	7	56.68	28.95	M	R44	MMP-1	4	5	37.06	24.02	M
R16	MMP-1	6	8	50.72	13.67	S	R44	MMP-1	4	6	23.14	34.41	M
R16	MMP-1	6	9	60.69	27.21	M	R44	MMP-1	4	7	47.34	35.48	M
R16	MMP-1	6	10	64.76	18.69	S	R44	MMP-1	4	8	46.38	23.35	M
R17	MMP-1	4	1	71.35	46.90	L	R44	MMP-1	4	9	34.95	24.83	M
R17	MMP-1	4	2	79.29	33.27	M	R44	MMP-1	4	10	80.31	16.67	S
R17	MMP-1	4	3	73.06	32.50	M	R44	MMP-1	5	1	28.77	15.49	S
R17	MMP-1	4	4	89.84	21.85	M	R44	MMP-1	5	2	22.95	16.15	S
R17	MMP-1	4	5	79.49	29.78	M	R44	MMP-1	5	3	30.55	26.68	M
R17	MMP-1	4	6	70.26	38.55	M	R44	MMP-1	5	4	27.99	20.14	S
R17	MMP-1	4	7	36.80	24.53	M	R44	MMP-1	5	5	22.03	27.02	M
R17	MMP-1	4	8	47.18	17.98	S	R44	MMP-1	5	6	25.57	21.36	M

φ: diameter; S: small; M: medium; L: large

Note: Table is continued on the next page.

Table E.7. continued

Rat	Group	image no.	cell no.	intensity	φ (μm)	bin	Rat	Group	image no.	cell no.	intensity	φ (μm)	bin
R44	MMP-1	5	7	38.92	22.70	M	R48	vehicle	5	7	71.72	24.35	M
R44	MMP-1	5	8	43.73	30.06	M	R48	vehicle	5	8	48.80	16.46	S
R44	MMP-1	5	9	51.75	20.62	S	R48	vehicle	5	9	55.06	26.48	M
R44	MMP-1	5	10	28.81	17.99	S	R48	vehicle	5	10	55.63	38.18	M
R46	MMP-1	3	1	66.84	61.91	L	R48	vehicle	6	1	54.78	20.17	S
R46	MMP-1	3	2	55.56	41.04	L	R48	vehicle	6	2	90.61	20.48	S
R46	MMP-1	3	3	73.94	27.60	M	R48	vehicle	6	3	61.31	23.05	M
R46	MMP-1	3	4	51.70	25.36	M	R48	vehicle	6	4	59.50	45.73	L
R46	MMP-1	3	5	75.08	62.48	L	R48	vehicle	6	5	47.85	18.38	S
R46	MMP-1	3	6	70.27	54.43	L	R48	vehicle	6	6	60.61	19.92	S
R46	MMP-1	3	7	53.87	40.69	L	R48	vehicle	6	7	67.42	46.15	L
R46	MMP-1	3	8	52.64	27.86	M	R48	vehicle	6	8	59.38	20.48	S
R46	MMP-1	3	9	64.93	45.08	L	R48	vehicle	6	9	51.13	19.59	S
R46	MMP-1	3	10	99.27	30.88	M	R48	vehicle	6	10	51.44	14.82	S
R46	MMP-1	6	1	52.37	21.56	M	R49	vehicle	2	1	123.30	19.75	S
R46	MMP-1	6	2	57.10	23.66	M	R49	vehicle	2	2	154.49	13.98	S
R46	MMP-1	6	3	35.68	30.70	M	R49	vehicle	2	3	114.78	20.91	S
R46	MMP-1	6	4	85.23	28.92	M	R49	vehicle	2	4	128.32	21.52	M
R46	MMP-1	6	5	49.46	42.16	L	R49	vehicle	2	5	106.50	29.45	M
R46	MMP-1	6	6	46.58	14.30	S	R49	vehicle	2	6	106.53	21.67	M
R46	MMP-1	6	7	51.12	30.63	M	R49	vehicle	2	7	111.63	30.44	M
R46	MMP-1	6	8	44.57	31.05	M	R49	vehicle	2	8	119.24	21.33	M
R46	MMP-1	6	9	57.86	23.28	M	R49	vehicle	2	9	96.66	14.81	S
R46	MMP-1	6	10	50.13	22.15	M	R49	vehicle	2	10	102.64	21.67	M
R47	MMP-1	3	1	73.27	24.99	M	R49	vehicle	6	1	59.78	21.37	M
R47	MMP-1	3	2	108.52	29.45	M	R49	vehicle	6	2	84.73	21.29	M
R47	MMP-1	3	3	98.54	15.89	S	R49	vehicle	6	3	56.74	25.26	M
R47	MMP-1	3	4	104.82	16.35	S	R49	vehicle	6	4	39.47	27.68	M
R47	MMP-1	3	5	76.63	17.45	S	R49	vehicle	6	5	86.42	23.45	M
R47	MMP-1	3	6	88.22	18.97	S	R49	vehicle	6	6	55.22	20.45	S
R47	MMP-1	3	7	88.25	50.32	L	R49	vehicle	6	7	46.54	18.61	S
R47	MMP-1	3	8	85.59	41.55	L	R49	vehicle	6	8	71.28	29.83	M
R47	MMP-1	3	9	88.77	46.23	L	R49	vehicle	6	9	58.95	41.97	L
R47	MMP-1	3	10	98.61	16.87	S	R49	vehicle	6	10	64.05	24.91	M
R47	MMP-1	5	1	82.21	27.15	M	R50	vehicle	4	1	61.96	23.23	M
R47	MMP-1	5	2	84.28	27.35	M	R50	vehicle	4	2	45.58	24.56	M
R47	MMP-1	5	3	67.20	27.77	M	R50	vehicle	4	3	35.73	28.63	M
R47	MMP-1	5	4	61.22	17.02	S	R50	vehicle	4	4	60.51	25.82	M
R47	MMP-1	5	5	80.13	18.81	S	R50	vehicle	4	5	35.52	22.83	M
R47	MMP-1	5	6	59.53	17.38	S	R50	vehicle	4	6	34.36	22.92	M
R47	MMP-1	5	7	71.76	22.16	M	R50	vehicle	4	7	35.16	22.07	M
R47	MMP-1	5	8	86.83	25.11	M	R50	vehicle	4	8	47.67	22.49	M
R47	MMP-1	5	9	73.93	31.40	M	R50	vehicle	4	9	36.37	29.61	M
R47	MMP-1	5	10	80.63	21.52	M	R50	vehicle	4	10	56.00	24.19	M
R48	vehicle	5	1	73.66	33.48	M	R50	vehicle	6	1	42.31	48.48	L
R48	vehicle	5	2	71.33	44.51	L	R50	vehicle	6	2	80.71	19.53	S
R48	vehicle	5	3	39.07	40.10	L	R50	vehicle	6	3	82.63	17.16	S
R48	vehicle	5	4	64.10	25.93	M	R50	vehicle	6	4	60.88	20.32	S
R48	vehicle	5	5	71.49	24.98	M	R50	vehicle	6	5	82.41	11.56	S
R48	vehicle	5	6	89.46	26.86	M	R50	vehicle	6	6	63.06	42.84	L

φ: diameter; S: small; M: medium; L: large

Note: Table is continued on the next page.

Table E.7. continued

Rat	Group	image no.	cell no.	intensity	φ (µm)	bin
R50	vehicle	6	7	55.83	36.84	M
R50	vehicle	6	8	74.57	43.10	L
R50	vehicle	6	9	50.13	30.29	M
R50	vehicle	6	10	72.03	43.93	L
R51	vehicle	3	1	38.99	28.38	M
R51	vehicle	3	2	65.45	31.41	M
R51	vehicle	3	3	48.71	20.87	S
R51	vehicle	3	4	59.06	20.81	S
R51	vehicle	3	5	76.17	32.66	M
R51	vehicle	3	6	77.26	38.10	M
R51	vehicle	3	7	74.27	40.94	L
R51	vehicle	3	8	65.33	31.35	M
R51	vehicle	3	9	47.62	40.64	L
R51	vehicle	3	10	40.31	18.24	S
R51	vehicle	6	1	62.56	24.27	M
R51	vehicle	6	2	81.87	16.34	S
R51	vehicle	6	3	108.06	21.31	M
R51	vehicle	6	4	69.39	22.31	M
R51	vehicle	6	5	92.90	26.77	M
R51	vehicle	6	6	56.38	35.84	M
R51	vehicle	6	7	96.75	37.14	M
R51	vehicle	6	8	89.08	37.70	M
R51	vehicle	6	9	58.68	28.81	M
R51	vehicle	6	10	74.41	20.97	S

φ: diameter; S: small; M: medium; L: large

Figure E.6. Immunolabeling of MMP-9 in DRG neurons as designated in Table E.7 (Chapter 7)

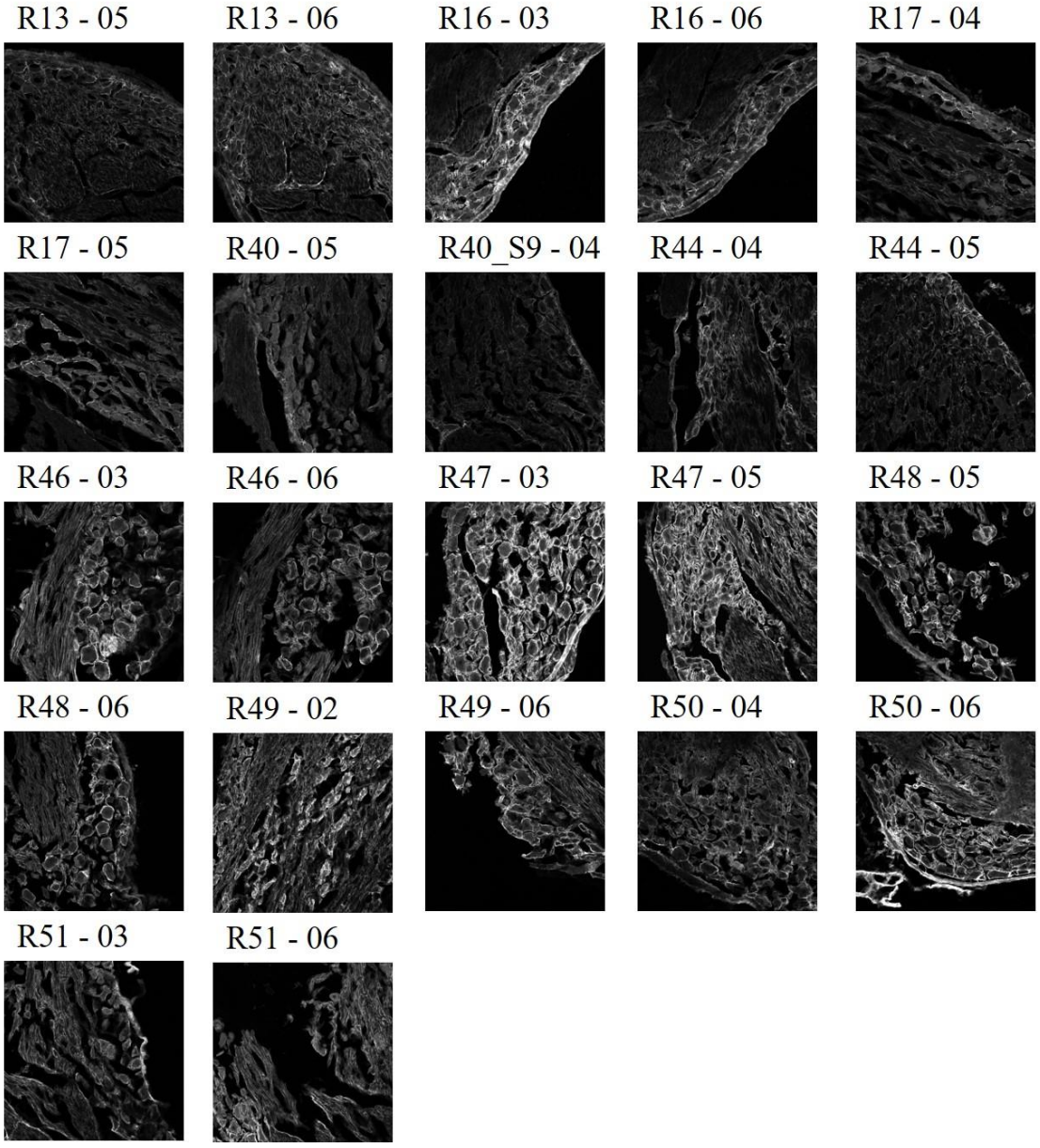

Table E.8. Densitometry of substance P immunolabeling in the superficial dorsal horn of the spinal cord from rats injected with MMP-1 or vehicle (Chapter 7)

Rat	Group	image no.	substance P (% positive)
R03	naïve	1	3.11%
R03	naïve	2	9.11%
R03	naïve	3	6.01%
R03	naïve	4	12.28%
R03	naïve	5	6.28%
R03	naïve	6	3.34%
R13	MMP-1	1	0.27%
R13	MMP-1	2	9.45%
R13	MMP-1	3	22.58%
R13	MMP-1	4	7.35%
R13	MMP-1	5	0.56%
R16	MMP-1	1	7.93%
R16	MMP-1	2	6.58%
R16	MMP-1	3	4.64%
R16	MMP-1	4	1.96%
R16	MMP-1	5	11.51%
R16	MMP-1	6	60.23%
R17	MMP-1	1	12.82%
R17	MMP-1	2	23.78%
R17	MMP-1	3	19.67%
R17	MMP-1	4	14.92%
R17	MMP-1	5	23.78%
R17	MMP-1	6	18.03%
R40_s1	naïve	1	1.26%
R40_s1	naïve	2	2.29%
R40_s1	naïve	3	1.46%
R40_s1	naïve	4	5.74%
R40_s1	naïve	5	2.59%
R40_s1	naïve	6	13.76%
R40_s2	naïve	1	15.49%
R40_s2	naïve	2	19.50%
R40_s2	naïve	3	5.90%
R40_s2	naïve	4	8.11%
R40_s2	naïve	5	24.54%
R40_s2	naïve	6	7.51%
R40_s3	naïve	1	1.96%
R40_s3	naïve	2	2.47%
R40_s3	naïve	3	43.15%
R40_s3	naïve	4	29.96%
R40_s3	naïve	5	4.81%
R40_s3	naïve	6	6.99%
R44	MMP-1	1	12.71%
R44	MMP-1	2	25.47%
R44	MMP-1	3	10.31%
R44	MMP-1	4	25.79%
R46	MMP-1	1	2.58%
R46	MMP-1	2	1.43%
R46	MMP-1	3	1.85%
R46	MMP-1	4	2.75%
R46	MMP-1	5	3.16%
R46	MMP-1	6	38.48%
R47	MMP-1	1	7.29%
R47	MMP-1	2	23.07%
R47	MMP-1	3	9.82%
R47	MMP-1	4	1.07%
R47	MMP-1	5	2.69%
R47	MMP-1	6	2.46%
R48	vehicle	1	10.81%
R48	vehicle	2	13.17%
R48	vehicle	3	13.17%
R48	vehicle	4	6.22%
R48	vehicle	5	6.26%
R48	vehicle	6	9.43%
R49	vehicle	1	5.62%
R49	vehicle	2	4.09%
R49	vehicle	3	3.57%
R49	vehicle	4	3.27%
R49	vehicle	5	3.28%
R49	vehicle	6	2.63%
R50	vehicle	1	2.41%
R50	vehicle	2	2.56%
R50	vehicle	3	2.60%
R50	vehicle	4	2.75%
R50	vehicle	5	3.87%
R50	vehicle	6	3.76%
R51	vehicle	1	0.78%
R51	vehicle	2	1.89%
R51	vehicle	3	3.10%
R51	vehicle	4	6.65%
R51	vehicle	5	2.83%
R51	vehicle	6	5.35%

Figure E.7. Immunolabeling of substance P in the superficial dorsal horn of the spinal cord as designated in Table E.8 (Chapter 7)

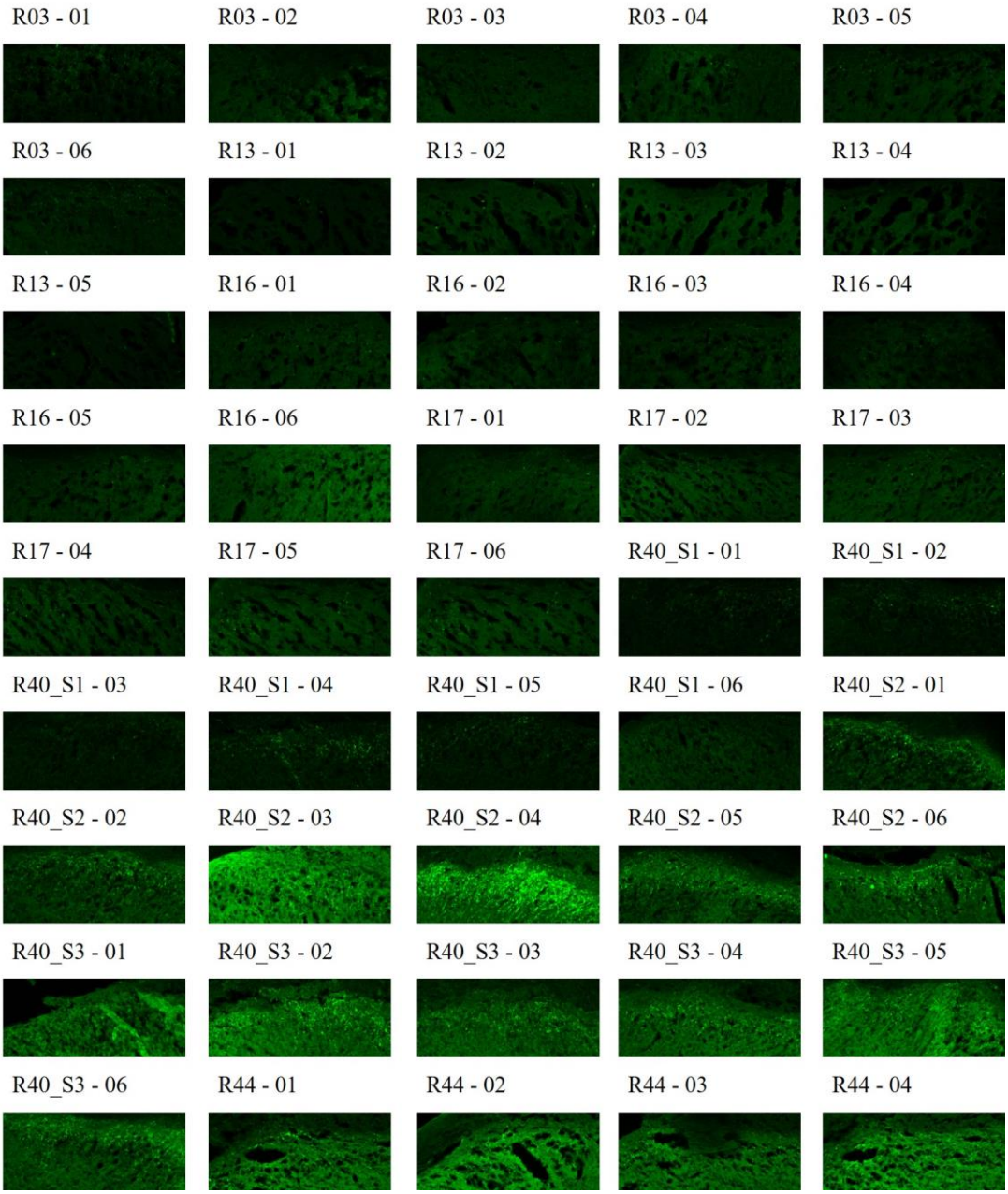

Note: Figure is continued on the next page.

Figure E.7. continued

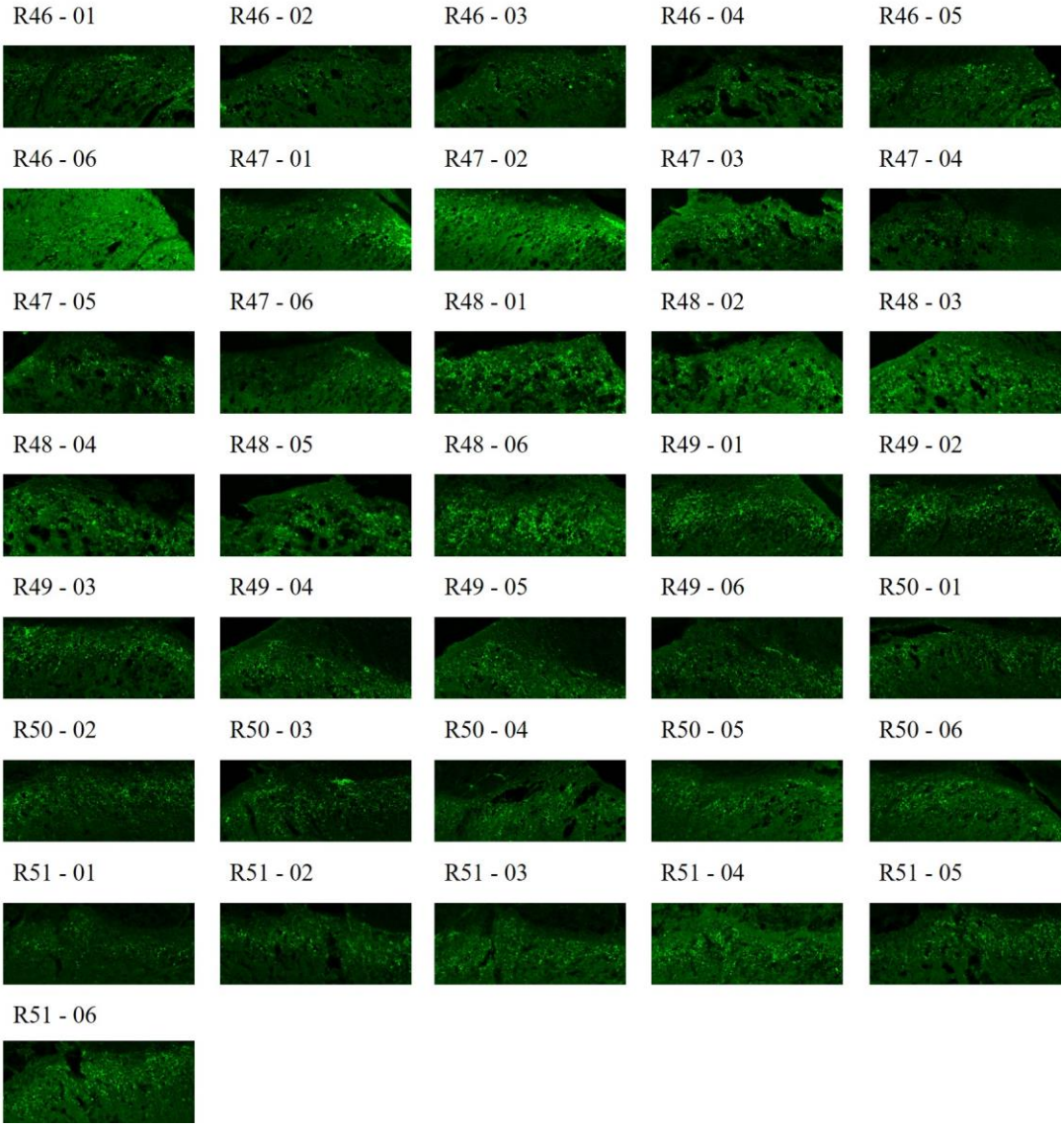

Table E.9. Densitometry of MMP-9 immunolabeling in the superficial dorsal horn of the spinal cord from rats injected with MMP-1 or vehicle (Chapter 7)

Rat	Group	image no.	substance P (% positive)	Rat	Group	image no.	substance P (% positive)
R13	MMP-1	1	0.33%	R46	MMP-1	1	47.40%
R13	MMP-1	2	1.52%	R46	MMP-1	2	2.76%
R13	MMP-1	3	0.23%	R46	MMP-1	3	11.23%
R13	MMP-1	4	0.90%	R46	MMP-1	4	24.95%
R13	MMP-1	5	1.68%	R46	MMP-1	5	0.76%
R13	MMP-1	6	0.06%	R46	MMP-1	6	0.07%
R16	MMP-1	1	0.24%	R47	MMP-1	1	63.20%
R16	MMP-1	2	7.54%	R47	MMP-1	2	73.19%
R16	MMP-1	3	43.89%	R47	MMP-1	3	29.59%
R16	MMP-1	4	15.13%	R47	MMP-1	4	2.30%
R16	MMP-1	5	28.99%	R47	MMP-1	5	35.20%
R16	MMP-1	6	0.10%	R47	MMP-1	6	57.17%
R17	MMP-1	1	75.60%	R48	vehicle	1	0.09%
R17	MMP-1	2	74.21%	R48	vehicle	2	20.39%
R17	MMP-1	3	9.27%	R48	vehicle	3	42.21%
R17	MMP-1	4	6.53%	R48	vehicle	4	32.03%
R17	MMP-1	5	21.16%	R48	vehicle	5	1.93%
R17	MMP-1	6	34.93%	R48	vehicle	6	11.03%
R40	naïve	1	72.62%	R49	vehicle	1	0.88%
R40	naïve	2	61.41%	R49	vehicle	2	0.05%
R40	naïve	3	11.50%	R49	vehicle	3	35.56%
R40	naïve	4	22.52%	R49	vehicle	4	35.90%
R40	naïve	5	44.50%	R49	vehicle	5	28.64%
R40	naïve	6	4.02%	R49	vehicle	6	1.32%
R40_S9	naïve	1	1.26%	R50	vehicle	1	19.39%
R40_S9	naïve	2	2.13%	R50	vehicle	2	19.37%
R40_S9	naïve	3	42.18%	R50	vehicle	3	0.12%
R40_S9	naïve	4	0.67%	R50	vehicle	4	1.10%
R40_S9	naïve	5	5.21%	R50	vehicle	5	0.33%
R40_S9	naïve	6	21.57%	R50	vehicle	6	2.78%
R44	MMP-1	1	0.82%	R51	vehicle	1	20.98%
R44	MMP-1	2	11.06%	R51	vehicle	2	11.16%
R44	MMP-1	3	0.18%	R51	vehicle	3	10.55%
R44	MMP-1	4	4.40%	R51	vehicle	4	31.89%
R44	MMP-1	5	0.35%	R51	vehicle	5	9.36%
R44	MMP-1	6	0.19%	R51	vehicle	6	4.97%

Figure E.8. Immunolabeling of MMP-9 in the superficial dorsal horn of the spinal cord as designated in Table E.9 (Chapter 7)

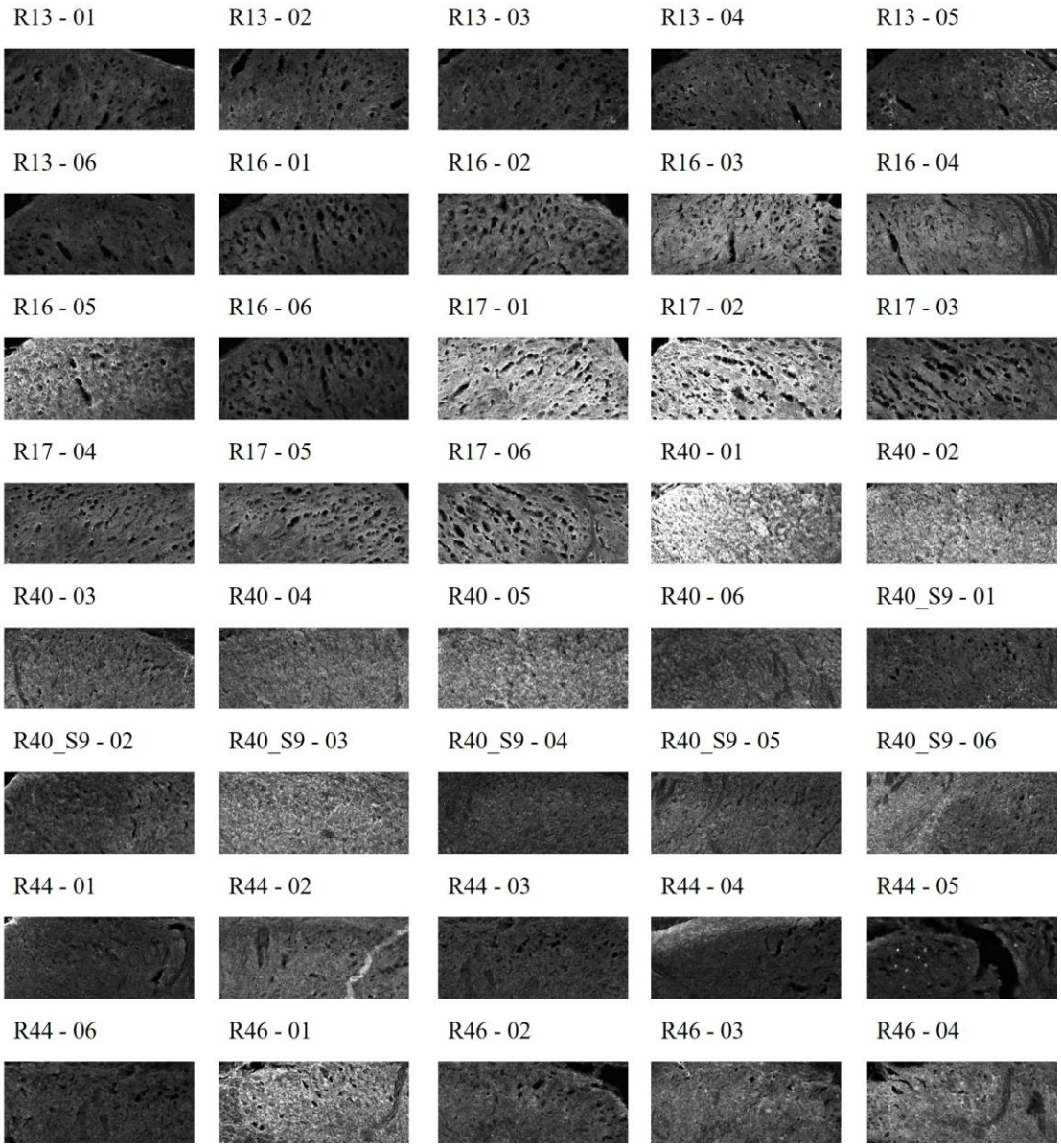

Note: Figure is continued on the next page.

Figure E.8. continued

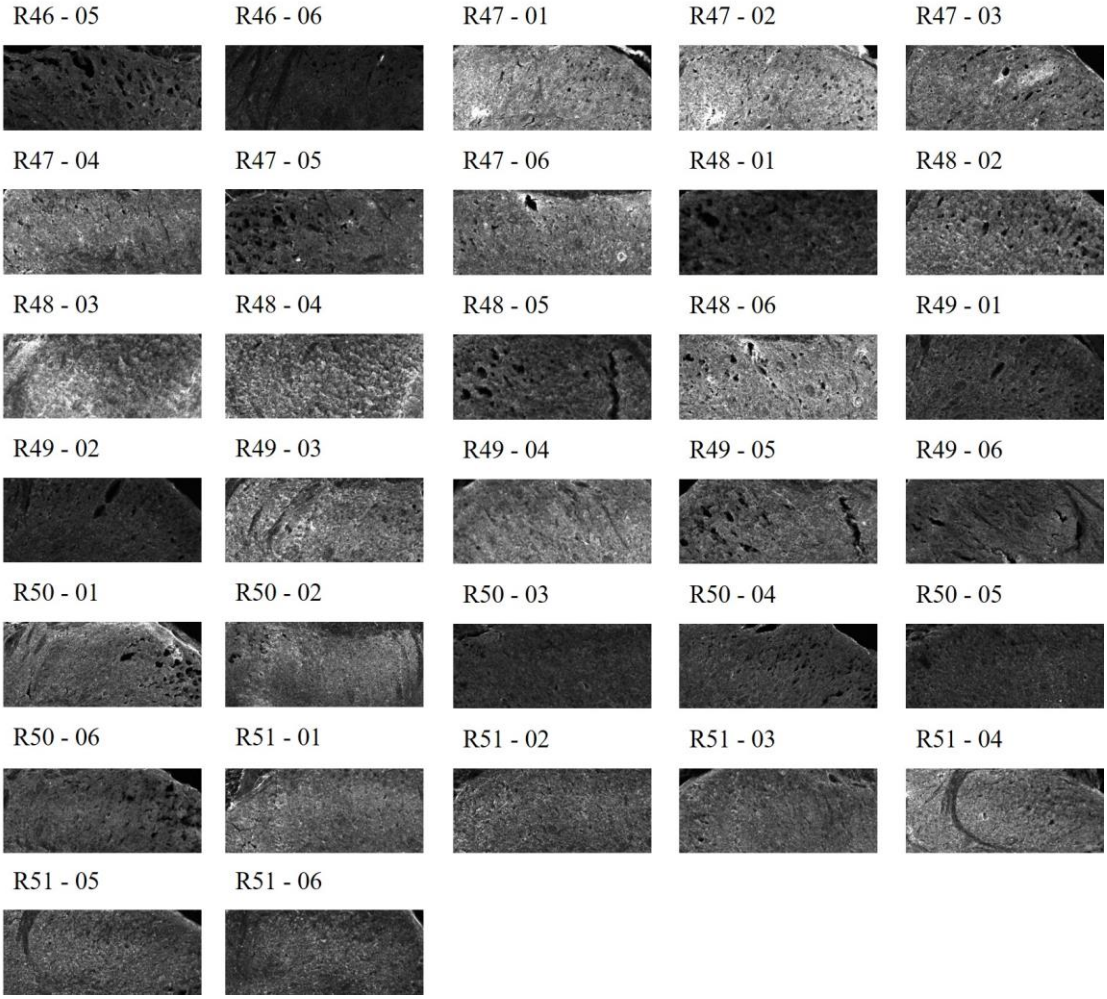

APPENDIX F

Mechanical & Immunolabeling Data for Bacterial Collagenase Exposure Studies in the Co-Culture Model

This appendix summarizes the force, strain, and immunolabeling data acquired for the studies presented in Section 5.5 of Chapter 5 that define the effects of bacterial collagenase exposure in the DRG-FLS co-culture model of the capsular ligament. In each of the tables and figures detailed in this appendix, data are identified by their sample ID number and the experimental group (collagenase; vehicle). Labels above each image within the figures that contain confocal images list the sample number followed by the image number (e.g. "S03 – 01" indicates image 1 from sample 3); the image number in the labels matches the image numbers listed in the corresponding data table.

The studies corresponding to the data summarized in this appendix incubated co-culture collagen gels in purified bacterial collagenase in DMEM (collagenase) or DMEM only (vehicle) for 20 minutes. In those studies, separate co-cultures were designated to exposure experiments performed under a physiological, constrained hold or under free-floating conditions. Table F.1 contains the force data acquired after 20 minutes of a biaxial physiological hold with collagenase or vehicle exposure; force data are presented as the change from baseline for the four load cells corresponding to each of the four actuator arms

on the planar biaxial test device. Figure F.1 summarizes the force traces versus time, for each load cell, for those same studies. Marker positions of fiducial markers were also digitized (Fiji software; NIH) before the addition of collagenase or vehicle solution and after the 20-minute hold for elemental strain analyses. LS-DYNA (LSTC) software was used to calculate the maximum principal strain (MPS) for each gel. Elemental MPS data are detailed in Table F.2 and the corresponding surface strain maps are visualized in Figure F.2.

Tables F.3 and F.4 and Figures F.3-F.6 summarize the data acquired from immunolabeling assays performed on co-culture collagen gels after 20 minutes of free-floating exposure to bacterial collagenase or a vehicle solution. Table F.3 and Figure F.3 detail the collagen immunolabel. Fiber orientation was quantified on the immunolabeled images by computing the anisotropy index as the ratio of the principal axes to describe orientation on a continuous scale from isotropic (random; 0) to aligned (1) (Sander and Barocas 2009). Densitometry computed the percent of positive collagen pixels using the script in Appendix B. Both of the quantified metrics of the anisotropy index and percent positive pixels are summarized in Table F.3.

Table F.4 details the neuronal and fibroblast-localized MMP-1 quantified using co-localization of βIII tubulin or vimentin, respectively, with MMP-1. Images of a βIII tubulin (Figure F.4), vimentin (Figure F.5), and MMP-1 (Figure F.6) triple-label were acquired in regions of the DRG axons and somas and in regions with only FLS cells. Labeling above a threshold for positive MMP-1, βIII tubulin, and vimentin was separately quantified, and MMP-1 co-localization to βIII tubulin and vimentin was computed, separately, to quantify

neuronal and fibroblast-localized MMP-1 using the co-localization densitometry script in Appendix B. MMP-1-βIII tubulin co-localized pixels were normalized to total βIII tubulin, and MMP-1-vimentin co-localized pixels to total vimentin as a measure of neuronal and fibroblast-localized MMP-1.

Table F.1. Force readings after a 20-minute biaxially-constrained hold of collagen gels during exposure to bacterial collagenase or a vehicle solution (Chapter 5) with each of the X and Y arms labeled

Sample	Group	X1L (mN)	X2L (mN)	Y1L (mN)	Y2L (mN)
S01	collagenase	6.2	-11.4	6.0	-6.9
S02	collagenase	5.5	-10.5	2.8	-9.0
S03	collagenase	5.7	3.5	13.2	-5.3
S04	vehicle	12.0	-4.2	9.6	28.2
S05	vehicle	1.2	-2.9	4.7	-23.8
S06	vehicle	3.7	-1.3	-23.6	-12.8

Table F.2. Elemental maximum principal strain after a 20-minute biaxially-constrained hold of collagen gels during exposure to bacterial collagenase or a vehicle solution (Chapter 5)

Sample	Group	element	MPS	Sample	Group	element	MPS
S01	collagenase	1	0.047	S04	vehicle	1	0.154
S01	collagenase	2	0.033	S04	vehicle	2	0.134
S01	collagenase	3	0.055	S04	vehicle	3	0.044
S01	collagenase	4	0.047	S04	vehicle	4	0.045
S01	collagenase	5	0.004	S04	vehicle	5	0.110
S01	collagenase	6	0.023	S04	vehicle	6	0.334
S01	collagenase	7	0.049	S04	vehicle	7	0.037
S01	collagenase	8	0.025	S04	vehicle	8	0.175
S01	collagenase	9	0.016	S04	vehicle	9	0.051
S01	collagenase	10	0.085	S04	vehicle	10	0.036
S01	collagenase	11	0.049	S04	vehicle	11	0.053
S01	collagenase	12	0.021	S04	vehicle	12	0.006
S02	collagenase	1	0.000	S05	vehicle	1	0.040
S02	collagenase	2	0.014	S05	vehicle	2	0.013
S02	collagenase	3	0.035	S05	vehicle	3	0.000
S02	collagenase	4	0.074	S05	vehicle	4	0.047
S02	collagenase	5	0.076	S05	vehicle	5	0.042
S02	collagenase	6	0.000	S05	vehicle	6	0.052
S02	collagenase	7	0.004	S05	vehicle	7	0.035
S02	collagenase	8	0.013	S05	vehicle	8	0.022
S02	collagenase	9	0.026	S05	vehicle	9	0.056
S02	collagenase	10	0.023	S05	vehicle	10	0.023
S02	collagenase	11	0.060	S05	vehicle	11	0.020
S02	collagenase	12	0.057	S05	vehicle	12	0.062
S03	collagenase	1	0.054	S06	vehicle	1	0.024
S03	collagenase	2	0.026	S06	vehicle	2	0.031
S03	collagenase	3	0.025	S06	vehicle	3	0.000
S03	collagenase	4	0.008	S06	vehicle	4	0.040
S03	collagenase	5	0.085	S06	vehicle	5	0.050
S03	collagenase	6	0.063	S06	vehicle	6	0.026
S03	collagenase	7	0.071	S06	vehicle	7	0.007
S03	collagenase	8	0.116	S06	vehicle	8	0.030
S03	collagenase	9	0.024	S06	vehicle	9	0.005

MPS: maximum principal strain

Figure F.1. Force traces shown separately for each load cell affixed to each actuator arm (X1, X2, Y1, Y2) during a 20-minute biaxially-constrained hold of collagen gels during exposure to bacterial collagenase or a vehicle solution as designated in Table F.1 (Chapter 5)

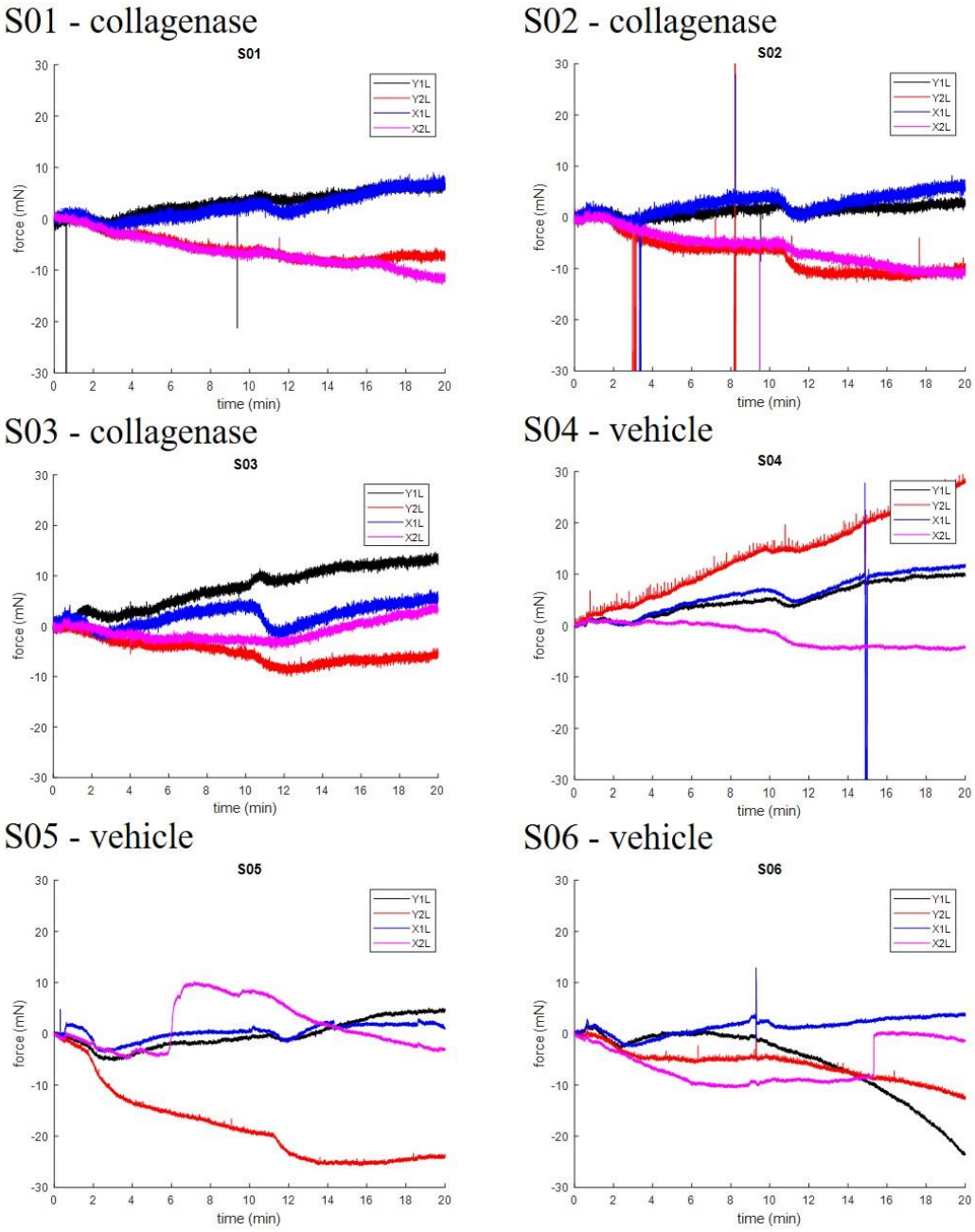

Figure F.2. Surface strain maps after a 20-minute biaxially-constrained hold of collagen gels during exposure to bacterial collagenase or a vehicle solution as designated in Table F.2 (Chapter 5). Elements are numbered sequentially from the bottom left to top right, as shown in sample S01.

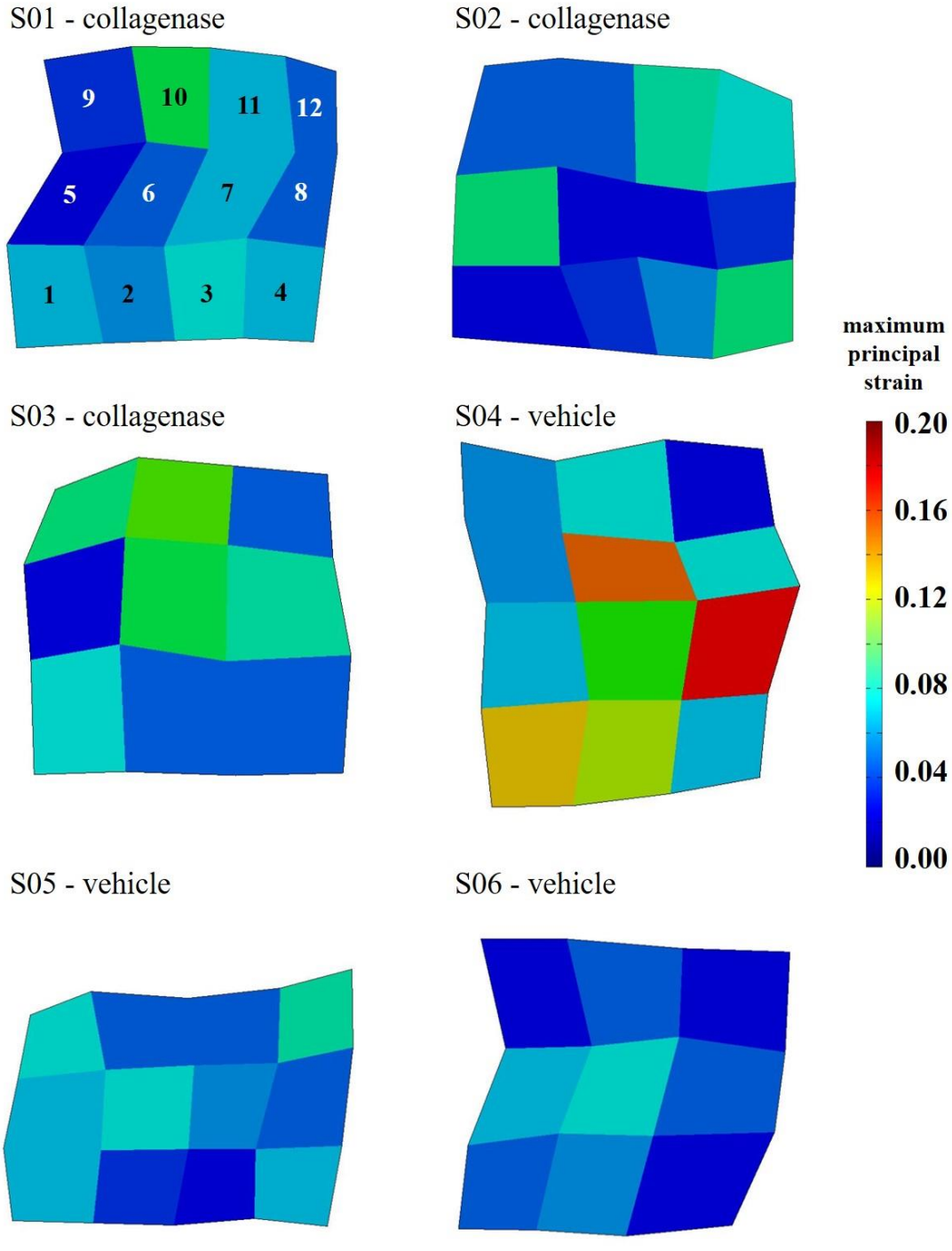

Table F.3. Anisotropy indices and percent positive pixels computed from collagen immunolabeling performed on co-culture gels after 20 minutes of collagenase exposure (Chapter 5)

Sample	Group	image no.	anisotropy index	collagen (% positive)
S01	collagenase	1	0.3999	7.78%
S01	collagenase	2	0.1630	1.91%
S02	collagenase	1	0.0512	0.76%
S02	collagenase	2	0.0302	1.09%
S02	collagenase	3	0.1183	3.84%
S02	collagenase	4	0.2581	3.60%
S03	collagenase	1	0.1567	12.91%
S03	collagenase	2	0.0364	0.83%
S03	collagenase	3	0.1226	0.59%
S04	collagenase	1	0.3302	4.32%
S04	collagenase	2	0.2207	28.80%
S04	collagenase	3	0.1062	4.87%
S04	collagenase	4	0.2325	3.64%
S05	vehicle	1	0.2336	1.15%
S06	vehicle	1	0.0450	3.65%
S06	vehicle	2	0.0909	46.61%
S07	vehicle	1	0.1308	28.72%
S07	vehicle	2	0.2578	56.80%
S07	vehicle	3	0.0722	8.40%
S07	vehicle	4	0.2471	82.88%
S08	vehicle	1	0.0867	42.31%
S08	vehicle	2	0.0792	58.55%
S08	vehicle	3	0.1083	33.73%

Figure F.3. Confocal images showing the collagen immunolabel as designated in Table F.3 (Chapter 5)

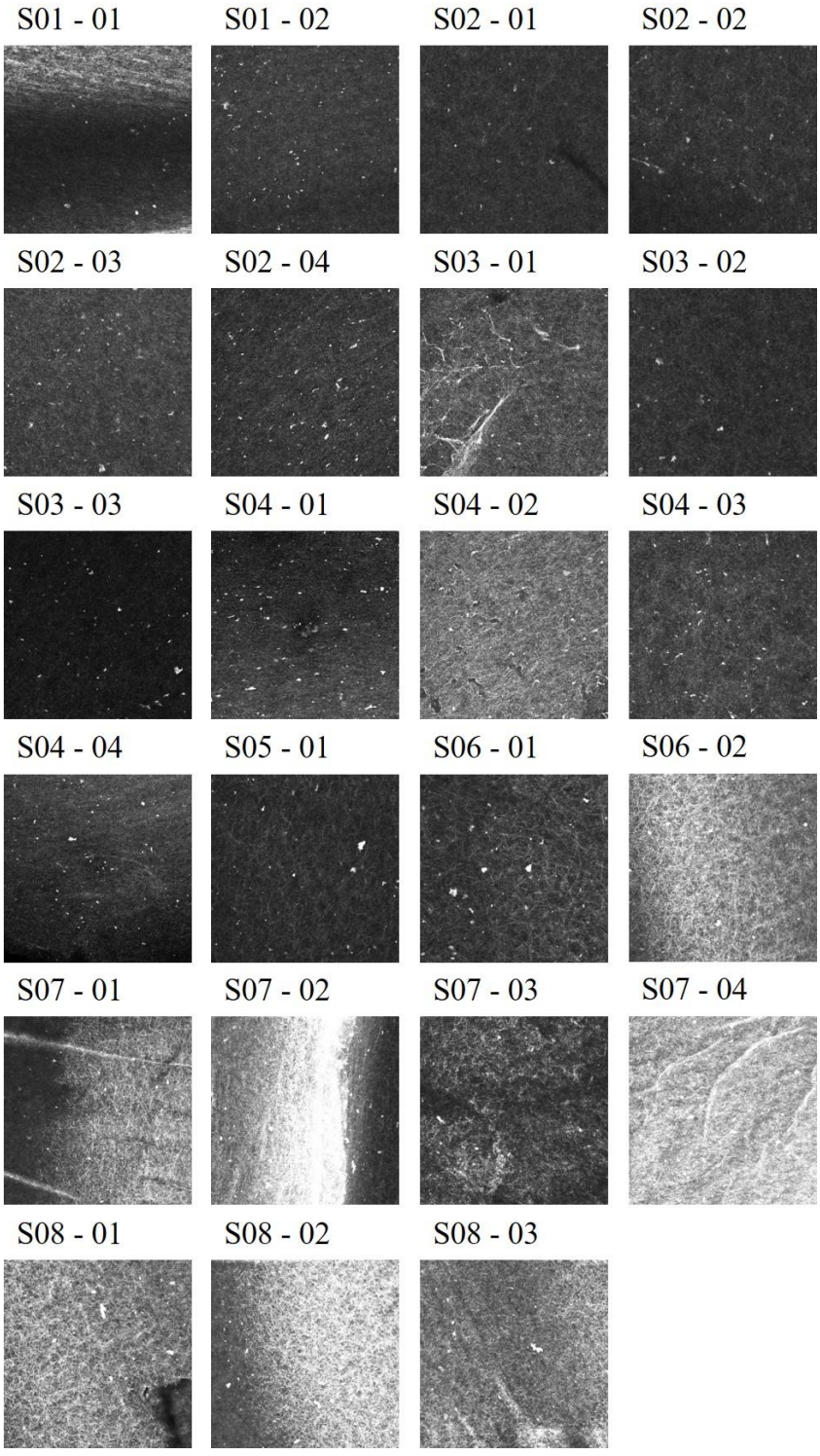

Table F.4. Densitometry analyses of DRG- and FLS- co-localized MMP-1 in co-culture gels after 20 minutes of collagenase exposure (Chapter 5)

Sample	Group	image no.	DRG-localized MMP-1 (% positive co-localized pixels)	FLS-localized MMP-1 (% positive co-localized pixels)
G01	collagenase	1	63.08%	60.77%
G01	collagenase	2	4.78%	4.16%
G01	collagenase	3	10.22%	11.05%
G01	collagenase	4	12.46%	20.00%
G01	collagenase	5	10.67%	15.67%
G01	collagenase	6	N/A	32.99%
G01	collagenase	7	N/A	48.46%
G01	collagenase	8	N/A	32.10%
G02	collagenase	1	10.93%	14.71%
G02	collagenase	2	11.79%	25.14%
G02	collagenase	3	27.38%	24.17%
G02	collagenase	4	18.23%	27.96%
G02	collagenase	5	18.97%	33.50%
G02	collagenase	6	N/A	15.69%
G02	collagenase	7	N/A	38.57%
G02	collagenase	8	N/A	54.01%
G03	collagenase	1	27.42%	44.33%
G03	collagenase	2	32.46%	47.24%
G03	collagenase	3	16.26%	24.75%
G03	collagenase	4	46.84%	71.03%
G03	collagenase	5	3.00%	7.31%
G03	collagenase	6	N/A	18.90%
G03	collagenase	7	N/A	15.68%
G03	collagenase	8	N/A	2.72%
G04	collagenase	1	70.32%	78.23%
G04	collagenase	2	35.20%	50.56%
G04	collagenase	3	6.34%	20.33%
G04	collagenase	4	6.07%	16.55%
G04	collagenase	5	82.75%	88.91%
G04	collagenase	6	N/A	25.73%
G04	collagenase	7	N/A	24.13%
G04	collagenase	8	N/A	26.43%
R01	vehicle	1	2.35%	14.64%
R01	vehicle	2	1.74%	3.12%
R01	vehicle	3	1.12%	1.03%
R01	vehicle	4	6.15%	3.62%
R01	vehicle	5	2.76%	3.13%
R01	vehicle	6	N/A	9.08%
R01	vehicle	7	N/A	21.70%
R01	vehicle	8	N/A	4.19%
R02	vehicle	1	2.47%	5.48%
R02	vehicle	2	0.00%	0.00%
R02	vehicle	3	0.05%	0.27%
R02	vehicle	4	0.15%	0.35%
R02	vehicle	5	N/A	3.64%

DRG: dorsal root ganglia; FLS: fibroblast-like synoviocyte
N/A indicates images taken in regions with FLS cells only and no evidence of βIII tubulin labeling

Figure F.4. Confocal images showing the βIII tubulin immunolabel as designated in Table F.4 (Chapter 5)

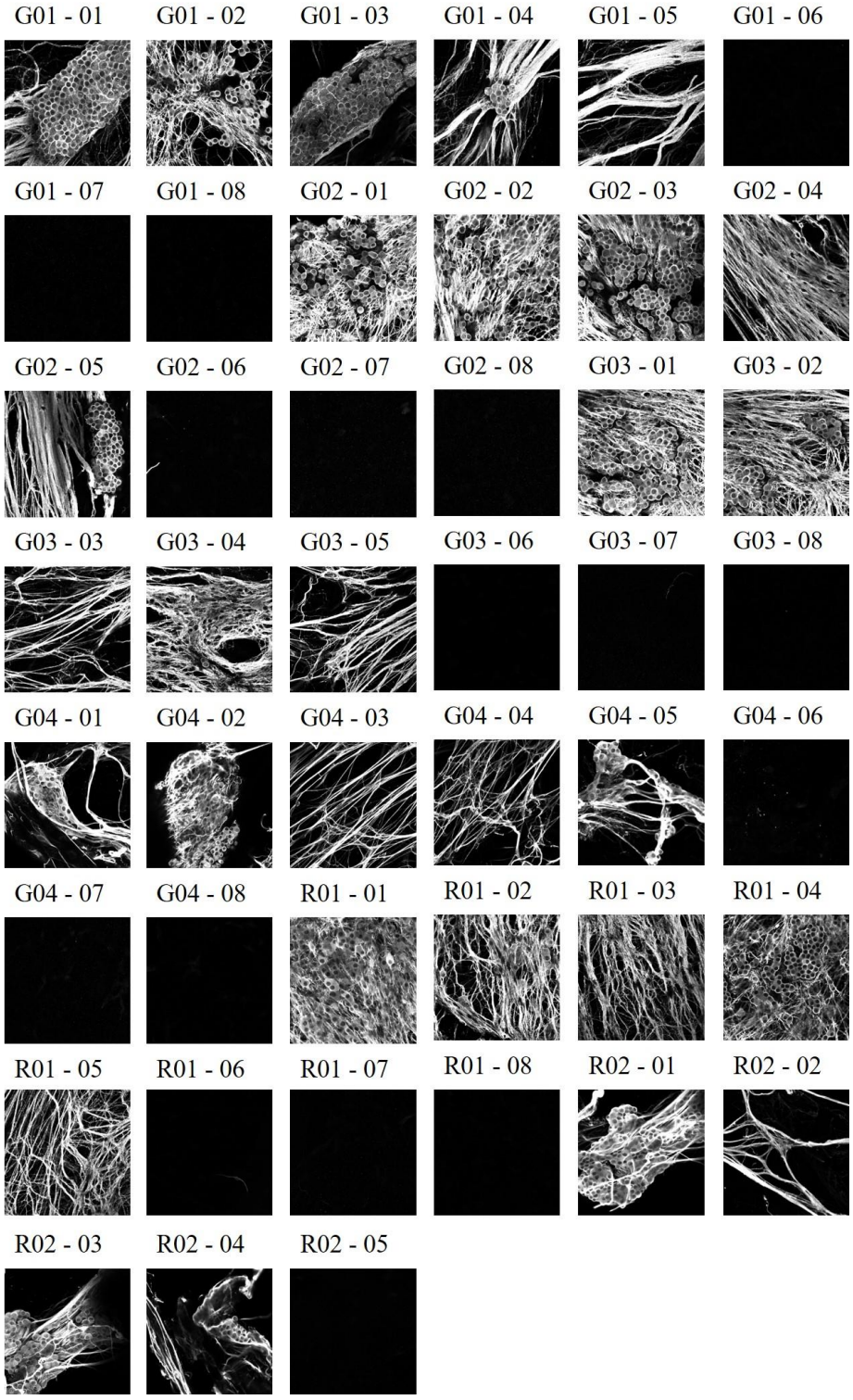

Figure F.5. Confocal images showing the vimentin immunolabel as designated in Table F.4 (Chapter 5)

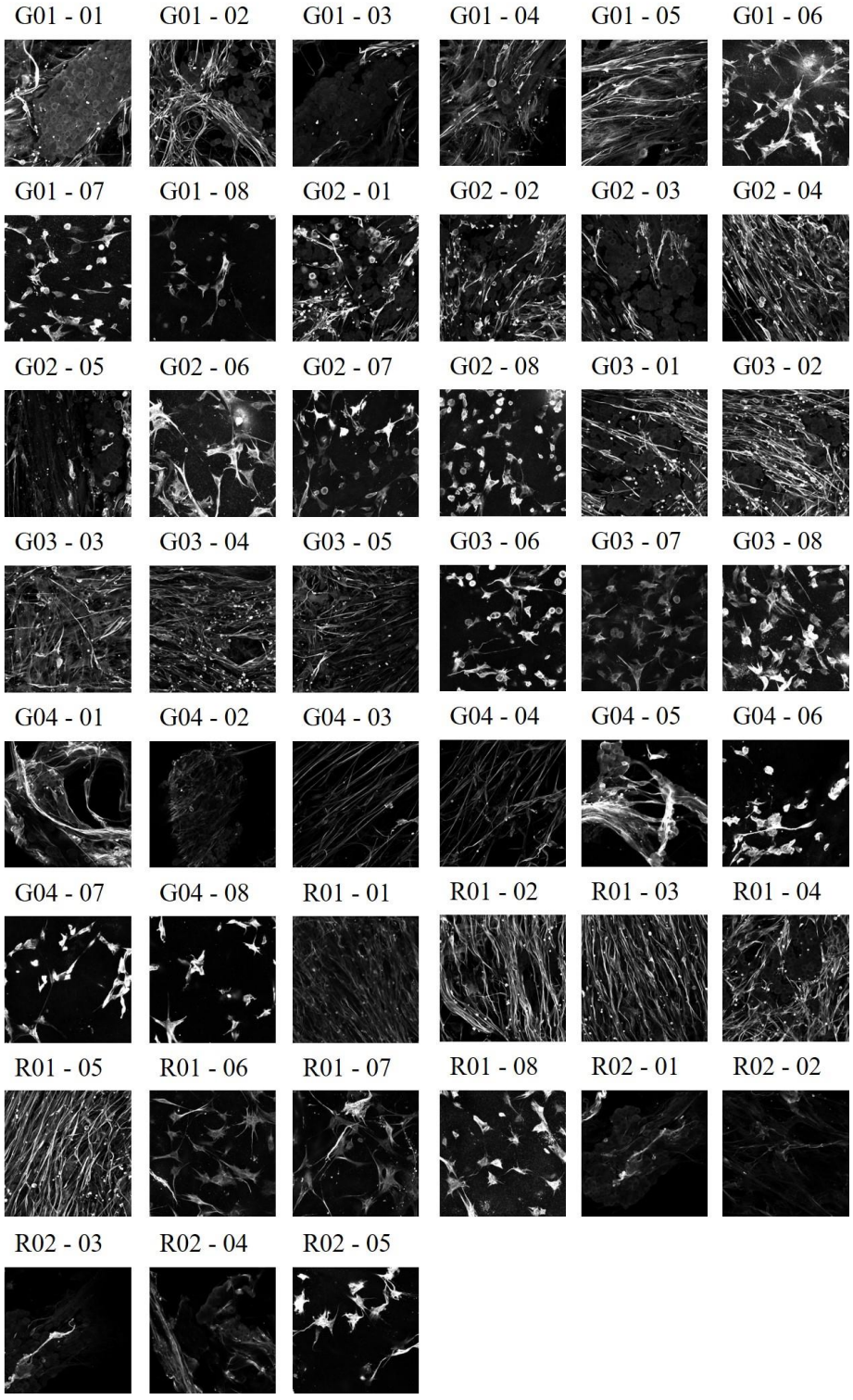

Figure F.6. Confocal images showing the MMP-1 immunolabel as designated in Table F.4 (Chapter 5)

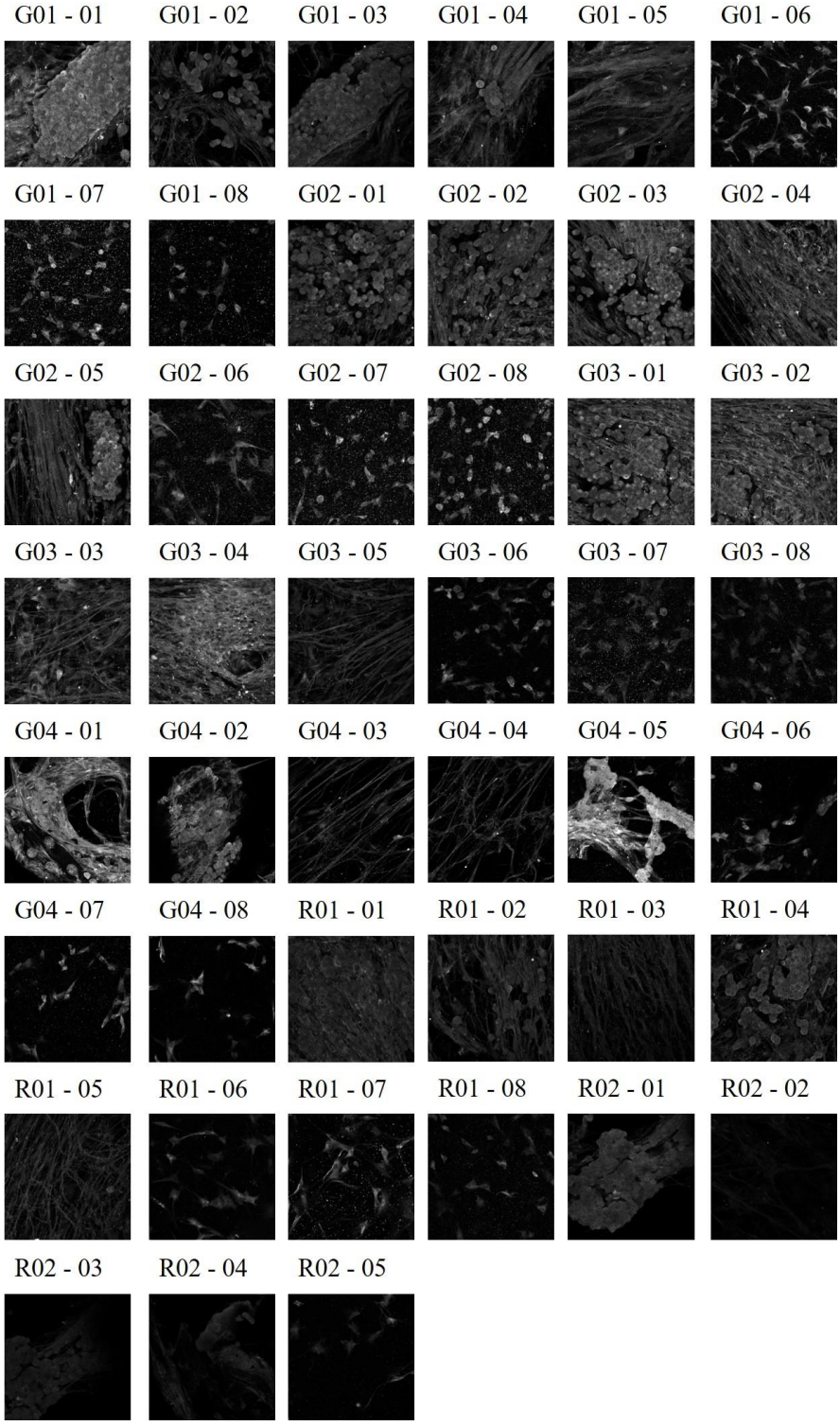

APPENDIX G

Mechanical & MMP-1 Immunolabeling Data for Comparative Studies of FLS vs. 3T3 Fibroblasts

This appendix summarizes the force, strain, polarized light imaging, and MMP-1 immunolabeling data acquired for the studies presented in Section 5.4 of Chapter 5 that defined the response of FLS cells to stretch. Parallel experiments were performed in parallel with fibroblasts from the NIH 3T3 immortalized cell line; 3T3 outcomes served as a comparison group for the FLS cells as a more extensively studied cell type (Mohammadi et al. 2015; Simon et al. 2012). In each of the tables and figures detailed in this appendix, data are identified by their sample ID number and the experimental group (FLS, 3T3; stretched, unstretched). Labels above and/or to the left of each image within the figures list the sample number followed by the group name and/or image number (e.g. "3T3 CTRL – 01" indicates image 1 from sample 3T3 CTRL).

Table G.1 and Figures G.1-G.3 contain the mechanical and microstructural data from uniaxial stretch-to-failure tests performed with FLS-collagen gels and 3T3-collagen gels. Two fibroblast concentrations of $5x10^4$ (low) and $1x10^5$ (high) cells/mL were also used to test the effect of cell concentration and to simulate the variable region-dependent concentrations in the capsular ligament (Yamashita et al. 1996). Figure G.1 summarizes the force-displacement curves acquired during failure loading. The maximum force

detected was taken as the failure point and is depicted as a pink circle. Stiffness was calculated using the force-displacement curves and defined as the slope of the curve from between 20% and 80% of the maximum force (Lee et al. 2006); in Figure G.1, 20% and 80% of the maximum force are designated by red data points and the dashed line indicates the linear fit between those two points that is used to calculate stiffness. The force, strain, and polarized light imaging data were compared at several displacement points during loading: 20% of the maximum force, 80% of the maximum force, and at the maximum force (failure). Quantification of all metrics at those displacement points are detailed in Table G.1.

Figure G.2 details the maximum principal strain (MPS) computed at the three displacement points (20%, 80%, and failure). MPS was computed by digitizing the locations of the fiducial markers on the gel for the unloaded image before any distraction and in the image immediately prior to the displacement points of interest. Grid position data were processed in LS-DYNA (Livermore Software Technology Corp.) to calculate the MPS for each element for each loaded gel (Figure G.2).

Figure G.3 depicts histograms that show the probability that collagen is oriented at a given angle for reference and at each displacement point. Histograms are computed from pixel-wise fiber alignment maps created using 20 consecutive high-speed images acquired both before distraction (reference) and immediately prior to the event of interest using polarized light imaging (Quinn et al. 2010; Quinn and Winkelstein 2008; Tower et al. 2002). The circular variance (CV) is computed from the spread of the collagen fiber angles that are depicted in the histograms; a larger spread of angles corresponds to a larger CV

value (Miller et al. 2012; Zhang et al. 2016). Table G.1 summarizes the raw CV values at reference that correspond to the data in Figure G.3 as well as the normalized CV over the reference value at 20%, 80%, and 100% of the maximum force.

Table G.2, Figure G.4, and Figure G.5 contain MMP-1 immunolabeling data acquired immediately after the stretch-to-failure for DRG-fibroblast co-culture gels fabricated with a low concentration of either FLS cells or 3T3 cells following a uniaxial stretch-to-failure. MMP-1 labeling was rated by five blinded graders as either absent (0) or present (1) (Villasmil et al. 2017), with the determination of MMP-1 taken as the majority rating. The majority rating for each image is detailed as the "score" in Table G.2. Figures G.4 and G.5 summarize confocal images of the MMP-1 immunolabeling in DRG-localized and fibroblast-localizes regions, respectively.

Table G.1. Summary of force, maximum principal strain (MPS), and microstructure (CV) at several displacement points during uniaxial stretch-to-failure experiments with FLS- or 3T3-collagen gels at a low or high concentration (Chapter 5)

		reference	20% of failure force			80% of failure force		
Sample	**Group**	**CV (x102)**	**force (mN)**	**MPS (%)**	**CV / ref**	**force (mN)**	**MPS (%)**	**CV / ref**
S02	low FLS	0.054	6.686	0.087	2.331	26.817	0.199	10.531
S05	low FLS	0.111	4.107	0.048	1.606	16.479	0.125	2.283
S08	low FLS	0.037	2.415	0.060	1.339	9.656	0.130	4.346
S17	low FLS	0.441	5.116	0.067	1.683	20.384	0.146	3.353
S19	low FLS	0.026	7.136	0.058	3.229	28.481	0.143	9.421
S49	low FLS	0.076	7.603	0.076	2.522	30.362	0.246	18.605
S15	low 3T3	0.096	6.122	0.066	1.313	24.486	0.125	1.961
S16	low 3T3	0.073	1.340	0.038	0.931	5.302	0.081	0.993
S21	low 3T3	0.103	1.987	0.042	0.943	7.968	0.086	1.295
S25	low 3T3	0.064	4.689	0.081	2.759	18.659	0.141	4.160
S55	low 3T3	0.019	3.178	0.095	2.141	12.689	0.149	6.377
S38	high FLS	N/A	0.540	0.056	N/A	2.166	0.430	N/A
S39	high FLS	0.128	0.225	0.110	1.340	0.896	0.402	2.476
S41	high FLS	21.593	1.432	0.105	0.628	5.693	0.353	0.171
S48	high FLS	2.493	2.913	0.076	2.158	11.709	0.445	3.361
S50	high FLS	26.470	4.172	0.040	0.967	16.637	0.320	0.229
S36	high 3T3	0.088	2.795	0.090	1.118	11.160	0.130	1.698
S37	high 3T3	0.156	13.515	0.073	1.542	54.045	0.166	31.630
S40	high 3T3	0.104	2.715	0.053	1.162	10.941	0.104	1.499
S42	high 3T3	1.024	12.163	0.071	N/A	48.635	0.162	0.369
S51	high 3T3	7.418	2.604	0.048	0.236	10.394	0.102	0.177
S52	high 3T3	0.069	11.997	0.120	3.772	47.966	0.249	4.952

		failure			
Sample	**Group**	**force (mN)**	**MPS (%)**	**CV / ref**	**stiffness (mN/mm)**
S02	low FLS	33.490	0.275	10.152	8.66
S05	low FLS	20.575	0.203	4.534	4.82
S08	low FLS	12.060	0.131	7.366	2.69
S17	low FLS	25.500	0.173	3.314	7.88
S19	low FLS	35.607	0.187	18.375	10.45
S49	low FLS	37.960	0.358	15.749	5.96
S15	low 3T3	30.605	0.172	1.544	8.94
S16	low 3T3	6.613	0.096	1.149	1.38
S21	low 3T3	9.964	0.103	1.783	3.51
S25	low 3T3	23.278	0.185	7.238	6.24
S55	low 3T3	15.844	0.177	10.138	5.05
S38	high FLS	2.708	0.469	N/A	0.16
S39	high FLS	1.121	0.369	5.654	0.40
S41	high FLS	7.125	0.390	0.151	0.87
S48	high FLS	14.638	0.605	2.779	3.06
S50	high FLS	20.796	0.371	0.115	4.30
S36	high 3T3	13.958	0.146	5.701	3.64
S37	high 3T3	67.515	0.217	N/A	15.04
S40	high 3T3	13.647	0.115	1.489	3.65
S42	high 3T3	60.787	0.191	0.722	11.80
S51	high 3T3	13.016	0.130	N/A	4.12

FLS: fibroblast-like synoviocyte; MPS: maximum principal strain; CV: circular variance
CV / ref is normalized to the reference CV
N/A data were not collected due to technical problems with data capture

Figure G.1. Force-displacement data during tensile loading to failure as designated in Table G.1 (Chapter 5). Red data points show 20 and 80% of maximum force; the pink data point shows the maximum force; the dotted line is a linear fit between 20 and 80% and calculates stiffness.

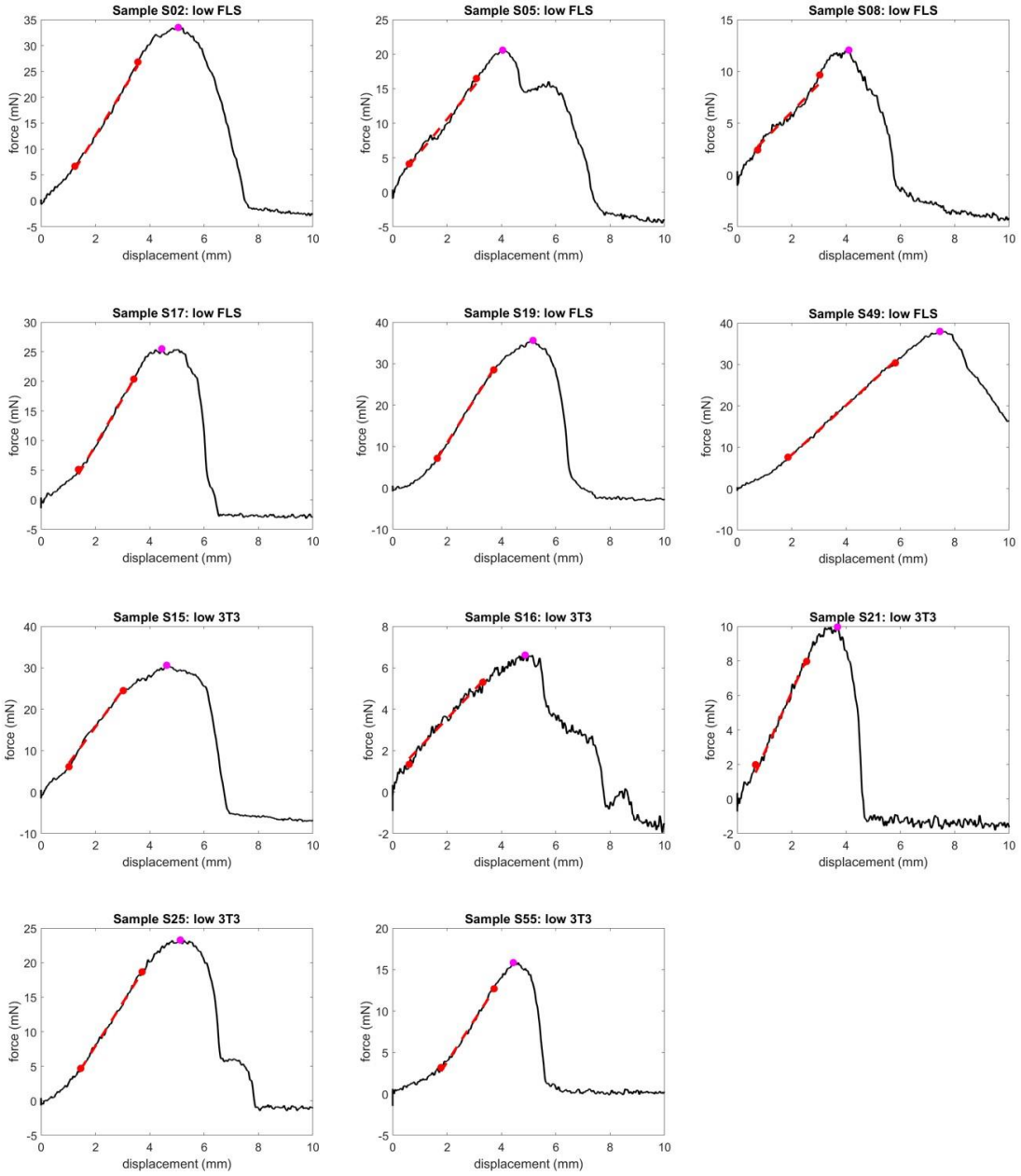

Note: Figure is continued on the next page.

Figure G.1. continued

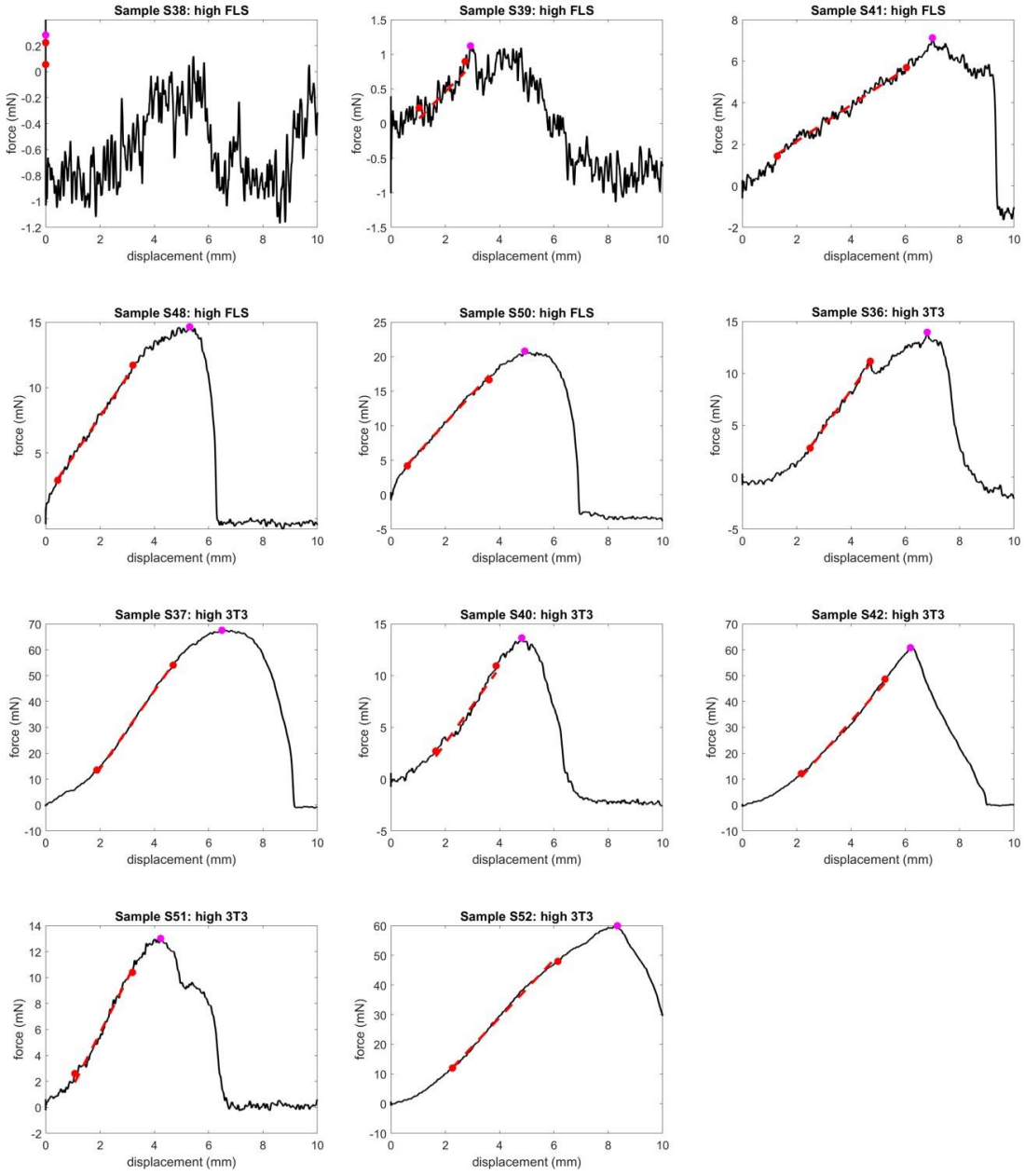

Figure G.2. Maximum principal strains sustained on the gel surface at 20% of maximum force, 80% of maximum force, and at the point of failure as designated in Table G.1 (Chapter 5)**.** Elements are numbered sequentially from the bottom left to top right, as shown in sample S02 for 80%.

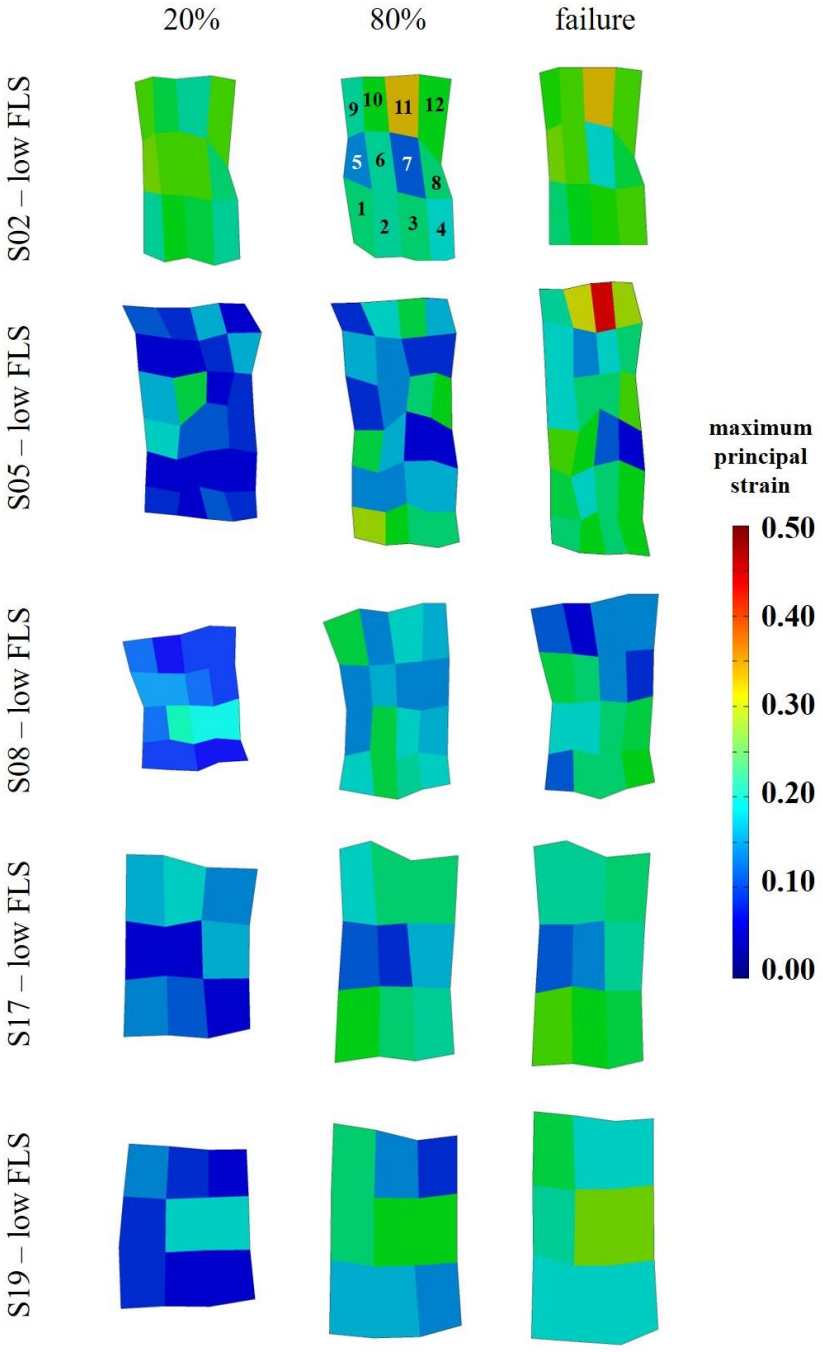

Note: Figure is continued on the next page.

Figure G.2. continued

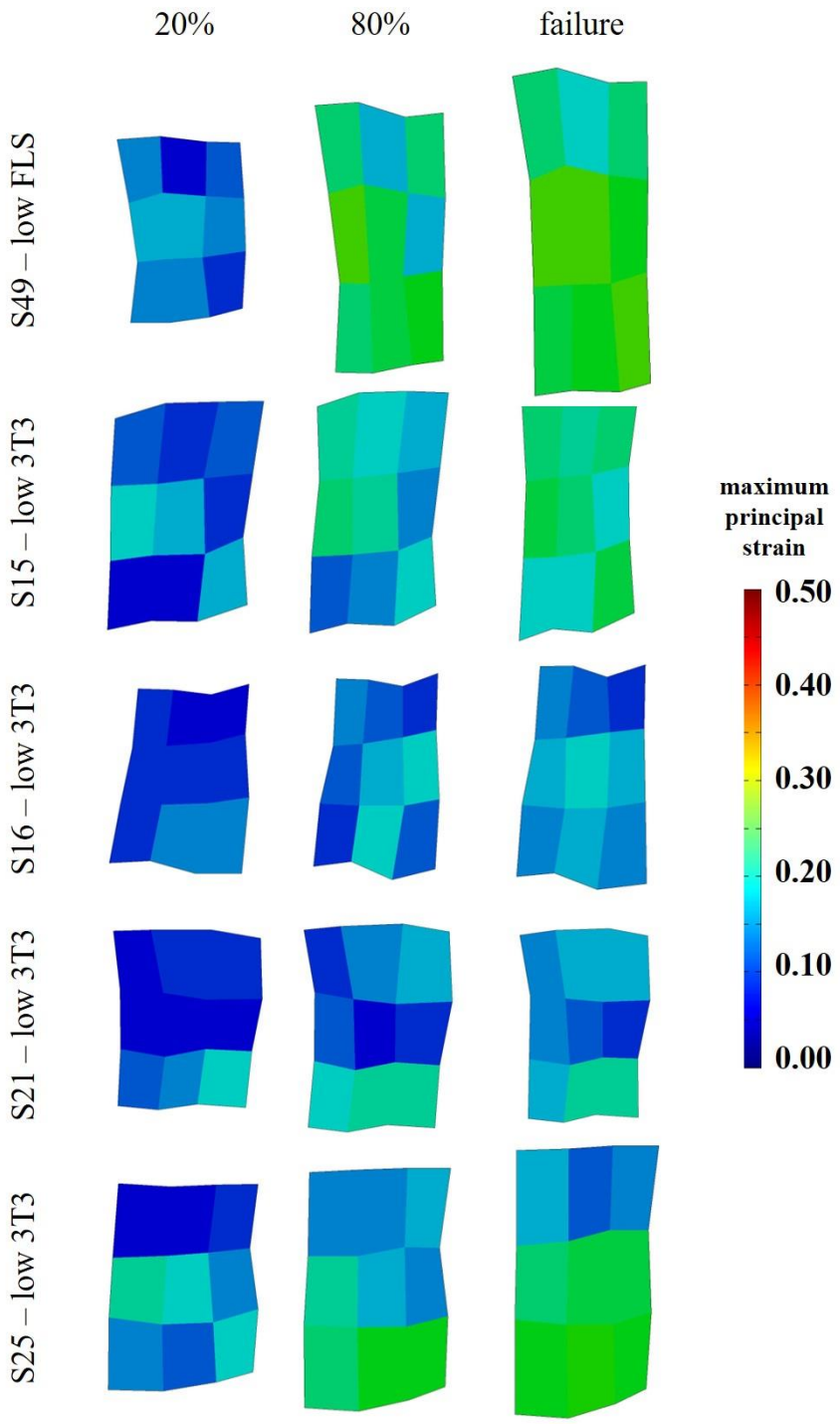

Note: Figure is continued on the next page.

Figure G.2. continued

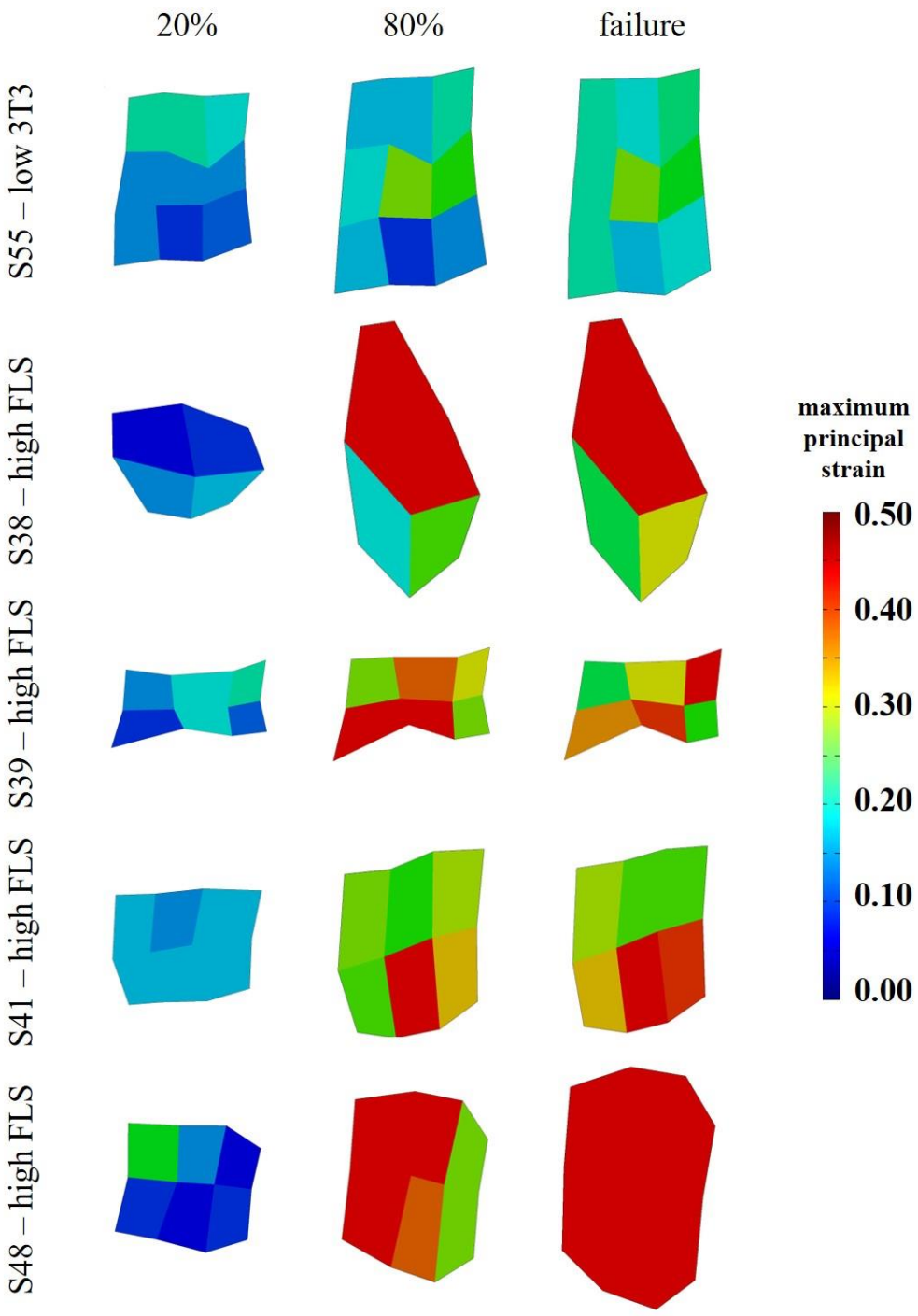

Note: Figure is continued on the next page.

Figure G.2. continued

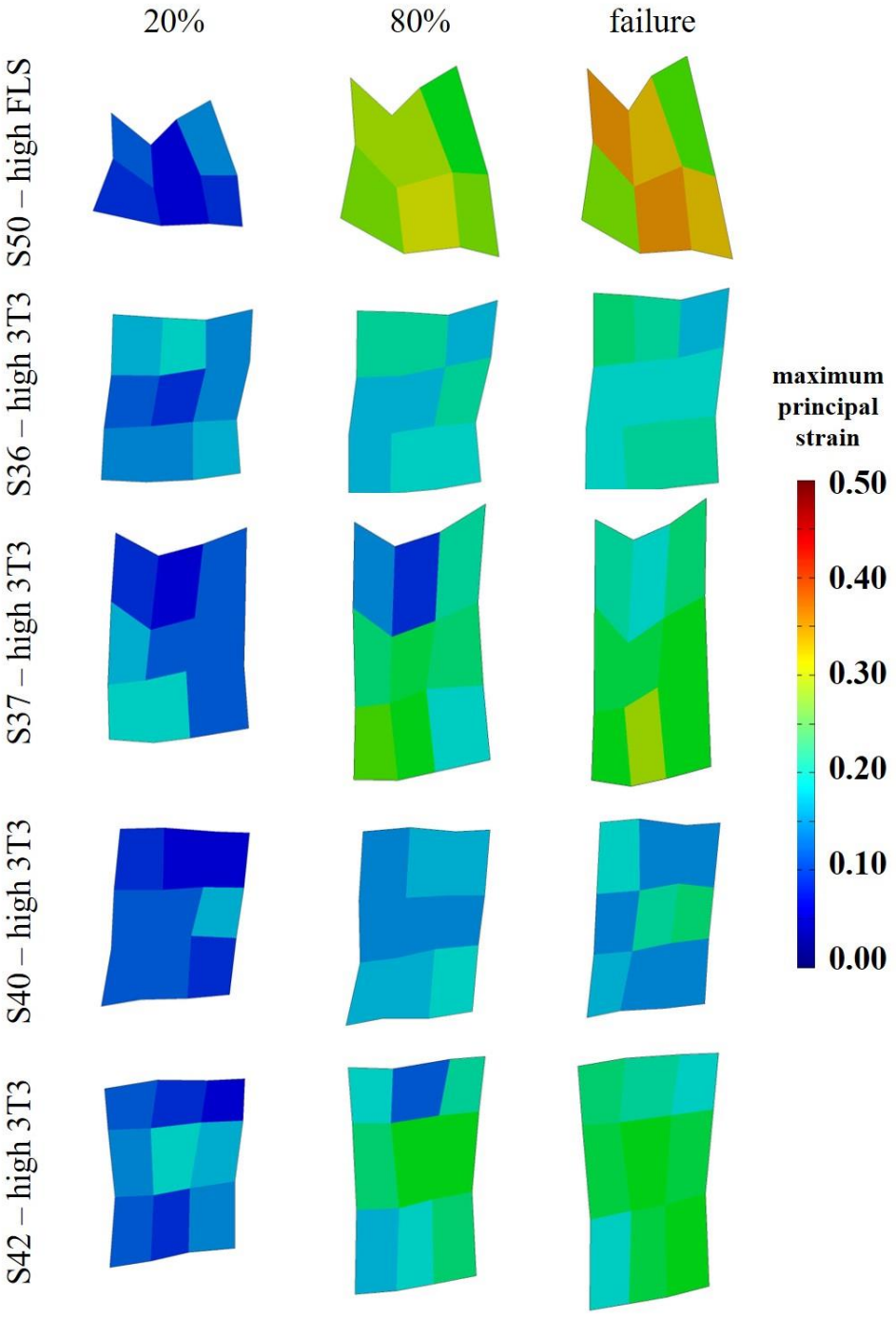

Note: Figure is continued on the next page.

Figure G.2. continued

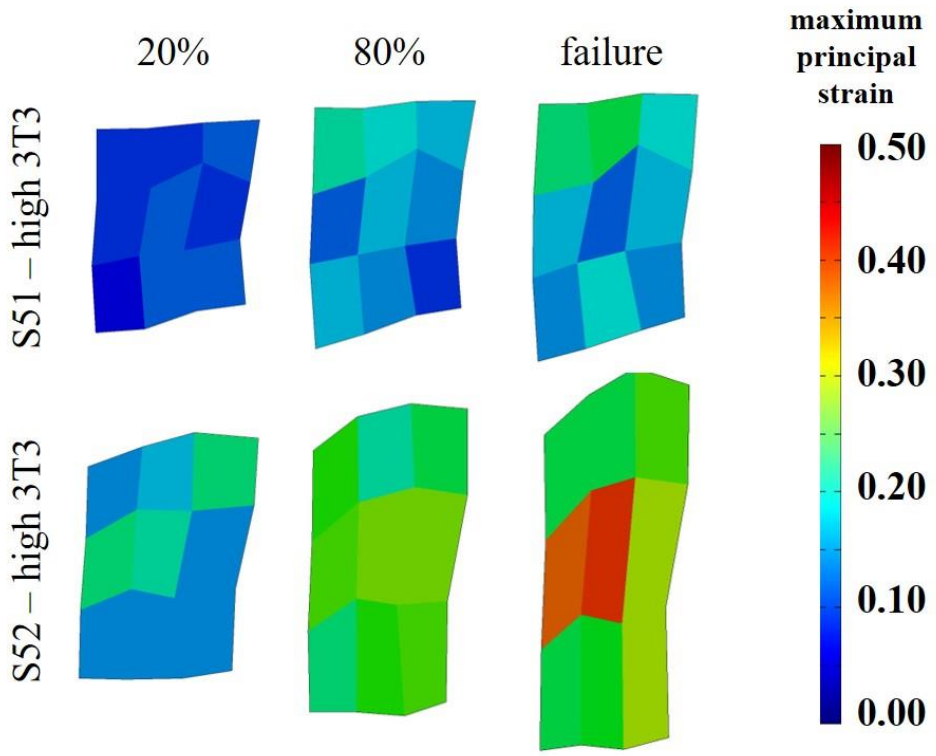

Figure G.3. Histograms of collagen fiber orientation angle at reference, 20% of maximum force, 80% of maximum force, and at the point of failure as designated in Table G.1 (Chapter 5)

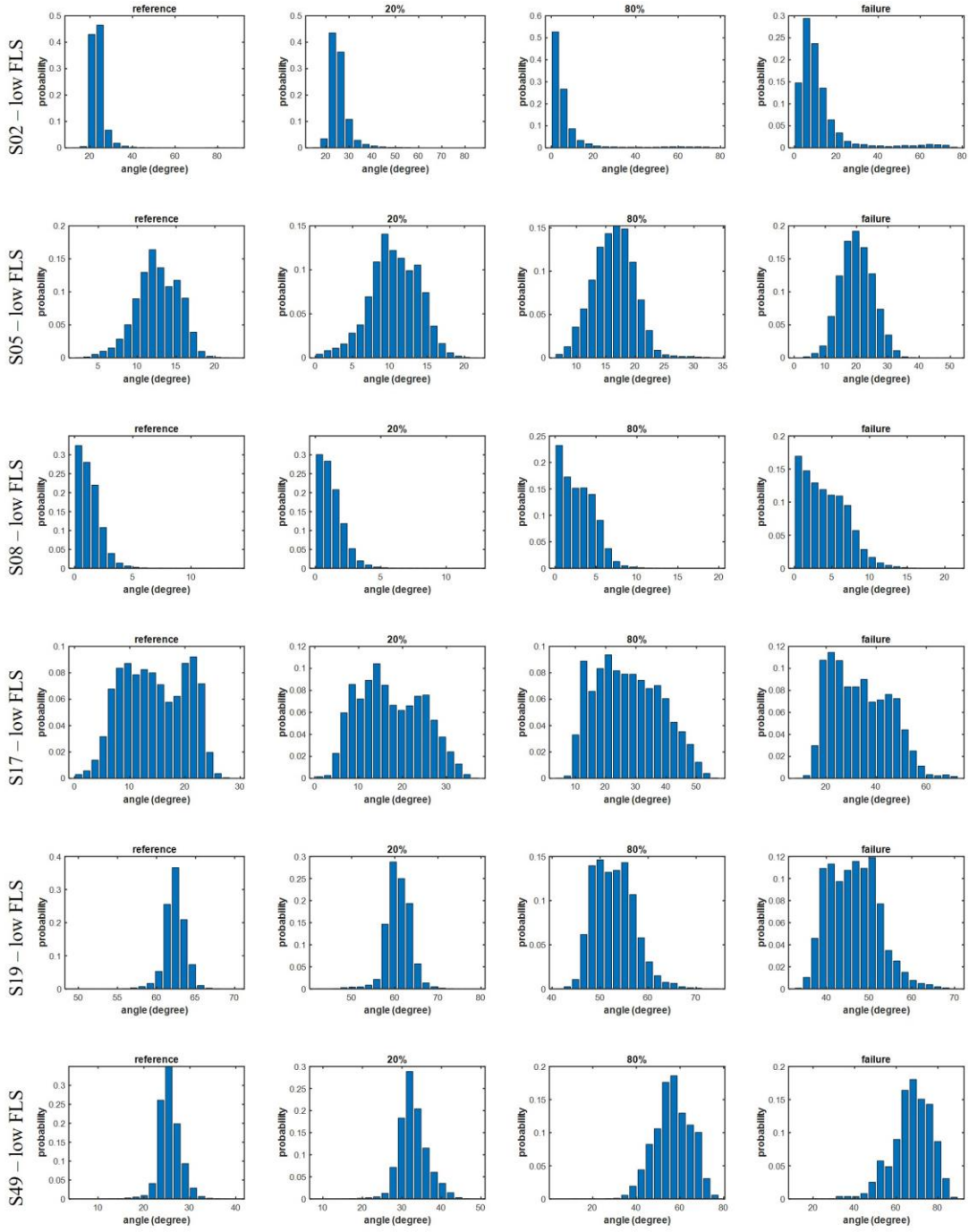

Note: Figure is continued on the next page.

Figure G.3. continued

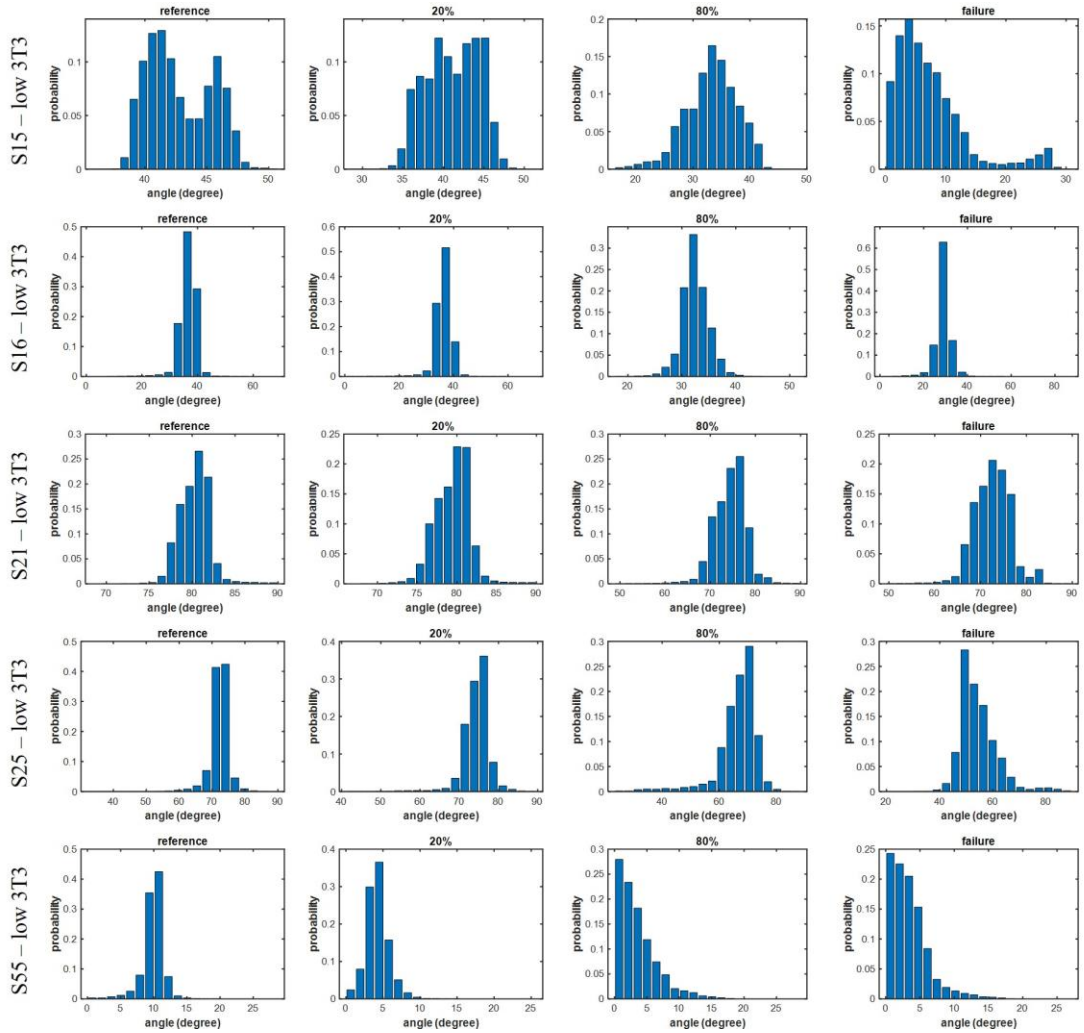

Note: Figure is continued on the next page.

Figure G.3. continued

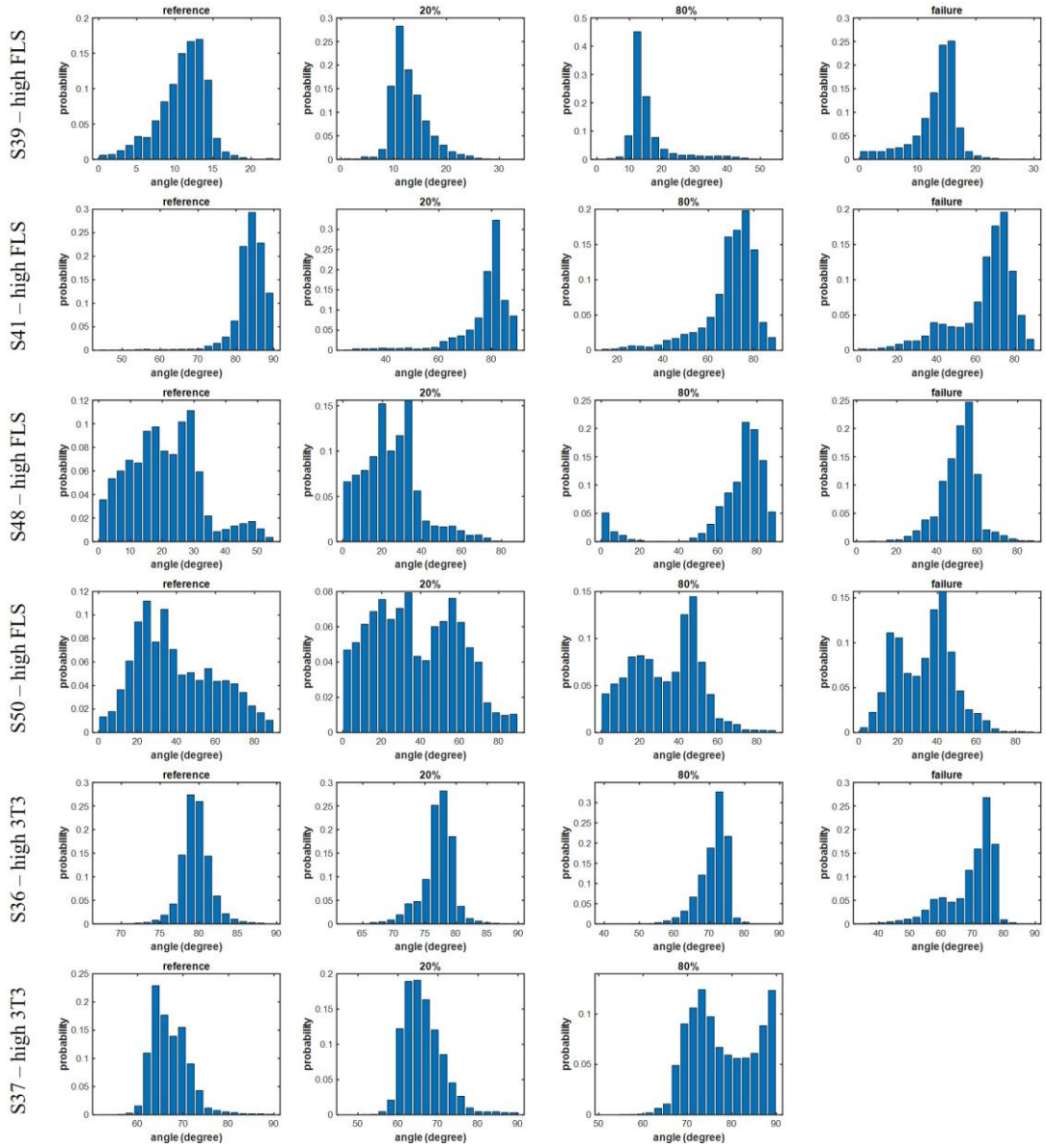

Note: Figure is continued on the next page.

Figure G.3. continued

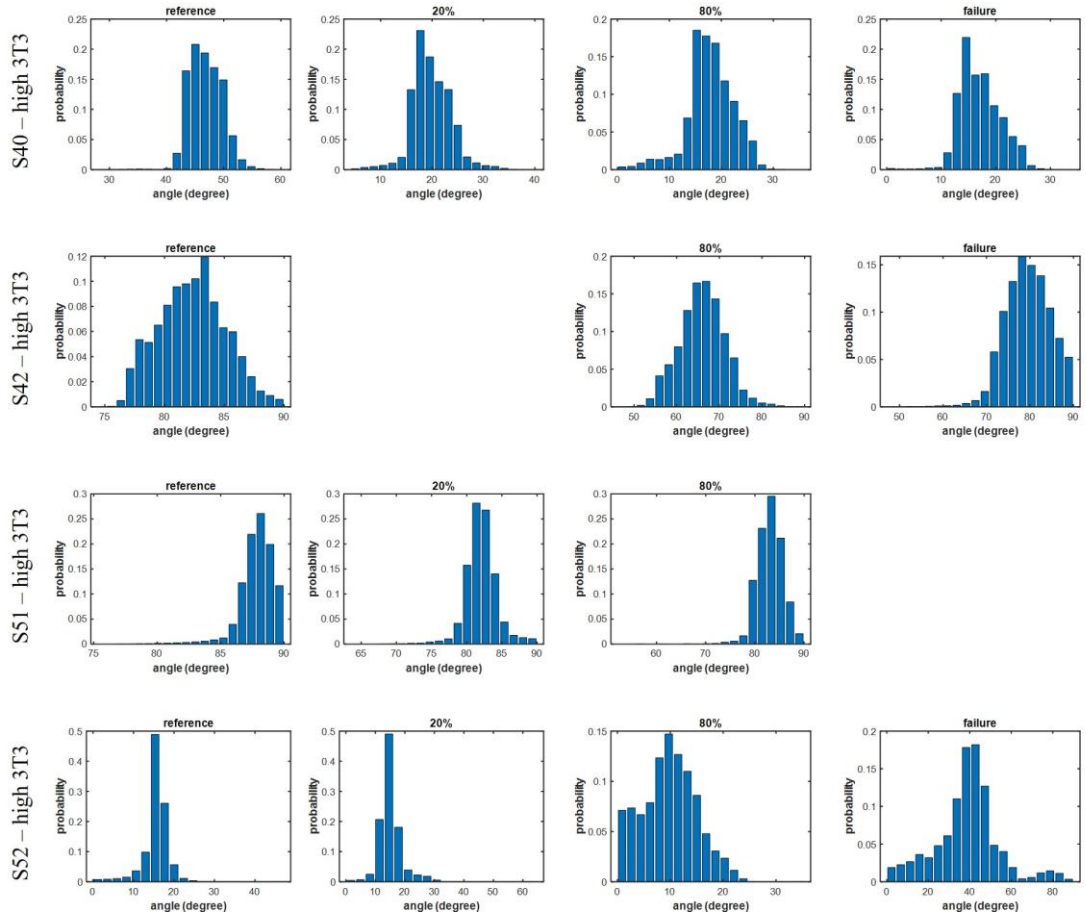

Table G.2. Scoring of MMP-1 immunolabeling in DRG- and fibroblast-localized regions in stretched and unstretched co-cultures with DRGs and a low concentration of FLS or 3T3 cells (Chapter 5)

DRG images (Figure G.4)				Fibroblast images (Figure G.5)			
Sample	Group	image no.	score	Sample	Group	image no.	score
3T3 CTRL	3T3 unstretched	1	1	3T3 CTRL	3T3 unstretched	1	1
FLS CTRL	FLS unstretched	1	2	3T3 CTRL	3T3 unstretched	2	2
FLS CTRL	FLS unstretched	2	0	3T3 CTRL	3T3 unstretched	3	2
FLS CTRL	FLS unstretched	3	0	3T3 CTRL	3T3 unstretched	4	0
FLS CTRL	FLS unstretched	4	0	3T3 CTRL	3T3 unstretched	5	1
FLS CTRL	FLS unstretched	5	0	3T3 CTRL	3T3 unstretched	6	2
S04	3T3 stretched	1	1	3T3 CTRL	3T3 unstretched	7	2
S04	3T3 stretched	2	0	3T3 CTRL	3T3 unstretched	8	0
S04	3T3 stretched	3	1	FLS CTRL	FLS unstretched	1	2
S04	3T3 stretched	4	1	FLS CTRL	FLS unstretched	2	2
S04	3T3 stretched	5	0	FLS CTRL	FLS unstretched	3	0
S04	3T3 stretched	6	0	FLS CTRL	FLS unstretched	4	0
S05	3T3 stretched	1	1	FLS CTRL	FLS unstretched	5	1
S05	3T3 stretched	2	1	FLS CTRL	FLS unstretched	6	2
S05	3T3 stretched	3	0	FLS CTRL	FLS unstretched	7	2
S05	3T3 stretched	4	0	S04	3T3 stretched	1	1
S07	FLS stretched	1	2	S04	3T3 stretched	2	0
S07	FLS stretched	2	1	S05	3T3 stretched	1	0
S07	FLS stretched	3	1	S05	3T3 stretched	2	0
S07	FLS stretched	4	1	S05	3T3 stretched	3	0
S08	FLS stretched	1	0	S07	FLS stretched	1	1
S08	FLS stretched	2	0	S07	FLS stretched	2	2
S08	FLS stretched	3	0	S07	FLS stretched	3	1
S08	FLS stretched	4	0	S08	FLS stretched	1	2
S08	FLS stretched	5	0	S08	FLS stretched	2	2
S12	3T3 stretched	1	0	S08	FLS stretched	3	0
S12	3T3 stretched	2	0	S12	3T3 stretched	1	1
S12	3T3 stretched	3	0	S12	3T3 stretched	2	0
S12	3T3 stretched	4	0	S12	3T3 stretched	3	0
S34	FLS stretched	1	2	S13	FLS stretched	1	1
S34	FLS stretched	2	1	S13	FLS stretched	2	1
S34	FLS stretched	3	1	S13	FLS stretched	3	2
S34	FLS stretched	4	0	S34	FLS stretched	1	1
S35	FLS unstretched	1	2	S34	FLS stretched	2	1
S35	FLS unstretched	2	1	S34	FLS stretched	3	1
S35	FLS unstretched	3	1	S35	FLS unstretched	1	2
S35	FLS unstretched	4	1	S35	FLS unstretched	2	2

DRG: dorsal root ganglia; FLS: fibroblast-like synoviocyte

Figure G.4. Immunolabeling of MMP-1 in DRG-localized regions of stretched and unstretched co-cultures as designated in Table G.2 (Chapter 5)

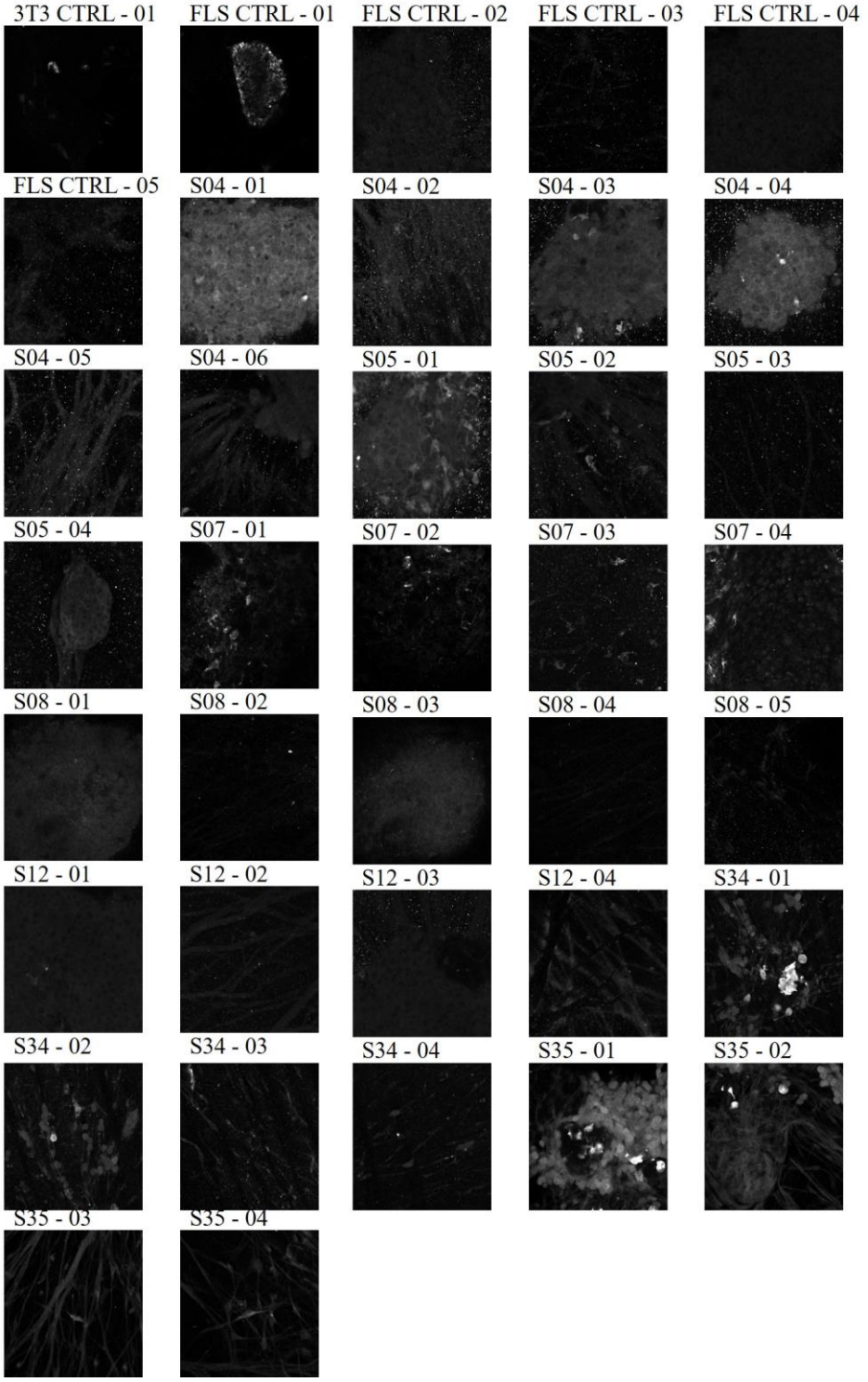

Figure G.5. Immunolabeling of MMP-1 in fibroblast-localized regions of stretched and unstretched co-cultures as designated in Table G.2 (Chapter 5)

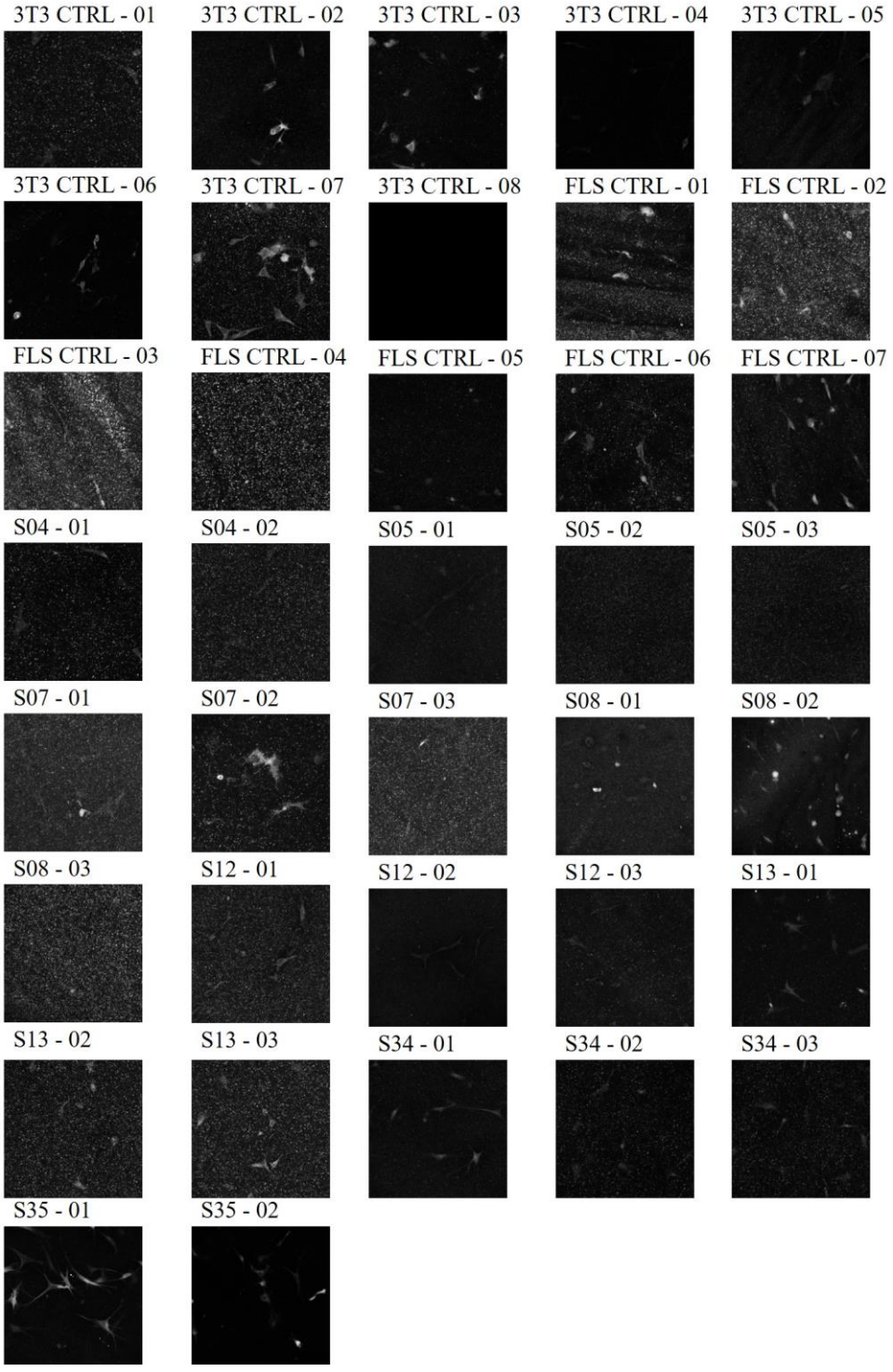

APPENDIX H

Multiscale Collagen Gel Mechanics in Response to Gel Distraction to Failure

This appendix summarizes the mechanical, strain, and collagen fiber alignment data acquired during tensile failure tests of co-culture collagen gels from the studies presented in Chapter 6. In the figures detailed in this appendix, data are identified by their sample ID number and the experimental group. Experimental groups include collagen gels seeded with only DRGs (none), DRGs and a low concentration of FLS ($5x10^4$ cells/mL; low FLS), or DRGs and a high concentration of FLS ($1x10^5$ cells/mL; high FLS). Gels were tested on either day-in-vitro (DIV) 7 or DIV9. Labels above each image within the figures list the DIV of testing, sample number, and experimental group (e.g. “DIV7: Sample S03: none” indicates sample 3 tested on DIV7 from a collagen gel with DRGs only).

Figure H.1 summarizes the force-displacement curves acquired during failure loading. The maximum force detected was taken as the failure point and is depicted as a pink circle for the curves in Figure H.1. Stiffness was calculated using the force-displacement curves and defined as the slope of the curve from between 20% and 80% of the maximum force (Lee et al. 2006); in Figure H.1, 20% and 80% of the maximum force are designated by red data points and the dashed line indicates the linear fit between those two points that is used to calculate stiffness.

Figure H.2 summarizes the maximum principal strain (MPS) computed at the point of failure. MPS was computed by digitizing the locations of the fiducial markers on the gel for the unloaded image before any distraction and in the image immediately prior to failure. Grid position data were processed in LS-DYNA (Livermore Software Technology Corp.) to calculate the MPS for each element for each loaded gel (Figure H.2).

Figure H.3 depicts histograms that show the probability that collagen is oriented at a given angle for reference and at failure, separately for each loaded gel. Histograms are computed from pixel-wise fiber alignment maps created using 20 consecutive high-speed images acquired both before distraction (reference) and immediately prior to failure using polarized light imaging (Quinn et al. 2010; Quinn and Winkelstein 2008; Tower et al. 2002). The circular variance (CV) is computed from the spread of the collagen fiber angles that are depicted in the histograms; a larger spread of angles corresponds to a larger CV value (Miller et al. 2012; Zhang et al. 2016).

Table 6.1 in Chapter 6 details the quantification of force, displacement, and normalized CV at failure, as well as the stiffness calculated for each stretched gel. Protein expression data were also acquired from the gel samples summarized in this appendix; the location of each image taken to acquire protein expression data was registered with the regional elements from each gel to relate physiological outcomes with the strain and collagen organization data. As such, the quantification of that *elemental* MPS and CV data are summarized with their corresponding protein expression data, by gel and element, in the following Appendix I.

Figure H.1. Force-displacement data during tensile loading to failure as designated in Table 6.1 (Chapter 6). Red data points show 20 and 80% of maximum force; the pink data point shows the maximum force; the dotted line is a linear fit between 20 and 80% and calculates stiffness.

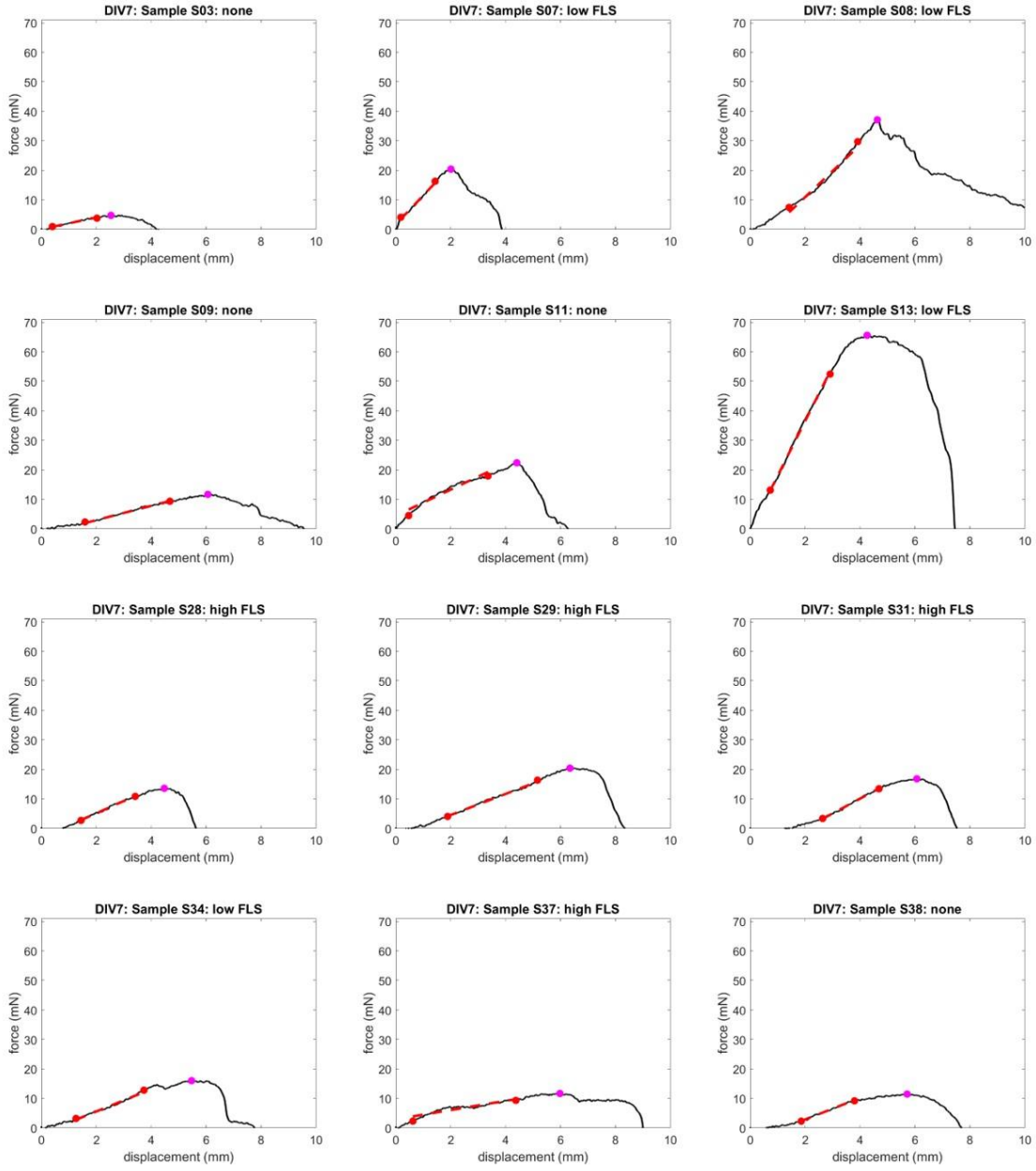

Note: Figure is continued on the next page.

Figure H.1. continued

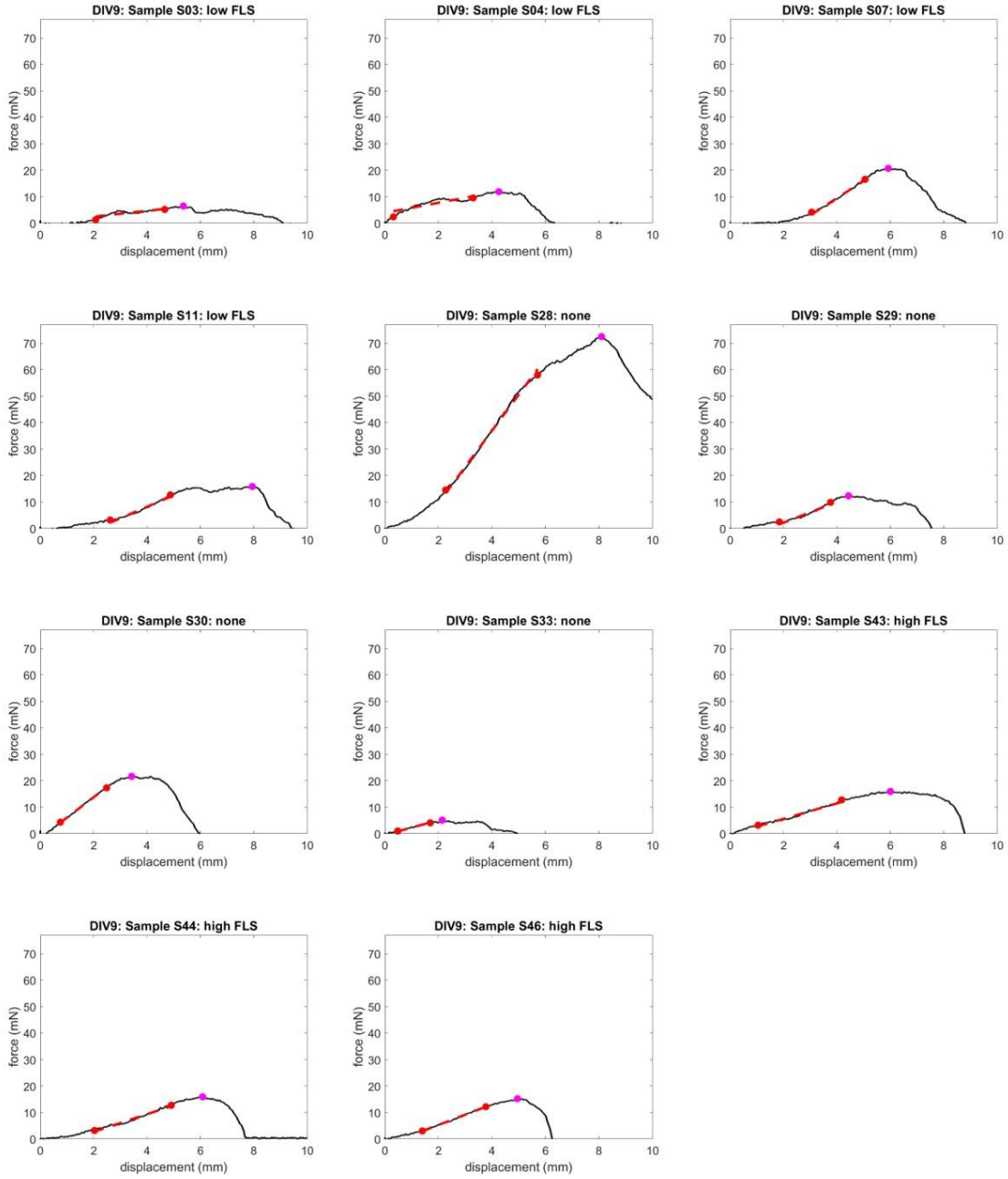

Figure H.2. Maximum principal strains sustained on the gel surface at the point of failure as designated in Table 6.1 and Figure H.1 (Chapter 6)

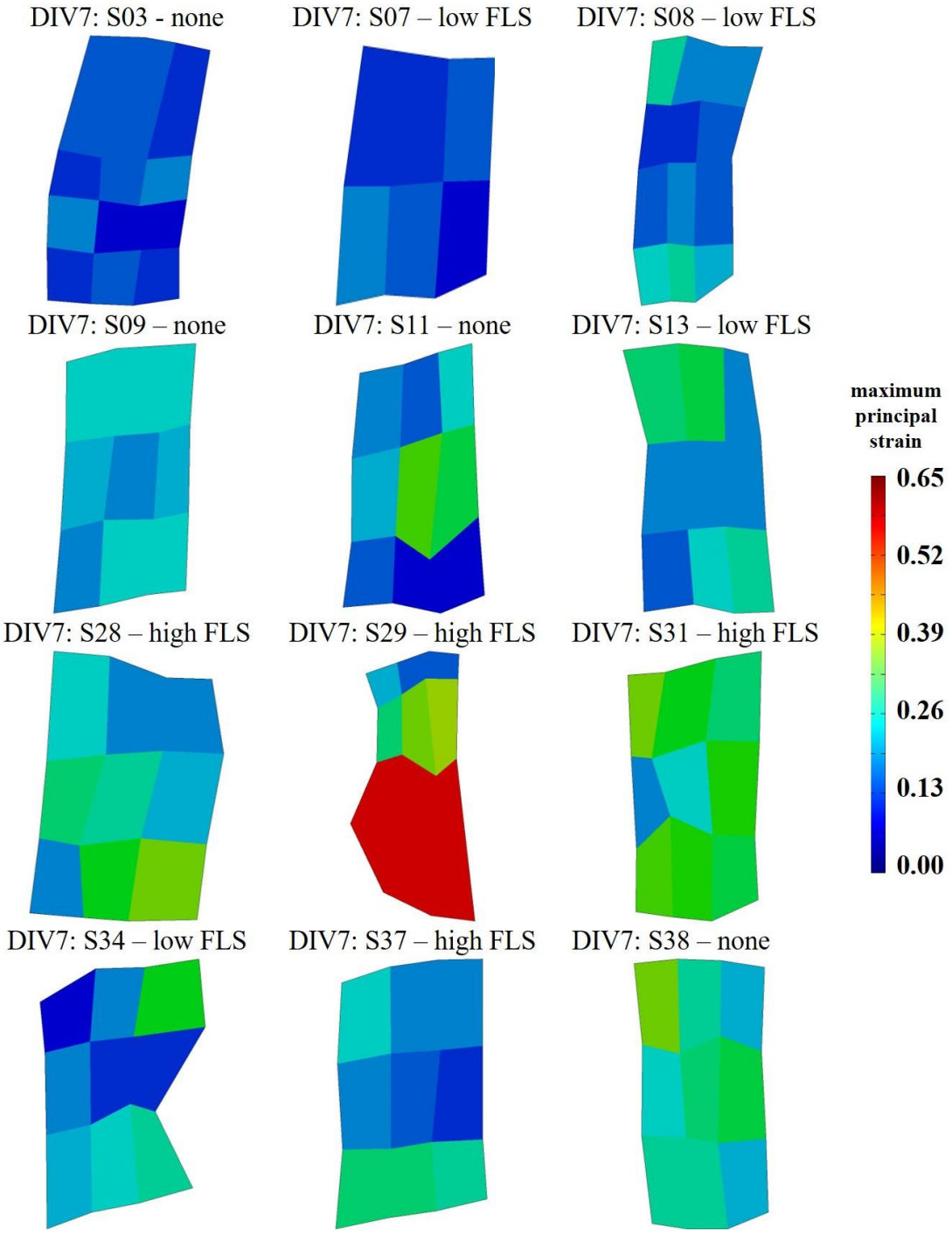

Note: Figure is continued on the next page.

Figure H.2. continued

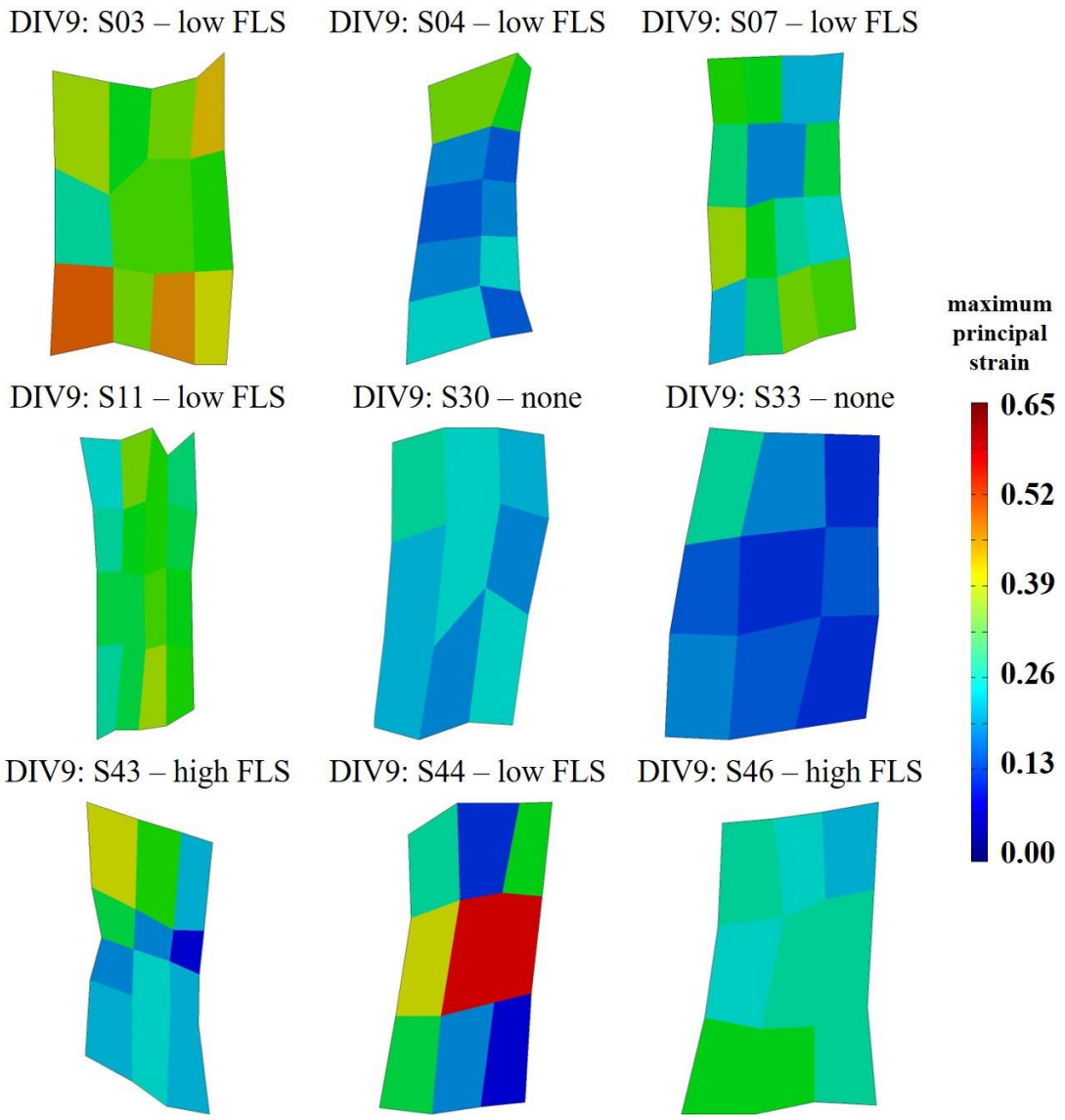

Figure H.3. Histograms of collagen fiber orientation angle at reference and at failure as designated in Table 6.1 and Figure H.1 (Chapter 6)

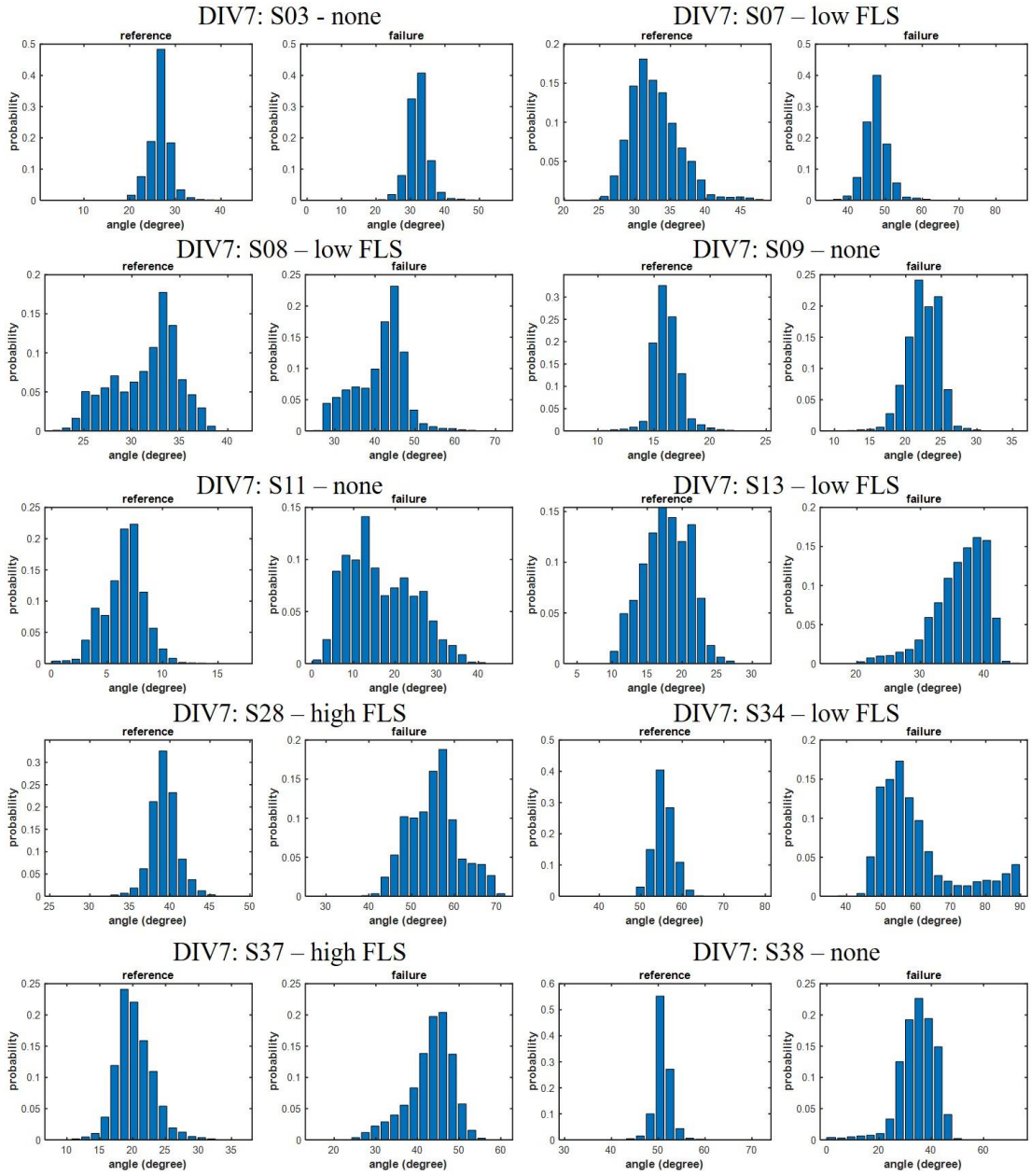

Note: Figure is continued on the next page.

Figure H.3. continued

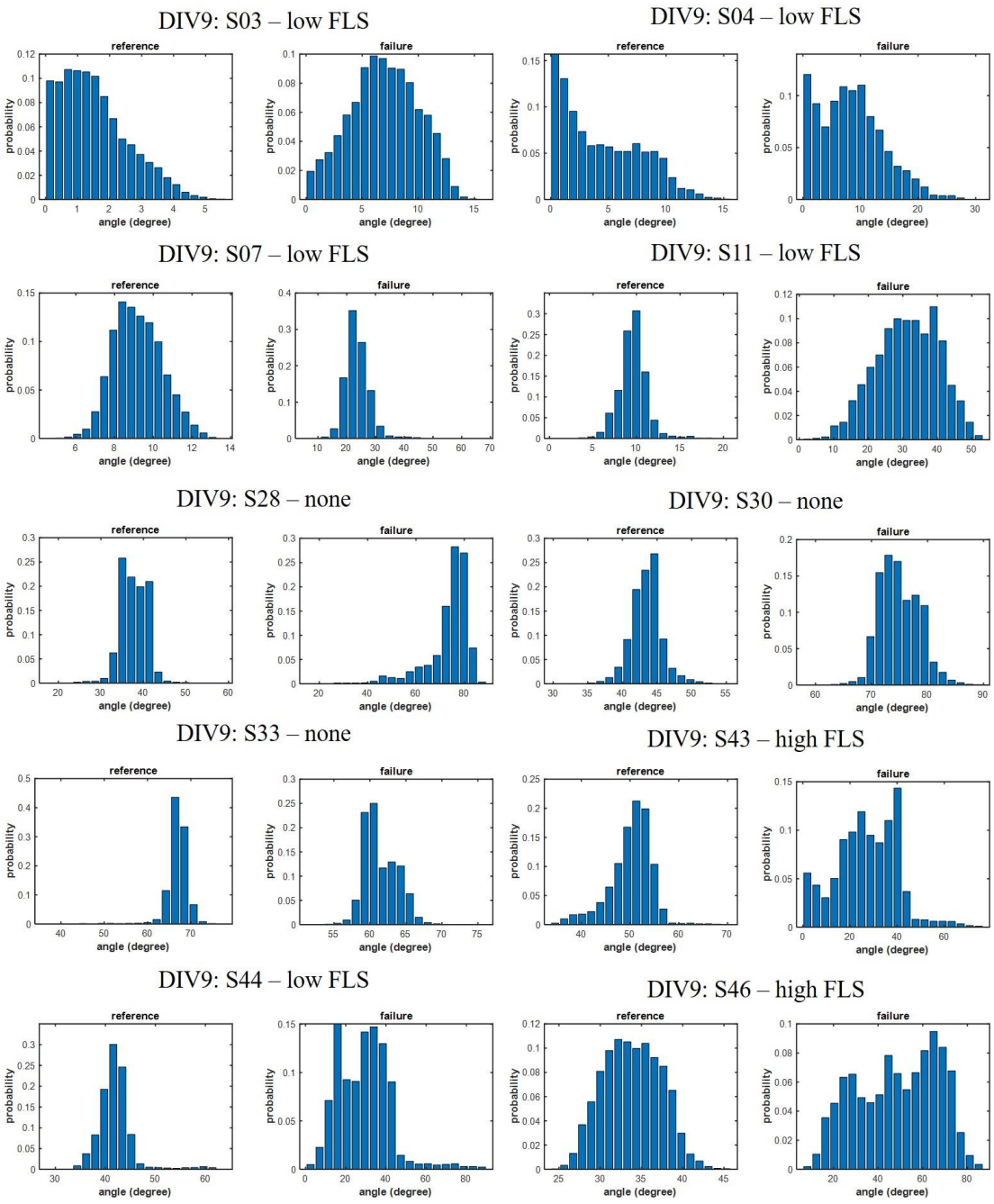

APPENDIX I

Immunolabeling of MMPs & Substance P in DRGs & DRG-FLS Co-Cultures & Cytotoxicity after Biomechanical or Biochemical Stimuli

This appendix summarizes the immunolabeling and cytotoxicity assays performed in the in vitro studies that are detailed in Chapter 6. In each of the tables and figures detailed in this appendix, data are identified by their sample ID number and the experimental group. Labels above each image within the figures list the sample number followed by the image number (e.g. "S03 – 01" indicates image 1 from sample 3); the image number in the labels matches the image numbers listed in the corresponding data table.

Table I.1 and Table I.2 summarize the immunolabeling assays performed to quantify total MMP-1 and neuronal substance P expression, respectively, in co-culture collagen gels immediately after uniaxial failure loading (Section 6.3). Experimental groups in those studies include collagen gels seeded with only DRGs (none), DRGs and a low concentration of FLS ($5x10^4$ cells/mL; low FLS), or DRGs and a high concentration of FLS ($1x10^5$ cells/mL; high FLS). Figure I.1 details the confocal images of the MMP-1 label and Figure I.2 details the confocal images of the substance P label. A custom MATLAB script for densitometry (found in Appendix B) was used to quantify the number of positive pixels above a threshold for positive labeling for MMP-1 and substance P, separately.

Confocal images were taken in regions with DRG soma or axons. The location of each image was also registered with the regional elements from each gel to relate cellular outcomes with the strain and collagen organization data. As such, the elemental maximum principal strain (MPS) and circular variance (CV) at failure are detailed in Tables I.1 and I.2 with the corresponding protein expression data. Appendix H contains the full-field MPS maps and the spread of the collagen fiber orientation angles that correspond to the data in Tables I.1 and I.2.

Table I.3 summarizes the MMP-1 and MMP-9 immunolabels performed on a subset of co-culture collagen gels with DRGs and a low FLS concentration immediately after uniaxial failure loading (Section 6.4.1). Studies compared protein expression between co-culture collagen gels stretched to failure with an unloaded control gel (unstretched). Confocal images were taken in regions with DRG soma, DRG axons, or FLS cells, and the cell type and/or cellular region for which images were acquired is detailed in Table I.3. MMP-1 and MMP-9 were quantified using densitometry (Appendix B). Figure I.3 summarizes the corresponding confocal images for MMP-1, and Figure I.4 has those images for MMP-9.

Studies that are detailed in Section 6.4.3 test the effect of exogenous MMP-1 exposure on MMP-9 expression and cytotoxicity in DRG monolayer cultures. Table I.4 details the MMP-9 protein expression data acquired after a 24-hour exogenous MMP-1 exposure and Table I.5 details the results from the cytotoxicity assay performed after that same 24-hour exogenous MMP-1 exposure. MMP-9 immunolabeling was quantified using densitometry (Appendix B) and the corresponding confocal images summarized in Figure

I.5. Cytotoxicity was assessed by quantifying the percent cell death using a lactate dehydrogenase (LDH) assay. MMP-9 protein expression and percent cell death were also quantified in DRG monolayer cultures that were not exposed to any treatment (naïve).

Table I.1. MMP-1 densitometry in stretched collagen gels with DRGs and no, low, or high FLS concentration with elemental MPS and CV at failure (Chapter 6)

Sample	DIV	Group	image no.	total MMP-1 (% positive)	MPS (%)	CV at failure
S03	DIV7	none	1	18.30%	7.60%	1.03
S03	DIV7	none	2	2.90%	6.60%	1.71
S07	DIV7	low	1	14.90%	6.10%	0.24
S07	DIV7	low	2	73.00%	8.50%	1.90
S08	DIV7	low	1	57.30%	22.50%	1.74
S08	DIV7	low	2	25.50%	15.60%	1.52
S08	DIV7	low	3	19.60%	7.50%	3.50
S09	DIV7	none	1	26.40%	18.50%	3.59
S11	DIV7	none	1	40.00%	0.00%	2.94
S11	DIV7	none	2	56.90%	0.00%	4.92
S11	DIV7	none	3	31.10%	27.60%	7.05
S13	DIV7	low	1	20.80%	18.00%	3.82
S13	DIV7	low	2	52.20%	7.50%	1.85
S28	DIV7	high	1	5.00%	41.70%	7.68
S28	DIV7	high	2	16.90%	30.00%	9.85
S28	DIV7	high	3	55.90%	14.40%	34.91
S29	DIV7	high	1	21.20%	N/A	N/A
S29	DIV7	high	2	0.40%	N/A	N/A
S29	DIV7	high	3	44.40%	N/A	N/A
S29	DIV7	high	4	2.80%	N/A	N/A
S29	DIV7	high	5	4.10%	N/A	N/A
S31	DIV7	high	1	57.20%	25.90%	N/A
S31	DIV7	high	2	69.60%	34.40%	N/A
S31	DIV7	high	3	3.60%	38.10%	N/A
S31	DIV7	high	4	10.60%	9.70%	N/A
S34	DIV7	low	1	24.50%	3.70%	5.92
S34	DIV7	low	2	12.50%	5.90%	7.69
S34	DIV7	low	3	7.00%	29.90%	3.38
S37	DIV7	high	1	14.90%	17.30%	0.94
S37	DIV7	high	2	14.80%	11.00%	4.18
S37	DIV7	high	3	5.00%	14.50%	1.95
S37	DIV7	high	4	3.90%	11.70%	2.43
S38	DIV7	none	1	34.00%	16.60%	12.18
S38	DIV7	none	2	25.40%	13.00%	1.89
S03	DIV9	low	1	21.90%	48.50%	3.82
S03	DIV9	low	2	97.40%	49.20%	8.43
S03	DIV9	low	3	8.80%	43.10%	25.46
S03	DIV9	low	4	43.30%	45.70%	17.25
S04	DIV9	low	1	16.20%	11.30%	1.91
S07	DIV9	low	1	24.30%	17.40%	3.16
S07	DIV9	low	2	69.10%	24.90%	7.03
S07	DIV9	low	3	9.50%	14.30%	12.06
S07	DIV9	low	4	66.10%	40.30%	8.99
S07	DIV9	low	5	4.20%	38.30%	5.87
S11	DIV9	low	1	9.40%	21.90%	45.80
S11	DIV9	low	2	71.00%	20.20%	51.39
S11	DIV9	low	3	67.30%	39.90%	11.81
S28	DIV9	none	1	0.10%	N/A	21.22
S28	DIV9	none	2	0.90%	N/A	6.69
S29	DIV9	none	1	4.00%	N/A	N/A
S29	DIV9	none	2	0.90%	N/A	N/A
S29	DIV9	none	3	4.50%	N/A	N/A
S29	DIV9	none	4	5.10%	N/A	N/A
S29	DIV9	none	5	11.20%	N/A	N/A
S30	DIV9	none	1	1.20%	15.20%	2.45
S30	DIV9	none	2	0.30%	16.30%	1.40
S30	DIV9	none	3	2.80%	17.90%	2.85
S33	DIV9	none	1	0.20%	4.20%	1.91
S33	DIV9	none	2	3.70%	7.30%	5.39
S33	DIV9	none	3	4.50%	12.10%	1.61
S43	DIV9	high	1	5.40%	35.10%	4.08
S43	DIV9	high	2	11.90%	13.20%	28.53
S44	DIV9	high	1	36.10%	26.60%	10.94
S44	DIV9	high	2	46.40%	17.50%	19.54
S44	DIV9	high	3	2.30%	22.50%	58.89
S44	DIV9	high	4	68.90%	23.30%	83.77
S46	DIV9	high	1	8.80%	15.90%	37.84
S46	DIV9	high	2	1.40%	21.80%	18.84
S46	DIV9	high	3	1.70%	17.20%	15.62

DRG: dorsal root ganglia; FLS: fibroblast-like synoviocyte
DIV: day-in-vitro; MPS: maximum principal strain; CV: circular variance
N/A data were not collected due to technical problems with data capture

Note: Table is continued on the next page.

Figure I.1. Immunolabeling of MMP-1 in DRGs as designated in Table I.1 (Chapter 6). Gels tested on day-in-vitro 7 are detailed before the red-dashed line; gels tests on day-in-vitro 9 are detailed after the line.

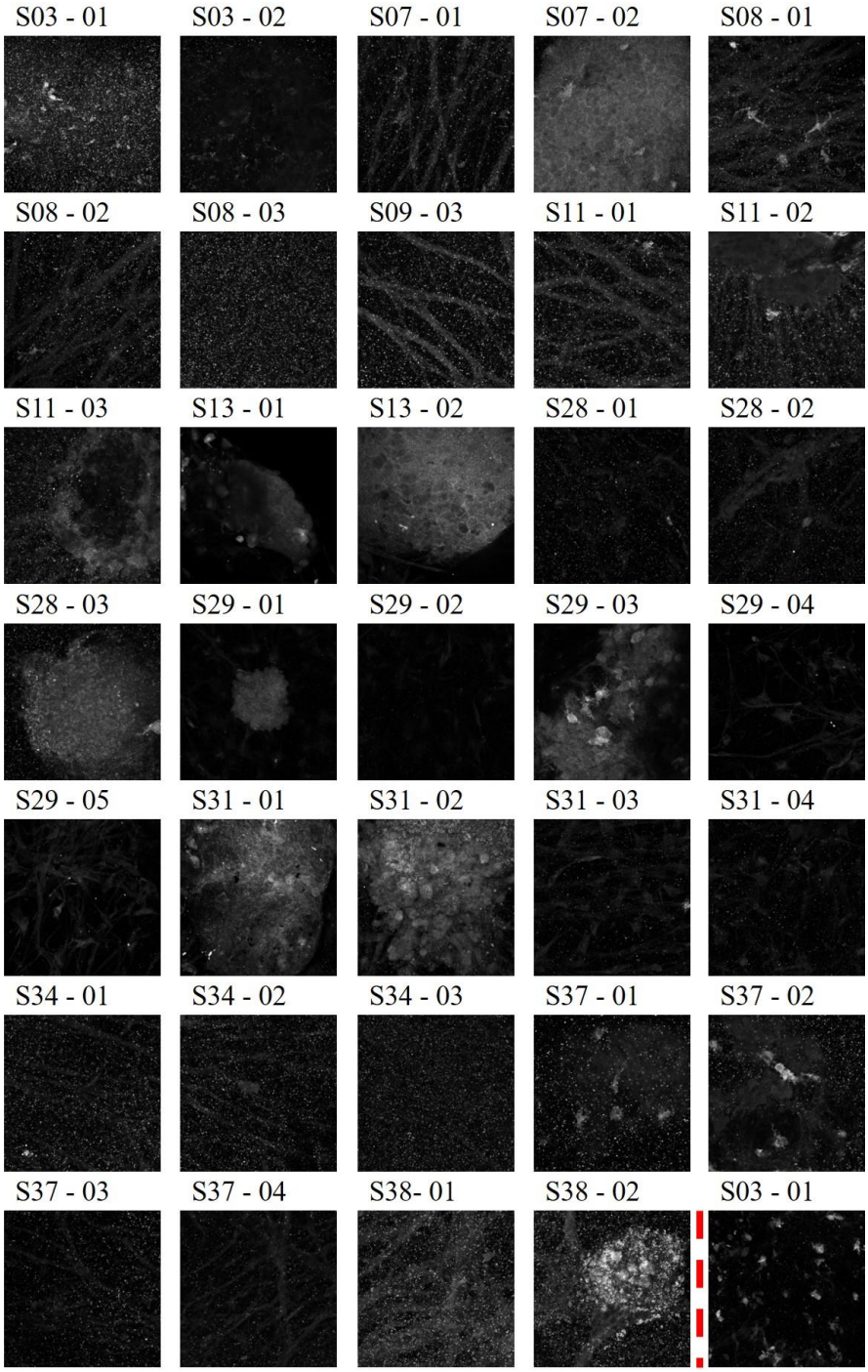

Note: Figure is continued on the next page.

Figure I.1. continued

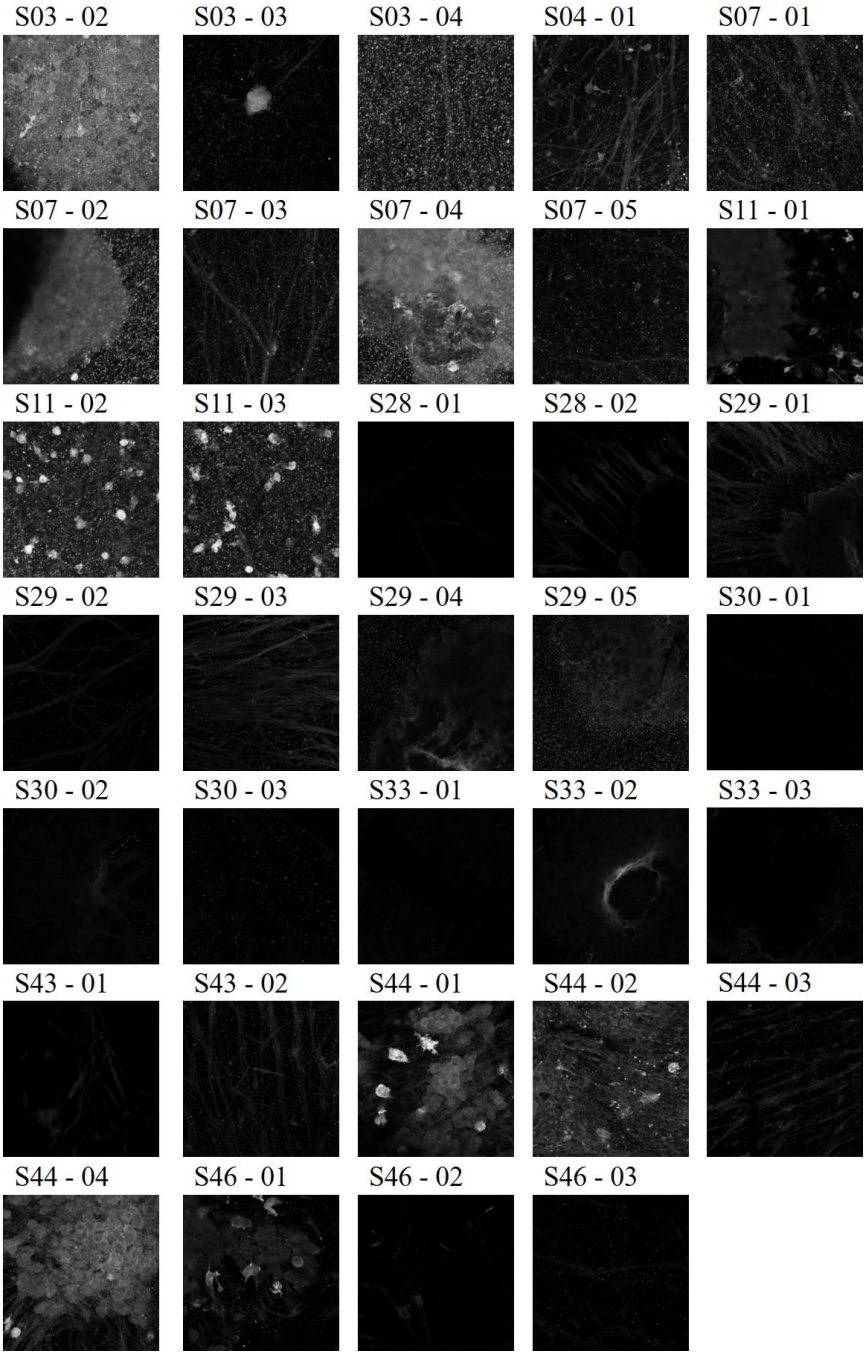

Table I.2. Neuronal substance P densitometry in stretched collagen gels with DRGs and no, low, or high FLS concentration with elemental MPS and CV at failure (Chapter 6).

Sample	DIV	Group	image no.	neuronal substance P (% positive)	MPS (%)	CV at failure
S03	DIV7	none	1	3.10%	7.60%	1.03
S03	DIV7	none	2	3.80%	6.60%	1.71
S07	DIV7	low	1	0.70%	6.10%	0.24
S07	DIV7	low	2	23.70%	8.50%	1.90
S08	DIV7	low	1	5.70%	22.50%	1.74
S08	DIV7	low	2	11.70%	15.60%	1.52
S08	DIV7	low	3	6.70%	7.50%	3.50
S09	DIV7	none	1	19.20%	18.50%	3.59
S11	DIV7	none	1	14.70%	0.00%	2.94
S11	DIV7	none	2	46.30%	0.00%	4.92
S11	DIV7	none	3	44.30%	27.60%	7.05
S13	DIV7	low	1	1.50%	18.00%	3.82
S13	DIV7	low	2	7.20%	7.50%	1.85
S28	DIV7	high	1	1.30%	41.70%	7.68
S28	DIV7	high	2	2.40%	30.00%	9.85
S28	DIV7	high	3	67.30%	14.40%	34.91
S29	DIV7	high	1	1.30%	N/A	N/A
S29	DIV7	high	2	0.00%	N/A	N/A
S29	DIV7	high	3	2.50%	N/A	N/A
S29	DIV7	high	4	0.60%	N/A	N/A
S29	DIV7	high	5	0.50%	N/A	N/A
S31	DIV7	high	1	12.70%	25.90%	N/A
S31	DIV7	high	2	75.50%	34.40%	N/A
S31	DIV7	high	3	0.10%	38.10%	N/A
S31	DIV7	high	4	1.50%	9.70%	N/A
S34	DIV7	low	1	1.10%	3.70%	5.92
S34	DIV7	low	2	2.30%	5.90%	7.69
S34	DIV7	low	3	2.10%	29.90%	3.38
S37	DIV7	high	1	1.70%	17.30%	0.94
S37	DIV7	high	2	0.60%	11.00%	4.18
S37	DIV7	high	3	0.20%	14.50%	1.95
S37	DIV7	high	4	0.20%	11.70%	2.43
S38	DIV7	none	1	0.80%	16.60%	12.18
S38	DIV7	none	2	12.50%	13.00%	1.89
S03	DIV9	low	1	92.10%	49.20%	8.43
S03	DIV9	low	2	22.50%	43.10%	25.46
S03	DIV9	low	3	32.50%	45.70%	17.25
S07	DIV9	low	1	67.80%	24.90%	7.03
S07	DIV9	low	2	38.10%	14.30%	12.06
S07	DIV9	low	3	86.50%	40.30%	8.99
S07	DIV9	low	4	20.70%	38.30%	5.87
S11	DIV9	low	1	59.00%	20.20%	51.39
S11	DIV9	low	2	56.40%	39.90%	11.81
S28	DIV9	none	1	0.40%	N/A	6.06
S28	DIV9	none	2	2.40%	N/A	5.74
S29	DIV9	none	1	1.90%	N/A	N/A
S29	DIV9	none	2	17.70%	N/A	N/A
S29	DIV9	none	3	2.60%	N/A	N/A
S29	DIV9	none	4	7.20%	N/A	N/A
S29	DIV9	none	5	6.10%	N/A	N/A
S30	DIV9	none	1	26.50%	15.20%	2.69
S30	DIV9	none	2	1.00%	14.70%	3.87
S30	DIV9	none	3	7.50%	20.00%	3.78
S30	DIV9	none	4	2.50%	18.90%	2.26
S33	DIV9	none	1	0.40%	4.20%	2.89
S33	DIV9	none	2	2.20%	4.20%	1.91
S33	DIV9	none	3	13.10%	8.10%	1.87
S33	DIV9	none	4	3.20%	12.10%	1.61
S43	DIV9	high	1	0.00%	35.10%	4.08
S43	DIV9	high	2	0.10%	13.20%	28.53
S44	DIV9	high	1	1.00%	26.60%	10.94
S44	DIV9	high	2	1.40%	17.50%	19.54
S44	DIV9	high	3	0.10%	22.50%	58.89
S44	DIV9	high	4	1.90%	23.30%	83.77
S46	DIV9	high	1	0.40%	15.90%	37.84
S46	DIV9	high	2	0.00%	21.80%	18.84
S46	DIV9	high	3	0.00%	17.20%	15.62

DRG: dorsal root ganglia; FLS: fibroblast-like synoviocyte
DIV: day-in-vitro; MPS: maximum principal strain; CV: circular variance
N/A data were not collected due to technical problems with data capture

Note: Table is continued on the next page.

Figure I.2. Immunolabeling of substance P in DRGs as designated in Table I.2 (Chapter 6). Gels tested on day-in-vitro 7 are detailed before the red-dashed line; gels tests on day-in-vitro 9 are detailed after the line.

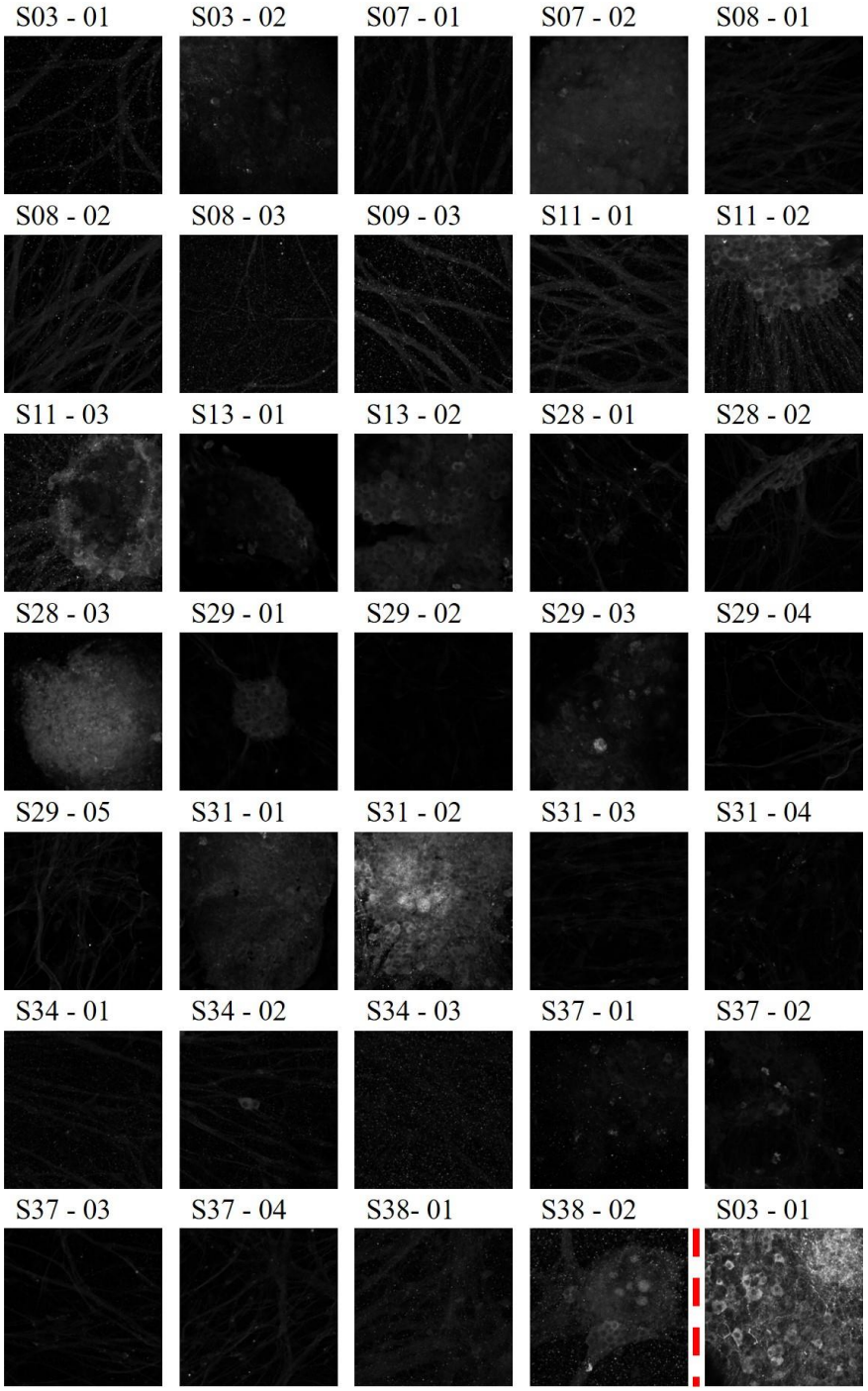

Note: Figure is continued on the next page.

Figure I.2. continued

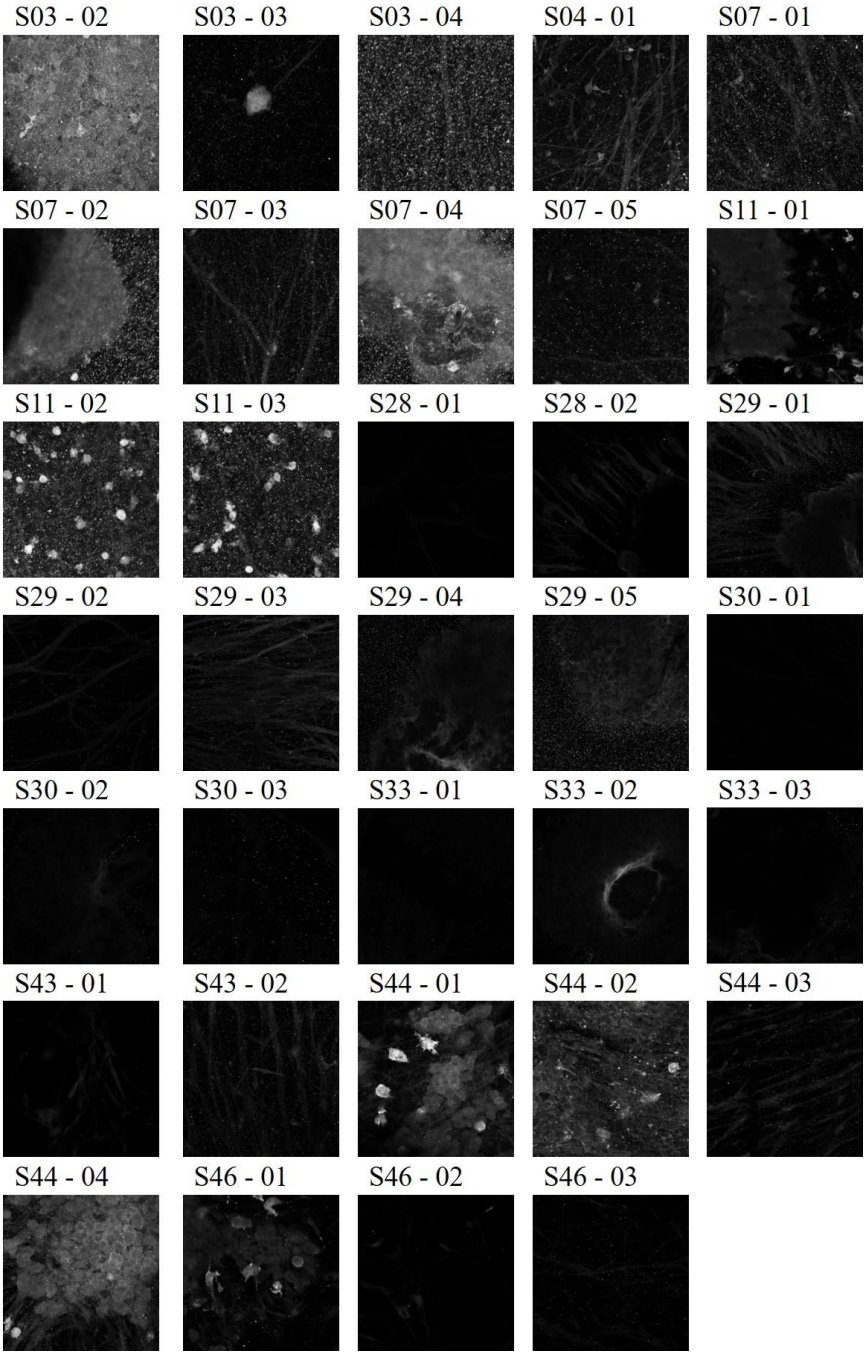

Table I.3. MMP-1 and MMP-9 densitometry in stretched and unstretched co-cultures with DRGs and a low concentration of FLS (Chapter 6)

Sample	Group	image no.	MMP-1 (% positive)	MMP-9 (% positive)	cell type
S07	stretched	1	15.18%	15.17%	axon
S07	stretched	2	9.24%	12.28%	axon
S07	stretched	3	10.95%	23.03%	FLS
S07	stretched	4	10.65%	12.90%	FLS
S08	stretched	1	22.02%	0.18%	soma
S08	stretched	2	3.32%	0.61%	axon
S08	stretched	3	10.02%	0.25%	soma
S08	stretched	4	5.64%	1.22%	axon
S08	stretched	5	6.69%	2.37%	axon
S08	stretched	6	8.14%	10.63%	FLS
S08	stretched	7	3.85%	7.67%	FLS
S08	stretched	8	3.21%	10.42%	FLS
S13	stretched	1	13.96%	2.03%	soma
S13	stretched	2	8.97%	5.28%	axon
S13	stretched	3	6.13%	14.46%	axon
S13	stretched	4	24.70%	5.10%	soma
S13	stretched	5	3.61%	3.47%	axon
S13	stretched	6	7.82%	13.82%	FLS
S13	stretched	7	8.11%	10.90%	FLS
S13	stretched	8	4.78%	11.28%	FLS
S35	unstretched	1	0.70%	7.69%	axon
S35	unstretched	2	1.38%	4.65%	axon
S35	unstretched	3	0.88%	1.41%	axon
S35	unstretched	4	10.25%	5.06%	soma
S35	unstretched	5	6.00%	8.71%	FLS
S35	unstretched	6	2.77%	4.18%	FLS
S35	unstretched	7	5.19%	4.66%	FLS

DRG: dorsal root ganglia; FLS: fibroblast-like synoviocyte

Figure I.3. Immunolabeling of MMP-1 in stretched and unstretched co-cultures as designated in Table I.3 (Chapter 6)

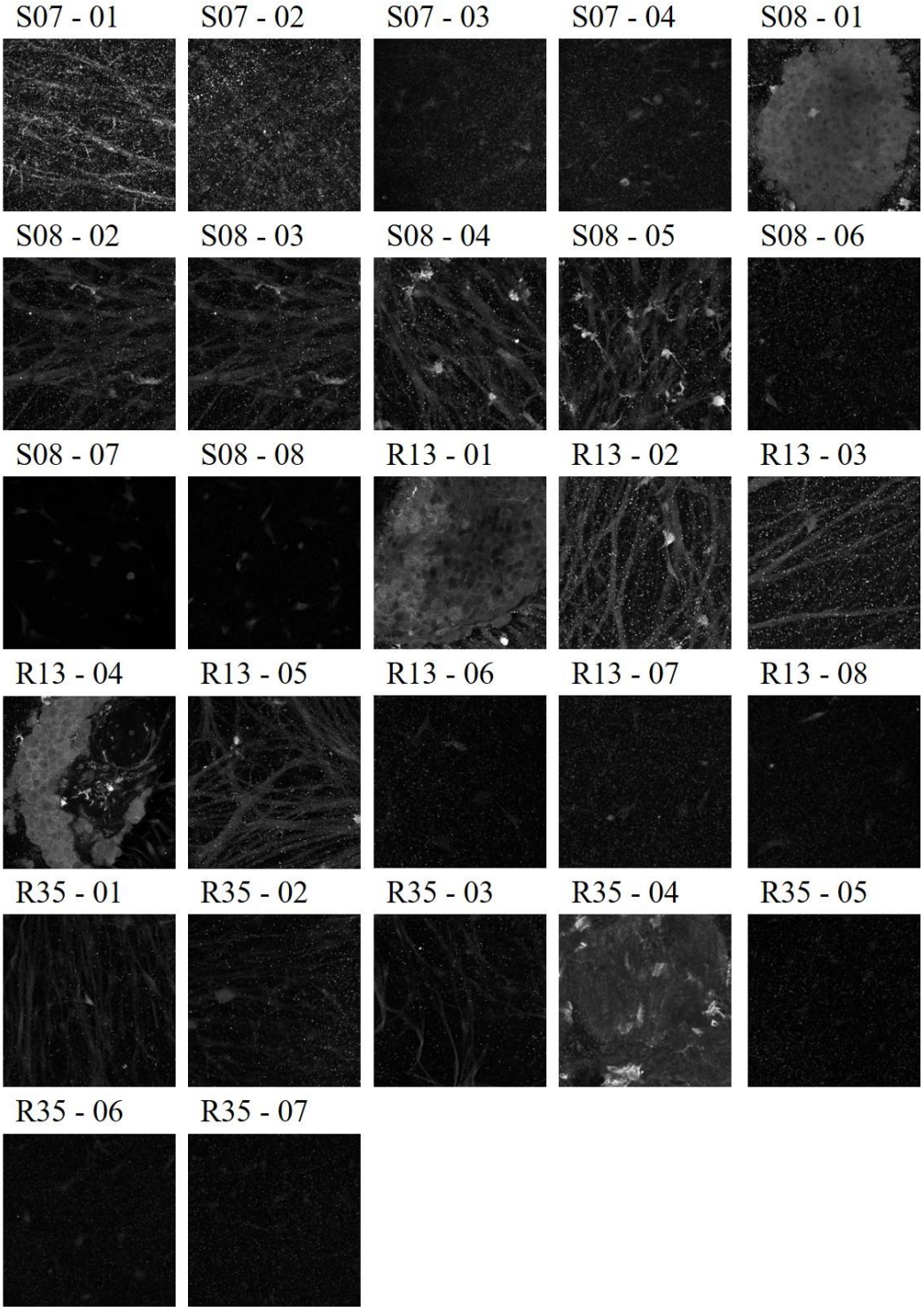

Figure I.4. Immunolabeling of MMP-9 in stretched and unstretched co-cultures as designated in Table I.3 (Chapter 6)

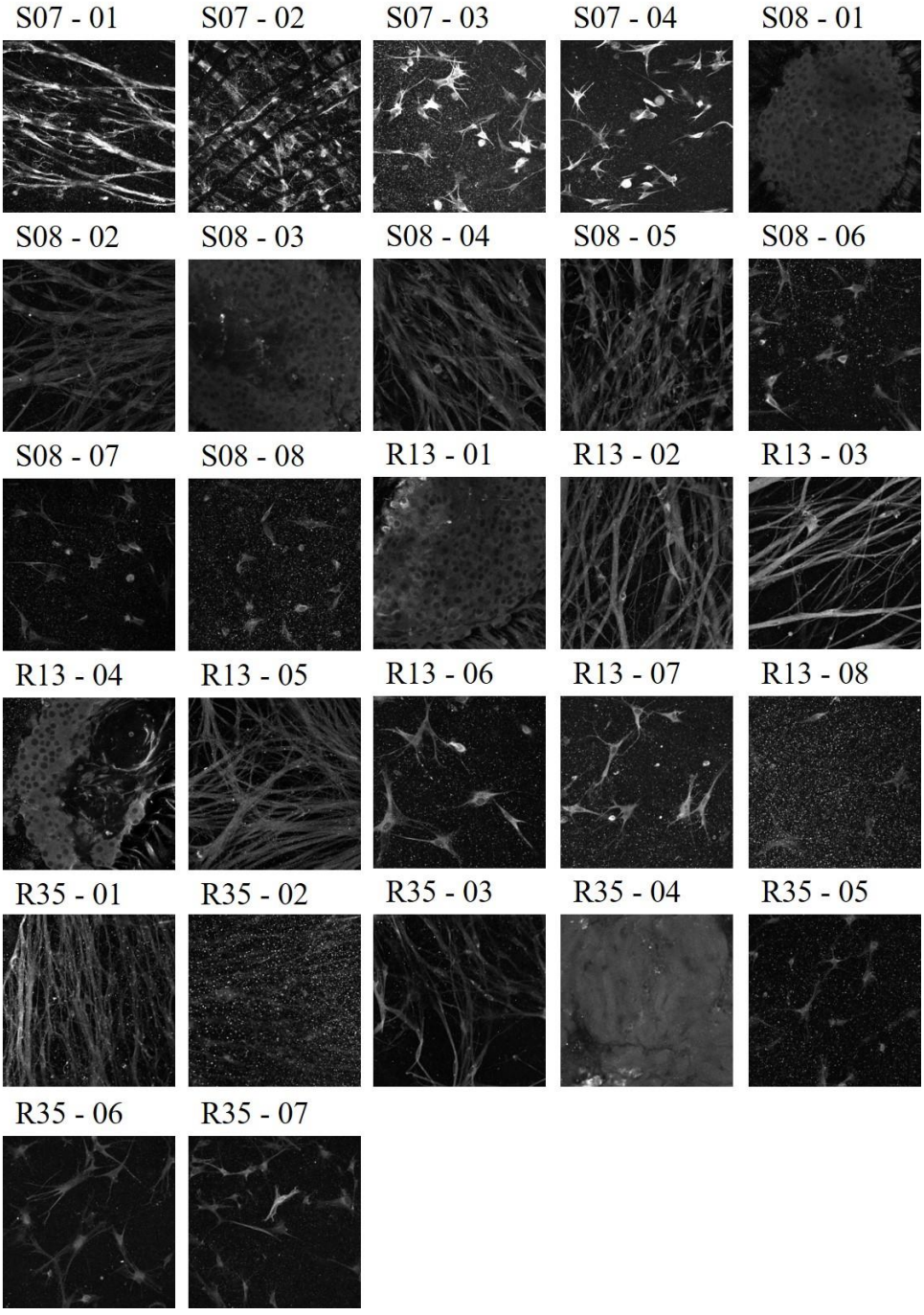

Table I.4. MMP-9 densitometry in DRG cultures exposed to exogenous MMP-1 (Chapter 6)

Sample	Group	image no.	MMP-9 (% positive)	DRG region
C01	MMP-1	1	71.22%	soma
C01	MMP-1	2	2.22%	axons
C01	MMP-1	3	49.48%	soma
C01	MMP-1	4	7.35%	axons
C01	MMP-1	5	21.02%	soma
C01	MMP-1	6	4.77%	axons
C02	MMP-1	1	52.70%	soma
C02	MMP-1	2	43.22%	soma
C02	MMP-1	3	42.12%	soma
C04	MMP-1	1	14.26%	soma
C04	MMP-1	2	8.53%	soma
C04	MMP-1	3	24.50%	axons
C04	MMP-1	4	20.19%	soma
C04	MMP-1	5	26.83%	axons
C05	MMP-1	1	9.19%	soma
C05	MMP-1	2	2.34%	soma
C05	MMP-1	3	1.51%	soma
C05	MMP-1	4	0.26%	axons
C05	MMP-1	5	2.38%	soma
C05	MMP-1	6	0.18%	soma
C05	MMP-1	7	0.60%	axons
C08	naïve	1	8.46%	soma
C08	naïve	2	11.05%	soma
C08	naïve	3	5.02%	axons
C08	naïve	4	0.64%	soma
C08	naïve	5	18.66%	axons
C09	naïve	1	12.08%	axons
C09	naïve	2	13.59%	soma
C09	naïve	3	15.63%	axons
C09	naïve	4	17.58%	axons
C09	naïve	5	5.04%	soma
C09	naïve	6	1.70%	soma

Table I.5. Percent cell death determined from cytotoxicity assays after exogenous MMP-1 exposure (Chapter 6)

Sample	Group	% cell death
C01	MMP-1	38.81
C02	MMP-1	23.32
C03	MMP-1	28.90
C04	MMP-1	39.00
C05	MMP-1	39.41
C08	naïve	7.39
C09	naïve	16.80

Figure I.5. Immunolabeling of MMP-9 in DRG cultures exposed to exogenous MMP-1 as designated in Table I.4 (Chapter 6)

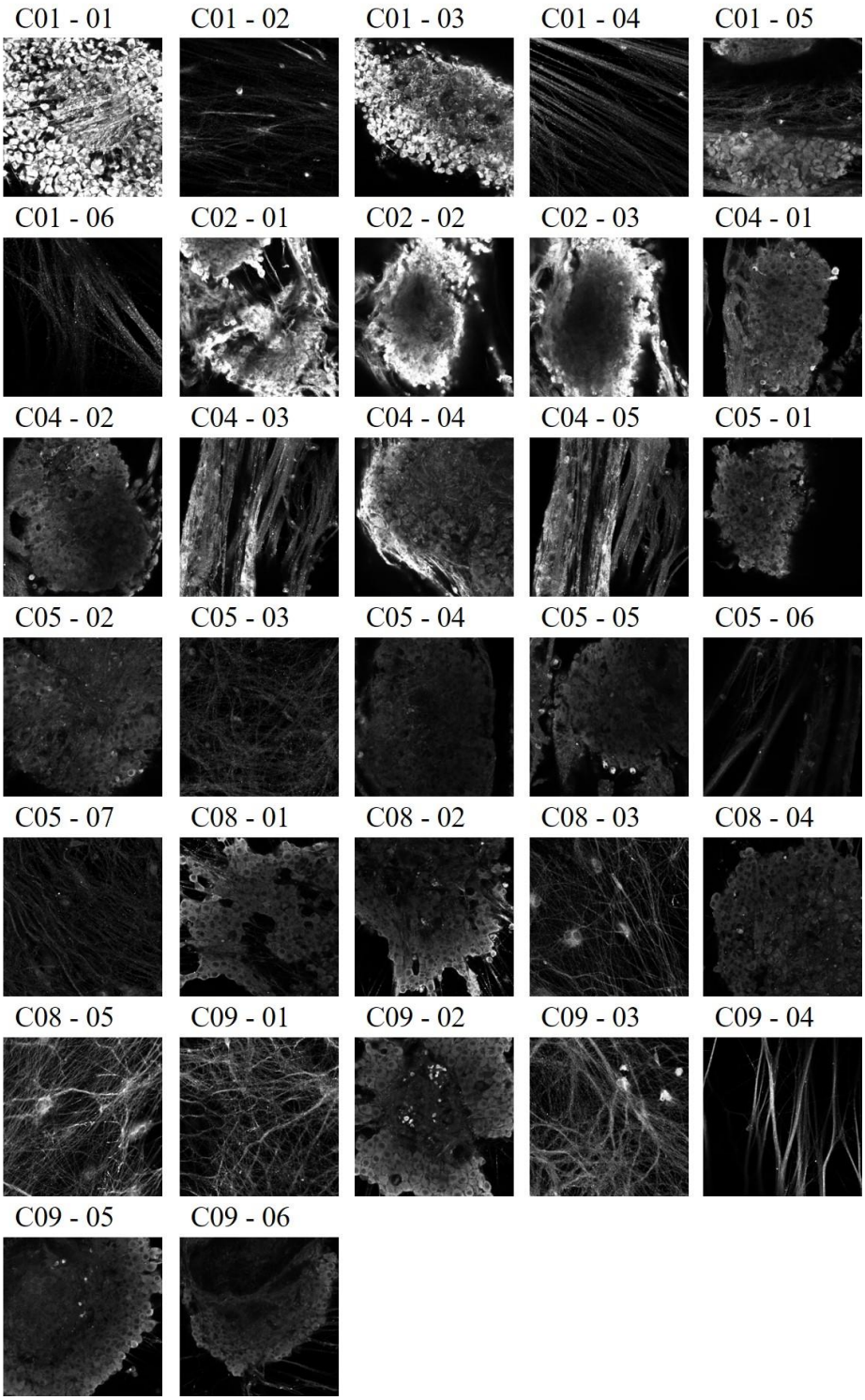

APPENDIX J

Mechanical, Strain, & Polarized Light Optical Data from Rat Facet Capsular Ligaments during Tensile Loading

This appendix summarizes the force-displacement, full-field surface strains, and collagen fiber kinematic data computed for the capsular ligaments tested from isolated joints under tensile load in the studies in Chapter 7. Capsular ligaments were isolated from the C6/C7 facet joints of rats 28 days after injection with MMP-1 or a matched vehicle and stretched to failure in tension. Mechanical, strain, and collagen fiber kinematic data in a capsular ligament from a naïve, un-operated rat are also included in this appendix. The behavioral data for rats included in this study are summarized in Appendix C. Histology and immunohistochemistry assays performed on the joint tissues of the rats from this study are summarized in Appendix D, and immunohistochemistry assays performed on the DRG and spinal cord tissues from those same rats are detailed in Appendix E. Data are identified by their injection group and rat number in the figures contained within this appendix.

Force, displacement, and optical data were used to define several events of interest throughout the stretch to failure: the first occurrence of anomalous collagen fiber realignment, yield, the first failure, and ultimate rupture of the ligament. Figure J.1 summarizes the force and displacement data that were acquired at 500Hz during loading,

separately for each stretched capsular ligament. Ultimate rupture, first failure, and yield were defined using the mechanical data in Figure J.1 for each test; first failure and yield are designated on the curves in Figure J.1 and the data are plotted to the event of ultimate rupture. The first occurrence of anomalous collagen fiber realignment is also shown on the force-displacement curves in Figure J.1; the first occurrence of collagen fiber realignment was computed from polarized light imaging data and that computation is described in detail below. Quantification of force and displacement at every event, as well as the stiffness computed from those curves (Ita and Winkelstein 2019; Lee et al. 2006), are summarized in Table 7.1 (Chapter 7).

Figure J.2 shows the average maximum principal strain, by element, computed using fiducial markers that were digitized from high-speed images using the centroid of each capsule marker. Marker coordinates were transformed into x-y coordinates using the ProAnalyst software and maximum principal strains were computed relative to the unloaded reference (Quinn et al. 2007; Quinn and Winkelstein 2010). Strain data are shown at the first occurrence of anomalous collagen fiber realignment, yield, the first failure, and ultimate rupture of the ligament. Table 7.1 in Chapter 7 details the strain quantification that corresponds to the strain maps that are visualized in Figure J.2.

Figure J.3 details the optical data acquired with polarized light imaging during the loading of capsular ligaments. In order to compute the first occurrence of anomalous collagen fiber realignment and to track microstructural kinematics throughout loading, vector correlations were generated for every acquired alignment map based on pixel-by-pixel correlation calculations (Quinn et al. 2010a). Anomalous collagen realignment was

defined by a decrease of 0.35 or more in the alignment vector correlation between maps, and a single region was defined as sustaining anomalous realignment when at least nine pixels were connected to one another (Quinn et al. 2010a). Alignment maps were also generated in the unloaded reference state to measure microstructural organization of each ligament prior to loading. At reference and at every mechanical event, circular variance (CV) was computed from the spread of collagen fiber angles, with a lower CV indicating a tighter clustering and a higher degree of fiber alignment (Miller et al. 2012; Zhang et al. 2016). Figure J.3 summarizes the vector correlation maps, histograms of the collagen fiber orientation angles, and the regions where anomalous collagen fiber realignment events were detected. Table 7.1 in Chapter 7 details the CV and the number of anomalous fiber realignment events that correspond to the data in Figure J.3.

Figure J.1. Force-displacement data during tensile loading to failure as designated in Table 7.1 (Chapter 7). Curves terminate at ultimate rupture.

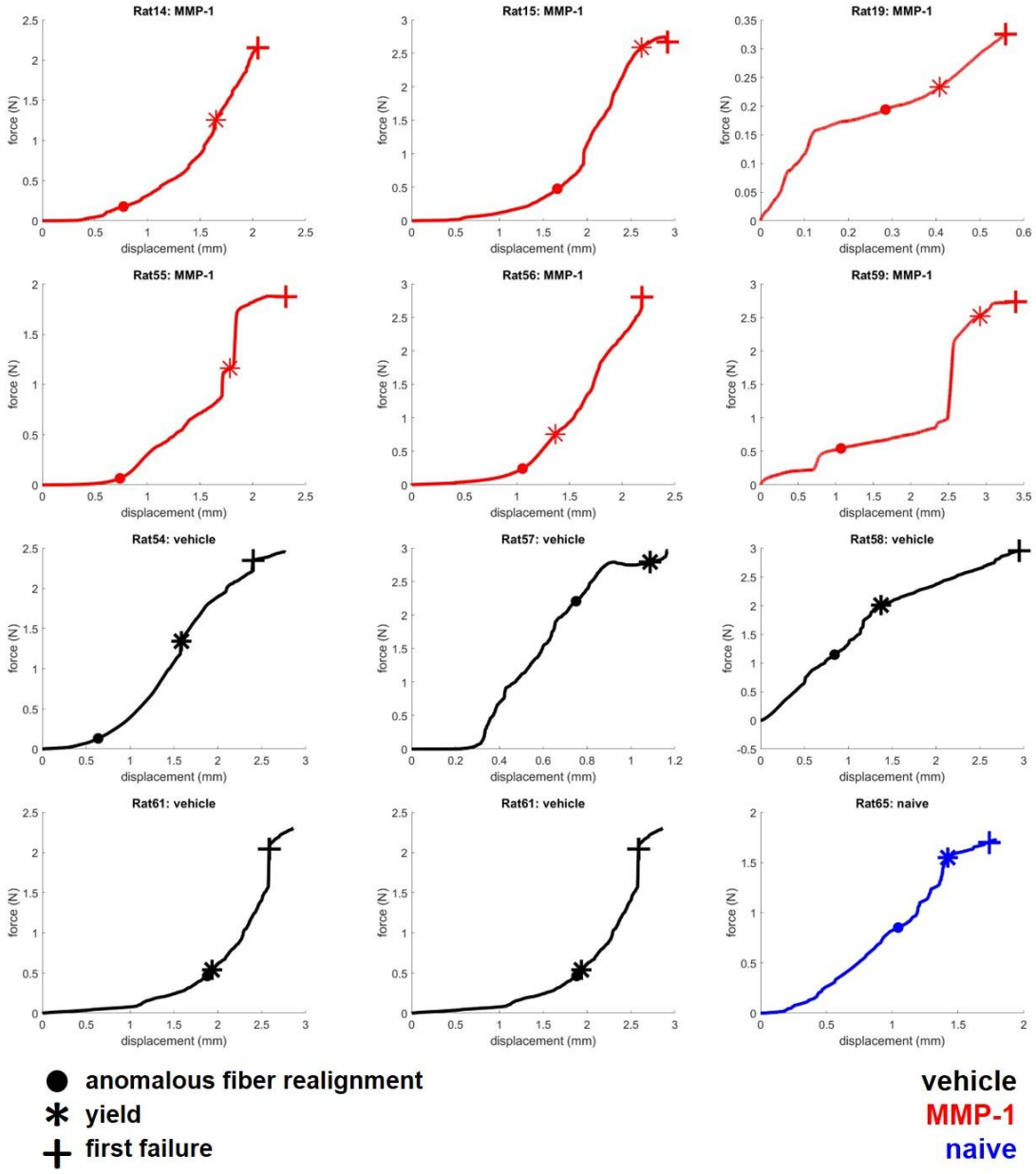

Figure J.2. Full-field strain maps showing the maximum principal strain in elements defined by fiducial markers on the surface of capsular ligaments injected with MMP-1 or a matched vehicle at mechanical events during tensile loading (Chapter 7). Asterisks indicate capsules with first failure and ultimate rupture as the same event.

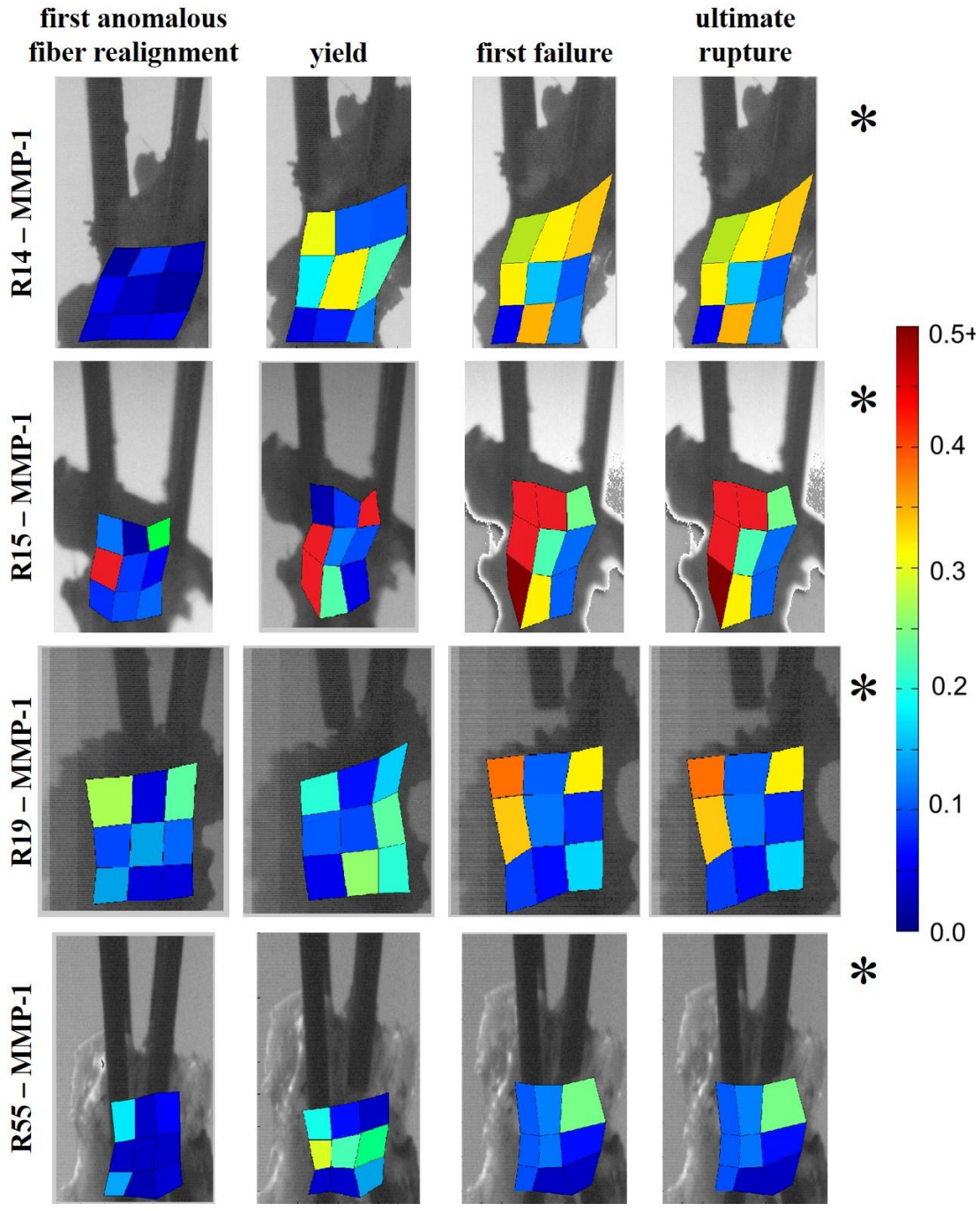

Note: Figure is continued on the next page.

Figure J.2. continued

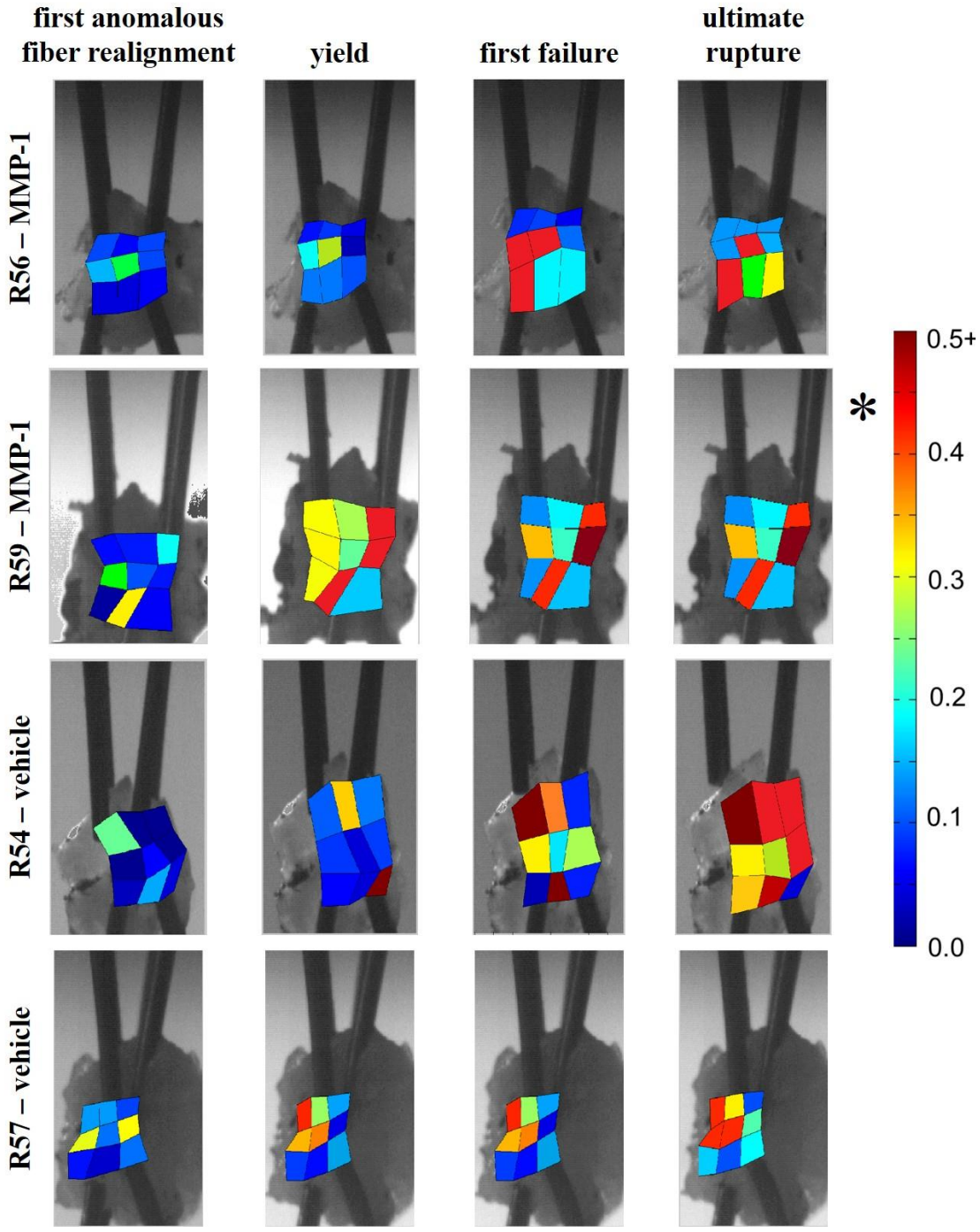

Note: Figure is continued on the next page.

Figure J.2. continued

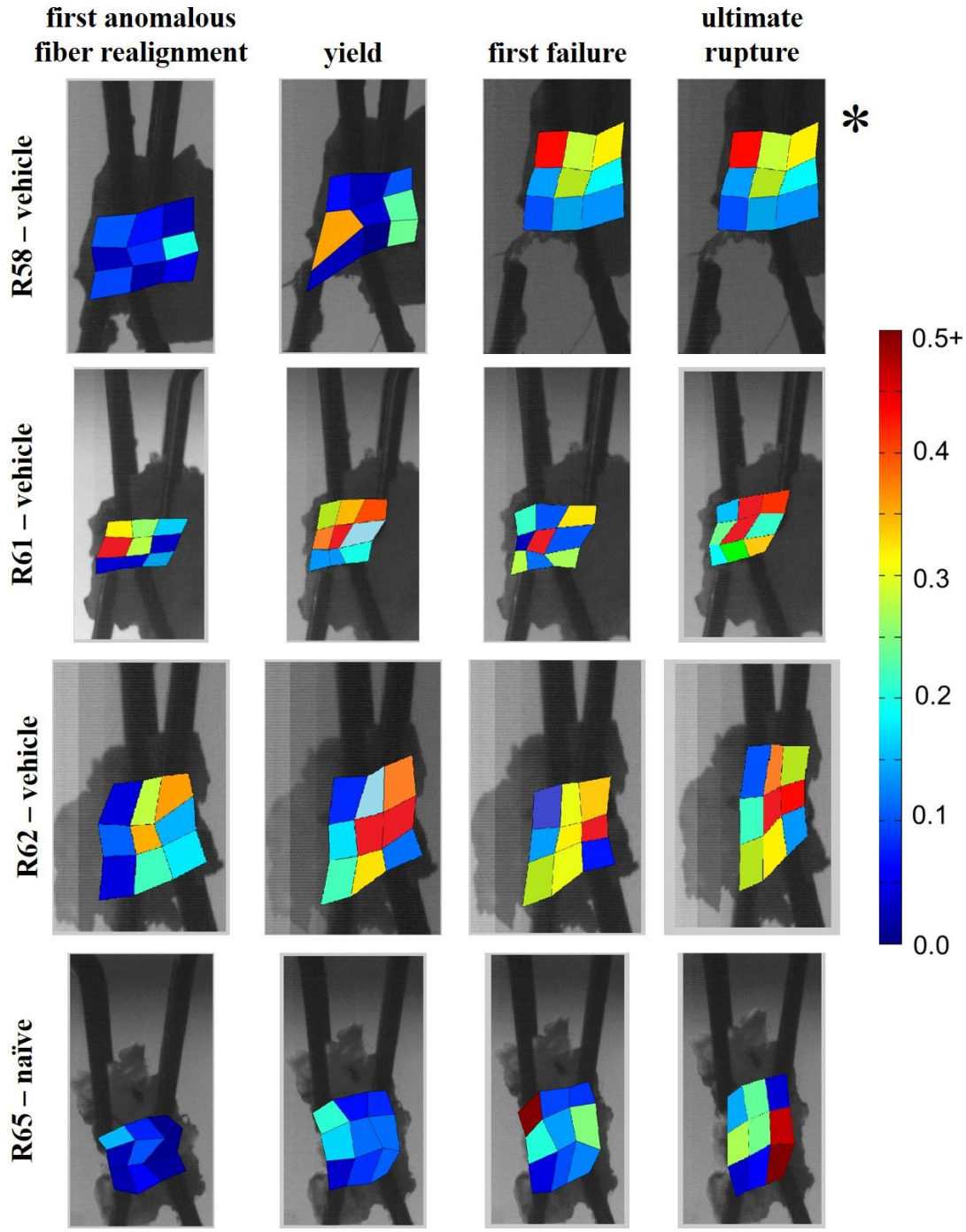

Figure J.3. High-speed images with collagen fiber alignment vectors (yellow), corresponding histograms depicting the spread of collagen fiber orientation angles, and the detection of anomalous fiber reorganization events (yellow circles in insets). Data are shown at reference, the first occurrence of anomalous realignment, yield, first failure, and ultimate rupture for loaded capsular ligaments, separately by rat (Chapter 7).

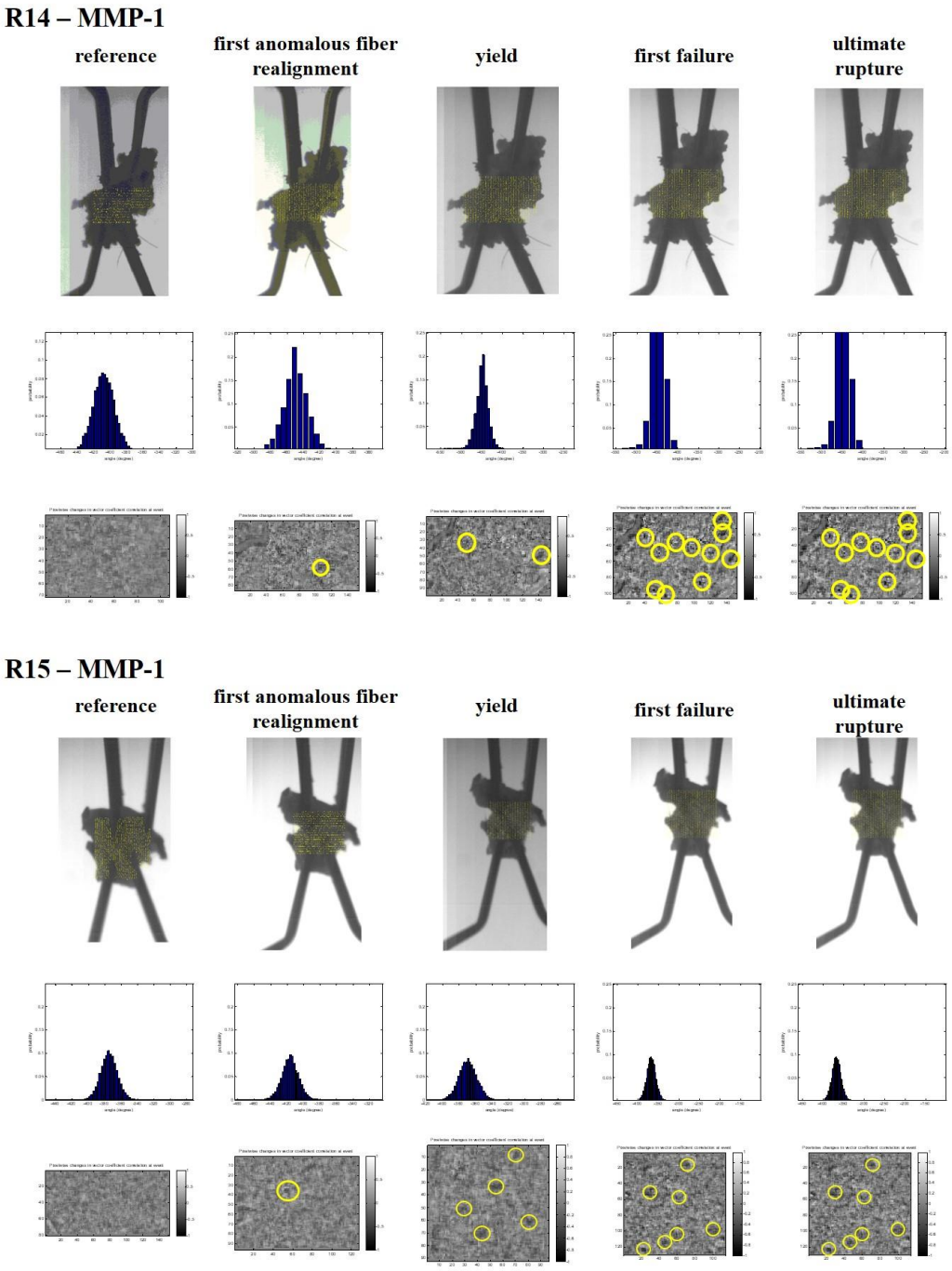

Figure J.3. continued

R19 – MMP-1

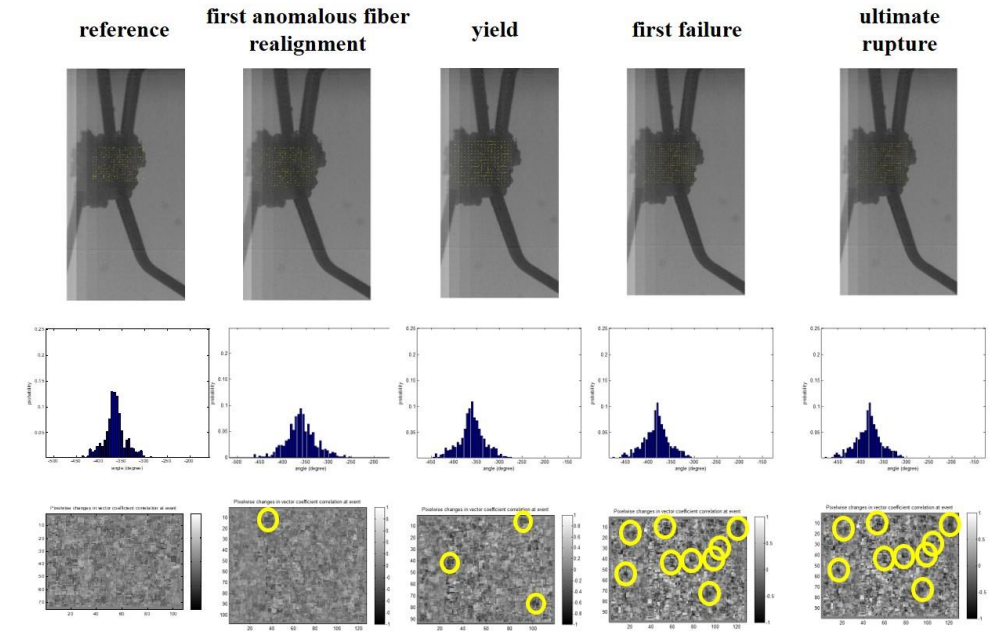

R55 – MMP-1

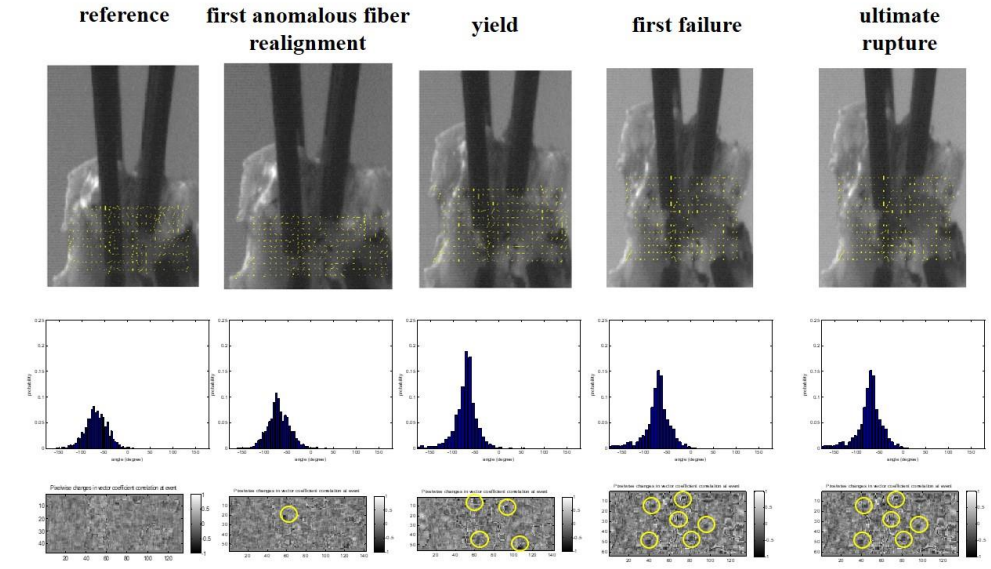

Note: Figure is continued on the next page.

Figure J.3. continued

R56 – MMP-1

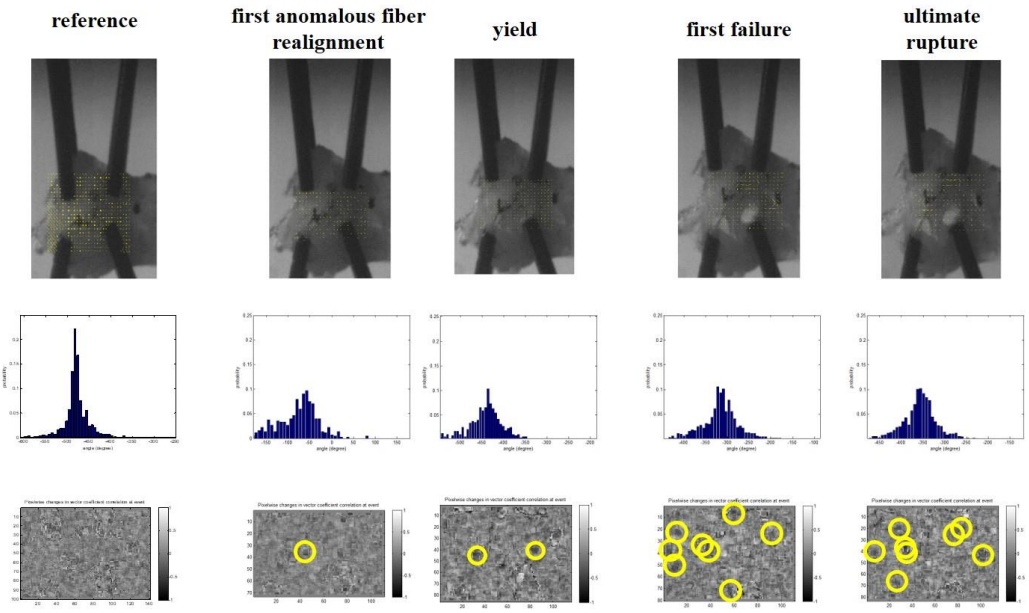

R59 – MMP-1

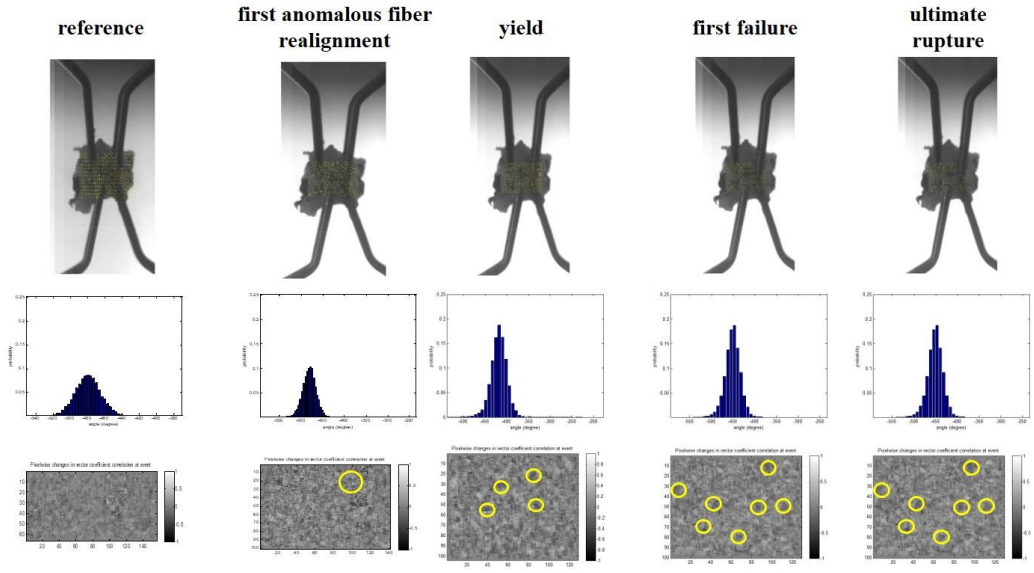

Note: Figure is continued on the next page.

Figure J.3. continued

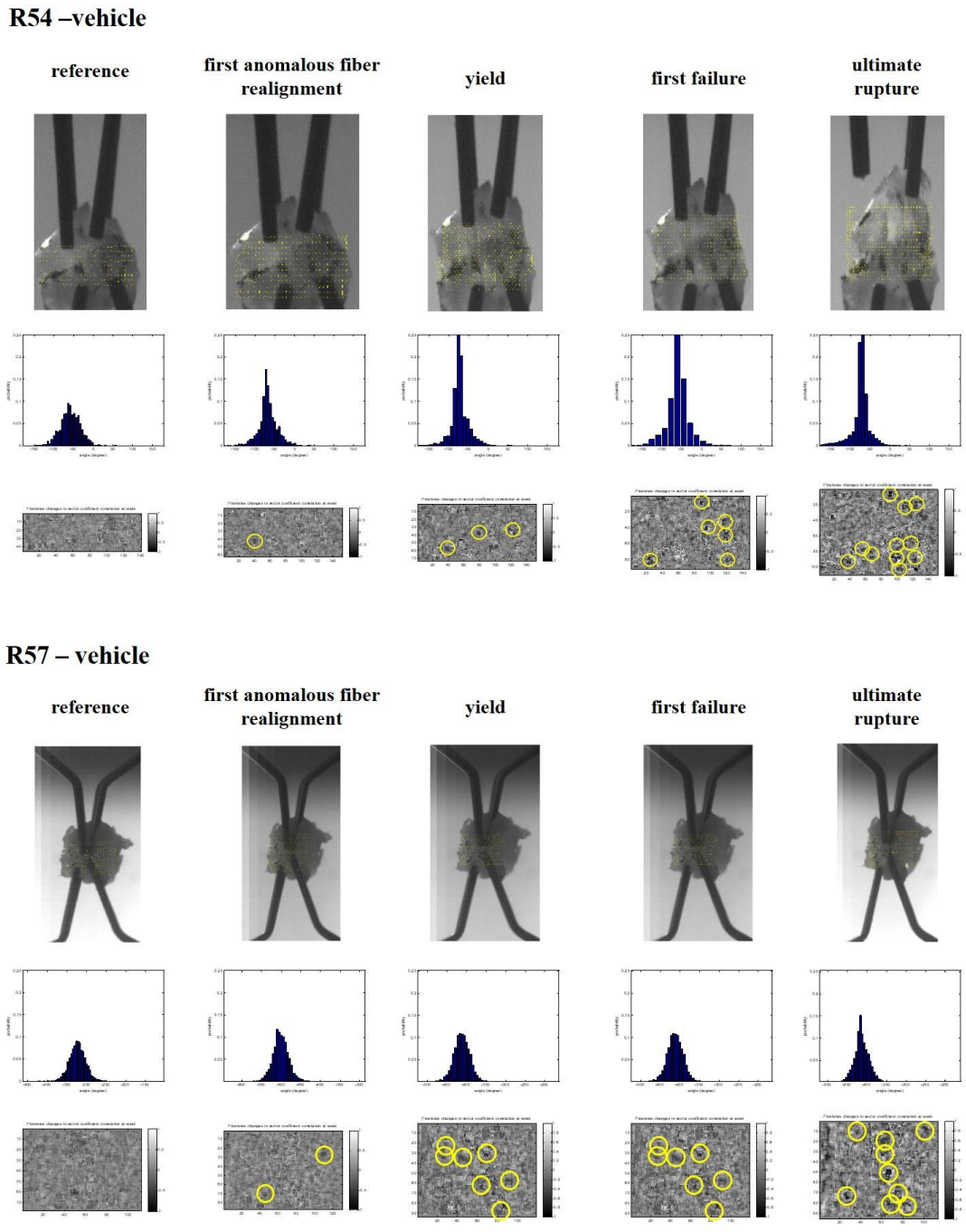

Note: Figure is continued on the next page.

Figure J.3. continued

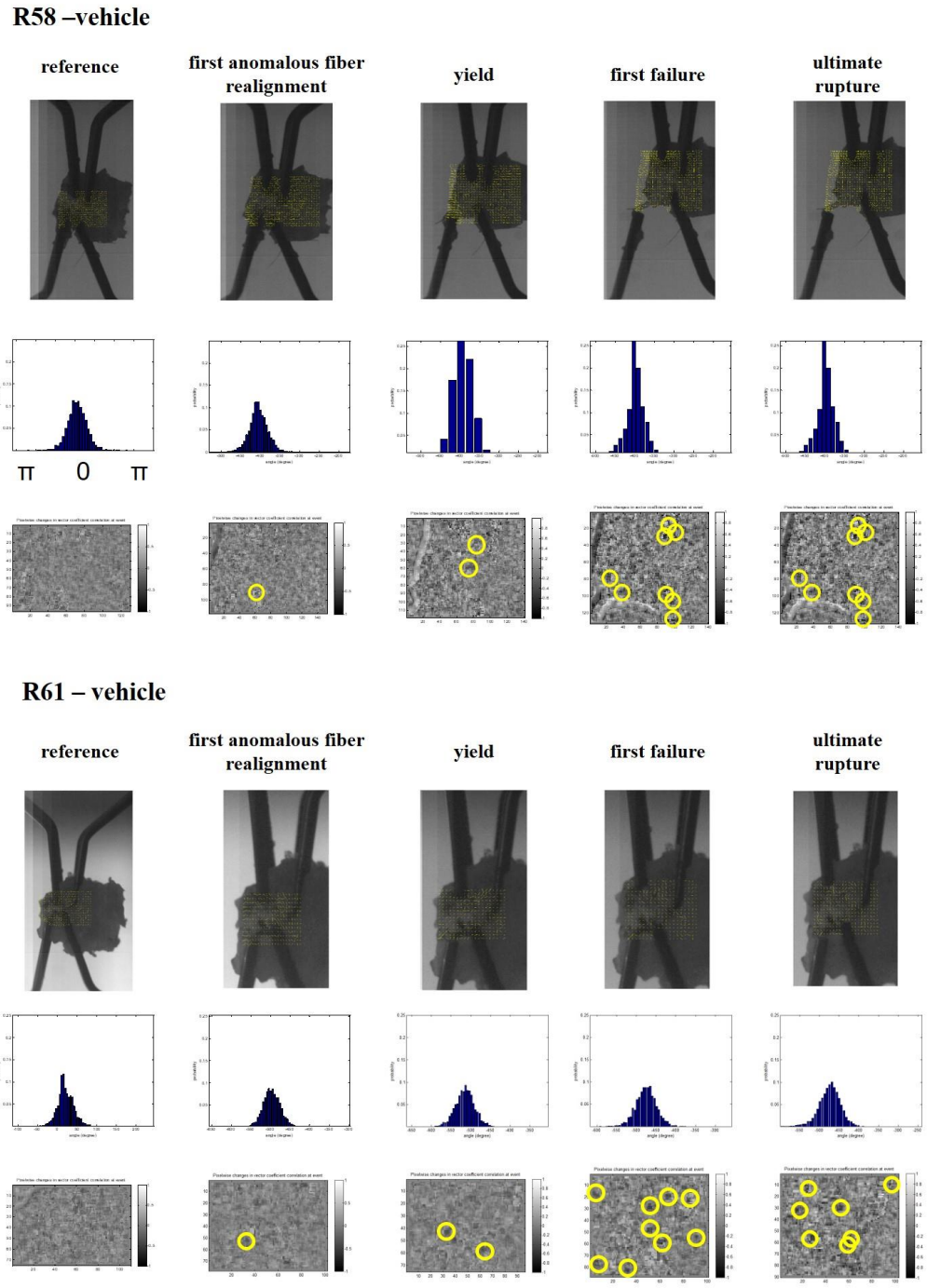

Note: Figure is continued on the next page.

Figure J.3. continued

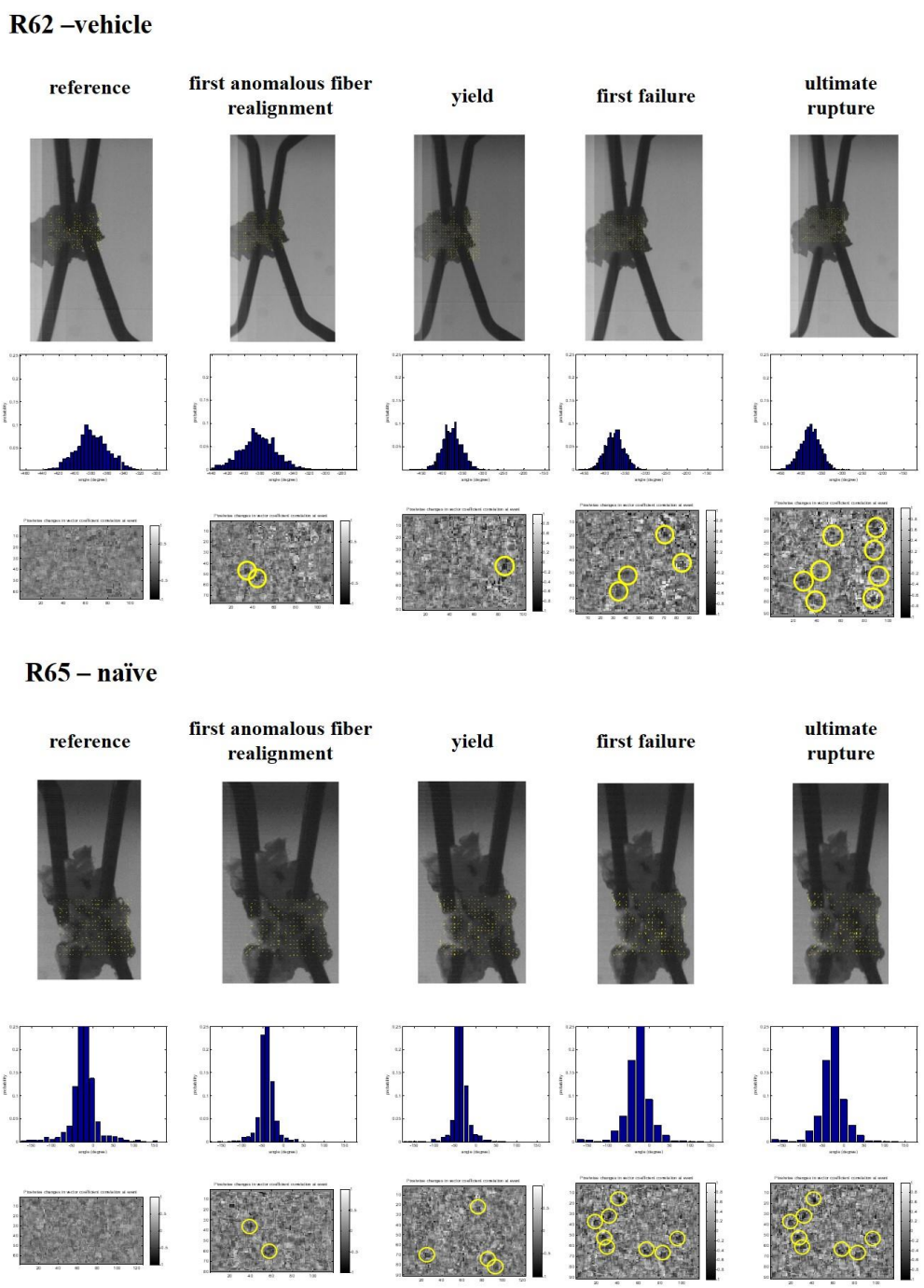

APPENDIX K

Collagen Gel Mechanics in Response to Sub-Failure Biaxial Loading

This appendix summarizes the force-displacement and strain data acquired during the sub-failure equibiaxial collagen gels from the studies presented in Section 8.3 and Section 8.4. In the figures detailed in this appendix, data are identified by their sample ID number and the experimental group. The studies in Section 8.3 defined whether sub-failure strains that induce nociceptive signaling in the previous neuron-collagen gel model (Zhang et al. 2017; Zhang et al. 2018) also increase substance P in the co-culture model. Experimental groups for the studies summarized in Section 8.3 include collagen gels seeded with only DRGs (DRG-only) or with DRGs and FLS cells ($5x10^4$ cells/mL; naïve). The studies in Section 8.4 utilized equibiaxial sub-failure loading and different dosing regimens of the MMP inhibitor ilomastat. Experimental groups for the studies summarized in Section 8.4 include several ilomastat dosing regimens: DMSO vehicle at every dosing time (vehicle), ilomastat one hour prior to stretch and DMSO five minutes after the stretch (pre), ilomastat only five minutes after the stretch (post), or ilomastat at every dosing time (pre+post).

Figure K.1 summarizes the force versus displacement traces, for each load cell (X1, X2, Y1, Y2), separately for the studies presented in Sections 8.3 and 8.4. The highest magnitude force acquired during sub-failure equibiaxial stretch was recorded for each load

cell trace and is detailed in Table K.1. The maximum magnitude of force during a gel stretch recorded by any of the four load cells was taken as the peak force for that gel and is also detailed in Table K.1. Figure K.2 details the maximum principal strain (MPS) computed by digitizing the locations of the fiducial markers in the unloaded reference image and the image immediately after the maximum force. Fiducial markers were digitized with FIJI software (NIH) and position data were processed in LS-DYNA (LSTC) to calculate the MPS. The largest magnitude MPS sustained out of all elements within a gel was taken as the peak MPS for that gel and is detailed in Table K.1.

Table K.1. Summary of force and maximum principal strain (MPS) recorded during an equibiaxial sub-failure stretch (Chapter 8). The peak force recorded from each load cell is separately detailed (X1, X2, Y1, Y2); the maximum force from any given load cell is also listed.

		peak force (mN)					
Sample	Group	X1	X2	Y1	Y2	max force (mN)	peak MPS (%)
E5-S01	DRG-only	-0.43	4.75	13.98	10.29	**13.98**	N/A
E5-S03	naive	13.79	23.56	18.41	18.93	**23.56**	7.39
E5-S05	DRG-only	1.71	7.95	2.06	2.73	**7.95**	24.76
E5-S08	naive	12.04	7.04	3.22	2.83	**12.04**	26.71
E5-S09	naive	15.62	16.11	2.87	5.39	**16.11**	21.02
E5-S11	DRG-only	2.17	3.34	0.45	2.02	**3.34**	25.32
E5-S13	naive	6.84	12.41	3.28	2.17	**12.41**	16.34
E5-S15	DRG-only	10.93	9.00	0.43	4.47	**10.93**	11.90
E5-S18	naive	9.82	12.37	8.45	16.92	**16.92**	18.09
E5-S19	DRG-only	0.03	1.00	5.48	2.00	**5.48**	30.31
S09	pre	2.85	4.77	1.15	6.36	**6.36**	10.09
S10	pre+post	1.90	2.43	0.61	2.12	**2.43**	25.94
S11	pre	2.42	1.72	0.26	2.44	**2.44**	22.47
S14	pre+post	5.93	4.91	5.35	11.47	**11.47**	10.89
S17	pre	4.43	9.15	8.54	12.00	**12.00**	19.75
S20	pre+post	6.71	6.97	7.98	12.06	**12.06**	19.74
S21	pre	2.22	3.34	2.96	2.10	**3.34**	18.13
S24	pre+post	3.71	6.90	4.49	8.21	**8.21**	10.83
S27	pre+post	11.10	15.45	17.77	7.74	**17.77**	28.66
S28	post	6.68	9.11	30.99	33.25	**33.25**	18.84
S30	pre+post	27.26	25.45	36.08	26.05	**36.08**	15.43
S33	pre+post	20.50	30.93	30.70	26.51	**30.93**	17.18
S34	post	10.45	6.38	0.41	7.03	**10.45**	11.31
S36	post	11.37	19.38	16.59	15.29	**19.38**	23.15
S38	vehicle	2.03	3.60	3.91	3.44	**3.91**	19.97
S41	pre	14.95	10.99	4.51	9.13	**14.95**	20.71
S43	vehicle	10.64	7.62	20.51	7.23	**20.51**	51.80
S44	pre	12.10	7.18	5.62	4.38	**12.10**	50.17
S46	vehicle	10.33	10.45	18.44	7.20	**18.44**	23.27
S49	pre	12.53	5.06	12.78	8.36	**12.78**	53.93
S50	vehicle	13.68	14.94	22.35	7.63	**22.35**	40.69
S53	post	13.35	15.48	3.39	16.86	**16.86**	15.39
S54	vehicle	17.91	16.33	16.08	21.58	**21.58**	17.35
S57	post	7.41	5.30	10.37	12.33	**12.33**	22.16
S64	post	3.29	6.91	7.78	9.36	**9.36**	20.33
S70	naive	13.99	9.25	12.80	6.51	**13.99**	22.28
S72	pre	8.61	19.68	12.21	21.06	**21.06**	17.26

DRG: dorsal root ganglia; MPS: maximum principal strain
N/A data were not collected due to technical problems with data capture

Figure K.1. Force-displacement traces shown separately for each load cell affixed to each actuator arm (X1, X2, Y1, Y2) during equibiaxial sub-failure stretch as designated in Table K.1 (Chapter 8)

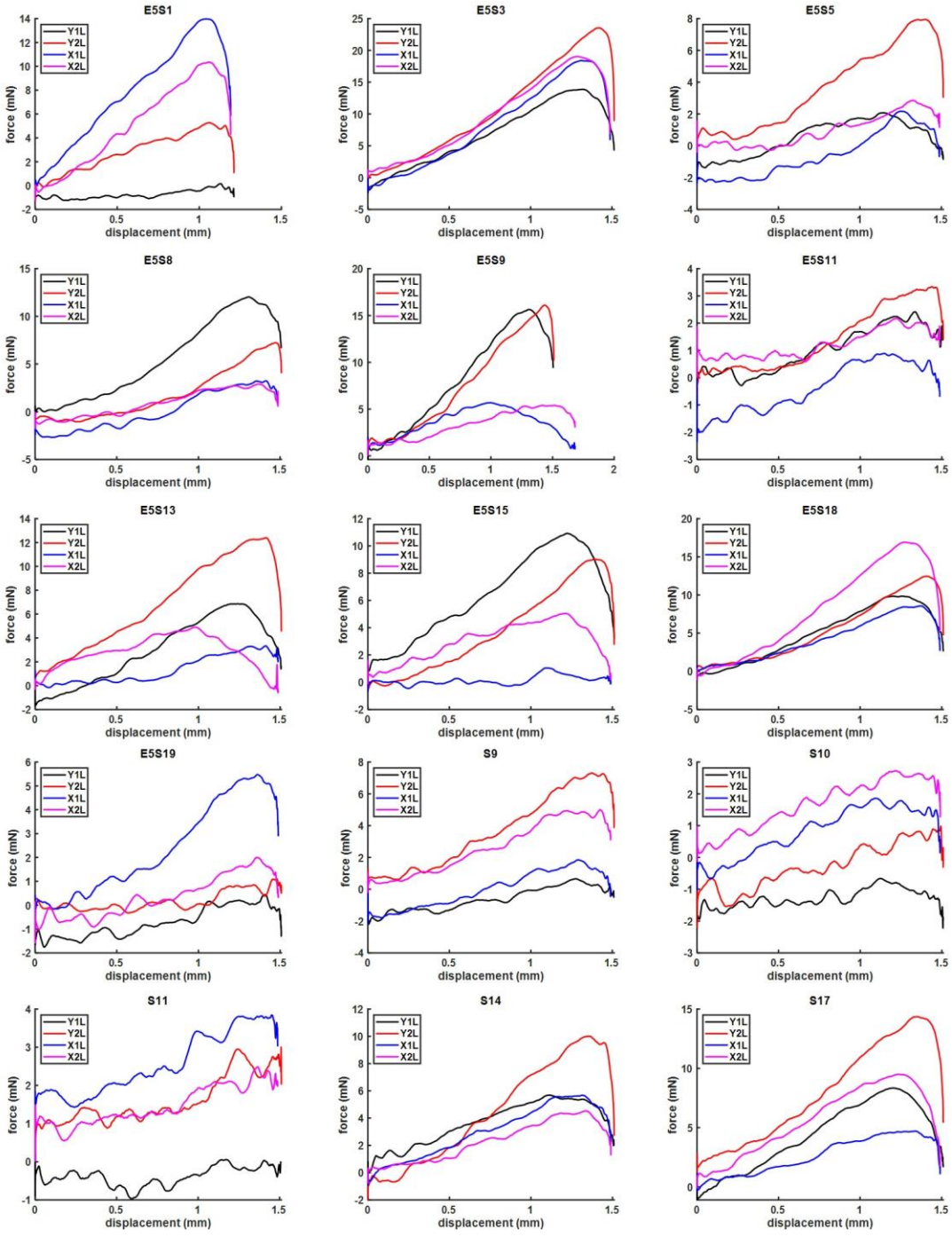

Note: Figure is continued on the next page.

Figure K.1. continued

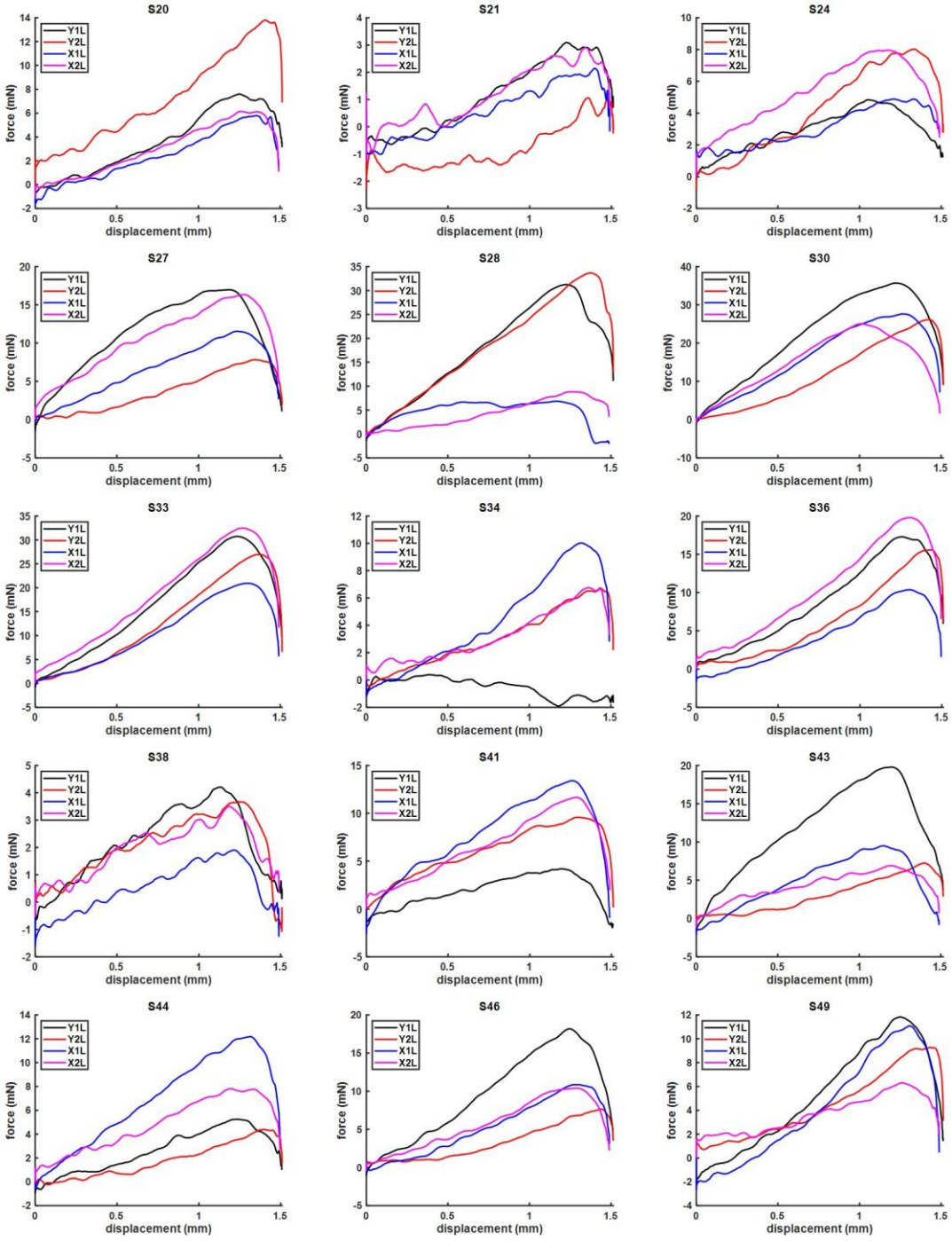

Note: Figure is continued on the next page.

Figure K.1. continued

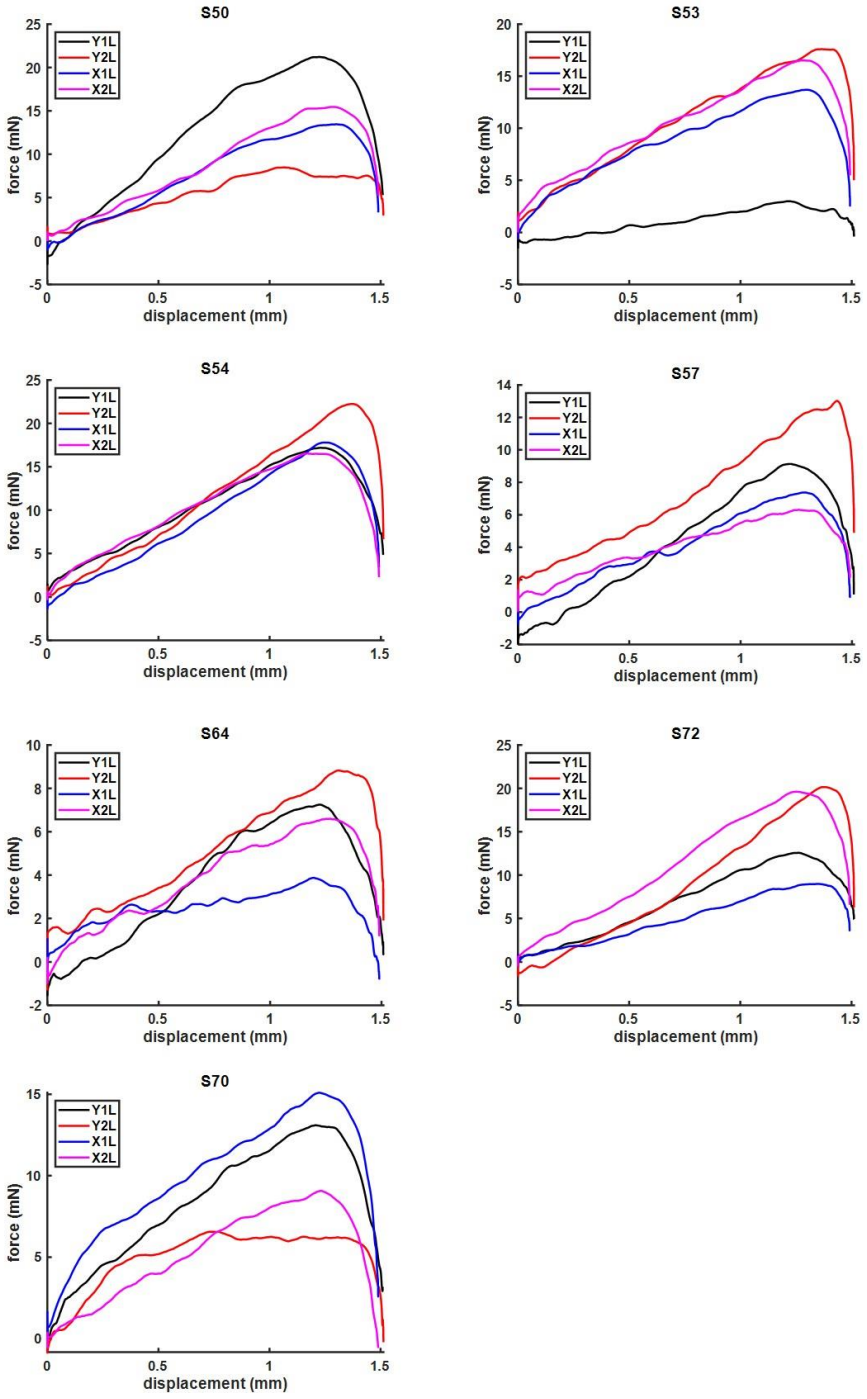

Figure K.2. Maximum principal strains sustained on the gel surface immediately following an equibiaxial sub-failure stretch as designated in Table K.1 (Chapter 8)**.** Elements are numbered sequentially from the bottom left to top right, as shown in sample E5-S11.

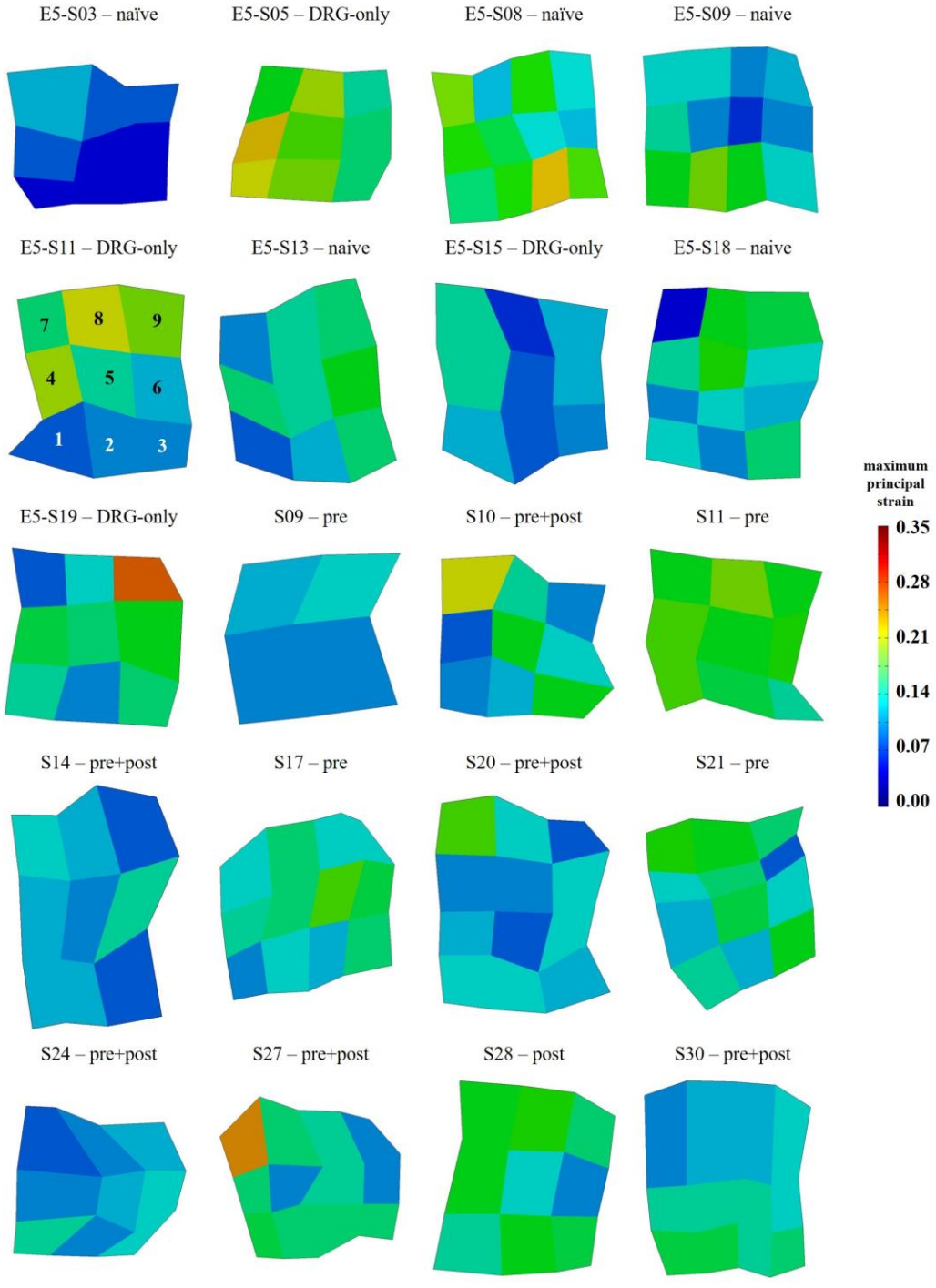

Note: Figure is continued on the next page.

Figure K.2. continued

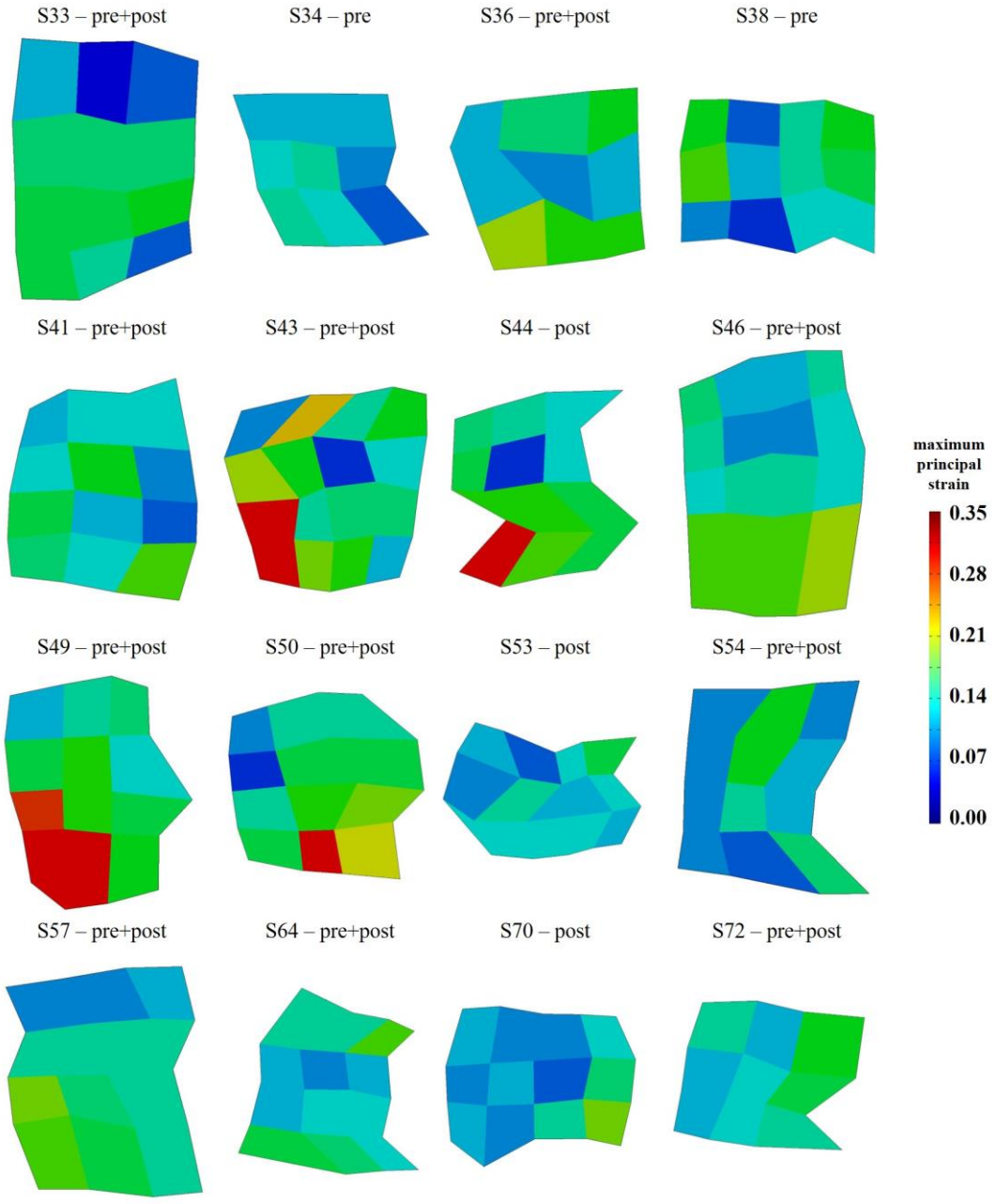

APPENDIX L

MMP-1, MMP-9 & Substance P Expression After Sub-Failure Stretch & MMP Inhibition

This appendix summarizes the immunolabeling and ELISA data acquired for the in vitro studies presented in Chapter 8. Data included in this appendix include those from the studies presented in Section 8.3 that utilized an equibiaxial sub-failure stretch, those from the studies presented in Section 8.4.1 that optimized the dosing regimen of the MMP inhibitor ilomastat using a bacterial collagenase exposure, and those from the studies presented in Section 8.4.2 that utilized equibiaxial sub-failure stretch with MMP inhibition. The immunolabeling data in this appendix are organized by whether gel samples underwent bacterial collagenase exposure (Section 8.4.1; Table L.1 and Figures L.1-L.3) or equibiaxial sub-failure stretch (Sections 8.3 and 8.4.2; Table L.2 and Figures L.4-L.8). Labels above each image within the figures list the gel sample number followed by the image number (e.g. "A1 – 01" indicates image 1 from gel sample A1); the image number in the labels matches the image numbers listed in the corresponding data table.

Table L.1 details the densitometry results for the MMP-1, MMP-9, and substance P immunolabeling data acquired for the ilomastat optimization dosing studies presented in Section 8.4.1. Experimental groups for those studies include co-cultures that received one of the five following treatment paradigms: (1) ilomastat daily and one hour before a

collagenase exposure (daily), (2) with every media change and one hour before a collagenase exposure (media Δ), (3) only one hour before a collagenase exposure (1hr before), (4) a sterile water vehicle (H2O veh), or (5) a DMSO vehicle (DMSO veh). Confocal images of MMP-1 (Figure L.1), MMP-9 (Figure L.2), and substance P (Figure L.3) that were acquired immediately following 20 minutes of exposure to bacterial collagenase are summarized in Figure L.1, Figure L.2, and Figure L.3, respectively. Gel samples were named based on their placement in a 24-well culture plate; as such, the gel sample identification numbers in Table L.1 and Figures L.1-L.3 consist of a letter (A-D) and a number (1-4) (e.g. A1). Confocal images were acquired for each co-culture gel in regions containing DRG soma, DRG axons, and in regions containing FLS cells and no DRGs. The amount of positive protein labeling was quantified using densitometry and a custom MATLAB script (Appendix B) for each image and each label separately. The maximum intensity projection of each stack was generated prior to quantification by densitometry for the FLS-localized images.

Table L.2 details the densitometry results for the MMP-1, MMP-9, and substance P immunolabeling data acquired for DRG-only or co-culture collagen gels subjected to equibiaxial sub-failure stretch presented in Sections 8.3 and 8.4.2. The corresponding force-displacement and strain data for those studies are detailed in Appendix K Experimental groups for the studies summarized in Section 8.3 include collagen gels seeded with only DRGs (DRG-only) or with DRGs and FLS cells (naïve) that underwent equibiaxial sub-failure stretch without MMP inhibition. Experimental groups for the studies summarized in Section 8.4.2 include several ilomastat dosing regimens given

before and/or after an equibiaxial sub-failure stretch: (1) DMSO vehicle at every dosing time (vehicle), (2) ilomastat one hour prior to stretch and DMSO five minutes after the stretch (pre), (3) ilomastat only five minutes after the stretch (post), or (4) ilomastat at every dosing time (pre/post). Confocal images were acquired to quantify immunolabeling performed for MMP-1 (Figure L.4), MMP-9 (Figure L.5), or substance P (Figure L.6) in DRG soma and/or axons in both of those studies. Separate confocal images were acquired in regions with FLS cells to measure FLS-localized protein expression of MMP-1 and MMP-9 and are summarized in Figure L.7 and Figure L.8, respectively. The amount of positive labeling was quantified using densitometry and the custom MATLAB script in Appendix B. For each image, MMP-1, MMP-9, and substance P were normalized to DAPI to account for different cell densities in each image, and then normalized to the unloaded control gel, separately for each label. Protein outcomes in the neuronal images for the studies presented in Section 8.4.2 were further binarized based on whether they were acquired in elements that sustained maximum principal strains (MPS) below or above 11.7% strain, the threshold for increasing phosphorylated ERK and collagen matrix reorganization in stretched neuron-collagen cultures (Zhang et al. 2016). As such, Table L.2 details the elemental MPS that corresponds to each image and includes whether that strain was above (a) or below (b) the 11.7% strain threshold.

Table L.3 summarizes the quantification for secreted MMP-1 levels measured using ELISA in the culture media (media) and trapped within the collagen gel (gel homogenate) in the studies that are presented in Section 8.3. For ELISA assays, culture media was sampled 24 hours after the sub-failure stretch. Gels were also homogenized at

that same time after stretch according to the kit protocol of the manufacturer (Sensolyte Plus 520 MMP-1 Assay Kit; Anaspec). MMP-1 values were quantified using a standard curve ranging from 20-0.625ng that was optimized for the range of MMP-1 concentrations expected in cell culture media; those data are summarized in Table L.3 in picograms/mL.

Table L.1. Densitometry of MMP-1, MMP-9, and substance P in DRGs and FLS cells from ilomastat inhibitor dosing studies using bacterial collagenase exposure (Section 8.4.1)

Corresponding Studies	Sample ID	Group	image no.	anatomy	MMP-1 (% positive pixels)	MMP-9 (% positive pixels)	substance P (% positive pixels)
Section 8.4.1	A1	daily	1	DRG axon	6.44%	11.50%	0.85%
Section 8.4.1	A1	daily	2	DRG axon	2.52%	6.60%	0.51%
Section 8.4.1	A1	daily	3	DRG axon	2.53%	5.11%	0.69%
Section 8.4.1	A1	daily	4	DRG soma	4.77%	6.74%	0.37%
Section 8.4.1	A1	daily	5	DRG soma	2.92%	0.37%	2.38%
Section 8.4.1	A1	daily	6	FLS	5.63%	4.01%	
Section 8.4.1	A1	daily	7	FLS	5.83%	4.55%	
Section 8.4.1	A2	media Δ	1	DRG axon	2.79%	3.61%	0.23%
Section 8.4.1	A2	media Δ	2	DRG axon	3.91%	1.17%	0.11%
Section 8.4.1	A2	media Δ	3	DRG axon	8.15%	2.71%	0.70%
Section 8.4.1	A2	media Δ	4	DRG soma	3.69%	0.37%	0.81%
Section 8.4.1	A2	media Δ	5	DRG soma	1.44%	0.15%	1.43%
Section 8.4.1	A2	media Δ	6	FLS	3.05%	6.22%	
Section 8.4.1	A2	media Δ	7	FLS	4.07%	8.94%	
Section 8.4.1	A3	1hr before	1	DRG axon	3.26%	5.05%	1.12%
Section 8.4.1	A3	1hr before	2	DRG axon	6.24%	2.29%	0.60%
Section 8.4.1	A3	1hr before	3	DRG axon	20.46%	6.05%	7.09%
Section 8.4.1	A3	1hr before	4	DRG soma	3.53%	6.64%	2.58%
Section 8.4.1	A3	1hr before	5	DRG soma	5.29%	0.47%	12.11%
Section 8.4.1	A3	1hr before	6	FLS	6.12%	4.29%	
Section 8.4.1	A3	1hr before	7	FLS	7.41%	3.53%	
Section 8.4.1	A4	H_2O veh	1	DRG axon	6.57%	3.58%	1.84%
Section 8.4.1	A4	H_2O veh	2	DRG axon	6.68%	12.85%	2.04%
Section 8.4.1	A4	H_2O veh	3	DRG axon	17.84%	9.73%	5.63%
Section 8.4.1	A4	H_2O veh	4	DRG soma	2.39%	0.06%	7.30%
Section 8.4.1	A4	H_2O veh	5	DRG soma	19.59%	2.84%	10.31%
Section 8.4.1	A4	H_2O veh	6	FLS	7.29%	4.89%	
Section 8.4.1	A4	H_2O veh	7	FLS	3.99%	2.93%	
Section 8.4.1	B1	media Δ	1	DRG axon	3.46%	1.23%	0.31%
Section 8.4.1	B1	media Δ	2	DRG axon	6.69%	0.96%	0.36%
Section 8.4.1	B1	media Δ	3	DRG axon	9.11%	0.93%	1.45%
Section 8.4.1	B1	media Δ	4	DRG soma	2.72%	0.27%	1.65%
Section 8.4.1	B1	media Δ	5	DRG soma	4.64%	1.01%	4.49%
Section 8.4.1	B1	media Δ	6	FLS	3.42%	5.13%	
Section 8.4.1	B1	media Δ	7	FLS	10.38%	3.24%	
Section 8.4.1	B2	daily	1	DRG axon	6.53%	3.88%	0.56%
Section 8.4.1	B2	daily	2	DRG axon	10.68%	1.51%	0.35%
Section 8.4.1	B2	daily	3	DRG axon	20.51%	5.08%	9.70%
Section 8.4.1	B2	daily	4	DRG soma	8.21%	0.44%	2.30%
Section 8.4.1	B2	daily	5	DRG soma	4.34%	3.80%	1.74%
Section 8.4.1	B2	daily	6	FLS	6.54%	2.00%	
Section 8.4.1	B2	daily	7	FLS	1.26%	1.95%	

DRG: dorsal root ganglia; FLS: fibroblast-like synoviocyte
N/A data were not collected due to technical problems with data capture
Shaded cells indicate where data were not quantified because FLS do not express substance P

Note: Table is continued on the next page.

Table L.1. continued

Corresponding Studies	Sample ID	Group	image no.	anatomy	MMP-1 (% positive pixels)	MMP-9 (% positive pixels)	substance P (% positive pixels)
Section 8.4.1	B3	H_2O veh	1	DRG axon	5.86%	3.40%	0.45%
Section 8.4.1	B3	H_2O veh	2	DRG axon	7.34%	1.20%	0.20%
Section 8.4.1	B3	H_2O veh	3	DRG axon	6.58%	0.50%	0.40%
Section 8.4.1	B3	H_2O veh	4	DRG soma	10.19%	0.39%	2.65%
Section 8.4.1	B3	H_2O veh	5	DRG soma	6.71%	0.23%	4.22%
Section 8.4.1	B3	H_2O veh	6	FLS	5.21%	2.12%	
Section 8.4.1	B3	H_2O veh	7	FLS	12.39%	2.90%	
Section 8.4.1	B4	1hr before	1	DRG axon	3.93%	1.74%	0.16%
Section 8.4.1	B4	1hr before	2	DRG axon	9.79%	2.26%	0.43%
Section 8.4.1	B4	1hr before	3	DRG axon	9.19%	8.04%	6.17%
Section 8.4.1	B4	1hr before	4	DRG soma	2.45%	2.92%	0.97%
Section 8.4.1	B4	1hr before	5	DRG soma	12.81%	0.24%	0.50%
Section 8.4.1	B4	1hr before	6	FLS	5.24%	8.23%	
Section 8.4.1	B4	1hr before	7	FLS	14.17%	4.09%	
Section 8.4.1	C1	1hr before	1	DRG axon	5.26%	2.29%	0.19%
Section 8.4.1	C1	1hr before	2	DRG axon	7.65%	2.76%	0.56%
Section 8.4.1	C1	1hr before	3	DRG axon	8.90%	1.96%	0.51%
Section 8.4.1	C1	1hr before	4	DRG soma	9.08%	0.82%	1.89%
Section 8.4.1	C1	1hr before	5	DRG soma	7.27%	0.49%	1.23%
Section 8.4.1	C1	1hr before	6	FLS	4.92%	1.46%	
Section 8.4.1	C1	1hr before	7	FLS	4.77%	1.91%	
Section 8.4.1	C2	H_2O veh	1	DRG axon	5.10%	8.62%	1.64%
Section 8.4.1	C2	H_2O veh	2	DRG axon	3.55%	3.67%	0.30%
Section 8.4.1	C2	H_2O veh	3	DRG axon	7.88%	2.54%	0.94%
Section 8.4.1	C2	H_2O veh	4	DRG soma	10.58%	1.20%	2.13%
Section 8.4.1	C2	H_2O veh	5	DRG soma	8.79%	0.71%	2.05%
Section 8.4.1	C2	H_2O veh	6	FLS	3.83%	1.94%	
Section 8.4.1	C2	H_2O veh	7	FLS	2.07%	0.68%	
Section 8.4.1	C3	daily	1	DRG axon	6.22%	3.27%	0.45%
Section 8.4.1	C3	daily	2	DRG axon	4.65%	11.41%	0.29%
Section 8.4.1	C3	daily	3	DRG axon	7.90%	6.99%	1.23%
Section 8.4.1	C3	daily	4	DRG soma	7.66%	2.37%	2.02%
Section 8.4.1	C3	daily	5	DRG soma	2.71%	0.80%	1.74%
Section 8.4.1	C3	daily	6	FLS	1.29%	1.49%	
Section 8.4.1	C3	daily	7	FLS	1.70%	3.23%	
Section 8.4.1	C4	media Δ	1	DRG axon	8.65%	0.77%	0.10%
Section 8.4.1	C4	media Δ	2	DRG axon	5.62%	3.76%	0.19%
Section 8.4.1	C4	media Δ	3	DRG axon	13.09%	0.74%	0.43%
Section 8.4.1	C4	media Δ	4	DRG soma	4.01%	0.17%	0.41%
Section 8.4.1	C4	media Δ	5	DRG soma	8.22%	0.70%	1.14%
Section 8.4.1	C4	media Δ	6	FLS	7.33%	4.15%	
Section 8.4.1	C4	media Δ	7	FLS	7.41%	5.00%	
Section 8.4.1	D1	H_2O veh	1	DRG axon	4.57%	4.42%	0.42%

DRG: dorsal root ganglia; FLS: fibroblast-like synoviocyte
N/A data were not collected due to technical problems with data capture
Shaded cells indicate where data were not quantified because FLS do not express substance P

Note: Table is continued on the next page.

Table L.1. continued

Corresponding Studies	Sample ID	Group	image no.	anatomy	MMP-1 (% positive pixels)	MMP-9 (% positive pixels)	substance P (% positive pixels)
Section 8.4.1	D1	H_2O veh	2	DRG axon	10.59%	10.40%	6.22%
Section 8.4.1	D1	H_2O veh	3	DRG axon	24.18%	4.86%	4.68%
Section 8.4.1	D1	H_2O veh	4	DRG soma	1.96%	0.20%	0.37%
Section 8.4.1	D1	H_2O veh	5	DRG soma	19.88%	1.86%	0.75%
Section 8.4.1	D1	H_2O veh	6	FLS	0.90%	1.56%	
Section 8.4.1	D2	1hr before	1	DRG axon	10.77%	3.94%	0.62%
Section 8.4.1	D2	1hr before	2	DRG axon	12.75%	2.24%	0.40%
Section 8.4.1	D2	1hr before	3	DRG axon	10.69%	3.10%	2.60%
Section 8.4.1	D2	1hr before	4	DRG soma	31.42%	5.90%	9.86%
Section 8.4.1	D2	1hr before	5	DRG soma	5.45%	0.41%	0.62%
Section 8.4.1	D2	1hr before	6	FLS	0.20%	2.84%	
Section 8.4.1	D2	1hr before	7	FLS	6.56%	1.58%	
Section 8.4.1	D3	media Δ	1	DRG axon	3.65%	1.99%	0.10%
Section 8.4.1	D3	media Δ	2	DRG axon	6.14%	0.86%	0.04%
Section 8.4.1	D3	media Δ	3	DRG axon	8.47%	0.19%	0.08%
Section 8.4.1	D3	media Δ	4	DRG soma	5.30%	1.33%	1.72%
Section 8.4.1	D3	media Δ	5	DRG soma	8.08%	0.32%	0.34%
Section 8.4.1	D3	media Δ	6	FLS	0.45%	2.15%	
Section 8.4.1	D3	media Δ	7	FLS	0.62%	2.81%	
Section 8.4.1	D4	daily	1	DRG axon	10.76%	0.78%	0.46%
Section 8.4.1	D4	daily	2	DRG axon	3.80%	7.19%	0.84%
Section 8.4.1	D4	daily	3	DRG axon	11.59%	17.92%	5.88%
Section 8.4.1	D4	daily	4	DRG soma	4.33%	0.27%	0.94%
Section 8.4.1	D4	daily	5	DRG soma	7.44%	1.70%	1.17%
Section 8.4.1	D4	daily	6	FLS	11.37%	2.49%	
Section 8.4.1	D4	daily	7	FLS	7.52%	3.83%	
Section 8.4.1	A2	media Δ	1	DRG axon	28.37%	0.98%	0.25%
Section 8.4.1	A2	media Δ	2	DRG axon	26.89%	0.40%	0.26%
Section 8.4.1	A2	media Δ	3	DRG axon	42.32%	1.88%	0.44%
Section 8.4.1	A2	media Δ	4	DRG soma	56.61%	0.67%	1.77%
Section 8.4.1	A2	media Δ	5	DRG soma	74.08%	0.11%	0.16%
Section 8.4.1	A2	media Δ	6	FLS	4.22%	4.98%	
Section 8.4.1	A2	media Δ	7	FLS	N/A	1.96%	
Section 8.4.1	B2	DMSO veh	1	DRG axon	5.51%	10.64%	0.32%
Section 8.4.1	B2	DMSO veh	2	DRG axon	13.42%	10.78%	1.96%
Section 8.4.1	B2	DMSO veh	3	DRG axon	7.46%	7.22%	0.12%
Section 8.4.1	B2	DMSO veh	4	DRG soma	25.65%	15.45%	1.83%
Section 8.4.1	B2	DMSO veh	5	DRG soma	63.21%	22.56%	6.02%
Section 8.4.1	B2	DMSO veh	6	FLS	3.44%	1.61%	
Section 8.4.1	B2	DMSO veh	7	FLS	0.49%	1.01%	
Section 8.4.1	B3	media Δ	1	DRG axon	1.12%	0.08%	0.08%
Section 8.4.1	B3	media Δ	2	DRG axon	4.16%	0.13%	0.16%
Section 8.4.1	B3	media Δ	3	DRG axon	0.70%	0.09%	0.02%
Section 8.4.1	B3	media Δ	4	DRG soma	5.84%	0.05%	0.57%
Section 8.4.1	B3	media Δ	5	DRG soma	0.46%	0.08%	0.49%
Section 8.4.1	B3	media Δ	6	DRG soma	9.07%	0.12%	0.55%
Section 8.4.1	B3	media Δ	7	FLS	1.08%	1.95%	
Section 8.4.1	B3	media Δ	8	FLS	4.40%	3.12%	

Figure L.1. Immunolabeling of MMP-1 in DRGs and FLS cells from ilomastat inhibitor dosing studies using bacterial collagenase exposure as designated in Table L.1 (Section 8.4.1)

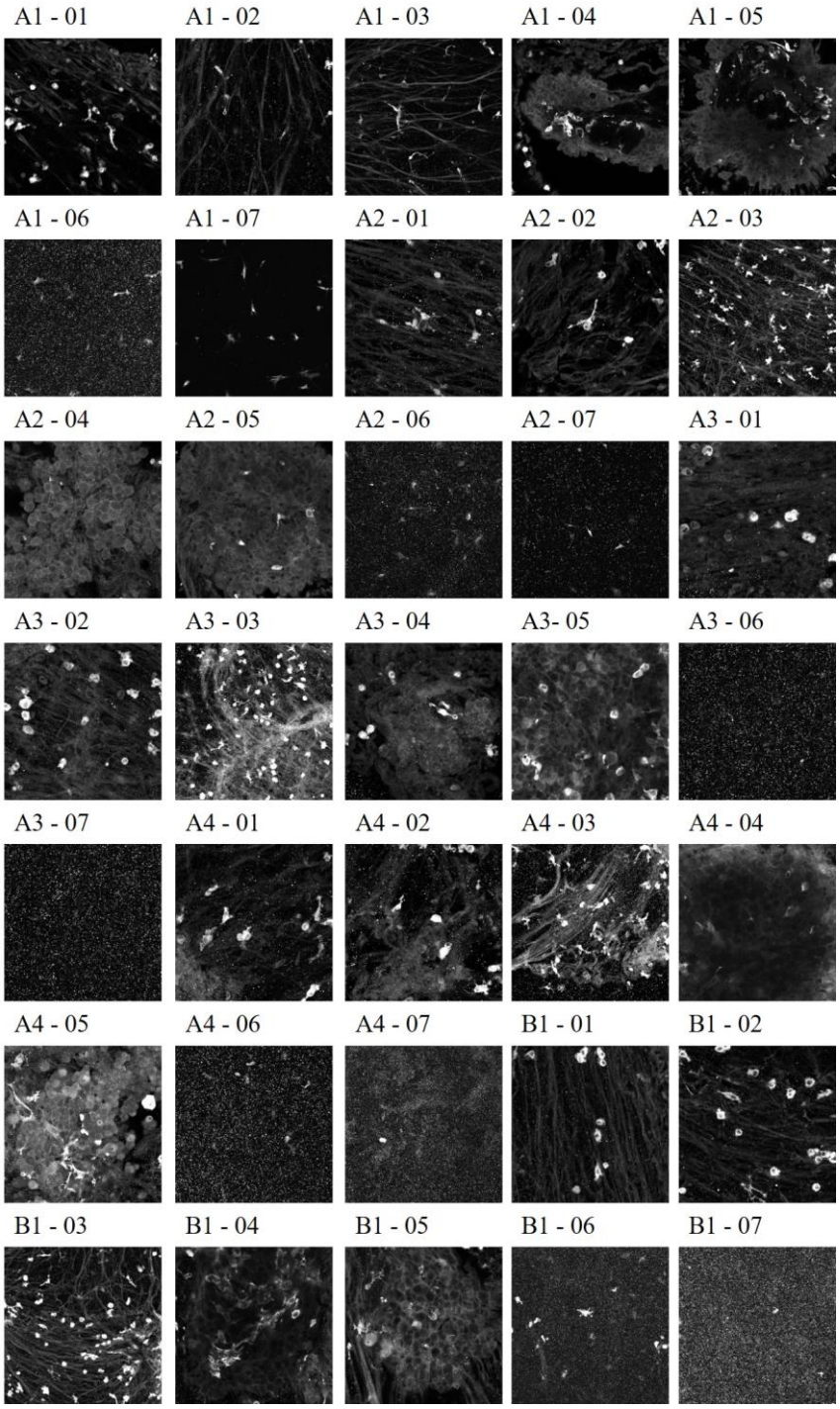

Note: Figure is continued on the next page.

Figure L.1. continued

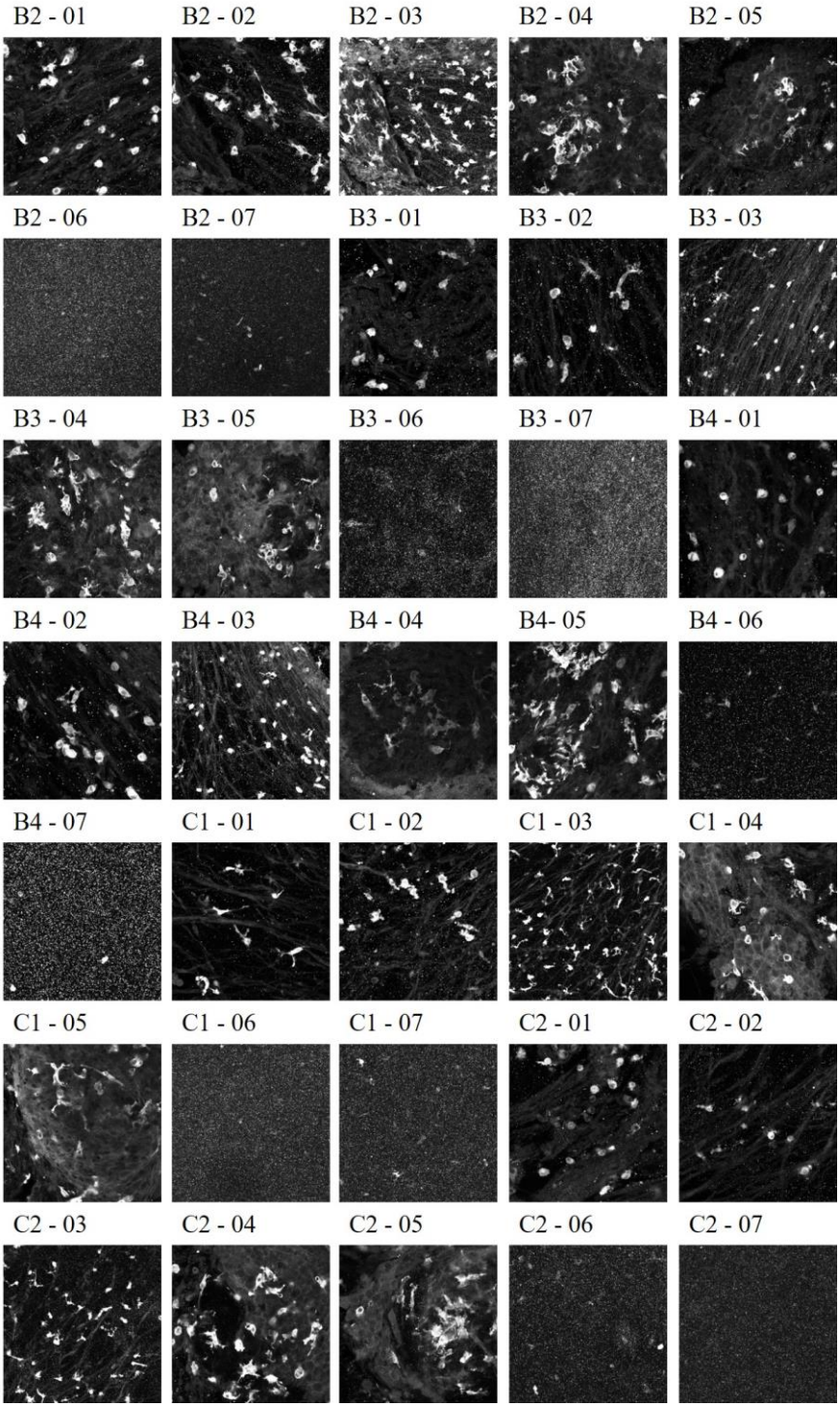

Note: Figure is continued on the next page.

Figure L.1. continued

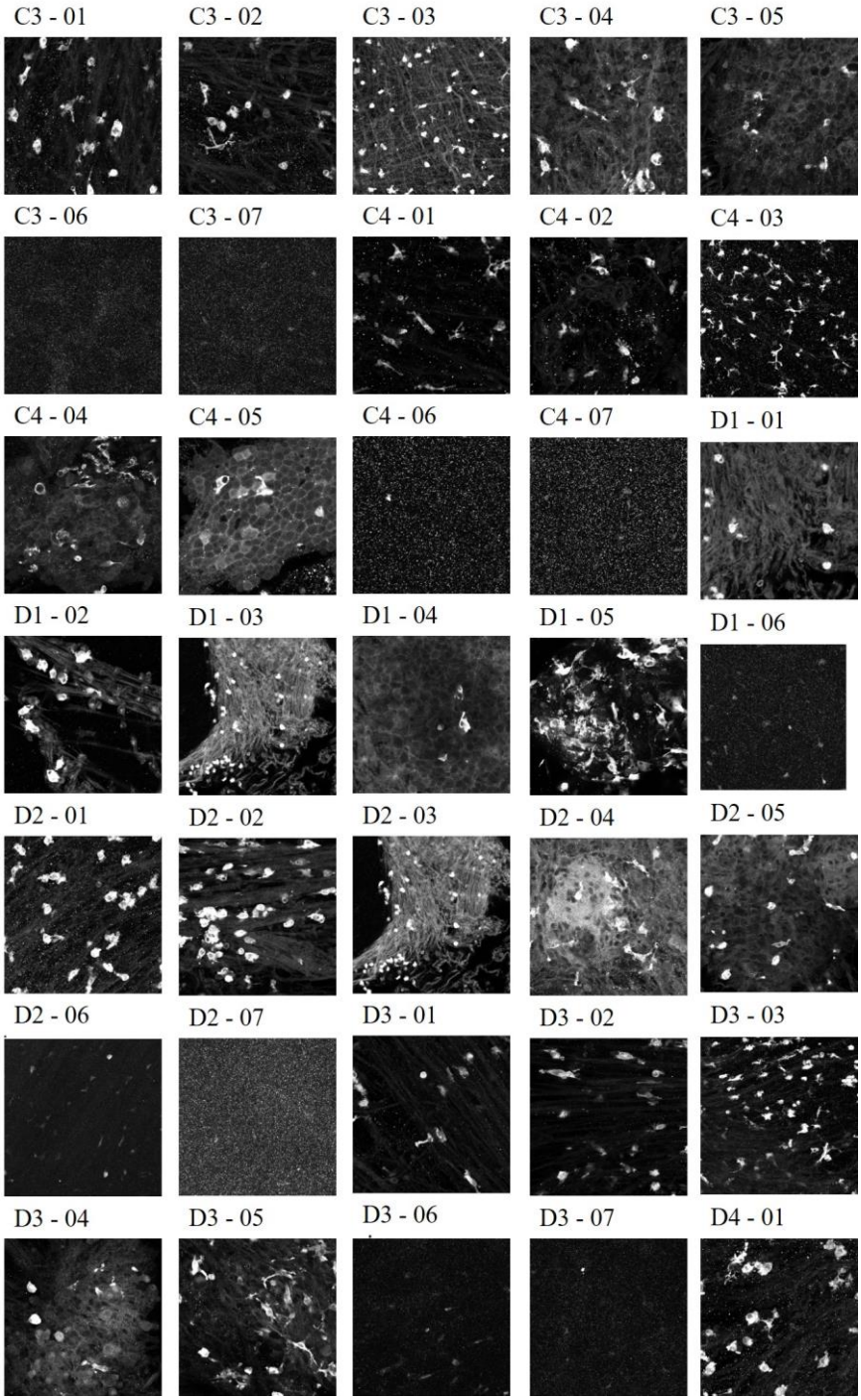

Note: Figure is continued on the next page.

Figure L.1. continued

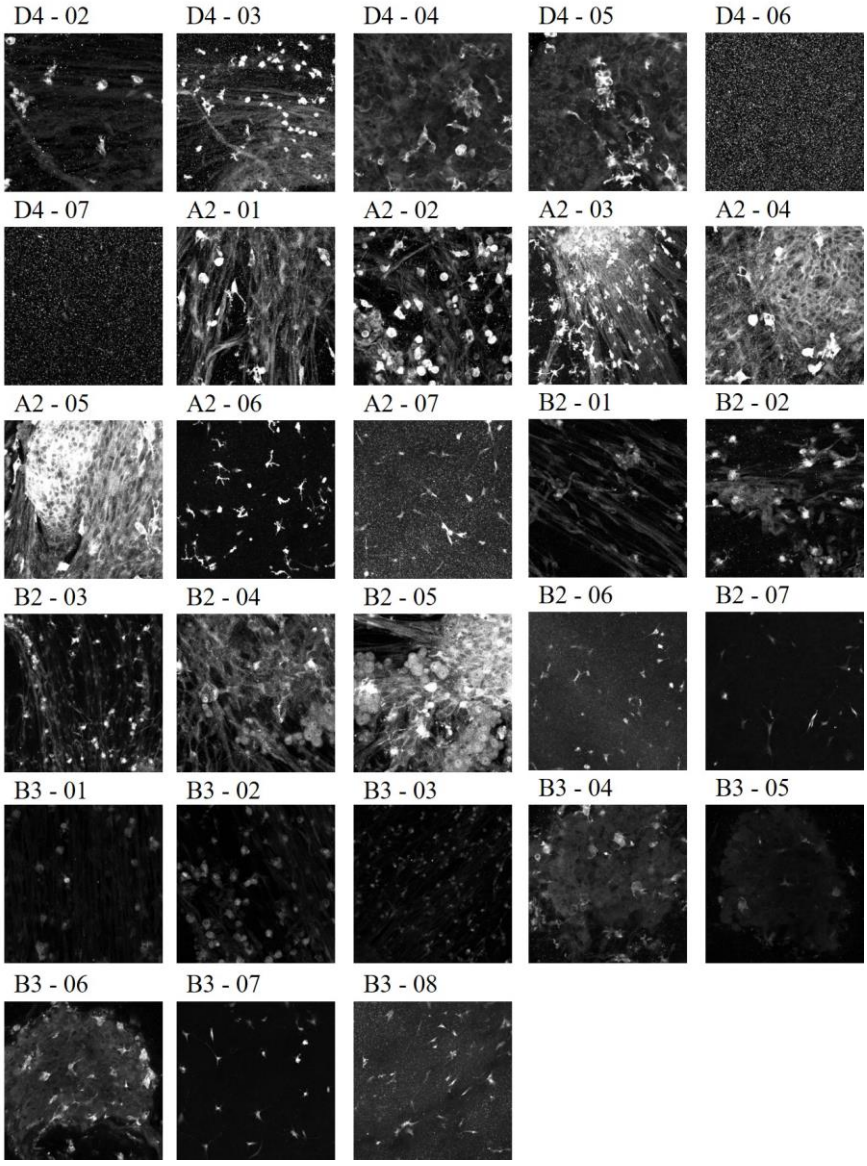

Figure L.2. Immunolabeling of MMP-9 in DRGs and FLS cells from ilomastat inhibitor dosing studies using bacterial collagenase exposure as designated in Table L.1 (Section 8.4.1)

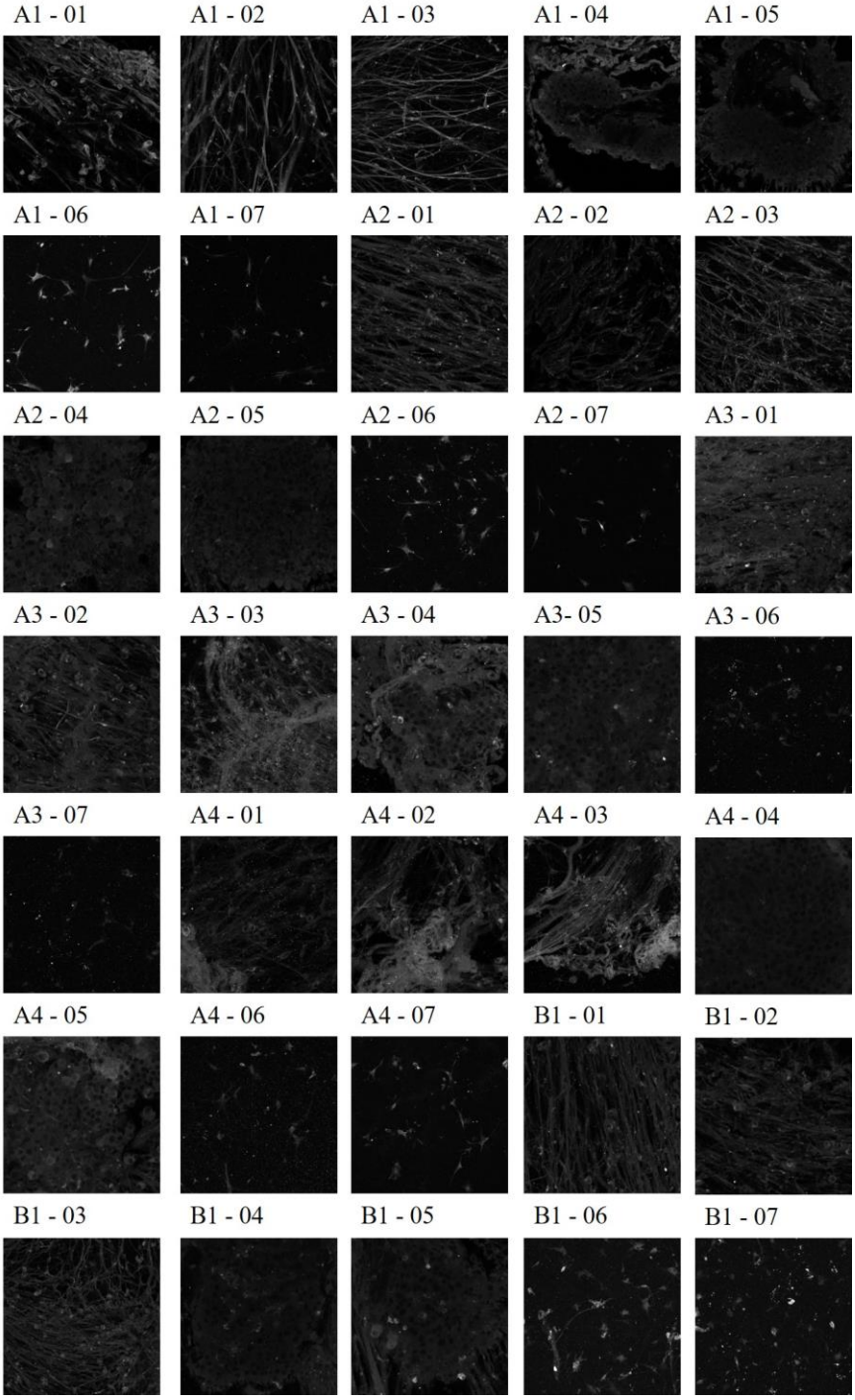

Note: Figure is continued on the next page.

Figure L.2. continued

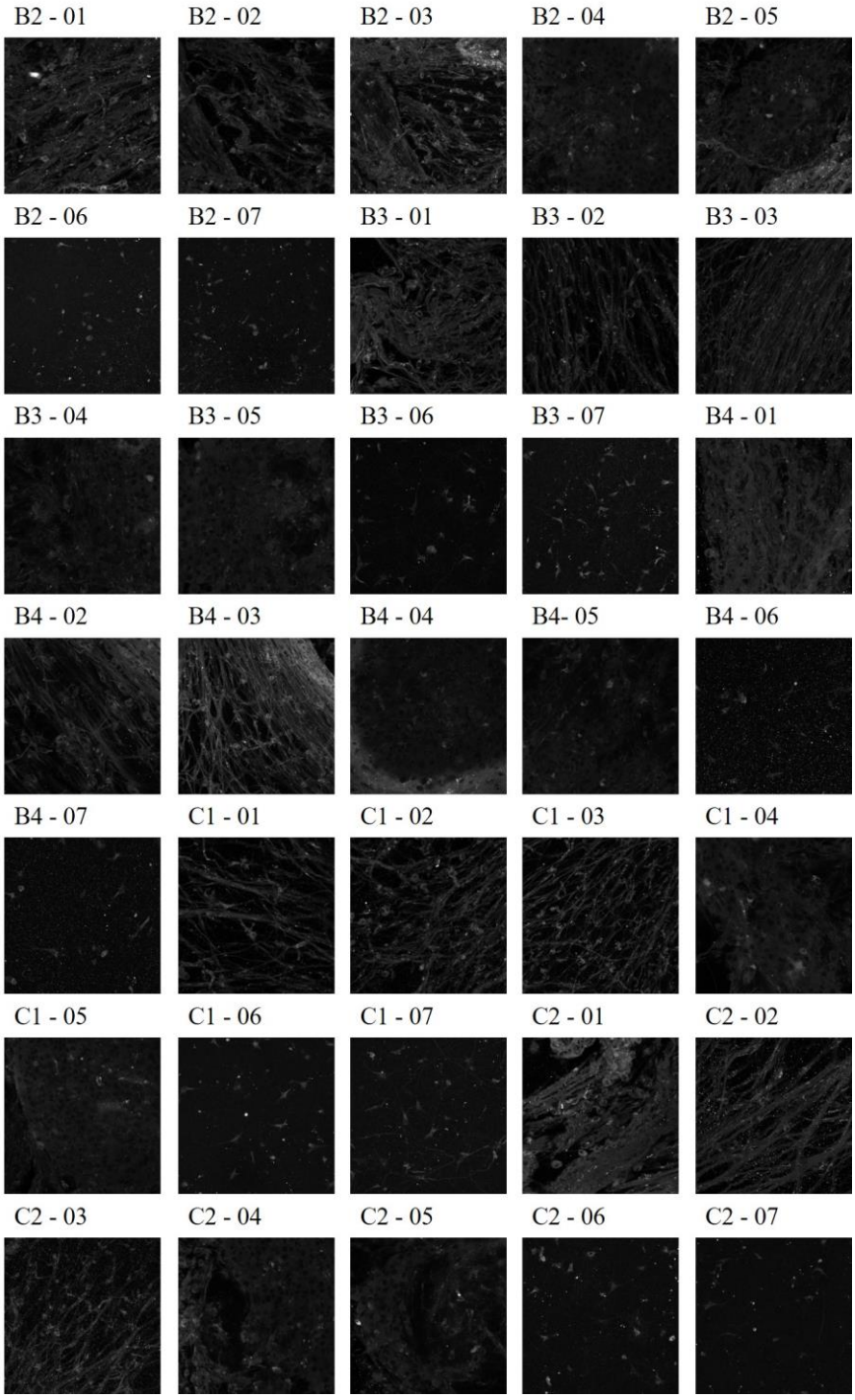

Note: Figure is continued on the next page.

Figure L.2. continued

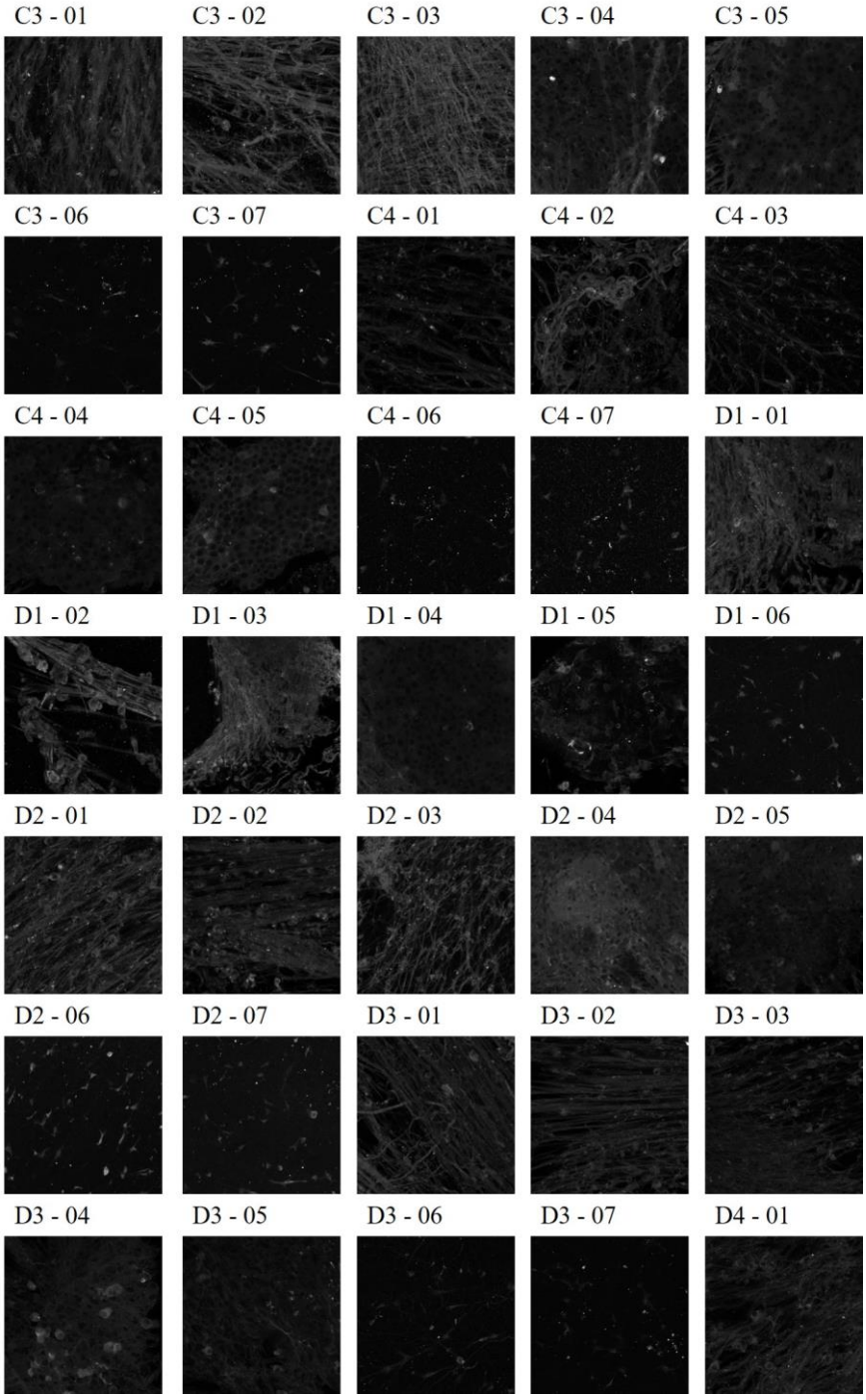

Note: Figure is continued on the next page.

Figure L.2. continued

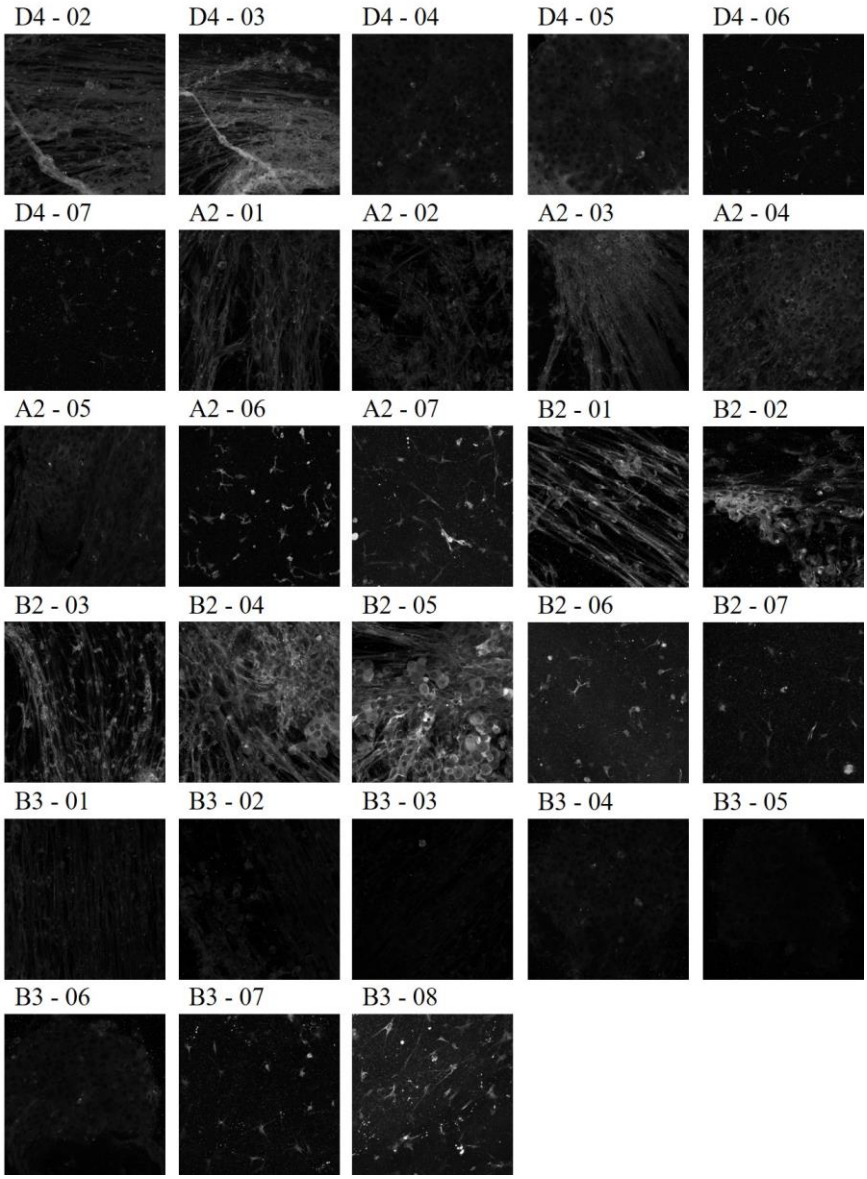

Figure L.3. Immunolabeling of substance P in DRGs and FLS cells from ilomastat inhibitor dosing studies using bacterial collagenase exposure as designated in Table L.1 (Section 8.4.1)

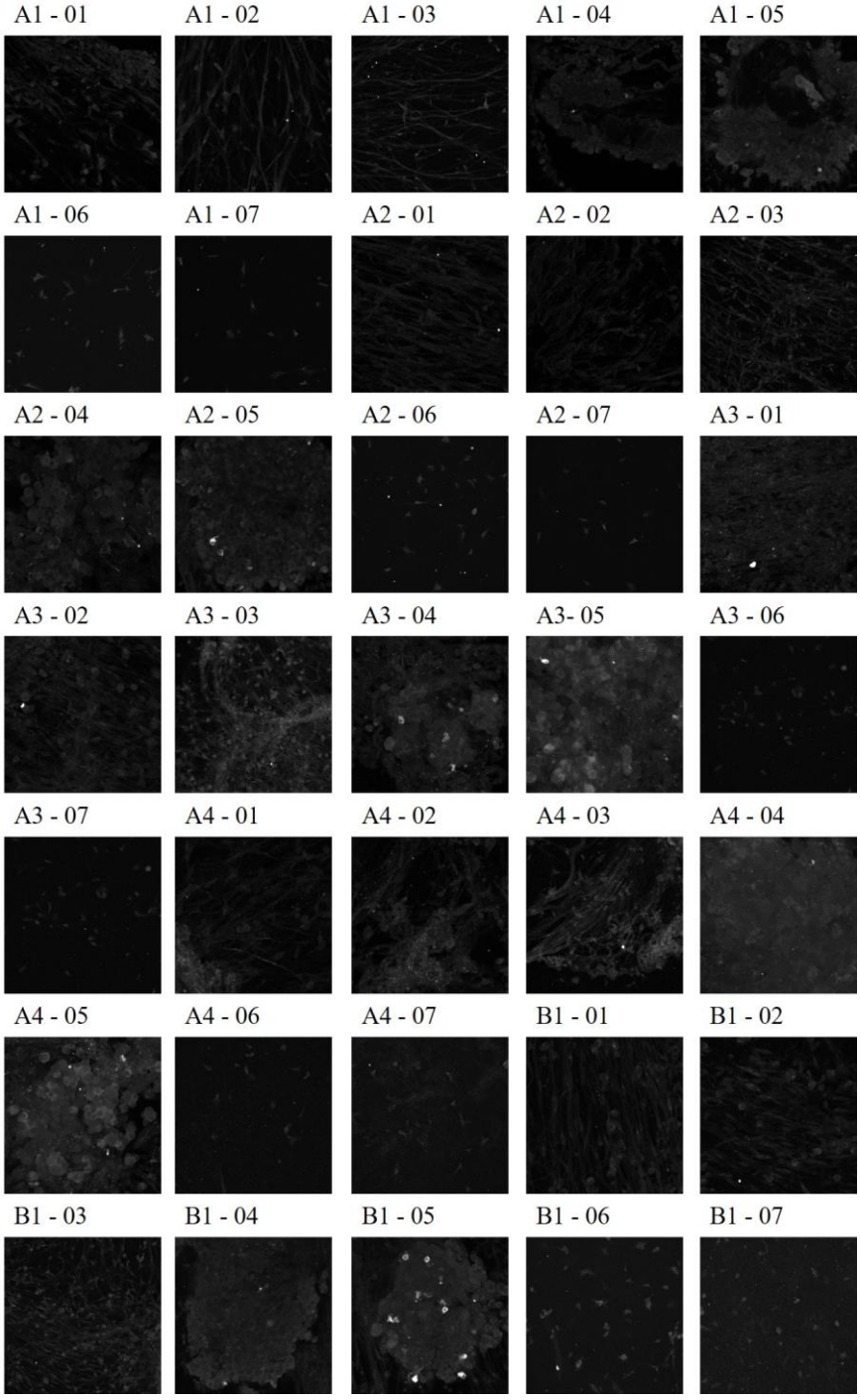

Note: Figure is continued on the next page.

Figure L.3. continued

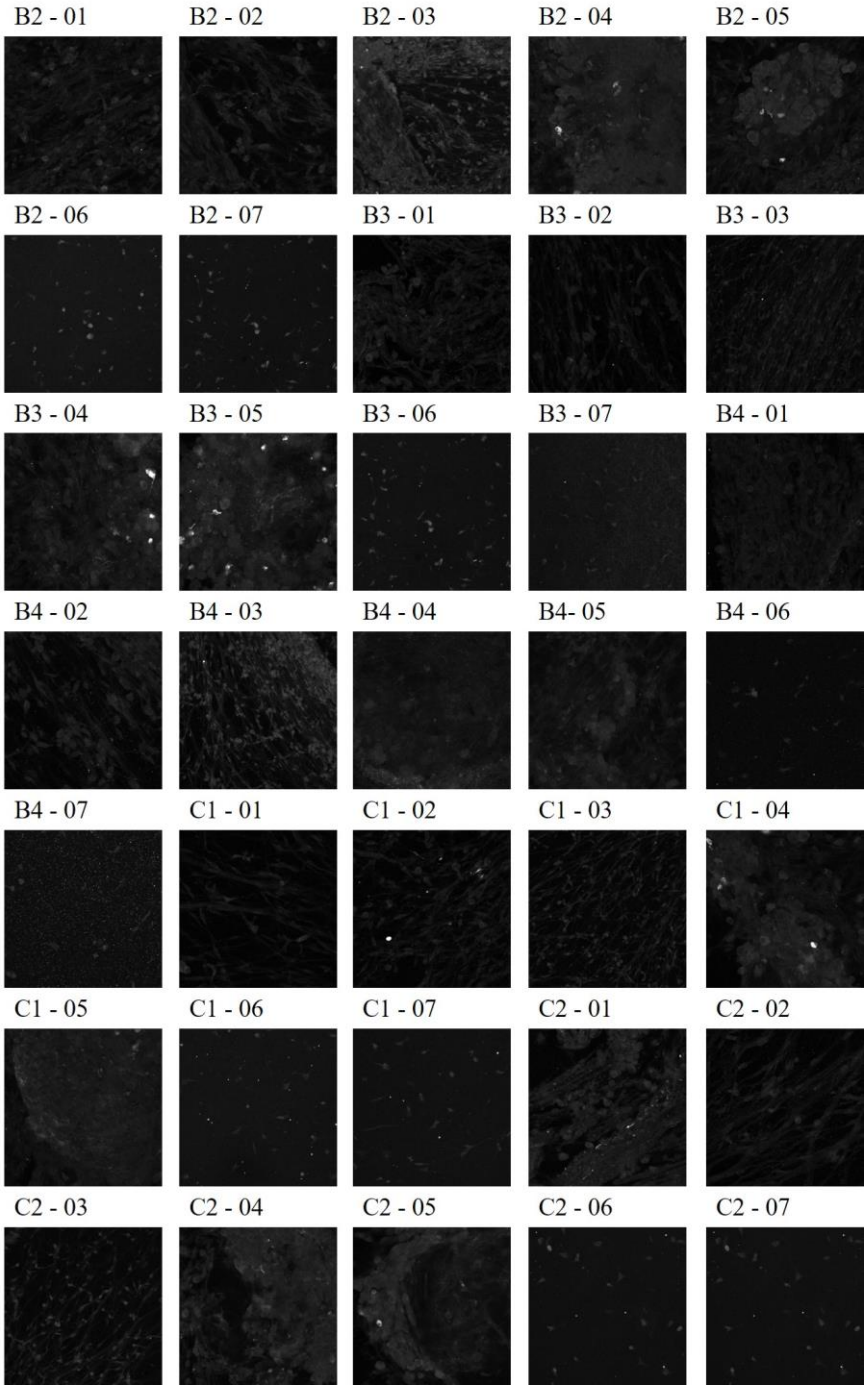

Note: Figure is continued on the next page.

Figure L.3. continued

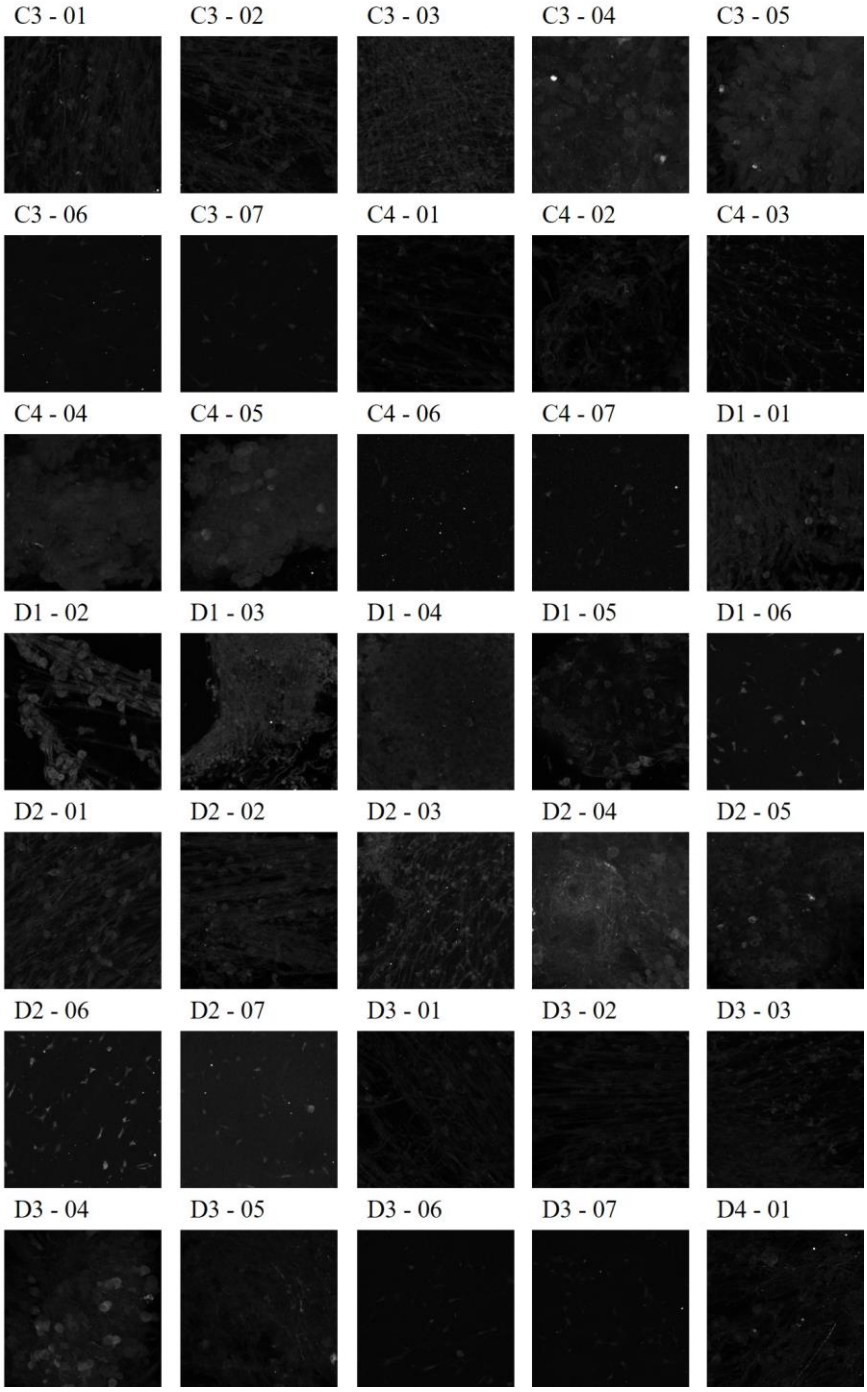

Note: Figure is continued on the next page.

Figure L.3. continued

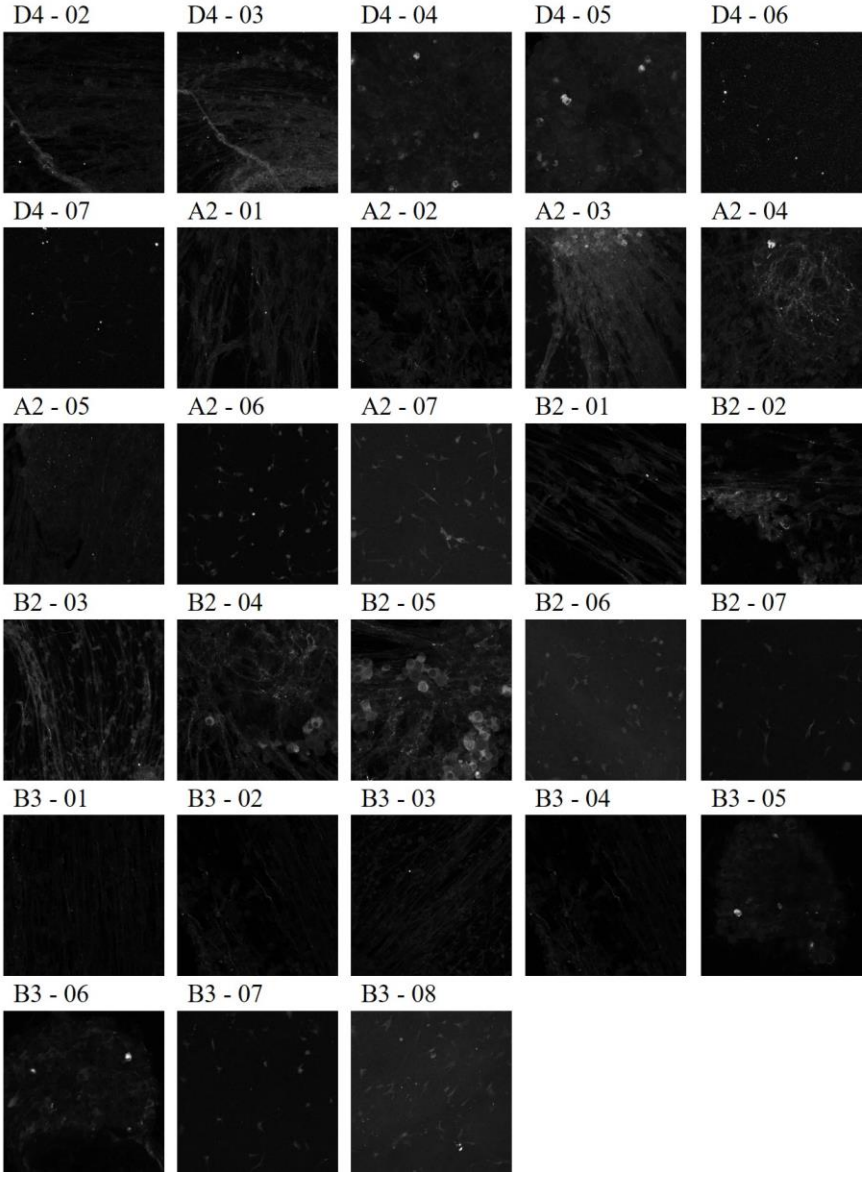

Table L.2. Densitometry of MMP-1, MMP-9, and substance P in DRGs and FLS cells at 24 hours after equibiaxial sub-failure stretch (Sections 8.3 and 8.4.2)

Corresponding Studies	Sample ID	image no.	Group	MMP-1	MMP-9	substance P	strain	threshold
Section 8.3	E5-S01	1	DRG only	0.56	0.34	0.20	NC	NC
Section 8.3	E5-S01	2	DRG only	0.11	0.03	0.23	NC	NC
Section 8.3	E5-S01	3	DRG only	0.39	0.31	0.52	NC	NC
Section 8.3	E5-S01	4	DRG only	0.38	0.22	0.07	NC	NC
Section 8.3	E5-S03	1	naïve	1.92	0.32	0.93	NC	NC
Section 8.3	E5-S03	2	naïve	2.25	0.18	0.11	NC	NC
Section 8.3	E5-S03	3	naïve	0.47	0.37	0.24	NC	NC
Section 8.3	E5-S03	4	naïve	3.15	12.73	4.42	NC	NC
Section 8.3	E5-S03	5	naïve	2.64	2.55	12.76	NC	NC
Section 8.3	E5-S05	1	DRG only	19.54	15.82	2.49	NC	NC
Section 8.3	E5-S05	2	DRG only	56.88	45.84	3.97	NC	NC
Section 8.3	E5-S05	3	DRG only	38.44	43.72	0.94	NC	NC
Section 8.3	E5-S05	4	DRG only	5.86	9.41	8.35	NC	NC
Section 8.3	E5-S05	5	DRG only	91.08	39.81	4.47	NC	NC
Section 8.3	E5-S08	1	naïve	0.43	0.46	1.05	NC	NC
Section 8.3	E5-S08	2	naïve	0.46	1.46	2.27	NC	NC
Section 8.3	E5-S08	3	naïve	0.64	1.52	2.16	NC	NC
Section 8.3	E5-S08	4	naïve	1.12	1.79	2.31	NC	NC
Section 8.3	E5-S08	5	naïve	0.55	0.68	0.70	NC	NC
Section 8.3	E5-S08	6	naïve	0.81	1.57	20.83	NC	NC
Section 8.3	E5-S08	7	naïve	1.27	2.14	1.57	NC	NC
Section 8.3	E5-S09	1	naïve	0.71	0.12	0.40	NC	NC
Section 8.3	E5-S09	2	naïve	1.23	0.66	0.40	NC	NC
Section 8.3	E5-S09	3	naïve	0.51	2.16	1.41	NC	NC
Section 8.3	E5-S09	4	naïve	0.70	0.86	1.63	NC	NC
Section 8.3	E5-S09	5	naïve	0.48	0.48	0.88	NC	NC
Section 8.3	E5-S09	6	naïve	0.74	0.75	1.30	NC	NC
Section 8.3	E5-S11	1	DRG only	0.01	0.86	0.69	NC	NC
Section 8.3	E5-S11	2	DRG only	0.02	0.09	0.46	NC	NC
Section 8.3	E5-S11	3	DRG only	0.02	0.05	0.42	NC	NC
Section 8.3	E5-S11	4	DRG only	0.12	0.54	0.66	NC	NC
Section 8.3	E5-S11	5	DRG only	6.36	37.70	9.75	NC	NC
Section 8.3	E5-S11	6	DRG only	0.13	3.39	1.06	NC	NC
Section 8.3	E5-S13	1	naïve	0.88	1.04	1.13	NC	NC
Section 8.3	E5-S13	2	naïve	0.90	0.32	0.73	NC	NC
Section 8.3	E5-S13	3	naïve	0.05	0.01	0.19	NC	NC
Section 8.3	E5-S13	4	naïve	0.19	0.20	0.67	NC	NC
Section 8.3	E5-S13	5	naïve	1.15	1.44	4.45	NC	NC
Section 8.3	E5-S15	1	DRG only	0.10	1.87	10.53	NC	NC
Section 8.3	E5-S15	2	DRG only	0.18	3.02	2.77	NC	NC
Section 8.3	E5-S15	3	DRG only	0.87	0.54	0.85	NC	NC
Section 8.3	E5-S15	4	DRG only	3.26	0.88	2.88	NC	NC
Section 8.3	E5-S15	5	DRG only	1.32	3.43	10.71	NC	NC
Section 8.3	E5-S18	1	naïve	0.85	0.48	0.34	NC	NC
Section 8.3	E5-S18	2	naïve	1.18	1.08	1.05	NC	NC
Section 8.3	E5-S18	3	naïve	1.20	1.20	2.44	NC	NC
Section 8.3	E5-S18	4	naïve	4.10	3.72	4.92	NC	NC

DRG: dorsal root ganglia; FLS: fibroblast-like synoviocyte; a: above; b: below
N/A data were not collected due to technical problems with data capture
NC: not collected during imaging acquisition; protein values are fold-change over unstretched control

Note: Table is continued on the next page.

Table L.2. continued

Corresponding Studies	Sample ID	image no.	Group	MMP-1	MMP-9	substance P	strain	threshold
Section 8.3	E5-S18	5	naïve	1.24	1.25	2.34	NC	NC
Section 8.3	E5-S18	6	naïve	1.77	1.24	1.50	NC	NC
Section 8.3	E5-S19	1	DRG only	0.85	1.02	0.15	NC	NC
Section 8.3	E5-S19	2	DRG only	0.54	1.04	0.75	NC	NC
Section 8.3	E5-S19	3	DRG only	1.10	1.05	0.46	NC	NC
Section 8.3	E5-S19	4	DRG only	0.09	0.43	0.20	NC	NC
Section 8.3	E5-S19	5	DRG only	0.48	0.17	0.15	NC	NC
Section 8.4.2	S09	1	pre	1.05	0.52	0.34	6.7%	b
Section 8.4.2	S09	2	pre	1.13	0.77	0.89	6.7%	b
Section 8.4.2	S09	3	pre	0.69	0.20	0.41	6.7%	b
Section 8.4.2	S09	4	pre	1.46	0.37	1.87	10.1%	b
Section 8.4.2	S09	5	pre	0.69	0.12	0.11	6.1%	b
Section 8.4.2	S09	6	pre	1.50	0.14	0.26	6.1%	b
Section 8.4.2	S10	1	pre/post	1.10	0.26	0.98	4.8%	b
Section 8.4.2	S10	2	pre/post	0.61	0.01	0.14	25.9%	a
Section 8.4.2	S10	3	pre/post	0.57	0.03	0.18	25.9%	a
Section 8.4.2	S10	4	pre/post	0.87	1.82	2.01	25.9%	a
Section 8.4.2	S10	5	pre/post	1.09	2.09	3.16	25.9%	a
Section 8.4.2	S10	6	pre/post	1.51	0.22	0.07	4.8%	b
Section 8.4.2	S11	1	pre	2.30	1.68	2.39	16.7%	a
Section 8.4.2	S11	2	pre	2.84	0.71	0.10	17.8%	a
Section 8.4.2	S11	3	pre	3.94	1.02	1.11	16.5%	a
Section 8.4.2	S11	4	pre	1.02	3.53	0.05	16.5%	a
Section 8.4.2	S11	5	pre	2.01	0.90	0.98	14.5%	a
Section 8.4.2	S11	6	pre	1.92	1.19	0.10	12.0%	a
Section 8.4.2	S14	1	pre/post	0.91	0.23	0.15	9.1%	b
Section 8.4.2	S14	2	pre/post	0.67	0.04	0.07	7.2%	b
Section 8.4.2	S14	3	pre/post	0.63	0.71	0.37	7.7%	b
Section 8.4.2	S14	4	pre/post	0.49	0.04	0.03	5.0%	b
Section 8.4.2	S14	5	pre/post	0.77	0.27	0.57	10.9%	b
Section 8.4.2	S14	6	pre/post	0.85	0.23	0.22	8.4%	b
Section 8.4.2	S17	1	pre	1.11	7.57	4.45	7.6%	b
Section 8.4.2	S17	2	pre	1.09	12.08	7.03	19.8%	a
Section 8.4.2	S17	3	pre	0.71	9.45	11.11	17.3%	a
Section 8.4.2	S17	4	pre	0.63	2.30	0.17	7.6%	b
Section 8.4.2	S17	5	pre	0.97	6.34	1.53	12.4%	a
Section 8.4.2	S17	6	pre	1.12	8.28	3.01	12.4%	a
Section 8.4.2	S20	1	pre/post	3.28	16.48	3.29	19.7%	a
Section 8.4.2	S20	2	pre/post	1.34	30.34	1.41	7.7%	b
Section 8.4.2	S20	3	pre/post	1.69	31.53	0.31	10.0%	b
Section 8.4.2	S20	4	pre/post	2.19	22.03	1.48	7.7%	b
Section 8.4.2	S20	5	pre/post	1.89	15.89	0.31	19.7%	a
Section 8.4.2	S21	1	pre	1.00	0.15	0.59	14.8%	a
Section 8.4.2	S21	2	pre	1.16	0.38	0.24	16.0%	a
Section 8.4.2	S21	3	pre	0.98	0.59	0.40	16.0%	a
Section 8.4.2	S21	4	pre	0.94	0.16	0.62	14.3%	a
Section 8.4.2	S21	5	pre	1.11	0.30	0.43	16.0%	a

DRG: dorsal root ganglia; FLS: fibroblast-like synoviocyte; a: above; b: below
N/A data were not collected due to technical problems with data capture
NC: not collected during imaging acquisition; protein values are fold-change over unstretched control

Note: Table is continued on the next page.

Table L.2. continued

Corresponding Studies	Sample ID	image no.	Group	MMP-1	MMP-9	substance P	strain	threshold
Section 8.4.2	S21	6	pre	0.30	0.70	0.08	12.7%	a
Section 8.4.2	S24	1	pre/post	1.28	0.14	0.63	8.5%	b
Section 8.4.2	S24	2	pre/post	0.38	1.55	0.65	8.7%	b
Section 8.4.2	S24	3	pre/post	0.97	1.04	0.50	7.6%	b
Section 8.4.2	S24	4	pre/post	0.21	5.62	0.18	7.6%	b
Section 8.4.2	S24	5	pre/post	1.14	0.50	0.44	3.6%	b
Section 8.4.2	S24	6	pre/post	1.16	0.43	1.20	3.6%	b
Section 8.4.2	S27	1	pre/post	0.94	1.64	13.64	12.7%	a
Section 8.4.2	S27	2	pre/post	0.94	1.03	9.29	13.6%	a
Section 8.4.2	S27	3	pre/post	1.03	0.68	10.13	13.6%	a
Section 8.4.2	S27	4	pre/post	0.78	1.21	9.75	13.6%	a
Section 8.4.2	S27	5	pre/post	0.82	0.44	12.80	13.6%	a
Section 8.4.2	S27	6	pre/post	1.45	0.29	14.81	5.7%	b
Section 8.4.2	S28	1	post	0.94	0.05	0.35	12.0%	a
Section 8.4.2	S28	2	post	0.86	0.17	0.23	14.2%	a
Section 8.4.2	S28	3	post	0.73	0.68	0.37	16.4%	a
Section 8.4.2	S28	4	post	0.94	0.23	0.41	16.4%	a
Section 8.4.2	S28	5	post	1.11	2.45	0.33	12.0%	a
Section 8.4.2	S28	6	post	0.94	0.28	0.61	12.0%	a
Section 8.4.2	S30	1	pre/post	0.66	0.74	0.02	8.2%	b
Section 8.4.2	S30	2	pre/post	0.62	0.19	0.04	6.9%	b
Section 8.4.2	S30	3	pre/post	0.56	0.03	0.02	6.9%	b
Section 8.4.2	S30	4	pre/post	0.57	0.26	0.09	8.2%	b
Section 8.4.2	S30	5	pre/post	0.60	0.14	0.04	8.1%	b
Section 8.4.2	S30	6	pre/post	0.71	0.23	0.20	11.4%	a
Section 8.4.2	S33	1	pre/post	5.93	0.38	0.59	4.9%	b
Section 8.4.2	S33	2	pre/post	4.44	0.20	0.81	17.2%	a
Section 8.4.2	S33	3	pre/post	5.86	0.86	3.03	17.2%	a
Section 8.4.2	S33	4	pre/post	4.81	0.35	1.70	1.5%	b
Section 8.4.2	S33	5	pre/post	1.68	3.42	0.19	1.5%	b
Section 8.4.2	S33	6	pre/post	2.28	4.61	0.15	1.5%	b
Section 8.4.2	S34	1	post	5.80	1.71	8.89	7.0%	b
Section 8.4.2	S34	2	post	15.56	3.45	24.95	8.1%	b
Section 8.4.2	S34	3	post	7.62	3.90	2.50	8.1%	b
Section 8.4.2	S34	4	post	16.61	1.45	28.32	7.5%	b
Section 8.4.2	S34	5	post	18.23	7.93	15.88	8.5%	b
Section 8.4.2	S34	6	post	15.53	4.43	11.10	9.4%	b
Section 8.4.2	S36	1	post	0.74	0.17	1.03	18.8%	a
Section 8.4.2	S36	2	post	0.81	0.57	1.12	8.1%	b
Section 8.4.2	S36	3	post	0.42	0.10	1.73	6.7%	b
Section 8.4.2	S36	4	post	0.44	0.22	0.99	6.7%	b
Section 8.4.2	S36	5	post	0.59	0.33	0.44	23.2%	a
Section 8.4.2	S36	6	post	1.30	1.84	1.38	7.9%	b
Section 8.4.2	S38	1	vehicle	0.96	0.11	0.41	13.0%	a
Section 8.4.2	S38	2	vehicle	1.14	0.03	0.68	9.6%	b
Section 8.4.2	S38	3	vehicle	0.55	0.09	0.57	8.8%	b
Section 8.4.2	S38	4	vehicle	0.37	0.01	0.18	2.4%	b

DRG: dorsal root ganglia; FLS: fibroblast-like synoviocyte; a: above; b: below
N/A data were not collected due to technical problems with data capture
NC: not collected during imaging acquisition; protein values are fold-change over unstretched control

Note: Table is continued on the next page.

Table L.2. continued

Corresponding Studies	Sample ID	image no.	Group	MMP-1	MMP-9	substance P	strain	threshold
Section 8.4.2	S38	5	vehicle	0.64	0.83	0.15	2.4%	b
Section 8.4.2	S38	6	vehicle	1.20	0.08	0.37	8.8%	b
Section 8.4.2	S41	1	pre	0.86	0.07	0.16	13.9%	a
Section 8.4.2	S41	2	pre	0.26	0.01	0.04	15.3%	a
Section 8.4.2	S41	3	pre	0.68	0.28	0.73	8.8%	b
Section 8.4.2	S41	4	pre	0.26	1.30	1.05	7.0%	b
Section 8.4.2	S41	5	pre	0.52	1.85	1.74	7.0%	b
Section 8.4.2	S41	6	pre	0.40	0.20	0.10	7.0%	b
Section 8.4.2	S43	1	vehicle	0.09	0.04	0.04	12.9%	a
Section 8.4.2	S43	2	vehicle	0.77	0.08	0.26	13.3%	a
Section 8.4.2	S43	3	vehicle	1.38	0.27	0.34	20.3%	a
Section 8.4.2	S43	4	vehicle	0.37	0.15	0.16	51.8%	a
Section 8.4.2	S43	5	vehicle	0.99	2.13	0.24	38.0%	a
Section 8.4.2	S43	6	vehicle	0.11	0.53	0.07	12.9%	a
Section 8.4.2	S44	1	pre	0.61	0.31	0.30	19.9%	a
Section 8.4.2	S44	2	pre	0.76	0.26	0.35	9.0%	b
Section 8.4.2	S44	3	pre	0.40	0.19	0.73	9.6%	b
Section 8.4.2	S44	4	pre	1.17	1.88	0.84	9.3%	b
Section 8.4.2	S44	5	pre	0.61	0.56	0.55	14.4%	a
Section 8.4.2	S44	6	pre	0.57	0.09	0.13	17.5%	a
Section 8.4.2	S46	1	vehicle	0.64	1.29	0.74	19.5%	a
Section 8.4.2	S46	2	vehicle	0.82	0.18	0.82	11.5%	a
Section 8.4.2	S46	3	vehicle	0.67	0.21	0.84	11.5%	a
Section 8.4.2	S46	4	vehicle	0.70	0.10	0.49	7.2%	b
Section 8.4.2	S46	5	vehicle	1.01	0.28	0.36	7.2%	b
Section 8.4.2	S46	6	vehicle	1.24	0.51	1.04	8.0%	b
Section 8.4.2	S49	1	pre	0.22	0.20	0.96	35.7%	a
Section 8.4.2	S49	2	pre	1.25	1.01	1.67	35.7%	a
Section 8.4.2	S49	3	pre	1.12	0.67	1.02	17.4%	a
Section 8.4.2	S49	4	pre	1.12	3.38	2.04	17.4%	a
Section 8.4.2	S49	5	pre	0.62	0.13	0.45	35.7%	a
Section 8.4.2	S49	6	pre	0.64	1.96	0.10	14.6%	a
Section 8.4.2	S50	1	vehicle	0.46	0.71	4.45	14.3%	a
Section 8.4.2	S50	2	vehicle	1.37	0.98	9.75	14.3%	a
Section 8.4.2	S50	3	vehicle	1.21	0.32	13.69	17.7%	a
Section 8.4.2	S50	4	vehicle	2.23	1.14	16.08	11.2%	b
Section 8.4.2	S50	5	vehicle	1.83	0.38	11.39	14.4%	a
Section 8.4.2	S50	6	vehicle	0.55	5.56	1.28	17.7%	a
Section 8.4.2	S53	1	post	0.21	0.02	0.09	8.7%	b
Section 8.4.2	S53	2	post	0.90	0.13	0.05	8.7%	b
Section 8.4.2	S53	3	post	0.44	0.14	0.39	8.7%	b
Section 8.4.2	S53	4	post	0.83	0.08	0.08	8.7%	b
Section 8.4.2	S54	1	vehicle	4.48	1.18	4.32	7.0%	b
Section 8.4.2	S54	2	vehicle	0.38	0.23	1.11	16.0%	a
Section 8.4.2	S54	3	vehicle	1.08	0.65	2.67	17.4%	a
Section 8.4.2	S54	4	vehicle	0.95	3.94	0.29	6.3%	b
Section 8.4.2	S54	5	vehicle	0.29	0.67	1.91	9.3%	b

DRG: dorsal root ganglia; FLS: fibroblast-like synoviocyte; a: above; b: below
N/A data were not collected due to technical problems with data capture
NC: not collected during imaging acquisition; protein values are fold-change over unstretched control

Note: Table is continued on the next page.

Table L.2. continued

Corresponding Studies	Sample ID	image no.	Group	MMP-1	MMP-9	substance P	strain	threshold
Section 8.4.2	S54	6	vehicle	0.36	0.49	2.21	9.3%	b
Section 8.4.2	S57	1	post	1.55	0.30	1.15	14.6%	a
Section 8.4.2	S57	2	post	0.66	0.14	6.56	14.6%	a
Section 8.4.2	S57	3	post	1.10	0.26	8.46	10.9%	b
Section 8.4.2	S57	4	post	0.79	0.24	7.23	10.9%	b
Section 8.4.2	S57	5	post	0.47	0.07	3.15	11.4%	a
Section 8.4.2	S57	6	post	0.71	0.77	1.02	11.4%	a
Section 8.4.2	S64	1	post	2.73	34.41	9.92	9.1%	b
Section 8.4.2	S64	2	post	2.74	13.08	8.51	6.5%	b
Section 8.4.2	S64	3	post	1.71	1.36	0.71	15.7%	a
Section 8.4.2	S64	4	post	1.29	0.41	0.21	15.7%	a
Section 8.4.2	S64	5	post	1.11	0.84	0.30	15.7%	a
Section 8.4.2	S64	6	post	1.97	1.49	3.09	15.7%	a
Section 8.4.2	S70	1	naïve	0.74	0.13	0.44	NC	NC
Section 8.4.2	S70	2	naïve	1.05	0.40	0.21	NC	NC
Section 8.4.2	S70	3	naïve	0.91	0.15	0.58	NC	NC
Section 8.4.2	S70	4	naïve	0.16	0.15	0.60	NC	NC
Section 8.4.2	S72	1	pre	1.50	1.41	0.30	17.3%	a
Section 8.4.2	S72	2	pre	0.46	0.73	0.07	17.3%	a
Section 8.4.2	S72	3	pre	2.22	1.65	0.43	17.3%	a
Section 8.4.2	S72	4	pre	1.62	1.17	0.36	17.3%	a
Section 8.4.2	S72	5	pre	1.86	0.48	1.11	12.7%	a
Section 8.4.2	S72	6	pre	2.00	1.24	0.46	17.3%	a
Section 8.3	E5-S03	FLS	naïve	3.85	2.22	6.25	NC	NC
Section 8.3	E5-S08	FLS	naïve	1.45	0.49	0.04	NC	NC
Section 8.3	E5-S18	FLS	naïve	0.78	1.40	0.84	NC	NC
Section 8.4.2	S09	FLS	pre	0.50	1.74	6.46	NC	NC
Section 8.4.2	S10	FLS	pre/post	0.40	0.89	6.54	NC	NC
Section 8.4.2	S11	FLS	pre	1.01	0.31	1.11	NC	NC
Section 8.4.2	S14	FLS-01	pre/post	1.48	0.60	0.94	NC	NC
Section 8.4.2	S14	FLS-02	pre/post	0.89	0.27	0.07	NC	NC
Section 8.4.2	S17	FLS	pre	0.60	5.58	2.09	NC	NC
Section 8.4.2	S30	FLS	pre/post	0.08	0.22	0.02	NC	NC
Section 8.4.2	S33	FLS	pre/post	3.43	2.26	15.58	NC	NC
Section 8.4.2	S36	FLS	post	0.18	0.23	0.87	NC	NC
Section 8.4.2	S38	FLS	vehicle	0.53	0.31	1.02	NC	NC
Section 8.4.2	S41	FLS	pre	0.35	0.78	#DIV/0!	NC	NC
Section 8.4.2	S43	FLS	vehicle	1.34	0.89	0.00	NC	NC
Section 8.4.2	S44	FLS	pre	1.12	0.67	1.24	NC	NC
Section 8.4.2	S50	FLS	vehicle	2.37	1.06	18.67	NC	NC
Section 8.4.2	S53	FLS	post	0.58	0.23	0.04	NC	NC
Section 8.4.2	S54	FLS	vehicle	0.30	0.27	0.01	NC	NC
Section 8.4.2	S57	FLS	post	0.58	0.40	6.92	NC	NC
Section 8.4.2	S64	FLS	post	1.07	4.64	0.48	NC	NC
Section 8.4.2	S70	FLS	naïve	1.66	0.76	1.51	NC	NC
Section 8.4.2	S72	FLS	pre	0.18	0.92	0.28	NC	NC

DRG: dorsal root ganglia; FLS: fibroblast-like synoviocyte; a: above; b: below
N/A data were not collected due to technical problems with data capture
NC: not collected during imaging acquisition; protein values are fold-change over unstretched control

Figure L.4. Immunolabeling of MMP-1 in DRGs at 24 hours after equibiaxial sub-failure stretch as designated in Table L.2 (Sections 8.3 and 8.4.2)

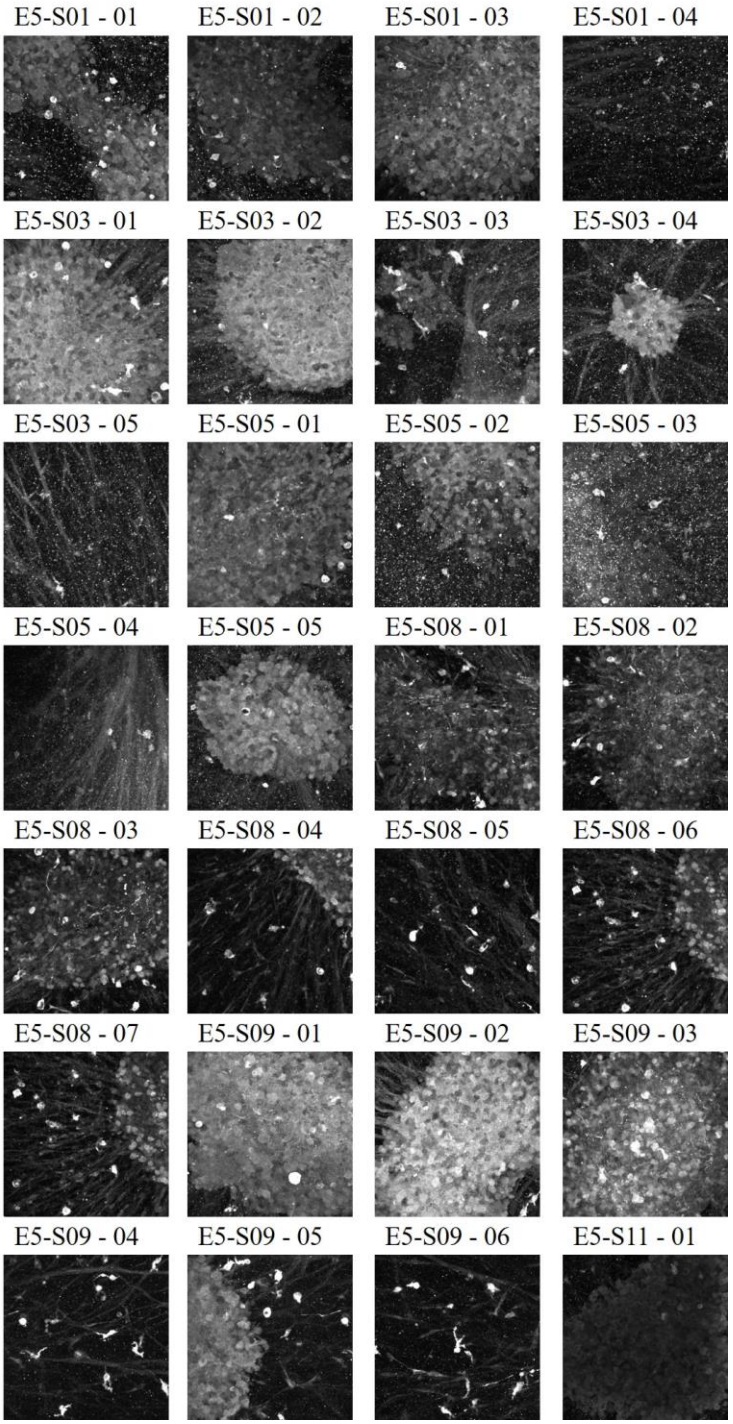

Note: Figure is continued on the next page.

Figure L.4. continued

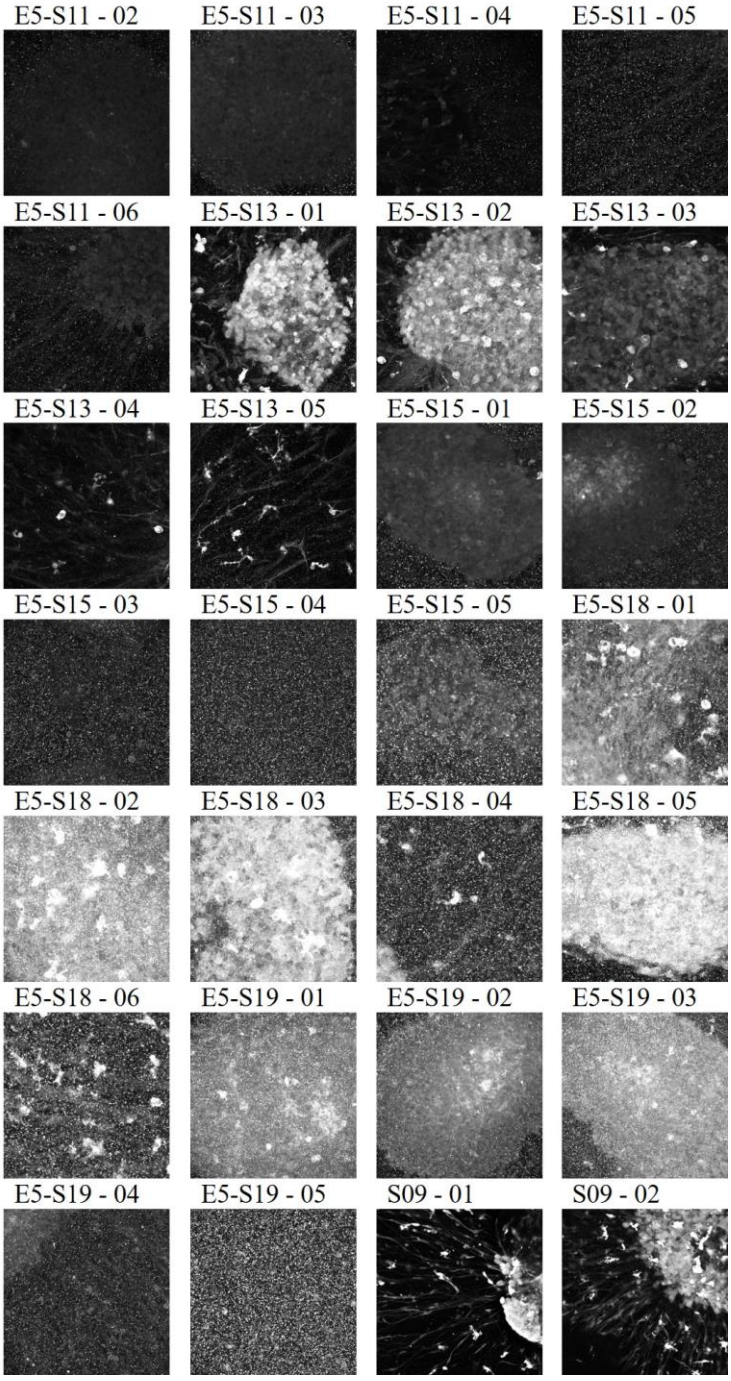

Note: Figure is continued on the next page.

Figure L.4. continued

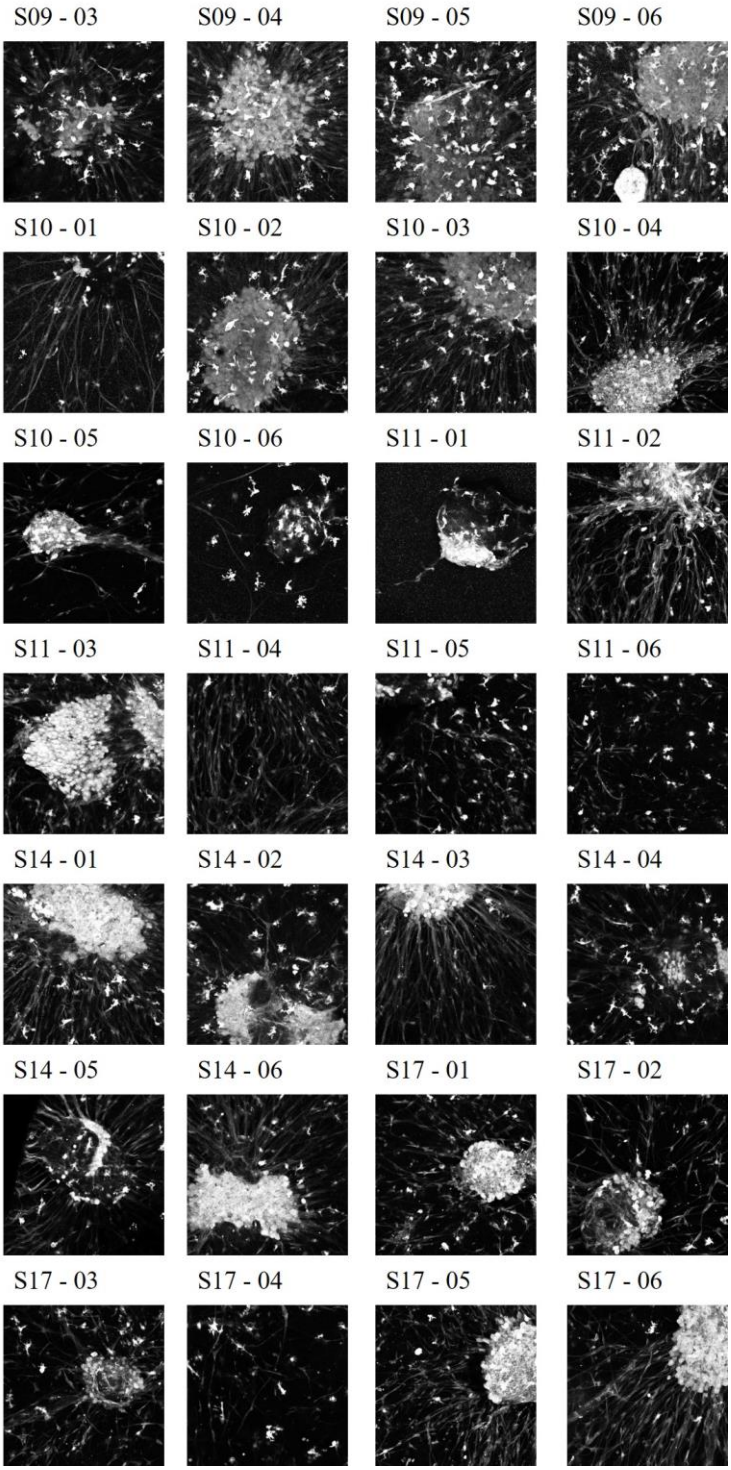

Note: Figure is continued on the next page.

Figure L.4. continued

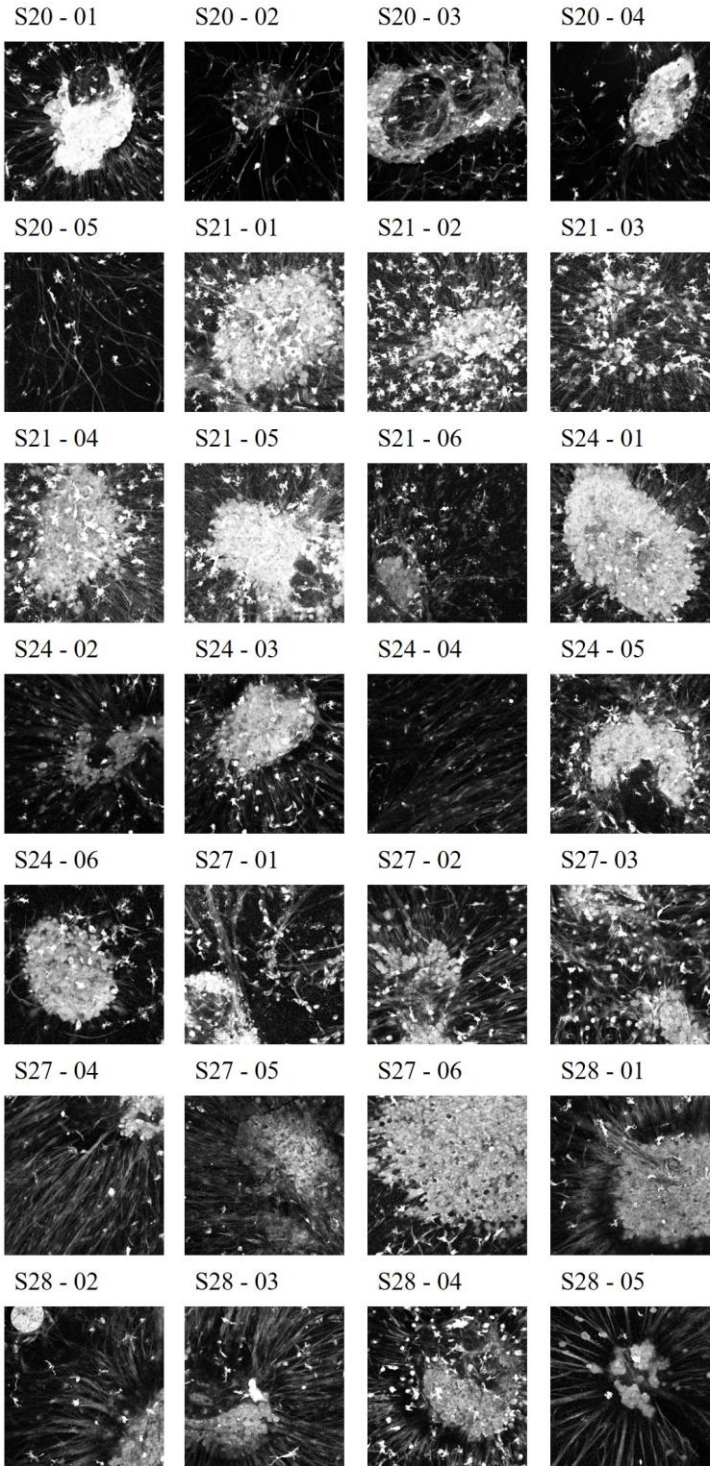

Note: Figure is continued on the next page.

Figure L.4. continued

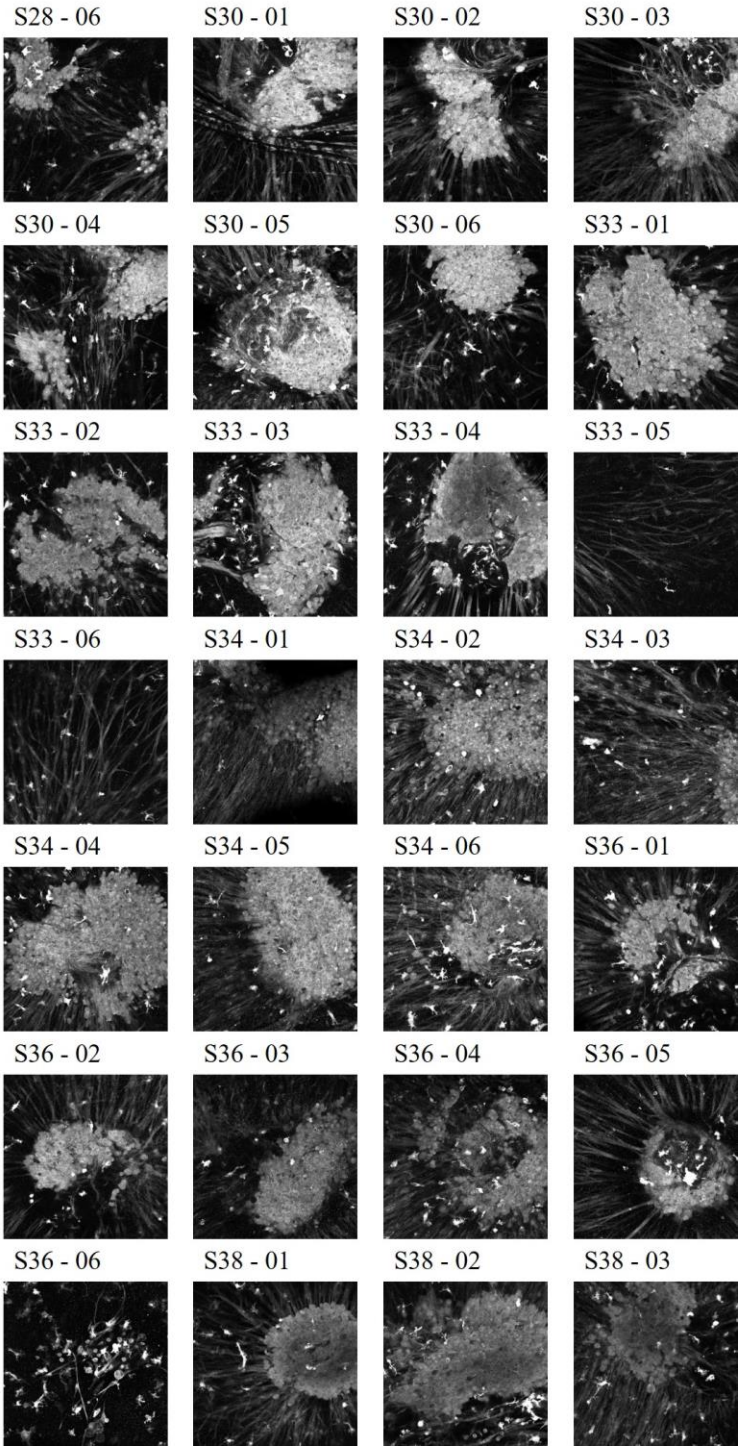

Note: Figure is continued on the next page.

Figure L.4. continued

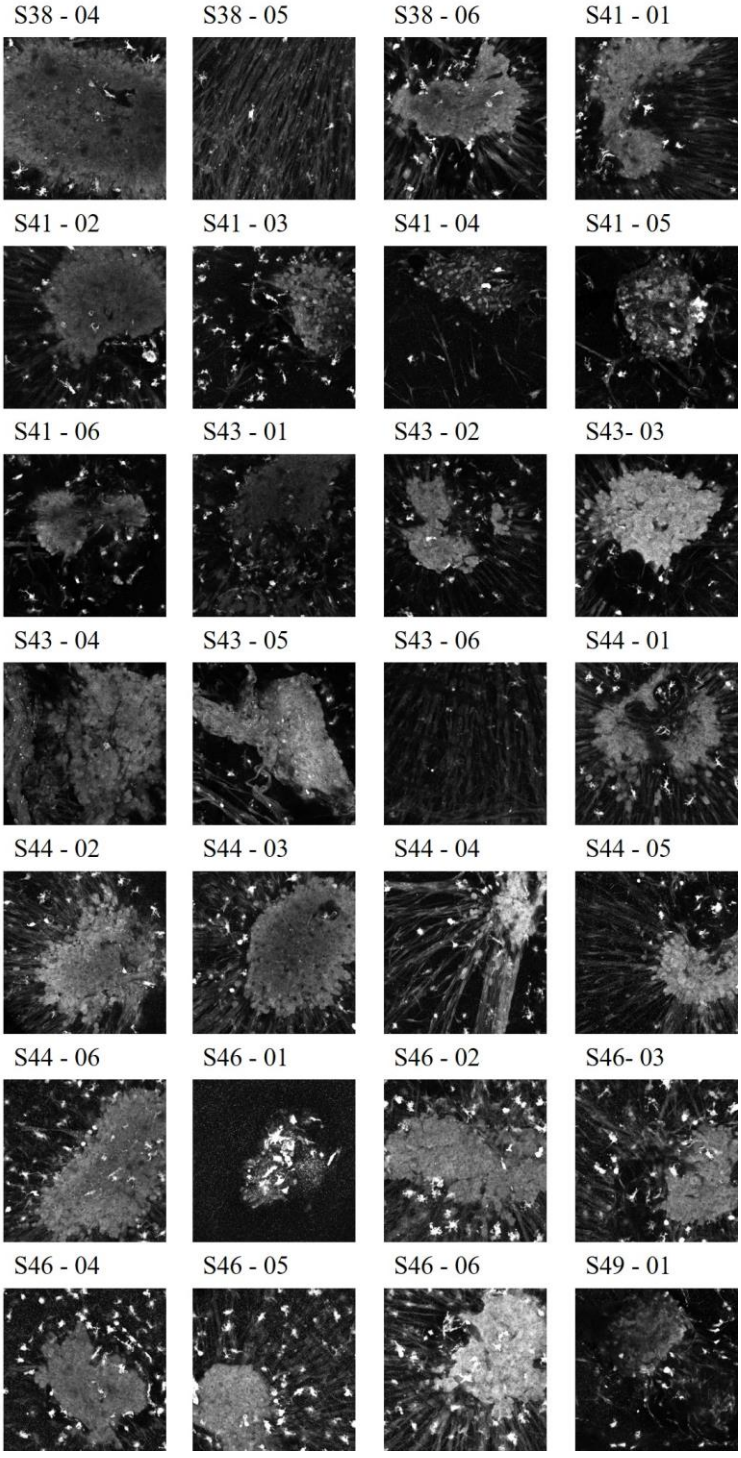

Note: Figure is continued on the next page.

Figure L.4. continued

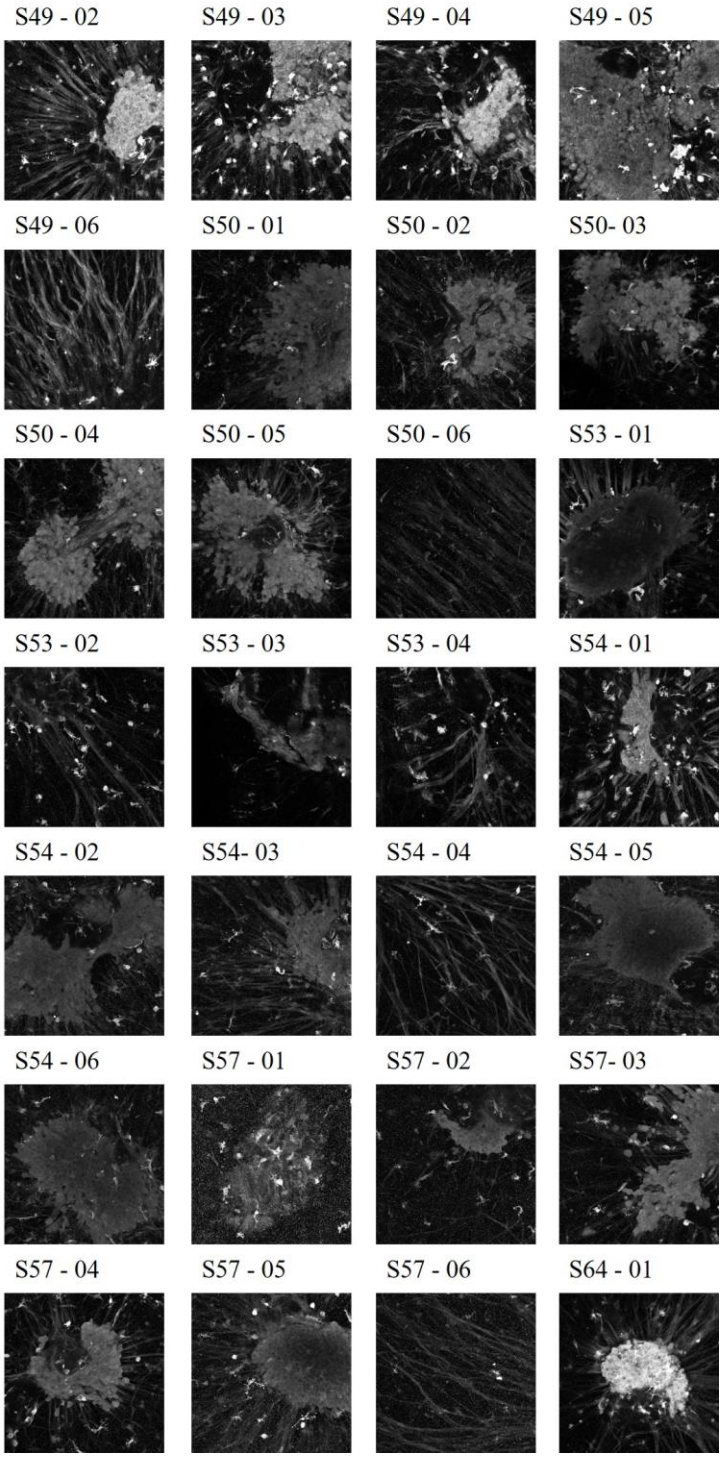

Note: Figure is continued on the next page.

Figure L.4. continued

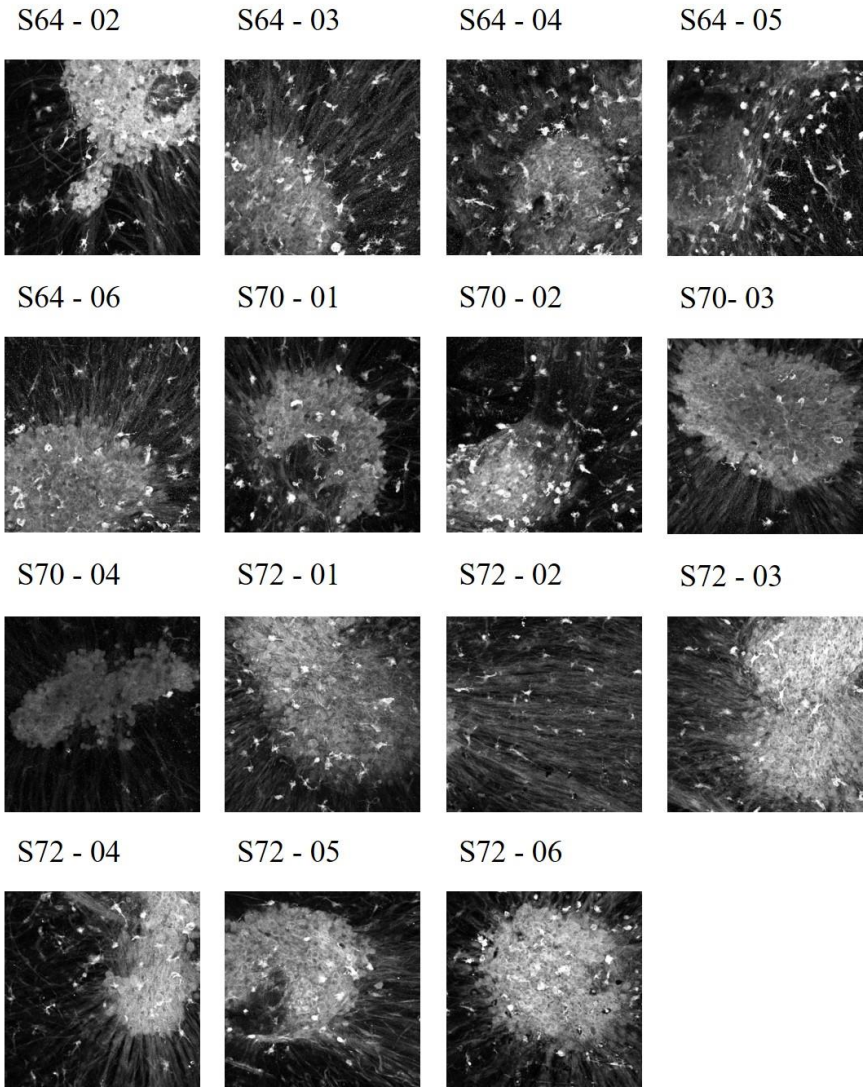

Figure L.5. Immunolabeling of MMP-9 in DRGs at 24 hours after equibiaxial sub-failure stretch as designated in Table L.2 (Sections 8.3 and 8.4.2)

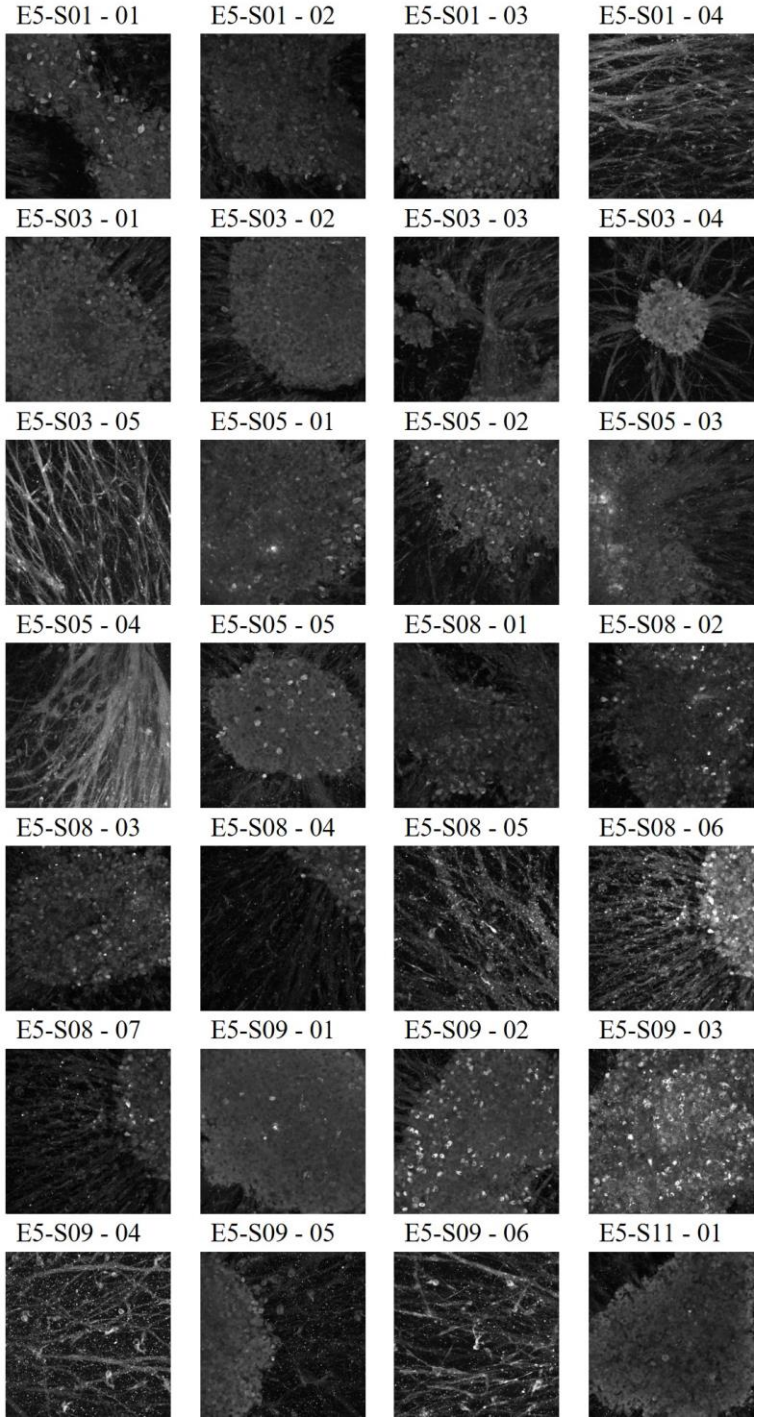

Note: Figure is continued on the next page.

Figure L.5. continued

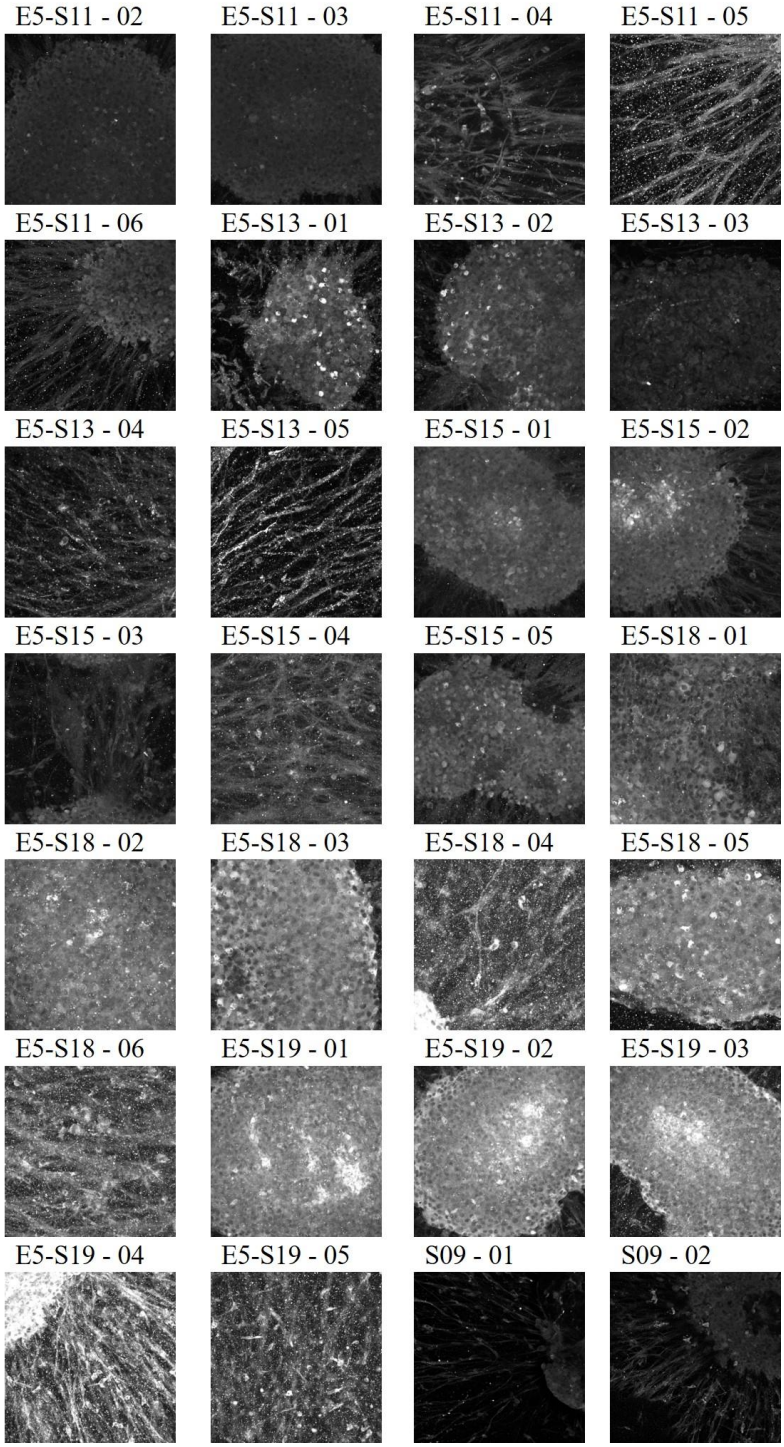

Note: Figure is continued on the next page.

Figure L.5. continued

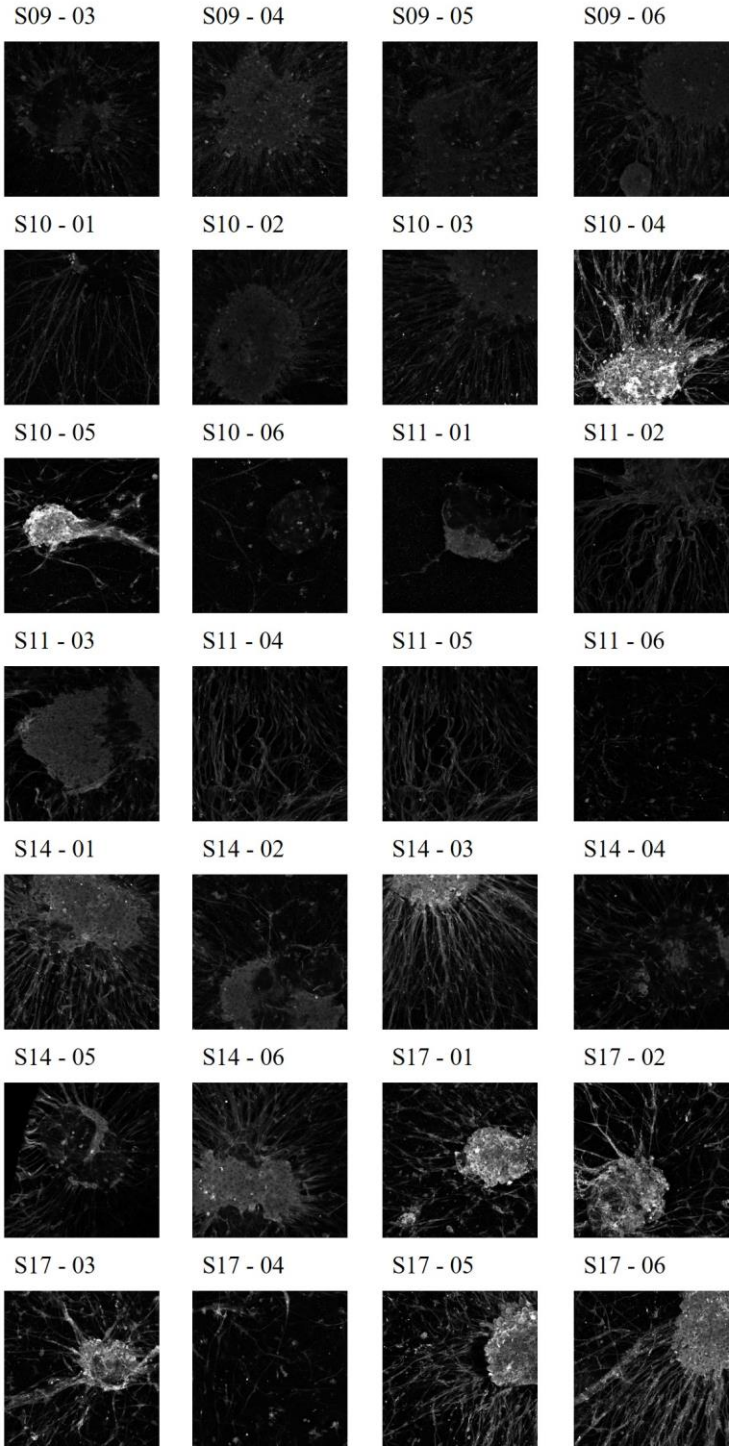

Note: Figure is continued on the next page.

Figure L.5. continued

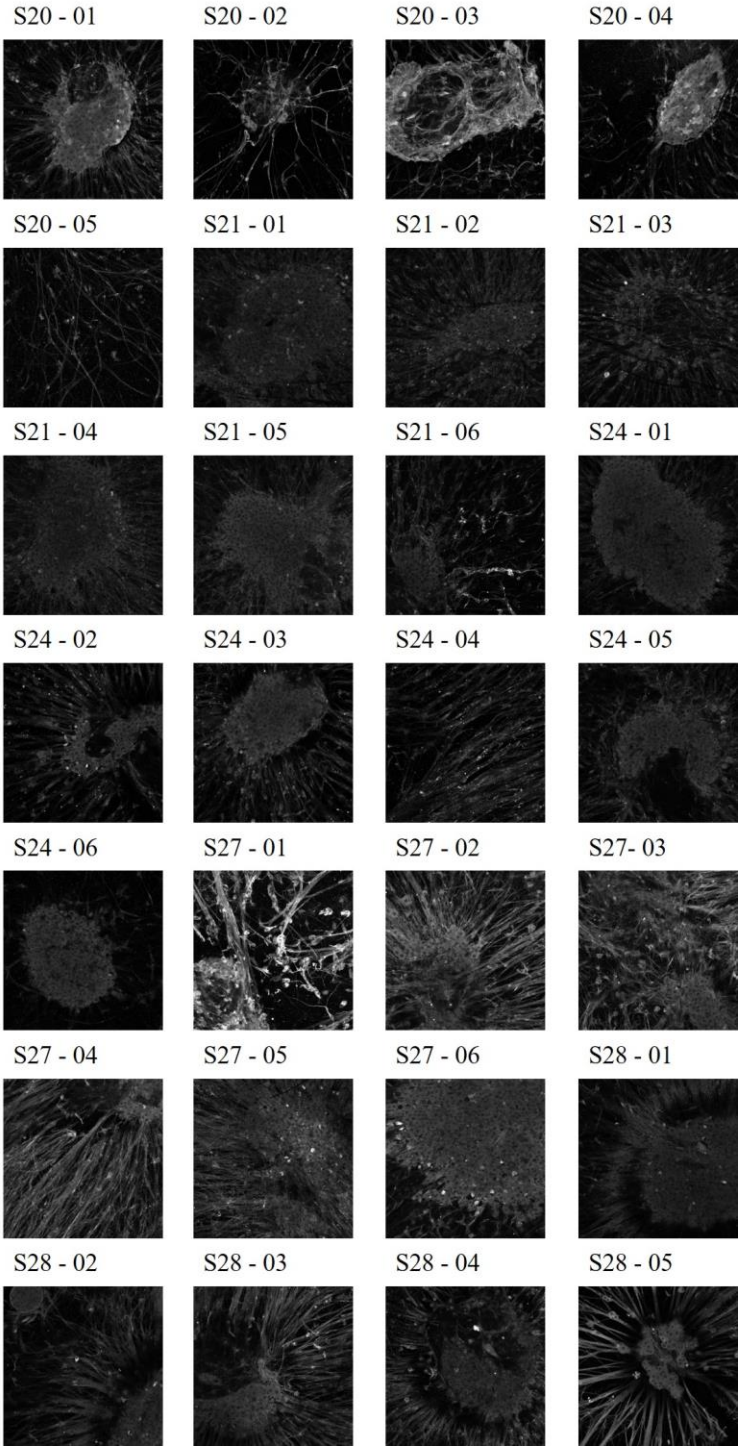

Note: Figure is continued on the next page.

Figure L.5. continued

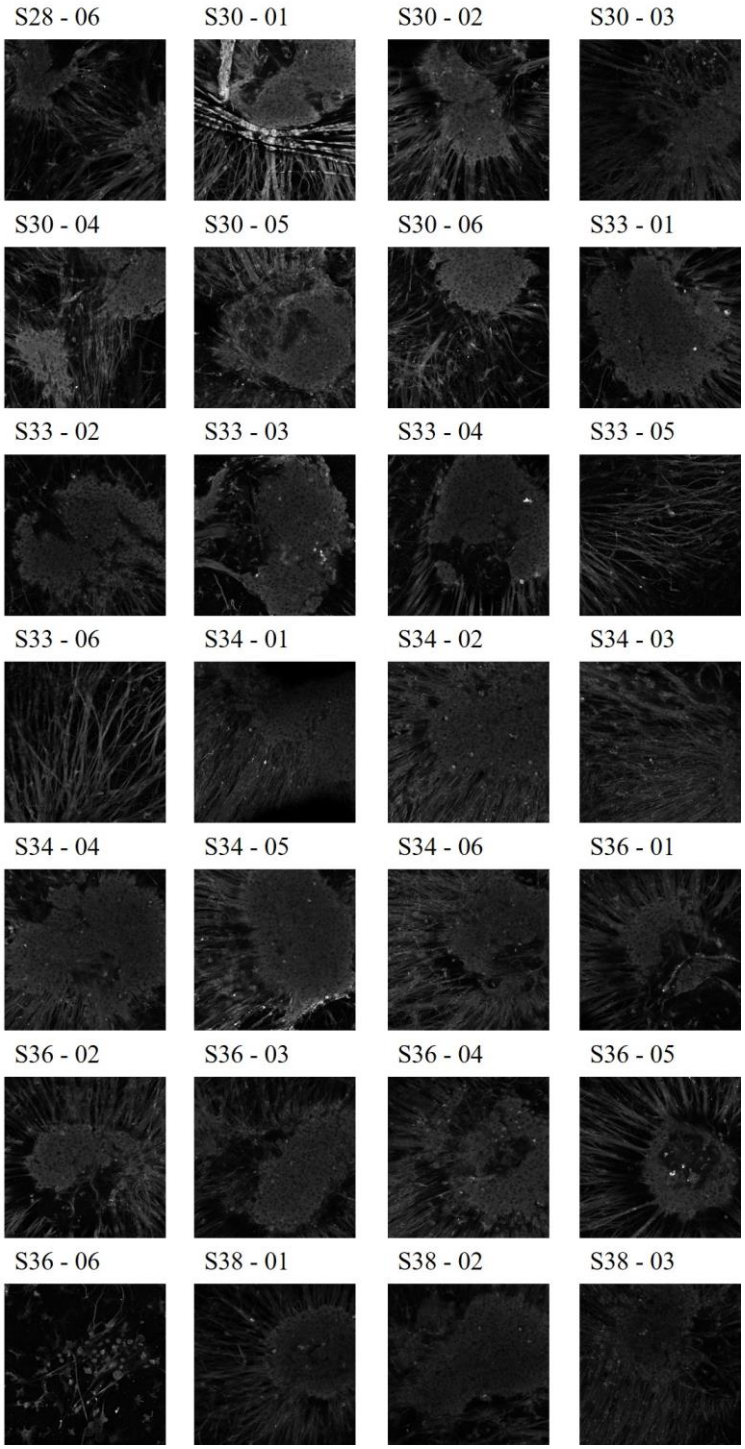

Note: Figure is continued on the next page.

Figure L.5. continued

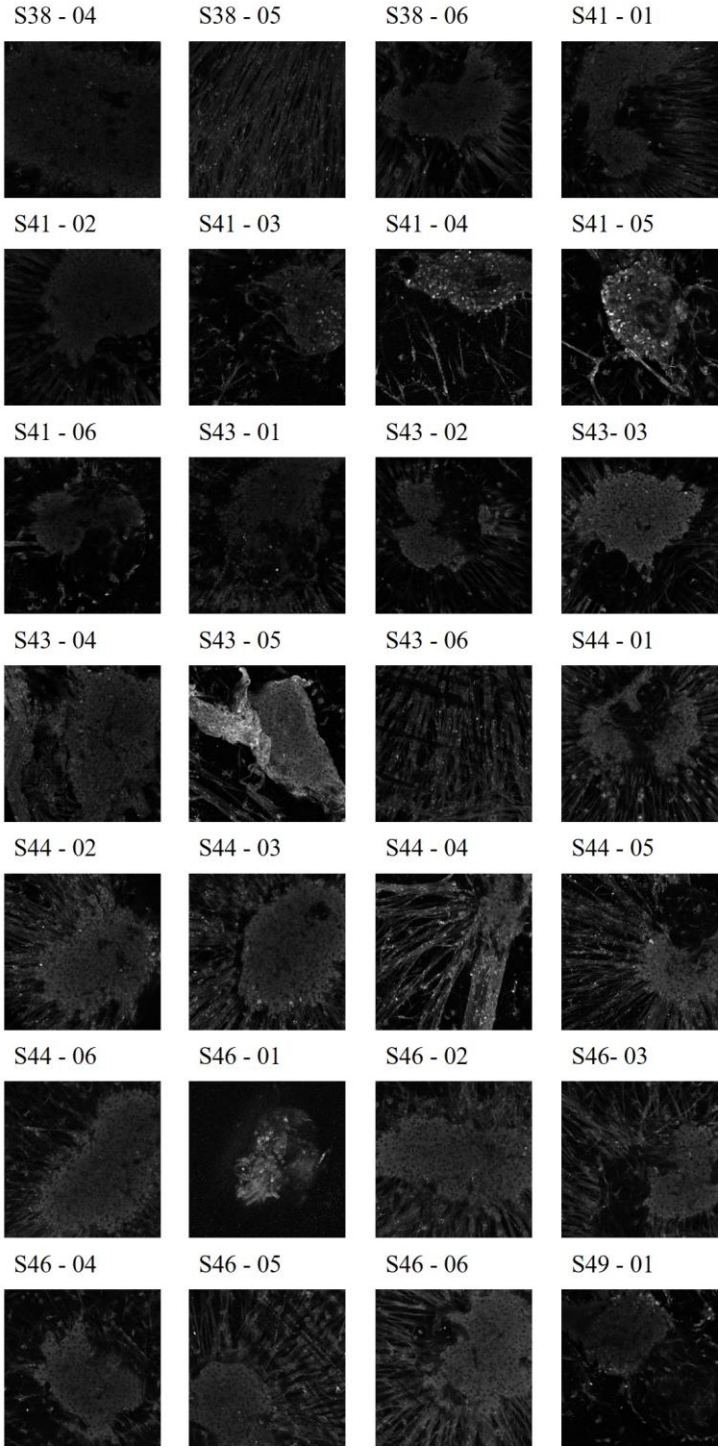

Note: Figure is continued on the next page.

Figure L.5. continued

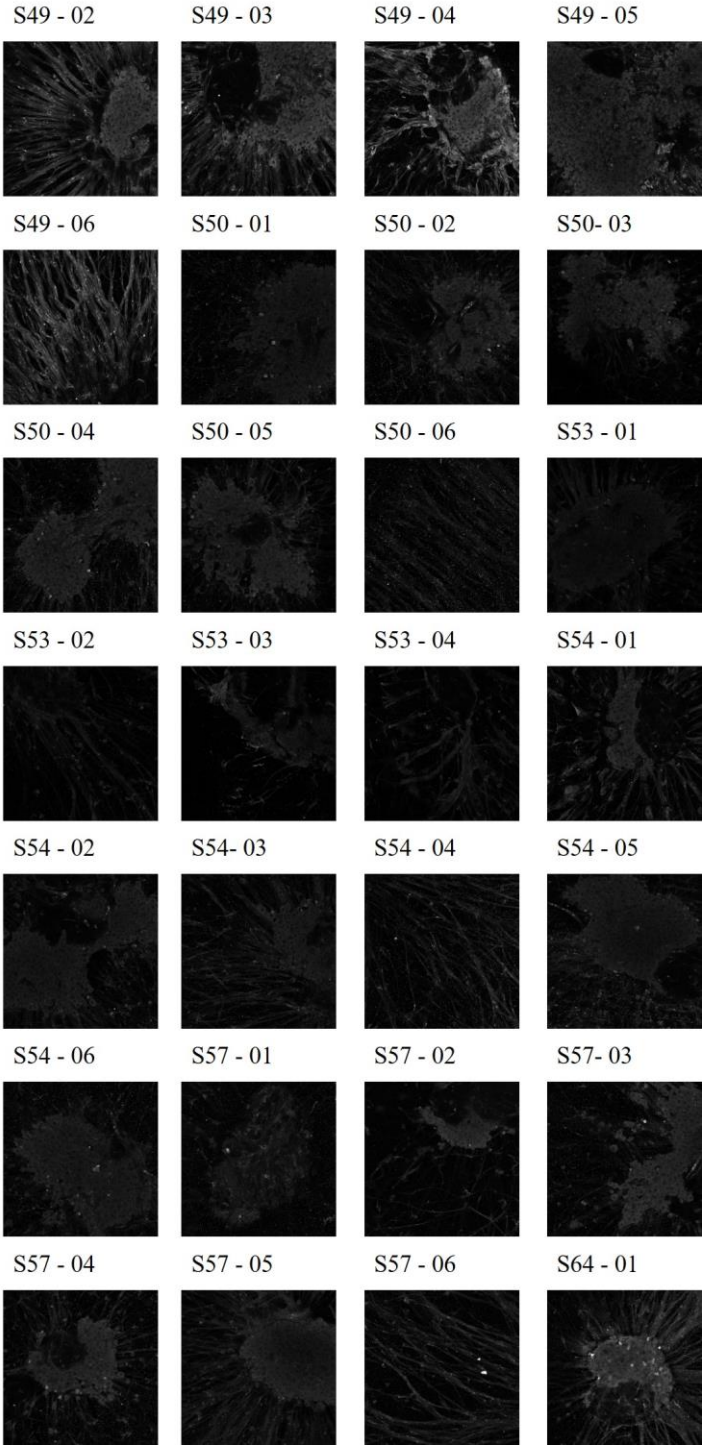

Note: Figure is continued on the next page.

Figure L.5. continued

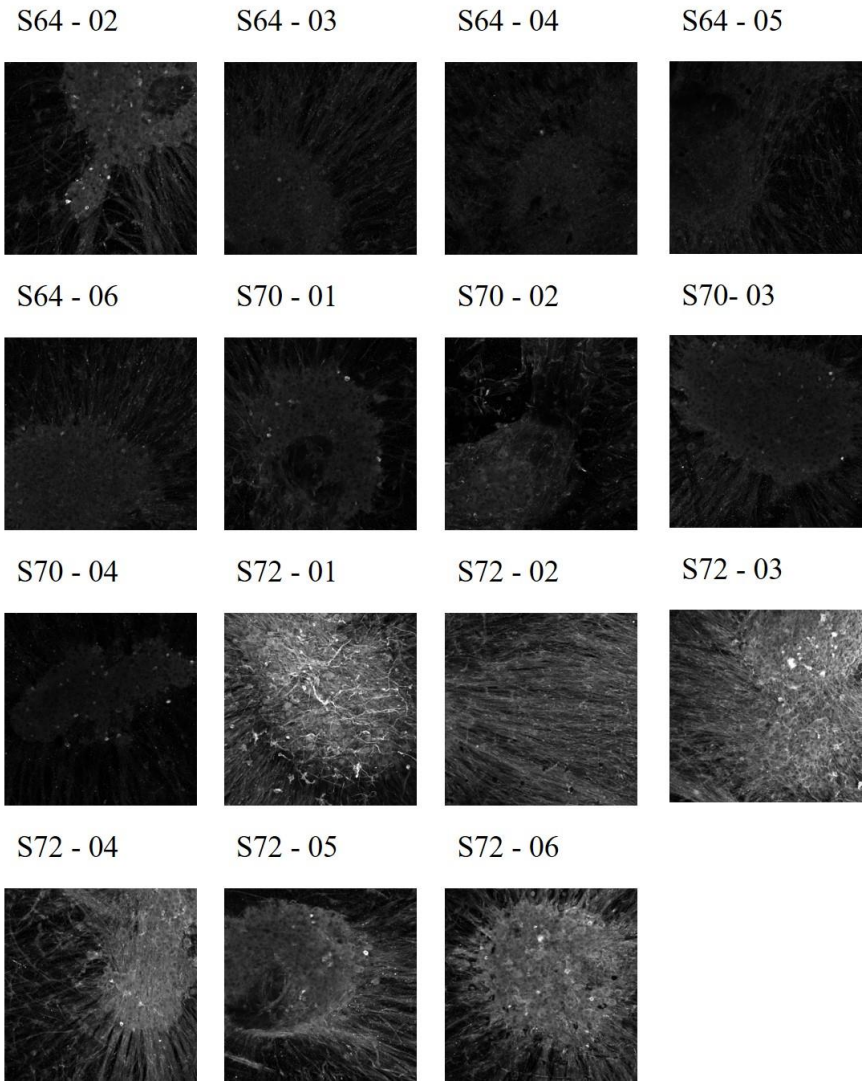

Figure L.6. Immunolabeling of substance P in DRGs at 24 hours after equibiaxial sub-failure stretch as designated in Table L.2 (Sections 8.3 and 8.4.2)

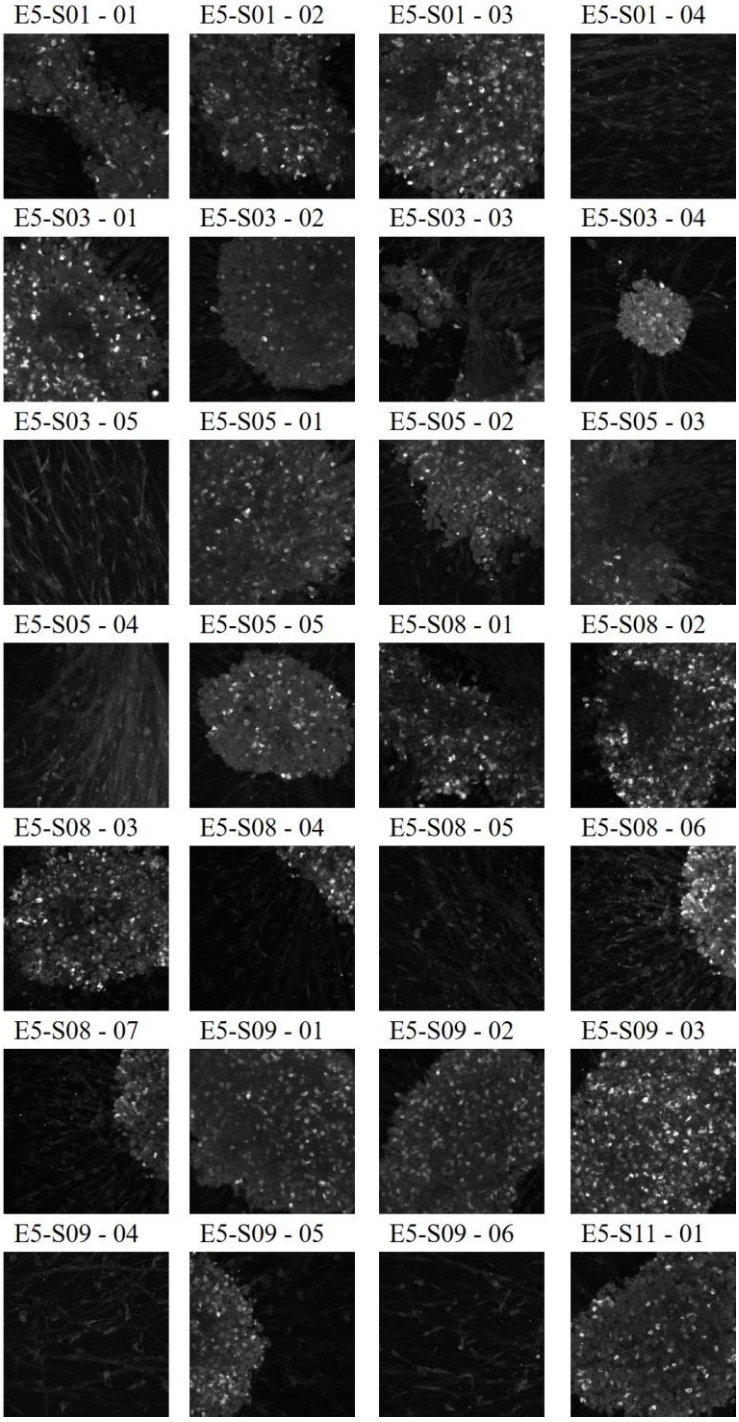

Note: Figure is continued on the next page.

Figure L.6. continued

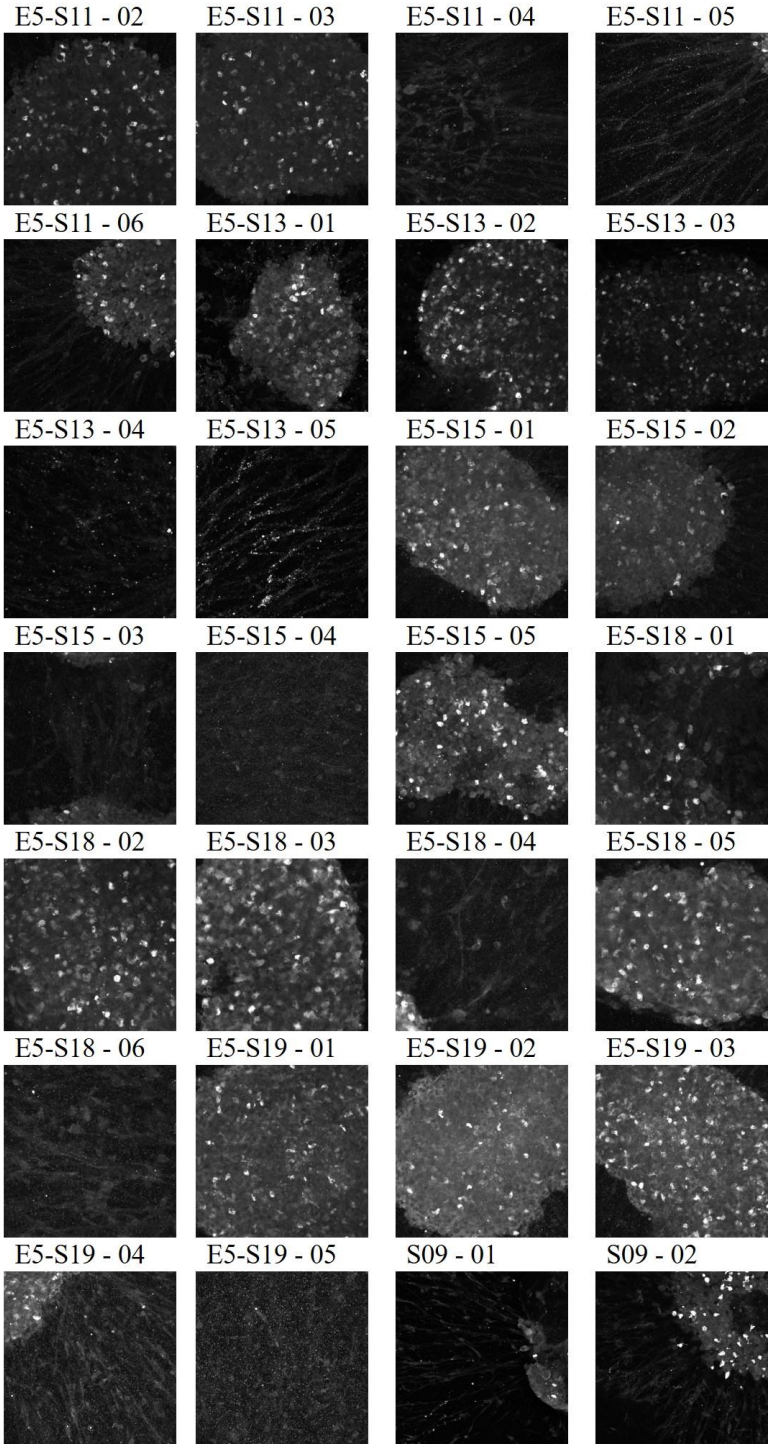

Note: Figure is continued on the next page.

Figure L.6. continued

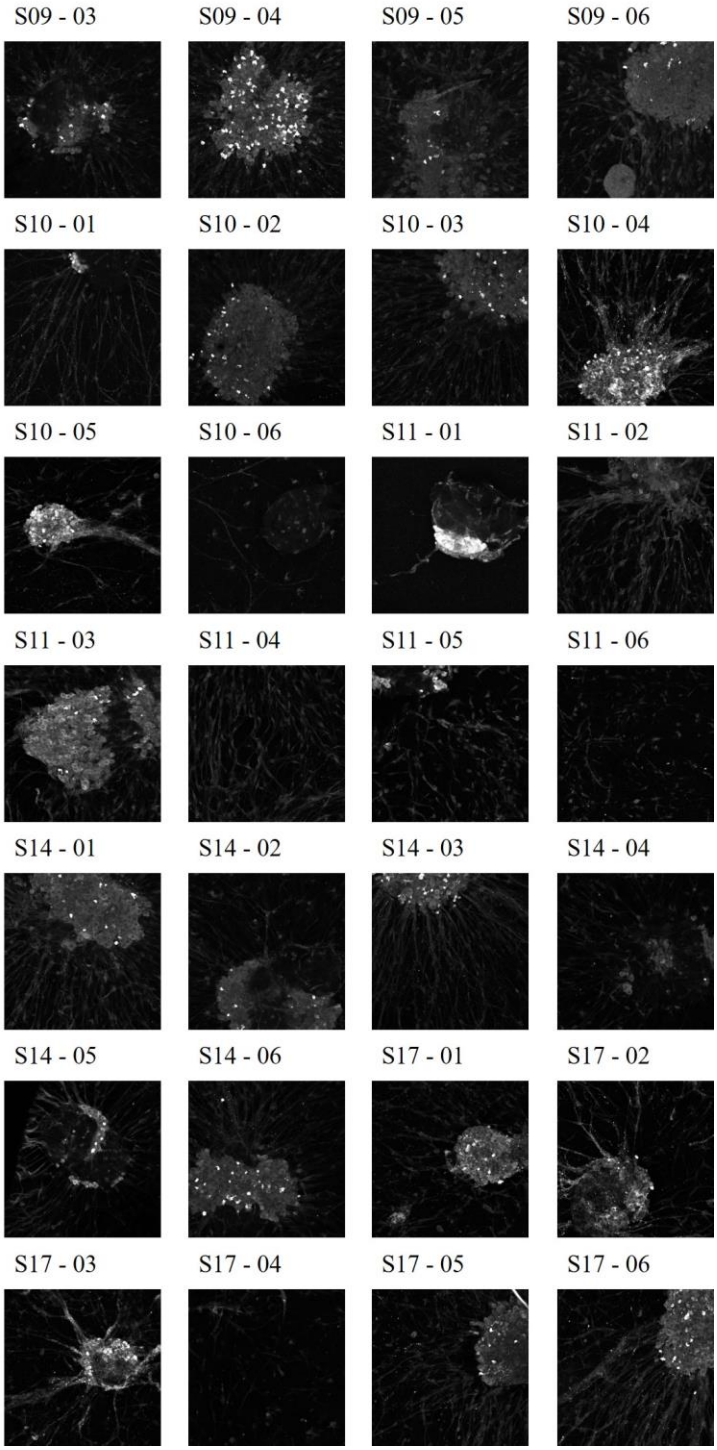

Note: Figure is continued on the next page.

Figure L.6. continued

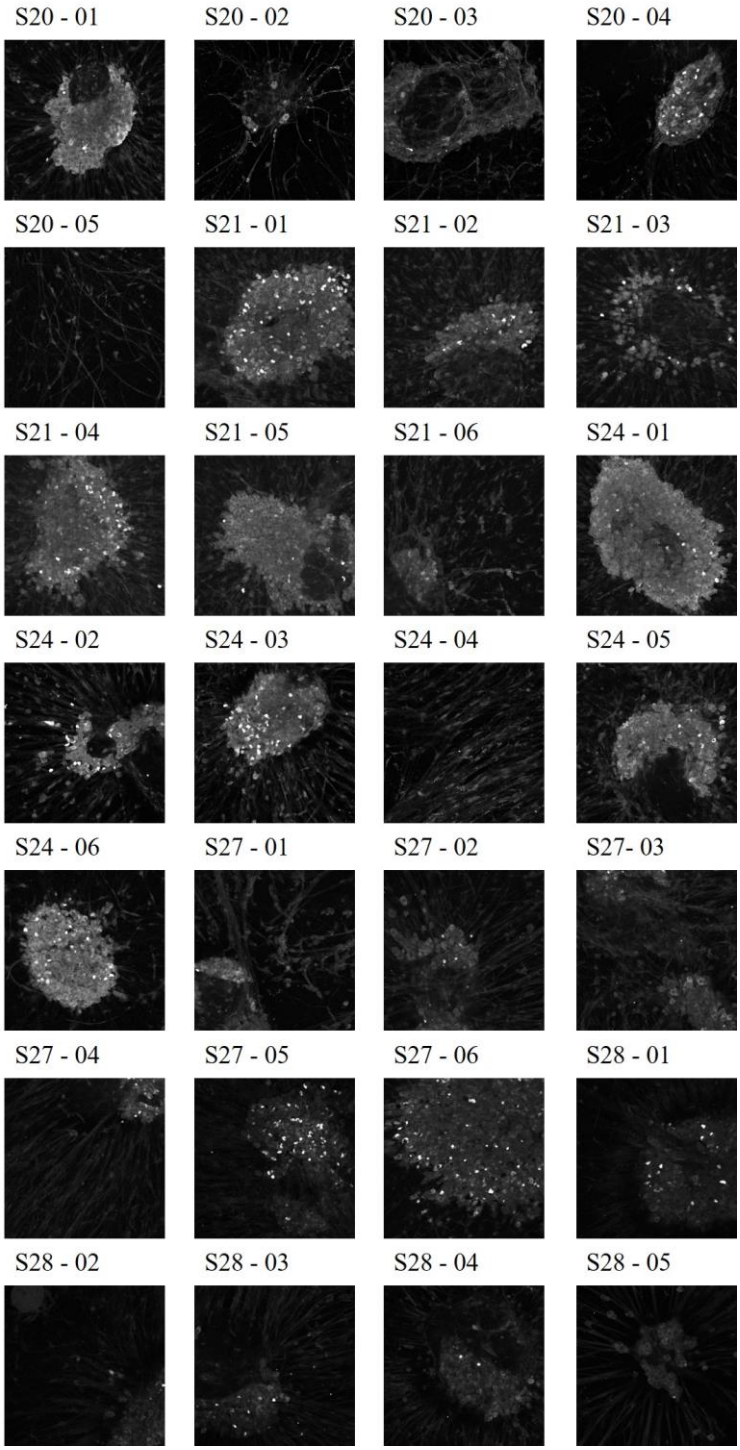

Note: Figure is continued on the next page.

Figure L.6. continued

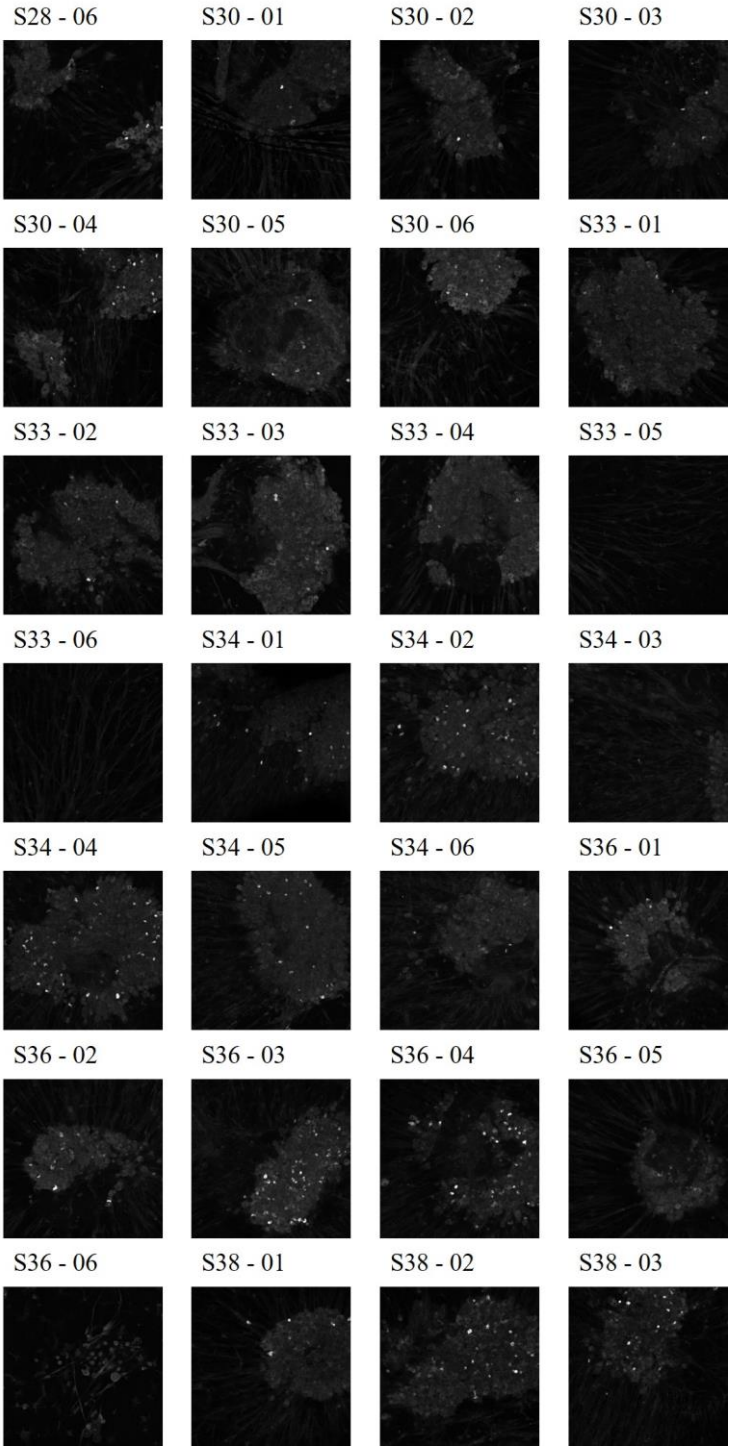

Note: Figure is continued on the next page.

Figure L.6. continued

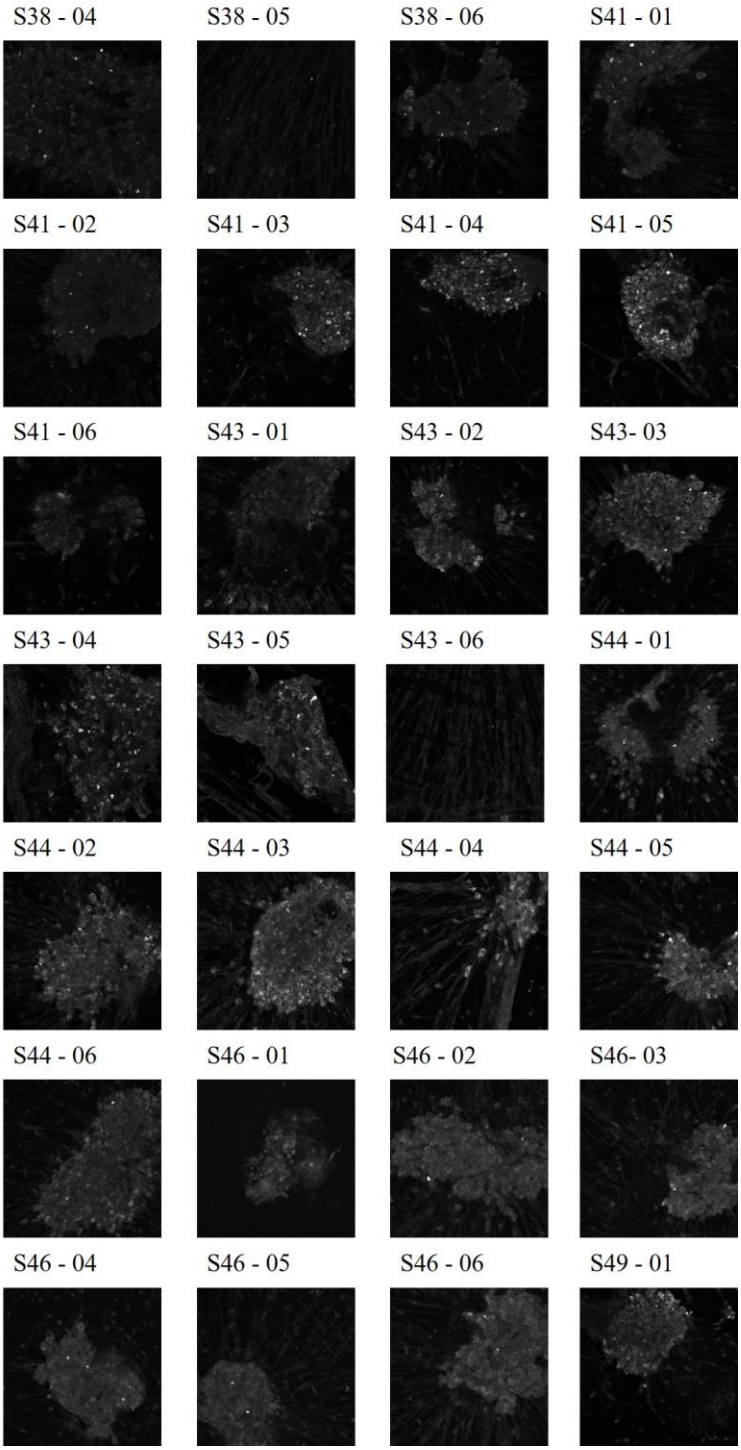

Note: Figure is continued on the next page.

Figure L.6. continued

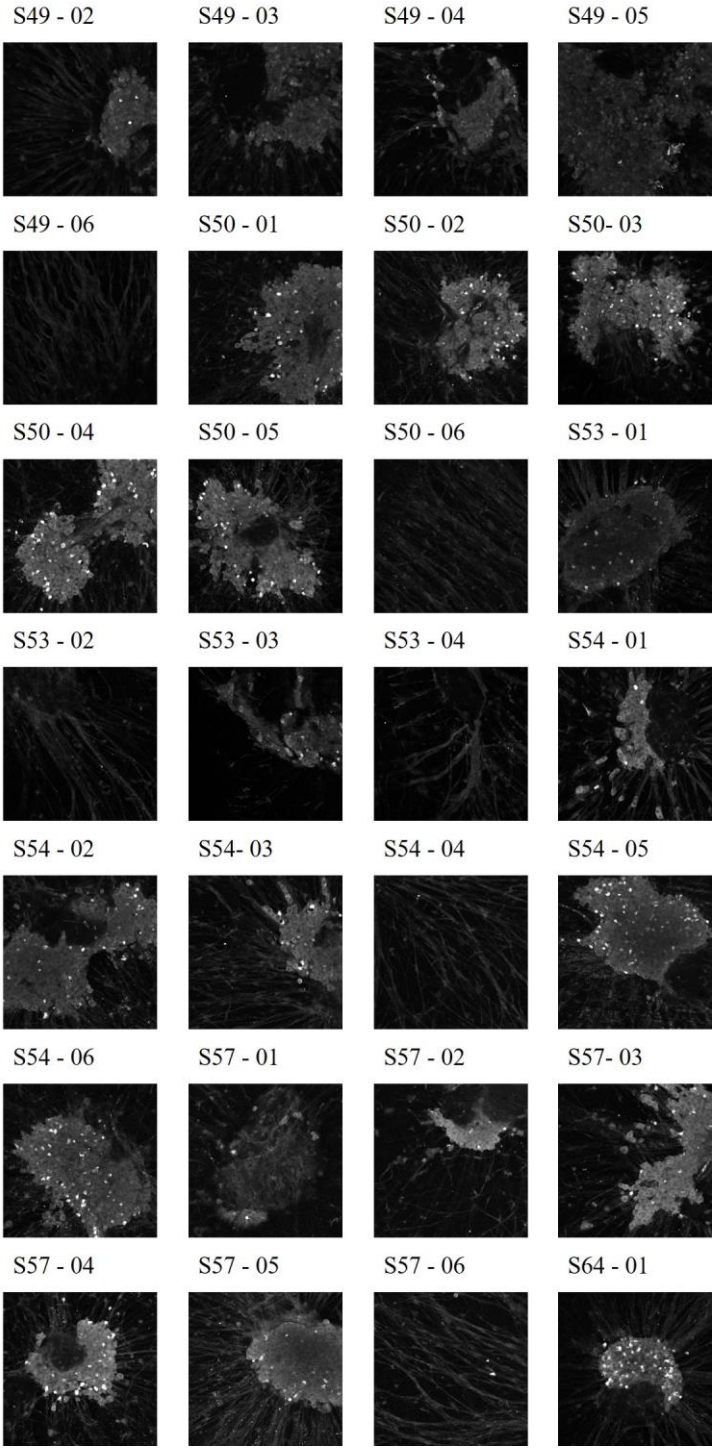

Note: Figure is continued on the next page.

Figure L.6. continued

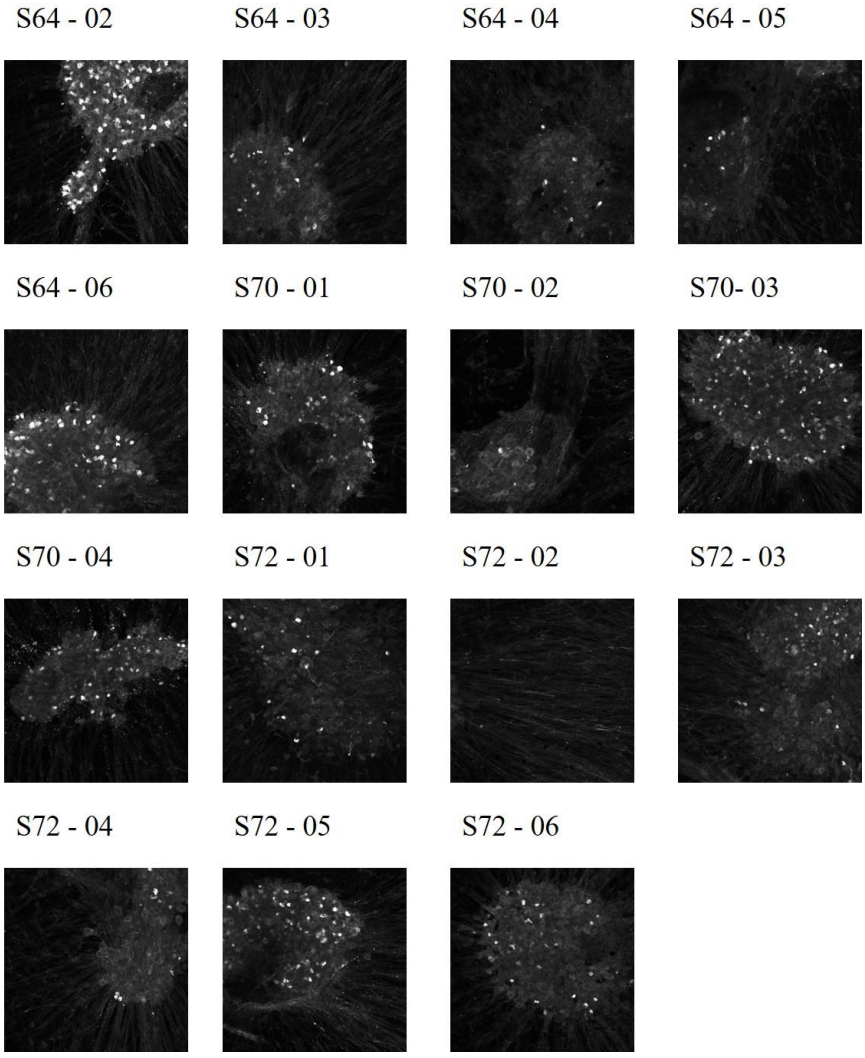

Figure L.7. Immunolabeling of MMP-1 in FLS cells at 24 hours after equibiaxial sub-failure stretch as designated in Table L.2 (Sections 8.3 and 8.4.2)

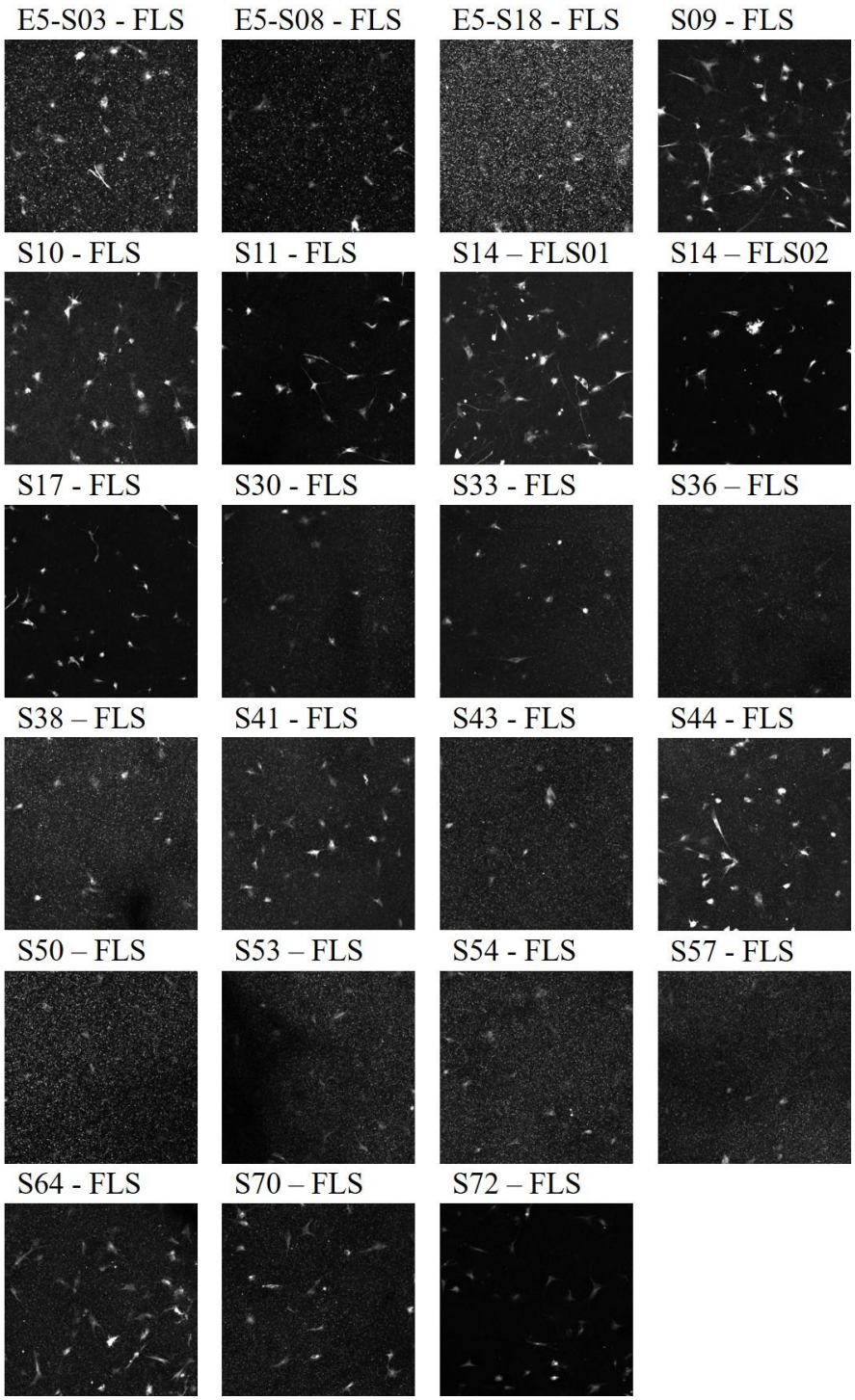

Figure L.8. Immunolabeling of MMP-9 in FLS cells at 24 hours after equibiaxial sub-failure stretch as designated in Table L.2 (Sections 8.3 and 8.4.2)

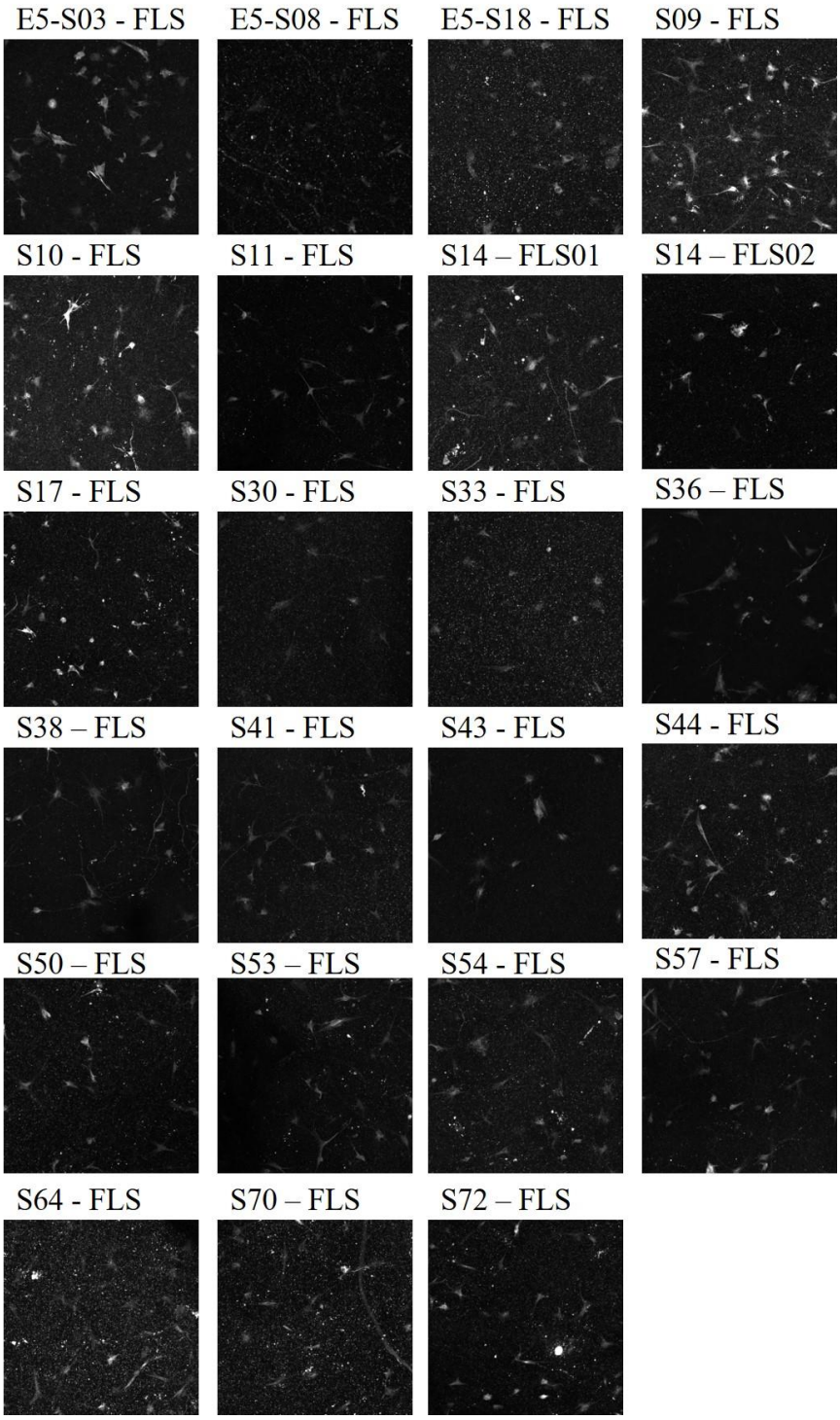

Table L.3. MMP-1 ELISA data from media and gel homogenate at 24 hours after equibiaxial sub-failure stretch (Section 8.3). Quantification of MMP-1 in media represents the average of duplicate measurements; gel homogenate measurements were taken in single wells.

Corresponding Studies	Sample ID	group	stretch	media (pg/mL)	gel homogenate (pg/mL)
Section 8.3	E05_S04	naïve	control	181.4	66.1
Section 8.3	E05_S07	naïve	control	131.5	119.3
Section 8.3	E05_S10	naïve	control	98.3	87.1
Section 8.3	E05_S14	naïve	control	117.0	167.3
Section 8.3	E05_S17	naïve	control	120.0	175.2
Section 8.3	E05_S03	naïve	sub-failure	156.1	106.8
Section 8.3	E05_S08	naïve	sub-failure	150.5	83.1
Section 8.3	E05_S09	naïve	sub-failure	126.2	142.3
Section 8.3	E05_S13	naïve	sub-failure	98.9	176.5
Section 8.3	E05_S18	naïve	sub-failure	96.3	175.8
Section 8.3	E05_S02	DRG-only	control	234.0	70.0
Section 8.3	E05_S06	DRG-only	control	204.1	35.2
Section 8.3	E05_S12	DRG-only	control	109.8	137.0
Section 8.3	E05_S16	DRG-only	control	160.7	188.3
Section 8.3	E05_S20	DRG-only	control	124.6	378.9
Section 8.3	E05_S01	DRG-only	sub-failure	-11.2	91.0
Section 8.3	E05_S05	DRG-only	sub-failure	98.6	421.0
Section 8.3	E05_S11	DRG-only	sub-failure	93.7	177.8
Section 8.3	E05_S15	DRG-only	sub-failure	115.7	77.9
Section 8.3	E05_S19	DRG-only	sub-failure	109.8	253.4

References

Abhilash A. S., Baker B. M., Trappmann B., Chen C. S., Shenoy V. B. (2014) Remodeling of fibrous extracellular matrices by contractile cells: predictions from discrete fiber network simulations. *Biophys. J.* 107(8):1829–1840.

Abramowicz S., Dolwick M. F. (2010) 20-Year Follow-Up Study of Disc Repositioning Surgery for Temporomandibular Joint Internal Derangement. *J. Oral Maxillofac. Surg.* 68(2):239–242.

Adães S., Almeida L., Potes C. S., Ferreira A. R., Castro-Lopes J. M., Ferreira-Gomes J., Neto F. L. (2017) Glial activation in the collagenase model of nociception associated with osteoarthritis. *Mol. Pain.* 13:1744806916688219.

Adães S., Ferreira-Gomes J., Mendonça M., Almeida L., Castro-Lopes J. M., Neto F. L. (2015) Injury of primary afferent neurons may contribute to osteoarthritis induced pain: An experimental study using the collagenase model in rats. *Osteoarthr. Cartil.* 23(6):914–924.

Adães S., Mendonça M., Santos T. N., Castro-Lopes J. M., Ferreira-Gomes J., Neto F. L. (2014) Intra-articular injection of collagenase in the knee of rats as an alternative model to study nociception associated with osteoarthritis. *Arthritis Res. Ther.* 16(1):R10.

Aghvami M., Billiar K. L., Sander E. A. (2016) Fiber Network Models Predict Enhanced Cell Mechanosensing on Fibrous Gels. *J. Biomech. Eng.* 138(10):101006.

Agrawal N., Dasaradhi P. V. N., Mohmmed A., Malhotra P., Bhatnagar R. K., Mukherjee S. K. (2003) RNA Interference: Biology, Mechanism, and Applications. *Microbiol. Mol. Biol. Rev.* 67(4):657–685.

Agrawal S. M., Lau L., Yong V. W. (2008) MMPs in the central nervous system: Where the good guys go bad. *Semin. Cell Dev. Biol.* 19(1):42–51.

Ahn J. K., Kim H., Lee J., Bae E.-K., Cha H.-S., Koh E.-M. (2008) Phenotypic Characterization and Invasive Properties of Synovial Fluid-Derived Adherent Cells in Rheumatoid Arthritis. *Inflammation*. 31(6):365–371.

Allen K. D., Griffin T. M., Rodriguiz R. M., Wetsel W. C., Kraus V. B., Huebner J. L., Boyd L. M., Setton L. A. (2009) Decreased physical function and increased pain sensitivity in mice deficient for type IX collagen. *Arthritis Rheum.* 60(9):2684–2693.

Allen M., Ghosh S., Ahern G. P., Villapol S., Maguire-Zeiss K. A., Conant K. (2016) Protease induced plasticity: matrix metalloproteinase-1 promotes neurostructural changes through activation of protease activated receptor 1. *Sci. Rep.* 6:35497.

Almeida L. E., Caporal K., Ambros V., Azevedo M., Noronha L., Leonardi R., Trevilatto P. C. (2015) Immunohistochemical expression of matrix metalloprotease-2 and matrix metalloprotease-9 in the disks of patients with temporomandibular joint

dysfunction. *J. Oral Pathol. Med.* 44(1):75–79.

Amar S., Smith L., Fields G. B. (2017) Matrix metalloproteinase collagenolysis in health and disease. *Biochim Biophys Acta Mol Cell Res*. 1864(11):1940–1951.

Anderst W. J., Donaldson W. F., Lee J. Y., Kang J. D. (2014) In vivo cervical facet joint capsule deformation during flexion-extension. *Spine (Phila. Pa. 1976).* 39(8):E514-20.

Arendt-Nielsen L., Eskehave T. N., Egsgaard L. L., Petersen K. K., Graven-Nielsen T., Hoeck H. C., Simonsen O., Siebuhr A. S., Karsdal M., Bay-Jensen A. C. (2014) Association Between Experimental Pain Biomarkers and Serologic Markers in Patients With Different Degrees of Painful Knee Osteoarthritis. *Arthritis Rheumatol.* 66(12):3317–3326.

Attia E., Bohnert K., Brown H., Bhargava M., Hannafin J. A. (2014) Characterization of Total and Active Matrix Metalloproteinases-1,-3, and-13 Synthesized and Secreted by Anterior Cruciate Ligament Fibroblasts in Three-Dimensional Collagen Gels. *Tissue Eng. Part A.* 20:171–177.

Balbín M., Fueyo A., Knäuper V., López J. M., Álvarez J., Sánchez L. M., Quesada V., Bordallo J., Murphy G., López-Otín C. (2001) Identification and Enzymatic Characterization of Two Diverging Murine Counterparts of Human Interstitial Collagenase (MMP-1) Expressed at Sites of Embryo Implantation. *J. Biol. Chem.* 276(13):10253–10262.

Ban E., Zhang S., Zarei V., Barocas V. H., Winkelstein B. A., Picu C. R. (2017) Collagen Organization in Facet Capsular Ligaments Varies with Spinal Region and with Ligament Deformation. *J. Biomech. Eng.* 139(7):071009.

Bank R. a, Krikken M., Beekman B., Stoop R., Maroudas A., Lafebers F. P. J. G., Koppele J. M. Te (1997) A simplified measurement of degraded collagen in tissues: Application in healthy, fibrillated and osteoarthritic cartilage. *Matrix Biol.* 16(5):233–243.

Baragi V. M., Becher G., Bendele A. M., Biesinger R., Bluhm H., Boer J., Deng H., et al. (2009) A new class of potent matrix metalloproteinase 13 inhibitors for potential treatment of osteoarthritis: Evidence of histologic and clinical efficacy without musculoskeletal toxicity in rat models. *Arthritis Rheum.* 60(7):2008–2018.

Barbir A., Michalek A. J., Abbott R. D., Iatridis J. C. (2010) Effects of enzymatic digestion on compressive properties of rat intervertebral discs. *J. Biomech.* 43(6):1067–1073.

Barnsley L., Lord S., Bogduk N. (1993) Comparative local anaesthetic blocks in the diagnosis of cervical zygapophysial joint pain. *Pain*. 55:99–106.

Bartok B., Firestein G. S. (2010) Fibroblast-like synoviocytes: key effector cells in rheumatoid arthritis. *Immunol. Rev.* 233(1):233–255.

Basbaum A. I., Bautista D. M., Scherrer G., Julius D. (2009) Cellular and Molecular Mechanisms of Pain. *Cell*. 139(2):267–284.

Bay-Jensen A. C., Reker D., Kjelgaard-Petersen C. F., Mobasheri A., Karsdal M. A., Ladel C., Henrotin Y., Thudium C. S. (2016) Osteoarthritis year in review 2015: Soluble biomarkers and the BIPED criteria. *Osteoarthr. Cartil.* 24(1):9–20.

Bedson J., Croft P. R. (2008) The discordance between clinical and radiographic knee osteoarthritis: A systematic search and summary of the literature. *BMC Musculoskelet. Disord.* 9(1):116.

Bettini L., Moore K. (2016) Central Sensitization in Functional Chronic Pain Syndromes: Overview and Clinical Application. *Pain Manag. Nurs.* 17(5):333–338.

Bhole A. P., Flynn B. P., Liles M., Saeidi N., Dimarzio C. A., Ruberti J. W. (2009) Mechanical strain enhances survivability of collagen micronetworks in the presence of collagenase: implications for load-bearing matrix growth and stability. *Philos. Trans. A. Math. Phys. Eng. Sci.* 367(1902):3339–62.

Bing Z., Linlin L., Jianguo Y., Shenshen R., Ruifang R., Xi Z. (2012) Effect of mechanical stretch on the expressions of elastin, LOX and Fibulin-5 in rat BMSCs with ligament fibroblasts co-culture. *Mol. Biol. Rep.* 39(5):6077–6085.

Bogduk N., Marsland A. (1988) The cervical zygapophysial joints as a source of neck pain. *Spine (Phila. Pa. 1976).* 13(6):610–617.

Boire A., Covic L., Agarwal A., Jacques S., Sherifi S., Kuliopulos A. (2005) PAR1 is a matrix metalloprotease-1 receptor that promotes invasion and tumorigenesis of breast cancer cells. *Cell.* 120(3):303–313.

Bosco R., Alvarado S., Quiroz D., Eblen-Zajjur A. (2010) Digital morphometric characterization of lumbar dorsal root ganglion neurons in rats. *J. Histotechnol.* 33(3):113–118.

Bottini N., Firestein G. S. (2013) Duality of fibroblast-like synoviocytes in RA: Passive responders and imprinted aggressors. *Nat. Rev. Rheumatol.* 9(1):24–33.

Braz J. M., Nassar M. A., Wood J. N., Basbaum A. I. (2005) Parallel "pain" pathways arise from subpopulations of primary afferent nociceptor. *Neuron*. 47(6):787–793.

Broussard G. J., Liang R., Tian L. (2014) Monitoring activity in neural circuits with genetically encoded indicators. *Front. Mol. Neurosci.* 7(97):1–17.

Burgeson R. E., Nimni M. E. (1992) Collagen types. Molecular structure and tissue distribution. *Clin. Orthop. Relat. Res.* (282):250–272.

Bushnell M. C., Čeko M., Low L. A. (2013) Cognitive and emotional control of pain and its disruption in chronic pain. *Nat Rev Neurosci*. 14(7):502–511.

Camelliti P., Borg T. K., Kohl P. (2005) Structural and functional characterisation of cardiac fibroblasts. *Cardiovasc. Res.* 65(1):40–51.

Camp R. J., Liles M., Beale J., Saeidi N., Flynn B. P., Moore E., Murthy S. K., Ruberti J. W. (2011) Molecular mechanochemistry: Low force switch slows enzymatic cleavage of human type I collagen monomer. *J. Am. Chem. Soc.* 133(11):4073–4078.

Campos L. S., Leone D. P., Relvas J. B., Brakebusch C., Fässler R., Suter U., Ffrench-Constant C. (2004) β1 integrins activate a MAPK signalling pathway in neural stem cells that contributes to their maintenance. *Development*. 131(14):3433–3444.

Cavanaugh J. M., Lu Y., Chen C., Kallakuri S. (2006) Pain generation in lumbar and cervical facet joints. *J. Bone Jt. Surg.* 88-A Suppl:63–67.

Chakrabarti S., Hore Z., Pattison L. A., Lalnunhlimi S., Bhebhe C. N., Callejo G., Bulmer D. C., Taams L. S., Denk F., Smith E. S. J. (2020) Sensitization of knee-innervating sensory neurons by tumor necrosis factor-α-activated fibroblast-like synoviocytes: an in vitro, coculture model of inflammatory pain. *Pain*. 161(9):2129–2141.

Chan V. W. L., Tobin W. R., Zhang S., Winkelstein B. A., Barocas V. H., Shephard M. S., Picu C. R. (2019) Image-based multi-scale mechanical analysis of strain amplification in neurons embedded in collagen gel. *Comput. Methods Biomech. Biomed. Engin.* 22(2):113–129.

Chandran P. L., Barocas V. H. (2004) Microstructural Mechanics of Collagen Gels in Confined Compression: Poroelasticity, Viscoelasticity, and Collapse. *J. Biomech. Eng.* 126(2):152–166.

Chen C., Lu Y., Kallakuri S., Patwardhan A., Cavanaugh J. M. (2006) Distribution of A-δ and C-Fiber Receptors in the Cervical Facet Joint Capsule. *J. Bone Jt. Surg.* 88:1807–1816.

Chen N.-F., Chen W.-F., Sung C.-S., Lu C.-H., Chen C.-L., Hung H.-C., Feng C.-W., et

al. (2016) Contributions of p38 and ERK to the antinociceptive effects of TGF-β1 in chronic constriction injury-induced neuropathic rats. *J. Headache Pain*. 17(1):72.

Chen T.-W., Wardill T. J., Sun Y., Pulver S. R., Renninger S. L., Baohan A., Schreiter E. R., et al. (2013) Ultrasensitive fluorescent proteins for imaging neuronal activity. *Nature*. 499(7458):295–300.

Chen Y., Li G., Huang L. Y. M. (2015) p38 MAPK mediates glial P2X7R-neuronal P2Y1R inhibitory control of P2X3R expression in dorsal root ganglion neurons. *Mol. Pain*. 11(1):1–10.

Cheng J.-K., Ji R.-R. (2008) Intracellular signaling in primary sensory neurons and persistent pain. *Neurochem. Res.* 33(10):1970–1978.

Chockalingam P. S., Glasson S. S., Lohmander L. S. (2013) Tenascin-C levels in synovial fluid are elevated after injury to the human and canine joint and correlate with markers of inflammation and matrix degradation. *Osteoarthr. Cartil.* 21(2):339–345.

Clark I. M., Swingler T. E., Sampieri C. L., Edwards D. R. (2008) The Regulation of Matrix Metalloproteinases and their Inhibitors. *Int. J. Biochem. Cell Biol.* 40(6–7):1362–1378.

Cohen M. S., Schimmel D. R., Masuda K., Hastings H., Muehleman C. (2007) Structural and biochemical evaluation of the elbow capsule after trauma. *J. Shoulder Elb. Surg.* 16(4):484–490.

Conant K., Haughey N., Nath A., Hillaire C. St., Gary D. S., Pardo C. A., Wahl L. M., Bilak M., Milward E., Mattson M. P. (2002) Matrix metalloproteinase-1 activates a pertussis toxin-sensitive signaling pathway that stimulates the release of matrix metalloproteinase-9. *J. Neurochem.* 82(4):885–893.

Conant K., Hillaire C. St., Nagase H., Visse R., Gary D., Haughey N., Anderson C., Turchan J., Nath A. (2004) Matrix Metalloproteinase 1 Interacts with Neuronal Integrins and Stimulates Dephosphorylation of Akt. *J. Biol. Chem.* 279(9):8056–8062.

Coussens L. M., Fingleton B., Matrisian L. M. (2002) Matrix metalloproteinase inhibitors and cancer: Trials and tribulations. *Science.* 295(5564):2387–2392.

Craig V. J., Zhang L., Hagood J. S., Owen C. A. (2015) Matrix metalloproteinases as therapeutic targets for idiopathic pulmonary fibrosis. *Am J Respir Cell Mol Biol*. 53(5):585–600.

Crofford L. J. (2015) Chronic Pain: Where the Body Meets the Brain, in *Trans. Am. Clin. Climatol. Assoc.*, Vol. 126, pp. 167–183. Trans Am Clin Climatol Assoc, Nashville, Tennessee.

Crosby N. D., Gilliland T. M., Winkelstein B. A. (2014) Early afferent activity from the facet joint after painful trauma to its capsule potentiates neuronal excitability and glutamate signaling in the spinal cord. *Pain*. 155(9):1878–1887.

Crosby N. D., Smith J. R. (2015) Pain Biomechanics, in *Accid. Inj.*, (Yoganandan N.,

Nahum A. M., Melvin J. W., eds), pp. 549–580. Springer-Verlag New York, New York.

Crosby N. D., Weisshaar C. L., Winkelstein B. A. (2013) Spinal neuronal plasticity is evident within 1 day after a painful cervical facet joint injury. *Neurosci. Lett.* 542:102–106.

Crosby N. D., Zaucke F., Kras J. V, Dong L., Luo Z. D., Winkelstein B. A. (2015) Thrombospondin-4 and excitatory synaptogenesis promote spinal sensitization after painful mechanical joint injury. *Exp. Neurol.* 264:111–120.

Cullen D. K., Lessing M. C., LaPlaca M. C. (2007) Collagen-Dependent Neurite Outgrowth and Response to Dynamic Deformation in Three-Dimensional Neuronal Cultures. *Ann. Biomed. Eng.* 35(5):835–846.

Cullen D. K., Tang-Schomer M. D., Struzyna L. A., Patel A. R., Johnson V. E., Wolf J. A., Smith D. H. (2012) Microtissue Engineered Constructs with Living Axons for Targeted Nervous System Reconstruction. *Tissue Eng. Part A.* 18(21–22):2280–2289.

Curatolo M., Müller M., Ashraf A., Neziri A. Y., Streitberger K., Andersen O. K., Arendt-Nielsen L. (2015) Pain Hypersensitivity and Spinal Nociceptive Hypersensitivity in Chronic Pain. *Pain*. 156(11):2373–2382.

Dai Y., Iwata K., Fukuoka T., Kondo E., Tokunaga A., Yamanaka H., Tachibana T., Liu Y., Noguchi K. (2002) Phosphorylation of extracellular signal-regulated kinase in

primary afferent neurons by noxious stimuli and its involvement in peripheral sensitization. *J. Neurosci.* 22(17):7737–7745.

Dallon J. C., Ehrlich H. P. (2008) A review of fibroblast-populated collagen lattices. *Wound Repair Regen.* 16(4):472–479.

Daniels J. T., Cambrey A. D., Occleston N. L., Garrett Q., Tarnuzzer R. W., Schultz G. S., Khaw P. T. (2003) Matrix metalloproteinase inhibition modulates fibroblast-mediated matrix contraction and collagen production in vitro. *Investig. Ophthalmol. Vis. Sci.* 44(3):1104–1110.

deLuca A. C., Faroni A., Reid A. J. (2015) Dorsal Root Ganglia Neurons and Differentiated Adipose-derived Stem Cells: An In Vitro Co-culture Model to Study Peripheral Nerve Regeneration. *J. Vis. Exp.* 26(96).

Diekmann O., Tschesche H. (1994) Degradation of kinins, angiotensins and substance P by polymorphonuclear matrix metalloproteinases MMP 8 and MMP 9. *Braz J Med Biol Res*. 27(8):1865–1876.

Dong L., Quindlen J. C., Lipschutz D. E., Winkelstein B. A. (2012) Whiplash-like facet joint loading initiates glutamatergic responses in the DRG and spinal cord associated with behavioral hypersensitivity. *Brain Res.* 1461:51–63.

Dong L., Smith J. R., Winkelstein B. A. (2013) Ketorolac reduces spinal astrocytic activation and PAR1 expression associated with attenuation of pain after facet joint injury. *J. Neurotrauma*. 30(10):818–825.

Dong L., Winkelstein B. A. (2010) Simulated Whiplash Modulates Expression of the Glutamatergic System in the Spinal Cord Suggesting Spinal Plasticity is Associated with Painful Dynamic Cervical Facet Loading. *J. Neurotrauma*. 174(27):163–174.

Donk J. van der, Schouten J. S., Passchier J., Romunde L. K. van, Valkenburg H. A. (1991) The associations of neck pain with radiological abnormalities of the cervical spine and personality traits in a general population. *J. Rheumatol.* 18(12):1884–1889.

Dumin J. A., Dickeson S. K., Stricker T. P., Bhattacharyya-Pakrasi M., Roby J. D., Santoro S. A., Parks W. C. (2001) Pro-collagenase-1 (Matrix Metalloproteinase-1) Binds the α2β1 Integrin upon Release from Keratinocytes Migrating on Type I Collagen. *J. Biol. Chem.* 276(31):29368–29374.

Elliott J. M., Noteboom J. T., Flynn T. W., Sterling M. (2009) Characterization of acute and chronic whiplash-associated disorders. *J. Orthop. Sports Phys. Ther.* 39(5):312–323.

Emshoff R., Brandlmaier I., Gerhard S., Strobl H., Bertram S., Rudisch A. (2003) Magnetic resonance imaging predictors of temporomandibular joint pain. *J. Am. Dent. Assoc.* 134(6):705–714.

Ernberg M. (2017) The role of molecular pain biomarkers in temporomandibular joint internal derangement. *J. Oral Rehabil.* 44(6):481–491.

Evans M. C., Barocas V. H. (2009) The Modulus of Fibroblast-Populated Collagen Gels

is not Determined by Final Collagen and Cell Concentration: Experiments and an Inclusion-Based Model. *J. Biomech. Eng.* 131(10):101014.

Evanson J. M., Jeffrey J. J., Krane S. M. (1967) Human collagenase: Identification and characterization of an enzyme from rheumatoid synovium in culture. *Science (80-.).* 158(3800):499–502.

Fernihough J., Gentry C., Bevan S., Winter J. (2005) Regulation of calcitonin gene-related peptide and TRPV1 in a rat model of osteoarthritis. *Neurosci. Lett.* 388(2):75–80.

Fields G. B. (2013) Interstitial collagen catabolism. *J. Biol. Chem.* 288(13):8785–8793.

Finan P. H., Buenaver L. F., Bounds S. C., Hussain S., Park R. J., Haque U. J., Campbell C. M., Haythornthwaite J. A., Edwards R. R., Smith M. T. (2013) Discordance between pain and radiographic severity in knee osteoarthritis: Findings from quantitative sensory testing of central sensitization. *Arthritis Rheum.* 65(2):363–372.

Fingleton B. (2008) MMPs as therapeutic targets-Still a viable option? *Semin. Cell Dev. Biol.* 19:61–68.

Flynn B. P., Bhole A. P., Saeidi N., Liles M., Dimarzio C. A., Ruberti J. W. (2010) Mechanical strain stabilizes reconstituted collagen fibrils against enzymatic degradation by mammalian collagenase matrix metalloproteinase 8 (MMP-8). *PLoS One*. 5(8):e12337.

Frank-Bertoncelj M., Trenkmann M., Klein K., Karouzakis E., Rehrauer H., Bratus A.,

Kolling C., et al. (2017) Epigenetically-driven anatomical diversity of synovial fibroblasts guides joint-specific fibroblast functions. *Nat. Commun.* 8:14852.

Freedman B. R., Bade N. D., Riggin C. N., Zhang S., Haines P. G., Ong K. L., Janmey P. A. (2015a) The (dys)functional extracellular matrix. *Biochim Biophys Acta*. Nov(1853(11 Pt B)):3153–3164.

Freedman B. R., Zuskov A., Sarver J. J., Buckley M. R., Soslowsky L. J. (2015b) Evaluating changes in tendon crimp with fatigue loading as an ex vivo structural assessment of tendon damage. *J. Orthop. Res.* 33(6):904–910.

Fu K., Robbins S. R., McDougall J. J. (2018) Osteoarthritis: the genesis of pain. *Rheumatology*. 57(suppl_4):iv43–iv50.

Fujita H., Morisugi T., Tanaka Y., Kawakami T., Kirita T., Yoshimura Y. (2009) MMP-3 activation is a hallmark indicating an early change in TMJ disorders, and is related to nitration. *Int. J. Oral Maxillofac. Surg.* 38(1):70–78.

Galardy R. E., Cassabonne M. E., Giese C., Gilbert J. H., Lapierre F., Lopez H., Schaefer M. E., et al. (1994) Low Molecular Weight Inhibitors in Corneal Ulceration. *Ann. N. Y. Acad. Sci.* 732(1):315–323.

Gege C., Bao B., Bluhm H., Boer J., Gallagher B. M., Korniski B., Powers T. S., Steeneck C., Taveras A. G., Baragi V. M. (2012) Discovery and evaluation of a non-Zn chelating, selective matrix metalloproteinase 13 (MMP-13) inhibitor for potential intra-articular treatment of osteoarthritis. *J. Med. Chem.* 55(2):709–716.

Gellhorn A. C., Katz J. N., Suri P. (2013) Osteoarthritis of the spine: the facet joints. *Nat. Rev. Rheumatol.* 9(4):216–224.

Ghasemi S., Sardari K., Mirshokraei P., Hassanpour H. (2018) In vitro study of matrix metalloproteinases 1, 2, 9, 13 and serum amyloid A mRNAs expression in equine fibroblast-like synoviocytes treated with doxycycline. *Can. J. Vet. Res.* 82(2):82–88.

Gho W. G., Choi Y., Park K. H., Huh J. K. (2018) Expression of collagenases (Matrix metalloproteinase-1, 8, 13) and tissue inhibitor of metalloproteinase-1 of retrodiscal tissue in temporomandibular joint disorder patients. *J. Korean Assoc. Oral Maxillofac. Surg.* 44(3):120–127.

Gong K., Shao W., Chen H., Wang Z., Luo Z. J. (2011) Rat model of lumbar facet joint osteoarthritis associated with facet-mediated mechanical hyperalgesia induced by intra-articular injection of monosodium iodoacetate. *J. Formos. Med. Assoc.* 110(3):145–152.

Gou Y., Tian F., Dai M., Li H., Lv Q., Kong Q., Chen T., et al. (2019) Salmon calcitonin exerts better preventive effects than celecoxib on lumbar facet joint degeneration and long-term tactile allodynia in rats. *Bone*. 127:17–25.

Grant T. M., Yapp C., Chen Q., Czernuszka J. T., Thompson M. S. (2015) The Mechanical, Structural, and Compositional Changes of Tendon Exposed to Elastase. *Ann. Biomed. Eng.* 43(10):2477–2486.

Grenier S., Bhargava M. M., Torzilli P. A. (2014) An in vitro model for the pathological

degradation of articular cartilage in osteoarthritis. *J. Biomech.* 47(3):645–652.

Grienberger C., Konnerth A. (2012) Imaging Calcium in Neurons. *Neuron*. 73(5):862–885.

Griffin D. J., Vicari J., Buckley M. R., Silverberg J. L., Cohen I., Bonassar L. J. (2014) Effects of enzymatic treatments on the depth-dependent viscoelastic shear properties of articular cartilage. *J. Orthop. Res.* 32(12):1652–1657.

Grinnell F. (2000) Fibroblast – collagen - matrix contraction : signalling and mechanical loading. *Cell*. 10(September):377–380.

Grinnell F. (2003) Fibroblast biology in three-dimensional collagen matrices. *Trends Cell Biol.* 13(5):264–269.

Grinnell F. (2008) Fibroblast mechanics in three-dimensional collagen matrices. *J. Bodyw. Mov. Ther.* 12(3):191–3.

Grinnell F., Petroll W. M. (2010) Cell Motility and Mechanics in Three-Dimensional Collagen Matrices. *Annu. Rev. Cell Dev. Biol.* 26(1):335–361.

Grobelny D., Poncz L., Galardy R. E. (1992) Inhibition of Human Skin Fibroblast Collagenase, Thermolysin, and Pseudomonas aeruginosa elastase by Peptide Hydroxamic Acids. *Biochemistry*. 31(31):7152–7154.

Hadi M. F., Barocas V. H. (2013) Microscale fiber network alignment affects macroscale failure behavior in simulated collagen tissue analogs. *J. Biomech. Eng.*

135(2):021026.

Hadi M. F., Sander E. A., Ruberti J. W., Barocas V. H. (2012) Simulated remodeling of loaded collagen networks via strain-dependent enzymatic degradation and constant-rate fiber growth. *Mech. Mater.* 44:72–82.

Hall M., Allison K., Wrigley T. V, Metcalf B. R., Pua Y.-H., Ginckel A. Van, Bennell K. L. (2018) Frontal plane hip joint loading according to pain severity in people with hip osteoarthritis. *J. Orthop. Res.* 36(6):1637–1644.

Haller J. M., Swearingen C. A., Partridge D., McFadden M., Thirunavukkarasu K., Higgins T. F. (2015) Intraarticular Matrix Metalloproteinases and Aggrecan Degradation Are Elevated After Articular Fracture. *Clin. Orthop. Relat. Res.* 473(10):3280–3288.

Hardy R. S., Hülso C., Liu Y., Gasparini S. J., Fong-Yee C., Tu J., Stoner S., et al. (2013) Characterisation of fibroblast-like synoviocytes from a murine model of joint inflammation. *Arthritis Res. Ther.* 15(1):R24.

Havelin J., Imbert I., Cormier J., Allen J., Porreca F., King T. (2015) Central sensitization and neuropathic features of ongoing pain in a rat model of advanced osteoarthritis. *J. Pain.* 17(3):374–382.

Hawellek T., Hubert J., Hischke S., Rolvien T., Krause M., Püschel K., Rüther W., Niemeier A. (2017) Microcalcification of lumbar spine intervertebral discs and facet joints is associated with cartilage degeneration, but differs in prevalence and its

relation to age. *J. Orthop. Res.* 35(12):2692–2699.

Hawker G. A., Mian S., Kendzerska T., French M. (2011) Measures of adult pain: Visual Analog Scale for Pain (VAS Pain), Numeric Rating Scale for Pain (NRS Pain), McGill Pain Questionnaire (MPQ), Short-Form McGill Pain Questionnaire (SF-MPQ), Chronic Pain Grade Scale (CPGS), Short Form-36 Bodily Pain Scale (SF-36 BPS), and Measure of Intermittent and Constant Osteoarthritis Pain (ICOAP). *Arthritis Care Res.* 63(SUPPL. 11):S240–S252.

Henninger H. B., Underwood C. J., Romney S. J., Davis G. L., Weiss J. A. (2013) Effect of elastin digestion on the quasi-static tensile response of medial collateral ligament. *J Orthop Res*. 31(8):1226–33.

Hill C. L., Seo G. S., Gale D., Totterman S., Gale M. E., Felson D. T. (2005) Cruciate ligament integrity in osteoarthritis of the knee. *Arthritis Rheum.* 52(3):794–799.

Hinz B. (2013) Matrix Mechanics And Regulation Of The Fibroblast Phenotype. *Periodontol. 2000*. 63(162):14–28.

Hjermstad M. J., Fayers P. M., Haugen D. F., Caraceni A., Hanks G. W., Loge J. H., Fainsinger R., Aass N., Kaasa S. (2011) Studies comparing numerical rating scales, verbal rating scales, and visual analogue scales for assessment of pain intensity in adults: A systematic literature review. *J. Pain Symptom Manage.* 41(6):1073–1093.

Hogg-Johnson S., Velde G. van der, Carroll L. J., Holm L. W., Cassidy J. D., Guzman J., Côté P., et al. (2008a) The Burden and Determinants of Neck Pain in the General

Population. *Spine (Phila. Pa. 1976).* 33(Supplement):S39–S51.

Hogg-Johnson S., Velde G. van der, Carroll L. J., Holm L. W., David Cassidy J., Guzman J., Côté P., et al. (2008b) The Burden and Determinants of Neck Pain in the General Population Results of the Bone and Joint Decade 2000 –2010 Task Force on Neck Pain and Its Associated Disorders. *Spine (Phila. Pa. 1976).* 33(4S):39–51.

Hong J.-I., Park I. Y., Kim H. A. (2020) Understanding the Molecular Mechanisms Underlying the Pathogenesis of Arthritis Pain Using Animal Models. *Int. J. Mol. Sci.* 21(2):533.

Hsieh A. H., Tsai C. M., Ma Q. J., Lin T., Banes A. J., Villarreal F. J., Akeson W. H., Sung K. L. (2000) Time-dependent increases in type-III collagen gene expression in medical collateral ligament fibroblasts under cyclic strains. *J. Orthop. Res.* 18:220–227.

Hu X., Laragione T., Sun L., Koshy S., Jones K. R., Ismailov I. I., Yotnda P., Horrigan F. T., Gulko P. S., Beeton C. (2012) KCa1.1 Potassium Channels Regulate Key Proinflammatory and Invasive Properties of Fibroblast-like Synoviocytes in Rheumatoid Arthritis. *J. Biol. Chem.* 287(6):4014–22.

Hunter D. J., Guermazi A., Roemer F., Zhang Y., Neogi T. (2013) Structural correlates of pain in joints with osteoarthritis. *Osteoarthr. Cartil.* 21(9):1170–1178.

Huntley G. W. (2012) Synaptic circuit remodelling by matrix metalloproteinases in health and disease. *Nat. Rev. Neurosci.* 13(11):743–757.

Hwang J., Huang Y., Burwell T. J., Peterson N. C., Connor J., Weiss S. J., Yu ⊥ S Michael, Li Y. (2017) In Situ Imaging of Tissue Remodeling with Collagen Hybridizing Peptides. *ACS Nano*. 11(10):9825–35.

IBM Corporation (2019) *IBM Pulse Poll: Pain*.

Inglis J. J., McNamee K. E., Chia S. L., Essex D., Feldmann M., Williams R. O., Hunt S. P., Vincent T. (2008) Regulation of pain sensitivity in experimental osteoarthritis by the endogenous peripheral opioid system. *Arthritis Rheum.* 58(10):3110–3119.

Institute of Medicine (2011) *Relieving pain in America: A blueprint for transforming prevention, care, education, and research*. Washington, DC.

Ita M. E., Adegoke M. A., Winkelstein B. A. (2017a) Collagenase exposure alters neuronal activity and biochemical regulators with implications for degenerative pain, in *Summer Biomech. Bioeng. Biotransport Conf.*, p. P123. Tucson, AZ.

Ita M. E., Crosby N. D., Bulka B. A., Winkelstein B. A. (2017b) Painful Cervical Facet Joint Injury Is Accompanied by Changes in the Number of Excitatory and Inhibitory Synapses in the Superficial Dorsal Horn That Differentially Relate to Local Tissue Injury Severity. *Spine (Phila. Pa. 1976).* 42(12):E695–E701.

Ita M. E., Ghimire P., Granquist E. J., Winkelstein B. A. (2020a) MMPs in tissues from TMJ disorders relate to pain more than joint damage. *J. Orthop. Res.* (submitted).

Ita M. E., Ghimire P., Welch R. L., Troche H. R., Winkelstein B. A. (2020b) Intra-articular collagenase in the spinal facet joint induces pain, DRG neuron

dysregulation and increased MMP-1 absent evidence of joint destruction. *Sci. Rep.* (under review).

Ita M. E., Leavitt O. M. E., Winkelstein B. A. (2018a) MMP-1 induces joint pain that may be mediated by increased activity in peripheral neurons, in *Orthop. Res. Soc. Annu. Meet.*, p. #2184. New Orleans, LA.

Ita M. E., Weisshaar C. L., Winkelstein B. A. (2018b) Collagenase in the spinal facet joint induces pain & alters genes in the DRG absent evident cartilage destruction., in *IASP World Congr. Pain*. Boston, MA.

Ita M. E., Winkelstein B. A. (2019a) MMP-1 & MMP-9 increase after tensile stretch: lessons from neuronal-fibroblast co-cultures simulating joint capsules, in *Biomed. Eng. Soc. Annu. Meet.*, p. #767. Philadelphia, PA.

Ita M. E., Winkelstein B. A. (2019b) Intraarticular MMP-1 is sufficient to induce pain & substance P regulation in DRG afferents absent any structural damage, in *Cerv. Spine Res. Soc. Annu. Meet.*, p. #40. New York, NY.

Ita M. E., Winkelstein B. A. (2019c) Concentration-Dependent Effects of Fibroblast-Like Synoviocytes on Collagen Gel Multiscale Biomechanics and Neuronal Signaling: Implications for Modeling Human Ligamentous Tissues. *J. Biomech. Eng.* 141(9):0910131–09101312.

Ita M. E., Zhang S., Holsgrove T. P., Kartha S., Winkelstein B. A. (2017c) The Physiological Basis of Cervical Facet-Mediated Persistent Pain: Basic Science and

Clinical Challenges. *J. Orthop. Sport. Phys. Ther.* 47(7):450–461.

Jackson K. L., Dayton R. D., Deverman B. E., Klein R. L. (2016) Better Targeting, Better Efficiency for Wide-Scale Neuronal Transduction with the Synapsin Promoter and AAV-PHP.B. *Front. Mol. Neurosci.* 9(November 2019):1–11.

Jaumard N. V, Welch W. C., Winkelstein B. A. (2011) Spinal facet joint biomechanics and mechanotransduction in normal, injury and degenerative conditions. *J. Biomech. Eng.* 133(7):071010.

Jenkins G., Redwood K. L., Meadows L., Green M. R. (1999) Effect of gel re-organization and tensional forces on α2β1 integrin levels in dermal fibroblasts. *Eur. J. Biochem.* 263(1):93–103.

Ji J., Tyurina Y. Y., Tang M., Feng W., Stolz D. B., Clark R. S. B., Meaney D. F., Kochanek P. M., Kagan V. E., Bayır H. (2012) Mitochondrial injury after mechanical stretch of cortical neurons in vitro: biomarkers of apoptosis and selective peroxidation of anionic phospholipids. *J. Neurotrauma*. 29(5):776–788.

Ji R.-R., Baba H., Brenner G. J., Woolf C. J. (1999) Nociceptive-specific activation of ERK in spinal neurons contributes to pain hypersensitivity. *Nat. Neurosci.* 2(12):1114–1119.

Ji R.-R., Zhen-Zhong X., Wang X., Lo E. H. (2008) MMP-2 and MMP-9 — Investigations in Neuropathic Pain Phases. *Neuropathic Pain.* 4(2):71–74.

Ji R. R., Gereau IV R. W., Malcangio M., Strichartz G. R. (2009) MAP kinase and pain.

Brain Res. Rev. 60(1):135–148.

Ji R. R., Nackley A., Huh Y., Terrando N., Maixner W. (2018) Neuroinflammation and central sensitization in chronic and widespread pain. *Anesthesiology*. 129(2):343–366.

Ji R. R., Samad T. A., Jin S. X., Schmoll R., Woolf C. J. (2002) p38 MAPK activation by NGF in primary sensory neurons after inflammation increases TRPV1 levels and maintains heat hyperalgesia. *Neuron*. 36(1):57–68.

Jiang L., Pan C.-L., Wang C.-Y., Liu B.-Q., Han Y., Hu L., Liu L., Yang Y., Qu J.-W., Liu W.-T. (2017) Selective suppression of the JNK-MMP2/9 signal pathway by tetramethylpyrazine attenuates neuropathic pain in rats. *J. Neuroinflammation*. 14(1):174.

Jüngel A., Ospelt C., Lesch M., Thiel M., Sunyer T., Schorr O., Michel B. A., et al. (2010) Effect of the oral application of a highly selective MMP-13 inhibitor in three different animal models of rheumatoid arthritis. *Ann. Rheum. Dis.* 69(5):898–902.

Kallakuri S., Li Y., Chen C., Cavanaugh J. M. (2012) Innervation of cervical ventral facet joint capsule: Histological evidence. *World J. Orthop.* 3(2):10–14.

Kallakuri S., Singh A., Chen C., Cavanaugh J. M. (2004) Demonstration of substance P, calcitonin gene-related peptide, and protein gene product 9.5 containing nerve fibers in human cervical facet joint capsules. *Spine (Phila. Pa. 1976).* 29(11):1182–1186.

Kallakuri S., Singh A., Lu Y., Chen C., Patwardhan A., Cavanaugh J. M. (2008) Tensile

stretching of cervical facet joint capsule and related axonal changes. *Eur. Spine J.* 17(4):556–563.

Kanyama M., Kuboki T., Kojima S., Fujisawa T., Hattori T., Takigawa M., Yamashita A. (2000) Matrix metalloproteinases and tissue inhibitors of metalloproteinases in synovial fluids of patients with temporomandibular joint osteoarthritis. *J. Orofac. Pain*. 14(1):20–30.

Kartha S., Weisshaar C. L., Philips B. H., Winkelstein B. A. (2018) Pre-treatment with Meloxicam Prevents the Spinal Inflammation and Oxidative Stress in DRG Neurons that Accompany Painful Cervical Radiculopathy. *Neuroscience*. 388:393–404.

Kartha S., Yan L., Weisshaar C. L., Ita M. E., Shuvaev V. V., Muzykantov V. R., Tsourkas A., Winkelstein B. A., Cheng Z. (2017) Superoxide Dismutase-Loaded Porous Polymersomes as Highly Efficient Antioxidants for Treating Neuropathic Pain. *Adv. Healthc. Mater.* 6(17).

Kartha S., Zhou T., Granquist E. J., Winkelstein B. A. (2016) Development of a Rat Model of Mechanically Induced Tunable Pain and Associated Temporomandibular Joint Responses. *J. Oral Maxillofac. Surg.* 74(1):54.e1-e10.

Kawasaki Y., Xu Z.-Z., Wang X., Park J. Y., Zhuang Z.-Y., Tan P.-H., Gao Y.-J., et al. (2008) Distinct roles of matrix metalloproteases in the early- and late-phase development of neuropathic pain. *Nat. Med.* 14(3):331–336.

Kellenberger C. J., Junhasavasdikul T., Tolend M., Doria A. S. (2018)

Temporomandibular joint atlas for detection and grading of juvenile idiopathic arthritis involvement by magnetic resonance imaging. *Pediatr. Radiol.* 48(3):411–426.

Kido M. A., Kiyoshima T., Kondo T., Ayasaka N., Moroi R., Terada Y., Tanaka T. (1993) Distribution of substance P and calcitonin gene-related peptide-like immunoreactive nerve fibers in the rat temporomandibular joint. *J. Dent. Res.* 72(3):592–8.

Kim J.-S., Ali M. H., Wydra F., Li X., Hamilton J. L., An H. S., Cs-Szabo G., et al. (2015) Characterization of degenerative human facet joints and facet joint capsular tissues. *Osteoarthr. Cartil.* 23(12):2242–2251.

Kim J.-S., Kroin J. S., Buvanendran A., Li X., Wijnen A. J. van, Tuman K. J., Im H.-J. (2011) Characterization of a new animal model for evaluation and treatment of back pain due to lumbar facet joint osteoarthritis. *Arthritis Rheum.* 63(10):2966–2973.

Kim S.-G., Akaike T., Sasagaw T., Atomi Y., Kurosawa H. (2002) Gene expression of type I and type III collagen by mechanical stretch in anterior cruciate ligament cells. *Cell Struct. Funct.* 27(3):139–144.

Kjaer P., Leboeuf-Yde C., Korsholm L., Sorensen J. S., Bendix T. (2005) Magnetic Resonance Imaging and Low Back Pain in Adults: A Diagnostic Imaging Study of 40-Year-Old Men and Women. *Spine (Phila. Pa. 1976).* 30(10):1173–1180.

Kobayashi H., Chattopadhyay S., Kato K., Dolkas J., Kikuchi S. ichi, Myers R. R.,

Shubayev V. I. (2008) MMPs initiate Schwann cell-mediated MBP degradation and mechanical nociception after nerve damage. *Mol. Cell. Neurosci.* 39(4):619–627.

Koh K.-J., List T., Petersson A., Rohlin M. (2009) Relationship Between Clinical and Magnetic Resonance Imaging Diagnoses and Findings in Degenerative and Inflammatory Temporomandibular Joint Diseases: A Systematic Literature Review. *J. Orofac. Pain*. 23(2):123–139.

Konttinen Y. T., Ainola M., Valleala H., Ma J., Ida H., Mandelin J., Kinne R. W., et al. (1999) Analysis of 16 different matrix metalloproteinases (MMP-1 to MMP-20) in the synovial membrane: different profiles in trauma and rheumatoid arthritis. *Ann. Rheum. Dis.* 58(11):691–697.

Kook S.-H., Hwang J.-M., Park J.-S., Kim E.-M., Heo J.-S., Jeon Y.-M., Lee J.-C. (2009) Mechanical force induces type I collagen expression in human periodontal ligament fibroblasts through activation of ERK/JNK and AP-1. *J. Cell. Biochem.* 106(January):1060–1067.

Kraan P. M. van der, Vitters E. L., Beuningen H. M. van, Putte L. B. van de, Berg W. B. van den (1990) Degenerative knee joint lesions in mice after a single intra-articular collagenase injection. A new model of osteoarthritis. *J. Exp. Pathol. (Oxford).* 71(1):19–31.

Kras J. V., Kartha S., Winkelstein B. A. (2015a) Intra-articular nerve growth factor regulates development, but not maintenance, of injury-induced facet joint pain &

spinal neuronal hypersensitivity. *Osteoarthr. Cartil.* 23:1999–2008.

Kras J. V., Weisshaar C. L., Pall P. S., Winkelstein B. A. (2015b) Pain from intra-articular NGF or joint injury in the rat requires contributions from peptidergic joint afferents. *Neurosci. Lett.* 604:193–198.

Kras J. V, Dong L., Winkelstein B. A. (2014) Increased interleukin-1α and prostaglandin E2 expression in the spinal cord at 1 day after painful facet joint injury: evidence of early spinal inflammation. *Spine (Phila. Pa. 1976).* 39(3):207–12.

Kras J. V, Tanaka K., Gilliland T. M., Winkelstein B. A. (2013a) An anatomical and immunohistochemical characterization of afferents innervating the C6-C7 facet joint after painful joint loading in the rat. *Spine (Phila. Pa. 1976).* 38(6):E325–E331.

Kras J. V, Weisshaar C. L., Quindlen J., Winkelstein B. A. (2013b) Brain-derived neurotrophic factor is upregulated in the cervical dorsal root ganglia and spinal cord and contributes to the maintenance of pain from facet joint injury in the rat. *J. Neurosci. Res.* 91(10):1312–1321.

Kraus V. B., Blanco F. J., Englund M., Karsdal M. A., Lohmander L. S. (2015) Call for standardized definitions of osteoarthritis and risk stratification for clinical trials and clinical use. *Osteoarthr. Cartil.* 23(8):1233–1241.

Kubota T., Kubota E., Matsumoto A., Kawai Y., Saito H., Mikuni-Takagaki Y., Sato S. (1998) Identification of matrix metalloproteinases (MMPs) in synovial fluid from patients with temporomandibular disorder. *Eur. J. Oral Sci.* 106(6):992–998.

Kural M. H., Billiar K. L. (2013) Regulating tension in three-dimensional culture environments. *Exp. Cell Res.* 319(16):2447–2459.

Kusiak J. W., Veasley C., Maixner W., Smith S., Fillingim R. B., Mogil J. S., Diatchenko L., et al. (2018) *The TMJ Patient-Led Round Table: A History and Summary of Work.*

Kuyinu E. L., Narayanan G., Nair L. S., Laurencin C. T. (2016) Animal models of osteoarthritis: Classification, update, and measurement of outcomes. *J. Orthop. Surg. Res.* 11(19):1–27.

Lafeber F. P. J. G., Spil W. E. van (2013) Osteoarthritis year 2013 in review: Biomarkers; reflecting before moving forward, one step at a time. *Osteoarthr. Cartil.* 21(10):1452–1464.

Lake S. P., Barocas V. H. (2011) Mechanical and structural contribution of non-fibrillar matrix in uniaxial tension: A collagen-agarose co-gel model. *Ann. Biomed. Eng.* 39(7):1891–1903.

Lake S. P., Barocas V. H. (2012) Mechanics and kinematics of soft tissue under indentation are determined by the degree of initial collagen fiber alignment. *J. Mech. Behav. Biomed. Mater.* 13:25–35.

Lake S. P., Hald E. S., Barocas V. H. (2011) Collagen-Agarose Co-Gels as a Model for Collagen-Matrix Interaction in Soft Tissues Subjected to Indentation. *J Biomed Mater Res A.* 99(4):507–515.

Lakes E. H., Allen K. D. (2016) Gait analysis methods for rodent models of arthritic disorders: Reviews and recommendations. *Osteoarthr. Cartil.* 24(11):1837–1849.

Latremoliere A., Woolf C. J. (2009) Central Sensitization: A Generator of Pain Hypersensitivity by Central Neural Plasticity. *J. Pain*. 10(9):895–926.

Lattermann C., Jacobs C. A., Proffitt Bunnell M., Huston L. J., Gammon L. G., Johnson D. L., Reinke E. K., Huebner J. L., Kraus V. B., Spindler K. P. (2017) A Multicenter Study of Early Anti-inflammatory Treatment in Patients With Acute Anterior Cruciate Ligament Tear. *Am. J. Sports Med.* 45(2):325–333.

Lee D. J., Winkelstein B. A. (2012) The failure response of the human cervical facet capsular ligament during facet joint retraction. *J. Biomech.* 45(14):2325–9.

Lee J. Y., Choi H. Y., Ahn H. J., Ju B. G., Yune T. Y. (2014) Matrix metalloproteinase-3 promotes early blood-spinal cord barrier disruption and hemorrhage and impairs long-term neurological recovery after spinal cord injury. *Am. J. Pathol.* 184(11):2985–3000.

Lee K. E., Davis M. B., Mejilla R. M., Winkelstein B. A. (2004a) In Vivo Cervical Facet Capsule Distraction: Mechanical Implications for Whiplash & Neck Pain. *Stapp Car Crash J.* 48(November):1–23.

Lee K. E., Davis M. B., Winkelstein B. A. (2008) Capsular ligament involvement in the development of mechanical hyperalgesia after facet joint loading: behavioral and inflammatory outcomes in a rodent model of pain. *J. Neurotrauma*. 25(11):1383–

1393.

Lee K. E., Franklin A. N., Davis M. B., Winkelstein B. A. (2006) Tensile cervical facet capsule ligament mechanics: failure and subfailure responses in the rat. *J. Biomech.* 39(7):1256–1264.

Lee K. E., Thinnes J. H., Gokhin D. S., Winkelstein B. A. (2004b) A novel rodent neck pain model of facet-mediated behavioral hypersensitivity: implications for persistent pain and whiplash injury. *J. Neurosci. Methods*. 137(2):151–159.

Lee K. E., Winkelstein B. A. (2009) Joint distraction magnitude is associated with different behavioral outcomes and substance P levels for cervical facet joint loading in the rat. *J. Pain*. 10(4):436–445.

Lee T. C., Midura R. J., Hascall V. C., Vesely I. (2001) The effect of elastin damage on the mechanics of the aortic valve. *J. Biomech.* 34(2):203–210.

Leeming D. J., He Y., Veidal S. S., Nguyen Q. H. T., Larsen D. V., Koizumi M., Segovia-Silvestre T., et al. (2011) A novel marker for assessment of liver matrix remodeling: An enzyme-linked immunosorbent assay (ELISA) detecting a MMP generated type I collagen neo-epitope (C1M). *Biomarkers*. 16(7):616–628.

Leonardi R., Perrotta R. E., Almeida L.-E., Loreto C., Musumeci G., Lu M. G. (2016) Lubricin in synovial fluid of mild and severe temporomandibular joint internal derangements- bricin in synovial fluid of mild and severe temporomandibular joint internal derangements. *Med Oral Patol Oral Cir Bucal*. 21(6):e793–e739.

Lin A. H., Zitnay J. L., Li Y., Yu S. M., Weiss J. A. (2019) Microplate assay for denatured collagen using collagen hybridizing peptides. *J. Orthop. Res.* 37(2):431–438.

Lluch E., Torres R., Nijs J., Oosterwijck J. Van (2014) Evidence for central sensitization in patients with osteoarthritis pain: A systematic literature review. *Eur. J. Pain (United Kingdom)*. 18(10):1367–1375.

Lluch Girbés E., Dueñas L., Barbero M., Falla D., Baert I. A. C., Meeus M., Sánchez-Frutos J., Aguilella L., Nijs J. (2016) Expanded Distribution of Pain as a Sign of Central Sensitization in Individuals With Symptomatic Knee Osteoarthritis. *Phys. Ther.* 96(8):1196–1207.

Lo E. H., Dalkara T., Moskowitz M. A. (2003) Neurological diseases: Mechanisms, challenges and opportunities in stroke. *Nat. Rev. Neurosci.* 4(5):399–414.

Loeser J. D., Treede R. D. (2008) The Kyoto protocol of IASP basic pain terminology. *Pain*. 137(3):473–477.

Loeser R. F., Goldring S. R., Scanzello C. R., Goldring M. B. (2012) Osteoarthritis: A disease of the joint as an organ. *Arthritis Rheum.* 64(6):1697–1707.

Löffek S., Schilling O., Franzke C.-W. (2011) Biological Role of Matrix Metalloproteinases: A Critical Balance. *Eur. Respir. J.* 38(1):191–208.

Lu Y., Chen C., Kallakuri S., Patwardhan A., Cavanaugh J. M. (2005a) Neural Response of Cervical Facet Joint Capsule to Stretch: A Study of Whiplash Pain Mechanism.

Stapp Car Crash J. 49:49–65.

Lu Y., Chen C., Kallakuri S., Patwardhan A., Cavanaugh J. M. (2005b) Development of an in vivo method to investigate biomechanical and neurophysiological properties of spine facet joint capsules. *Eur. Spine J.* 14:565–572.

Lu Y., Chen C., Kallakuri S., Patwardhan A., Cavanaugh J. M. (2005c) Neurophysiological and biomechanical characterization of goat cervical facet joint capsules. *J. Orthop. Res.* 23(4):779–87.

Malfait A. M., Little C. B., McDougall J. J. (2013) A commentary on modelling osteoarthritis pain in small animals. *Osteoarthr. Cartil.* 21(9):1316–1326.

Malfait A. M., Miller R. J. (2016) Emerging Targets for the Management of Osteoarthritis Pain. *Curr. Osteoporos. Rep.* 14(6):260–268.

Malfait A. M., Schnitzer T. J. (2013) Towards a mechanism-based approach to pain management in osteoarthritis. *Nat. Rev. Rheumatol.* 9(11):654–664.

Manchikanti L., Boswell M. V., Singh V., Pampati V., Damron K. S., Beyer C. D. (2004) Prevalence of facet joint pain in chronic spinal pain of cervical, thoracic, and lumbar regions. *BMC Musculoskelet. Disord.* 5(15).

Manchikanti L., Kaye A. D., Boswell M. V., Bakshi S., Gharibo C. G., Grami V., Grider J. S., et al. (2015) A systematic review and best evidence synthesis of effectiveness of therapeutic facet joint interventions in managing chronic spinal pain. *Pain Physician*. 18(4):E535–E582.

Marchetti C., Cornaglia I., Casasco A., Bernasconi G., Baciliero U., Stetler-Stevenson W. G. (1999) Immunolocalization of gelatinase-A (matrix metalloproteinase-2) in damaged human temporomandibular joint discs. *Arch. Oral Biol.* 44:297–304.

May J. O., Looney S. W. (2020) Biometrics & Biostatistics Sample Size Charts for Spearman and Kendall Coefficients. *J. Biom. Biostat.* 11(2).

McLain R. (1994) Mechanoreceptor endings in human cervical facet joints. *Spine (Phila. Pa. 1976).* 19(5):495–501.

Mehnert J. M., Kisch T., Brandenburger M. (2014) Co-Culture Systems of Human Sweat Gland Derived Stem Cells and Peripheral Nerve Cells: An in Vitro Approach for Peripheral Nerve Regeneration. *Cell. Physiol. Biochem.* 34(4):1027–1037.

Melli G., Höke A. (2009) Dorsal Root Ganglia Sensory Neuronal Cultures: a tool for drug discovery for peripheral neuropathies. *Expert Opin Drug Discov.* 4(10):1035–1045.

Milam S. B., Klebe R. J., Triplett R. G., Herbert D. (1991) Characterization of the extracellular matrix of the primate temporomandibular joint. *J. Oral Maxillofac. Surg.* 49(4):381–391.

Miller E. J., Rhodes R. K. (1982) Preparation and characterization of the different types of collagen. *Methods Enzymol.* 82 Pt A:33–64.

Miller K. S., Connizzo B. K., Soslowsky L. J. (2012) Collagen fiber re-alignment in a neonatal developmental mouse supraspinatus tendon model. *Ann. Biomed. Eng.*

40(5):1102–1110.

Miller R. E., Kim Y. S., Tran P. B., Ishihara S., Dong X., Miller R. J., Malfait A. M. (2018) Visualization of Peripheral Neuron Sensitization in a Surgical Mouse Model of Osteoarthritis by In Vivo Calcium Imaging. *Arthritis Rheumatol.* 70(1):88–97.

Miller R. E., Miller R. J., Malfait A. M. (2014) Osteoarthritis joint pain: The cytokine connection. *Cytokine*. 70(2):185–193.

Miller R. E., Tran P. B., Ishihara S., Syx D., Ren D., Miller R. J., Valdes A. M., Malfait A. M. (2020) Microarray analyses of the dorsal root ganglia support a role for innate neuro-immune pathways in persistent pain in experimental osteoarthritis. *Osteoarthr. Cartil.* 28(5):581–592.

Miotla Zarebska J., Chanalaris A., Driscoll C., Burleigh A., Miller R. E., Malfait A. M., Stott B., Vincent T. L. (2017) CCL2 and CCR2 regulate pain-related behaviour and early gene expression in post-traumatic murine osteoarthritis but contribute little to chondropathy. *Osteoarthr. Cartil.* 25(3):406–412.

Mitchell A. J., Lone A. M., Tinoco A. D., Saghatelian A. (2013) Proteolysis Controls Endogenous Substance P Levels. *PLoS One*. 8(7):68638.

Mizui T., Ishimaru J. I., Miyamoto K., Kurita K. (2001) Matrix metalloproteinase-2 in synovial lavage fluid of patients with disorders of the temporomandibular joint. *Br. J. Oral Maxillofac. Surg.* 39(4):310–314.

Mohammadi H., Arora P. D., Simmons C. A., Janmey P. A., Mcculloch C. A. (2015)

Inelastic behaviour of collagen networks in cell-matrix interactions and mechanosensation. *J R Soc Interface*. 12(102):20141074.

Moore D. (2020) *Level of Evidence: AAOS Evidence-Based Practice Committee*.

Mort J. S., Billington C. J. (2001) Articular cartilage and changes in arthritis: matrix degradation. *Arthritis Res.* 3(6):337–41.

Mow V. C., Ateshian G. A., Spilker R. L. (1993) Biomechanics of Diarthrodial Joints: A Review of Twenty Years of Progress. *J. Biomech. Eng.* 115(4B):460–467.

Muir E. M., Adcock K. H., Morgenstern D. A., Clayton R., Stillfried N. Von, Rhodes K., Ellis C., Fawcett J. W., Rogers J. H. (2002) Matrix metalloproteases and their inhibitors are produced by overlapping populations of activated astrocytes. *Mol. Brain Res.* 100(1–2):103–117.

Munster S., Jawerth L. M., Leslie B. A., Weitz J. I., Fabry B., Weitz D. A. (2013) Strain history dependence of the nonlinear stress response of fibrin and collagen networks. *Proc. Natl. Acad. Sci.* 110(30):12197–12202.

Murphy G. (2017) Riding the Metalloproteinase Roller Coaster. *J. Biol. Chem.* 292(19):7708–7718.

Murphy G., Nagase H. (2009) Progress in matrix metalloproteinase research. *Mol. Aspects Med.* 29(5):290–308.

Nascimento G. C., Rizzi E., Gerlach R. F., Leite-Panissi C. R. A. (2013) Expression of

MMP-2 and MMP-9 in the rat trigeminal ganglion during the development of temporomandibular joint inflammation. *Brazilian J. Med. Biol. Res.* 46(11):956–967.

National Academies of Sciences, Engineering, and Medicine (2020) *Temporomandibular Disorders: Priorities for Research and Care*. Washington, DC.

Neidhart M., Seemayer C. A., Hummel K. M., Michel B. A., Gay R. E., Gay S. (2003) Functional characterization of adherent synovial fluid cells in rheumatoid arthritis: Destructive potential in vitro and in vivo. *Arthritis Rheum.* 48(7):1873–1880.

Neogi T. (2013) The epidemiology and impact of pain in osteoarthritis. *Osteoarthr. Cartil.* 21(9):1145–1153.

NIDCR (2014) *Facial Pain*.

Nishida K., Kuchiiwa S., Oiso S., Futagawa T., Masuda S., Takeda Y., Yamada K. (2008) Up-regulation of matrix metalloproteinase-3 in the dorsal root ganglion of rats with paclitaxel-induced neuropathy. *Cancer Sci.* 99(8):1618–1625.

Nobe K., Nobe H., Obara K., Paul R. J. (2000) Preferential role of intracellular Ca2+ stores in regulation of isometric force in NIH 3T3 fibroblast fibres. *J. Physiol.* 529 Pt 3(Pt 3):669–79.

Noble L. J., Donovan F., Igarashi T., Goussev S., Werb Z. (2002) Matrix metalloproteinases limit functional recovery after spinal cord injury by modulation of early vascular events. *J. Neurosci.* 22(17):7526–7535.

Norris S. H., Watt I. (1983) The prognosis of neck injuries resulting from rear-end vehicle collisions. *J. Bone Jt. Surg.* 65-B(5):608–611.

Nwosu L. N., Mapp P. I., Chapman V., Walsh D. A. (2016) Relationship between structural pathology and pain behaviour in a model of osteoarthritis (OA). *Osteoarthritis Cartilage*. 24(11):6–13.

O'Leary S. A., Paschos N. K., Link J. M., Klineberg E. O., Hu J. C., Athanasiou K. A. (2018) Facet Joints of the Spine: Structure-Function Relationships, Problems and Treatments, and the Potential for Regeneration. *Annu. Rev. Biomed. Eng*. 20:145–70.

Obata K., Noguchi K. (2004) MAPK activation in nociceptive neurons and pain hypersensitivity. *Life Sci.* 74(21):2643–2653.

Obeidat A. M., Miller R. E., Miller R. J., Malfait A. M. (2019) The nociceptive innervation of the normal and osteoarthritic mouse knee. *Osteoarthr. Cartil.* 11:1669–79.

Oliviero F., Ramonda R., Punzi L. (2010) New horizons in osteoarthritis. *Swiss Med. Wkly.* 140:w13098.

Oosterwijck J. Van, Nijs J., Meeus M., Paul L. (2013) Evidence for central sensitization in chronic whiplash: A systematic literature review. *Eur. J. Pain (United Kingdom)*. 17(3):299–312.

Osch G. J. V. M. van, Blankevoort L., Kraan P. M. van der, Janssen B., Hekman E.,

Huiskes R., Berg W. B. van den (1995) Laxity characteristics of normal and pathological murine knee joints in vitro. *J. Orthop. Res.* 13(5):783–791.

Osch G. J. V. M. van, Kraan P. M. van der, Berg W. B. van den (1994) Site-specific cartilage changes in murine degenerative knee joint disease induced by iodoacetate and collagenase. *J. Orthop. Res.* 12(2):168–175.

Otterness I. G., Bliven M. L., Eskra J. D., Koppele J. M. Te, Stukenbrok H. A., Milici A. J. (2000) Cartilage damage after intraarticular exposure to collagenase 3. *Osteoarthr. Cartil.* 8(5):366–373.

Pan F., Jones G. (2018) Clinical Perspective on Pain and Pain Phenotypes in Osteoarthritis. *Curr. Rheumatol. Rep.* 20(79).

Panjabi M. M., Cholewicki J., Nibu K., Grauer J., Vahldiek M. (1998) Capsular ligament stretches during in vitro whiplash simulations. *J. Spinal Disord.* 11(3):227–232.

Park M. S., Lee Y. B., Moon S.-H., Lee H.-M., Kim T.-H., Oh J. B., Riew K. D. (2014) Facet joint degeneration of the cervical spine: A computed tomographic analysis of 320 patients. *Spine (Phila. Pa. 1976).* 39(12):E713–E718.

Patel T. P., Man K., Firestein B. L., Meaney D. F. (2015) Automated quantification of neuronal networks and single-cell calcium dynamics using calcium imaging. *J. Neurosci. Methods*. 243:26–38.

Pearle A. D., Warren R. F., Rodeo S. A. (2005) Basic science of articular cartilage and osteoarthritis. *Clin. Sports Med.* 24(1):1–12.

Pearson A. M., Ivancic P. C., Ito S., Panjabi M. M. (2004) Facet Joint Kinematics and Injury Mechanisms During Simulated Whiplash. *Spine (Phila. Pa. 1976).* 29(4):390–397.

Pekny M., Nilsson M. (2005) Astrocyte activation and reactive gliosis. *Glia*. 50(4):427–434.

Pereira D., Peleteiro B., Araújo J., Branco J., Santos R. A., Ramos E. (2011) The effect of osteoarthritis definition on prevalence and incidence estimates: A systematic review. *Osteoarthr. Cartil.* 19(11):1270–1285.

Perrot S. (2015) Osteoarthritis pain. *Best Pract. Res. Clin. Rheumatol.* 29(1):90–97.

Petersen A., Joly P., Bergmann C., Korus G., Duda G. N. (2012) The Impact of Substrate Stiffness and Mechanical Loading on Fibroblast-Induced Scaffold Remodeling. *Tissue Eng. Part A.* 18(17–18):1804–1817.

Provenzano P. P., Alejandro-Osorio A. L., Valhmu W. B., Jensen K. T., Vanderby R. (2005) Intrinsic fibroblast-mediated remodeling of damaged collagenous matrices in vivo. *Matrix Biol.* 23:543–555.

Provenzano P. P., Heisey D., Hayashi K., Lakes R., Vanderby R. (2002) Subfailure damage in ligament: a structural and cellular evaluation. *J. Appl. Physiol.* 92:362–371.

Provenzano P. P., Vanderby R. (2006) Collagen fibril morphology and organization: Implications for force transmission in ligament and tendon. *Matrix Biol.* 25:71–84.

Quinn K. P., Bauman J. A., Crosby N. D., Winkelstein B. A. (2010a) Anomalous fiber realignment during tensile loading of the rat facet capsular ligament identifies mechanically induced damage and physiological dysfunction. *J. Biomech.* 43(10):1870–1875.

Quinn K. P., Dong L., Golder F. J., Winkelstein B. A. (2010b) Neuronal hyperexcitability in the dorsal horn after painful facet joint injury. *Pain*. 151(2):414–21.

Quinn K. P., Lee K. E., Ahaghotu C. C., Winkelstein B. A. (2007) Structural Changes in the Cervical Facet Capsular Ligament : Potential Contributions to Pain Following Subfailure Loading. *Stapp Car Crash J.* 51:169–187.

Quinn K. P., Winkelstein B. A. (2007) Cervical facet capsular ligament yield defines the threshold for injury and persistent joint-mediated neck pain. *J. Biomech.* 40(10):2299–306.

Quinn K. P., Winkelstein B. A. (2008) Altered collagen fiber kinematics define the onset of localized ligament damage during loading. *J Appl Physiol*. 105(6):1881–1888.

Quinn K. P., Winkelstein B. A. (2009) Vector correlation technique for pixel-wise detection of collagen fiber realignment during injurious tensile loading. *J. Biomed. Opt.* 14(5):054010.

Quinn K. P., Winkelstein B. A. (2010) Full field strain measurements of collagenous tissue by tracking fiber alignment through vector correlation. *J. Biomech.* 43(13):2637–40.

Quinn K. P., Winkelstein B. A. (2011) Detection of altered collagen fiber alignment in the cervical facet capsule after whiplash-like joint retraction. *Ann. Biomed. Eng.* 39(8):2163–2173.

Rahman W., Dickenson A. H. (2015) Osteoarthritis-dependent changes in antinociceptive action of Nav1.7 and Nav1.8 sodium channel blockers: An in vivo electrophysiological study in the rat. *Neuroscience*. 295:103–116.

Raja S. N., Carr D. B., Cohen M., Finnerup N. B., Flor H., Gibson S., Keefe F. J., et al. (2020) The revised International Association for the Study of Pain definition of pain: concepts, challenges, and compromises. *Pain*. 161(9):1976–1982.

Ren K., Dubner R. (2008) Neuron–glia crosstalk gets serious: role in pain hypersensitivity. *Curr. Opin. Anaesthesiol.* 21(5):570–579.

Rhee S., Grinnell F. (2007) Fibroblast mechanics in 3D collagen matrices. *Adv. Drug Deliv. Rev.* 59(13):1299–305.

Rinn J. L., Bondre C., Gladstone H. B., Brown P. O., Chang H. Y. (2006) Anatomic Demarcation by Positional Variation in Fibroblast Gene Expression Programs. *PLoS Genet.* 2(7):e119.

Roeder B. A., Kokini K., Sturgis J. E., Robinson J. P., Voytik-Harbin S. L. (2002) Tensile mechanical properties of three-dimensional type I collagen extracellular matrices with varied microstructure. *J. Biomech. Eng.* 124(2):214–222.

Rogers N. K., Clements D., Dongre A., Harrison T. W., Shaw D., Johnson S. R. (2014)

Extra-Cellular Matrix Proteins Induce Matrix Metalloproteinase-1 (MMP-1) Activity and Increase Airway Smooth Muscle Contraction in Asthma. *PLoS One*. 9(2):e90565.

Rojas F. P., Batista M. A., Lindburg C. A., Dean D., Grodzinsky A. J., Ortiz C., Han L. (2014) Molecular adhesion between cartilage extracellular matrix macromolecules. *Biomacromolecules*. 15(3):772–780.

Rosenberg G. A. (2002) Matrix metalloproteinases in neuroinflammation. *Glia*. 39(3):279–291.

Rosengren S., Boyle D. L., Firestein G. S. (2007) Acquisition, Culture, and Phenotyping of Synovial Fibroblasts, in *Methods Mol. Med.*, (A. P. Cope, ed), Vol. 135, pp. 365–375. Humana Press Inc., Totowa, NJ.

Rothman S. M., Winkelstein B. A. (2010) Cytokine antagonism reduces pain and modulates spinal astrocytic reactivity after cervical nerve root compression. *Ann. Biomed. Eng.* 38(8):2563–2576.

Ruberti J. W., Hallab N. J. (2005) Strain-controlled enzymatic cleavage of collagen in loaded matrix. *Biochem. Biophys. Res. Commun.* 336(2):483–9.

Saddiq Z. A., Barbenel J. C., Grant M. H. (2009) The mechanical strength of collagen gels containing glycosaminoglycans and populated with fibroblasts. *J. Biomed. Mater. Res. - Part A*. 89(3):697–706.

Sander E. A., Barocas V. H. (2009) Comparison of 2D fiber network orientation

measurement methods. *J. Biomed. Mater. Res. - Part A.* 88(2):322–331.

Sander E. A., Barocas V. H., Tranquillo R. T. (2011) Initial fiber alignment pattern alters extracellular matrix synthesis in fibroblast-populated fibrin gel cruciforms and correlates with predicted tension. *Ann. Biomed. Eng.* 39(2):714–729.

Sander E. A., Stylianopoulos T., Tranquillo R. T., Barocas V. H. (2009a) Image-based multiscale modeling predicts tissue-level and network-level fiber reorganization in stretched cell-compacted collagen gels. *Proc. Natl. Acad. Sci. U. S. A.* 106(42):17675–17680.

Sander E., Stylianopoulos T., Tranquillo R., Barocas V. (2009b) Image-based biomechanics of collagen-based tissue equivalents. *IEEE Eng. Med. Biol. Mag.* 28(3):10–18.

Saravanan S., Hairul Islam V. I., Thirugnanasambantham K., Pazhanivel N., Raghuraman N., Paulraj M. G., Ignacimuthu S. (2014) Swertiamarin ameliorates inflammation and osteoclastogenesis intermediates in IL-1b induced rat fibroblast-like synoviocytes. *Inflamm. Res.* 63(6):451–462.

Saxler G., Löer F., Skumavc M., Pförtner J., Hanesch U. (2007) Localization of SP- and CGRP-immunopositive nerve fibers in the hip joint of patients with painful osteoarthritis and of patients with painless failed total hip arthroplasties. *Eur. J. Pain.* 11(1):67.

Sbardella D., Fasciglione G. F., Gioia M., Ciaccio C., Tundo G. R., Marini S., Coletta M.

(2012) Human matrix metalloproteinases: An ubiquitarian class of enzymes involved in several pathological processes. *Mol. Aspects Med.* 33:119–208.

Schindelin J., Arganda-Carreras I., Frise E., Kaynig V., Longair M., Pietzsch T., Preibisch S., et al. (2012) Fiji: an open-source platform for biological-image analysis. *Nat. Methods*. 9(7):676–682.

Schmitz N., Laverty S., Kraus V. B., Aigner T. (2010) Basic methods in histopathology of joint tissues. *Osteoarthr. Cartil.* 18(SUPPL. 3):S113–S116.

Schofferman J., Bogduk N., Slosar P. (2007) Chronic whiplash and whiplash-associated disorders: an evidence-based approach. *J. Am. Acad. Orthop. Surg.* 15(10):596–606.

Schonbeck U., Mach F., Libby P. (1998) Generation of biologically active IL-1 beta by matrix metalloproteinases: a novel caspase-1-independent pathway of IL-1 beta processing. *J. Immunol.* 161(7):3340–3346.

Schultz S. R., Kitamura K., Post-Uiterweer A., Krupic J., Häusser M. (2009) Spatial Pattern Coding of Sensory Information by Climbing Fiber-Evoked Calcium Signals in Networks of Neighboring Cerebellar Purkinje Cells. *J. Neurosci.* 29(25):8005–8015.

Schurigt U., Pfirschke C., Irmler I. M., Hückel M., Gajda M., Janik T., Baumgrass R., Bernhagen J., Bräuer R. (2008) Interactions of T helper cells with fibroblast-like synoviocytes: Up-regulation of matrix metalloproteinases by macrophage migration inhibitory factor from both Th1 and Th2 cells. *Arthritis Rheum.* 58(10):3030–3040.

Scrivani S. J., Keith D. A., Kaban L. B. (2008) Temporomandibular disorders. *N. Engl. J. Med.* 359(25):2693–2705.

Sellers A., Cartwright E., Murphy G., Reynolds J. J. (1977) Evidence that latent collagenases are enzyme inhibitor complexes. *Biochem. J.* 163(2):303–307.

Sessle B. J. (2011) Peripheral and central mechanisms of orofacial inflammatory pain, in *Int. Rev. Neurobiol.*, Vol. 97, pp. 179–206. Academic Press Inc.

Sharma L. (2016) Osteoarthritis year in review 2015: clinical. *Osteoarthr. Cartil.* 24(1):36–48.

Shuang F., Zhu J., Song K., Hou S., Liu Y., Zhang C., Tang J. (2014) Establishment of a Rat Model of Adjuvant-Induced Osteoarthritis of the Lumbar Facet Joint. *Cell Biochem Biophys*. 70:1545–51.

Siebert H.-C., Burg-Roderfeld M., Eckert T., Stötzel S., Kirch U., Diercks T., Humphries M. J., et al. (2010) Interaction of the α2A domain of integrin with small collagen fragments. *Protein Cell*. 1(4):393–405.

Siebuhr A. S., Petersen K. K., Arendt-Nielsen L., Egsgaard L. L., Eskehave T., Christiansen C., Simonsen O., et al. (2014) Identification and characterisation of osteoarthritis patients with inflammation derived tissue turnover. *Osteoarthr. Cartil.* 22(1):44–50.

Simon D. D., Horgan C. O., Humphrey J. D. (2012) Mechanical restrictions on biological responses by adherent cells within collagen gels. *J. Mech. Behav. Biomed. Mater.*

14:216–26.

Singh S., Kartha S., Bulka B., Stiansen N., Winkelstein B. A. (2019) Physiologic facet capsule stretch can induce pain & upregulate matrix metalloproteinase-3 in the dorsal root ganglia when preceded by a physiological mechanical or nonpainful chemical exposure. *Clin. Biomech.* 64:122–130.

Singh S., Winkelstein B. A. (2020) Bacterial Collagenase Exposure Decreases Macromechanical Properties & Local Fiber Realignment in the C6/C7 Rat Facet Joint Capsule Under Tensile Load, in *Summer Biomech. Bioeng. Biotransport Conf.*, p. #352. remote.

Skaper S. D. (2012) Neurotrophic Factors. *Neurotrophic Factors Methods Protoc. Methods Mol. Biol.* 846:1–12.

Slade G. D., Ohrbach R., Greenspan J. D., Fillingim R. B., Bair E., Sanders A. E., Dubner R., et al. (2016) Clinical Review Painful Temporomandibular Disorder: Decade of Discovery from OPPERA Studies. *J. Dent. Res.* 95(10):1084–1092.

Sluzalska K. D., Liebisch G., Lochnit G., Ishaque B., Hackstein H., Schmitz G., Rickert M., Steinmeyer J. (2017) Interleukin-1β affects the phospholipid biosynthesis of fibroblast-like synoviocytes from human osteoarthritic knee joints. *Osteoarthr. Cartil.* 25:1890–9.

Smith J. R., Galie P. A., Slochower D. R., Weisshaar C. L., Janmey P. A., Winkelstein B. A. (2016) Salmon-derived thrombin inhibits development of chronic pain through an

endothelial barrier protective mechanism dependent on APC. *Biomaterials*. 80:96–105.

Smith J. R., Winkelstein B. A. (2017) The role of spinal thrombin through protease-activated receptor 1 in hyperalgesia after neural injury. *J Neurosurg Spine*. 26(4):532–541.

Smith L. J., Byers S., Costi J. J., Fazzalari N. L. (2008) Elastic fibers enhance the mechanical integrity of the human lumbar anulus fibrosus in the radial direction. *Ann. Biomed. Eng.* 36(2):214–223.

Song R. H., Tortorella M. D., Malfait A. M., Alston J. T., Yang Z., Arner E. C., Griggs D. W. (2007) Aggrecan degradation in human articular cartilage explants is mediated by both ADAMTS-4 and ADAMTS-5. *Arthritis Rheum.* 56(2):575–585.

Sorsa T., Konttinen Y. T., Lindy O., Ritchlin C., Saari H., Suomalainen K., Eklund K. K., Santavirta S. (1992) Collagenase in synovitis of rheumatoid arthritis. *Semin. Arthritis Rheum.* 22(1):44–53.

Sperry M. M., Granquist E. J., Winkelstein B. A. (2021) Early changes in brain network topology and activation of affective pathways predict persistent pain in the rat. *Pain*. 162(1):45–55.

Sperry M. M., Ita M. E., Kartha S., Zhang S., Yu Y. H., Winkelstein B. (2017) The Interface of Mechanics and Nociception in Joint Pathophysiology: Insights from the Facet and Temporomandibular Joints. *J. Biomech. Eng.* 139(2):021003-1-021003–

13.

Sperry M. M., Kartha S., Winkelstein B. A., Granquist E. J. (2019) Experimental Methods to Inform Diagnostic Approaches for Painful TMJ Osteoarthritis. *J. Dent. Res.* 98(4):388–397.

Sperry M. M., Yu Y.-H., Kartha S., Ghimire P., Welch R. L., Winkelstein B. A., Granquist E. J. (2020) Intra-articular etanercept attenuates pain and hypoxia from TMJ loading in the rat. *J. Orthop. Res.* 38(6):1316–1326.

Sperry M. M., Yu Y. H., Welch R. L., Granquist E. J., Winkelstein B. A. (2018) Grading facial expression is a sensitive means to detect grimace differences in orofacial pain in a rat model. *Sci. Rep.* 8(1):13894.

Srinivas R., Sorsa T., Tjäderhane L., Niemi E., Raustia A., Pernu H., Teronen O., Salo T. (2001) Matrix metalloproteinases in mild and severe temporomandibular joint internal derangement synovial fluid. *Oral Surgery, Oral Med. Oral Pathol. Oral Radiol. Endodontology*. 91(5):517–525.

Sterling M. (2010) Differential development of sensory hypersensitivity and a measure of spinal cord hyperexcitability following whiplash injury. *Pain.* 150(3):501–6.

Sterling M., Hodkinson E., Pettiford C., Souvlis T., Curatolo M. (2008) Psychologic factors are related to some sensory pain thresholds but not nociceptive flexion reflex threshold in chronic whiplash. *Clin. J. Pain.* 24(2):124–30.

Sterling M., Jull G., Vicenzino B., Kenardy J. (2003) Sensory hypersensitivity occurs

soon after whiplash injury and is associated with poor recovery. *Pain*. 104(3):509–517.

Suri P., Hunter D. J., Rainville J., Guermazi A., Katz J. N. (2013) Presence and extent of severe facet joint osteoarthritis are associated with back pain in older adults. *Osteoarthr. Cartil.* 21(9):1199–1206.

Syx D., Miller R. E., Obeidat A. M., Tran P. B., Vroman R., Malfait Z., Miller R. J., Malfait F., Malfait A. M. (2020) Pain-related behaviors and abnormal cutaneous innervation in a murine model of classical Ehlers-Danlos syndrome. *Pain*. 161(10):2274–2283.

Syx D., Tran P. B., Miller R. E., Malfait A.-M. (2018) Peripheral Mechanisms Contributing to Osteoarthritis Pain. *Curr. Rheumatol. Rep.* 20(9):1–11.

Takahashi Y., Nakajima Y. (1996) Dermatomes in the rat limbs as determined by antidromic stimulation of sensory C-fibers in spinal nerves. *Pain*. 67(1):197–202.

Tan H. K., Heywood D., Ralph G. S., Bienemann A., Baker A. H., Uney J. B. (2003) Tissue inhibitor of metalloproteinase 1 inhibits excitotoxic cell death in neurons. *Mol. Cell. Neurosci.* 22(1):98–106.

Tanaka A., Kumagai S., Kawashiri S., Takatsuka S., Nakagawa K., Yamamoto E., Matsumoto N. (2001) Expression of matrix metalloproteinase-2 and -9 in synovial fluid of the temporomandibular joint accompanied by anterior disc displacement. *J. Oral Pathol. Med.* 30(1):59–64.

Tanaka E., Detamore M. S., Mercuri L. G. (2008) Degenerative disorders of the temporomandibular joint: etiology, diagnosis, and treatment. *J. Dent. Res.* 87(4):296–307.

Tanner M. R., Hu X., Huq R., Tajhya R. B., Sun L., Khan F. S., Laragione T., Horrigan F. T., Gulko P. S., Beeton C. (2015) KCa1.1 Inhibition Attenuates Fibroblast-like Synoviocyte Invasiveness and Ameliorates Disease in Rat Models of Rheumatoid Arthritis. *Arthritis Rheumatol.* 67(1):96–106.

Tchetverikov I., Lohmander L. S., Verzijl N., Huizinga T. W. J., TeKoppele J. M., Hanemaaijer R., DeGroot J. (2005) MMP protein and activity levels in synovial fluid from patients with joint injury, inflammatory arthritis, and osteoarthritis. *Ann. Rheum. Dis.* 64(5):694–698.

Thomopoulos S., Fomovsky G. M., Chandran P. L., Holmes J. W. (2007) Collagen fiber alignment does not explain mechanical anisotropy in fibroblast populated collagen gels. *J. Biomech. Eng.* 129(October 2007):642–650.

Tomar R. (2019) Review: Methods of firing rate estimation. *BioSystems*. 183:103980.

Torres L., Dunlop D. D., Peterfy C., Guermazi A., Prasad P., Hayes K. W., Song J., et al. (2006) The relationship between specific tissue lesions and pain severity in persons with knee osteoarthritis. *Osteoarthr. Cartil.* 14(10):1033–1040.

Torrie A., Adams M. A. (2012) Basic science of spinal degeneration. *Surg. (United Kingdom)*. 33(6):233–7.

Tower T. T., Neidert M. R., Tranquillo R. T. (2002) Fiber Alignment Imaging During Mechanical Testing of Soft Tissues. *Ann. Biomed. Eng.* 30(10):1221–1233.

Treede R. D., Rief W., Barke A., Aziz Q., Bennett M. I., Benoliel R., Cohen M., et al. (2019) Chronic pain as a symptom or a disease: The IASP Classification of Chronic Pain for the International Classification of Diseases (ICD-11). *Pain*. 160(1):19–27.

Vader D., Kabla A., Weitz D., Mahadevan L. (2009) Strain-induced alignment in collagen gels. *PLoS One*. 4(6):e5902.

Valencia X., Higgins J. M. G., Kiener H. P., Lee D. M., Podrebarac T. A., Dascher C. C., Watts G. F. M., et al. (2004) Cadherin-11 Provides Specific Cellular Adhesion between Fibroblast-like Synoviocytes. *J. Exp. Med.* 200(12):1673–1679.

Vandenabeele F., Bari C. De, Moreels M., Lambrichts I., Dell'Accio F., Lippens P. L., Luyten F. P. (2003) Morphological and immunocytochemical characterization of cultured fibroblast-like cells derived from adult human synovial membrane. *Arch. Histol. Cytol.* 66(2):145–153.

Vandenbroucke R. E., Libert C. (2014) Is there new hope for therapeutic matrix metalloproteinase inhibition? *Nat. Rev. Drug Discov.* 13(12):904–927.

Varady N. H., Grodzinsky A. J. (2016) Osteoarthritis year in review 2015: mechanics. *Osteoarthr. Cartil.* 24:27–35.

Varani K., Mattei M. De, Vincenzi F., Gessi S., Merighi S., Pellati A., Ongaro A., Caruso A., Cadossi R., Borea P. A. (2008) Characterization of adenosine receptors in bovine

chondrocytes and fibroblast-like synoviocytes exposed to low frequency low energy pulsed electromagnetic fields. *Osteoarthr. Cartil.* 16(3):292–304.

Vellani V., Kinsey A. M., Prandini M., Hechtfischer S. C., Reeh P., Magherini P. C., Giacomoni C., McNaughton P. A. (2010) Protease activated receptors 1 and 4 sensitize TRPV1 in nociceptive neurones. *Mol. Pain*. 6(61).

Villasmil A. J., Ita M. E., Singh S., Winkelstein B. A. (2017) Tension simulating ligament loading induces changes in neuronal morphology even at strains below those sustrained in painful injury, in *Biomed. Eng. Soc. Annu. Meet.*, p. #3084. Phoenix, AZ.

Visse R., Nagase H. (2003) Matrix metalloproteinases and tissue inhibitors of metalloproteinases: Structure, function, and biochemistry. *Circ. Res.* 92(8):827–839.

Vos C. M. P., Sjulson L., Nath A., McArthur J. C., Pardo C. A., Rothstein J., Conant K. (2000) Cytotoxicity by Matrix Metalloprotease-1 in Organotypic Spinal Cord and Dissociated Neuronal Cultures. *Exp. Neurol.* 163(2):324–330.

Wadhwa S., Kapila S. (2008) TMJ Disorders: Future Innovations in Diagnostics and Therapeutics. *J. Dent. Educ.* 72(8):930–947.

Wang J. H. C., Thampatty B. P., Lin J. S., Im H. J. (2007) Mechanoregulation of gene expression in fibroblasts. *Gene*. 391(1–2):1–15.

Wang X., Hunter D. J., Jin X., Ding C. (2018) The importance of synovial inflammation in osteoarthritis: Current evidence from imaging assessments and clinical trials.

Osteoarthr. Cartil. 26(2):165–174.

Wang X. Y., Chen Y., Tang X. J., Jiang L. H., Ji P. (2016) AMD3100 Attenuates Matrix Metalloprotease-3 and -9 Expressions and Prevents Cartilage Degradation in a Monosodium Iodo-Acetate-Induced Rat Model of Temporomandibular Osteoarthritis. *J. Oral Maxillofac. Surg.* 74(5):927.e1-927.e13.

Weisshaar C. L., Dong L., Bowman A. S., Perez F. M., Guarino B. B., Sweitzer S. M., Winkelstein B. A. (2010) Metabotropic glutamate receptor-5 and protein kinase C-epsilon increase in dorsal root ganglion neurons and spinal glial activation in an adolescent rat model of painful neck injury. *J. Neurotrauma*. 27(12):2261–71.

Wilkes C. H. (1989) Internal Derangements of the Temporomandibular Joint. *Arch Otolaryngol Head Neck Surg*. 115(2):469–477.

Williamson A., Hoggart B. (2005) Pain: A review of three commonly used pain rating scales. *J. Clin. Nurs.* 14(7):798–804.

Winkelstein B. A. (2011) How Can Animal Models Inform on the Transition to Chronic Symptoms in Whiplash? *Spine (Phila. Pa. 1976).* 36(25S):218–225.

Winkelstein B. A., Nightingale R. W., Richardson W. J., Myers B. S. (2000) The Cervical Facet Capsule and Its Role in Whiplash Injury: A Biomechanical Investigation. *Spine (Phila. Pa. 1976).* 25(10):1238–1246.

Winkelstein B. A., Santos D. G. (2008) An intact facet capsular ligament modulates behavioral sensitivity and spinal glial activation produced by cervical facet joint

tension. *Spine (Phila. Pa. 1976).* 33(8):856–62.

Wolford L. M., Mercuri L. G., Schneiderman E. D., Movahed R., Allen W. (2015) Twenty-Year Follow-up Study on a Patient-Fitted Temporomandibular Joint Prosthesis: The Techmedica/TMJ Concepts Device. *J. Oral Maxillofac. Surg.* 73(5):952–960.

Woolf C. J., Shortland P., Coggeshall R. E. (1992) Peripheral nerve injury triggers central sprouting of myelinated afferents. *Nature*. 355(6355):75–78.

Wyatt K. E.-K., Bourne J. W., Torzilli P. A. (2009) Deformation-dependent enzyme mechanokinetic cleavage of type I collagen. *J. Biomech. Eng.* 131(5):051004.

Xu L., Polur I., Lim C., Servais J. M., Dobeck J., Li Y., Olsen B. R. (2009) Early-onset osteoarthritis of mouse temporomandibular joint induced by partial discectomy. *Osteoarthr. Cartil.* 17(7):903–908.

Yahia L., Garzon S. (1993) Structure on the capsular ligaments of the facet joints. *Ann Anat*. 175(2):185–188.

Yamashita T., Minaki Y., Ozaktay A. C., Cavanaugh J. M., King A. I. (1996) A morphological study of the fibrous capsule of the human lumbar facet joint. *Spine (Phila. Pa. 1976).* 21(5):538–543.

Yang G., Im H.-J., Wang J. H.-C. (2005) Repetitive mechanical stretching modulates IL-1β induced COX-2, MMP-1 expression, and PGE2 production in human patellar tendon fibroblasts. *Gene*. 363:166–172.

Yang Y., Kaufman L. J. (2009) Rheology and confocal reflectance microscopy as probes of mechanical properties and structure during collagen and collagen/hyaluronan self-assembly. *Biophys. J.* 96(4):1566–85.

Yeh T.-T., Wen Z.-H., Lee H.-S., Lee C.-H., Yang Z., Jean Y.-H., Wu S.-S., Nimni M. E., Han B. (2008) Intra-articular injection of collagenase induced experimental osteoarthritis of the lumbar facet joint in rats. *Eur. Spine J.* 17(5):734–742.

Yeh T.-T., Wu S.-S., Lee C.-H., Wen Z.-H., Lee H.-S., Yang Z., Nimni M. E., Han B. (2007) The short-term therapeutic effect of recombinant human bone morphogenetic protein-2 on collagenase-induced lumbar facet joint osteoarthritis in rats. *Osteoarthritis Cartilage*. 15(12):1357–66.

Yong V. W., Power C., Forsyth P., Edwards D. R. (2001) Metalloproteinases in biology and pathology of the nervous system. *Nat. Rev. Neurosci.* 2(7):502–511.

Zarei V., Zhang S., Winkelstein B. A., Barocas V. H. (2017) Tissue loading and microstructure regulate the deformation of embedded nerve fibers: predictions from single-scale and multiscale simulations. *J. R. Soc. Interface*. 14(135):20170326.

Zareian R., Church K. P., Saeidi N., Flynn B. P., Beale J. W., Ruberti J. W. (2010) Probing collagen/enzyme mechanochemistry in native tissue with dynamic, enzyme-induced creep. *Langmuir*. 26(12):9917–26.

Zhang H. H., Zhang X. Q., Wang W. Y., Xue Q. S., Lu H., Huang J. L., Gui T., Yu B. W. (2012) Increased Synaptophysin Is Involved in Inflammation-Induced Heat

Hyperalgesia Mediated by Cyclin-Dependent Kinase 5 in Rats. *PLoS One*. 7(10):e46666.

Zhang R. X., Ren K., Dubner R. (2013) Osteoarthritis pain mechanisms: Basic studies in animal models. *Osteoarthr. Cartil.* 21(9):1308–1315.

Zhang S., Cao X., Stablow A., Shenoy V., Winkelstein B. A. (2016) Tissue Strain Reorganizes Collagen with a Switch-Like Response That Regulates Neuronal ERK Phosphorylation in Vitro: Implications for Ligamentous Injury and Mechanotransduction. *J. Biomech. Eng.* 138(2):021013.

Zhang S., Singh S., Winkelstein B. A. (2018a) Collagen organization regulates stretch-initiated pain-related neuronal signals in vitro: Implications for structure-function relationships in innervated ligaments. *J. Orthop. Res.* 36(2):770–777.

Zhang S., Zarei V., Winkelstein B. A., Barocas V. H. (2018b) Multiscale mechanics of the cervical facet capsular ligament, with particular emphasis on anomalous fiber realignment prior to tissue failure. *Biomech. Model. Mechanobiol.* 17(1):133–145.

Zhang S., Zhao E., Winkelstein B. A. (2017) A Nociceptive Role for Integrin Signaling in Pain After Mechanical Injury to the Spinal Facet Capsular Ligament. *Ann. Biomed. Eng.* 45(12):2813–2825.

Zhang Y. Z., Ran L. Y., Li C. Y., Chen X. L. (2015) Diversity, structures, and collagen-degrading mechanisms of bacterial collagenolytic proteases. *Appl. Environ. Microbiol.* 81(18):6098–6107.

Zhou Y., Cui Z., Xia X., Liu C., Zhu X., Cao J., Wu Y., et al. (2014) Matrix Metalloproteinase-1 (MMP-1) Expression in Rat Spinal Cord Injury Model. *Cell. Mol. Neurobiol.* 34(8):1151–1163.

Zieglgänsberger W. (2019) Substance P and pain chronicity. *Cell Tissue Res.* 375(1):227–241.

Zimmermann M. (1983) Ethical guidelines for investigations of experimental pain in conscious animals. *Pain*. 16(2):109–110.

Zimmermann T., Kunisch E., Pfeiffer R., Hirth A., Stahl H. D., Sack U., Laube A., et al. (2001) Isolation and characterization of rheumatoid arthritis synovial fibroblasts from primary culture - primary culture cells markedly differ from fourth-passage cells. *Arthritis Res.* 3(1):72–76.